# R&T

## 2006 Research and Technology

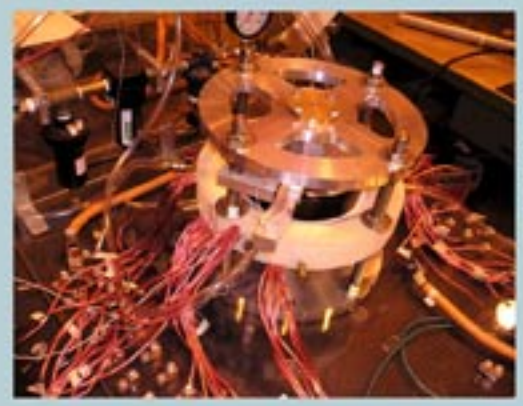

National Aeronautics and
Space Administration

Glenn Research Center at Lewis Field
Cleveland • Ohio

NASA/TM—2007-214479

# RESEARCH & TECHNOLOGY 2006

National Aeronautics and
Space Administration

**Glenn Research Center**
Cleveland, Ohio 44135–3191

NASA/TM—2007-214479

Trade names or manufacturers' names are used in this report for identification only. This usage does not constitute an official endorsement, either expressed or implied, by the National Aeronautics and Space Administration.

**Notice for Copyrighted Information**

This document contains material copyrighted by the parties submitting it to NASA—see the copyright notices on pages 93 and 202. The figures referred to may be reproduced, used to prepare derivative works, displayed, or distributed only by or on behalf of the Government and not for private purposes. All other rights are reserved under the copyright law.

Available from

NASA Center for Aerospace Information
7121 Standard Drive
Hanover, MD 21076

National Technical Information Service
5285 Port Royal Road
Springfield, VA 22100

Available electronically at http://www.grc.nasa.gov/WWW/RT/

# Introduction

At the NASA Glenn Research Center, in partnership with U.S. industry, universities, and other Government institutions, we develop critical systems technologies and capabilities that address national priorities. Our world-class research, technology, and capability development efforts are keys to advancing space exploration of our solar system and beyond while maintaining global leadership in aeronautics. Our work is focused on technological advancements in space flight systems development, aeropropulsion, space propulsion, power systems, nuclear systems, communications, and human-related systems.

Glenn's main campus, Lewis Field, is situated on 350 acres adjacent to the Cleveland Hopkins International Airport. It has more than 140 buildings that include 24 major facilities and over 500 specialized research and test facilities. In addition, Plum Brook Station, located 50 miles west of Cleveland, offers four large, world-class facilities for space technology and capability development on a 6400-acre installation. All Center capabilities are available for Government and industry programs through Interagency or Space Act Agreements.

The Glenn team consists of over 3100 civil service employees and support service contractor personnel. Scientists and engineers comprise more than half of our workforce, while technical specialists, skilled workers, and an administrative staff support them. We aggressively strive for technical excellence through continuing education, increased diversity in our workforce, and continuous improvement in our management and business practices so that we can expand the boundaries of space and aeronautics technology.

The Center's activities support all NASA missions and the major programs of our Agency. We contribute to economic growth and national security by developing technology for safe, superior, and environmentally compatible U.S. aircraft propulsion systems. Glenn leads NASA's research in the fields of fluids, combustion, and reacting flow systems, including gravity variation. Glenn also leads in the testing and evaluation of materials and structures for atmospheric and space environments by utilizing our first-rate facilities and world-class researchers. Almost every space shuttle science mission has had an experiment managed by Glenn, and we have conducted a wide array of experiments on the *International Space Station.*

Knowledge generation and management are among our most important activities. Our annual Research & Technology report helps make this knowledge available to potential users in the technical community. This report is organized such that a broad cross section of people can readily use it. Each article begins with a short introductory paragraph and continues with a summary of the progress made during the year in various scientific and technical areas.

I hope that this information is useful to you. If additional information is desired, you are encouraged to contact the researchers identified at the end of each article and to visit Glenn's Web site at http://www.nasa.gov/glenn/.

Woodrow Whitlow, Jr.

Woodrow Whitlow, Jr., Ph.D.
Director

# NASA Glenn Research Center Senior Management

CD–48534
May 30, 2007

*Acting

# NASA Glenn Research Center at Lewis Field

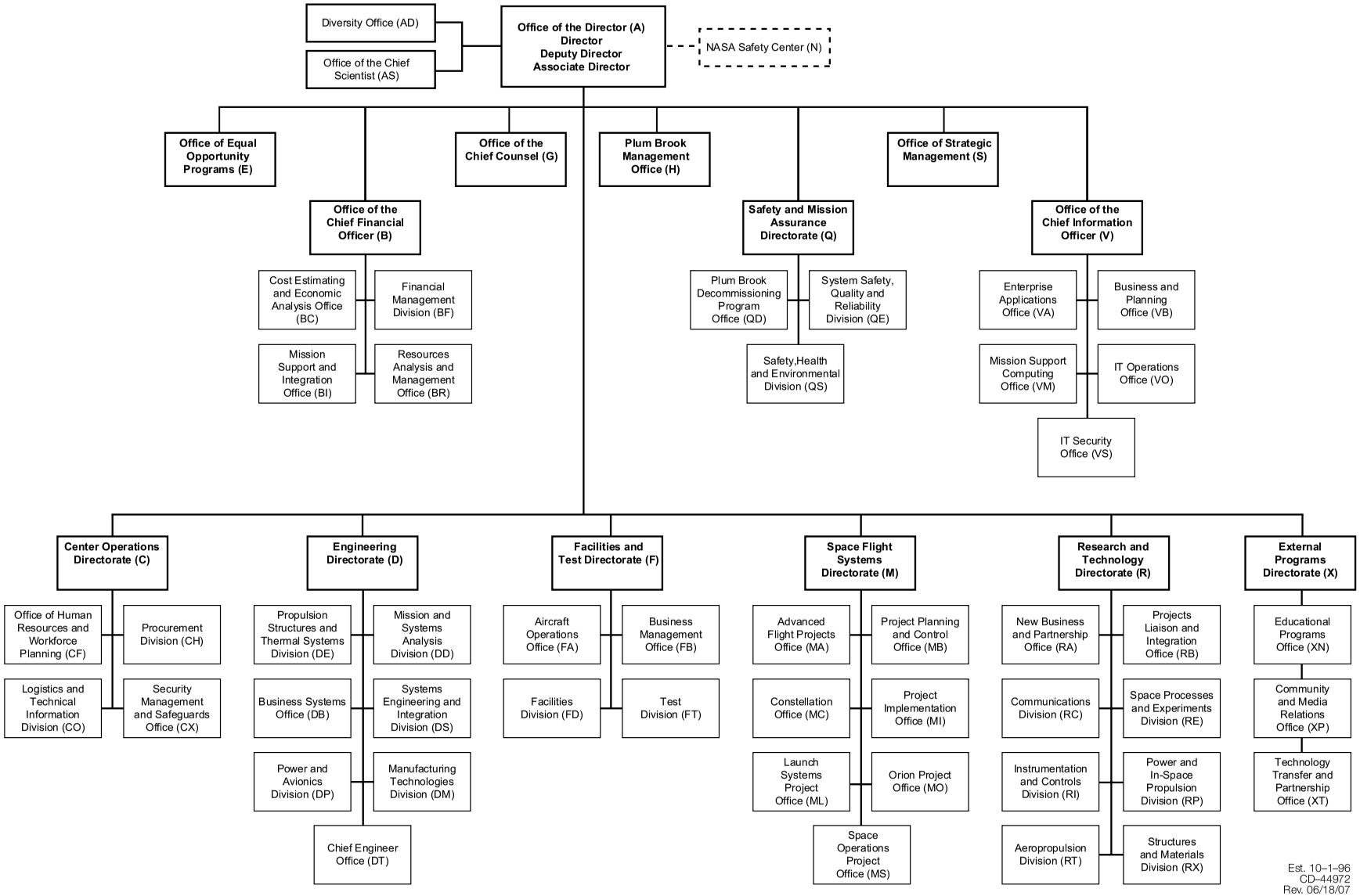

# CONTENTS

## Programs and Projects

### Systems Analysis

Logic-Evolved Decision Analysis Methodology Used To Assess Risk and Prioritize Technologies for Aviation Security . . . 2
Adaptive Engine Technologies Assessed To Reduce Aviation Carbon Dioxide Emissions . . . 3
Environmental Design Space Developed To Assess Aircraft Technology and Operational Tradeoffs . . . 5
P–BEAT: Initial Version of a Process-Based Economic Analysis Tool Released . . . 6
OTIS 4 Software Released . . . 8
A Lunar In Situ Explorer (ALISE) Conceptual Design Developed . . . 10

### Exploration Systems

First Lithium-Ion Engineering Model Battery Developed and Tested for Human Space Flight for Low Earth Orbit and Lunar Mission Applications . . . 11
New Catalytic Gas Generator Developed and Tested With a Turbine Power Unit . . . 12
Crew Launch Vehicle Upper-Stage Thrust-Vector-Control Architecture Selected . . . 13
Intravenous Fluid Mixing Times Quantified by Planar Laser-Induced Fluorescence . . . 15
Model To Predict Risk of Bone Fracture During Space Missions Developed . . . 17

## Research and Technology

Microenergy Rates Used To Determine Damage Tolerance and Durability of Composite Structures . . . 20
Corrosion of Composites Modeled by Computational Simulation . . . 22
Composite Mechanics Used To Evaluate Composite-Enhanced Concrete Structures . . . 24

### Communications

Steerable Space-Fed Lens Array Developed for Low-Cost Adaptive Ground Station Applications . . . 26
Small-Size Active Antenna Developed That Integrates the Oscillator and the Radiating Element . . . 28
Parabolic Equation Extended to the Analysis of Wide-Angle Scattering in Random Propagation Media . . . 29
Interspacecraft Communications and Ranging System Developed and Demonstrated . . . 31
Low-Power, Silicon-on-Insulator, Complementary Metal-Oxide Semiconductor Receiver Chip Developed for Planetary Robotic and Distributed Sensor Network Applications . . . 32
Space Telecommunications Radio System Software Architecture Concepts Investigated . . . 34
Space Network Router Developed . . . 36
Software-Defined Radio Architecture Framework Released for Space-Based Radios . . . 37
Applicability of the Joint Tactical Radio System Software Communications Architecture to Space-Based Radios Examined . . . 39
High-Speed Network Interface Controller Based on SpaceWire Designed and Characterized . . . 40
Space Audio Development and Evaluation Laboratory Created To Improve Audio Transmission to and From Space Suits . . . 42
Bench-Top Antigen-Detection Technique Developed That Utilizes Nanofiltration and Fluorescent Dyes Which Emit and Absorb Light in the Near Infrared . . . 43
Radiofrequency Mass Gauging of Propellants Simulated by Modern Computational Tools . . . 44
Lunar-Based Lunar Surface Navigation Analyzed . . . 46
Earth-Based Lunar Surface Navigation Analyzed . . . 48
Lunar Surface Mobility Autonomous Navigation Assessed . . . 51
Satellite Laser-Ranging Benefits Assessed for Orbit Determination at Global Positioning System Orbit . . . 53
Reflector Antenna Surface Photogrammetry Studied . . . 54

Extravehicular Activity Subsystems Being Developed: Communications Equipment and Crew Displays Demonstrated and Field Tested . . . 56
Dynamic Channel Emulator That Models Space Data Links Developed . . . 58
Communication, Navigation, and Surveillance Models Integrated Into National Airspace System Simulation . . . 59

## Instrumentation and Controls

Variable-Frequency Fluidic Actuator Developed, Fabricated, and Tested for Flow-Control Applications . . . 62
Novel Predictive Control Concept Developed for Improved Turbine Tip-Clearance Performance . . . 63
Hybrid Kalman Filter Developed for In-Flight Detection of Aircraft Engine Faults . . . 65
Efficient Algorithm Developed To Enable Real-Time Implementation of Model Predictive Control for a Turbofan Engine Application . . . 66
Sensor Data Qualification System Developed and Evaluated for Assessing the Health of Ares I Upper-Stage Sensors . . . 68
Large-Scale Pulsejet-Driven Ejector System Investigated . . . 70
Cruciform Specimen Used To Assess Long-Term Creep for Characterizing Advanced Aerospace Materials Under In-Plane Biaxial Loading . . . 72
Linux-Based Image-Acquisition System Tested for Use With a Hyperspectral Imager . . . 74
Cratos—Tracked Test Rover Designed and Built at NASA Glenn . . . 75
Model Developed To Assess a Vibration-Based Crack-Detection Approach for the In Situ Health Monitoring of Rotors . . . 77
Great Lakes Hyperspectral Water Quality Instrument Suite Designed, Developed, Integrated, and Flight Tested for the Airborne Monitoring of Algal Blooms . . . 78
Candidate Thermal Protection System Materials Evaluated Following Simulated Space Environment and Reentry Conditions . . . 80
Molecular Rayleigh Scattering Technique Developed To Measure Temperature, Velocity, and Density Fluctuations in Gas Flows . . . 81
Communication Over Direct-Current Power Line Demonstrated for Distributed Engine Control Using High-Temperature Electronics . . . 83
Flaw Resolution Improved by New Signal-Processing Approaches for Terahertz Data Obtained From Inspection of Space Shuttle External Tank Thermal Protection System Foam . . . 85
Phase-Only Filtering Developed for Improved Particle Image Velocimetry Data Reduction . . . 87
Improved Modeling of Forward-Scattered Light From an Optically Trapped Particle Demonstrated . . . 89
Deep Reactive Ion Etching Process Optimized for Silicon Carbide Micromachining . . . 90
Small-Area, Fast-Response Heat Flux Sensor With Large Output Signal Developed . . . 92
Smart Leak-Detection Systems Being Matured for Crew Launch Vehicle . . . 93
Nanosensor Technology Tools Being Explored—Tools Advanced To Overcome Three Technical Barriers . . . 95
High-Temperature Amplifier Based on a Silicon Carbide Metal-Semiconductor Field Effect Transistor and Ceramic Packaging Designed, Fabricated, and Electrically Operated at 500 °C . . . 97

## Power and Electric Propulsion

Closed-Cycle Hydrogen-Oxygen Proton-Exchange-Membrane Regenerative Fuel Cell Demonstrated at the NASA Glenn Research Center . . . 99
Thermal Stability of Lithium Ion Cells Studied . . . 101
High-Altitude Long-Endurance Unmanned Air Vehicle Configurations Assessed . . . 103
NASA's Proton Exchange Membrane Fuel Cell Engineering Model Powerplant Evaluated . . . 104
Lithium-Ion Cells From Multiple Vendors Demonstrated 10,000 Low-Earth-Orbit Cycles at Various Conditions . . . 106
Hall Thruster Developed for Increased Mission Life . . . 108
Next-Generation Ion Propulsion System Development Program Achieved Major Goals: Prototype and Engineering Model Thruster Tested . . . 109
High-Temperature Titanium-Water Heat Pipes Built and Tested . . . 111
High-Power Alternator Testbed Results Reported . . . 112
Closed Brayton Power System Prototype Developed for Future Space Nuclear Power Applications . . . 113

Stirling Power Convertors Continued Extended Operation . . . . . 115
Control Architecture Developed for Dual-Opposed Stirling Convertors With Active Power Factor Correction Controllers . . . . . 116
Active Power Factor Correction Controller Achieved High-Power Operation of Dual Stirling Convertors . . . . . 117
Change in Solar Array Orientation Successfully Reduced *International Space Station* Propellant Usage . . . . . 118
Dust on Mars Solar Arrays Examined With Microscopic Imager . . . . . 120
Galium Arsenide on Silicon Advanced Photovoltaic Devices Flight Tested on the Exterior of the *International Space Station* as Part of the Materials International Space Station Experiment 5 (MISSE5) . . . . . 122
Results From Scattered Atomic Oxygen Characterization Experiment Evaluated . . . . . 123
Solar Effects on Tensile and Optical Properties of Hubble Space Telescope Silver-Teflon Insulation Investigated . . . . . 124
Optical and Mechanical Properties Determined of Polymer Film Samples Exposed on the Materials International Space Station Experiment (MISSE) 1 and 2 . . . . . 127
Lunar Simulation Chamber Completed . . . . . 130
*International Space Station* Experiment Used To Correlate Erosion Observed on Orbit for Coated Polymers to That Measured in Ground-Based Atomic Oxygen Facilities . . . . . 131
L-Band Global Positioning System Preamplifiers Space-Qualified for Low-Temperature Use Onboard the Space Shuttle . . . . . 132

## Propulsion Systems

Trailing Edge Blowing Tested for Fan Blade Wake Management . . . . . 134
New Procedure Created for Studying Core Noise . . . . . 136
Technique Improved for Measuring Noise Sources in a Supersonic Jet Via Two-Point Space-Time Correlations . . . . . 138
Planar Laser-Induced Fluorescence and Particle Imaging Velocimetry Used To Characterize a Baseline Nine-Point Lean Direct Injector for Comparison With National Combustor Code Results . . . . . 140
Fuel Injector-Mixer Concepts Examined for Kerosene and Diesel Fuel Reformer Applications Using Laser-Based Techniques . . . . . 143
Alternative Fuels Research Laboratory Being Designed and Constructed . . . . . 146
End-to-End System Analysis Tool Developed for Studying Lunar In Situ Resource Utilization . . . . . 148
Alternative Rotational Raman Thermometry Developed for Turbulent Combustion . . . . . 149
Quantitative, Single-Shot, Multiscalar Measurements Demonstrated in a High-Pressure, Swirl-Stabilized Turbulent Flame . . . . . 152
High-Throughput Triple-Grating Spectrograph Developed for Nonintrusive Measurements of Combustion-Generated Plasmas . . . . . 154
Outer Planet Mining Vehicle Design Issues Identified and Analyzed . . . . . 156
Aerospace Fuels Assessed for Future Aerospace Vehicles . . . . . 157
Fuel-Injector Concepts Investigated in the Fuel-Reforming Injector Test Facility . . . . . 159
Aerosol Microphysics in a Pressure-Reduction Chamber Predicted by Numerical Simulations . . . . . 160
Compressor Stability Model Developed . . . . . 163
Baseline Inlet Tests Conducted for Supersonic Inlet Flow Control in a Partial Isentropic External Compression Inlet . . . . . 164
Wind-US Code Updated . . . . . 165
Effect of Wedge-Shaped Deflectors on the Flow Field of a High-Bypass-Ratio Nozzle Studied . . . . . 166
SmaggIce 2D Version 2.0: Capabilities Added for the Interactive Grid Generation of Iced Airfoils . . . . . 168
Liquid Acquisition Devices Evaluated . . . . . 169
Catalytic Reforming Technologies Investigated for Hydrogen Production and Onboard Aerospace Power Generation . . . . . 171
Low-Gravity Gauging Concept Extended to Cryogenic Propellants . . . . . 173
Liquid Oxygen-Liquid Methane Ignition Demonstrated for Application to Reaction Control Engines . . . . . 174

## Microgravity

Noninvasive Laser Doppler Flowmetry Used To Measure In Vivo Blood Flow in Distal Fingertips . . . . . .176
Enzyme-Linked Immunosorbent-Assay-Based Optical Biosensors Investigated for Exploration Applications . . . 177
Microvascular Remodeling Analysis Developed for Advances in Human Health . . . . . .179
Smoke-Detection Model Developed for the Destiny Laboratory on the *International Space Station* . . . . . 182
Portable Unit for Metabolic Analysis Benchmarked for Measuring Human Metabolic Activity . . . . . 183
Distribution of Micrometer and Submicrometer Content of the Lunar Regolith Measured . . . . . 185
Experimental Rig Built and Used To Investigate Supercritical Water Oxidation for Solid Waste Management and Water Reclamation Systems . . . . . 187
Narrow Channel Apparatus Used To Simulate Low-Gravity Flames on Earth . . . . . .189
Equivalent Low Stretch Apparatus Developed for Testing Flammability. . . . . 190
Gravitational Effects Evaluated in Swirl-Stabilized Fluidized Bed . . . . . .191
Durable Coating Technology Tested for Lunar Dust Protection and Mitigation . . . . . .193
Porous-Media-Based Condensing Heat Exchanger Investigated for Space Systems . . . . . 195

## Materials and Structures

Long-Term Creep Resistance of a Cast Superalloy Investigated . . . . . 197
Low-Density, Creep-Resistant Superalloys Developed for Turbine Blades . . . . . 199
Compatibility of Titanium With Liquid-Metal NaK (78 wt% Potassium/22 wt% Sodium) Evaluated . . . . . 200
GRCop-84 Tubing Produced Using Optimized Production Methods . . . . . 202
Nickel Chromium Aluminum Yttrium (NiCrAlY) Overlay Coatings Successfully Deposited on GRCop-84 Subscale Combustion Chamber Liners . . . . . 204
Fiber Architecture Used To Increase the Matrix Cracking Stress of Silicon Carbide (SiC)/SiC Ceramic Composites for Propulsion and Power Applications . . . . . 206
Physics-Based Models Developed for Predicting Creep Effects in Silicon Carbide (SiC)/SiC Composite Components . . . . . 207
Thermal- and Environmental-Barrier-Coated Silicon Nitride Vanes Tested in NASA Glenn's High Pressure Burner Rig . . . . . .208
Current Limits for High-Temperature Nickel-Titanium-Based Shape-Memory Alloys Defined . . . . . 211
Electrical and Piezoelectric Properties of Piezoelectric Ceramics Measured at High Temperatures . . . . . .212
Multifunctional, Foam Core, Ceramic Matrix Composite Integrated Structures Developed . . . . . 214
Moisture-Induced Hydrogen Embrittlement of the Alumina-Metal Interface Demonstrated . . . . . 216
New Burner-Rig-Based Erosion Test With High-Temperature (>2200 °F) Capability Developed. . . . . 218
Photocured Polyimides Developed. . . . . .219
High Glass Transition Temperature, Low-Melt Viscosity Polyimides Developed for Resin Transfer Molding. . . . . 220
Reaction Zones Associated With Joining Nickel-Based Superalloys to Titanium Investigated . . . . . 222
Diffusion Bonding of Silicon Carbide to Silicon Carbide Developed for a Lean Direct Injector Application . . . . . 224
Adhesive Joining of Titanium to Carbon-Carbon Composite and Foam Structures Demonstrated . . . . . 225
Effect of Processing Conditions on Chemical Makeup of Di-Isocyanate Crosslinked Silica Aerogels Studied . . . 226
X-Aerogel Processing Time Reduced by One-Pot Synthesis. . . . . 229
Computer Simulation Developed for Modeling the Thermal Conductivity of Silica Aerogels . . . . . 231
Carbon-Nanofiber-Reinforced Polymer Crosslinked Aerogels Studied . . . . . .232
Mechanical Strength and Physical Properties of Functionalized Graphene-Epoxy Nanocomposites Studied . . . 234
Photo-Oxidation of Single-Walled Carbon Nanotubes Examined . . . . . .235
Boron Nitride Nanotubes Demonstrated as Solid-State Hydrogen Storage Media . . . . . .238
Water Electrolysis and Regenerative Tests Conducted on NASA Glenn Solid Oxide Cell Demonstrated High Efficiency. . . . . 240
Protonic-Conducting Ceramic Films Fabricated Using Pulsed Laser Deposition. . . . . 241
Novel Polymers Synthesized for High-Temperature Use in Proton Exchange Membrane Fuel Cells . . . . . 243
Novel Polymer Membranes Synthesized for Lithium Batteries Doped With Ionic Liquids . . . . . 245
High-Temperature Regenerator Developed and Demonstrated for a High-Temperature Stirling Convertor . . . . . 247
Structural Benchmark Testing Completed for 110-W Stirling Radioisotope Generator Heater Head Life Prediction. . . . . 248

Novel Cascade Technique Developed for Accelerated Testing of Advanced Stirling Convertor Heater Heads . . . .250
Organics Evaluated for Advanced Stirling Convertor . . . . . 252
Sublimation Suppression Coatings Evaluated for Advanced Thermoelectric Materials . . . . . 254
Reliable Manufacturing Process Developed for Magnetic Materials Used in Hall Thrusters . . . . . 255
Applicability of Fracture Mechanics to Foams Examined . . . . . 256
Framework Developed for Performing Multiscale Stochastic Progressive Failure Analysis of Composite Structures . . . . . 258
Level of Risk in an Optimal Design Solution Quantified by a Stochastic Calculation . . . . . 260
Multiaxial Failure Response of Nuclear Grade Graphite Predicted With Ceramics Analysis Reliability Evaluation of Structures/Life (CARES/*Life*) Software . . . . . 262
Composite Gyroscope Momentum Wheels Optimized . . . . . .264
Computationally Efficient Blade Mistuning Analysis Codes Studied for Mistuned Bladed Disk Analysis: Subset of Nominal Modes (SNM) and Fundamental Mistuning Model (FMM) . . . . . 266
Turbo-Reduce Code Used To Predict Blade Stress Levels Directly From Reduced-Order Vibration Models of Mistuned Bladed Disks . . . . . 268
Preliminary Tests Showed That Turbomachinery Blade Damping Coatings Are Effective . . . . . .270
New Turbulence and Transition Models Implemented Into Turbomachinery Aeroelastic Analysis Code . . . . . 272
Hybrid Pulse Detonation Engine Turbine Blades Analyzed . . . . . .273
Power Electronics for Switched-Reluctance Motor Improved . . . . . 274
Self-Levitated Switched-Reluctance Motor Demonstrated Successfully at Low Temperatures for Non-Combustion-Based Propulsion . . . . . 276
Electrical Model Developed To Predict Blade Tip Drive Rig Performance . . . . . 277
Room-Temperature Bearingless Electric Motor Technology Demonstrated for Future NASA and Aerospace Missions . . . . . 279
Specific Power of Cryogenic Motor Increased 50 Percent . . . . . 281
Magnesium Diboride Superconducting Coils Evaluated for Electric Aircraft Propulsion . . . . . .282
Novel Bearingless Switched-Reluctance Motor Characterized by One-Dimensional Electromagnetic Radial Force Equations . . . . . .284
Ironless High-Power-Density Permanent Magnet Electric Motor Evaluated for Non-Combustion-Based Air Vehicles . . . . . .285
Liquid-Hydrogen-Cooled Electric Motors Test Facility Completed for Aircraft Propulsion . . . . . .286
High-Temperature Active Clearance Control System Concept Performance Tests Successfully Completed at NASA Glenn . . . . . .288
Leak Rates of Candidate Docking System Seal Materials Determined After Simulated Space Exposure . . . . . .290
Preliminary Turbomachinery Seal Power Loss Data Completed for Competing Engine Seal Applications . . . . . .293
Influence of Operational Parameters on the Thermal Behavior of High-Speed Helical Gear Trains Studied . . . . . .296
Testing Began in New Wave Bearing Test Facility . . . . . .297
Face Gear Endurance Testing Conducted . . . . . .299
Foil-Bearing Research Capabilities Expanded in Support of Oil-Free Turbomachinery . . . . . .300
Integrating Sphere Used With Fourier Transform Infrared Spectroscopy To Characterize Lubricants on Ball Bearings . . . . . .301
Long-Term Compression and Recovery Tests Completed on Space Shuttle Main Landing Gear Door Seals . . . .303
Mechanical Response Experiments Designed for Full-Scale Testing of Orbiter Composite Overwrap Pressure Vessels . . . . . .305
Mechanical Characteristics of Kevlar/Epoxy Overwrap From Columbia's Composite Overwrap Pressure Vessels Investigated . . . . . .307
Raman-Based Strain Measurements Successfully Incorporated Into Composite Overwrapped Pressure Vessel Pressurization Tests . . . . . .309
Microstructure of Kevlar Fibers Used in Composite Overwrapped Pressure Vessels Characterized . . . . . .310
Digital Image Correlation Utilized To Obtain Full-Field Strains of a Full-Scale Orbiter Composite Overwrapped Pressure Vessel During Stress Rupture Life Testing . . . . . .312
Ballistic Impact Response of Kevlar and Zylon Evaluated . . . . . .314
Candidate Materials Examined for Ice Mitigation on the External Tank Liquid Oxygen Feedline Bracket . . . . . .315
Methodology Based on Vertical Scanning Interferometry Developed for Space Shuttle Window Inspection . . . . .317

Composite Crew Module Designed and Sized for Orion . . . . . .318
Polymer Matrix Composites Evaluated for Advanced Space Radiators . . . . . .321
Crew Exploration Vehicle Landing Concept Designed . . . . . 323
Lightweight Cryogenic Hydrogen Storage Tanks—Preliminary Design for Unmanned Aerial Vehicle Applications Evaluated . . . . . 324
Nanoindentation Hardness of Compacted JSC–1 Lunar Soil Simulant Determined . . . . . .326

# Engineering and Technical Services

## Engineering Development

Hybrid Power Management Program: Grid-Tie Photovoltaic Power System Designed, Developed, and Is Providing Power to NASA Glenn . . . . . 330
Large-Scale Levitated Ducted Fan Conceptual Design Developed . . . . . 331
Acoustical Testing Laboratory Developed Automated Aeroacoustic Characterization Capability for Cooling Fans . . . . . 332
Exercise Countermeasures Laboratory—New Ground-Based Analog for Space Exploration Developed . . . . . .334
Gravity-Replacement Load Device Developed and Implemented for the Cleveland Clinic . . . . . .335

## Research Testing

Particulate Aerosol Laboratory Reactivated in NASA Glenn's Engine Research Building . . . . . 337
Aero-Acoustic Propulsion Laboratory Piping Enhancements Reduced Facility Background Noise by 20 dB . . . . 338
NASA Glenn's 8- by 6-Foot Supersonic Wind Tunnel/9- by 15-Foot Low-Speed Wind Tunnel Control System Upgraded . . . . . .339

# Appendixes

Index of Authors and Contacts . . . . . 341

# Programs and Projects

## Systems Analysis
## Exploration Systems

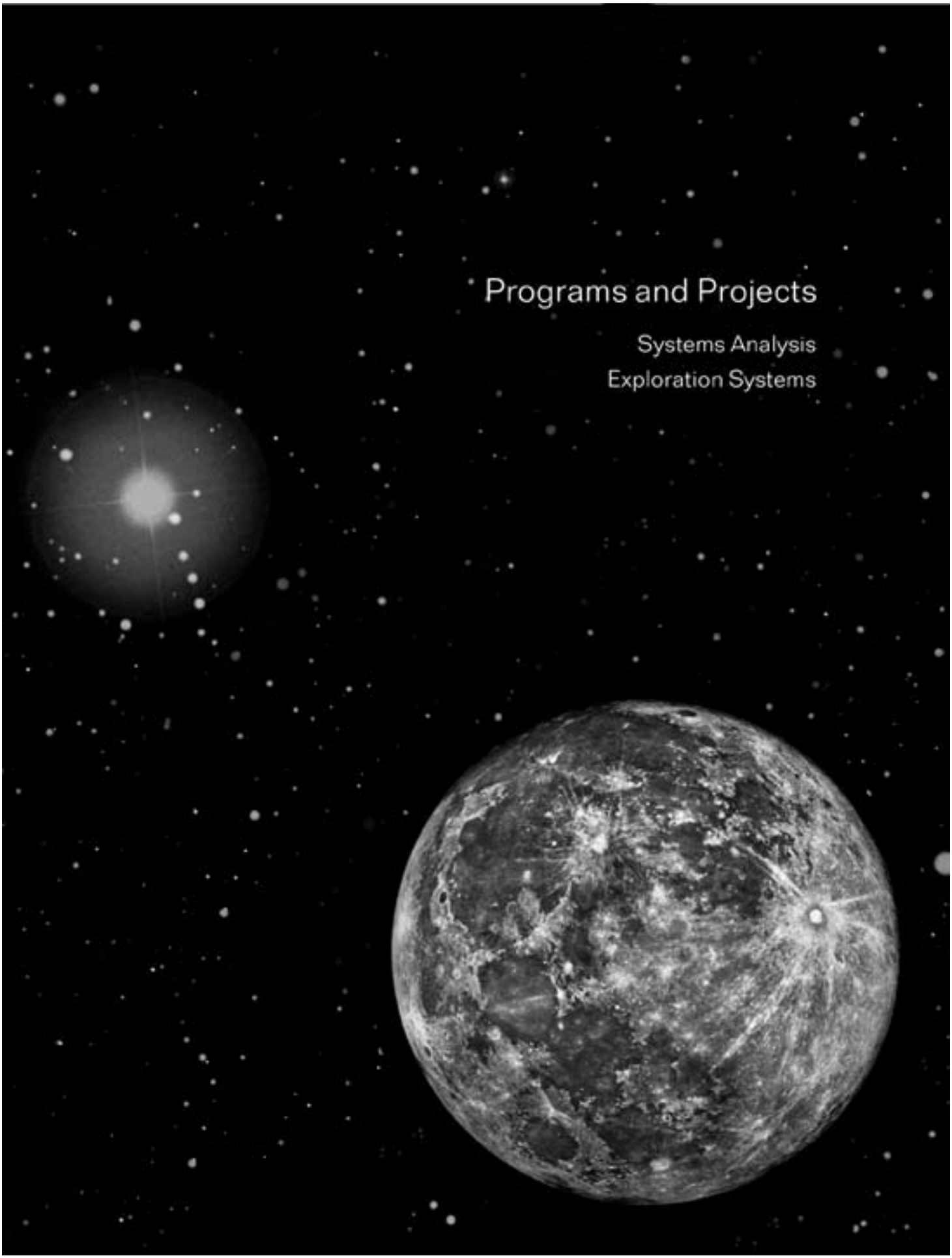

# Logic-Evolved Decision Analysis Methodology Used To Assess Risk and Prioritize Technologies for Aviation Security

**Glenn contact:**
Kenneth L. Fisher, 216–433–5655, Kenneth.L.Fisher@nasa.gov

**Author:**
Kenneth L. Fisher

**Headquarters program office:**
Aeronautics Research Mission Directorate

**Programs/projects:**
Aviation Safety Program

The events of 9/11 led the NASA Glenn Research Center to introduce a security component to its Aviation Safety Program, with a robust portfolio of advanced technologies designed to make flight more secure. The portfolio needed to be prioritized and managed to ensure that investment payoffs were maximized in the most promising technologies. In addition, an assessment was desired to identify the integration issues that the technologies could have with each other as well as within the overall National Airspace System (NAS).

To accomplish this, NASA needed a new approach. A complete vulnerability assessment of the NAS would have to be performed to formulate a baseline risk so that NASA technologies could be applied to find how much each technology reduced risk. This enormous task was performed through the use of a computational methodology called logic-evolved decision (LED) analysis, which was developed at the Los Alamos National Laboratory for modeling the behavior of complex systems with respect to decision-support applications. The LED computational algorithm uses linked, formal logic models to represent the basic functions of a decision analysis tool. LED incorporates fuzzy logic, approximate reasoning, possibility, probability, multi-attribute scoring, and graph theory to construct decision-support models. It is a flexible, self-contained, comprehensive, and traceable software tool for risk-based prioritization and portfolio management across a broad spectrum of applications.

Using the LED tool, in 2006 researchers from the NASA Glenn Research Center and the NASA Langley Research Center developed a comprehensive set of several million attack scenarios, using fault tree analysis to define terrorist threats to aircraft, airports, and the airspace. Then a much smaller, representative set of attacks were chosen to apply the technologies to determine the effective risk reduction. Technology readiness levels, technical development risks, implementation risks, cultural and certification issues, and cost-to-benefit ratios were considered. The LED methodology allowed the researchers to use approximate reasoning to construct inference models for analyzing each attack scenario. Expertise from NASA technologists, experts in all aspects of aviation operations and security, and national security analysts was input to the attack scenarios and inference models to define the threats, the security technologies, and the impact of the technologies. By applying these inference models to the attack scenarios, the researchers could determine the final risk and compare it with the baseline risks to determine the effective risk reduction. Risk-reduction technologies were analyzed both as standalone operations and coupled with one or more other technologies for increased risk reduction.

The objective of these assessments was to provide a decision-support tool for prioritizing NASA research in aviation security. This top-down analysis and modeling approach utilized LED methodologies and techniques to rank order proposed NASA security research projects according to their effectiveness in reducing risk.

# Adaptive Engine Technologies Assessed To Reduce Aviation Carbon Dioxide Emissions

Emissions reduction is a worldwide priority because of increasing concern over local air quality, climate change, and the health effects of emissions. The transportation sector accounted for about 27 percent of total U.S. greenhouse gas emissions in 2003, with aircraft contributing 9 percent of the transportation sector total, or about 2 percent of total greenhouse gas emissions. Aviation is projected to contribute an increasingly larger share of carbon dioxide ($CO_2$) emissions as air traffic continues to grow. Technology improvements have substantially reduced the amount of emissions generated from aircraft over the past 50 years, and advancements must continue in order to mitigate the effect of a projected doubling of aircraft operations over the next 20 to 25 years (see the graph).

At the NASA Glenn Research Center, numerous technologies are under development to adaptively modify aircraft turbine engine performance. These adaptive technologies could lead to improved engine component efficiency and/or reduced weight, reducing overall fuel burn and $CO_2$ emissions. The primary classes of these adaptive technologies are flow control (see the table and see the figure on the next page), structural control, combustion control, and the enabling technologies that are applicable to each. Some specific technology examples include inlet, fan, and compressor flow control; compressor stall control; blade clearance control; combustion control; active bearings; and enabling technologies, such as active materials and wireless sensors.

Over the past several years, system analyses have been performed to quantify the emissions-reduction potential of a number of adaptive engine technologies. These assessments, concluded in 2006, show that adaptive technologies have the potential to significantly reduce aircraft $CO_2$ emissions. Possible emissions-reduction values range from a fraction of one percent for enabling technologies to as much as 13 percent for flow control in S-shaped inlets on a blended-wing-body transport aircraft. As a group, flow-control technologies show potential for the largest $CO_2$ reduction. From the structural-control technologies, a significant benefit is possible through the development of a shape-memory-alloy-actuated, variable-area fan nozzle when coupled with a low-fan-pressure-ratio/high-bypass-ratio engine. These assessment results can guide the development of a robust adaptive engine technology portfolio.

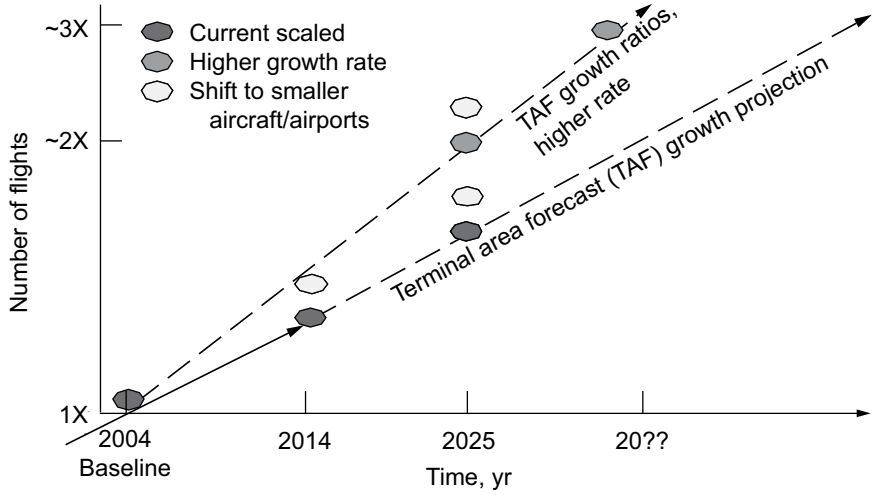


*Some aviation growth scenarios predict a doubling of flights as early as 2025.*

| Engine component | Focus of technology |
|---|---|
| Inlets | Maintain performance, engine stability, and durability with shorter inlets (lower weight)<br>Reduce bleed drag and bleed systems weight |
| Fan | Improve operability with shorter inlets |
| Compressors and turbines | Improve flow quality and operability to improve loading conditions, enabling reduced weight |

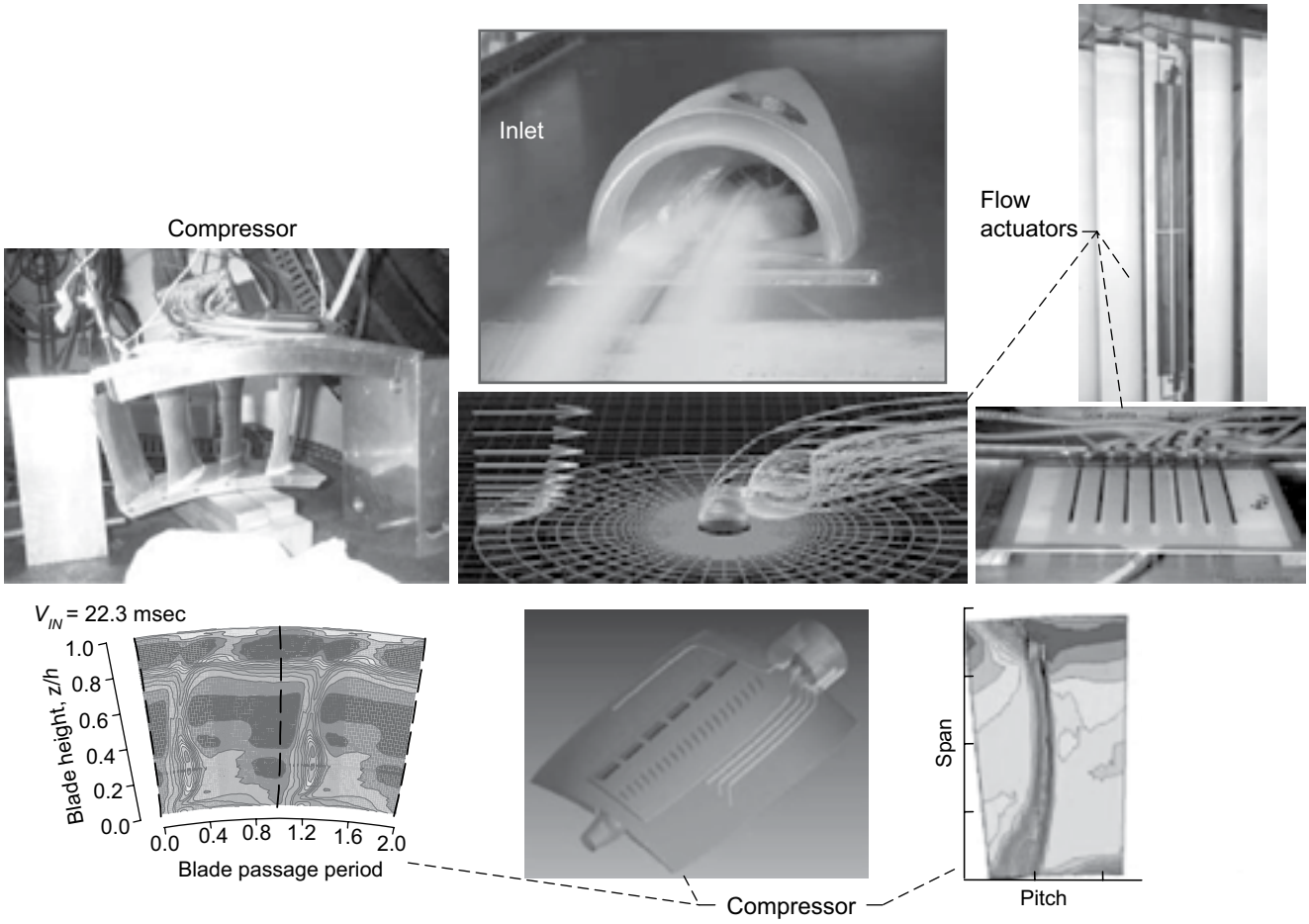


*Adaptive flow-control technologies are just a few of the technologies under investigation at NASA. As a class, these technologies manipulate the flow in turbine engine components to enable improved efficiency, better flow qualities, and lower weight—resulting in better aircraft fuel economy and lower emissions. NASA flow-control technologies focus on the inlets, fan, and compressors and turbines.*

**Bibliography**

Mercer, Carolyn R.; Haller, William J.; and Tong, Michael T.: Adaptive Engine Technologies for Aviation $CO_2$ Emissions Reduction. AIAA–2006–5105 (NASA/TM—2006-214392), 2006. http://gltrs.grc.nasa.gov/Citations.aspx?id=155

**Glenn contacts:**

Dr. Carolyn R. Mercer, 216–433–3411, Carolyn.R.Mercer@nasa.gov

William J. Haller, 216–977–7004, William.J.Haller@nasa.gov

Michael T. Tong, 216–433–6739, Michael.T.Tong@nasa.gov

**Authors:**

Dr. Carolyn R. Mercer, William J. Haller, and Michael T. Tong

**Headquarters program office:**

Aeronautics Research Mission Directorate

**Programs/projects:**

Intelligent Propulsion System Foundation Technology Project, Ultra-Efficient Engine Technology Project, Revolutionary Concepts in Propulsion Project

# Environmental Design Space Developed To Assess Aircraft Technology and Operational Tradeoffs

The continuing growth in air traffic and increasing public awareness have made environmental considerations one of the most critical aspects of commercial aviation today. The focus of commercial aircraft design has been on producing airplanes that meet performance goals at minimum operating costs. Environmental performance has been considered mostly at the postdesign analysis phase, during which adjustments have been made to satisfy the noise and emissions requirements of individual airlines or airports. This sequential design approach does not guarantee that the final aircraft is of overall optimal design with respect to operating costs and environmental considerations, but it served its purpose as long as only localized, minor adjustments were necessary to bring aircraft into environmental compliance. However, the gradual tightening of environmental requirements has increased the cost and complexity of achieving compliance in the postdesign phase significantly. Therefore, there is a need for integrating environmental considerations at an early stage of the aircraft design process and for more systematic investigation and quantification of the tradeoffs involved in meeting specific noise and emissions constraints.

Under a research grant from the NASA Glenn Research Center, the Massachusetts Institute of Technology (MIT) and Stanford University explored the feasibility of including environmental performance as an optimization objective at the aircraft conceptual design stage, allowing a quantitative analysis of the tradeoffs between environmental performance and operating cost. During 2006, a preliminary design framework was developed that uses a multiobjective genetic algorithm to determine optimal aircraft configuration and to estimate the sensitivities between the conflicting objectives of low noise, low emissions, and low operating costs. The framework incorporates the Aircraft Noise Prediction Program (ANOPP, a detailed noise-prediction code developed by NASA), the NASA Engine Performance Program (NEPP, an engine simulator developed by NASA Glenn), and aircraft operation procedures, analysis, and optimization modules developed at MIT and Stanford University. It allows tradeoffs between aircraft design, operations, and environmental impact to be explored and quantitatively articulated, resulting in assessments of the relative benefits of different opportunities for improving air transportation. The figure shows the design framework and its components.

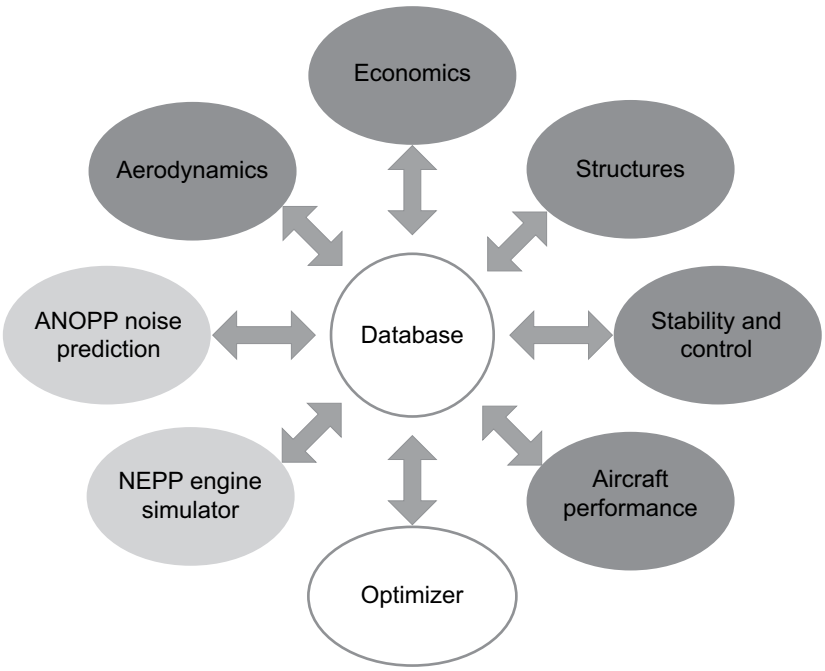


*Design framework and its components.*

**Bibliography**
Willcox, Karen E., et al.: An Environmental Design Space to Assess Aircraft Technology and Operational Trades. Final Report, NASA Grant NAG3–2897, 2006.

**Glenn contact:**
Michael T. Tong, 216–433–6739, Michael.T.Tong@nasa.gov

**Author:**
Michael T. Tong

**Headquarters program office:**
Aeronautics Research Mission Directorate

**Programs/projects:**
Ultra-Efficient Engine Technology Project

# P–BEAT: Initial Version of a Process-Based Economic Analysis Tool Released

The NASA Glenn Research Center is developing the Process-Based Economic Analysis Tool (P–BEAT): an engineering-focused economic analysis code for engineering tradeoff studies and technology investment decision analyses for all phases of a product life cycle. Version 1.0 of the code, released in 2006 and currently available upon request, combines decision analysis and economic analysis capabilities in a Microsoft Excel spreadsheet-based format. Included with the deterministic economic analysis tool is an Excel add-in simulation module (CpSimulation) that can be used for uncertainty and statistics analyses.

The initial release version of P–BEAT estimates development and production costs using an innovative process rollup-based methodology to calculate product complexity and its impact on cost. It offers multiuser capabilities, network-based configuration control, and data security features. It provides decision-support tools that can be used to generate utility curves that quantify desirability to stakeholders and a pair-wise method to determine system attribute priorities. P–BEAT includes an extensive database of over 14,000 materials and hundreds of manufacturing processes plus context-sensitive help and graphic tools for sensitivity analyses and identification of cost drivers, as well as the CpSimulation add-in module for uncertainty and cost-risk analyses.

The P–BEAT architecture is template-based and provides four usage modes (straight-cost rollup mode and dual-pane analogy mode, each using either the innovative process-based methodology or a traditional high-level parametric methodology). This analysis tool is presented in a multipaned graphical user interface with default values and bounds-checking for all user input parameters, along with context-sensitive help and parameter-specific charts and tables. Depending on available data, the fidelity of the analyses can range from first-order, system-level tradeoff studies to detailed, investment-grade, component-level product cost breakdowns. This allows the tool to be used to manage product cost throughout its full life-cycle from conception to production to retirement.

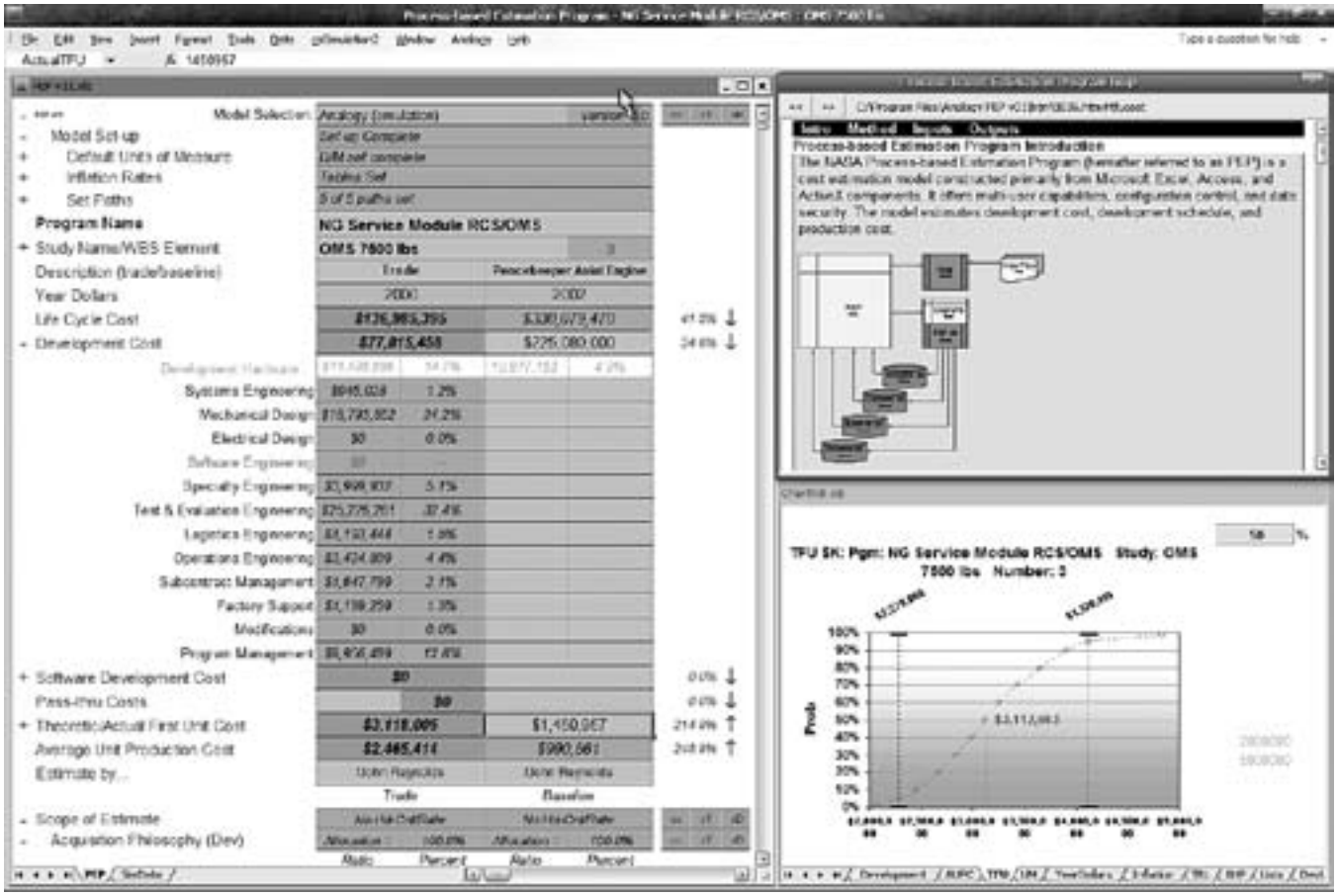


*P–BEAT multipaned user interface.*

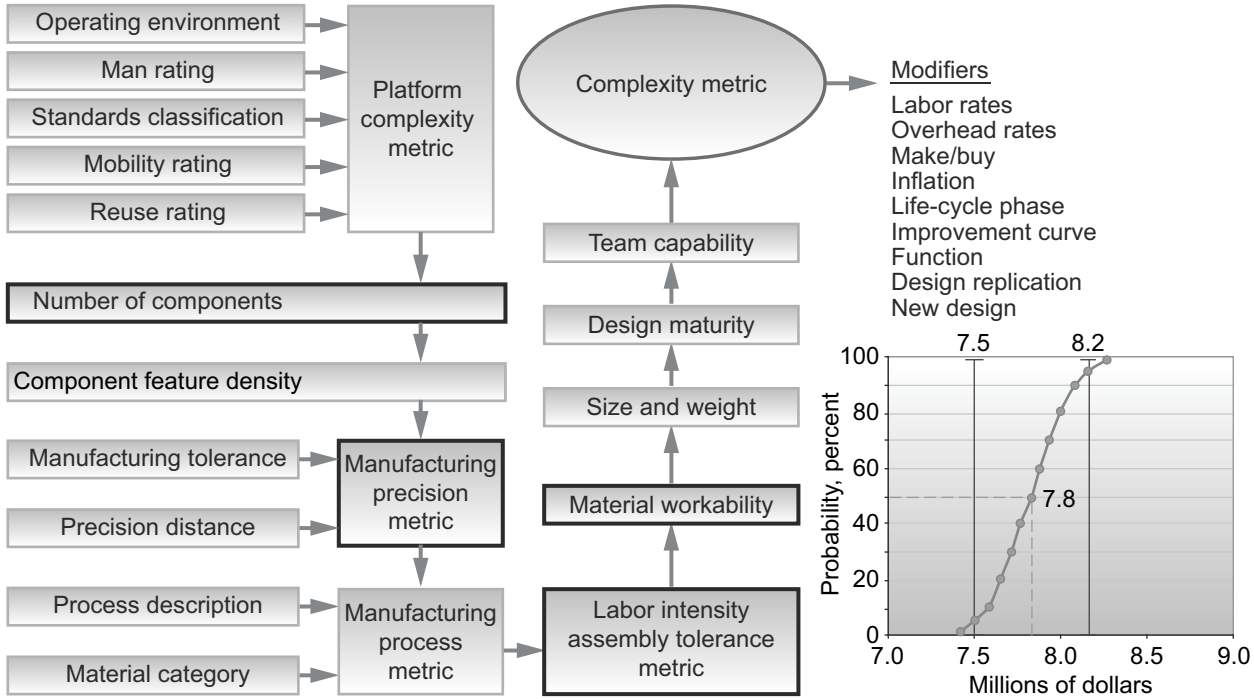


*P–BEAT process-based economic analysis methodology.*

Compared with traditional cost-estimation tools, which are not usually intended for use by engineers, P–BEAT provides the following benefits:

- Predicted costs are based on the known, actual cost of similar products: Estimates are credible to engineers.
- Self-documenting studies describe why costs vary, in terms understandable to engineers and managers.
- Turnaround is fast: An experienced practitioner can generate a first-order cost estimate in about 15 min when working with product development team members.
- Researchers can use high-level parametric input data and/or detailed design characteristics, such as design tolerance and material alternatives, within a single tool. The same tool can be used throughout all life-cycle phases.
- The decision module provides a hybrid analytic hierarchy process/utility function method for evaluating multiple criteria in a consistent manner for any number of design tradeoffs.
- Cost-estimating relationships, input data, and results are archived in a Microsoft Access database to ensure both access security and data integrity.
- A built-in automation mode allows batch processing of thousands of related studies for regression analysis and cost-driver assessment.
- A context-sensitive help system provides on-the-fly user instruction as well as model and cost-estimation documentation.

**Find out more about the research of the Glenn's Aeropropulsion Systems Analysis Office:**
http://www-psao.grc.nasa.gov

**Glenn contacts:**
Leo A. Burkardt, 216–977–7021, Leo.A.Burkardt@nasa.gov

Felix J. Torres, 216–977–7026, Felix.J.Torres@nasa.gov

Robert M. Plencner, 216–977–7010, Robert.M.Plencner@nasa.gov

Jonathan A. Seidel, 216–977–7039, Jonathan.A.Seidel@nasa.gov

Joseph F. Baumeister, 216–433–2179, Joseph.F.Baumeister@nasa.gov

**Author:**
Felix J. Torres

**Headquarters program office:**
Aeronautics Research Mission Directorate

**Programs/projects:**
Intercenter Systems Analysis Team

# OTIS 4 Software Released

Trajectory, mission, and vehicle engineers concern themselves with finding the best way for an object to get from one place to another. These engineers rely upon special software to assist them in this. For a number of years, many engineers have relied upon the OTIS program for this assistance. With OTIS, an engineer can fully optimize trajectories for airplanes, launch vehicles like the space shuttle, interplanetary spacecraft, and orbital transfer vehicles. OTIS provides two modes of operation with each mode, providing successively stronger simulation capability. The most powerful mode uses a mathematical method called implicit integration to solve what engineers and mathematicians call the optimal control problem. OTIS 4, the latest release of this industry workhorse, features a wide range of modifications that solve these problems more efficiently and faster. OTIS 4 was developed at the NASA Glenn Research Center in cooperation with the NASA Kennedy Space Center and Boeing Phantom Works and was released in 2006.

OTIS stands for Optimal Control by Implicit Simulation, and it is implicit integration that makes the OTIS software so powerful at solving trajectory optimization problems. Why is this so important? The optimization process not only determines how to get from point *A* to point *B*, but it can also determine how to do this with the least amount of propellant, with the lightest starting weight, or in the fastest time possible while avoiding certain obstacles along the way.

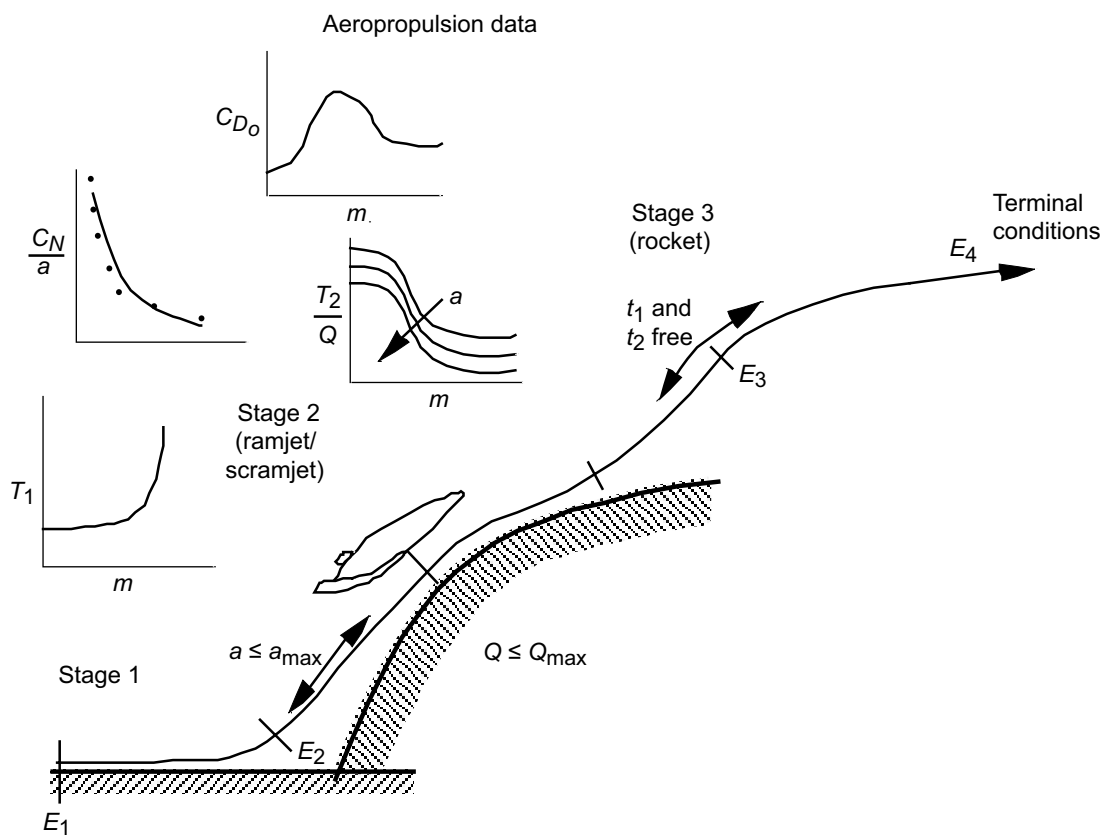


*Typical trajectory optimization problem. $C_N$, coefficient of normal force; a, angle of attack; $C_{Do}$, coefficient of base drag; m, mach number; $T_1$ and $T_2$, temperatures during phases 1 and 2; Q, dynamic pressure during phase 2; $t_1$ and $t_2$, initial and final phase times; $E_x$, phase times in seconds.*

There are numerous conditions that engineers can use to define optimal, or best. OTIS provides a framework for defining the starting and ending points of the trajectory (point *A* and point *B*), the constraints on the trajectory (requirements like "avoid these regions where obstacles occur"), and what is being optimized (e.g., "minimize propellant"). The implicit integration method can find solutions to very complicated problems when there is not much information available about what the optimal trajectory might be. The method was first developed for solving two-point boundary value problems and was adapted for use in OTIS. Implicit integration usually allows OTIS to find solutions to problems much faster than programs that use explicit integration and parametric methods. Consequently, OTIS is best suited to solving very complicated and highly constrained problems.

Typical OTIS input includes a description of the objective function (the thing that is the measure of goodness), general specifications that describe what the program should output, and specifications about how these results should be formatted. OTIS also provides input items for modeling vehicles by the phase of operation. Within each phase, the user specifies the current constraints on the operation of the vehicle, the initial and final conditions of the phase, the bounds on the problem, and the control parameters—such as steering angles and engine throttle parameters. See the diagram on the preceding page for a notional representation of the phases.

Although OTIS 4 is intended to solve trajectory optimization problems, it can be readily modified to solve optimal control problems in other engineering disciplines. The Boeing Company wrote the first versions of OTIS for the U.S. Air Force in 1985. Since 1995, the NASA Glenn Research Center has taken ownership of OTIS and has systematically improved and updated it. OTIS is written in Fortran 77 and uses the SNOPT 7 nonlinear programming package. The OTIS program is restricted to users within the United States who are working for the Federal Government, its entities, contractors, and subcontractors. Eligible users can obtain OTIS from Glenn's Technology Transfer & Partnership Office by following the links at http://otis.grc.nasa.gov/request.shtml.

**Find out more about this research:**

**OTIS:**
http://otis.grc.nasa.gov/

**Space Propulsion & Mission Analysis Office at Glenn:**
http://trajectory.grc.nasa.gov

**Glenn contact:**
John P. Riehl, 216–977–7061,
John.P.Riehl@nasa.gov

**Authors:**
John P. Riehl, Waldy K. Sjauw, and Stephen W. Paris

**Headquarters program office:**
Exploration Systems Mission Directorate

**Programs/projects:**
In-Space Systems

# A Lunar In Situ Explorer (ALISE) Conceptual Design Developed

The Clementine, Lunar Prospector, and SMART–1 missions to the Moon provided tantalizing data that indicated the possible presence of hydrogen volatiles within permanently shadowed craters at the lunar poles. These missions also indicated that there may be areas of high elevation that have much shorter “night-time” durations than the typical 14-day lunar night. If the hydrogen volatiles exist as water ice, and if nearby areas with longer durations of solar illumination can be exploited for power generation, the combination could be a boon to future human lunar exploration.

A Lunar In Situ Explorer (ALISE) is a conceptual design developed at the NASA Glenn Research Center in fiscal year 2006 for a robotic lander that would characterize the lunar environment and determine the presence of water ice in a permanently shadowed area in a lunar polar region. ALISE would provide ground truth measurements and demonstrate technologies that support the design of future robotic and human lunar exploration elements in the Vision for Space Exploration. From lunar orbit, the ALISE lander would deploy penetrators that would descend to a permanently shadowed area to determine the presence of water ice in the regolith and the subsurface strata. The lander would remain in orbit during this mission phase to act as an Earth data relay for the penetrators. Once the penetrator mission was completed, the lander would descend to a polar region that exhibits shortened night-time durations to provide in situ measurements of the lunar environment for at least 1 year. The lander would demonstrate precision landing capability in targeting one of these areas.

ALISE would provide significant data on the lunar polar environment, including radiation levels, neutron albedo, electrical characteristics of the lunar surface during the lunar day and night, surface and subsurface temperature profiles during the lunar day and night, characterization of the regolith dust properties and behavior, and the variation of solar illumination at the landing site over the course of a full year. The penetrators and the lander would contain passive devices that would act as beacons, providing navigational reference points for future robotic and human missions. ALISE would demonstrate power, navigation, communication, and in situ regolith processing technologies to support future robotic and human missions to the lunar surface. ALISE also would provide a design for a common lander platform that could support future robotic lander missions to the Moon or other extraterrestrial bodies.

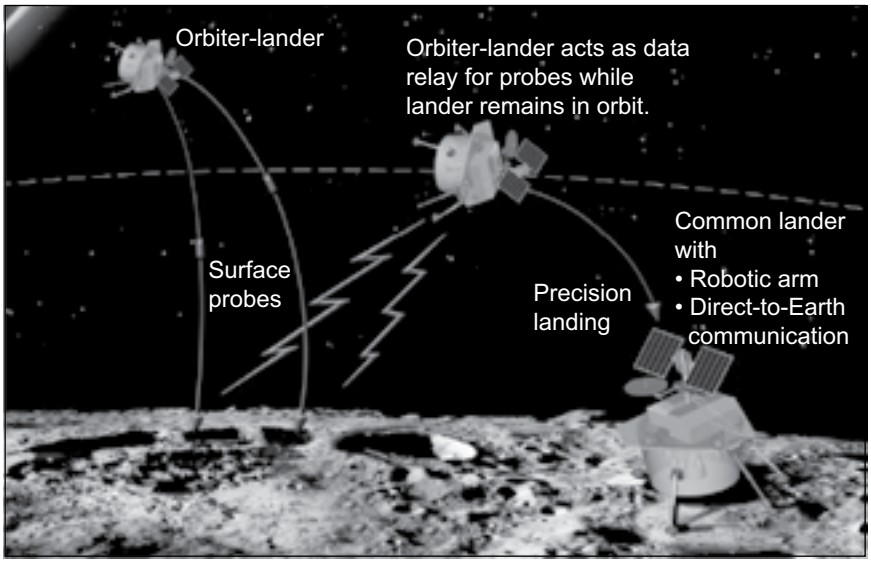


*ALISE mission profile.*

**Bibliography**
Woytach, Jeffrey M.; and Hojnicki, Jeffrey S.: A Lunar In-Situ Explorer (ALISE). AIAA–2006–7398, 2006.

**Glenn contacts:**
Jeffrey M. Woytach, 216–977–7075, Jeffrey.M.Woytach@nasa.gov

Jeffrey S. Hojnicki, 216–433–5393, Jeffrey.S.Hojnicki@nasa.gov

**Authors:**
Jeffrey M. Woytach and Jeffrey S. Hojnicki

**Programs/projects:**
Exploration, Lunar Precursor Robotics Program, Constellation

# EXPLORATION SYSTEMS

## First Lithium-Ion Engineering Model Battery Developed and Tested for Human Space Flight for Low Earth Orbit and Lunar Mission Applications

With a renewed spirit of discovery in space exploration, NASA plans to replace the aging space shuttle fleet with the new Crew Exploration Vehicle to travel beyond low Earth orbit (LEO) and return astronauts to the Moon. One of the critical components in a space-flight system is electrical energy storage. This year, researchers and engineers developed and tested the first high-energy lithium-ion (Li-ion) engineering model (EM) battery for human space flight for LEO and lunar missions.

The Li-ion EM (see the photograph) is a twin battery with eight 50-A-hr Li-ion cells connected in series on each side. It weighs about 100 lb. Although the EM was designed as a twin battery for an efficient power system packaging concept, a single battery could easily be built from the basic twin-battery design. The single battery could be used in a distributed power system in a space-flight vehicle where volume was limited. The battery is sized for both LEO and low lunar orbit (LLO) cycle regimes and with an N+2 battery level redundancy scheme to provide 5 to 7 kW of power during a 35-min Earth shadow and a 46.5-min lunar shadow. The N+2 redundancy scheme provides a fault-tolerant system while maintaining full performance capability and reducing battery system mass. An example of an N+2 redundancy scheme follows: A five-battery system with each battery sized for one-third performance capability can maintain full performance capability after two battery failures. The five-battery system mass is lower than the mass of three batteries with full performance capability.

The Li-ion EM has successfully passed protoflight vibration levels and thermal cycles, and it has demonstrated the required LEO and LLO charge-discharge cycle capability. The mission requirements include 240 LEO cycles, a 2.5- to 6-day cruise period, 2200 LLO cycles, and a 2.5- to 6-day return period with 8 LEO cycles. Demonstrations of the battery included LEO cycles at 45-percent depth-of-discharge (DOD) and LLO cycles at 60-percent DOD at 20 °C. Short-circuit and overcharge safety tests that were performed on battery cells of the same design provided valuable engineering data for the battery design. Furthermore, limited LEO/LLO cycle tests were performed with a separate eight-cell stack (same cell design). Another eight-cell stack was built for the life-cycle test. In addition, a battery charge-control system (BCCS) was built and demonstrated with the Li-ion EM battery. The BCCS features a nondissipative charge-control method that provides charging and individual cell balancing for the battery. The Li-ion EM battery system has been delivered to the NASA Glenn Research Center, and the battery with the BCCS will continue to undergo additional LLO cycle testing to evaluate performance.

The Li-ion EM and BCCS development effort has significantly advanced the technology readiness level, and the EM battery design is now a strong candidate for human space flight in LEO and lunar missions that require a battery for energy storage. The development effort is led by Glenn, with a Lockheed Martin Space Systems Company contract for hardware development, integration, and testing.

*Li-ion EM battery (front) and battery charge-control system (back).*

**Find out more about Exploration Systems research at Glenn:**
http://exploration.grc.nasa.gov

**Glenn contacts:**
Nang Pham, 216–433–6165,
Nang.T.Pham@nasa.gov

Tom Miller, 216–433–6300,
Thomas.B.Miller@nasa.gov

Scott Graham, 216–977–7123,
Scott.R.Graham@nasa.gov

**Authors:**
Nang T. Pham and Thomas B. Miller

**Headquarters program office:**
Exploration Systems Mission Directorate

**Programs/projects:**
Exploration Systems Research and Technology

# New Catalytic Gas Generator Developed and Tested With a Turbine Power Unit

A new catalytic gas generator (GG) was successfully built and tested with a turbine power unit (TPU) to demonstrate nontoxic power generation for launch vehicle applications that require high power for short durations, such as flight-control systems. Unlike the space shuttle's hydrazine auxiliary power unit (APU) and other similar APU's, which provide mechanical power to the hydraulic flight-control system, the GG/TPU combination provides electrical power for an all-electric flight-control system or for loads requiring high electrical power for short durations. The GG is designed to operate with gaseous hydrogen and oxygen. The GG/TPU (left photograph) was successfully demonstrated with gaseous hydrogen and oxygen propellants through catalytic reaction to produce 138.7 kWe. Hot restart was also demonstrated successfully with the GG/TPU configuration. The hot restart testing verified that the GG/TPU can be shut down at anytime and restarted after any shutdown interval.

The GG (right photograph) properly mixes the gaseous hydrogen and gaseous oxygen propellants, initiates their reaction through a Honeywell 405 granular catalyst, and channels the hot gas to the TPU to spin the turbine. The turbine directly drives a generator that produces electrical power. The GG is designed to operate at a combustion gas temperature of 1500 °F, an oxygen-to-fuel ratio of 0.80 (fuel rich), a flow rate of 0.336 lb/sec at maximum power, and a pressure of 170 psia to the TPU. It is pulsed on and off at 0.25 to 2 Hz to regulate power.

Numerous GG/TPU integration and GG design issues have been solved with the new catalytic GG. A remaining technical challenge for the GG is extending the catalyst operating life. The GG catalyst has a cumulative demonstrated operating life of about 55 min, with a projected life of about 1.1 hr. Extending the GG's operating life for longer durations or for reusable applications like the shuttle APUs will require significant catalyst life improvement for the GG design. Leveraging from this GG effort, Honeywell, under their internally funded research development, recently explored modifications to the GG and has demonstrated a significant increase in the GG catalyst operating life. With modifications to the GG, the catalyst operating life is projected to have 17 to 90 times the original catalytic GG life. The GG effort was led by

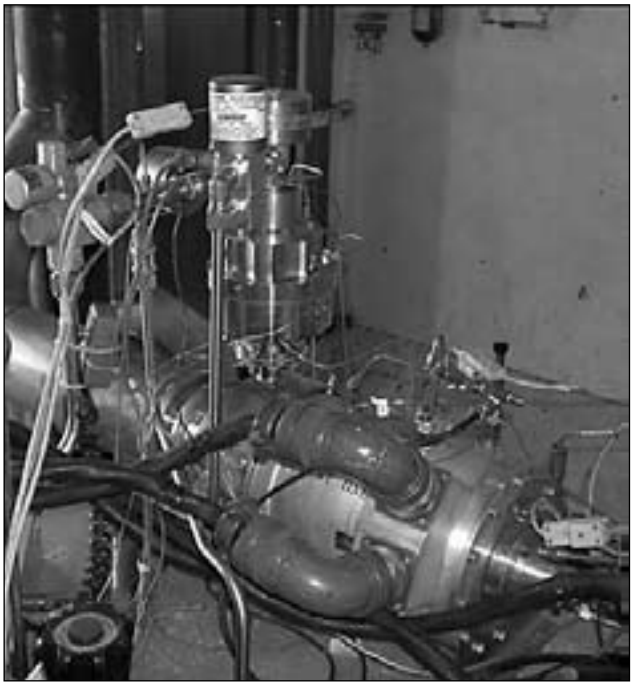

*Left: GG tested with TPU. Right: Catalytic GG.*

the NASA Glenn Research Center, with a Lockheed Martin Space Systems Company prime contract and a subcontract with Honeywell for nondissipative charge control for the GG development, integration, and testing.

**Find out more about Exploration Systems research at Glenn:**
http://exploration.grc.nasa.gov

**Glenn contacts:**
Nang Pham, 216–433–6165, Nang.T.Pham@nasa.gov

Clint Ensworth, 216–433–6297, Clinton.B.Ensworth@nasa.gov

Scott Graham, 216–977–7123, Scott.R.Graham@nasa.gov

**Authors:**
Nang T. Pham and Clinton B. Ensworth

**Headquarters program office:**
Exploration Systems Mission Directorate

**Programs/projects:**
Exploration Systems Research and Technology

## Crew Launch Vehicle Upper-Stage Thrust-Vector-Control Architecture Selected

In early spring to mid-summer 2006, a multi-NASA-center team led by the NASA Glenn Research Center—including the NASA Marshall Space Flight Center, the NASA Johnson Space Center, the NASA Kennedy Space Center, and industry input—conducted comprehensive thrust vector control (TVC) tradeoff studies leading to the selection of a TVC architecture for the Crew Launch Vehicle (CLV) Upper Stage (US). The NASA TVC team defined and evaluated a broad number of TVC architectures that included electric, hydraulic, and pneumatic actuation and power technologies. Quantitative and qualitative figures of merit consistent with the program mission and objectives and engineering judgment were used in selecting the TVC architecture.

The selected TVC architecture for the CLV US is a hydraulic actuation system with a primary and backup power system (see the diagram on the next page). Hydraulic actuators are driven by two high-pressure hydraulic pumps that are powered by a turbine power assembly (TPA) or a high-voltage battery-powered electric hydraulic pump assembly (EHPA). For redundancy, both power sources are sized for full power capability for the entire ascent. The selector valve in the actuators is used to choose the primary or redundant hydraulic system. The TPA is powered by pressurized hydrogen gas supplied by the US Main Propulsion System (MPS). The gas spins the turbine with the connecting gearbox to drive the hydraulic pump. A power takeoff (PTO) from a rocket engine liquid oxygen turbopump driving a hydraulic pump or a second TPA is being considered as a potential candidate instead of a battery-powered EHPA. The hydraulic system A/B (see the diagram) transmits the source power to the actuators and absorbs the regenerative actuator power. The main components in the hydraulic system A/B are an accumulator, a reservoir, a check valve, and a filter assembly. A circulation motor-pump circulates the hydraulic fluid for thermal conditioning, and hydraulic locks are provided to lock the rocket engine in the null position during the first stage of the flight. Low-voltage power from the vehicle electric power system provides all housekeeping power to the TVC. Command for TVC actuation is through a Mil-Std1553 communication bus.

The CLV US TVC steers the launch vehicle during US ascent in the vehicle pitch and yaw or rock and tilt axes by gimbaling the rocket engine to provide thrust vectoring. Two TVC actuators are positioned 90° apart relative to each other to provide the engine's gimbal function.

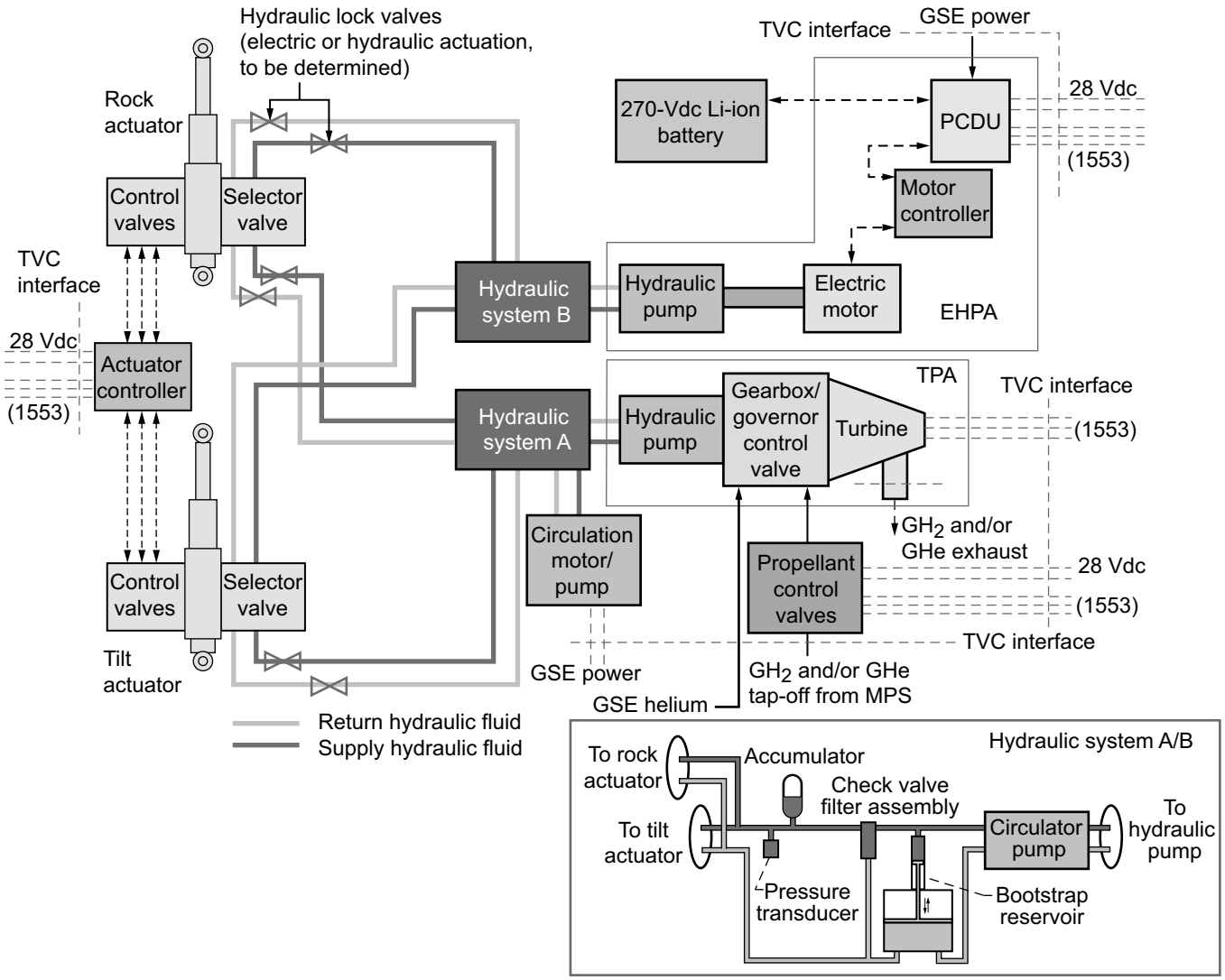


*Simplified TVC architecture diagram for the CLV US. GSE, ground support equipment; $GH_2$, gaseous hydrogen; GHe, gaseous helium; PCDU, power conversion and distribution unit.*

Now that the CLV US TVC architecture is selected, the detailed design and analysis of the various components within the architecture will proceed into the requirements-definition phase, leading to breadboard and engineering model hardware development and testing. An additional power tradeoff study is being conducted to decide on the second hydraulic power. Some of the assemblies will be developed under advanced development contracts, leading to a critical design review by 2009. Other components will be developed by Glenn, the overall integration activities will be performed by Glenn, and testing of breadboard and engineering model hardware will be performed at Glenn.

**Glenn contacts:**
Nang Pham, 216–433–6165, Nang.T.Pham@nasa.gov

Robert Tornabene, 216–433–3045, Robert.T.Tornabene@nasa.gov

Dave Frate, 216–433–8329,
David.T.Frate@nasa.gov

Scott Graham, 216–977–7123,
Scott.R.Graham@nasa.gov

Mark Hickman, 216–977–7105,
John.M.Hickman@nasa.gov

**Authors:**
Nang T. Pham and David T. Frate

**Headquarters program office:**
Exploration Systems Mission Directorate

**Programs/projects:**
Constellation Systems

# Intravenous Fluid Mixing Times Quantified by Planar Laser-Induced Fluorescence

Longer duration missions as outlined in the Vision for Space Exploration increase the likelihood of requiring intravenous (IV) fluids to treat a medical emergency. In some instances, as in the case of severe burns, proper medical treatment may require up to 32 liters of intravenous fluid weighing over 32 kg (70.5 lb), see reference 1. Because a system to generate medical grade water and mix it with powders or concentrates would reduce the mass requirements for IV fluids, in fiscal year 2006 the NASA Glenn Research Center analyzed several potential methods for mixing powders or concentrates with sterile water to produce IV fluid. The researchers found that a standard magnetic stirrer would be highly effective, being low in mass and high in mixing efficiency. Ground experiments were performed to validate the efficiency of this mixing method. More specifically, the amount of time required to mix the fluid to concentration tolerances defined by the Food and Drug Administration (FDA) was determined, and a noninvasive optical diagnostic technique was used to quantify these mixing times.

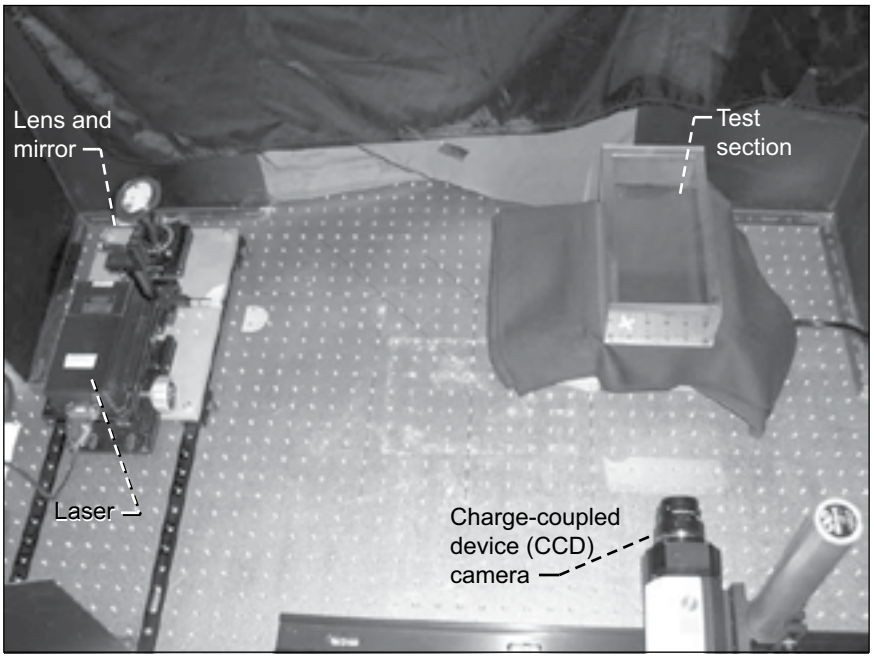


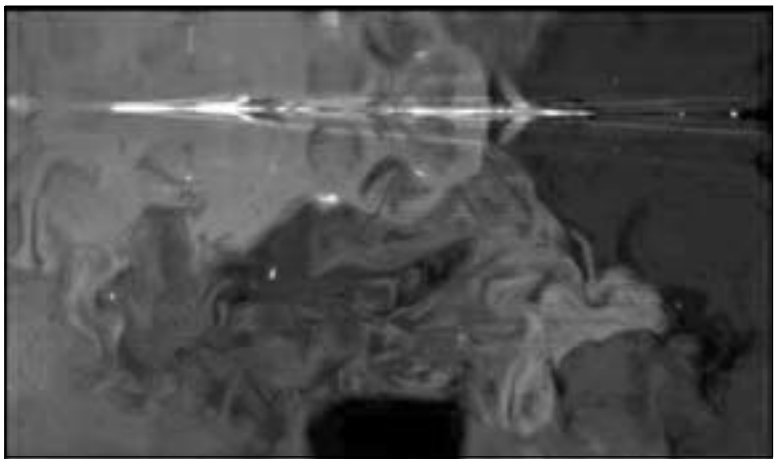

*Top: PLIF experimental setup. Bottom: An example of a PLIF image (enhanced for publication).*

Planar Laser-Induced Fluorescence (PLIF) is an optical technique in which a laser source is used to form a thin sheet of light that traverses a flow field of interest. If the laser wavelength is resonant with the optical shift of a species present in the flow, a portion of the incident light will be absorbed and emitted, at a longer wavelength, by that species at each point within the illumination plane. When the emitted light, or fluorescence, is imaged, the amount of light detected by a pixel of the camera depends on the concentration of the species of interest within the corresponding measurement volume and the local flow field conditions (i.e., temperature, pressure). The PLIF experimental setup at Glenn included a continuous-wave, 200-mW, 532-nm Nd: YAG laser that was passed through a planoconvex lens to create a divergent laser sheet. An optically flat mirror deflected the laser sheet into an acrylic test section, which approximated a 1-liter commercial IV bag. A 12-bit monochromatic 1024- by 768-pixel camera with a 35-mm lens was placed perpendicular to the laser sheet and focused on a cross section of interest. PLIF image sequences were acquired of a salt solution containing fluorescent dye (Rhodamine 6G) mixed with distilled water to mimic the production of a standard IV fluid: normal saline. The experimental setup and a sample image are shown in the top and bottom photographs, respectively.

A histogram analysis of the normalized pixel intensity for the series of images was used to plot the peak intensity over time (see the left graph on the next page). A fully mixed solution was indicated when

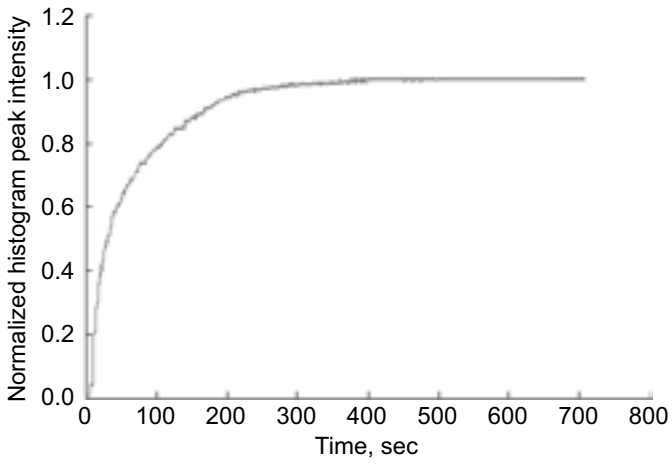


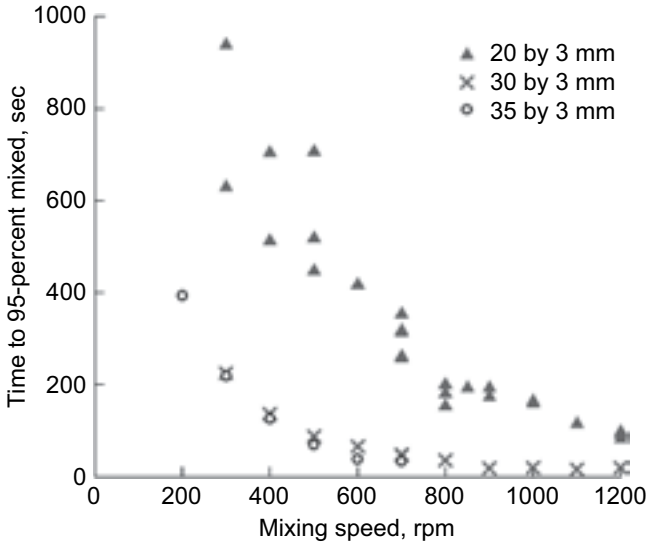


*Left: Normalized histogram peak intensity over time. Right: Time versus revolutions per minute required to achieve a 95-percent homogenous solution with various stir bar sizes.*

the mean intensity curve formed an asymptote to the normalized final intensity. Mixing times for a 95-percent homogenous solution were plotted for stir bars of various sizes (see the right graph). The plot indicates that these solutions can mix within a few seconds, particularly with the longer stir bars. Analysis is under way to determine the effect of gravity on the mixing time. If convective mixing is similar in microgravity, this mixing method would be able to produce IV fluids in emergency situations.

**Reference**

1. The United States Naval Flight Surgeon Handbook, 2nd ed., The Society of U.S. Naval Flight Surgeons, 1998.

**Glenn contacts:**
Karen L. Barlow, 216–433–3543, Karen.L.Barlow@nasa.gov

Charles E. Niederhaus, 216–433–5461, Charles.E.Niederhaus@nasa.gov

**Authors:**
Karen L. Barlow and Dr. Charles E. Niederhaus

**Headquarters program office:**
Exploration Systems Mission Directorate

**Programs/projects:**
Exploration Medical Capabilities

# Model To Predict Risk of Bone Fracture During Space Missions Developed

The Integrated Medical Model (IMM) is a decision-analysis tool using the principles of probabilistic risk assessment to help optimize astronaut health and mission integrity during space missions by predicting the risk of medical hazards, including cardiac arrest, radiation exposure, kidney stones, and bone fracture. The observation that astronauts in space lose bone mass more quickly than their counterparts on Earth leads to the concern that the crew members are vulnerable to bone fracture, particularly during long-duration space flight. Since treatment facilities are scarce and crew and mission consequences are severe, the reliable prediction of bone fracture is crucial. In support of multi-NASA-center IMM development, a team from the NASA Glenn Research Center and the Cleveland Clinic developed the Bone Fracture Risk Module (BFRM) to analyze fracture risk in any specified mission scenario.

Using the latest biomechanical and clinical research, the BFRM evaluates the risk of bone fracture in the hip and spine. Crew- and mission-specific data are input, as shown in the following figure, to define relevant mission scenarios and crew capabilities. The forces generated by hazards, such as falling from a ladder or lifting heavy objects, are input to biomechanical models that quantify applied skeletal load. The bone quality is then assessed to determine the maximum load that can be tolerated by the bone; that is, the ultimate load, which varies with time in space as a result of bone loss, aging, bone structural changes, and skeletal location. These measures are used to estimate the likelihood of fracture under such conditions. Outcomes from the evaluation of treatment options are coupled with the fracture risk prediction to generate a sensitivity analysis. This analysis identifies the parameters that can most affect the likelihood and successful treatment of fracture, such as spacesuit padding or medical training and supplies. On the basis of these results, the BFRM generates an assessment of crew impairment and mission impact.

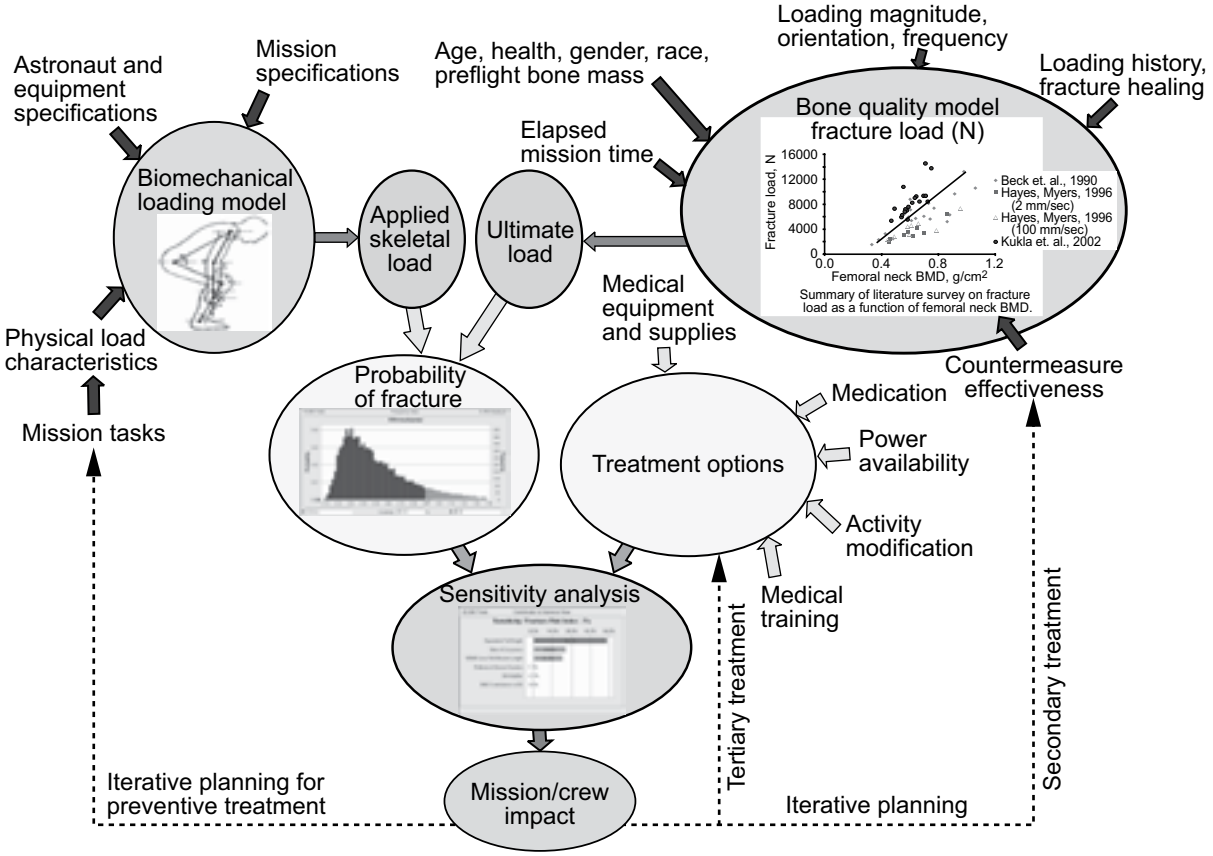


*Description of the BFRM. BMD, bone mineral density.*

Mission planning can be iterated to avoid hazardous activities during a mission as preventive treatment. Secondary treatment includes countermeasures such as exercise, medication, and dietary supplements. If a fracture does occur, tertiary treatment is recommended by evaluating outcomes from available treatment protocols. Optimization simulations can be performed to determine the most likely combination of countermeasures, medical equipment, supplies, and training to reduce mission impact due to fracture.

Although preliminary results indicate that the risk of bone fracture during a Mars mission is small, it does not appear to be negligible. In the event of fracture, the impact of astronaut impairment in an environment with limited treatment options is large. Consequently, future work aims at increasing the scope of the biomechanical models to improve precision in fracture prediction. One key area is the evaluation of repetitive or repeated loading on bone quality, which can result in fracture at substantially reduced loading levels (stress fracture progression). In summary, the BFRM can be used as an aid in planning missions before launch, in determining countermeasures during missions, and in prescribing treatment in the event of a fracture.

**Glenn contact:**
Dr. Jerry G. Myers, 216–433–2864, Jerry.G.Myers@nasa.gov

**Cleveland Clinic contact:**
Dr. Angelo Licata, 216–444–6248, LicataA@ccf.org

**Authors:**
Angelo Licata, M.D., Ph.D.; Jerry Myers, Ph.D.; Beth Lewandowski, M.S.; and Emily S. Nelson, Ph.D.

**Headquarters program office:**
Human Systems Research and Technology Development

**Programs/projects:**
Human Research Program

# Research and Technology

Communications
Instrumentation and Controls
Power and Electric Propulsion
Propulsion Systems
Microgravity
Materials and Structures

# Microenergy Rates Used To Determine Damage Tolerance and Durability of Composite Structures

For effective structural health monitoring in fuselages and in engines, it is important to quantify the damage tolerance of a candidate structure. New aircraft designs, both commercial and military, are increasingly relying on composite structures to reduce aircraft weight and fuel consumption. Fiber composites, by their multiscale nature, are able to arrest cracks and prevent self-similar crack propagation, and composite structures have received a great deal of consideration for designs that emphasize damage tolerance. However, the number of design parameters involved—such as fiber-orientation patterns, choices of constituent material combinations, ply drops, and hybridization—make the design of composite structures very complex. Thus, designers must evaluate damage initiation in a composite structure, as well as fracture propagation characteristics, in the early design phase in order to achieve a rational damage-tolerant design.

Compared with homogeneous materials, fiber composites have much more complicated damage initiation and progression characteristics. Composite structures often contain some preexisting flaws or flaws that were induced in the matrix and fibers during fabrication. At lower stresses, the matrix is likely to be cracked because of flaw-induced stress concentrations, and these flaws can propagate across the composite. By using established material modeling and finite element models—and considering the influence of local defects, through-the-thickness cracks, and residual stresses—researchers can use computational simulation to evaluate the details of progressive damage and fracture in composite structures.

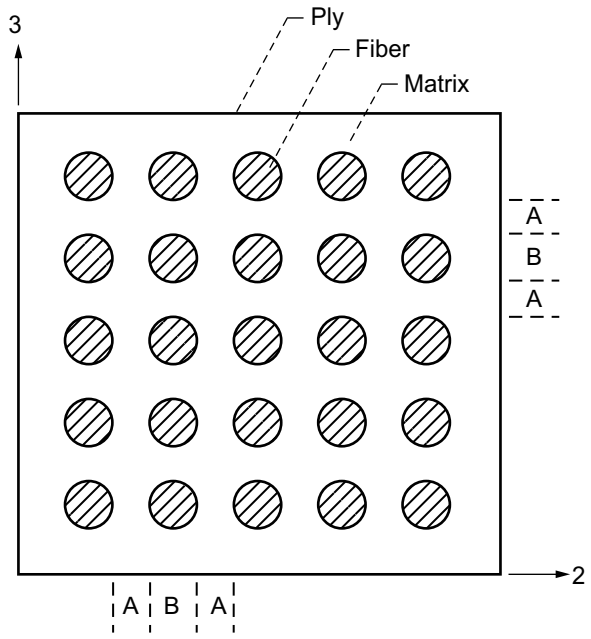


*Definitions of regions for ply microstress calculations. The numbers 2 and 3 indicate material axes.*

In a computational simulation, a damage evolution quantifier such as the damage volume, exhausted damage energy, or the damage energy release rate (DERR) are used to quantify the structural damage tolerance at different stages of degradation. Low DERR levels usually indicate that degradation takes place with minor resistance by the structure. Structural resistance to damage propagation is often dependent on structural geometry and boundary conditions as well as on the applied loading and the state of stress. In certain cases, such as the room-temperature behavior of composites designed for high-temperature applications, internal microcracks initiated in the matrix grow large enough to be externally visible. Thus, matrix cracking and its effect on damage propagation and damage tolerance need to be evaluated.

Damage initiation, growth, accumulation, and propagation to fracture were studied at the NASA Glenn Research Center. Since the complete evaluation of ply- and sub-ply-level damage and fracture processes is the fundamental premise of computational simulation, a microstress-level damage index was added to identify and track sub-ply-level damage processes. Computed damage regions were similarly correlated with ultrasonically scanned damage regions. Then, the simulation was compared with data from acoustic ultrasonic testing to validate it. Results showed that computational simulation can be used with suitable nondestructive evaluation (NDE) methods for credible inservice monitoring of composites.

At Glenn, we evaluated the microstresses by considering the model on the preceding page. In this model, the different regions where failure will occur are labeled. For example, A represents an all-matrix region, and B represents a mixed region of matrix, interface, and fiber. The concept is illustrated in the following graphs where the acoustic signal is plotted. The top graph shows the envelope curve for an epoxy-resin-bonded specimen, and the bottom graph shows the envelope curve for a prepreg-bonded specimen. The area under the envelope represents the total damage energy detected by the acoustic emission during the period monitored. Thus, we could correlate the microstress damage energy through computational simulation with the relative total damage energies represented by the envelope areas. The envelope area in the top graph is $1.22986\times10^{-3}$ and that in the bottom graph is $1.30145\times10^{-3}$. The ratio of the energies from the bottom graph to those of the top graph is 1.058. Comparatively, the ratio of damage energies computed from the NDE test results (ultrasonically scanned damage regions, ref. 1) is 1.168, which is 10 percent higher. Results showed that computational simulation can be used with suitable NDE methods for credible inservice monitoring of composites.

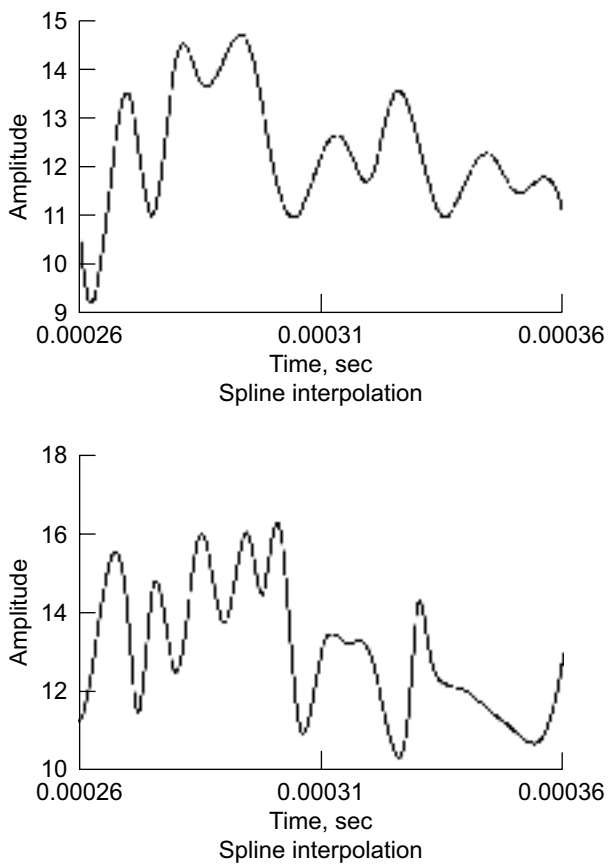


*Energy envelope of acoustic emission signals for bonded specimens. A special curve "spline" was fit through several distinct points for the interpolation. Top: Epoxy resin. Bottom: Prepreg.*

**Reference**

1. Chamis, Christos C.; and Minnetyan, Levan: Micro-Energy Rates for Damage Tolerance and Durability of Composite Structures. NASA/TM—2006-214037, 2006. http://gltrs.grc. nasa.gov/Citations.aspx?id=249

**Glenn contact:**
Dr. Christos C. Chamis, 216–433–3252, Christos.C.Chamis@nasa.gov

**Author:**
Dr. Christos C. Chamis

**Headquarters program office:**
Aeronautics Research Mission Directorate

**Programs/projects:**
Subsonic Fixed Wing

# Corrosion of Composites Modeled by Computational Simulation

New aircraft designs, both commercial and military, are increasingly relying on composite structures to reduce aircraft weight and fuel consumption. In the case of high-performance aircraft, the desired performance is often unobtainable using "traditional" structural designs (such as riveted or welded aluminum alloys). Corrosion is a critical design concern when composites are to be used in corrosive environments, and it needs to be addressed in the initial design phases of these aircraft. Corrosive environments, which are characterized by their pH factor, temperature, and moisture, continuously degrade composites until they cannot sustain the load that they were initially designed to carry. Even though the corrosion of metals has been investigated extensively—particularly in regards to test methods and experimental investigation—only a limited number of laminates can be investigated experimentally and in only a limited number of corrosive environments. This leaves a knowledge gap because composite system designs require lots of flexibility. A convenient computational simulation method was needed to predict the ability of composites to endure corrosive environments. Just such a method was developed at the NASA Glenn Research Center. It correlates the pH factor of the corrosive environment with the damage tolerance of the composite laminate, which is simulated by micro-, macro-, and laminate-level composite theories. The corrosive environment is assumed to cause polymer composite degradation on a ply-by-ply basis. The degradation is correlated with the measured pH factor, a parabolic distribution of voids through the laminate thickness, and a linear distribution of temperature and moisture.

Simulations are performed by the Integrated Composite Analyzer (ICAN), a computational composite mechanics computer code that includes microlevel, macrolevel, combined stress failure, and laminate-level theories. A simulation starts with constitutive material properties and models behavior up to the laminate scale, accounting for exposure of the laminate to the corrosive environment. The simulation procedure follows:

(1) Assume that the pH factor (see the graph) will corrode the first exposed ply in the polymer matrix only.
(2) Assume that the corrosion will pit the polymer matrix in a parabolic shape from zero at the last ply to about 0.3 at the top ply (ply 8). Voids of 0.3 are close to the limit of ply strength.
(3) Assume that the ply is subjected to a linearly varying temperature and moisture content, from 0 °F and a moisture content of 0 percent at the last ply (ply 1), to close to the transition temperature of about 270 °F and a moisture content of 4 percent at the top ply (ply 8). Both of these are limiting cases of ply strength.
(4) Use these as input data to ICAN (see the illustration on the next page), and run the program.
(5) Use the combined-stress failure; criterion to degrade the plies one or more at a time from the first ply to the last ply, or several last plies, until the simulation shows failure; that is, until each ply has degraded to the point that it cannot carry any more design load.
(6) The simulation ends when the laminate has been completely degraded.

Results obtained for one laminate indicate that the ply-by-ply simulation degrades the laminate to the last ply or last several plies. Results also demonstrate that the simulation is applicable to other polymer composite systems. The final figure illustrates the degradation procedure with the negative combined-stress failure criterion. Details of this simulation method are given in reference 1.

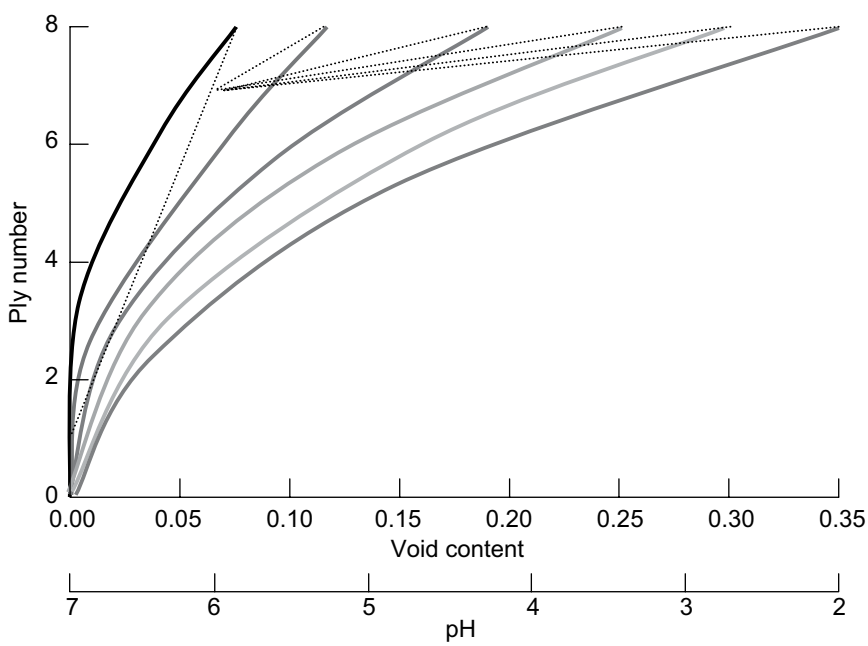


*Approximate pH correlation with ply degradation of AS/E $[0\pm45/90]_s$ composite (assuming that voids vary parabolically through the laminate thickness and that temperature and moisture vary linearly). (AS/E is an AS graphite fiber in an epoxy matrix.)*

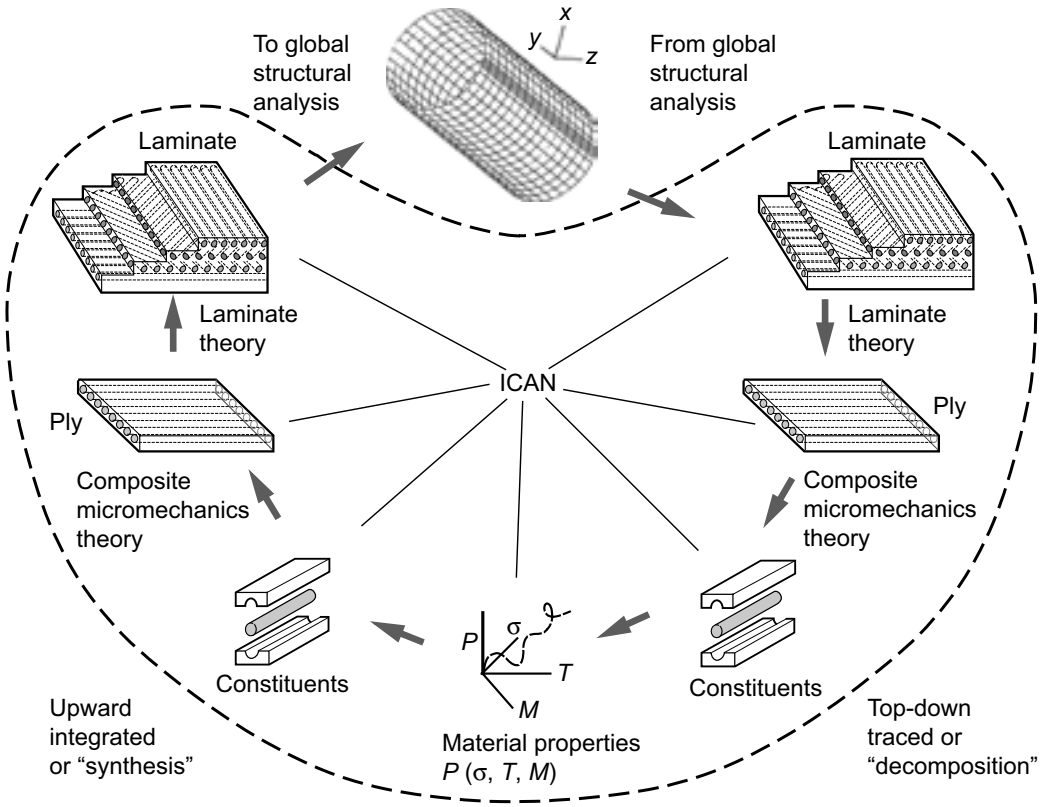


*ICAN simulation cycle.*

| | | | | | | |
|---|---|---|---|---|---|---|
| $\sigma_{\ell 11T}$ | 1.6 | 9.1 | 1.3 | 6.2 | 4.9 | 4.7 |
| $\sigma_{\ell 22T}$ | 1.1 | 0.4 | 2.7 | 2.9 | 2.5 | 1.6 |
| $\sigma_{\ell 12S}$ | ~0.0 | 0.1 | 0.7 | –1.1 | –1.0 | ~0.0 |
| FC(0) | –194 | –153.3 | –432 | –429 | –1200 | –396 |
| FC(2) | 0.568 | 0.521 | –7.7 | –8.45 | –7.18 | –0.48 |
| FC(3) | | | –1.5 | –1.56 | 0.48 | –0.72 |
| FC(4) | | | –0.07 | 0.48 | | |
| FC(5) | | | 0.62 | | | |

*Ply corrosion degradation [0±45/90]s of AS/HMHS laminate. Corrosion simulated by parabolic distribution of voids through the thickness of the laminate and linear distribution of temperature (first ply stresses and combined-stress failure criterion, FC). (AS/HMHS, AS graphite fiber in a high-modulus, high-strength matrix; $\sigma_{11T}$, longitudinal tensile stress; $\sigma_{12S}$, intraply shear stress.)*

**Reference**

Chamis, Christos C.; and Minnetyan, Levon: Structural Composites Corrosive Management by Computational Simulation. NASA/TM—2006-214221, 2006. http://gltrs.grc.nasa.gov/Citations.aspx?id=83

**Glenn contact:**

Dr. Christos C. Chamis, 216–433–3252, Christos.C.Chamis@nasa.gov

**Author:**

Dr. Christos C. Chamis

**Headquarters program office:**

Aeronautics Research Mission Directorate

**Programs/projects:**

Subsonic Fixed Wing

# Composite Mechanics Used To Evaluate Composite-Enhanced Concrete Structures

Reinforced concrete, which is widely used in the construction industry, tends to crack, chip, and be damaged as a result of inadvertent loads or overloads that may not have been accounted for in the initial design. The damage may be extensive enough that the safety of a structure becomes a major concern. Recently, a considerable effort was expended on using fiber-reinforced composites to repair or upgrade concrete structures, and several sessions were devoted to this subject at a recent International SAMPE Symposium and Exhibition in Long Beach, California. It is natural to use composites for repair since the repairing composites tend to be thin laminates. These materials are easily bonded to damaged concrete structures, which usually have cylindrical or flat surfaces.

Different methods for designing and analyzing thin laminates have been developed and are available in many computer codes. Recent research demonstrates that damaged concrete structures and the composites used to repair them can be simulated simultaneously by the composite mechanics included in some computer codes. With composite mechanics, we can represent any concrete structural section by assuming that it consists of several layers through its thickness. In so doing, we take advantage of all the composite mechanics features available in such computer codes as the Integrated Composite Analyzer (ICAN). This demonstrates that computer codes developed at the NASA Glenn Research Center for aeronautics research are applicable to civil engineering problems.

An approach developed at Glenn, and applied to selected reinforced-concrete structural sections and structures, takes advantage of those features and attendant computer codes. It represents a new and effective method for designing composites to repair or improve the overload strength of a concrete structure. The method uses the composite mechanics in ICAN to simulate reinforced-concrete sections that have a typical infrastructure as well as selected reinforced-concrete structures.

Structural sections were modeled by a number of layers through the thickness, where some layers represented concrete and others represented the composite. The reinforced-concrete structures were represented with finite elements, where the element stiffness parameters were from structural sections represented by composite mechanics. The load-carrying capability of the structure was determined by progressive structural fracture embedded in Composite Durability Structural Analysis (CODSTRAN). Results show that the addition of a relatively small composite laminate thickness resulted in up to 40 percent improvement in the damage and overload resistance of structural sections and up to 3 times improvement of the selected composite-enhanced structures (i.e., arches and domes).

Researchers at Glenn illustrated the new method by using composites to improve the damage resistance of a reinforced-concrete dome section, as shown in this diagram. The section configuration is illustrated in the diagram on the next page. The results obtained for different composite enhancements are shown in the graph on the next page: placement of the composite enhancement at the top of the dome improved the dome's damage resistance about 2½ times. Reference 1 describes this work in greater detail.

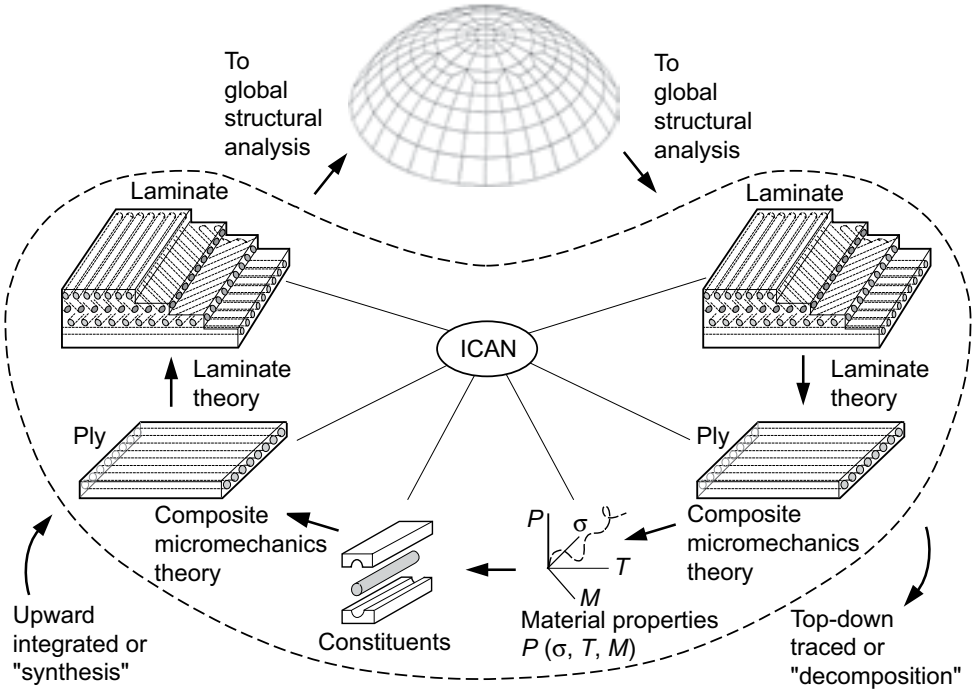


*CODSTRAN simulation cycle.*

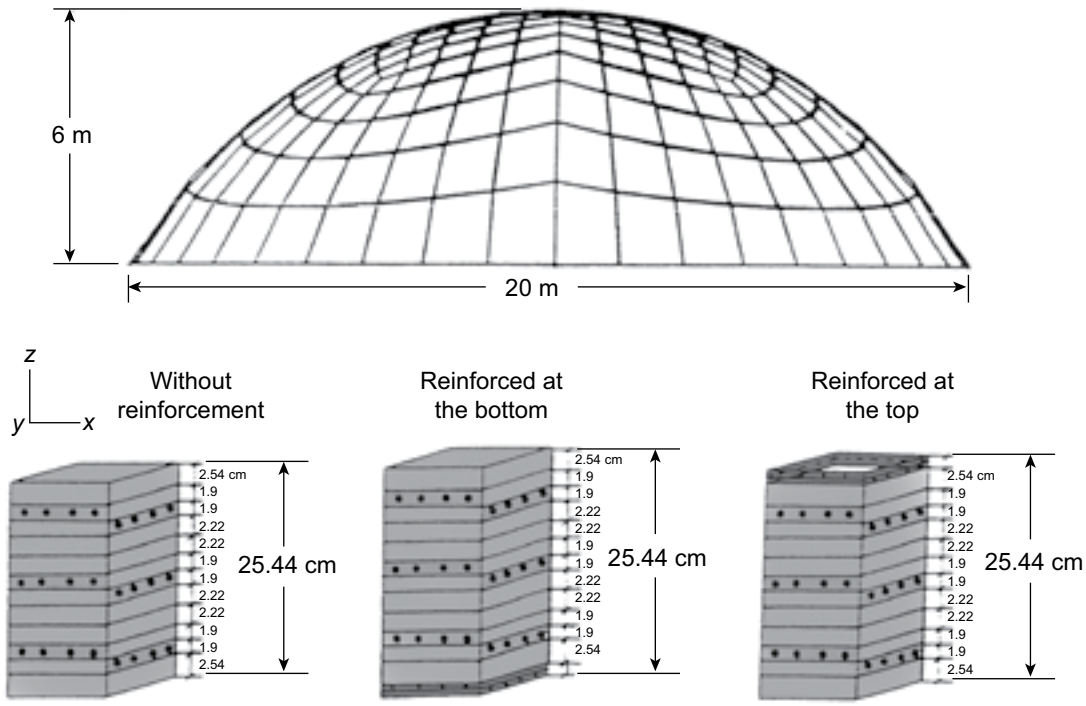


*Reinforced-concrete dome geometry and structural sections.*

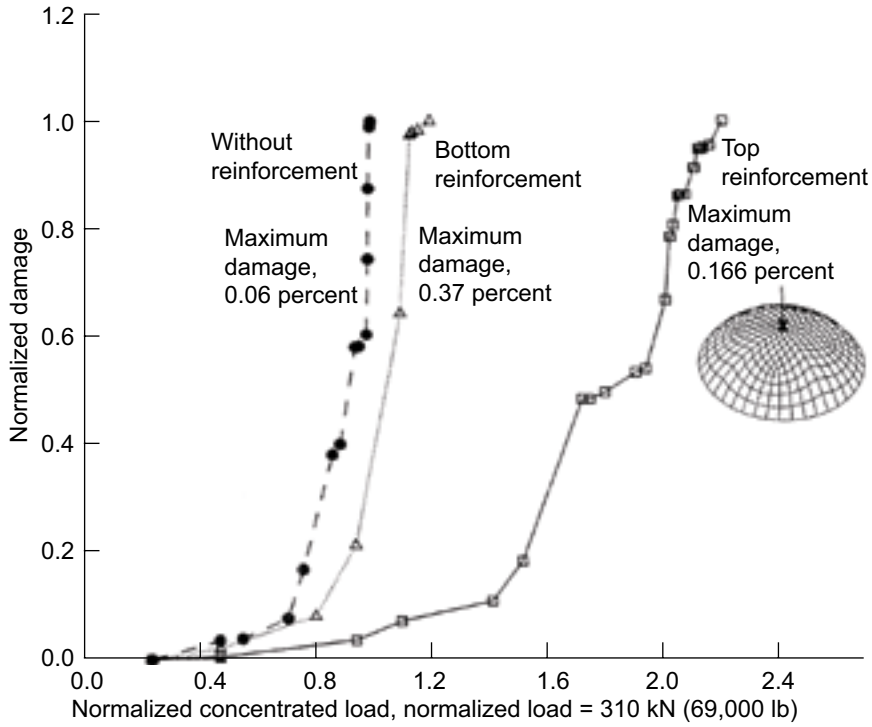


*Effect of applied concentrated load on the damage to a reinforced-concrete dome.*

**Reference**

1. Chamis, Christos C.; and Gotsis, Pascal K.: Application of Composite Mechanics to Composites Enhanced Concrete Structures. NASA/TM—2006-214038, 2006. http://gltrs.grc.nasa.gov/Citations.aspx?id=250

**Glenn contact:**
Dr. Christos C. Chamis, 216–433–3252, Christos.C.Chamis@nasa.gov

**Author:**
Dr. Christos C. Chamis

**Headquarters program office:**
Aeronautics Research Mission Directorate

**Programs/projects:**
Subsonic Fixed Wing, Research and Technology Tools Enhancement

## Steerable Space-Fed Lens Array Developed for Low-Cost Adaptive Ground Station Applications

The NASA Glenn Research Center, in collaboration with the University of Colorado, Boulder, has developed a 952-element Space-Fed Lens Array (SFLA) for ground stations to use to communicate with low-Earth-orbiting satellites. The SFLA is an alternative to a phased-array antenna that replaces large numbers of expensive solid-state phase shifters with a single spatial feed network. The SFLA has lower cost in comparison to a phased array at the expense of total volume and complete beam continuity. These tradeoff parameters are not important for ground station applications and can be exploited to lower costs.

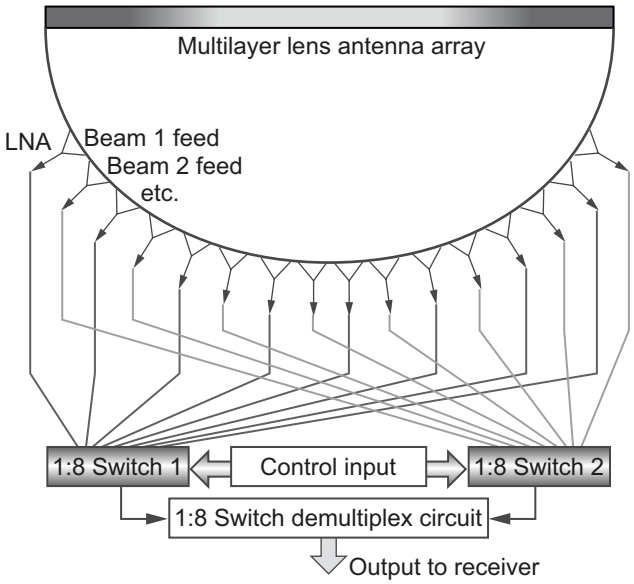


*SFLA and feed-switching connections for a 16-beam feed network.*

The basic SFLA scanning architecture is shown in the preceding diagram for the receiving mode only. The SFLA consists of three antenna arrays: the receiving-side array, the feed-side array, and the array of feed elements. The pairs of antenna elements on the two former arrays are connected through appropriate true-time delay lines. The front-end array (receiving-side) determines the beamwidth as in standard antenna array theory. The multiple beams are obtained with multiple spatial feeds. When a plane wave is incident from some direction (azimuth and elevation), the receive array antennas sample the wave front at approximately the Nyquist criterion, depending on the antenna element radiation pattern. Each sample is then appropriately time-delayed and reradiated by a second array of antennas, focusing the power onto the focal surface. The field is now sampled on the focal surface so that each feed antenna element preferentially receives incoming waves from a single direction. Thus, an SFLA can be viewed as a hardware discrete Fourier transform of an arbitrary linear combination of plane waves onto a focal surface. The SFLA can be implemented using standard printed-circuit-board technology and can incorporate power amplifiers for the transmit mode or low-noise amplifiers (LNAs) for the receive mode. The polarization can be chosen to be different on the two sides of the array for isolation purposes and for design simplicity. The LNAs also can be placed after the feed antennas, since the spatial feed does not contribute resistive loss.

The SFLA is a low-cost approach using multiple relatively small SFLAs to replace a 10- to 11-m reflector and to achieve beam scanning nonmechanically. The photographs below show the 952-element SFLA, which was designed to

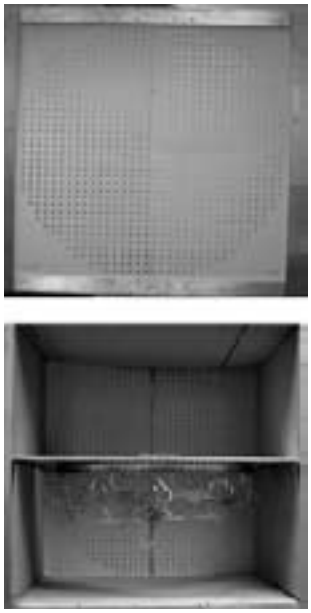

*The 952-element SFLA. Top: Receiving-side array. Bottom: Feed-side array, array feed elements, and switching network*

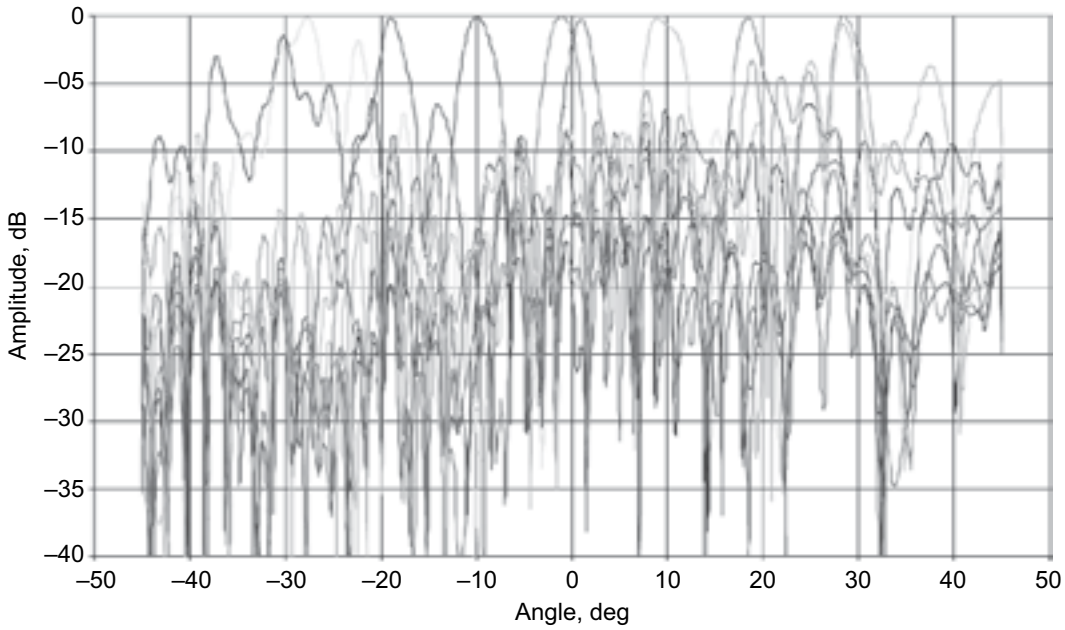


*Measured radiation patterns along the scan plane for various beam positions.*

operate at 8.386 GHz with circular polarization on the receiving side and linear polarization on the feed side. The elements in the array are patch antennas, and there are two dielectric substrates with metallized vias[1] interconnecting the corresponding antenna elements of the two arrays. The feed array, which is located along a focal arc, has 32 feed elements, with each feed receiving a beam from a different direction. In this architecture, scanning is accomplished by switching between independent beams, thus eliminating a need for microwave phase shifters. High-speed switches are not needed because the pass of a satellite allows many seconds per beam.

The SFLA was characterized using Glenn's planar Near-Field Antenna Facility. The final graph shows the radiation patterns along the scan plane for different beam positions. The scan loss was found to have a dependence with the scan angle $\theta$ of approximately cos $\theta$. For the prototype demonstration, the beam was scanned only in one plane (elevation), and scanning in the other plane (azimuth) was accomplished mechanically. In general, scanning in the elevation plane is sufficient to track a satellite if it does not drift too far away from its orbital plane; however, a two-dimensional scan can be accomplished with a two-dimensional feed array over the focal plane. Our results demonstrate the feasibility of the SFLA for the aforementioned application.

**Glenn contacts:**
Dr. Richard Q. Lee, 216–433–3489, Richard.Q.Lee@nasa.gov

Dr. Félix A. Miranda, 216–433–6589, Felix.A.Miranda@nasa.gov

**University of Colorado contacts:**
Zoya Popovic, 303–492–0374, zoya.popovic@colorado.edu

Sébastien Rondineau, 303–492–8719, sebastien.rondineau@colorado.edu

**Authors:**
Dr. Richard Q. Lee, Zoya Popovic, and Sébastien Rondineau

**Headquarters program office:**
Earth-Sun System Technology Office

**Programs/projects:**
Ground Network

[1]Vertical interconnects in a printed circuit.

# Small-Size Active Antenna Developed That Integrates the Oscillator and the Radiating Element

Active integrated antennas (AIAs), which integrate one or more active solid-state devices and circuits within an antenna element, are highly relevant to NASA applications. They could be the foundation for highly efficient, beam-steerable phased-array antenna systems that would be tailored to meet a wide range of mission requirements. For optimal direct-current-to-radiofrequency (RF) efficiency, the active solid-state device is a transistor mounted close to or directly into the radiating structure. This minimizes the conductor losses that are inherent in circuits where the active devices and radiating elements are spatially separated. In an AIA, there is no distinction between the microwave circuit and the antenna—the antenna serves both as a load and a radiator for the active device—and the integrated solid-state device may serve as a local oscillator for a self-oscillating antenna.

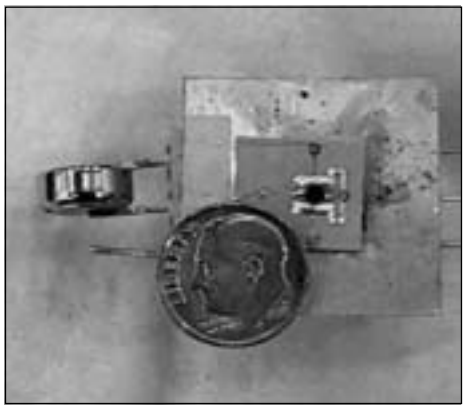

*AIA radiating element powered by a single 1.5-V battery.*

To demonstrate the concept, researchers at the NASA Glenn Research Center fabricated and tested AIA elements on a high-dielectric-constant ($\varepsilon_r$ = 10.2) microwave laminate that was 0.635 mm thick. A gallium arsenide (GaAs) transistor was mounted inside the radiating element, and the entire device occupied a 5- by 6-mm$^2$ area (see the photograph). The AIA demonstrated very stable oscillations and excellent radiation patterns at the X-band (8- to 12-GHz) frequencies.

Comparison between simulated and experimental data confirmed that the oscillation frequency was controlled by the length of the feedback loop between the drain and gate terminals and that radiated power and radiation efficiency were maximized when the feedback length was one wavelength long. With the device biased solely with a 1.5-V battery and with the gate terminal open, the effective isotropic radiated power (EIRP) was 13.2 mW. The RF power generated by the AIA was 2.8 mW, and the antenna directivity was 4.72. The RF power spectrum of the AIA at these bias conditions is shown in the graph to the left. When the AIA was biased for higher power levels, with the drain and gate voltages at 3.5 and –0.6 V, respectively, the EIRP increased to 52.2 mW. Under these bias conditions, the RF power generated by the AIA was 9.4 mW, and the antenna directivity was 5.55.

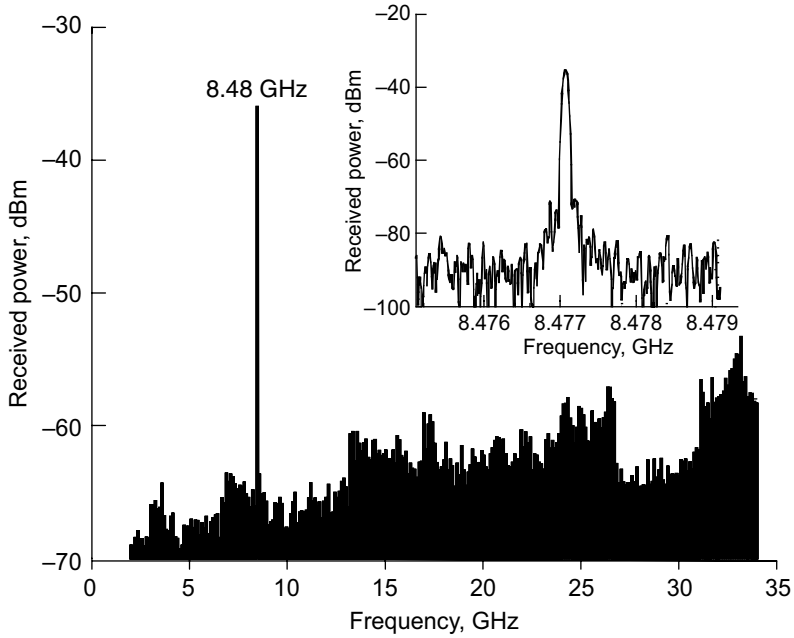


*Radiated power from single radiating antenna element, with the detector located 132 cm away from the AIA. The transistor was biased without a gate connection, with a drain voltage of 1.5 V, an open gate voltage, and a drain current of 17.7 mA. Data taken over a wide frequency range show that the fundamental signal at 8.48 GHz dominated the spectrum. For the inset, the frequency was 8.477 GHz and the maximum power was –35.4 dBm.*

The electric and magnetic field radiation patterns are shown on the left and right graphs, respectively, in the figure on the next page. The cross-polarization levels in the electric field scan did not exceed –10 dB. At broadside (0°), there was sharp null in the cross-polarization power level, indicating that the circuit was balanced and symmetric and that the pattern was free of perturbations that could cause higher order modes to propagate. In the magnetic field scan, cross-polarization levels did not exceed –15 dB. The radiation pattern at higher

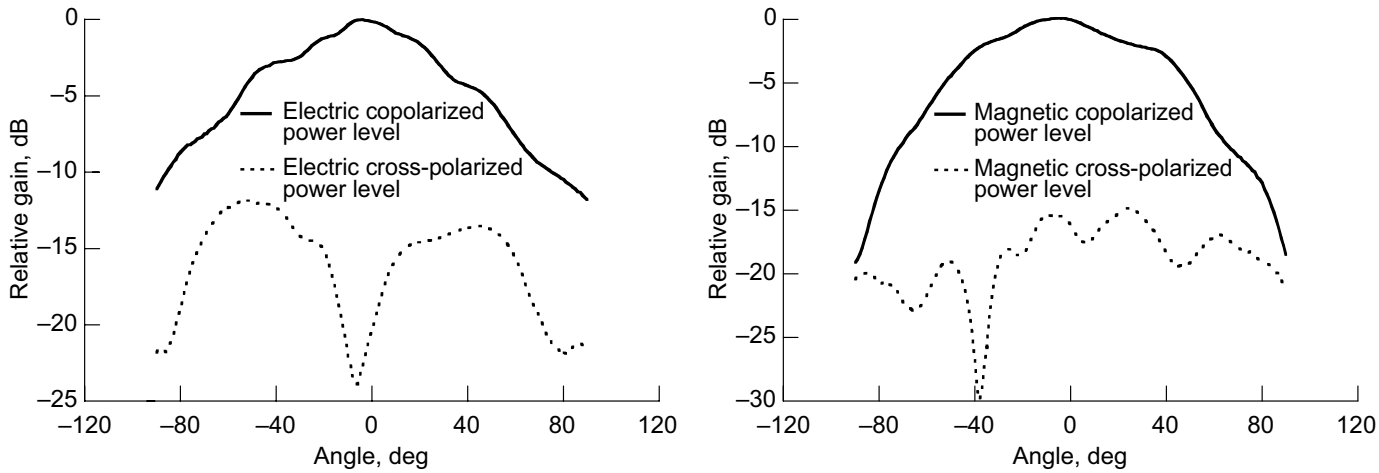


*Field data from a single AIA element. Power was supplied via a single 1.5-V battery connected between the source and drain electrodes, the gate terminal was open, and the EIRP of the AIA was 13.2 mW. Frequency, 8,48 GHz; maximum power, –46.28 dBm. Left: Electric field data. Right: Magnetic field data.*

bias levels was identical to that shown in the graph on the preceding page. The results obtained thus far suggest that this design can be scaled to multielement phased-array antennas, and we expect that these AIAs will serve as the foundation for phased-array antennas, wherein the active and passive circuitry is fully integrated onto a single substrate.

**Glenn contacts:**

Dr. Richard Q. Lee, 216–433–3489, Richard.Q.Lee@nasa.gov

Dr. Robert R. Romanofsky, 216–433–3507, Robert.R.Romanofsky@nasa.gov

Dr. Félix A. Miranda, 216–433–6589, Felix.A.Miranda.nasa.gov

**Authors:**

Dr. Carl H. Mueller, Dr. Carol L. Kory, and Kevin M. Lambert

**Programs/projects:**

Space Communications, Glenn Independent Research and Development

## Parabolic Equation Extended to the Analysis of Wide-Angle Scattering in Random Propagation Media

For the last 36 years, the analysis of electromagnetic wave propagation through random media, such as atmospheric turbulence, has been aided by the parabolic equation method. The resulting theory has been applied to everything from laser beam propagation to image propagation within the Earth's atmosphere and ocean as well as in other planetary atmospheres. Here, the general stochastic scalar Helmholtz wave equation is reduced to a corresponding stochastic parabolic differential equation for the random electric field. From this equation, various statistical moments of the propagating wave field can be derived.

This approximate treatment is applicable so long as the wavelength $\lambda$ of the electromagnetic wave is small in comparison to the characteristic size $l_0$ of the random inhomogeneity of the permittivity field of the medium. In this case, the scattered radiation from the inhomogeneities is concentrated in a narrow cone with a vertex angle $\theta \sim \lambda / l_0 << 1$. Hence, the scattered waves propagate in essentially the same direction as the primary wave. This defines the small scattering angle scenario of wave propagation to which the parabolic equation applies. The most important statistical quantity derived from the parabolic equation is the mutual coherence function (MCF), which is defined by the ensemble average of the product of the electric field with its complex conjugate in a plane transverse to the direction of propagation. This is an important

quantity for describing the degradation of a laser beam or an image propagating through a random medium.

The use of the parabolic equation comes into question, however, when $\lambda$ is on the order of $l_0$ and the scattering angle becomes large. This situation is encountered in the propagation of millimeter waves through the Earth's atmosphere or through sandstorms on the surface of Mars. Consequently, at the NASA Glenn Research Center, a complete mathematical analysis of the basis of the parabolic equation was made to extend its applicability to wide-scattering-angle situations in which $\theta \sim \lambda/l_0 \sim 1$. An operator form of the extended parabolic equation was written on which operator techniques were employed in the solution for a corresponding MCF. This theoretical exercise not only extended the parabolic equation to wide scattering angles, but also revealed the multiple scattering structure of the Green functions that enter into the theory. This resulted in an extended parabolic equation that can describe wide-angle scattering and that, unlike the traditional treatment, can consider longitudinal variations of the MCF of a wave field along the direction of propagation. The latter capability is due to the incorporation of higher order scattering processes into the theory.

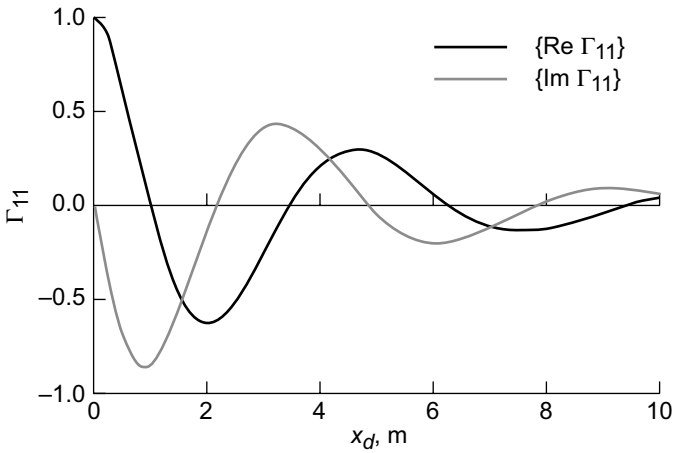


*$\Gamma_{11} = (x_c, x_d, 0)$ versus $x_d$ (in meters) for $\lambda = 0.63$ μm, $l_0 = 1.0$ mm, $x_c = 5$ km, and $C_n^2 = 10^{-12}$ m$^{-2/3}$.*

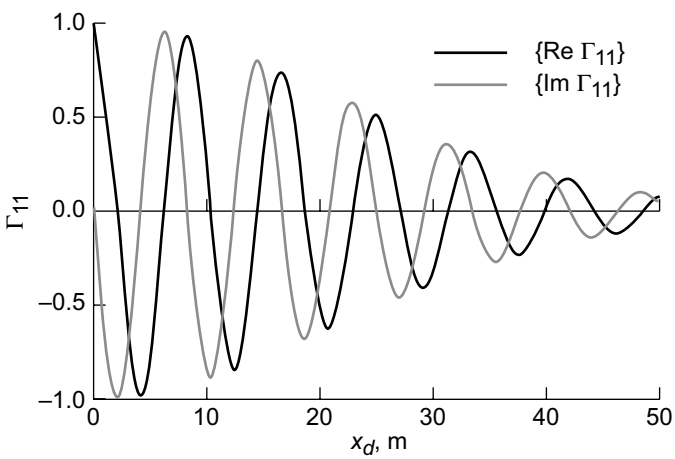


*$\Gamma_{11} = (x_c, x_d, 0)$ versus $x_d$ (in meters) for $\lambda = 0.63$ μm, $l_0 = 1.0$ cm, $x_c = 5$ km, and $C_n^2 = 10^{-12}$ m$^{-2/3}$.*

The figures show the behavior of the on-axis longitudinal MCF, $\Gamma_{11}(x_c, x_d, 0)$, as a function of longitudinal separation, $x_d$, for a typical Earth atmosphere propagation scenario for a wave source of wavelength $\lambda = 0.63$ μm (red light from, e.g., a helium-neon laser), placed $x_c = 5$ km from the measurement point, for two values of inner scale size (i.e., the smallest inhomogeneity of the turbulent fluctuations): $l_0 = 1.0$ mm and $l_0 = 1.0$ cm, respectively. In both figures, the structure constant of refractive index fluctuations is $C_n^2 = 1\times10^{-12}$ m$^{-2/3}$. Both the real and imaginary values of the MCF are displayed. The oscillatory behavior of the longitudinal MCF is due simply to the movement of the difference coordinate through the Fresnel zones intersecting the longitudinal axis. The oscillations decay because of the loss of longitudinal coherence as the difference coordinate becomes larger.

The characteristic behavior of the longitudinal MCF suggests a potential remote-sensing technique for atmospheric turbulence whereby the inner scales of turbulence can be ascertained on the basis of the spatial frequency of the longitudinal variations. Other results from this study are (1) a complete expression for the transverse and longitudinal MCF for any random medium for which the condition $\lambda \leq l_0$ prevails and (2) a verification of the fact that the classical parabolic equation is applicable for use in a medium characterized by the Kolmogorov spectrum of fluctuations even though $\lambda \sim l_0$. This latter fact is due to the Kolmogorov spectral density level near the inner scale of turbulence being much smaller than it is at the larger scale sizes at which most of the narrow-angle scattering occurs.

**Bibliography**

Manning, Robert M.: Application of an Extended Parabolic Equation to the Calculation of the Mean Field and the Transverse and Longitudinal Mutual Coherence Functions Within Atmospheric Turbulence. NASA/TM—2005-213841, 2005. http://gltrs.grc.nasa.gov/cgi-bin/GLTRS/browse.pl?2005/TM-2005-213841.html

Manning, Robert M.: An Extended Parabolic Equation and Its Application to the Calculation of Transverse and Longitudinal Mutual Coherence Functions in Atmospheric Turbulence. Waves in Random and Complex Media, vol. 15, no. 3, 2005, pp. 405–416.

**Glenn contact:**
Dr. Robert M. Manning, 216–433–6750, Robert.M.Manning@nasa.gov

**Author:**
Dr. Robert M. Manning

**Headquarters program office:**
Space Communications

**Programs/projects:**
Exploration Systems Research and Technology

## Interspacecraft Communications and Ranging System Developed and Demonstrated

The Geodetic Autonomous Inter-Spacecraft Network (GAIN) program, which builds on the successes of two NASA-sponsored programs, has produced a miniaturized, flexible, and autonomous interspacecraft communications and ranging system that meets the constraints of mass, size, power, cost, simplicity, flexibility, and autonomy demanded by distributed systems of small spacecraft. GAIN's operational concept for communications and ranging was developed and validated under NASA Goddard Space Flight Center's Magnetospheric Multi-Scale Mission, Inter-Satellite Ranging and Alarm System program. GAIN's transmitter and receiver designs are based on those developed under NASA's University-class Explorer (UNEX) program for the Cooperative Astrophysics and Technology Satellite (CATSAT).

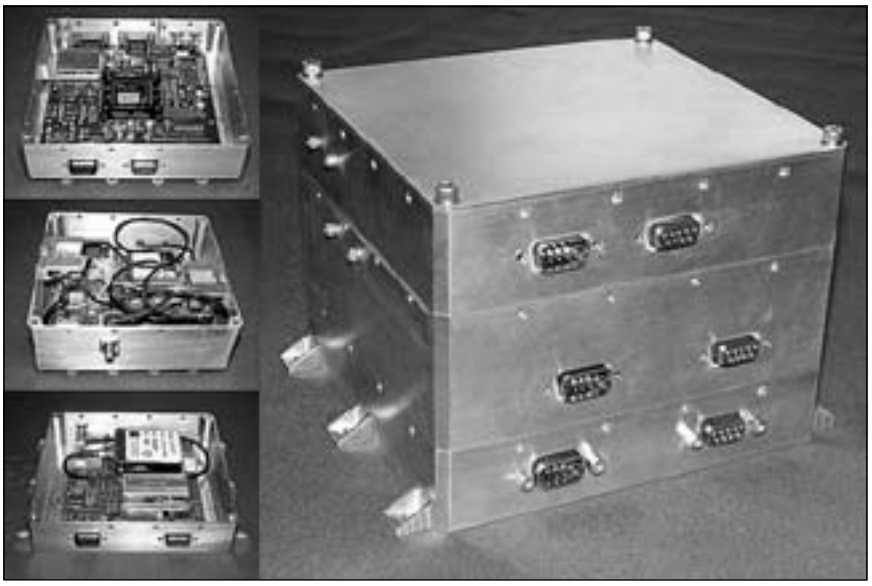

*GAIN electronics box (communications and ranging electronics, transmitter, and receiver).*

Two GAIN radios were developed and demonstrated, and were delivered (in 2006) to the NASA Glenn Research Center. Each radio consists of a laptop computer and an electronics box. The computer functions as the user interface and as the main processing unit. The electronics box consists of three boards: the communications and ranging board, the transmitter board, and the receiver board. These boards are 164 $cm^2$ each, with a total combined weight of 1429 g (including the enclosure).

The GAIN system enables packet-based communications between members of a satellite constellation at data rates of 125 bps, 1 kbps, 8 kbps, or 32 kbps. The operating frequency is S-Band (2039.65 MHz). In addition, the GAIN system enables range measurements between all spacecraft pairs in the constellation with an accuracy of 1 percent (or better) for distances of 100 to 6400 km and with an accuracy of 1 km (or better) for distances from 10 to 100 km. Extensive testing in both wired and wireless configurations verified proper operation of the radios.

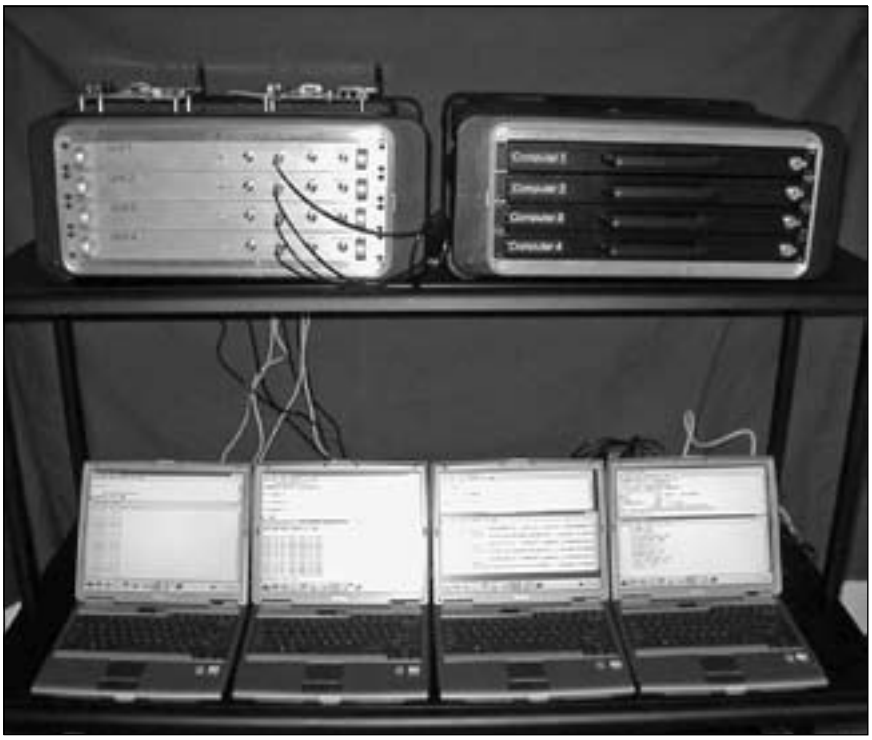

*Testing of GAIN radios (wired configuration).*

The GAIN radios can be upgraded or modified easily since much of the functionality is defined in software residing on the laptop computer. One example is the application of the GAIN radios to a robotics demonstration. For this demonstration, Glenn personnel were able to quickly expand the radio capabilities to provide an integrated command and ranging channel. The GAIN program was executed by SpaceWorks, Inc., under NASA contract NAS3–03090.

**Glenn contact:**
Thomas P. Bizon, 216–433–8121, Thomas.P.Bizon@nasa.gov

**Author:**
Thomas P. Bizon

**Headquarters program office:**
Exploration Systems Mission DIrectorate

**Programs/projects:**
Computing, Information, and Communications Technology Program, Space Communications Project

## Low-Power, Silicon-on-Insulator, Complementary Metal-Oxide Semiconductor Receiver Chip Developed for Planetary Robotic and Distributed Sensor Network Applications

In addressing NASA's planetary robotic and distributed sensor network needs, a low-power, silicon-on-insulator (SOI) complementary metal-oxide semiconductor (CMOS) transceiver chip has been successfully designed, fabricated, and demonstrated for use in energy-efficient, reliable, miniaturized wireless radiofrequency (RF) communications systems. The receiver supports a wide range of data rates (0.1 to 100 kilobits per second, kbps). A team led by North Carolina A&T State University, with coinvestigators at North Carolina State University and the Jet Propulsion Laboratory, worked closely with the NASA Glenn Research Center in accomplishing this effort.

Future Mars missions will require low-power, radiation-hardened ultra-high-frequency (UHF) receivers for orbiter-lander communication. To meet these requirements, Honeywell's 0.35-μm SOI CMOS process was chosen for the design and implementation of a UHF single-chip receiver (see the block diagram). The SOI CMOS process provides high-quality passives such as spiral inductors, resistors, and capacitors. The buried oxide layer and semi-insulating substrate provide excellent isolation between digital and analog circuit blocks (mixed-signal circuits). The device-to-device isolation is similar to that of gallium arsenide but is achievable at a lower cost.

A prototype single-chip receiver (see the photomicrograph) was designed at a frequency of 435 MHz with a maximum gain measured at 85 dB, a cascaded noise figure of 5.2 dB, and a current dissipation of 21 mA at 3 V. The UHF band

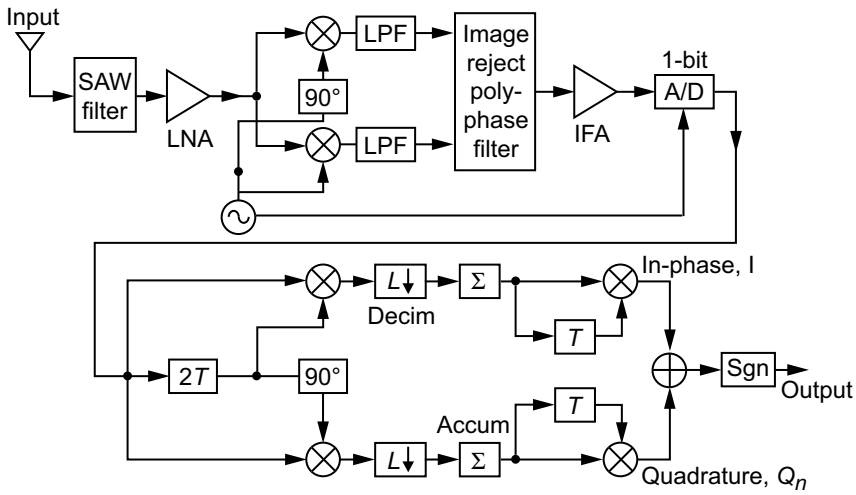


*Low-power UHF SOI CMOS receiver circuit. SAW, surface acoustic wave; LNA, low-noise amplifier; LPF, low-pass filter; IFA, intermediate frequency amplifier; A/D, analog-to-digital converter; L, decimation rate; T, symbol period; sgn, signum function (sgn = 1 when >0, sgn = 0 when ≤ 0); $Q_n$, quadrature signal at the output of the accumulator; Decim, decimator; Accum, accumulator.*

was selected because it has been designated as a forward-link spectrum allocation from a Mars relay satellite to surface and orbital user assets. This architecture is particularly good for applications in the presence of strong random Doppler frequency shift because the receiver circuit is targeted to address needs for an orbiter-lander communication system around Mars. For data rates on the order of 100 kbps or less, orbital analysis indicates that the Doppler shift is significant enough to require compensation. The double-differential phase-shift-keying (DDPSK) receiver circuit was invariant to frequency offset because of the use of a double-differential technique. This resulted in a simplified circuit implementation, thereby saving power.

A number of circuits and components were designed and tested including low-noise amplifiers; double-balanced in-phase and quadrature mixers; image reject intermediate-frequency bandpass active filters; DDPSK baseband circuits, a bandgap reference circuit; voltage-controlled oscillators at 435, 870, and 1740 MHz; and phase-lock loop circuits to generate quadrature local oscillator signals. These designs are now available for use as reference circuits for future low-power transceiver implementations. Twelve receiver chips in 88-pin carriers were completed in the final chip development effort. The low-power, SOI CMOS transceiver chip was successfully developed and tested under a grant to North Carolina A&T State University in Greensboro, North Carolina, and managed by Glenn.

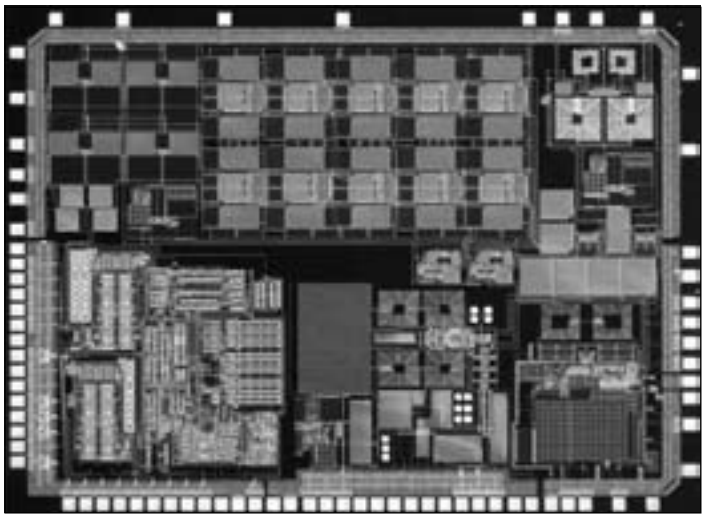

*Final prototype receiver chip.*

**Bibliography**

Dogan, Numan, S.: Advanced Low-Power Silicon on Insulator (SOI) Complimentary Metal Oxide Silicon (CMOS) Transceiver for Distributed Sensor Networks; Progress Report. NASA Grant Number NAG3–2584, 2005. Available from the NASA Center for Aerospace Information.

**Glenn contact:**
Gene Fujikawa, 216–433–3495, Gene.Fujikawa@nasa.gov

**North Carolina A&T State University contact:**
Dr. Numan S. Dogan, 336–334–7348, ext. 223, dogan@ncat.edu

**Authors:**
Dr. Numan S. Dogan and Gene Fujikawa

**Headquarters program office:**
Exploration Systems Mission Directorate

**Programs/projects:**
Computing, Information, and Communications Technology Program, Space Communications Project

# Space Telecommunications Radio System Software Architecture Concepts Investigated

This year, the Space Telecommunications Radio System (STRS) project investigated various software-defined radio architectures suitable for NASA's missions subject to the constraints of the space environment. The STRS architecture was developed at the NASA Glenn Research Center and includes both use cases and Unified Modeling Language (UML; see http://www.uml.org) diagrams. The STRS architecture (see the following UML figure) separates the STRS operating environment (OE) from its various waveform applications and abstracts any specialized hardware to limit its effect on the operating environment. The STRS OE enables the startup, operation, and teardown of the waveform applications. The waveform applications are implemented in firmware and software to transform information to or from signals that are transmitted over the air. Separating functionality within the radio promotes waveform portability and reuse.

The processing capability of the software-defined radio enables the radio to implement functionality previously limited to the flight computer. The command and control subsystem validates commands from the flight computer and translates them to appropriate method calls.

When a waveform function becomes a required part of the radio, the waveform is transitioned to a service by being configured as part of the infrastructure. Examples of functions likely to become part of the STRS infrastructure are the Global Positioning System (GPS) or ranging, navigation, and dynamic discovery service.

Use cases capture the requirements of a system by describing how the system should interact with the users or other systems (the actors) to achieve a specific goal. The diagram on the next page shows groupings of the use cases and how the actors are involved. Use cases are textual and contain a description, information about the external actors, related use cases, preconditions, a triggering event, a resulting event, postconditions, and a sequential list of the steps necessary to accomplish the desired result and alternatives.

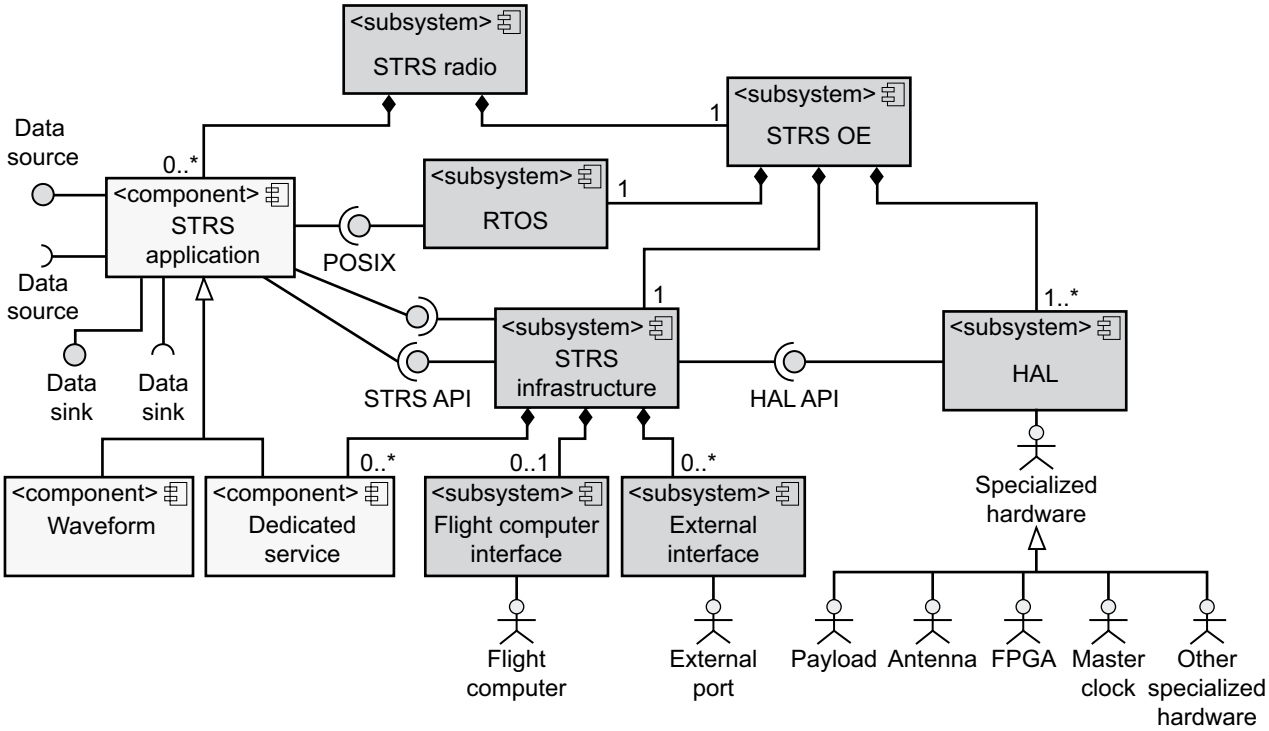


*STRS software architecture. POSIX, Portable Operating System Interface; RTOS, real-time operating system; HAL, Hardware Abstraction Layer; API, application programming interface; FPGA, field-programmable gate array. (See http://www.uml.org for a detailed explanation of the notation in this figure.)*

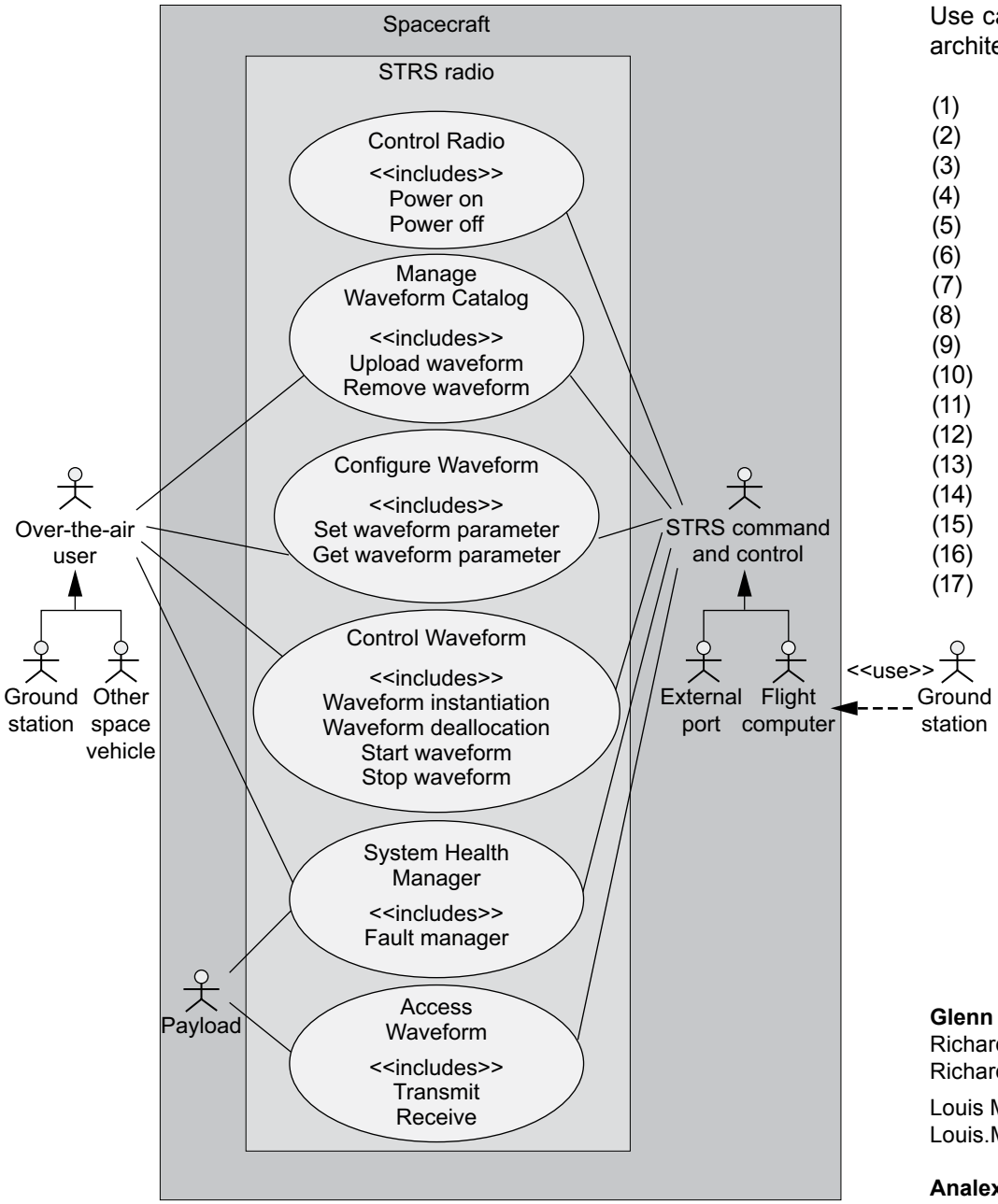


*Top-level use case diagram.*

The users are shown as stick figures both inside and outside of the spacecraft system boundary. The over-the-air users communicate with or control the radio by means of a communication channel realized by the STRS radio itself. The STRS command-and-control users communicate with the radio via an onboard interface. The ground station can configure a waveform over the air directly or can configure a waveform indirectly by sending the command to the onboard flight computer by means of another radio. This is why the ground station is shown twice. The interaction of the ground station and the flight computer shown on the right indicates that the ground station uses the flight computer to command the STRS radio.

Use cases identified for the STRS architecture follow:

(1) Power on
(2) Power off
(3) Waveform upload
(4) STRS OE upload
(5) Waveform instantiation
(6) Waveform start
(7) Processor resource sharing
(8) Set waveform parameter
(9) Get waveform parameter
(10) Transmit a packet
(11) Receive a packet
(12) Waveform stop
(13) Waveform deallocate
(14) Waveform abort
(15) Waveform remove
(16) Fault management
(17) Commanded built-in test

**Glenn contacts:**
Richard C. Reinhart, 216–433–6588, Richard.C.Reinhart@nasa.gov

Louis M. Handler, 216–433–8286, Louis.M.Handler@nasa.gov

**Analex contact:**
Charles S. Hall, 216–433–3036, Charles.S.Hall@nasa.gov

**Authors:**
Louis M. Handler, Tammy M. Blaser, Janette C. Briones, and Charles S. Hall

**Headquarters program office:**
Space Operations Mission Directorate

**Programs/projects:**
Space Communications and Data Systems Project

# Space Network Router Developed

The NASA Glenn Research Center, through a contract with General Dynamics C4 Systems, Spectrum Astro Space Systems, has developed a radiation-tolerant, single-board, four-port 10/100-Mbps Ethernet router as an enabling technology for future spacecraft architectures. Under a previous contract, General Dynamics C4 Systems (previously Spectrum Astro, Inc.), developed other space network hardware, including a 10/100 Mbps-Ethernet network interface controller (NIC) and a four-port 100-Mbps Ethernet hub. These space network hardware devices utilize Open Systems Interconnection (OSI) standards for space-based communications applications. The OSI standard is a well-recognized layered reference model that specifies how data should be sent node to node in a communications network. For some time, the terrestrial industry has recognized the benefits and flexibility of targeting hardware developments around OSI standards, in particular the commonly used Transmission Control Protocol/Internet Protocol (TCP/IP). The Internet would not be what it is today without OSI. The space community can leverage these standards and technologies, developed for ground networks, to reduce flight mission schedule, cost, system complexity, mass, and power requirements. In the future, even lower costs and streamlined options could result from using modular, commercial-off-the-shelf hardware in test and flight hardware.

A space router is an enabling or bridge technology for implementing IP addressing over a communications system in space. Space communications architectures differ considerably from ground networks in that many entities typically share a ground network. In ground applications, data packet collisions and congestion are more of a problem, and the hardware and software techniques used to mitigate these are more important. Space communications links are usually controlled by a single entity, such as a ground station linking to a single spacecraft asset, or cross communications links between spacecraft. Links in space usually do not fail because of data packet collisions or congestion but because of poor signal quality created by insufficient transmit power or available bandwidth from the ground link or cross link. Glenn has been working on developing versions of TCP that are tuned specifically for the parameters that are significant on space links.

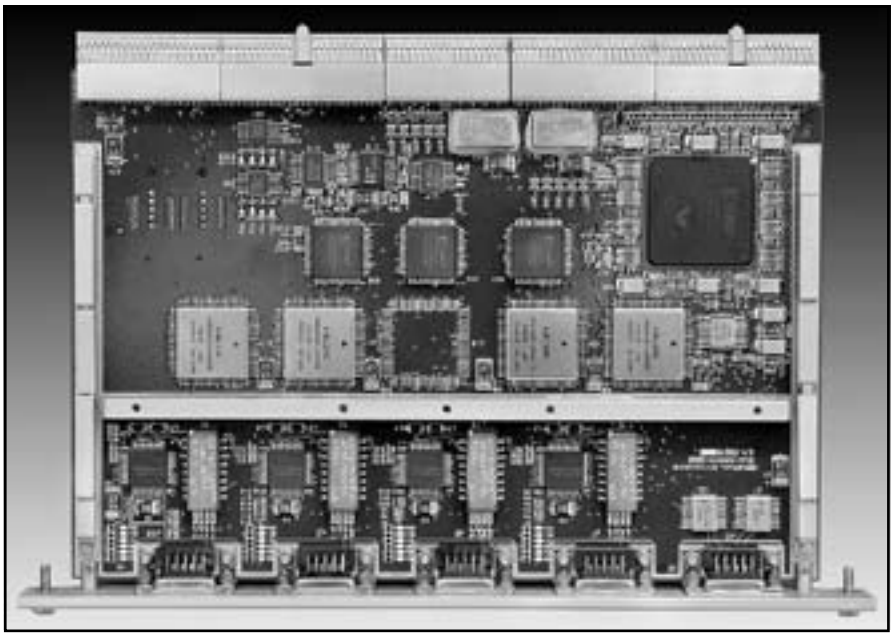

*Space network router board.*

Four aggregate key areas of router design were analyzed through trade-off studies: (1) architectures, (2) protocols, (3) data processing, and (4) control and network management. On the basis of the results of these studies, a radiation-tolerant 6U factor (six rack units, or 10.5 in. high), compact Peripheral Component Interconnect (cPCI) space network router (see the photograph) was developed at General Dynamics C4 Systems through a contract managed at Glenn. The board was designed to flight specifications including thermal and mechanical standards, according to flight manufacturing procedures.

The space network router can support various architecture configurations suitable for a spacecraft with a typical downlink connection. For data processing, the router used a field-programmable gate array (FPGA) design with an embedded 32-bit reduced instruction set computer (RISC) processor. The router has four 10/100-Mbps Ethernet ports and expansion capability for additional Ethernet, serial (HDLC/RS–422), SpaceWire, FireWire, or Universal Serial Bus (USB) ports. The routing protocol implemented was Routing Information Protocol (RIP); however, for future considerations and scalability, the Open Shortest Path First (OSPF) protocol was recommended. The space router was implemented with a console port with an RS–422 standard

interface that could interface to other spacecraft serial interfaces for control and configuration while in flight.

In conclusion, the space router is an enabling or bridge technology that will be useful in a variety of space communications applications including point-to-point links, onboard instrument and asset control, IP-compliant operation, and spacecraft command and data handling. It represents one piece of the architecture required to enable a principal investigator on a terrestrial Internet site to seamlessly interact with spacecraft assets in near real time.

**Find out more about the research of Glenn's Communications Division:**
http://ctd.grc.nasa.gov

**Glenn contact:**
Robert E. Jones, 216–433–3457, Robert.E.Jones@nasa.gov

**Authors:**
Robert E. Jones, James Joseph, and Jennifer Lazbin

**Headquarters program office:**
Earth Science Technology Office

**Programs/projects:**
Advanced Information Systems Technology, Constellation

## Software-Defined Radio Architecture Framework Released for Space-Based Radios

The NASA Glenn Research Center has released an open architecture framework for space-based software-defined radios. The Space Telecommunication Radio System (STRS) architecture description and standard provides a standard framework for future NASA space radios with greater degrees of interoperability and flexibility to meet new mission requirements. The goal is to improve capability by using this common standard across NASA missions and services. An open architecture reduces system development and operation costs by promoting and enabling multiple vendor solutions and interoperability between independent hardware and software technologies. The architecture supports existing communications needs and capabilities while providing a path to more capable, advanced waveform development and mission concepts. It provides an effective approach to designing and utilizing communications systems; radios are designed, managed, and operated through the adoption of common standards.

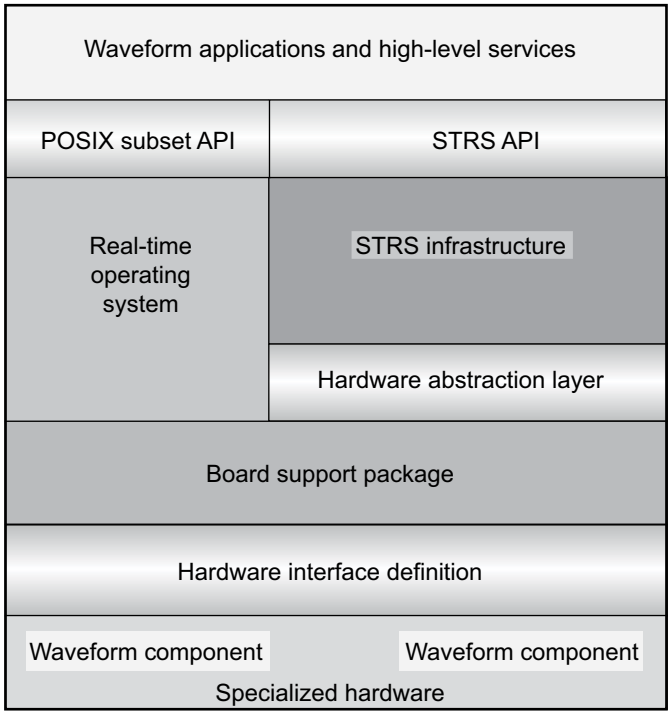


*STRS software architecture. API, application programming interface; POSIX, Portable Operating System Interface.*

The architecture effort defined the components and rule set framework for both software and hardware architectures. A key concept was the reuse of previously developed hardware and software components. The ability to reuse components was accomplished by defining the various hardware and software interfaces and providing additional layers to the architecture to abstract the software from the platform hardware. Because these interfaces are specified consistently and published as part of the architecture specification, and because rules are provided for each component, the various modules can be replaced and updated with a minimum amount of changes.

The software architecture provides a framework for the resulting software components. It describes the functions of each software component, the interfaces between components, and the services used to communicate with the underlying hardware. The layer between the waveform application and the operating environment is a key concept for the STRS architecture. Development of this layer required a careful balance to keep the operating environment from overwhelming the processing requirements of the radio, especially for the space environment. Minimizing the required resources of the operating environment (e.g., power and mass) for the constrained space case is important because the radiation-hardened electronics used in the radios will lag at least a generation or two in processing capability from commercial equivalents. The approach was to identify the core interfaces to provide application software (e.g., waveforms) development flexibility and portability by standardizing the interface provided by the radio processing platform through standard services.

The architecture provides an initial description of the functionality and interfaces of the software-defined radio system. Instead of a static description, it provides a framework that will evolve over time as technologies mature. This year, Glenn released the STRS Architecture Description Document, and it was reviewed by experts from different NASA centers. An industry day was held to solicit comments from those developing and/or integrating radios for NASA, the Department of Defense, and commercial space applications. These comments are being incorporated into the architecture, and future work will improve the architecture so that it can be recommended as an Agency standard.


**Bibliography**

Reinhart, Richard C.; Farrington, Allen; and Israel, Dave: Space Telecommunications Radio System STRS Open Architecture Description, Rev. 1.0, Space Operations Mission Directorate, Apr. 2006. Available from NASA Glenn Research Center's Digital Communications Branch.

Reinhart, Richard C.; Farrington, Allen; and Israel, Dave: Space Telecommunications Radio System STRS Open Architecture Standard, Rev. 1.0, Space Operations Mission Directorate, Apr. 2006. Available from NASA Glenn Research Center's Digital Communications Branch.



**ZIN Technologies, Inc., contact:**
Thomas J. Kacpura, 216–925–1266, Thomas.J.Kacpura@nasa.gov

**Glenn contact:**
Richard C. Reinhart, 216–433–6588, Richard.C.Reinhart@nasa.gov

**Authors:**
Thomas J. Kacpura and Richard C. Reinhart


**Headquarters program office:**
Space Operations Mission Directorate

**Programs/projects:**
Space Communications and Data Systems Project

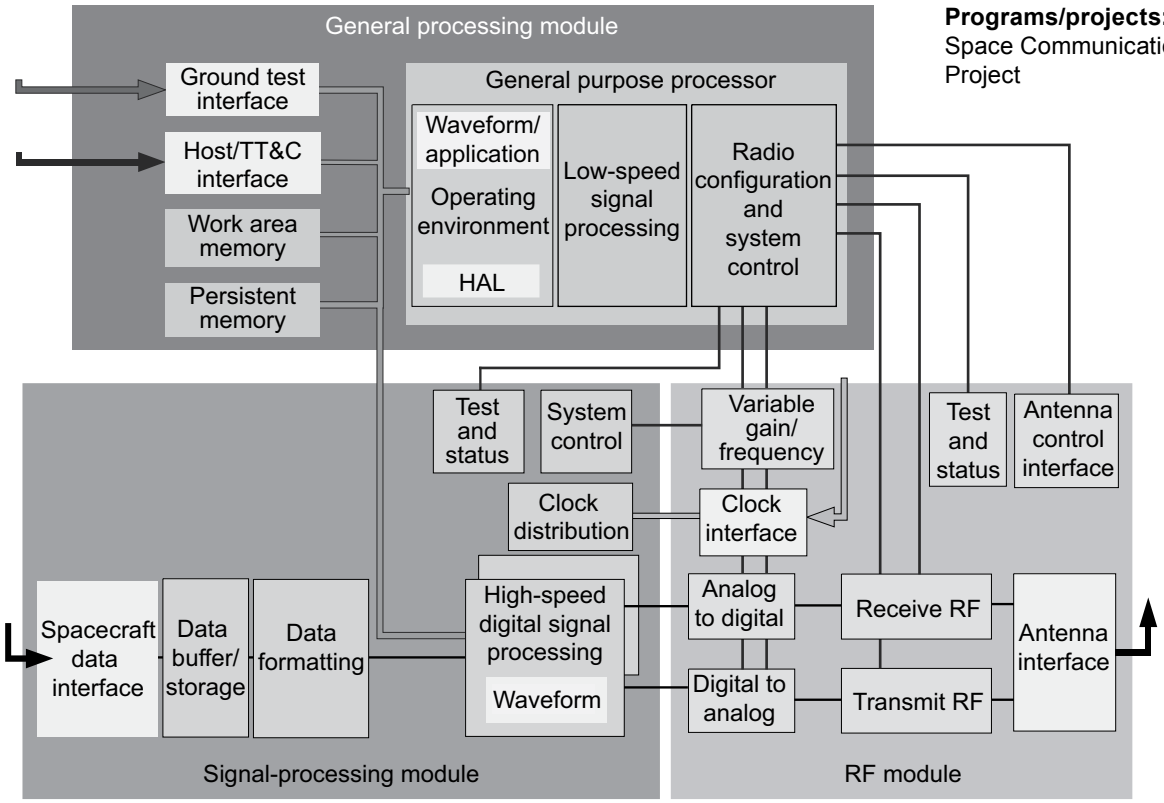


*STRS hardware architecture. RF, radiofrequency; TT&C, Telemetry, Tracking, and Control; HAL, Hardware Abstraction Layer.*

# Applicability of the Joint Tactical Radio System Software Communications Architecture to Space-Based Radios Examined

The Space Telecommunication Radio System (STRS), an open architecture specification based on software-defined reconfigurable technologies, is being developed by NASA for future space-radio communications and navigation systems. This includes software-defined radios (SDRs), which offer advanced operational capabilities that will reduce mission life-cycle costs for space platforms. The objective of the open architecture is to provide a consistent, extensible environment on which to develop, manage, and operate the increasingly complex software radios used in NASA space missions. The open STRS architecture provides a framework for leveraging earlier efforts by reusing various architecture-compliant system components developed previously in NASA programs.

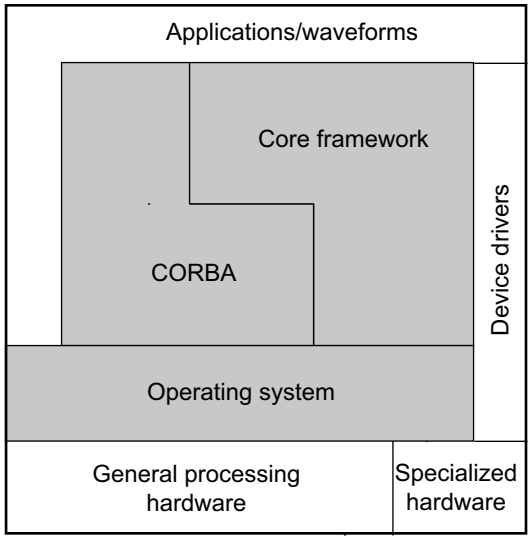


*SCA application/hardware separation. CORBA, Common Object Request Broker Architecture.*

The U.S. Department of Defense (DoD) and industry spent a considerable amount of effort on the development of the Software Communications Architecture (SCA), an open architecture for next-generation military radio communication systems. The STRS architecture and the SCA share many goals; however, the constraints of space-based systems currently prevent full utilization of the SCA by NASA. The size, power, and mass of the system need to be minimized for the constrained space environment. Processors and other electronic devices used in space require radiation hardening. NASA radios generally operate at higher frequencies and higher data rate transmissions than the current SCA-compliant radios. Space SDRs also have to address concerns about added software complexity and its effect on system reliability. During NASA missions, access is generally limited to remote uploads to change the behavior of the radios.

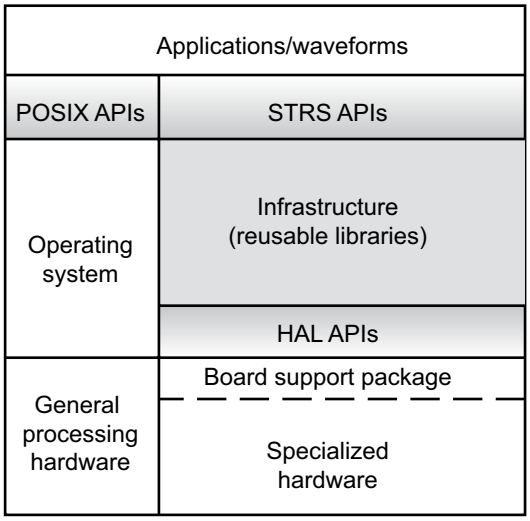


*STRS Application Software/Hardware Separation. POSIX, Portable Operating System Interface; API, application programming interface; HAL, Hardware Abstraction Layer.*

To leverage the DoD work, the NASA Glenn Research Center prepared a report that examines aspects of the SCA that could facilitate the design and implementation of the STRS architecture. STRS compatibility with the SCA would allow NASA to utilize commercial development and testing tools, share waveform components, and reduce the programmatic costs of maintaining a separate architecture. Highly effective commercial software development tools are reducing the time and cost of developing SCA-compliant waveforms and platforms. STRS adoption of these commercial tools would provide a consistent set of standards and practices, possibly lowering the costs of platform and waveform development.

There is commonality in a number of areas of the two architectures where NASA might be able to leverage assets derived from the SCA. However, the requirements and constraints associated with space-based systems prevent NASA from utilizing the current SCA specification, primarily because of the large footprint and resources, as well as the complexity due to the dynamic deployment capability of SCA waveform applications. For a NASA SDR architecture to be sustainable, it must accommodate the unique constraints and needs of the space environment. However, as technologies for the space environment evolve, they should allow the STRS architecture to incorporate more features and capabilities of the SCA.

**Bibliography**

Software Communications Architecture Specification. MSRC–5000SCA V2.2, Joint Tactical Radio System (JTRS) Joint Program Office, Nov. 17, 2001. http://jtrs.spawar.navy.mil/sca/downloads.asp?ID=2.2.2Ext2

Quinn, Todd M.: Space Telecommunication Radio System: JTRS SCA Applicability to Space-Based Radios, Nov. 2005. Available from NASA Glenn Research Center's Communications Technology Division.

Quinn, Todd; and Kacpura, Thomas: Strategic Adaptation of SCA for STRS. SDR Forum Technical Conference '06, session 4.2–01, Orlando, FL, Nov. 13–16, 2006.

Reinhart, Richard C.; Farrington, Allen; and Israel, Dave: Space Telecommunications Radio System STRS Open Architecture Description, Rev. 1.0, Space Operations Mission Directorate, Apr. 2006. Available from NASA Glenn Research Center's Digital Communications Branch.

Reinhart, Richard C.; Farrington, Allen; and Israel, Dave: Space Telecommunications Radio System STRS Open Architecture Standard, Rev. 1.0, Space Operations Mission Directorate, Apr. 2006. Available from NASA Glenn Research Center's Digital Communications Branch.

**Find out more about the research of the Digital Communications Technology Branch:**
http://ctd.grc.nasa.gov/organization/branches/dcb/dcb.html

**ZIN Technologies, Inc., contacts:**
Thomas J. Kacpura, 216–925–1266, Thomas.J.Kacpura@nasa.gov

**Glenn contact:**
Richard C. Reinhart, 216–433–6588, Richard.C.Reinhart@nasa.gov

**Authors:**
Thomas J. Kacpura and Todd M. Quinn

**Headquarters program office:**
Space Operations Mission Directorate

**Programs/projects:**
Space Communications and Data Systems Project

## High-Speed Network Interface Controller Based on SpaceWire Designed and Characterized

All spacecraft use networks of wires to transport commands and data between subsystems. Data networks onboard current spacecraft are generally standardized on a MIL–STD–1553/1773 bus with the Consultative Committee for Space Data Systems (CCSDS) protocol, which has a maximum speed of 1 Mbps. This is sufficient to pass commands from command and data handling (C&DH) to the various subsystems onboard the spacecraft, with a couple hundred kilobits available to transport science data from instruments to the downlink or mass storage. In addition to the 1553/1773 harness, there are usually custom discrete harnesses of up to hundreds of wires to transport high-speed data around the spacecraft. The custom harnesses add tens of kilograms, tens of watts, and complexity to the overall payload design. The current spacecraft network architecture dates back decades, and in the interim, ground-based commercial networks using new data protocols and physical layers have exploded in capability with multi-gigabit networks now commonplace in long-haul applications, Also, the CCSDS protocols used in current spacecraft are not compatible with commercial ground networks.

*BAE SpaceWire ASIC.*

The overall objective of this research was to develop low-power, miniaturized, high-data-rate onboard networking technology for distributed communications based on standards that would be beneficial to high-data-rate programs such as the National Polar Orbiting Operational Environmental Satellite System (NPOESS), Geostationary Operational Environmental Satellite Program R Series (GOES–R), Lunar Reconnaissance Orbiter, Space Interferometry Mission, James Webb Space Telescope, and others. The project addresses the development and delivery of prototype SpaceWire bus Application Specific Integrated Circuit (ASIC) chips capable of >100 Mbps throughput. The SpaceWire ASIC achieved 260 MHz, or 260 Mbps raw data rate, which is at least an order of magnitude increase in the current state of the art for spacecraft bus data rates. Also, the SpaceWire ASIC represents an innovative approach to solving onboard network communication. Integrating the

input/output interface with a complete system on a single chip (microcontroller, memory subsystem, back panel interface Peripheral Component Interconnect (PCI), direct memory access (DMA) controller, programmable input/output, timers, four SpaceWire ports, and a router), the SpaceWire ASIC achieves a high level of capability and density not obtainable in previous technologies.

The SpaceWire ASIC was successfully developed and tested under contract by BAE Systems in Manassas, Virginia, and delivered to the NASA Glenn Research Center in December 2005.

At least two NASA programs have applied this new technology to their missions. The C&DH subsystem of the Lunar Reconnaissance Orbiter will baseline the SpaceWire ASIC, and the orbiter's single board computer will use it to communicate with various other subsystems.

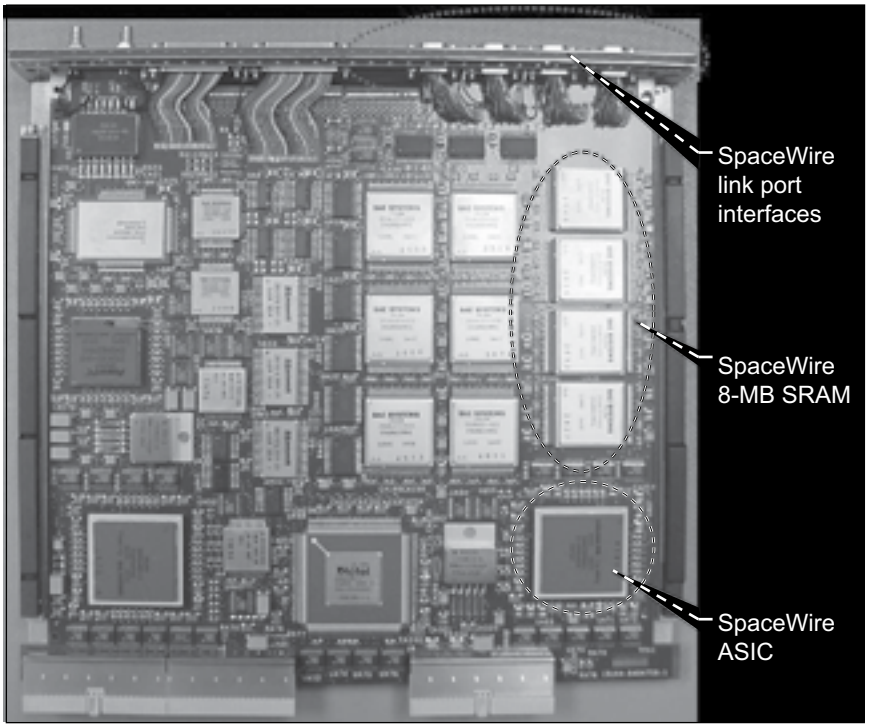


*Lunar Reconnaissance Orbiter processor board with SpaceWire ASIC. SRAM, static random access memory.*

The GOES–R weather satellite is being developed jointly by NASA and the National Oceanic and Atmospheric Administration. The satellite has a complement of four instrument suites ranging from 200 Kbps to 65 Mbps. The SpaceWire design will be used as a primary interface for C&DH and science data. A prototype board was tested, and the ASIC's functionality and performance was verified.

**Bibliography**

Jones, Robert E.: Design and Characterization of a State-of-the-Art High Speed Payload Interface Device for Use on Satellites Using RAD Hard Technology Based on Spacewire. Contract number NAS3–03086, 2003.

**Glenn contact:**
Nam T. Nguyen, 216–433–3425, Nam.T.Nguyen@nasa.gov

**Authors:**
Nam T. Nguyen and Myrna Milliser

**Headquarters program office:**
Exploration Systems Missions Directorate

**Programs/projects:**
Computing, Information, and Communications Technology Program, Space Communications Project

# Space Audio Development and Evaluation Laboratory Created To Improve Audio Transmission to and From Space Suits

Under the Advanced Extravehicular Activity program, the NASA Glenn Research Center is responsible for Communications, Avionics, and Information subsystems for next-generation exploration space suits. As part of the communications subsystem, the audio signals to and from the space suit are critical to mission success, providing voice communications between astronauts and mission control, between astronauts, and potentially from astronauts to voice-commanded robots and computers.

The space suit environment presents a unique challenge for capturing and transmitting speech. Inside the space suit, high levels of reverberation, flow noise, and machine noise exist together with very short direct-propagation paths. Static pressure levels can range from a fraction of an atmosphere during actual extravehicular activity operations to strong hyperbaric conditions during terrestrial field testing. Because an astronaut is afforded a wide range of motion within the suit, the physical geometry between an astronaut's mouth or ear and any particular fixed location on the inside of the suit varies significantly over time. In addition, problems were identified recently regarding the proper function of existing communications caps over wide ranges of pressure and regarding flow noise.

The resolution of technical issues surrounding speech audio capture and transmission systems—cap-based or otherwise—requires a testing facility that can support the development and evaluation of in-helmet audio solutions and that can provide a full complement of engineering data on the acoustic environment in a rigorous and repeatable fashion. The Space Audio Development and Evaluation Laboratory (SPADEL) at Glenn fills this requirement by providing the ability to measure in-helmet acoustic characteristics as well as the ability to evaluate the speech quality associated with in-helmet audio production and sensing devices.

*A NASA engineer tests sound-pressure levels on an anthropomorphic mannequin inside a space shuttle hard upper torso and helmet.*

The basic focus of SPADEL is to provide a means to assess the effects of the acoustic path on the speech communications channel to and from an astronaut. Current capabilities include traditional testing and evaluation methods that focus on engineering quantities such as frequency response and distortion levels. SPADEL also can evaluate speech in terms of listening quality and listening effort. Speech quality testing is accomplished primarily through the use of a computerized device that implements International Telecommunication Union (ITU)-recommended speech-quality algorithms.

In addition, SPADEL's controlled acoustic environment, together with its sophisticated sound production and recording capabilities, can be used to develop reference recordings for subsequent jury testing that produces true Mean Opinion Score (MOS) assessments of speech quality. SPADEL's computerized speech-quality testing device produces estimates of the MOS that have been shown to be highly correlated with the actual MOS created using jury testing, but with significantly less time and cost. Note that SPADEL's speech-quality testing tool can evaluate other portions of the speech channel such as speech coding and packetizing. Thus, in addition to measuring the speech quality of the acoustic paths within a space suit, SPADEL can measure the intelligibility of almost any part of the speech communications channel. Speech quality testing can be extended to the complete, end-to-end speech channel.

**Glenn contacts:**
Alan N. Downey, 216–433–3508, Alan.N.Downey@nasa.gov

Dr. O. Scott Sands, 216–433–2607, Obed.S.Sands@nasa.gov

Glenn R. Lindamood, 216–433–8582, Glenn.R.Lindamood@nasa.gov

Amy R. Asmus, 216–433–3703, Amy.R.Asmus@nasa.gov

David A. Carek, 216–433–8396, David.A.Carek@nasa.gov

**Authors:**
Alan N. Downey and Dr. O. Scott Sands

**Headquarters program office:**
Exploration Systems Mission Directorate

**Programs/projects:**
Human System Research and Technology

# Bench-Top Antigen-Detection Technique Developed That Utilizes Nanofiltration and Fluorescent Dyes Which Emit and Absorb Light in the Near Infrared

This year, a bench-top technique was developed at the NASA Glenn Research Center to detect antigenic proteins in fluids. The detection of these proteins is a tremendous concern at NASA because of the importance of ensuring astronaut safety onboard the International Space Station, the space shuttles, and the Crew Exploration Vehicle and in human habitats for the upcoming Moon and Mars missions. The detection of these antigenic proteins is also of great importance in keeping terrestrial waterways, treatment plants, and food-processing centers safe from contamination. The technique involves the use of near infrared (NIR) fluorescent dyes conjugated to antibodies, centrifugation, nanofilters, and spectrometry. The system used to detect the antigens utilizes a miniature spectrometer, fiber-optic cables, a tunable miniature NIR laser, and a laptop computer—making the system portable and ideally suited for desktop analysis (see the photograph).

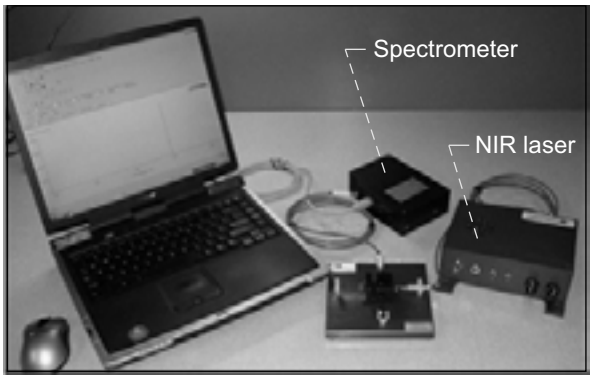


*Bench-top antigen-detection system, including laptop computer, spectrometer, cuvette holder, NIR laser, and fiber-optic cables.*

For this technique, antibody/fluorescent dye pairs that absorb in the NIR region and emit an offset emission at a longer wavelength in the NIR region are mixed into a solution containing antigens and are then centrifuged. Each antibody/dye pair is specific to one antigen and absorbs and emits at unique wavelengths, making the pairs distinguishable during analysis.

Because of the size difference between the antibody/fluorescent dye pairs and the large protein antigens used in this experiment, antibody/fluorescent dye pairs can be filtered through the nanofilter, but pairs that have bound with antigens cannot. Consequently, antibody/fluorescent dye pairs that have not bound with any of the antigenic proteins can be filtered away from the fluid sample by centrifugation and nanofilters, leaving only antibody/fluorescent dye pairs that have combined with their specific antigen.

After filtration, the fluid sample is excited with a tunable NIR laser that causes the fluorescent dyes to emit an offset wavelength. The different wavelengths are detected by spectrometry, thus revealing which antigens are present in the fluid sample. In the proof-of-concept experiment, the IRDye 800 CW (Rockland Immunochemicals) conjugated to the primary antibody, anti-IgM, was combined to the antibody (used as our antigen) IgM. An offset emission of 804 nm was detected when the antibody/dye-antigen complexes were excited by the tunable laser at 778 nm and is shown in the graph on this page. To validate this concept, researchers mixed IRDye 800 CW conjugated to the antibody anti-IgM with the nonspecific antigens β galactosidase and thyroglobulin. For both nonspecific antigens, no signal was observed, as illustrated in the graphs on the next page, thus proving that the anti-IgM did not bind to the nonspecific antigens, which were consequently filtered away.

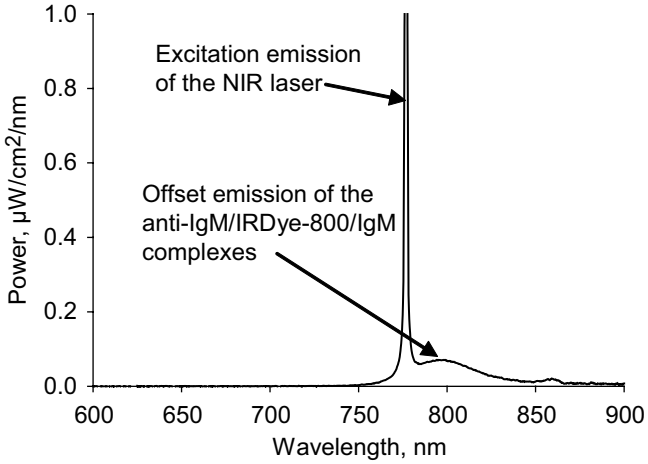


*Emission of the anti-IgM + IgM complexes in 1× phosphate buffer saline (1× PBS) solution (after nanofiltration) at 804 nm as excited by the NIR laser.*

This technique could potentially be used in fluids to detect multiple antigens from microorganisms onboard spacecraft and in human habitats on the Moon and Mars. Because of its portability, the technique is ideally suited for laboratory and clinical diagnostics as well as field testing. With further development, this novel technique could be used to detect antigenic microorganism cell proteins in more complex fluids, such as blood.

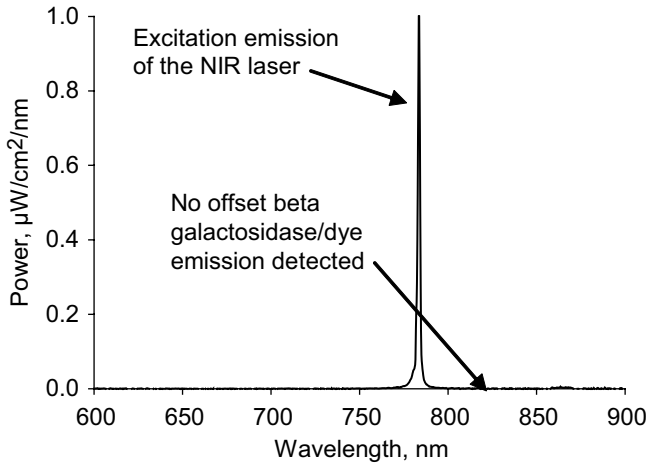


*Anti-IgM + beta galactosidase in 1× PBS solution (after nanofiltration) as excited by the NIR laser.*

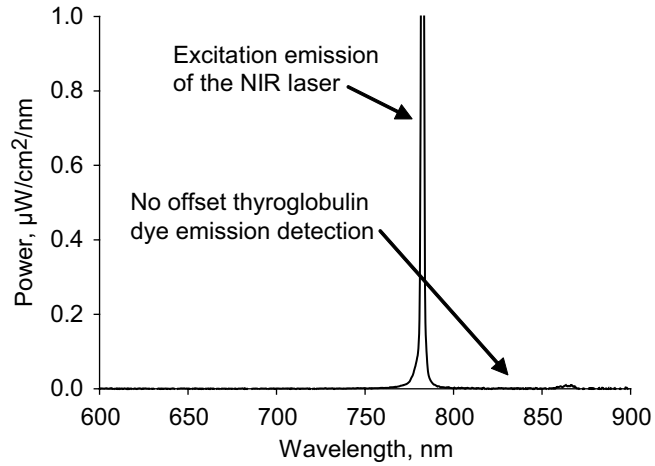


*Anti IgM + thyroglobulin in 1× PBS solution (after nanofiltration) as excited by the NIR laser.*

**Glenn contact:**
Maximilian C. Scardelletti, 216–433–9704, Maximilian.C.Scardelletti@nasa.gov

**University of Georgia contact:**
Vanessa A. Varaljay-Spence, 706–255–6540, vspence@uga.edu

**Authors:**
Maximilian C. Scardelletti and
Vanessa A. Varaljay-Spence

**Programs/projects:**
Crew Exploration Vehicle, Constellation Systems, Independent Research and Development

## Radiofrequency Mass Gauging of Propellants Simulated by Modern Computational Tools

The NASA Glenn Research Center used modern simulation tools to model a mass-gauging technique based on the electromagnetic radiofrequency (RF) resonance spectrum of closed cavities. Changing the quality or quantity of a dielectric, such as a propellant, from a cavity will shift the resonant frequencies of that cavity. The measurement of those frequency shifts can be incorporated into an algorithm to determine the weight of the propellant inside a cryogenic tank.

RF mass gauging is a promising technique that was investigated by a number of NASA contracts from 1964 to 1988. Most notable was the 1988 NASA contract with Ball Aerospace. Using a solid wax to emulate low-gravity fluid configurations, Ball Aerospace demonstrated up to 1 percent of full-scale accuracy. In comparison to other methods, RF mass gauging showed the following advantages: fast measurement time; simple, rugged, low-weight, low-power electronics; and technology that is applicable to any dielectric liquid (e.g., hydrogen, oxygen, or methane). In previous attempts, analytical or numerical methods could only be used to predict the response of tanks with very simple structures and basic Earth gravity (1g) liquid configurations. Today, the combination of powerful, yet relatively inexpensive, computers and highly advanced three-dimensional electromagnetic analysis software allows the simulation of arbitrary liquid configurations in cryogenic tanks containing baffles, struts, and many other internal devices and structures.

Glenn researchers validated the three-dimensional electromagnetic software by comparing simulated data with experimental data gathered on a 12-in.-diameter, 24-in.-high tank (shown in the photograph), which was incrementally filled with liquid oxygen. The preceding graph shows excellent agreement between the experimental and simulated data. The excellent results assure us that we can use the software to predict the resonance spectrum of complex cryogenic tanks, create electromagnetic field plots to identify specific resonance modes, and determine the optimum shape and location(s) of antenna to couple to specific resonance modes.

Ongoing work at Glenn includes performing extensive numerical simulations to predict resonance modes in various tanks that contain internal hardware, determining of the optimum shape and location of antenna for those tanks, simulating low-gravity fluid configurations, and developing a mass-gauging algorithm. We also plan to perform an in-flight validation of the algorithm.

This work is part of a larger RF mass-gauging effort being performed in-house that is funded by Exploration Systems Research and Technology, and Propulsion and Cryogenics Advanced Development.

*12- by 22-in. cryogenic tank being filled with liquid oxygen.*

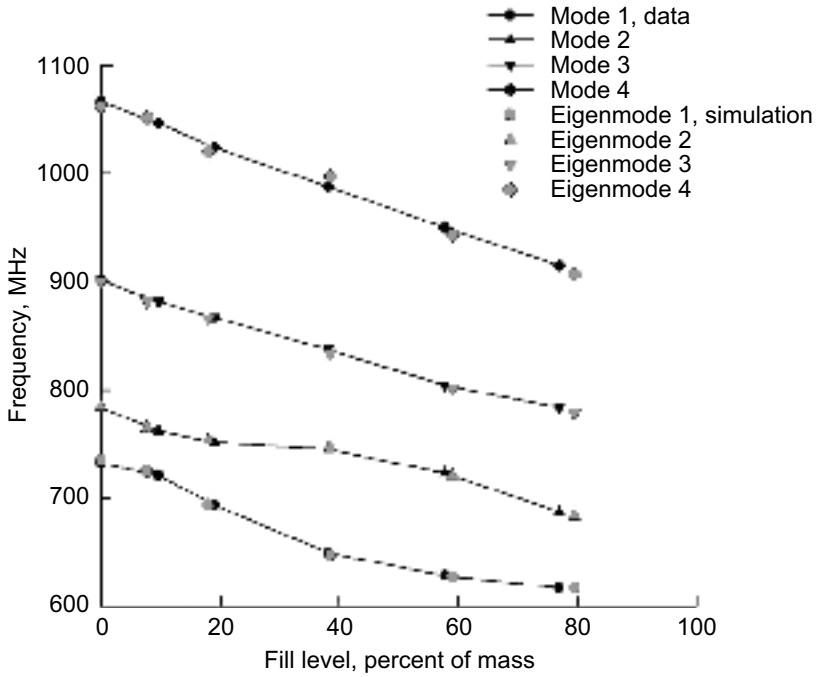


*Comparison of experimental and eigenmode simulated RF tank resonances for a tank incrementally filled with liquid oxygen.*

**Glenn contacts:**
Karl R. Vaden: 216–433–8131, Karl.R.Vaden@nasa.gov

Dr. Gregory A. Zimmerli, 216–433–6577, Greg.Zimmerli@nasa.gov

**Author:**
Karl R. Vaden

**Headquarters program office:**
Exploration Systems Mission Directorate

**Programs/projects:**
Exploration Systems Research and Technology, Propulsion and Cryogenics Advanced Development, Highly Reliable/Autonomous Deep-Space Cryogenic Propellant Refueling Systems Technology Theme; High Energy Space Systems Element Technology Maturation Program

# Lunar-Based Lunar Surface Navigation Analyzed

Lunar surface navigation is an important area of research, with the need to define the architecture of how science rovers, manned sortie missions, manned outpost missions, and lunar surface operations will perform navigation. Decisions need to be made as to what navigation aids these vehicles will use to gain knowledge of their lunar surface position. One idea that was investigated at the NASA Glenn Research Center was the use of a constellation of satellites around the Moon providing continuous global coverage. The Lunar-Based Lunar Surface Navigation Analysis characterized the performance of four types of satellite constellations that could be placed around the Moon. The constellations were designed to implement continuous communication and navigation over the entire lunar surface. Constellations included inclined Walker, inclined elliptical, Lang-Meyer, and polar orbit orientations.

Two forms of navigation were investigated: one-way and two-way navigation. The Global Positioning System (GPS) is considered to be a one-way navigation system because signals are only broadcast in one direction. In the one-way navigation system, the user receives broadcast pseudorange signals from satellites and determines their own position and time bias on the basis of pseudorange and range-rate measurements.

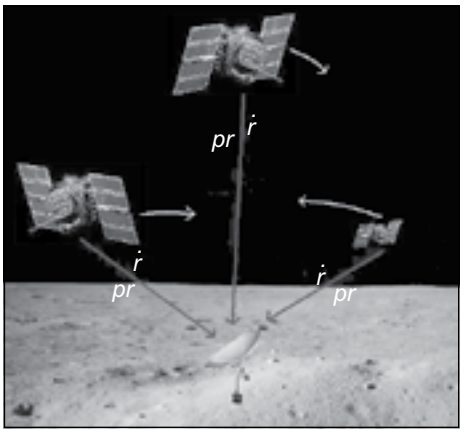


*One-way navigation system; pr, pseudorange; ṙ, range rate.*

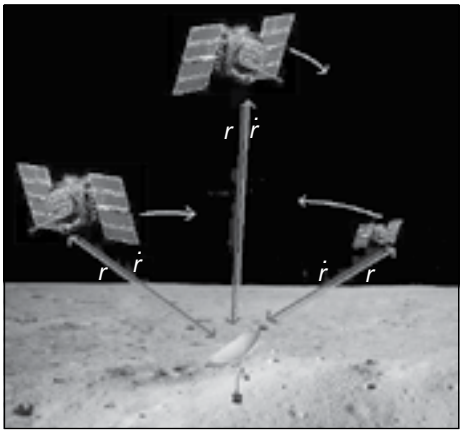


*Two-way navigation system; r, range; ṙ range rate.*

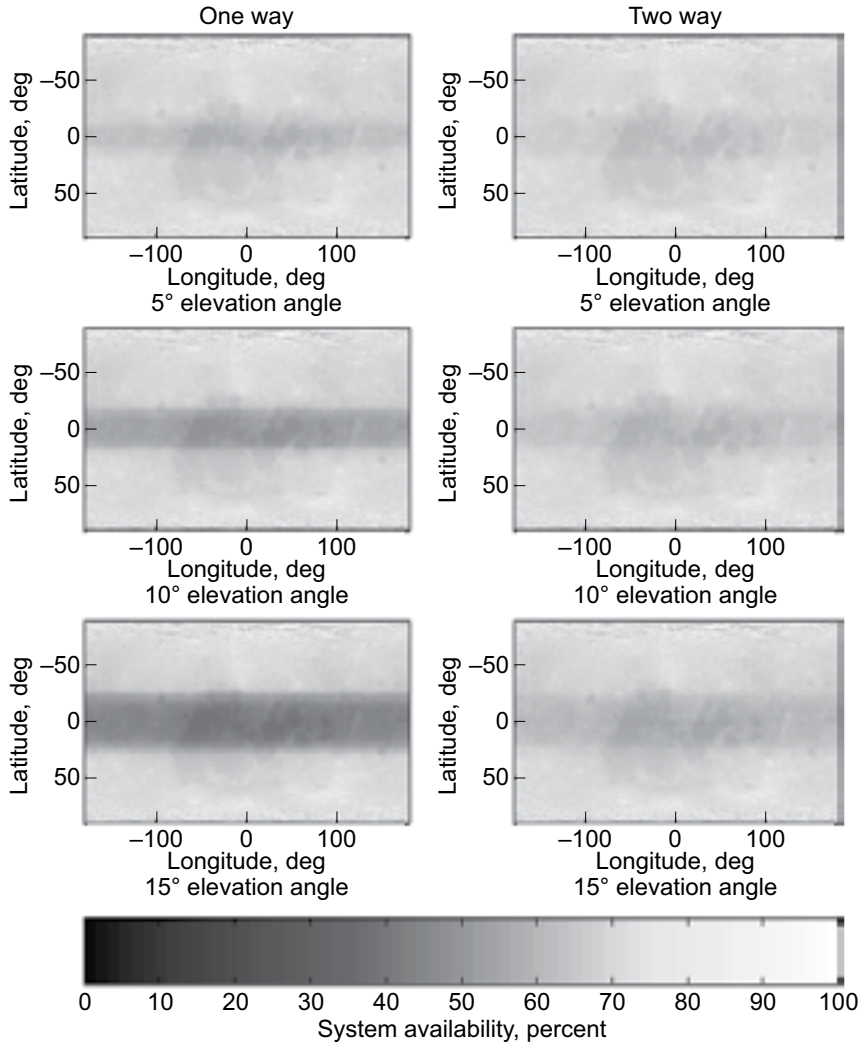


*SA results for the Polar 6/2/1 satellite constellation. This figure is shown in color in the online version of this article (http://www.grc.nasa.gov/WWW/RT/2006/RC/RCI-welch1.html).*

The two-way navigation method would eliminate the need to determine time bias, because the time-stamped signal would be retransmitted back to the source for processing. In the two-way system, the user retransmits broadcast range signals from satellites and determines their own position on the basis of range and range-rate measurements.

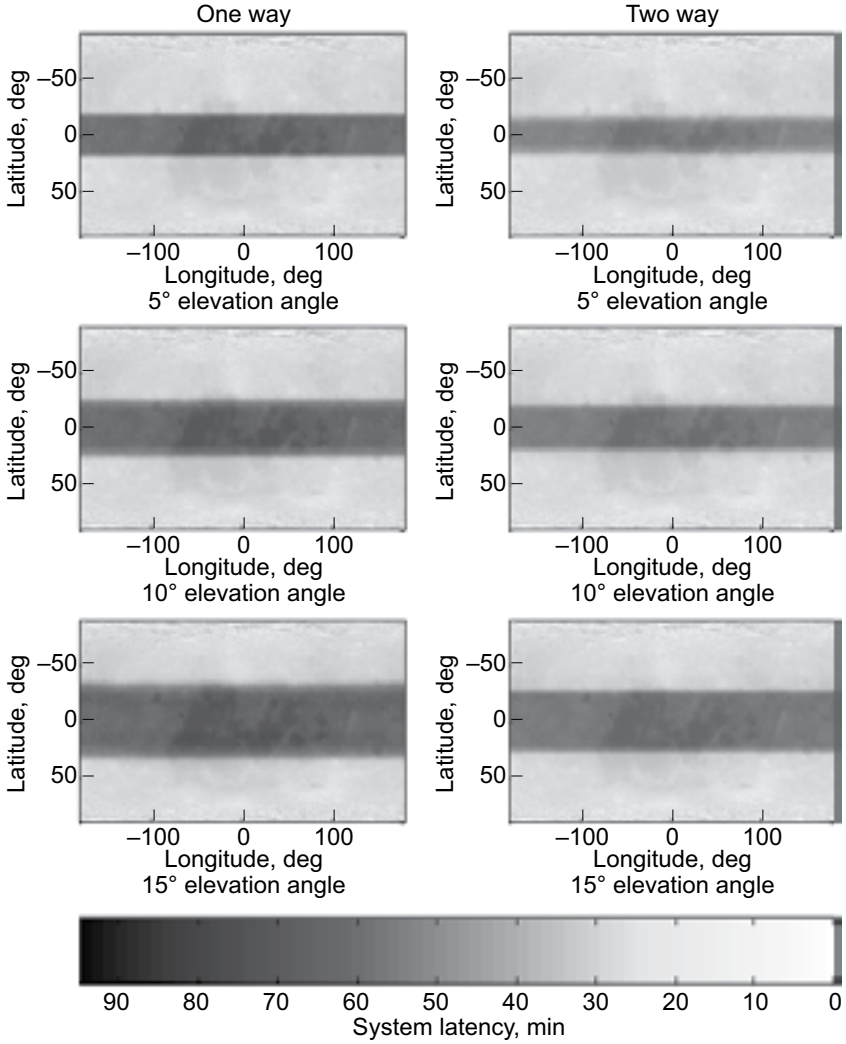


*SL results for the Polar 6/2/1 satellite constellation. This figure is shown in color in the online version of this article (http://www.grc.nasa.gov/WWW/RT/2006/RC/RCI-welch1.html).*

Two metrics used to characterize the navigation performance of the constellations were system availability (SA) and system latency (SL), both of which utilize the Dilution of Precision (DoP) technique. DoP is a high-level geometrical analysis of the view angles, from the user to the satellites in view, which is used to determine the effect of geometrical spacing on solution error. This can take several forms depending on the state variables being analyzed. One-way navigation methods, called Geometrical DoP (GDoP), require solving for a topocentric Cartesian position and time. In comparison, two-way navigation methods, called the Positional DoP (PDoP), only solve for a topocentric Cartesian position.

The SA and SL metrics compared the DoP results with a threshold. In the SA analysis, the DoP results, with a given integration latency, were compared with a threshold of 10, and the number of instances where the DoP was less than the threshold was weighted spatially to determine the overall SA. In the SL analysis, integration latency was increased until the SA was 90 percent of the DoP results, from which the integration latency was spatially weighted to determine the overall SL. These metrics were analyzed with 5°, 10°, and 15° minimum elevation angles from the lunar surface points.

The study concluded that the Polar 12/4/1 constellation had the best performance, as it also had the most satellites in the constellation. The recommended constellation was the Polar 8/2/1 because it could degrade to the Polar 6/2/1 if a failure was present. The Polar 6/2/1 was an acceptable constellation on the basis of performance and latency results.

The Lunar-Based Lunar Surface Navigation Analysis effort is managed under the Space Communications and Data Systems Project at Glenn. The work was performed in-house by members of the Communications Systems Integration Branch in Glenn's Communications Technology Division.

**Find out more about the research of Glenn's Communications Technology Division:**
http://ctd.grc.nasa.gov

**Glenn contacts:**
Bryan W. Welch, 216–433–3390, Bryan.W.Welch@nasa.gov

Dr. O. Scott Sands, 216–433–2607, Obed.S.Sands@nasa.gov

Joseph W. Connolly, 216–433–8728, Joseph.W.Connolly@nasa.gov

**Author:**
Bryan W. Welch

**Headquarters program office:**
Space Communications Technology Program

**Programs/projects:**
Space Communications and Data Systems Project, Space Communication Architecture Working Group

# Earth-Based Lunar Surface Navigation Analyzed

Lunar surface navigation is an important area of research that needs to address existing capabilities. Decisions need to be made in regards to how the current communication and tracking infrastructure will be used for lunar surface navigation. One idea that was investigated at the NASA Glenn Research Center was the use of the Deep Space Network (DSN), geostationary orbit satellites (GEO), and combinations thereof (DSNGEO).

The Earth-Based Lunar Surface Navigation Analysis characterized the performance of various types of Earth-based tracking assets. Ground stations located at the DSN locations were analyzed with multiple minimum-elevation-angle requirements. Satellites located in GEO at the Tracking and Data Relay Satellite System (TDRSS) orbit locations were analyzed with various nadir and zenith beam-width patterns. Finally, combinations of the GEO satellite assets with the DSN ground stations were analyzed.

Two forms of navigation were investigated: one-way and two-way navigation. One-way navigation systems use signals that are only broadcast in one direction. The user receives broadcast pseudorange signals from satellites and determines their own position and time bias on the basis of pseudorange and range-rate measurements. Two-way navigation systems use systems that are transponded back to the initiator. The user receives ranging signal measurements from the initiator and determines their own position on the basis of range and range-rate measurements.

Two metrics used to characterize the navigation performance of the Earth assets were system availability (SA) and system latency (SL), both of which utilize the Dilution of Precision (DoP) technique. DoP is a high-level geometrical analysis of the view angles from the user to the satellites in view, which is used to determine the effect of geometrical spacing on solution error. This can take several forms depending on the state variables being analyzed. One-way navigation methods, called the Geometrical DoP (GDoP), require solving for a topocentric Cartesian position and time. In comparison, two-way navigation methods, called Positional DoP (PDoP), only solve for a topocentric Cartesian position.

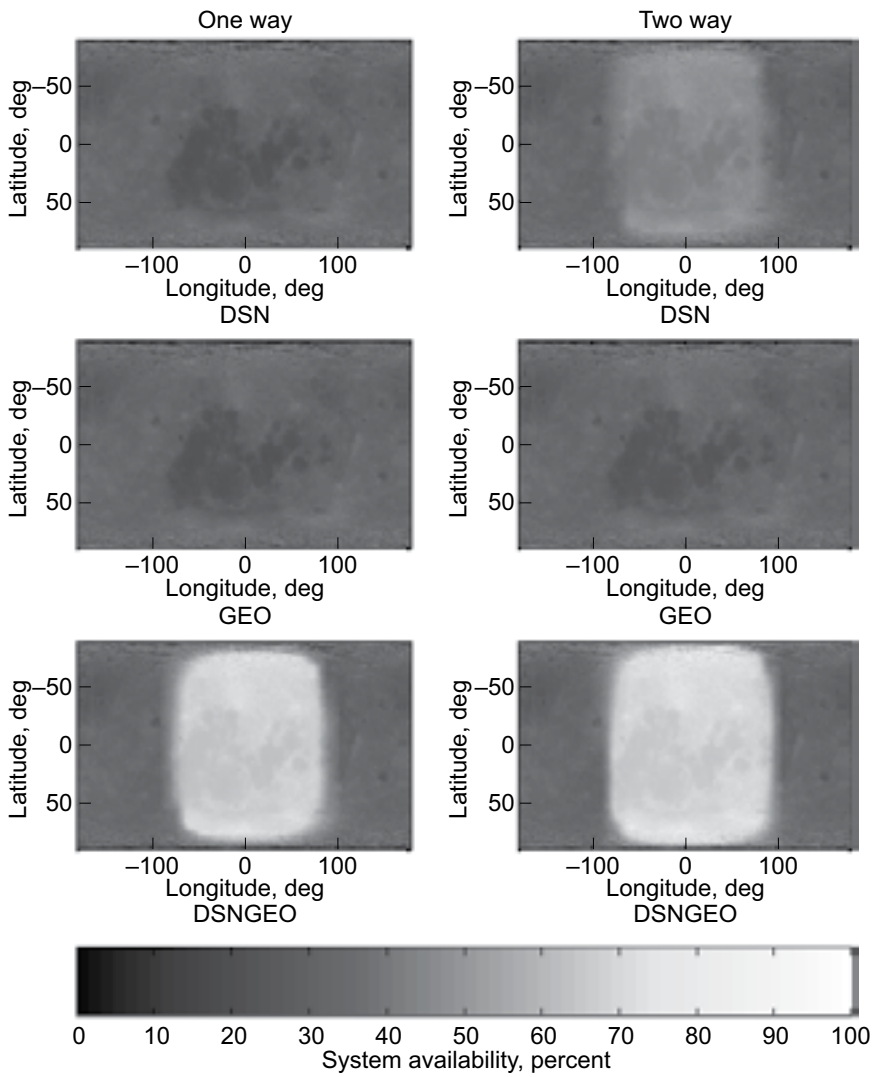


*SA results for Earth assets for an integration period of 1 hr. This figure is shown in color in the online version of this article (http://www.grc.nasa.gov/WWW/RT/2006/RC/RCI-welch2.html).*

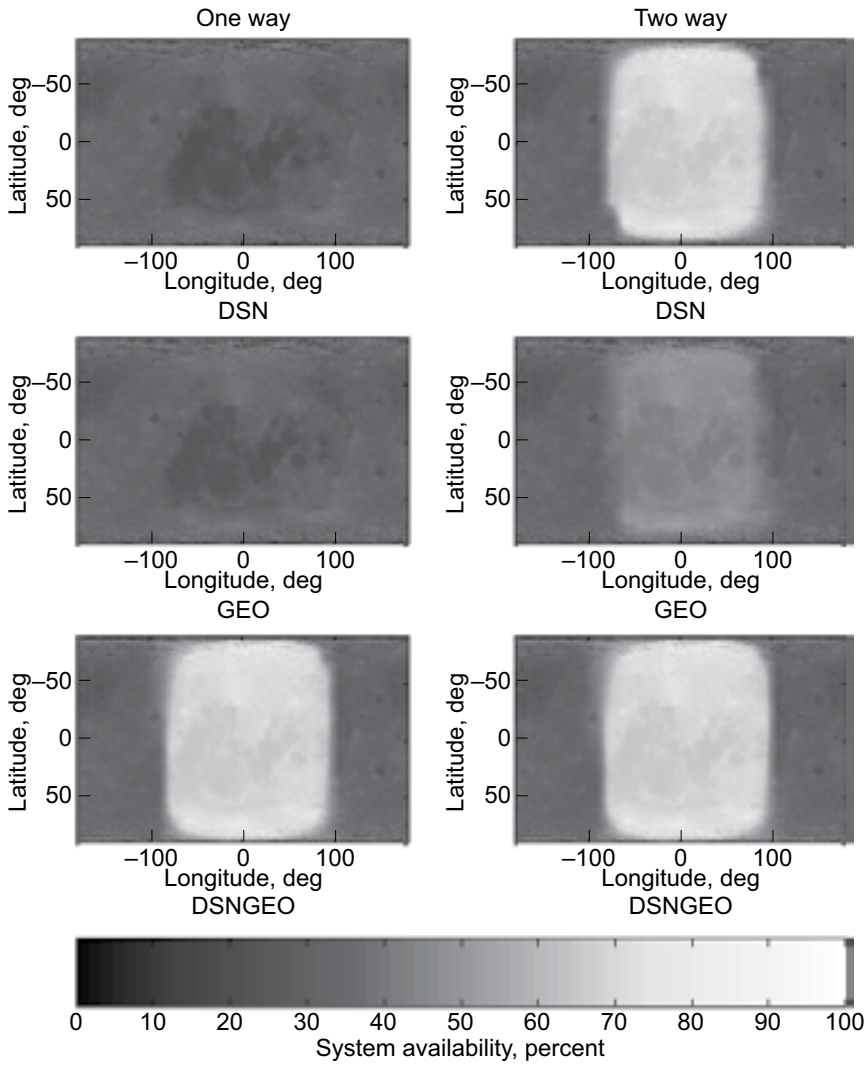


*SA results for Earth assets for an integration period of 12 hr. This figure is shown in color in the online version of this article (http://www.grc.nasa.gov/WWW/RT/2006/RC/RCI-welch2.html).*

The SA and SL metrics compare the DoP results with a threshold. In the SA analysis, the DoP results, with a given integration latency, were compared with a threshold of 10, and the number of instances where the DoP was less than the threshold was weighted spatially to determine the overall SA. In the SL analysis, integration latency was increased until the SA was 90 percent of the DoP results, from which the integration latency was spatially weighted to determine the overall SL. These metrics were analyzed with a 5° minimum elevation angle from the lunar surface points. Various dynamic integration time periods were used, ranging from 15 min to 12 hr.

Earth-based assets of any type can work well if long solution integration periods are acceptable, but only in the Apollo landing zone region on the lunar surface. Earth-based assets do not perform well for regions such as the lunar south pole or far side, and are not recommended for these regions. The study concluded that the system that worked best was the GEO constellation with the largest view angles (GEO 150/150). See reference 1 for an evaluation of lunar-based navigation.

The Earth-Based Lunar Surface Navigation Analysis effort is managed under the Space Communications and Data Systems Project at Glenn. The work was performed in-house by members of the Communications Systems Integration Branch in Glenn's Communications Technology Division.

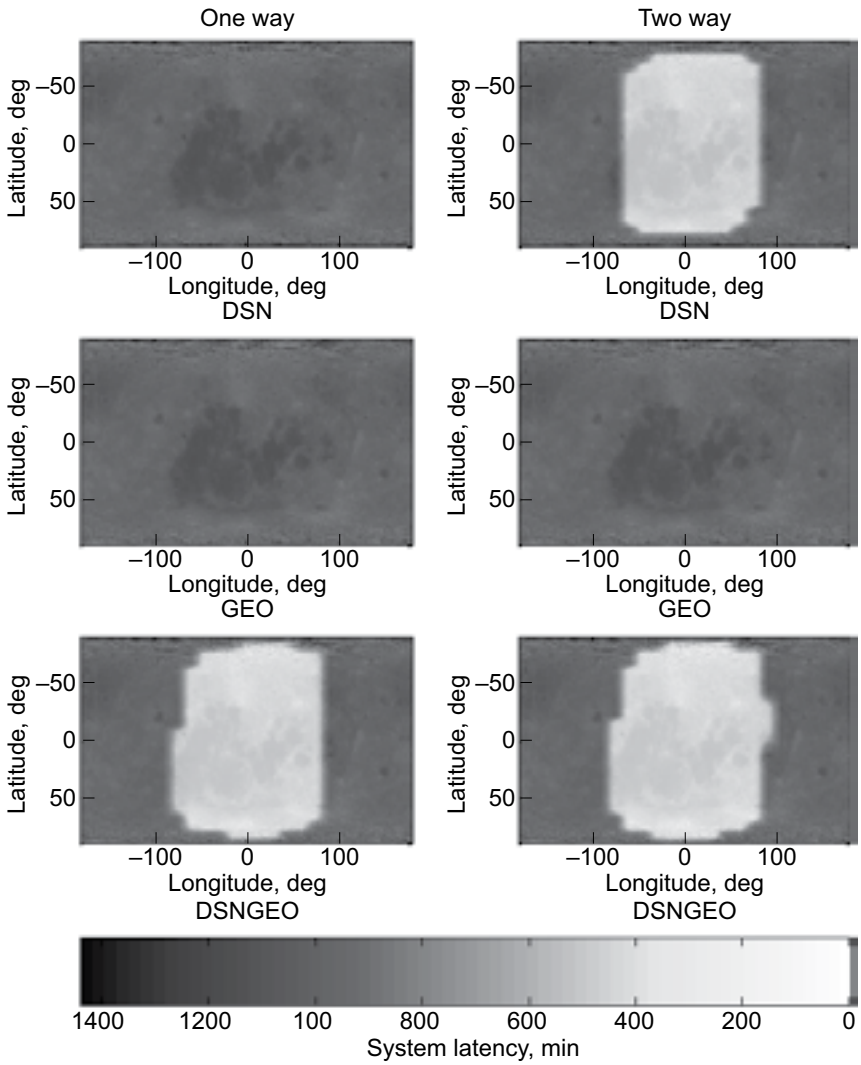


*SL results for Earth assets for an integration period of 1 hr. This figure is shown in color in the online version of this article (http://www.grc.nasa.gov/WWW/RT/2006/RC/RCI-welch2.html).*

**Reference**


1. Welch, Bryan W.: Lunar-Based Lunar Surface Navigation Analyzed. Research & Technology 2006. NASA/TM—2006-214479, 2006, pp. 28–29. http://www.grc.nasa.gov/WWW/RT/2006/RC/RCI-welch1.html


**Find out more about the research of Glenn's Communications Technology Division:**
http://ctd.grc.nasa.gov


**Glenn contacts:**
Bryan W. Welch, 216–433–3390, Bryan.W.Welch@nasa.gov

Dr. O. Scott Sands, 216–433–2607, Obed.S.Sands@nasa.gov

Joseph W. Connolly, 216–433–8728, Joseph.W.Connolly@nasa.gov

**Author:**
Bryan W. Welch


**Headquarters program office:**
Space Communications Technology Program

**Programs/projects:**
Space Communications and Data Systems Project, Space Communication Architecture Working Group

# Lunar Surface Mobility Autonomous Navigation Assessed

Lunar surface mobility autonomous navigation is becoming an important area of research again as the need arises to define the architecture of how science rovers and manned sortie missions will perform surface mobility navigation missions. Decisions need to be made as to what navigation aids and devices these vehicles will use to gain knowledge of their lunar surface position. During the Apollo era, surface mobility navigation missions utilized an autonomous navigation system consisting of an inertial measurement unit and star trackers.

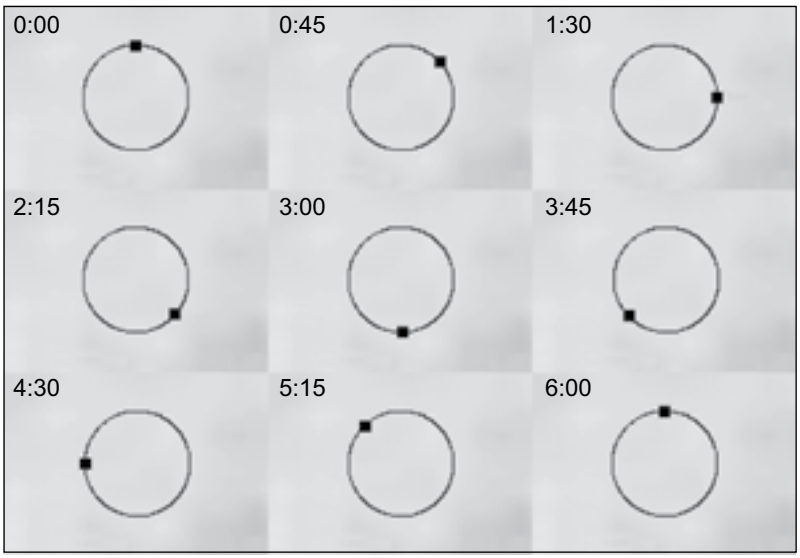


*Circular-track, constant-velocity profile.*

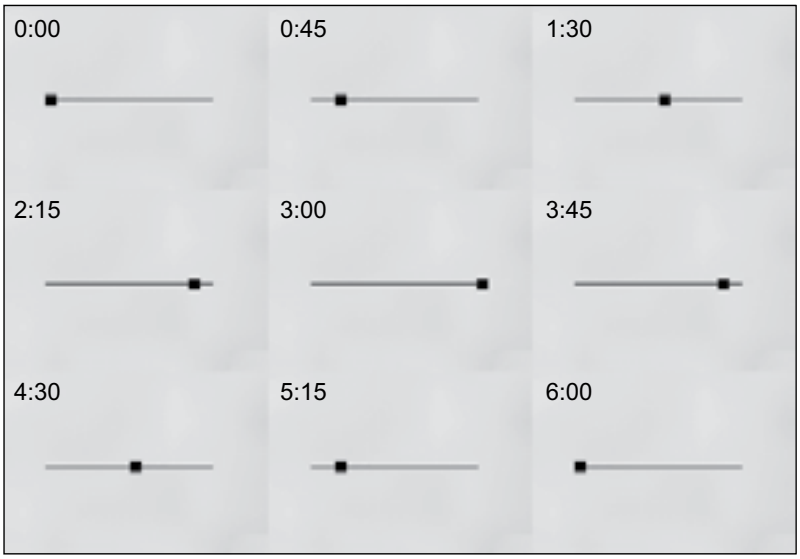


*Straight-track, variable-velocity profile.*

The Lunar Surface Mobility Autonomous Navigation Assessment, conducted at the NASA Glenn Research Center, characterized the performance of two surface mobility profiles that could be used to traverse from the lunar module to the mission destination. The first of the surface mobility profiles was a circular path with a constant velocity. The radius of the path was 15 km. Instead of stopping at the destination 30 km from the lunar module, the profile followed the circular path to return to base. The second of the surface mobility profiles was a straight path with a variable velocity. The path length was 30 km in one direction. This profile stopped at the endpoint before returning to the lunar module.

The navigation assessment was based on using an autonomous navigation system. The system would contain measurements from a gyroscope and an accelerometer. Sources of gaussian error in the gyroscope instruments that were modeled included bias drift, scale factor, and random walk. Two sources of error in the accelerometer instruments that were modeled included bias repeatability and scale factor. Nonorthogonality in the gyroscope and accelerometer instruments were not modeled for this analysis. The performance of the surface mobility profiles was assessed for 20 different noise profiles to attempt to characterize the performance of the navigation system. Results of the simulations were computed in terms of the error in the three local Cartesian dimensions from the location of the lunar module. Results show that maximum errors of up to 5 km in a single Cartesian dimension[1] could arise with this type of autonomous navigation system.

[1]This analysis examined results in each of the three local-topocentric Cartesian dimensions.

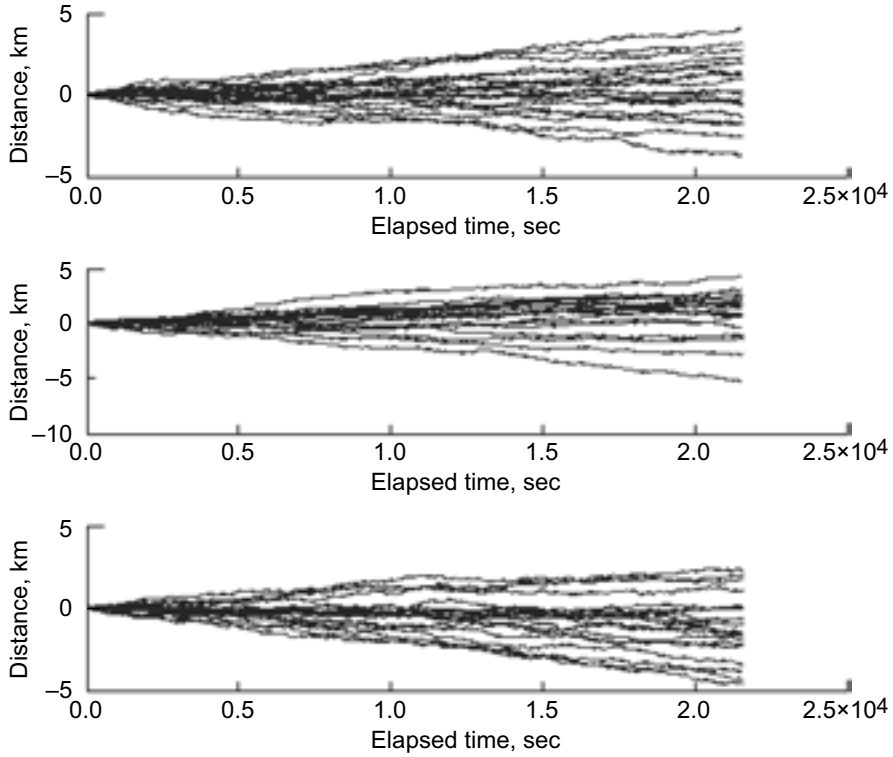


*Circular-track, constant-velocity profile results, showing topocentric position errors for 20 cases. The three subplots correspond to local Cartesian coordinates x, y, and z (top to bottom).*

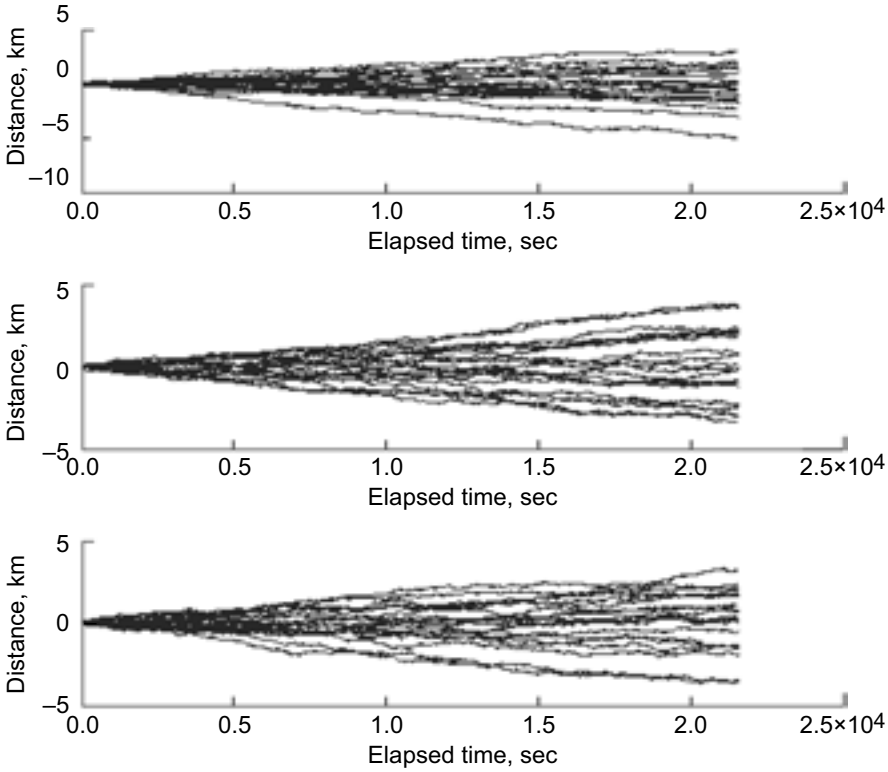


*Straight-track, variable-velocity profile results, showing topocentric position errors for 20 cases. The three subplots correspond to local Cartesian coordinates x, y, and z (top to bottom).*

The Lunar Surface Mobility Autonomous Navigation Assessment effort is managed under the Space Communications and Data Systems Project at Glenn. The work was performed in-house by members of the Communications Systems Integration Branch in Glenn's Communications Technology Division.

**Find out more about the research of Glenn's Communications Technology Division:**
http://ctd.grc.nasa.gov

**Glenn contacts:**
Bryan W. Welch, 216–433–3390, Bryan.W.Welch@nasa.gov

Joseph W. Connolly, 216–433–8728, Joseph.W.Connolly@nasa.gov

**Author:**
Bryan W. Welch

**Headquarters program office:**
Space Communications Technology Program

**Programs/projects:**
Space Communications and Data Systems Project, Space Communication Architecture Working Group

# Satellite Laser-Ranging Benefits Assessed for Orbit Determination at Global Positioning System Orbit

Although navigation systems for determining the orbit of the Global Positioning System (GPS) have proven to be very effective, the current issues involve lowering the error in the GPS satellite ephemerides below their current level.

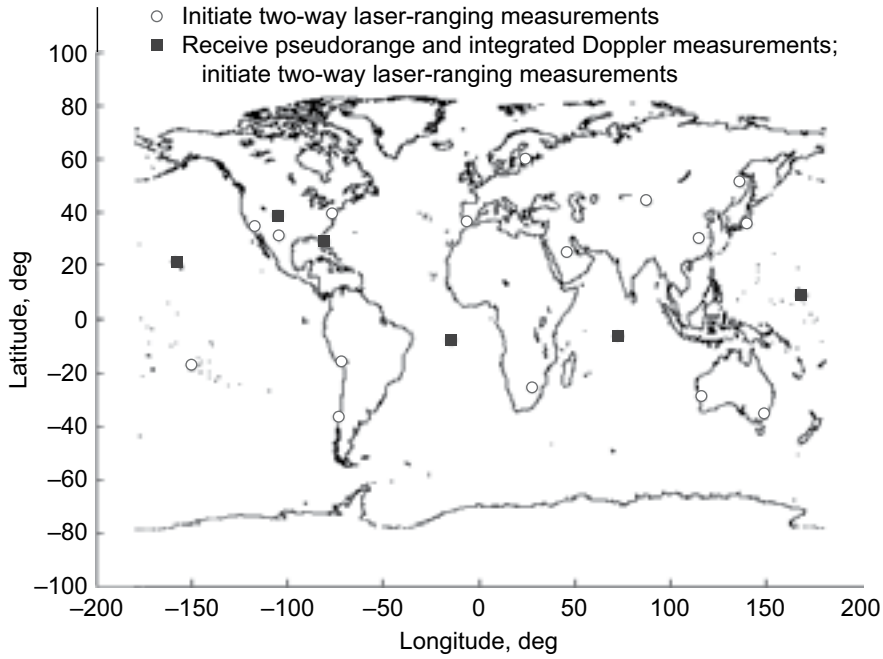


*Locations of ground stations utilized.*

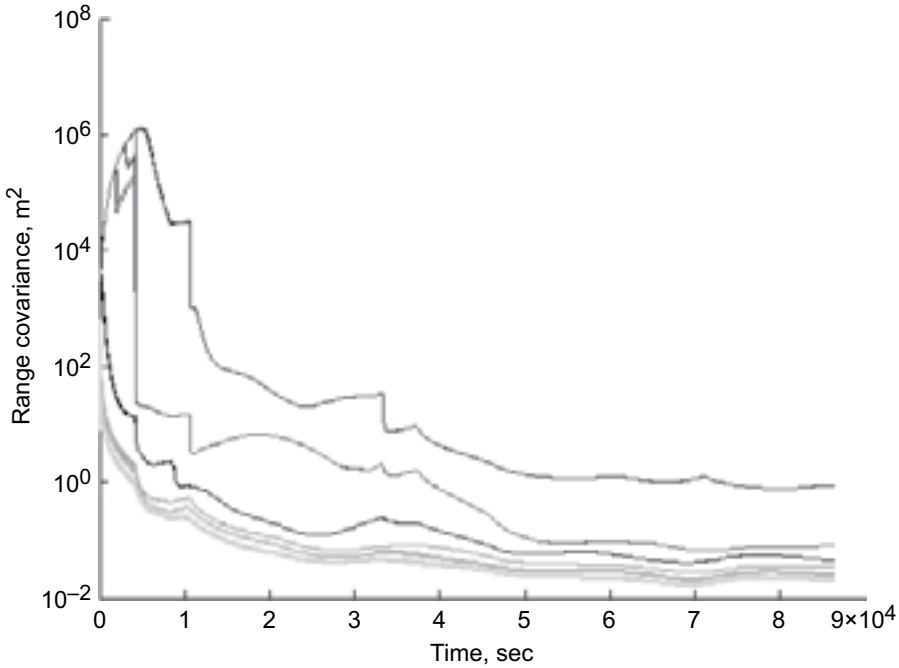


*Range covariance plots for initial longitude 0° east.*

An idea being discussed is incorporating two-way laser-ranging measurements into the operational methodology for determining the orbit of the GPS satellites.

The Satellite Laser Ranging Benefits for Orbit Determination at GPS Orbit Assessment, conducted at the NASA Glenn Research Center, characterized the performance of multiple ground system scenarios. The first ground system consisted of pseudorange and integrated Doppler measurements from the six GPS monitor stations around the world. Additional ground system scenarios started with the same measurements from the current system and included laser-ranging measurements from those same ground stations with additional laser-ranging measurements from various numbers of additional ground stations. Five modified systems were analyzed with between 2 and 16 additional ground stations.

The orbit determination assessment was based on an extended Kalman filter (EKF) covariance analysis for GPS orbit. State parameters included Cartesian position, velocity, clock bias, and clock drift. Nine different initial covariance studies were performed for two different initial longitude conditions for the location of the GPS satellite at the start of the simulation.

Measurements included pseudorange signals originating from the GPS satellite, integrated Doppler measurements originating from the GPS satellite, and two-way laser-ranging measurements originating from the ground stations. The simulation was performed under discrete time and measurement conditions for a duration of 1 day and a step size of 1 sec. Ten noise profiles were used to compare the performance of the EKF since the covariance profile of the EKF depends

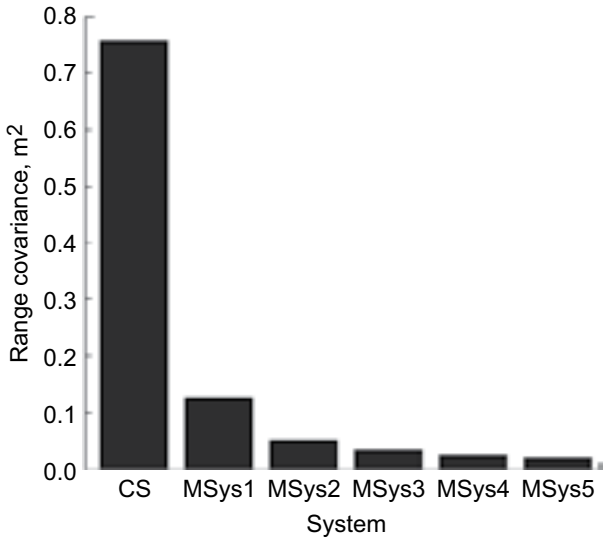


*Range covariance results comparison by system. CS, current system; MSys1 to MSys5, modified system 1 to modified system 5.*

on real noise values. Results show that an increase in the number of ground stations reduced the steady-state range covariance when the initial covariance of the velocity components was not greater than that of the position components. Results also show that as the number of laser-ranging ground stations was increased from 14 to 18, and then from 18 to 22, there were only small reductions in the range covariance.

Most benefits (most percent reductions in range covariance) come from transitions from CS to MSys1, MSys1 to MSys2, and MSys2 to MSys3. Further additions to the number of laser ranging ground stations as part of the simulation do not reduce the range covariance by a percentage comparable to the number of stations being utilized.

The Satellite Laser Ranging Benefits for Orbit Determination at GPS Orbit Assessment effort is managed under the Space Communications and Data Systems Project at Glenn. The work was performed in-house by a member of the Communications Systems Integration Branch in Glenn's Communications Technology Division.

**Find out more about the research of Glenn's Communications Technology Division:**
http://ctd.grc.nasa.gov

**Glenn contact:**
Bryan W. Welch, 216–433–3390, Bryan.W.Welch@nasa.gov

**Author:**
Bryan W. Welch

**Headquarters program office:**
Space Communications Technology Program

**Programs/projects:**
Space Communications and Data Systems Project, Space Communication Architecture Working Group

## Reflector Antenna Surface Photogrammetry Studied

Inflatable reflector antennas offer low-mass, low-volume options when high-gain antennas are required. While the antennas are inflating from their packaged state, their geometrical properties change over the inflation time. It is desirable to characterize the radiofrequency performance of the antennas during inflation so that the solar effects can be emulated from the coefficient of thermal expansion and solar flux variation experienced by the antenna in the space environment, where the changes occur on time scales on the order of minutes. Changes in the solar effects will impact antenna performance over the lifetime of the antenna. These solar effects can only be emulated within a thermal-vacuum chamber. Although near-field and/or far-field laboratory equipment is not available in the vacuum chamber in which inflation takes place, antenna surface characteristics can be obtained by laser-ranging the antenna surface with mirrors from the outside of the vacuum chamber.

The Reflector Antenna Surface Photogrammetry Study is the first part of an effort at the NASA Glenn Research Center to characterize the radiofrequency secondary patterns of an inflatable antenna. Initial laser scans in combination with near-field antenna patterns of the antenna surface show that the commonly used Ruze theory, which estimates gain degradation from the wavelength and the root-mean-square surface error overstates the loss in gain for inflatable antennas.

The Ruze theory assumes that the surface errors are random gaussian-distributed errors. However, inflatable antennas experience non-gaussian-distributed surface errors that are correlated, for example, with a wrinkle. Ideally, reflector antennas have reflections that are in the direction that the antenna is pointing. However, when surface errors are introduced, the direction of the reflections can vary depending on the location of the surface error and the geometry of the error in comparison to the ideal antenna surface.

The next phase in analyzing the secondary patterns of the inflatable antennas is to examine the laser photogrammetry data and to compute not only the correct gain (and therefore the correct degradation from the ideal antenna surface), but also the secondary pattern. The second phase of the planned analysis is not accounted for by the Ruze theory because the theory assumes random gaussian-distributed surface errors. The goal is to obtain the secondary patterns and the antenna gain from the photogrammetry data, such that vacuum chamber tests can be performed while photogrammetry data are obtained to characterize how the inflation of the inflatable antenna changes the antenna performance over time.

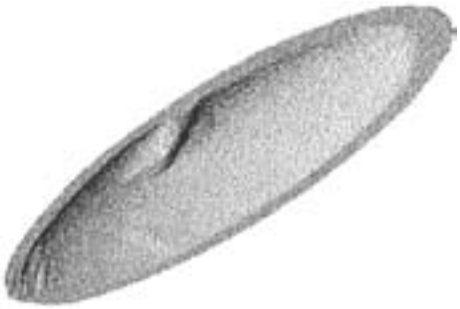

*Photogrammetry data of antenna surface.*

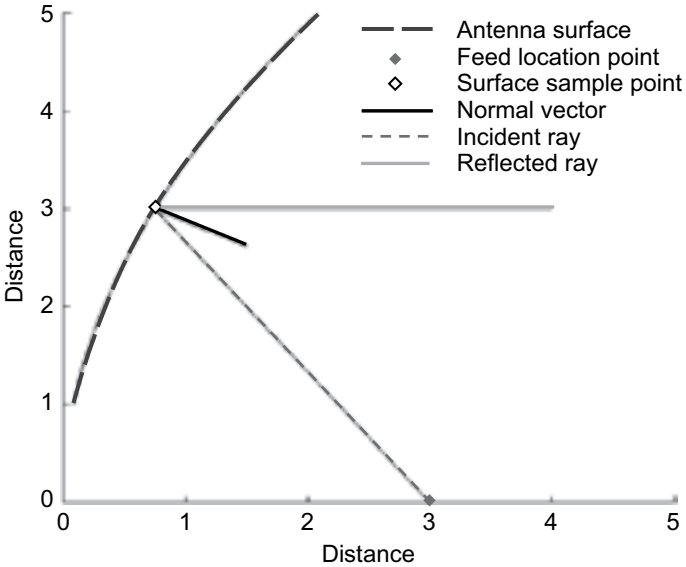


*Reflection from ideal parabolic surface.*

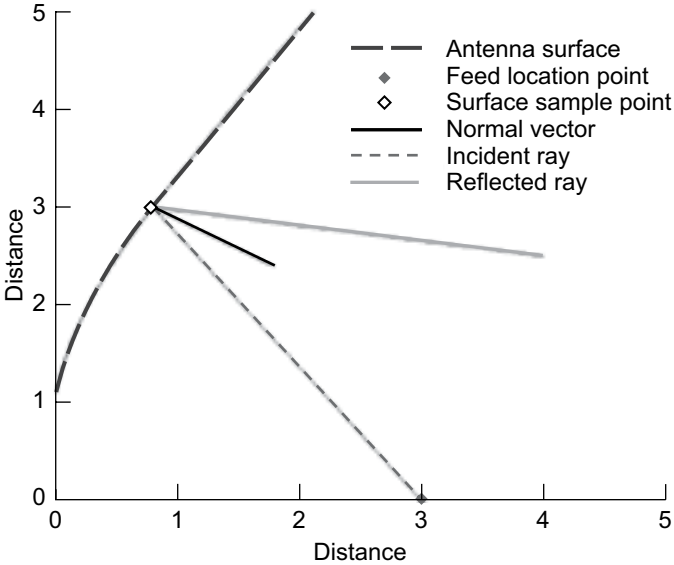


*Reflection from corrupted parabolic surface.*

The Reflector Antenna Surface Photogrammetry Study effort is managed under the Space Communications and Data Systems Project at Glenn. The work was performed in-house by a member of the Communications Systems Integration Branch in Glenn's Communications Technology Division.

**Find out more about the research of Glenn's Communications Technology Division:**
http://ctd.grc.nasa.gov

**Glenn contact:**
Bryan W. Welch, 216–433–3390, Bryan.W.Welch@nasa.gov

**Author:**
Bryan W. Welch

**Headquarters program office:**
Space Communications Technology Program

**Programs/projects:**
Space Communications and Data Systems Project

# Extravehicular Activity Subsystems Being Developed: Communications Equipment and Crew Displays Demonstrated and Field Tested

As part of the Extravehicular Activity (EVA) Project, the NASA Glenn Research Center is responsible for Communications, Avionics, and Information (CAI) subsystems for next-generation exploration space suits. Part of this effort involves prototypical development and testing of various CAI subsystems. This particular effort included the development of an EVA audio laboratory and digital signal processor (DSP) voice interface, an EVA crew display subsystem, an EVA suit information subsystem, and an EVA sensor subsystem.

Glenn's Space Audio Development and Evaluation Laboratory (SPADEL) is useful for precise characterization of in-suit acoustics and the evaluation of forward and return speech channels for prospective and operational systems. Audio system technology development of headset and DSP-based voice interfaces (helmet-mounted microphones and speakers) may improve outbound speech quality, in-suit noise levels, and duplex channel feedback levels. The SPADEL supports evaluation of speech quality through creation of an utterance database for jury testing, as well as objective evaluation of speech quality using International Telecommunications Union- (ITU-) recommended algorithms. The portability of SPADEL's test equipment allows for low-cost and low-risk environmental testing at various EVA operating pressures. A successful demonstration and field testing of suit-mounted microphones, speakers, and DSP-based noise suppression in the Mark III suit took place during the 2006 Desert Research and Technology Studies (D–RATS) outing. In addition, an improved headset concept is being developed to mitigate current EVA audio limitations.

*SPADEL and DSP subsystem.*

Another effort at Glenn involved the development of EVA crew displays. EVA design constraints were evaluated for various display concepts. Optical characteristics were evaluated for both displays inside the EVA helmet and displays located on the crewmember's arm. An optics analysis for a Glenn-developed internal helmet mounted display concept yielded promising results. A detailed prototype design is currently in progress. System design must allow for the required low volume, power, and safety considerations for operating in a pure oxygen environment.

Development is underway of an EVA suit information system prototyping platform that integrates displays, voice interfaces, computers, sensor systems, and software for evaluation of advanced EVA information system concepts. Candidate applications include using voice recognition for command and control of an on-suit computer, tracking and monitoring suit life support consumables such as oxygen and battery, displaying timeline procedures and checking off tasks, displaying crew biomedical information such as heart rate and metabolic rate for pacing of work activities, and navigating and tracking during surface operations.

The fourth CAI effort at Glenn involves development of a sensor system that promotes autonomous crew performance and health monitoring, such as heart rate and metabolic rate determination. Although Apollo-era metabolic rates were calculated on the ground, future EVA systems need to be able to operate autonomously. For the sensor system, $CO_2$ sensors are being developed with reduced size, power, and mass. This

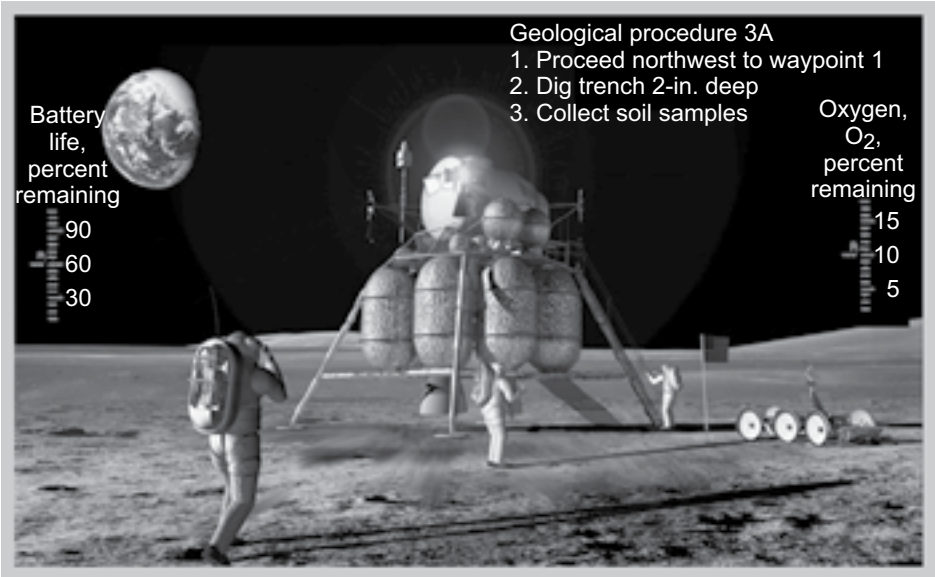


*Snapshot of EVA information system.*

*PUMA and integration testing.*

activity also supports near-term ground-based integrated testing activities such as walk-back testing to determine safe EVA traverse requirements. This technology is also coupled with the system requirements definition of an EVA information system.

Finally, the Portable Unit for Metabolic Analysis (PUMA) was upgraded to increase accuracy and portability to support EVA integrated testing. This technology development is also being evaluated for inclusion into the EVA system for real-time metabolic determination while astronauts are operating on the Moon.

**Glenn contact:**
David A. Carek, 216–433–8396, David.A.Carek@nasa.gov

**Authors:**
David A. Carek and David P. Irimies

**Headquarters program office:**
Constellation, Exploration Technology Development Program, Human Research Program

**Programs/projects:**
Exploration Systems

# Dynamic Channel Emulator That Models Space Data Links Developed

Future space networks will be a combination of private industry, government, and academia that will be adaptable and extensible to accommodate dynamic nodes. The Communication Technology Division's Network Emulation Laboratory (NEL) at the NASA Glenn Research Center is emulating different architectures, based on Space Communication Architecture Working Group studies, and technologies to determine how they will impact future net-centric architectures and communications. The emulations revolve around a dynamic channel emulator (CE), which provides dynamic space-based data link characteristics during the execution of the scenarios.

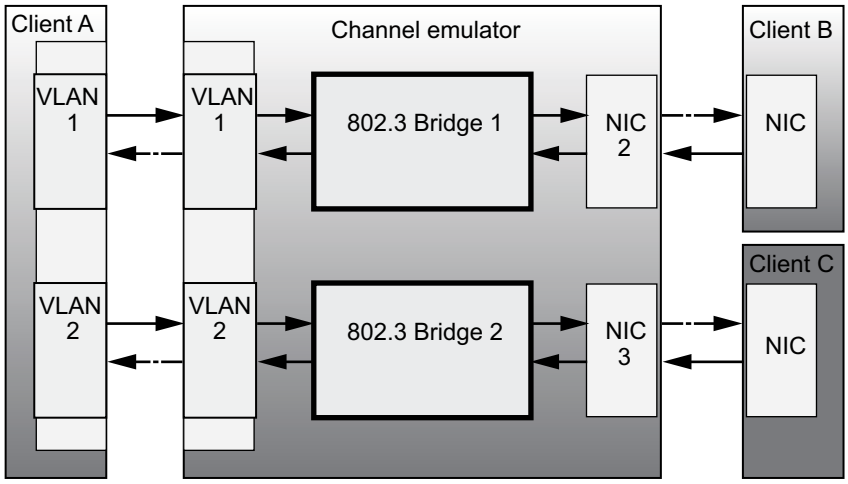


*The channel emulator with two channels configured using virtual interfaces. NIC, network interface card.*

The CE is a realistic, flexible platform that functions as a Level 2 link-layer 802.3 bridge, which allows it to accommodate a number of protocols in addition to the Internet Protocol. To apply emulated network attributes, the CE configures the queuing discipline (qdisc) on the egress queue of each interface, where packet delay, loss, corruption, and duplications are set. The CE also incorporates the 802.1q virtual (tag-based Virtual Local Area Network (VLAN)) interface, which creates virtual interfaces to permit the partitioning of a single pair of networking interfaces into many that represent physical devices on a satellite. The current version is distributed on a Knoppix LiveCD to simplify the installation and setup procedures.

The CE currently provides the following capabilities:

**Delay:** The quantity of time that a packet should be held at the CE before it is transmitted to the receiver; for each time interval, the delay represents a static quantity. The CE can also introduce a dynamic delay, which changes with respect to time (i.e., the delay is static at each time interval). Dynamic delays permit the emulation of an object approaching or receding from another object, such as the Crew Exploration Vehicle approaching the Moon. Delays have been validated for the Moon (3.4-sec round trip) and Mars (20-min round trip).

**Jitter:** The CE supports jitter, which is a variable amount of time that the packet is held at the CE before it is transmitted to the receiver; the additional delta time is added to the delay. Jitter can result in packet reordering, since each packet is held for a random amount of time; and conversely, when jitter is not implemented, the emulator should only produce a constant delay.

**Stream mangling—packet corruption (bit errors), loss, and duplication:** The CE can flip a random bit in a random packet at a configurable statistical rate that is sent to the receiver in that condition to force it to compensate for the error. The emulator must also be able to drop packets at a configurable rate, forcing the receiver to detect the missing packet by relying on packets already received.

**Maximum throughput:** Currently, the CE can support a maximum throughput of 622 Mbits/sec. Since potential throughput is primarily a hardware limitation, the bandwidth delay product dictates how much memory will be required to achieve the maximum throughput.

**Midscenario attribute changes:** The CE can process dynamic midscenario changes, where objects are moving and getting closer or farther apart, gaining or losing visibility, or changing weather conditions, without disrupting active data streams.

**Remote configurability:** The CE provides remote configuration through simple remote shell sessions and a programmatic interface. The CE supports SSH (Secure Shell) and Web access for direct user interaction and Simple Object Access Protocol (SOAP) and Web Services Description Language (WSDL) for programmatic functions.

**Data collection:** The CE uses the Linux ulog facility to collect packet headers and counters for both real-time and post-scenario analysis and visualization.

**One-way communication:** The CE can mimic one-way communications by ignoring packets that are directed to it from the receiver's side. It is not uncommon for a receiver in space to be unable, by design, to reply back to a sender.

**Serial connections:** The CE provides a unique ability to connect to a satellite modem via an RS–422 serial port rather than an Ethernet connection.

**Find out more about the research of Glenn's Satellite Networks and Architectures Branch:**
http://ctd.grc.nasa.gov/organization/branches/snab/snab.html

**Glenn contact:**
Richard A. Slywczak, 216–433–3493, Richard.A.Slywczak@nasa.gov

**Authors:**
Richard A. Slywczak and Thaddeus J. Kollar

**Headquarters program office:**
Exploration Systems Mission Directorate

**Programs/projects:**
Crew Exploration Vehicle, Life Support & Habitation, Next Generation Launch Technology, Return to Flight, Vehicle Systems, Satellite Missions

## Communication, Navigation, and Surveillance Models Integrated Into National Airspace System Simulation

The Airspace Concept Evaluation System (ACES) was developed by NASA's Airspace System Program to simulate flights and National Airspace System (NAS) operations, as an event-based, simulation application that has proven to be very effective for conceptual air traffic studies. During fiscal year 2006, an improvement to ACES was made at the NASA Glenn Research Center that involved implementing communication, navigation, and surveillance (CNS) system models into this application. Detailed system models were incorporated in three technology areas: (1) communications—voice communication and controller-pilot data link communications (CPDLC), (2) surveillance—secondary surveillance radar (SSR) and automatic dependent surveillance broadcast (ADS–B), and (3) navigation—Global Positioning System (GPS) and very high frequency (VHF) omnidirectional radar and digital measuring equipment (VOR/DME). These models were integrated into a version of ACES called ACES with CNS Models (AwCNS).

Along with the nominal operation of these systems to provide communications, navigation, and surveillance systems, three additional features were added that more realistically simulate their air traffic control (ATC) implementation. These include

(1) Communication-activated maneuvers, which provides a sequence of the ATC-to-pilot instruction and acknowledgment messages required to be delivered before an aircraft maneuver can be initiated
(2) Enhanced frequency and channel allocations—providing a more realistic distribution of VHF voice messages over multiple channels within the Terminal Radar Control Facility (TRACON) and airport airspace for specific airports
(3) A short sector transition time feature that mimics ATC of whether or not a new frequency is communicated to an aircraft when the length of time that the aircraft will reside in a portion of a sector is limited

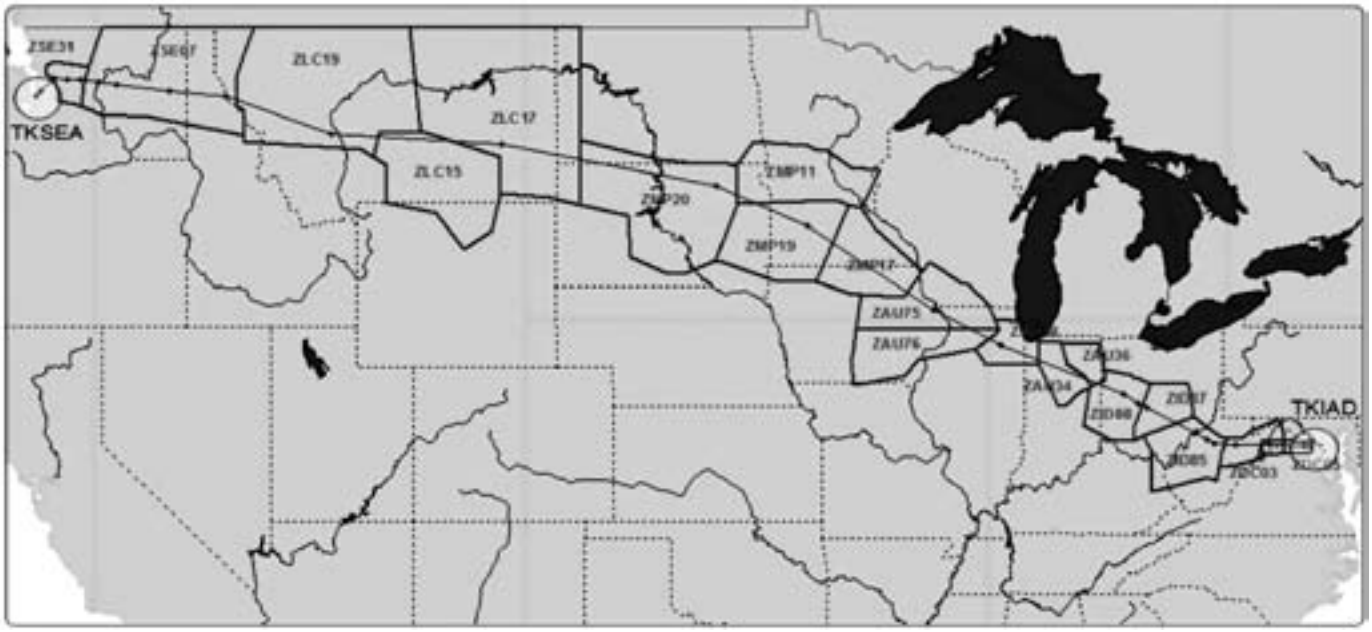


*Section of the northern United States overlayed with the flight path of an aircraft that flies from Dulles Airport near Washington DC to Seattle International Airport in Washington State. At both the Dulles and Seattle airports, the TRACON airspace regions are indicated as well as all sector boundaries that the aircraft flies through along its flight path.*

To enhance the use of the flight physics model in ACES, closed-loop operation features were introduced using the navigation and surveillance models. With closed-loop operation for navigation, the system provides feedback of the navigation system model output to the aircraft. With closed-loop operation using the surveillance system, a simulation can provide feedback of the reported position to ATC agents in ACES. ACES NAS agents can use this information to generate new maneuvers for the aircraft or to identify traffic restriction violations due to the variation of the aircraft from its anticipated or desired position, leading to a more realistic and dynamic flight scenario.

AwCNS models developed in this effort offer a diverse array of experimentation possibilities for investigating the NAS infrastructure with a proven, NAS-wide simulation tool. With these new modeling capabilities, existing NAS operations and new concept simulations that target NAS operational improvements can include CNS infrastructure systems, and results can be used to evaluate their ability to support those operations and concept objectives.

The project team consisted of in-house personnel from Glenn and contractors from Analex Corporation, Intelligent Automation, Inc., and Computer Networks and Software, Inc.

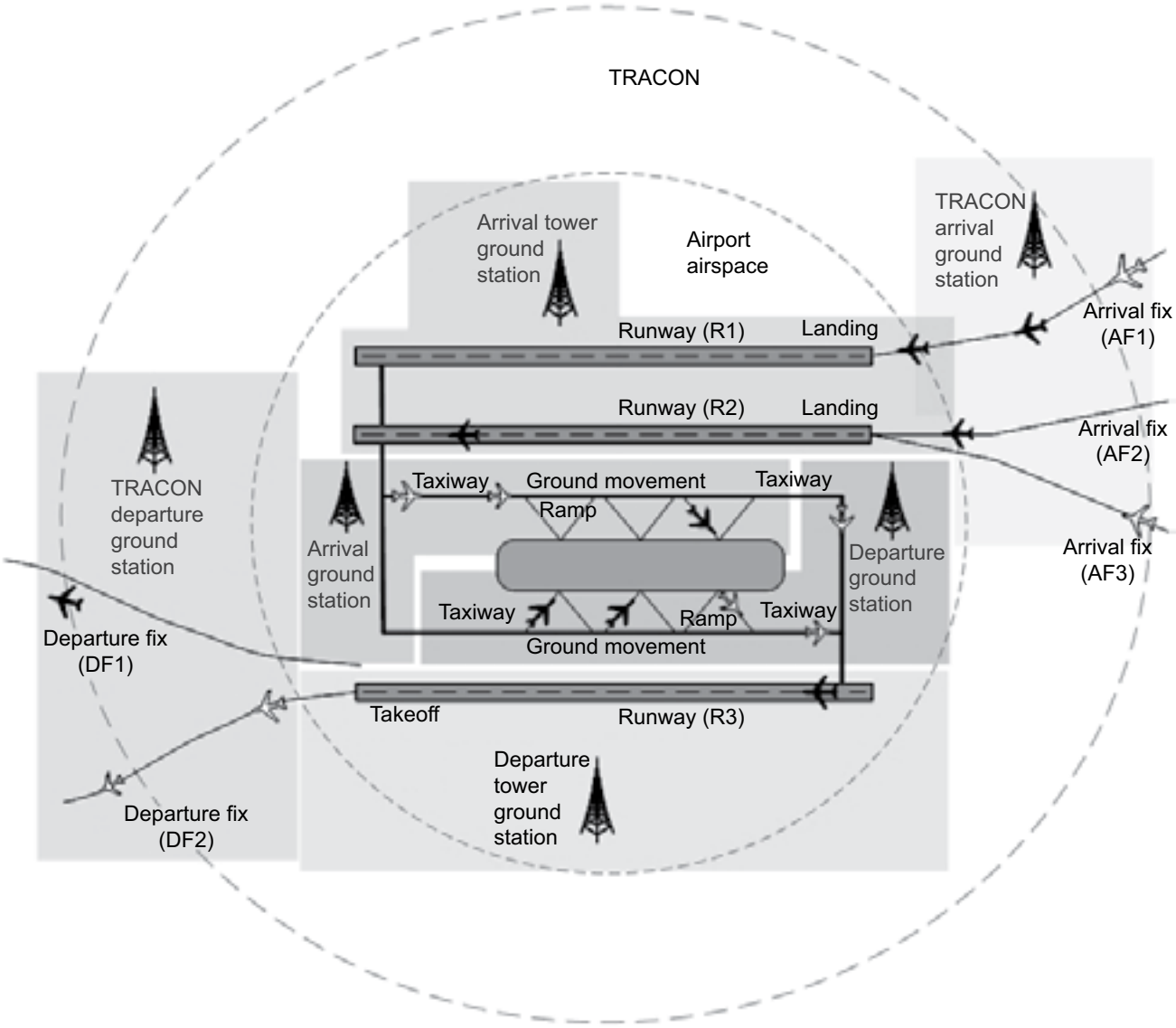


*Typical airport layout with terminals, arriving and departing runways, and the airport and TRACON airspaces detailed where communications to and from aircraft occur. A separate radio tower is located in each airspace shown to indicate the per-airspace, channel separation provided for airport communication simulations.*

**Glenn contact:**
Donald Van Drei, 216–433–9089, Donald.E.VanDrei@nasa.gov

**Analex Corp. contact:**
Greg Kubat, 216–433–8123, Gregory.Kubat@Analex.com

**Authors:**
Donald E. Van Drei and Gregory Kubat

**Headquarters program office:**
Aeronautics Research Mission Directorate

**Programs/projects:**
Airspace Systems Program

## Variable-Frequency Fluidic Actuator Developed, Fabricated, and Tested for Flow-Control Applications

Aeropropulsion system performance improvements are becoming increasingly dependent on the use of control technologies. As aeropropulsion engines evolve from rigid mechanical designs to adaptable systems, the need for new, embeddable sensors and actuators becomes critical. The variable-frequency fluidic actuator is a new device developed at the NASA Glenn Research Center that could be built into the components of an engine, thereby enabling advanced technologies known as active flow control.

Flow control is the technology of manipulating the aerodynamic flow over a surface, such as a wing, to enhance its ability to produce lift or to reduce the drag force, especially under severe operating conditions. This has been an area of basic research for many years. In an airframe, flow control is important because it affects the aircraft's operability, maneuverability, and fuel consumption. In a turbine engine, there are similar concerns because the many small airfoils in the engine must operate over a large range of flow conditions. Only in recent years have these flow-control concepts been extended to the internal workings of a turbine engine.

Research on air-injection flow control in turbomachinery performed at Glenn has reduced loss dramatically because of the mitigation of flow separation on compressor stators. These results, while demonstrating effective means to enhance performance, have also pointed to the lack of suitable actuation devices to effectively implement flow control in the hostile environment inside a jet engine. To further flow-control research and perhaps enable flow control in production engines, Glenn researchers developed the variable-frequency fluidic actuator, an actuation device capable of pulsed injection at variable frequency and duty cycle.

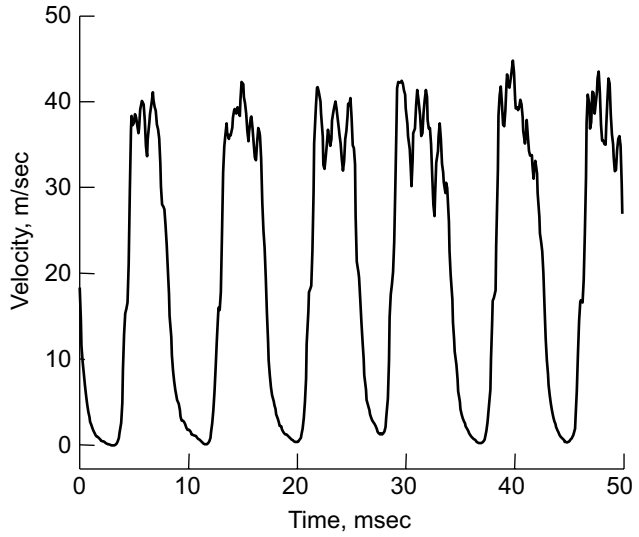


*Example of the output flow from a single channel of the actuator.*

The actuator produces two highly modulated output flows from a single pressure source. The graph depicts the flow from one channel. The output of the second channel would appear similar but would be 90° out of phase. The device operates on the Coanda effect to switch the source flow to one of the two output channels, thereby forming a stable jet. By applying a very small and momentary force at the control point, as shown in the drawing on the next page, the input flow can be diverted to the opposite channel, where a stable jet is once more formed. Reapplying the momentary control force again results in a switching action at the output. This can be repeated at any frequency and duty cycle up to the acoustic limit of the fluidic channels.

The device has been fabricated and tested using miniature, high-speed electromechanical operators to apply the control force as shown in the photograph on the next page. An effort is underway to replace the electromechanical operators with an all-electronic operator that will enable further miniaturization and improved high-frequency performance.

**Find out more about research at the NASA Glenn Research Center:**
http://www.grc.nasa.gov

**Glenn contact:**
Dennis E. Culley, 216–433–3797, Dennis.E.Culley@nasa.gov

**Author:**
Dennis E. Culley

**Headquarters program office:**
Aeronautics Research Mission Directorate

**Programs/projects:**
Independent Research and Development, Fundamental Aeronautics, Subsonic Fixed Wing

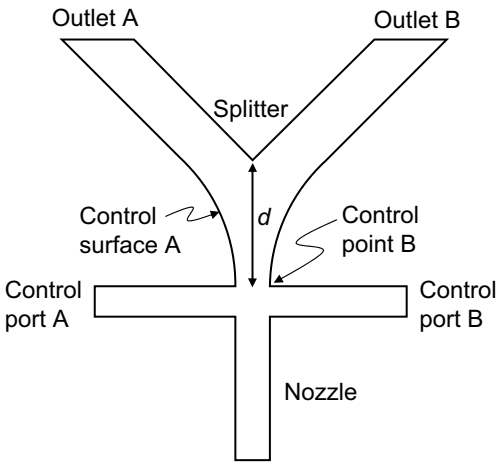


*Functional description of the actuator.*

*Actuator with miniature operators installed.*

## Novel Predictive Control Concept Developed for Improved Turbine Tip-Clearance Performance

Closed-loop active turbine tip clearance control methods are being sought by industry to improve the efficiency and longevity of modern-day gas turbine engines. Efforts are underway at the NASA Glenn Research Center to develop rapid-response actuation systems that regulate a segmented shroud ring that is free to move radially relative to the turbine blades. When used in conjunction with a tip clearance proximity sensor, the system enables tight clearances to be maintained throughout the operating envelope, even when rapid changes in the rotor diameter are experienced during power-up events.

Targeted reductions in specific fuel consumption and peak exhaust gas temperatures, which will negatively impact engine service life, are in excess of 1 percent and 10 °C, respectively. As progress continues on developing fast tip-clearance actuators and high-temperature proximity sensors, there is a strong need to develop control laws that can protect the engine from damaging blade rubs at the tight clearances required to achieve the targeted reductions in fuel consumption and exhaust temperatures. NASA researchers have identified model predictive control (MPC) as offering the most promise for attaining this challenging objective. With this method, a model of the engine is used to compute a trajectory of the clearance evolution through time; the controller uses this trajectory as a basis for optimizing future actuator commands. The advantage is that the controller can actively avoid operating limits, such as a minimum acceptable clearance to prevent the actuator from moving the shroud to within an unsafe proximity to the blades. MPC, therefore, improves the robustness of the system, allowing tighter clearance setpoints than those that are used with controllers designed with conventional methods.

There are inherent limitations to MPC when it is applied to a highly nonlinear turbofan engine. Linear parameter-varying models used to describe such systems lose fidelity when high-magnitude transients occur, such as takeoff or reacceleration, resulting in degraded MPC performance and loss of robustness to blade rubs, and therefore, reduced tip-clearance performance. In this work, a rate-based linear parameter-varying model was used instead to greatly reduce the model's dependence on statically derived parameters, thereby extending fidelity to rapid transients. As shown in the block diagram on the next page, this rate-based model was used in conjunction with standard quadratic programming optimizers to derive a new MPC with enhanced performance throughout the flight trajectory.

Extensive simulation studies of a tip-clearance system and high-fidelity engine simulation were used to verify

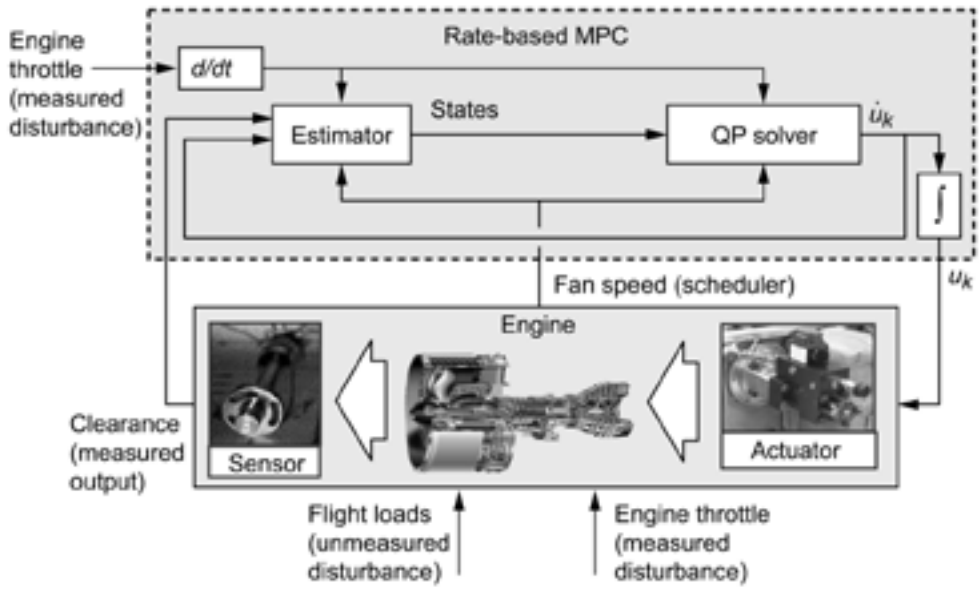


*Rate-based MPC. The "Estimator" block reconstructs the model states at the current time step on the basis of sensed output data. The "QP solver" block (quadratic programming) uses the estimated states at the current step to generate a model-predicted trajectory and computes an optimal rate-based controller output, $\dot{u}_k$. In the rate-based framework, this output is integrated to form the actuator command, $u_k$. The d/dt block represents signal differentiation.*

the improved performance achievable with this novel MPC algorithm. In the evaluation, both thermal- and servohydraulic-type actuators were evaluated; the results for three transient event scenarios using the servohydraulic are shown in the following time traces and are summarized in the table. Note that a zero-clearance setpoint is used here for illustration; in actual systems, negative values would correspond to clearances smaller than the setpoint. It is shown that, using this MPC controller, the minimum clearances in response to takeoff, thrust reversal, and airplane stall events were significantly smaller than those generated by a conventional control with no constraints. Applying worst-case analysis on the results reveals that the achievable setpoint of an MPC-based controller may be 2.55 mils tighter than that of a conventional controller, improving engine efficiency by approximately 0.25 percent. This improvement is considerable when compared with the 1.0-percent gain in efficiency realized by replacing open-loop thermally activated clearance control with a closed-loop mechanically actuated device. Efforts are underway to implement and evaluate the controller in a nonrotating turbine clearance control test rig.

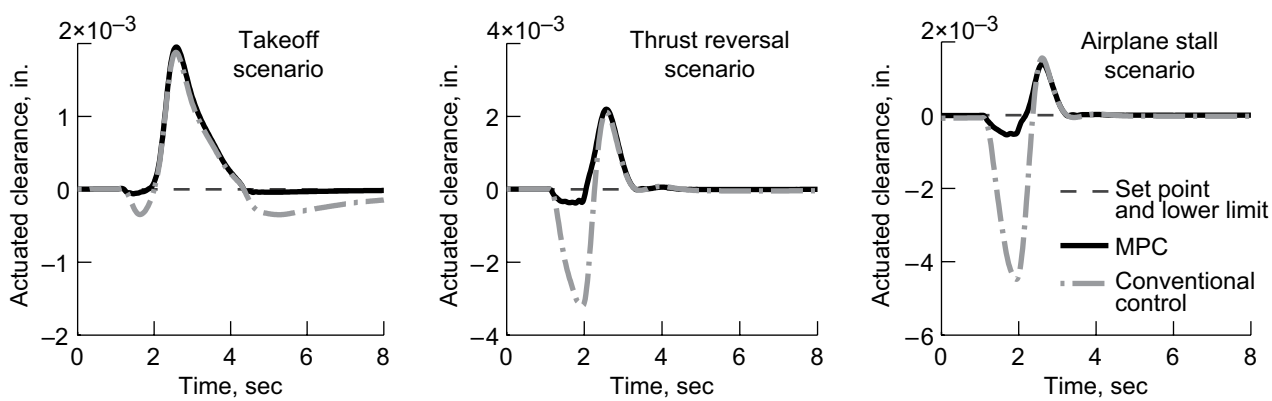


*Time histories of the high-pressure turbine clearance disturbance rejection with the rate-based MPC and a conventional linear controller. Both controllers have zero-clearance setpoints, but the MPC imposes a lower limit (also set at zero clearance) in order to realize tight clearances without blade rubs.*

PERFORMANCE IMPROVEMENTS OF AN MPC TIP–CLEARANCE CONTROL SYSTEM

| Mission event | Minimum clearance, mils | | |
|---|---|---|---|
| | Conventional control | Model predictive control | Delta improvement |
| Takeoff | –0.80 | –0.18 | 0.62 |
| Thrust reversal | –2.29 | –0.50 | 1.79 |
| Airplane stall | –3.26 | –0.71 | 2.55 |

**Bibliography**
DeCastro, J.: Rate-Based Model Predictive Control of Turbofan Engine Clearance. AIAA–2006–5107 (NASA/CR—2006-214419), 2006. http://gltrs.grc.nasa.gov/Citations.aspx?id=219

**ASRC Aerospace contact:**
Jonathan A. DeCastro, 216–433–3946, Jonathan.A.DeCastro@nasa.gov

**Glenn contact:**
Kevin J. Melcher, 216–433–3743, Kevin.J.Melcher@nasa.gov

**Authors:**
Jonathan A. DeCastro and Kevin J. Melcher

**Headquarters program office:**
Aeronautics Research Mission Directorate

**Programs/projects:**
Propulsion 21

# Hybrid Kalman Filter Developed for In-Flight Detection of Aircraft Engine Faults

Improved aviation safety and reliability can be achieved through enhanced in-flight diagnostic capabilities for aircraft gas turbine engines. Since faults in sensors, actuators, or components can lead the aircraft engine into undesirable operating conditions, it is critical to detect faults as early as possible so that the necessary corrective actions can be taken. A challenge in developing an in-flight fault-detection system is to make it adaptive to engine health degradation. Engine health degradation is a normal, expected process that all aircraft engines will undergo, whereas a fault is an abnormal, unexpected event. However, both health degradation and faults influence the engine output, from which the existence of faults is detected. If an in-flight fault-detection system cannot adapt to health degradation, it will eventually lose its diagnostic effectiveness.

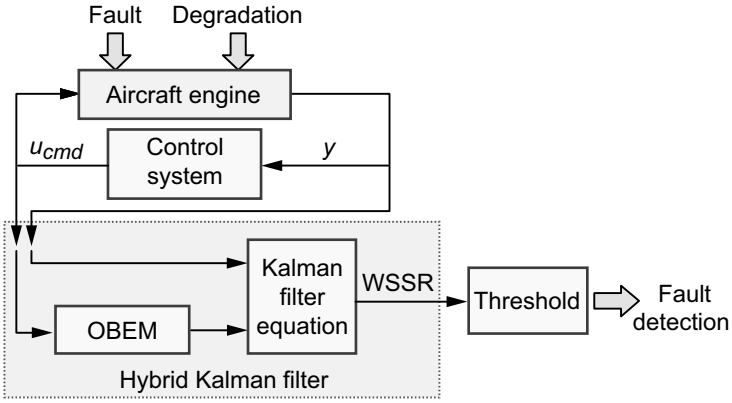


*Structure of the in-flight fault-detection system: y, measured engine output; $u_{cmd}$, control commands; WSSR (weighted sum of squared residuals), fault indicator signal.*

To address this issue, researchers at the NASA Glenn Research Center developed a hybrid Kalman filter (HKF). This new type of estimation technique combines the advantages of the linear and nonlinear Kalman filter approaches. The uniqueness of the HKF is its structure: a hybrid of a nonlinear onboard engine model (OBEM) and piecewise linear models. Because of this hybrid structure, the HKF possesses significant advantages that make this technique well suited for in-flight, real-time diagnostic applications.

The first advantage is that the reference health baseline of the HKF can be updated to the health condition of the degraded engine in a relatively simple manner. In-flight diagnostics is accomplished by processing the measured information relative to an established reference health baseline. As the aircraft engine degrades over time because of usage, its operating condition deviates from this baseline, causing health-degradation-induced shifts in the measurements. Such health degradation

influences are compensated for by periodic updates to the reference health baseline. Although this baseline update is a necessary step, some diagnostic techniques have a structure that makes this update highly complex and impractical. Therefore, the structure of the HKF, which lends itself to a simple health baseline update, is a significant advantage.

The second advantage is the HKF capability to capture nonlinear, off-design engine operations. Aircraft engines undergo such operations as the engine control system responds to faults or non-fault-related factors, such as bleed air or horsepower extractions for aircraft services. This HKF capability is due to the utilization of the OBEM in which the nonlinear relationships between the engine parameters are embedded.

The third advantage is the numerical robustness of the HKF. An OBEM can be a concern for numerical stability depending on how it is implemented and used in the diagnostics process. In the HKF approach, the OBEM runs as a standalone engine model; it generates expected engine output for given control command input. On the basis of the information provided by the OBEM, the HKF estimates engine variables. Therefore, the numerical stability of the OBEM is not influenced by the estimation performance of the HKF.

The HKF-based fault-detection system was developed, and its diagnostic capability was investigated in a simulation environment. Extensive study indicates that HKF is a promising technology for aircraft engine in-flight diagnostics.

**Bibliography**

Kobayashi, Takahisa; and Simon, Donald L.: Hybrid Kalman Filter Approach for Aircraft Engine In-Flight Diagnostics: Sensor Fault Detection Case. ASME Paper GT2006–90870 (NASA/TM—2006-214418), 2006, pp. 745–755. http://gltrs.grc.nasa.gov/Citations.aspx?id=167

**ASRC Aerospace Corp. contact:**
Takahisa Kobayashi, 216–433–3739, Takahisa.Kobayashi-1@nasa.gov

**U.S. Army Research Laboratory at Glenn contact:**
Donald L. Simon, 216–433–3740, Donald.L.Simon@nasa.gov

**Authors:**
Takahisa Kobayashi and Donald L. Simon

**Headquarters program office:**
Aeronautics Research Mission Directorate

**Programs/projects:**
Aviation Safety Program

## Efficient Algorithm Developed To Enable Real-Time Implementation of Model Predictive Control for a Turbofan Engine Application

Model Predictive Control (MPC) utilizes a model of the system under control to simulate performance over a time horizon into the future, and then optimizes the current control input data to achieve a future goal. This necessitates that the algorithm run much faster than real time. Although MPC has been applied extensively in industrial process control where the processes tend to have relatively long time constants, its application to aerospace systems has been limited because the large computational effort required precludes real-time operation. The time necessary to calculate a solution is a function of several factors including the time horizons selected, the number of state variables, and the data that are input to the system. The NASA Glenn Research Center, in collaboration with the Cleveland State University, has utilized a modified approach to enable a real-time implementation of MPC to aerospace systems while maintaining closed-loop performance close to that obtained by using the original MPC implementation.

The control application considered for this study is a large commercial turbofan engine simulation, capable of running faster than real time. A non-real-time implementation of MPC incorporating this simulation had demonstrated the capability to achieve complex tradeoffs in engine control, such as minimizing turbine temperature to extend part life while still maintaining acceptable transient performance during takeoff, and minimizing fuel consumption during cruise. This original MPC algorithm was not able to run in real time because of the number of variables

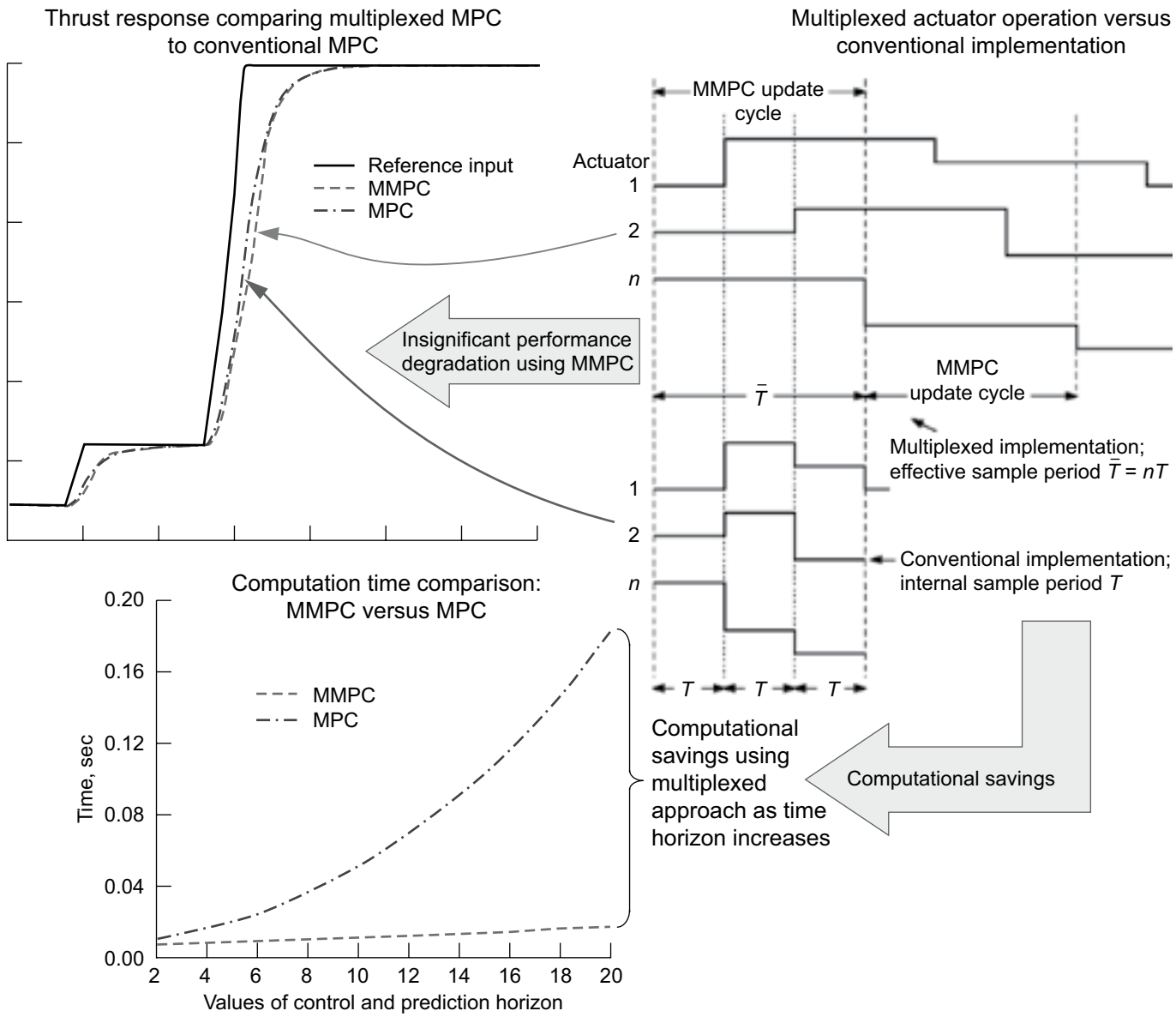


*MMPC performance compared with MPC performance, and comparison of the computation time required per control interval.*

that had to be optimized at each control interval. Specifically, the simulation has three fast-acting control input variables: fuel flow, variable guide vanes, and variable stator vanes. To simplify the model and thus reduce the computational load, the researchers used a multiplexed actuation approach. This multiplexed MPC (MMPC) technique computes a change in a single actuator at each control interval, holding the others constant. The algorithm rotates through each of the actuators over three time steps, thus significantly reducing the computational effort required.

The closed-loop system performance achieved with the multiplexed approach was similar to the original case where all actuators were updated together, whereas the computation time was reduced to about one-eighth. In addition, no convergence problems were observed with the optimization algorithms. These results indicate that the MMPC approach can effectively enhance the control of complex aerospace systems. For the propulsion system used for this study, the faster-than-real-time execution of MMPC allows users to extend the control time horizon or to reduce the control interval, thus potentially further reducing the small performance gap between the original MPC and the MMPC.

This work was performed under the grant “Computationally Efficient Predictive Control Strategies for Real-Time Implementation” with the Cleveland State University, with Prof. Hanz Richter as the principal investigator. This work was supported by the Propulsion 21 project under the Fundamental Aeronautics program.

**Find out more about the research of Glenn’s Controls & Dynamics Branch:**
http://www.grc.nasa.gov/WWW/cdtb/

**U.S. Army Research Laboratory at Glenn contact:**
Jonathan S. Litt, 216–433–3748,
Jonathan.S.Litt@nasa.gov

**Cleveland State University contact:**
Dr. Hanz Richter, 216–687–5232,
h.richter@csuohio.edu

**Author:**
Jonathan S. Litt

**Headquarters program office:**
Fundamental Aeronautics

**Programs/projects:**
Propulsion 21

## Sensor Data Qualification System Developed and Evaluated for Assessing the Health of Ares I Upper-Stage Sensors

Given the requirements for autonomous control and human rating for the next generation of space exploration vehicles, control and diagnostic functions for these vehicles will require that data used by these functions be analyzed and qualified to represent the state of the system being measured. A Sensor Data Qualification System (SDQS) is one approach for addressing data qualification requirements. Sensor data qualification is the development of a mathematical network of constraints using analytical redundancy to assess the health of a particular sensor in a suite of sensors that are measuring the condition of a given system. An SDQS for a power distribution unit (PDU) testbed was developed and evaluated at the NASA Glenn Research Center as part of a longer term activity to develop methodologies for assessing the health of Ares I upper-stage systems.

Algorithmically, the SDQS has three primary functions: predict, detect, and decide. To predict the value of a given sensor in time, measurements from related sensors are used in conjunction with predefined mathematical equations (i.e., local models) that describe how each sensor relates to the other sensors measuring the system state. The residual, the difference between the measured value and predicted value, is then computed for each relationship. A relationship failure is detected when the residual exceeds a preset threshold for a specified number of consecutive cycles. The decision to declare a sensor failed is made when the frequency and number of failed relationships for that sensor reaches predefined limits over some sampling interval—said limits being determined by the use of sensor reliability information and the application of Bayesian probability theory to the joint probability distributions.

As part of a feasibility demonstration to support the Avionics System Requirements Review for Ares I, SDQS networks were applied to a testbed developed by Glenn’s Advanced Electrical Systems Branch. The testbed was composed of a single power supply, a prototype PDU, and three load banks. A schematic of the testbed and a photograph of the PDU hardware are shown in the top figure on the next page. The system was operated in one of three modes depending on the number of active loads—one, two, or all three. The magnitude of each load was variable and unknown during operation.

The active sensor network consisted of 6, 9, or 12 active sensors, depending on the number of active loads. Relay states and output load requests were also available as discrete data. Three nominal runs provided data for determining the mathematical relationships between the

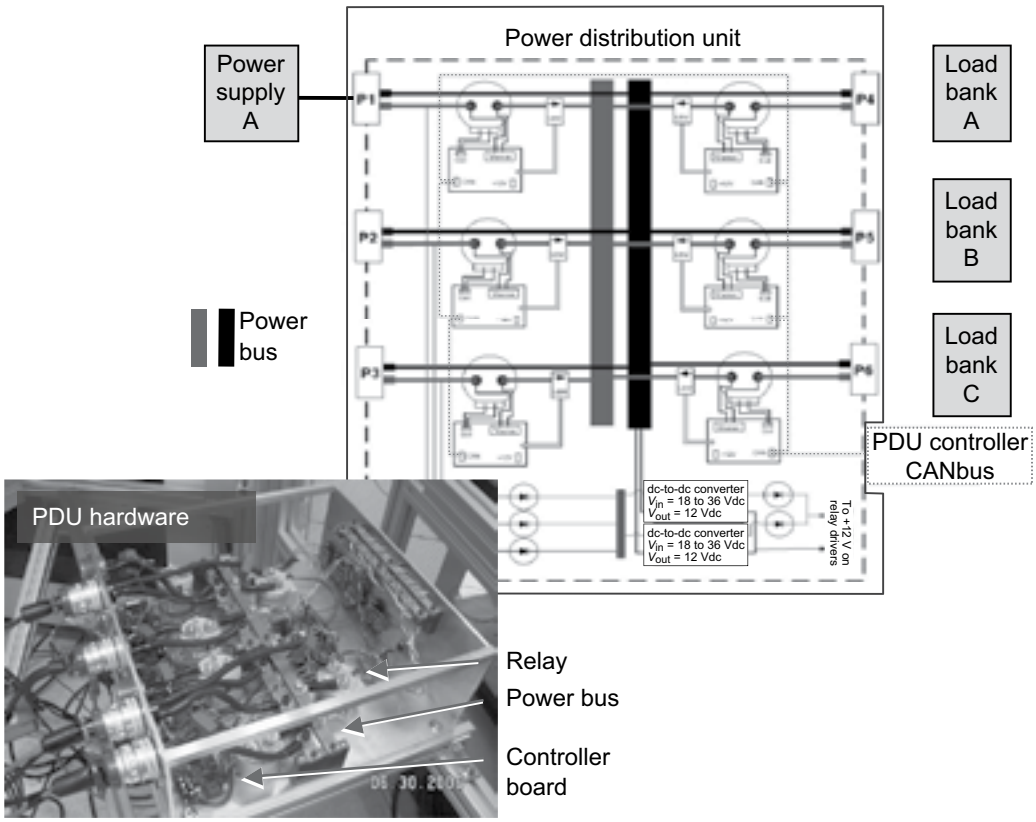


*PDU testbed and the PDU hardware used during testing. CANbus, Controller Area Network Bus (high-speed, high-integrity, serial data communications bus for real-time control applications, http://www.mjschofield.com); $V_{sense}$, voltage sensor; LEM, current sensor; CAN, port used to connect to the CANbus.*

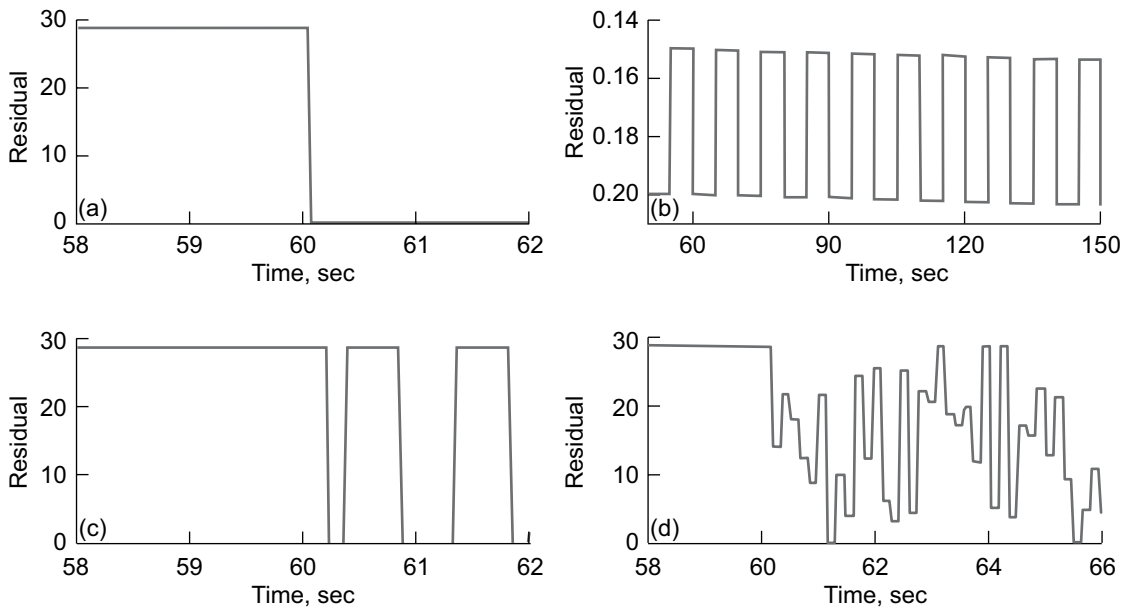


*Four primary fault signatures were simulated and superimposed on the nominal data to test the diagnostic performance of the SDQS. (a) Hard failure (open or short circuit). (b) Drift failure (thermal or resistance change). (c) Intermittent, binary (loose connector). (d) Intermittent, filtered (cracked solder joint).*

sensors. Sensor failure data were obtained by superimposing simulated fault signatures on nominal data during data acquisition. Four primary sensor faults were identified as shown in the graphs on the preceding page: hard (high or low), drift (low, medium, or high), intermittent-binary, and intermittent-filtered. Using these faults in combination with various sensors, Glenn researchers simulated 13 different sensor failures for each mode. The SDQS correctly identified all 13 faults in each of the three operating modes, with no false alarms or missed detections.

This study used data playback to investigate the failure of a single sensor in a network of sensors. Future research is planned for detecting multiple sensor failures, identifying sensor failures in the presence of a failed component or in a closed-loop control system, and investigating issues associated with real-time implementation.

**Bibliography**

Maul, William A., et al: Sensor Data Qualification for Autonomous Operation of Space Systems. American Association for Artificial Intelligence 2006 Fall Symposium on Spacecraft Autonomy, Washington, DC, Oct. 13–15, 2006, AAAI Technical Report FS–06–07 (NASA/TM—2006-214475), pp. 59–66, 2006. http://gltrs.grc.nasa.gov/Citations.aspx?id=192

**Find out more about the research of Glenn's Controls & Dynamics Branch:**
http://www.grc.nasa.gov/WWW/cdtb/

**Glenn contact:**
Kevin J. Melcher, 216–433–3743, Kevin.J.Melcher@nasa.gov

**Analex Corporation contact:**
William A. Maul, 216–977–7496, William.A.Maul@nasa.gov

**Authors:**
Kevin J. Melcher and William A. Maul

**Headquarters program office:**
Exploration Systems Mission Directorate

**Programs/projects:**
Crew Launch Vehicle Project

## Large-Scale Pulsejet-Driven Ejector System Investigated

Ejectors are passive devices that, when placed aft of a thrust-producing jet, entrain ambient air and increase thrust. In recent years there has been renewed interest in the concept of ejectors or thrust augmentors driven by periodic, unsteady propulsion devices (i.e., pulsed propulsion). The reason for this stems primarily from the interest in pulse detonation engines (PDEs), which are decidedly unsteady, and which therefore seem natural candidates on which to use an ejector. It has been demonstrated convincingly in recent experiments that, under the proper operating conditions, and with a well-designed ejector, thrust augmentation levels approaching or even exceeding 2.0 can be achieved with unsteady thrust sources as drivers. Thrust augmentation is defined as the total time-averaged thrust provided by the ejector and driver system divided by the thrust of the driver alone.

Studies have been conducted using a variety of unsteady thrust sources including actual PDEs, simple pulsed valves, Hartmann-Sprenger resonance tubes, synthetic jets, and pulsejets. The results from each of these experiments have helped to identify the factors that optimize unsteady ejector systems.

Despite the many unsteady ejector experiments performed to date and the growing body of understanding associated with them, some results could not be generalized because all the experiments shared a common small scale. The thrust levels were low (less than 15 $lb_f$), and the driver diameters were between 1 and 2 in. Thus, although rules have been suggested relating, for example, the optimal diameter of the ejector as a fixed ratio relative to that of the driver, they were not definitive because all the drivers tested were nearly the same size.

To address this issue, a pulsejet approximately an order of magnitude larger in exhaust cross-sectional area and thrust

than most recent tests was operated with a series of ejectors of varying diameter, length, and shape (cylindrical and tapered). The ejector parameters were systematically varied to determine the configuration yielding the highest thrust augmentation. The installed rig is shown in the photograph.

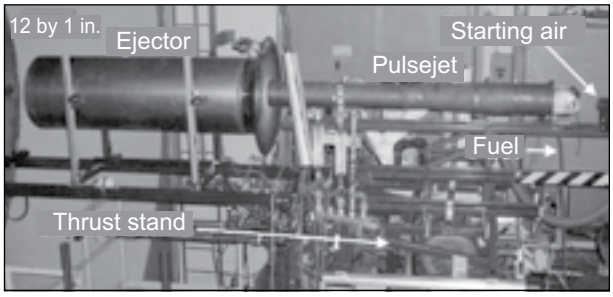


*Pulsejet and one of the tested ejectors installed on a thrust measuring rig.*

Typical results are shown in the graph. A peak thrust augmentation value of 1.71 was obtained using ejectors with parallel walls. The optimized ejector diameter was found to be 2.46 times the pulsejet driver diameter of 6.5 in. This ratio was consistent with the small-scale experiments and may, therefore, be considered a sizing rule. The optimal length was found to be 10 times the driver diameter. This result was found to be the same as for another small-scale pulsejet experiment but to be somewhat different from those where another driving source was used, suggesting that other parameters, such as pulsing frequency, determine optimal ejector length. It was found that the tapered profile ejector yielded a higher thrust augmentation than the best of the straight profile series. The value obtained was 1.81. This result was consistent with numerous other unsteady thrust augmentation experiments. Additional research is needed to determine if there is an optimal ejector taper angle and if that angle can be related to parameters of the driver. The large-scale ejector fabrication and testing were performed at the Air Force Research Laboratory in Dayton, Ohio.

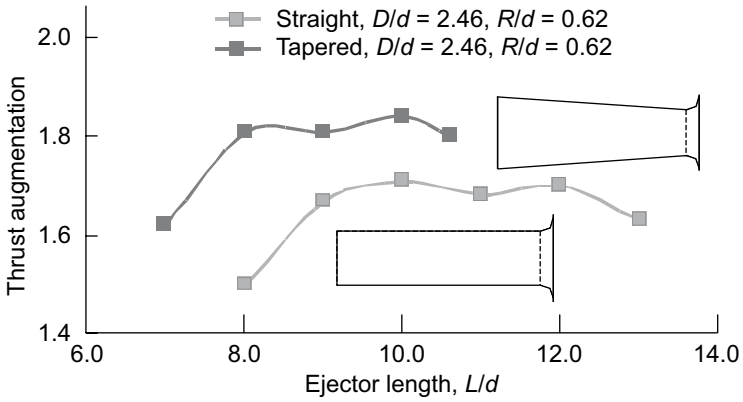


*Thrust augmentation as a function of ejector length for tapered- and straight-walled ejectors. D/d, ratio of ejector throat diameter to pulsejet exit diameter; R, radius of ejector inlet rounding (as viewed from the side, or axial radial plane).*

**Bibliography**

Litke, P., et al.: Assessment of the Performance of a Pulsejet and Comparison With a Pulsed-Detonation Engine. AIAA–2005–0228, 2005.

Paxson, D.; Wilson, J.; and Dougherty, K.: Unsteady Ejector Performance: An Experimental Investigation Using a Pulsejet Driver. AIAA–2002–3915 (NASA/TM—2002-211711), 2002. http://gltrs.grc.nasa.gov/cgi-bin/GLTRS/browse.pl?2002/TM-2002-211711.html

Wilson, J.; and Paxson, D.E.: Unsteady Ejector Performance: An Experimental Investigation Using a Resonance Tube Driver. AIAA–2002–3632 (NASA/TM—2002-211474), 2002. http://gltrs.grc.nasa.gov/cgi-bin/GLTRS/browse.pl?2002/TM-2002-211474.html

Wilson, J., et al.: Parametric Investigation of Thrust Augmentation by Ejectors on a Pulsed Detonation Tube. AIAA–2005–4208 (NASA/TM—2005-213823), 2005. http://gltrs.grc.nasa.gov/cgi-bin/GLTRS/browse.pl?2005/TM-2005-213823.html

**Glenn contact:**
Dr. Daniel E. Paxson, 216–433–8334, Daniel.E.Paxson@nasa.gov

**Author:**
Dr. Daniel E. Paxson

**Headquarters program office:**
Aeronautics Research Mission Directorate

**Programs/projects:**
Vehicle Systems Program, Constant Volume Combustion Cycle Engine Project

# Cruciform Specimen Used To Assess Long-Term Creep for Characterizing Advanced Aerospace Materials Under In-Plane Biaxial Loading

The Department of Energy and NASA are developing a high-efficiency Stirling radioisotope power system for potential use on NASA missions, including deep-space missions, Mars rovers, and lunar applications (refs. 1 and 2). A key qualification criterion for flight hardware is long-term durability for the critical hot-section components of the power convertor. One such critical component is the power convertor heater head. The heater head is a high-temperature pressure vessel that transfers heat to and from the working gas of the convertor, which is typically helium. The efficiency of a successful heater head design depends on balancing specific requirements, such as having thin walls for minimizing heat conduction losses between the hot and cold ends and having thick walls to lower the stresses and thus improve creep resistance for durability. In the current design of the Advanced Stirling Radioisotope Generator (ASRG), the heater head of the Advanced Stirling Convertor (ASC) is fabricated from the nickel-base superalloy INCONEL 718 (Special Metals Welding Products Company). Another version of the ASC is being developed with a MAR–M 247 (Lockheed Martin) heater head, which allows increased hot-end temperatures and, thus, increased efficiency and specific power. The vessel walls are subjected to temperatures as high as 650 °C (1200 °F) with INCONEL 718 and as high as 850 °C (1560 °F) with MAR–M 247, for lifetimes up to 17 years (refs. 3 and 4).

Material behavior under complex stress states is often investigated using an in-plane biaxial loading approach. Utilizing this technique requires cruciform-type specimens fabricated from plate material. The specimen is gripped at four locations and loaded along two orthogonal axes in servohydraulic systems. These testing capabilities currently exist at the NASA Glenn Research Center, where biaxial cruciform specimen testing is supporting the formulation and verification of an analytical life-prediction methodology for the flight-design heater head.

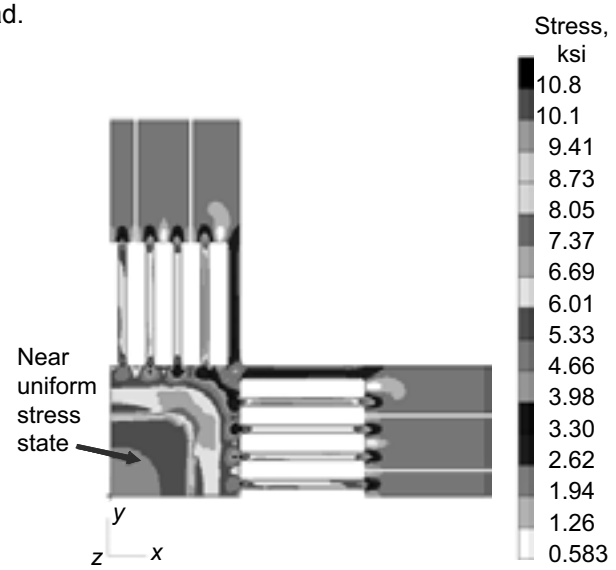


*Von Mises stress distribution under equibiaxial loading conditions. This figure is shown in color in the online version of this article (http://www.grc.nasa.gov/WWW/RT/2006/RI/RIO-abdul-aziz.html).*

This work is intended to continue the development of a specimen design that is fully compatible with the in-plane biaxial testing systems at Glenn (ref. 5). Details of the specimen design and its applicability to the ongoing experimental activities are reported and discussed in reference 5.

Analytical activities at Glenn led to a thorough finite element analysis to optimize the geometry of a cruciform specimen made of a nickel-base superalloy, INCONEL 718, and evaluating the stress response under biaxial loading conditions (ref. 6). Results reported indicated that the specimen can be used to investigate deformation behavior under general forms of biaxial loading, provided measurement and observation are limited to a 1-in.- (2.54-cm-) diameter circular region at the specimen's center. However, the conditions could be more complex in experiments investigating strength and fracture behavior.

This figure shows a nearly uniform stress state in the test region under linear elastic, equibiaxial loading, demonstrating the applicability of the specimen design for equibiaxial loading. A similar analysis was performed for nonequibiaxial loading under linear elastic conditions. Additional analyses were carried out under steady-state creep to further validate the biaxial test loading conditions with a heater head test specimen called Bitec1. The figure on the left (next page) shows the x-component of creep strain within the test section. More details are noted in the figure on the right, where the x-component of creep strain is reported for different time intervals as a function of the axial distance. The analyses were carried out for 750 hr, and the results indicate that the creep strain, as expected, increases with time. The analytical activities are progressing as planned to support ongoing benchmark tests on ASC heater heads and upcoming biaxial experiments on cruciform specimens.

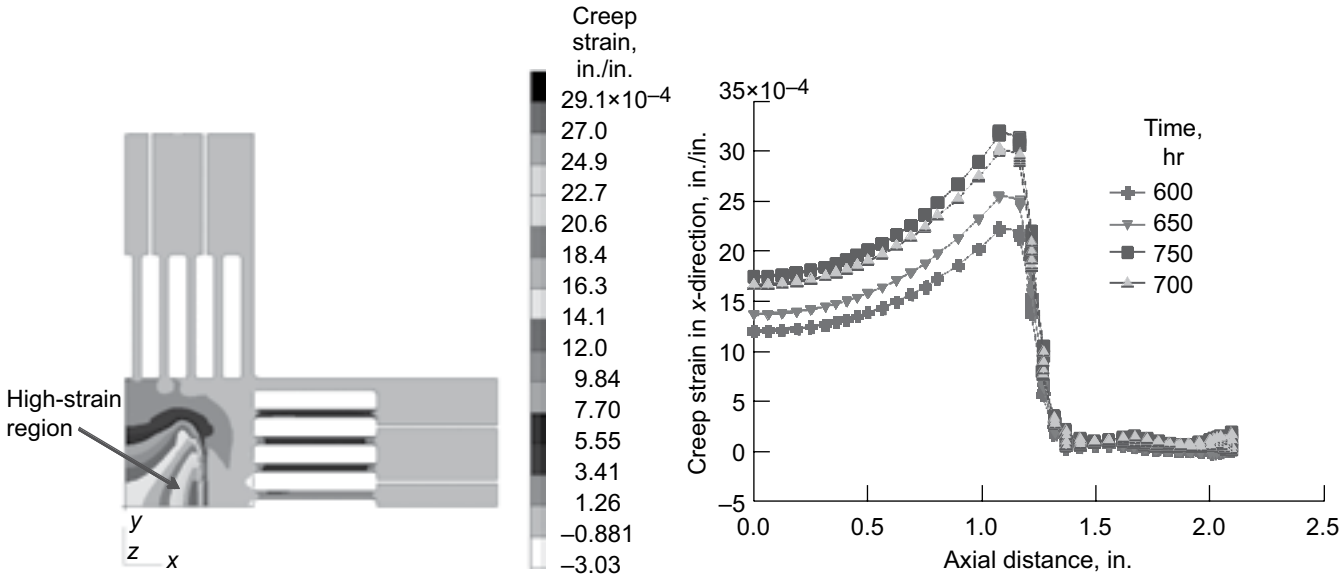


*Left: x-component of creep strain after 750 hr of nonequibiaxial loading. Right: x-component of creep strain after different time intervals of nonequibiaxial loading. This figure is shown in color in the online version of this article (http://www.grc.nasa.gov/WWW/RT/2006/RI/RIO-abdul-aziz.html).*

**References**


1. Schreiber, J.: Developmental Considerations on the Free-Piston Stirling Power Convertor for Use in Space. AIAA–2006–4015, 2006.
2. Chan, J.; Wood, J.G.; and Schreiber, J.G.: Development of Advanced Stirling Radioisotope Generator for Space Exploration. Proceedings of Space Technology and Applications International Forum (STAIF–2007), M.S. El-Genk, ed., American Institute of Physics, Melville, NY, Feb. 11–15, 2007.
3. Bowman, Randy R.: Long-Term Creep Assessment of a Thin-Walled Inconel 718 Stirling Power-Convertor Heater Head. Proc. Intersoc. Energy Convers. Eng. Conf., vol. 1, 2001, pp. 435–440.
4. Johnson, A.E.: Creep Under Complex Stress Systems at Elevated Temperatures. Proc. Inst. Mech. Eng. Proc., vol. 164, 1951, pp. 432–447.
5. Abdul-Aziz, Ali; and Krause, David: Combined Experimental and Analytical Study Using Cruciform Specimen for Testing Advanced Aeropropulsion Materials Under In-Plane Biaxial Loading. Proc. SPIE Int. Soc. Opt. Eng., vol. 6176, 2006.
6. Ellis, John R.; and Abdul-Aziz, Ali: Specimen Designs for Testing Advanced Aeropropulsion Materials Under In-Plane Biaxial Loading. NASA/TM—2003-212090, 2003. http://gltrs.grc.nasa.gov/cgi-bin/GLTRS/browse.pl?2003/TM-2003-212090.html



**Cleveland State University contact:**
Dr. Ali Abdul-Aziz, 216–433–6729, Ali.Abdul-aziz-1@nasa.gov

**Glenn contact:**
David L. Krause, 216–433–5465, David.L.Krause@nasa.gov

**Ohio Aerospace Institute (OAI) contact:**
Dr. Sreeramesh Kalluri, 216–433–6727, Sreeramesh.Kalluri-1@nasa.gov

**Authors:**
Dr. Ali Abdul-Aziz, David L. Krause, and Dr. Sreeramesh Kalluri


**Headquarters program office:**
Science Mission Directorate

**Programs/projects:**
110–W Stirling Radioisotope Generator

# Linux-Based Image-Acquisition System Tested for Use With a Hyperspectral Imager

In fiscal year 2006, a Linux-based image-acquisition system was demonstrated at the NASA Glenn Research Center. The system consists of an off-the-shelf industrial computer with a 100-GB hard drive, a Global Positioning System (GPS) receiver, an orientation sensor, and a custom image-acquisition board, which was developed in Glenn's Flight Electronics Lab to acquire "pushbroom" hyperspectral data as a part of the Great Lakes Environmental Monitoring project, which is a collaboration between Glenn and the National Oceanic and Atmospheric Administration.

The system is built around an industrial personal computer running Linux-2.6.9 (Free Software Foundation, Incorporated, MA) with custom software. The software consists of a device driver for the image acquisition board, a GPS daemon, an orientation daemon, a memory management daemon, and application software, which transfers image data from the image acquisition board to the database. The application software and daemons communicate via a region of shared memory. Furthermore, there is a small server that implements a subset of the Hypertext Transfer Protocol (HTTP). The server provides live Portable Network Graphics (PNG) snapshots of the context camera and hyperspectral imager, a histogram of hyperspectral data, and GPS and orientation data. It allows users to download the database. In addition, the software controls the camera exposure and gain and data bus timing.

The database is stored on an unformatted, 99-GB partition on the hard drive and is written via raw input/output: that is, there is no file system. It is organized as a series of up to approximately 160,000 records. Each record is of fixed size and contains image, position, and orientation information needed to reconstruct images from the hyperspectral data.

The device driver provides access to the image data and allows software to acquire snapshots. In order to maximize the data rate, the driver changes the clock speed of the PC–104 bus to 16.7 MHz upon initialization.

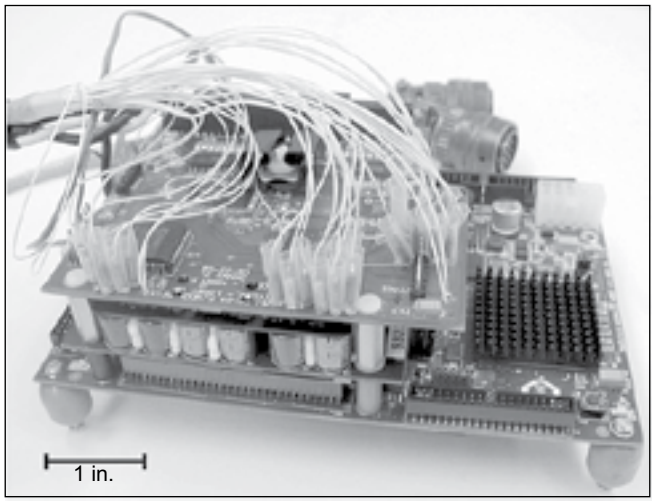


*Image acquisition system: industrial computer (bottom board), power supply (middle), image acquisition board (top board and cabling). The 2.5-in. hard drive is not shown.*

The GPS, orientation, and memory management daemons are small applications that continuously run in the background. Each daemon is responsible for a particular task. For example, the GPS daemon parses data from the GPS receiver and stores the position in shared memory. Shared memory usage allows several applications to have access to current data simultaneously.

The system was tested aboard a manned aircraft, and images were acquired at approximately 2 frames per second. The results are currently being analyzed. It is expected that the system will be demonstrated in an unmanned-aerial-vehicle-based experiment in the near future.

The system has been shown to operate in the field. It is a low-power system consuming approximately 13 W over a range of 6 to 40 V and is compact. The personal computer, with the power supply and acquisition board shock absorbers, is 4.5 in. wide, 6.5 in. long, and approximately 4 in. high (see the photograph).

In the future, hardware changes will allow us to increase the frame rate and to acquire data from additional sensors, such as a point spectrometer. The combined operating system and application software can be reduced to under 16 MB by eliminating unused libraries and other files. The system can also be adapted to other image-acquisition applications where power and weight are a concern.

**Ohio Aerospace Institute (OAI) contact:**
Joseph M. Flatico, 216–433–5053,
Joseph.M.Flatico@nasa.gov

**Glenn contact:**
Dr. Quang-Viet Nguyen, 216–433–3574,
Quang-Viet.Nguyen-1@nasa.gov

**Author:**
Joseph M. Flatico

**Program/projects:**
Independent Research and Development

# Cratos—Tracked Test Rover Designed and Built at NASA Glenn

In Greek mythology Cratos was the personification of strength and power. His character typified the goals of the researchers at the NASA Glenn Research Center when they were designing a tracked test rover called Cratos (shown in the top photograph). A heavy-duty aluminum frame, two powerful direct-current motors, and a versatile sensor-laden control system made this an ideal test vehicle for studying various track designs and control algorithms. Cratos will be tested in various terrains and with different track designs to help determine the feasibility of using tracks to descend into a crater on the Moon.

*Cratos tracked rover.*

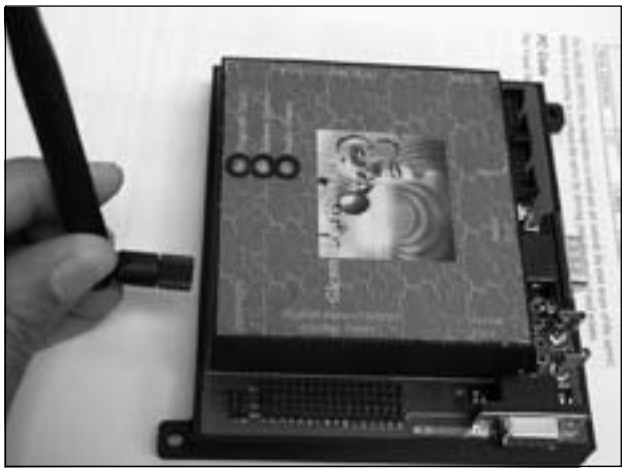

*Glenn controller.*

Cratos was a multidivisional effort led by the Flight Electronics Lab within Glenn's Instrumentation and Controls Division. It was funded under the Exploration Science Mission Directorate at Glenn and was part of a rover codevelopment program with the Carnegie Mellon University (CMU) Robotics Institute. CMU developed Highlander, a tracked rover to develop and test methods for lunar crater wall descent. As part of this effort, engineers at Glenn built and used Cratos to specify, develop, and test inertial measurement, tilt and odometry instruments, control algorithms with sensor fusion, and communications protocols for the CMU Highlander. As needs were determined at CMU, Glenn responded by developing and integrating new capabilities into Cratos. Once ready for use, these new components, techniques, and software downloads were delivered to CMU and were integrated into Highlander.

Because of cost and time constraints, off-the-shelf hardware and software components are often incorporated into test rigs such as Cratos. But in this case, many of the vehicle control components had to be customized to meet the design criteria. It proved to be more expedient to design a unique control system to implement Glenn's customized data packet structure for telemetering the sensor data. This new Glenn design includes a flexible controller with 16 pulse-width-modulated output ports, six relay output ports, two external interrupts, a RS232 serial port, a radio-link serial port, and 16 analog-to-digital input/output lines (see the bottom photograph). The radio link utilizes Maxstream's 900-MHz Extend-Radio with a maximum 40-mi range when its full 1 W of power is used. Data and control packets are telemetered between the controller and either a hand-held remote or a personal computer with a LabView program that emulates the remote and records the sensor data (see the photograph and screen capture on the next page).

In its current configuration Cratos has an electronic gyro, a two-axis accelerometer configured as tilt sensors, current sensors, and optical encoders for both track motors and a battery voltage/ampere-hour monitor (see the final photograph on the next page). Also included in Glenn's design is a Global Positioning System (GPS) unit that will interface to the controller through the RS232 serial line.

At the heart of the controller are two 8051 core processors from Silicon Laboratories. These processors use a pipelined architecture allowing the execution of 25 million instructions per second. One processor controls all of the communication, motor control, and battery monitoring, whereas the other controller is used to read the digital-to-analog and interrupt input as well as to

*Left: Hand-held remote. Right: LabView remote and data logger.*

*Gyro, tilt sensors, and current monitors.*

implement the user code. All the code is written in C and includes modules for easy input/output setup, motor control, and radio network (RNET) communication between the controller and host. The Joint Test Action Group interface between the personal computer and microcontrollers allows for quick troubleshooting during debugging sessions. Furthermore, status indicators for program fault, RNET fault, and low battery power give users a quick indication of the controller status. We hope to use this test rover to validate and/or improve various track designs as well as to test a variety of control algorithms for locomotion and navigation.

**Glenn contacts:**
Lawrence Greer, 216–433–8770,
Lawrence.C.Greer@nasa.gov

Mike Krasowski, 216–433–3729,
Michael.J.Krasowski@nasa.gov

John Caruso, 216–433–3324,
John.J.Caruso@nasa.gov

**Authors:**
Lawrence C. Greer and
Michael J. Krasowski

**Headquarters program office:**
Exploration Systems Mission Directorate

**Programs/projects:**
Surface Mobility

# Model Developed To Assess a Vibration-Based Crack-Detection Approach for the In Situ Health Monitoring of Rotors

Rotor health monitoring and online damage detection are increasingly gaining the interest of aircraft engine manufacturers. This is due primarily to the need for improved safety during operation and for lower maintenance costs. Applied techniques for damage detection and health monitoring of rotors are essential for engine safety, reliability, and life prediction. NASA's Aviation Safety Program provides research and technology products to help the aerospace industry improve aviation safety. The Nondestructive Evaluation (NDE) Group of the NASA Glenn Research Center's Optical Instrumentation and NDE Branch is developing propulsion-system-specific technologies for detecting damage prior to catastrophe.

Currently, the NDE group is assessing the feasibility of utilizing real-time vibration data for detecting cracks in turbine disks. The data are obtained from radial blade tip clearances and shaft clearances measured by a variety of sensors. The spectrum of sensors ranges from capacitive, to eddy current, to microwave-based technologies, all of which are designed for the extreme environments encountered within turbine engines. Damage can be detected in a rotating disk because the development of a disk crack distorts the strain field within the component. This causes a small deformation in the disk's geometry as well as a possible change in the system's center of mass. The geometric change and the center of mass shift are determined by monitoring the amplitude and phase of the first harmonic (i.e., the 1× component) of the vibration data. Spin pit experiments and full-scale engine tests have been conducted while this vibration-based crack-detection methodology was being used to monitor for crack growth. Even so, published data are extremely limited, and the basic foundation of the methodology has not been studied fully. To address these limitations, the NDE group developed a theoretical model that can assess the feasibility of this disk crack-detection approach.

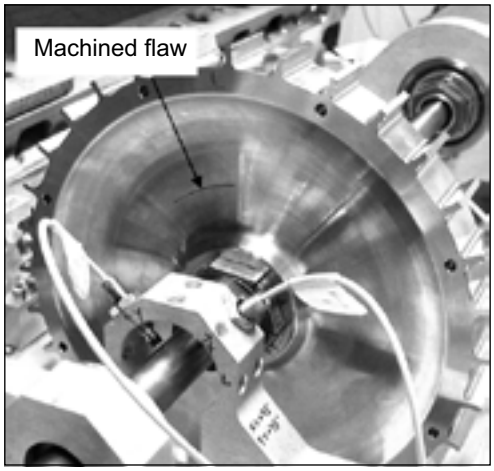


*Image of notched disk emulated by the model.*

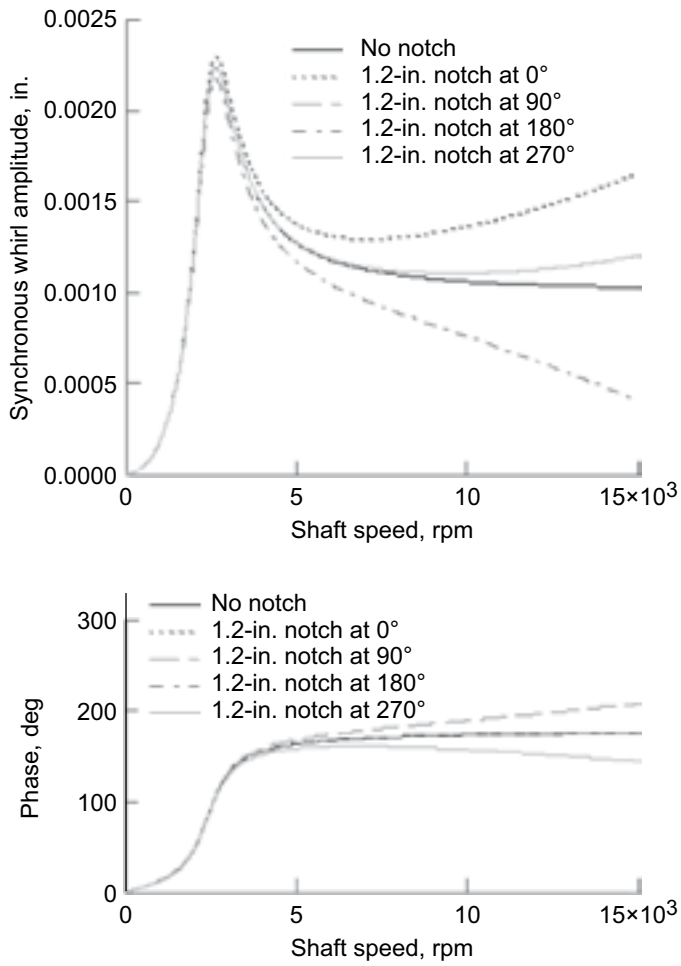


*Predictions of the amplitude and phase of the 1× vibration component for a disk located midspan on a flexible shaft. Results show various notch orientations in relation to the initial eccentricity.*

The vibration response obtained from the newly developed model provides a quantitative view of the method's sensitivity. The model was characterized using numerical and experimental data that emulated the Glenn spin rig that will be utilized for verification tests. For this setup, it appears that monitoring the

crack-induced shift in the center of mass is a feasible approach for identifying damage in a disk during operation. For the notched disk shown in the photograph, the model predicted an amplitude deviation on the order of 0.0005 in. at 15,000 rpm. The plots show the predicted response for multiple notch orientations. Further laboratory tests will be conducted to verify the data. The next steps involve modifying the vibration-based damage-detection methodologies to address more complex systems (e.g., multiple disks).

Lastly, localized approaches, where wireless sensors "ride on the spinning disk," are also being developed and studied as a complement to the global, vibration-based methodologies. An example of the local approach includes using piezoelectric patches (actuators/sensors) attached to the disk for conducting in situ ultrasonic and impedance-based measurements.

**Ohio Aerospace Institute (OAI) contact:**
Dr. Andrew L. Gyekenyesi,
216–433–8155,
Andrew.L.Gyekenyesi@nasa.gov

**Glenn contact:**
Dr. George Y. Baaklini, 216–433–6016,
George.Y.Baaklini@nasa.gov

**Authors:**
Dr. Andrew L. Gyekenyesi,
Prof. Jerzy T. Sawicki,
Dr. Wayne C. Haase, and
Dr. George Y. Baaklini

**Headquarters program office:**
Aeronautics Research Mission Directorate

**Programs/projects:**
Aviation Safety Program

## Great Lakes Hyperspectral Water Quality Instrument Suite Designed, Developed, Integrated, and Flight Tested for the Airborne Monitoring of Algal Blooms

In just 8 months, members of the Great Lakes Environmental Aerial Monitoring (GLEAM) mission—consisting of a multidisciplinary team of researchers, scientists, engineers, and technicians from the NASA Glenn Research Center, the National Oceanic and Atmospheric Administration (NOAA), and the Ohio Aerospace Institute (OAI)—designed, developed, integrated, and flight tested a highly specialized suite of instruments for the aerial measurement of water quality. During 2006, these instruments obtained spectral data of a sediment-laden river plume in Lake Michigan and an algal bloom in Lake Erie (shown in the photograph on the right). The suite of instruments consists of a Glenn-designed point spectrometer, a Glenn-designed hyperspectral imager, a commercial-off-the-shelf Global Positioning System (GPS) receiver, a commercial-off-the-shelf three-axis gyroscopic-stabilized inclinometer, and a Glenn-designed data-acquisition system (see the top photograph on the next page).

*Algal bloom in Lake Erie photographed on September 5, 2006. The algal bloom shown covers several square kilometers.*

The custom hyperspectral imager obtains wavelength-resolved images of a lake in narrow 2-nm-wide bands of light (see the sketch on the next page). The hyperspectral imager wavelength range is approximately 400 to 900 nm, thus approximately 250 distinct spectral band two-dimensional slices of data constitute a single three-dimensional image cube as shown in the sketch. The point spectrometer significantly adds to the capability of the instrument suite because it can provide highly accurate measurements of the incident solar spectrum as well as of the atmospheric water vapor content. This combined sensor suite will allow for more accurate spectral radiometric

measurements of lake constituents, allowing researchers to detect lower concentrations of pollutants or of harmful algal blooms.

The entire suite of instruments weighs less than 2.3 kg and uses less than 15 W of power. This allows the package to be deployed on many types of aircraft. For example, the team was able to mount the instrument on the avionics door of a T–34 aircraft to obtain the desired data in a very cost effective manner (see the final photograph). This instrumentation suite demonstrates Glenn's ability to deliver custom-designed flight-capable optoelectronic instrumentation and hardware for Earth science and space missions in a short amount of time.

*Glenn-designed water quality sensor suite mounted on the T–34 aircraft.*

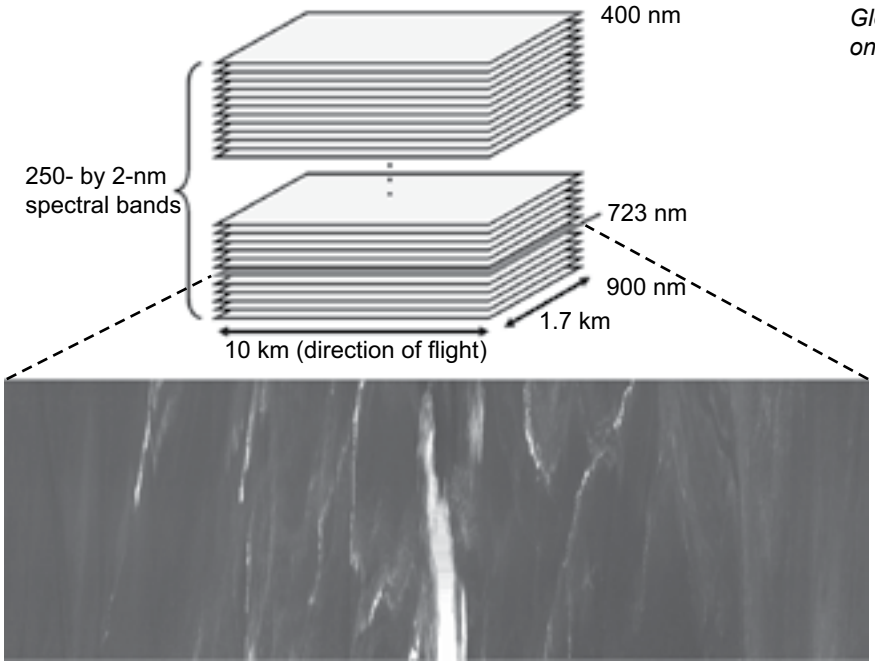


*Hyperspectral image "cube" data set obtained using the Glenn-built hyperspectral imager. The lower image is actual data from a slice of a near-infrared spectral band centered at 723 nm that correlates with a spectral feature in chlorophyll. At this wavelength, the contrast of an algal bloom in Lake Erie on September 5, 2006, is significantly enhanced in comparison to conventional imaging techniques. The large area of white in the middle is a cloud, and the rest of the white is the algal bloom.*

**Find out more about this research:**

**Glenn's Optical Instrumentation & NDE Branch:**
http://www.grc.nasa.gov/WWW/OptInstr/

**Glenn's Combustion Branch:**
http://www.grc.nasa.gov/WWW/combustion/

**Glenn's combustion diagnostics research:**
http://www.grc.nasa.gov/WWW/combustion/zDiag.htm

**Glenn contacts:**
John Lekki, 216–433–5650, John.D.Lekki@nasa.gov

Dr. Quang-Viet Nguyen, 216–433–3574, Quang-Viet.Nguyen-1@nasa.gov

**Authors:**
John D. Lekki and Dr. Quang-Viet Nguyen

**Programs/projects:**
Independent Research and Development

*Team that developed and deployed the instrument suite along with the instrument mounted on the side of the T–34 aircraft.*

# Candidate Thermal Protection System Materials Evaluated Following Simulated Space Environment and Reentry Conditions

In 2005 and 2006, NASA Glenn Research Center researchers tested and characterized thermal protection system candidate materials in support of the Lightweight Nonmetallic Thermal Protection Materials Technology Project. Efforts at Glenn included a nondestructive evaluation (NDE) study of six different state-of-the-art ceramic matrix composite and carbon-carbon composite thermal protection system candidate materials (55 specimens total). The materials are applicable to space/hypersonic vehicle heat shields, control surfaces, and leading edges.

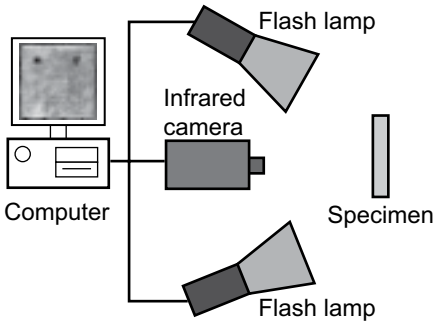


*Pulsed thermography setup. High-intensity flash lamps impart a short pulse of heat into the specimen. The thermal response to this input is monitored using an infrared camera and is recorded and processed using a computer.*

A pulsed thermography study was designed and conducted by Glenn researchers to characterize 1- by 4-in. ceramic matrix composite and carbon-carbon specimens in the as-fabricated condition and following exposure to simulated space environments at the NASA Marshall Space Flight Center, which included micrometeoroid object damage, atomic oxygen exposure, or combined radiation effects conditioning. All samples were subsequently exposed to a simulated Earth entry from lunar return in NASA Langley Research Center's Multiparameter Mission Simulation Facility (MMSF), followed by pulsed thermography and surface and microstructure examination at Glenn. Pulsed thermography is a nondestructive evaluation method that involves the heating of a specimen with a short-duration pulse of energy and monitoring the transient thermal response of the surface of the specimen with an infrared camera (see the sketch). Anomalous subsurface areas can then be identified on the basis of deviations in cooling behavior at the surface.

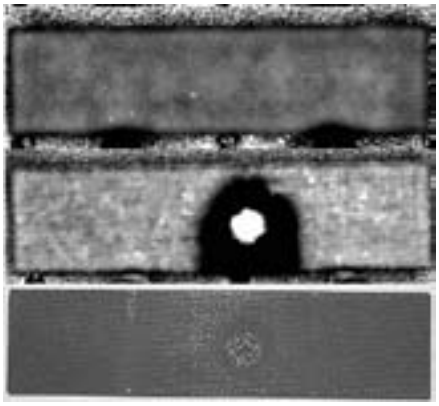

*Top: Thermography results for a carbon-carbon composite specimen in the as-received (undamaged) condition. Center: Thermography image obtained following simulated micrometeoroid damage. Subsurface damage is revealed by dark areas. Bottom: Optical image. Subsurface damage cannot be seen.*

The ability to use pulsed thermography to locate and monitor damage and material changes at and beneath the surface of the composites was demonstrated (see the figure to the left). The collection of thermography data in the as-fabricated condition proved useful in providing baseline condition information and in tracking material changes following environmental exposure. This NDE technique was shown to be particularly well-suited for assessing hidden material damage due to micrometeoroid object damage exposure and MMSF conditioning. Microstructural and chemical characterization of the sample surfaces, and sectioning and microscopy of samples at selected areas where thermography "indications" occurred, were performed to aid in understanding the source of changes in the NDE signals, and in an attempt to reduce the need for destructive evaluation of parts manufactured from these materials. The NDE results are documented and summarized in the NASA Marshall project report (Gubert et al.).

**Bibliography**

Hurwitz, Frances I., et al.: Oxidation Behavior of CMC Candidate Materials for Lightweight Nonmetallic TPS for NASA Exploration Missions. Proceedings of the 2006 National Space and Missile Materials Symposium, Orlando, FL, 2006.

Hurwitz, Frances I., et al.: Microstructural Characterization of Candidate Thermal Protection Materials Following Simulated Space Environments Exposure. 31st Annual Conference on Composite Materials and Structures, Afternoon Jan. 25, Session 1: Hypersonic Materials 4, Daytona Beach, FL, Jan. 22–25, 2007. Available only on DVD from Zimmerman Associates Inc. (ZAI), Arlington, VA.

Martin, Richard E.; Gyekenyesi, Andrew L.; and Shepard, Steven M.: Interpreting the Results of Pulsed Thermography Data. Mater. Eval., vol. 61, no. 5, 2003, pp. 611–616.

Gubert, Michael K., et al.: MSFC–RPT–3486: Effects of Space and Planetary Environments on TPS Materials—Integrated Test Report, pp. 39-45, August 31, 2006. Also Martin, Richard E.; Kiser, J. Douglas; and Hurwitz, Frances I.: Appendix G: Thermography and Post-Exposure Images, pp. 380–458.

**Find out more about the research of Glenn's Optical Instrumentation & NDE Branch:**
http://www.grc.nasa.gov/WWW/OptInstr/

**Cleveland State University contact:**
Richard E. Martin, 216–433–3684, Richard.E.Martin-1@nasa.gov

**Glenn contact:**
J. Douglas Kiser, 216–433–3247, James.D.Kiser@nasa.gov

**Authors:**
Richard E. Martin, J. Douglas Kiser, and Dr. Frances I. Hurwitz

**Headquarters program office:**
Exploration Systems Research and Development

**Programs/projects:**
Crew Exploration Vehicle, Hypersonics

# Molecular Rayleigh Scattering Technique Developed To Measure Temperature, Velocity, and Density Fluctuations in Gas Flows

A nonintrusive optical point-wise measurement technique utilizing the principles of molecular Rayleigh scattering was developed at the NASA Glenn Research Center to obtain turbulent temperature, velocity, and density fluctuation measurements in unseeded gas flows. This type of information is necessary for validating computational fluid dynamics and computational aeroacoustic codes. Dynamic property measurements allow the calculation of statistical quantities such as power spectra and mean square fluctuations. These types of measurements are used for jet noise studies in which sound pressure fluctuations are correlated with flow property fluctuations to ascertain the sources of noise in free jet flows.

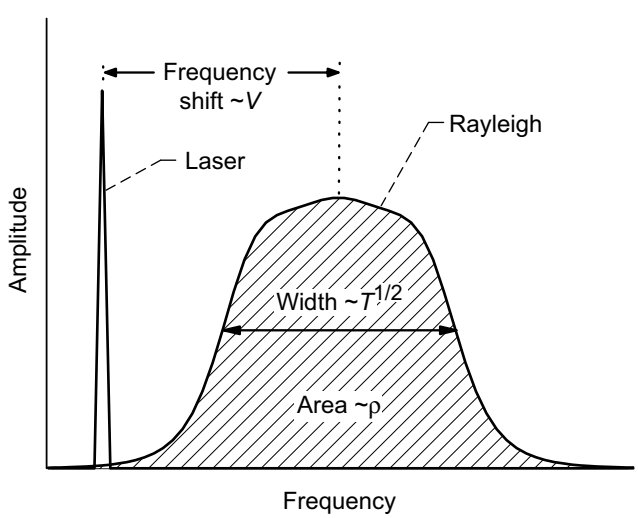


*Rayleigh scattering spectrum.*

Molecular Rayleigh scattering is the result of elastic light scattering from gas molecules. When light from a single-frequency laser beam passes through a gas, the scattered light is shifted in frequency by the Doppler effect because of the bulk motion of the molecules. The optical frequency spectrum of Rayleigh-scattered light contains information about the gas density, bulk velocity, and temperature. This graph shows a Rayleigh scattering spectrum containing the narrow laser line and the broadened Rayleigh spectral peak. If the gas composition is known, the total intensity of the Rayleigh spectrum is directly proportional to the gas density. The frequency shift between the laser peak and the Rayleigh peak is proportional to the bulk flow velocity. The width of the spectral peak is broadened by thermal motion of the molecules and, hence, is related to gas temperature. The spectra of the laser light and the Rayleigh-scattered light are analyzed using a Fabry-Perot interferometer operated in the static imaging mode. The resulting circular fringe pattern contains spectral information about the light (see the illustration on the next page).

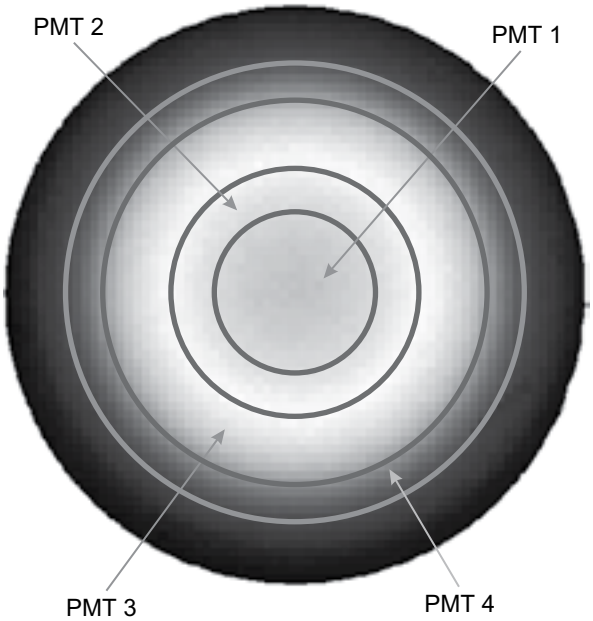


*Dissection of Fabry-Perot fringe pattern into four annular regions; PMT, photomultiplier tube.*

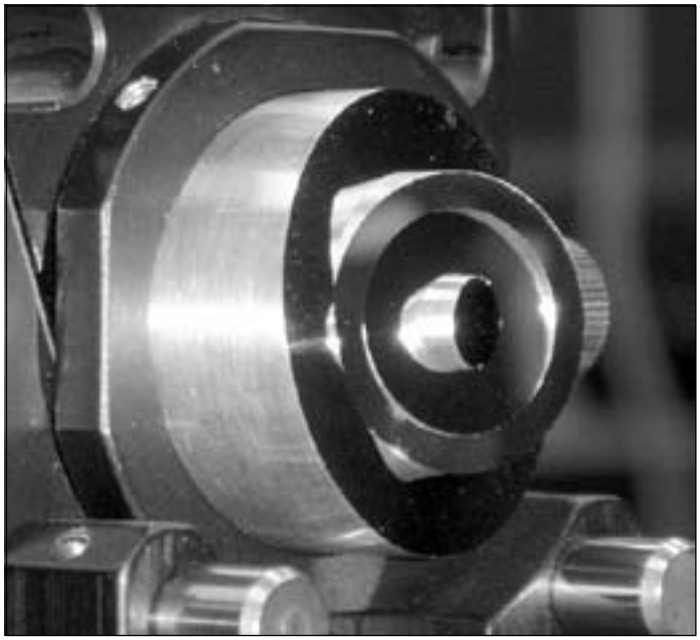

*Concentric angled mirror system used to dissect the Fabry-Perot fringe pattern as shown in the preceding figure.*

The interference fringe pattern is divided into four concentric regions (see the illustration) using a series of mirrors angled with respect to one another (see the photograph). Light from each of these regions is directed toward photomultiplier tubes and sampled at rates up to 16 kHz using photon-counting electronics. Monitoring the width of the spectrum allows for measurement of the gas temperature. Monitoring the spectral peak location provides a measure of a single component of the flow velocity. Independently monitoring the total scattered intensity provides a measure of the gas density. Gas temperature, velocity, and density were measured in a low-speed heated air jet (left graph on the next page) as well as in an acoustically modulated nozzle flow (right graph on the next page).

Upon completion of additional development and validation tests, this measurement system will be implemented in the Aero-Acoustic Propulsion Laboratory and other facilities at Glenn for use in jet noise research. These tests are related to milestones under the Supersonics and Subsonic Fixed Wing thrust areas.

**Bibliography**

Mielke, Amy F.; and Elam, Kristie A.: Molecular Rayleigh Scattering Diagnostic for Measurement of High Frequency Temperature Fluctuations. Proc. SPIE Int. Soc. Opt. Eng., vol. 5880, 2005, pp. 1–12.

Mielke, A.; Elam, K.; and Sung, C.: Molecular Rayleigh Scattering Diagnostic for Dynamic Temperature, Velocity, and Density Measurements. AIAA–2006–2969, 2006.

Mielke, A.; Elam, K.; and Sung, C.: Rayleigh Scattering Diagnostic for Measurement of Temperature, Velocity, and Density Fluctuation Spectra. AIAA–2006–0837, 2006.

Panda, J.; and Seasholtz, R.G.: Experimental Investigation of Density Fluctuations in High-Speed Jets and Correlation With Generated Noise. J. Fluid Mech., vol. 450, 2002, pp. 97–130.

Seasholtz, R.G.; Panda, J.; and Elam, K.A.: Rayleigh Scattering Diagnostic for Measurement of Velocity and Density Fluctuation Spectra. AIAA–2002–0827, 2002.

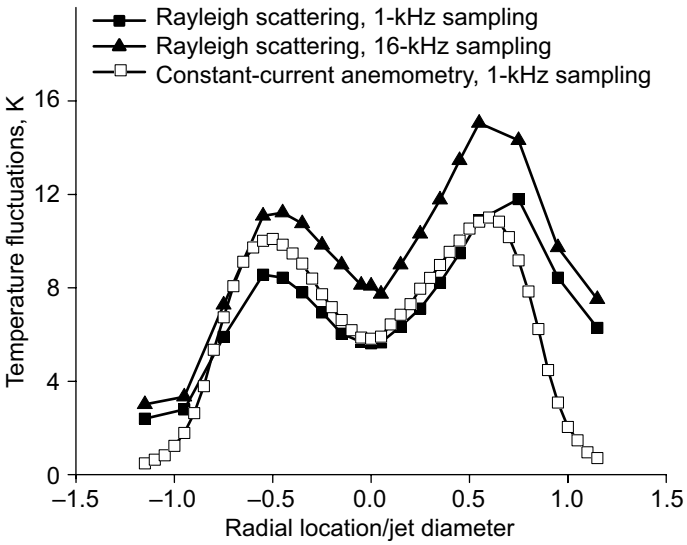


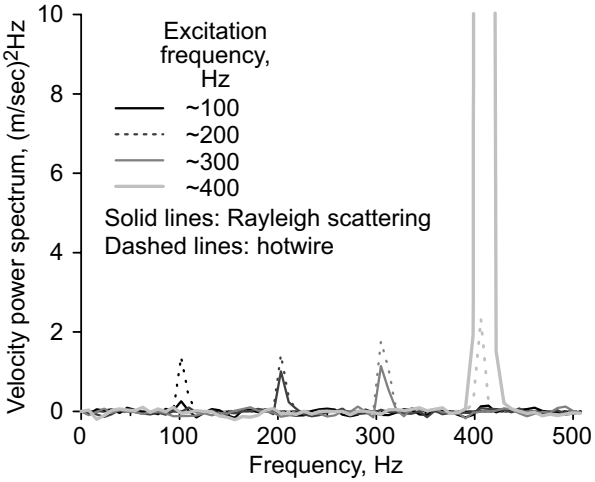


*Left: Temperature fluctuation profiles measured by Rayleigh scattering and constant current anemometry at an axial location four diameters downstream of the heated jet exit. Right: Velocity power spectra calculated from Rayleigh and hotwire velocity data acquired at a 16-kHz sampling rate in acoustically modulated nozzle flow at the given excitation frequencies.*

**Find out more about the research of Glenn's Optical Instrumentation & NDE Branch:**
http://www.grc.nasa.gov/WWW/OptInstr/

**Glenn contact:**
Amy F. Mielke, 216–433–6757, Amy.F.Mielke@nasa.gov

**Authors:**
Amy F. Mielke and Kristie A. Elam

**Headquarters program office:**
Aeronautics Research Mission Directorate

**Programs/projects:**
Supersonics, Hypersonics, Subsonic Fixed Wing, Independent Research and Development

## Communication Over Direct-Current Power Line Demonstrated for Distributed Engine Control Using High-Temperature Electronics

In the effort to lighten engine control systems, future engine control functions may be distributed throughout a network to different smart nodes, which may contain a sensor, an actuator, and signal conditioning. In addition to weight savings from lightening the central engine controller, significant weight savings might be achieved by decreasing the number of wires and the length of wiring in engine instrument/control wiring harnesses. Wireless smart nodes are one approach that could be developed, but the nodes would have to be constructed with currently available high-temperature electronics, which are limited in available components. In addition to requiring complex components, wireless nodes must be provided with power through at least two conductors (power and ground).

Although energy harvesting may enable complete wireless sensing and actuation, state-of-the-art energy harvesting will not support the power budget required. One method that will decrease wiring weight and complexity, while taking advantage of the necessary power lines, is communication over the power lines. One type of distributed engine control involves smart nodes that can condition signals from the sensors and generate actuating signals for the actuators, effectively

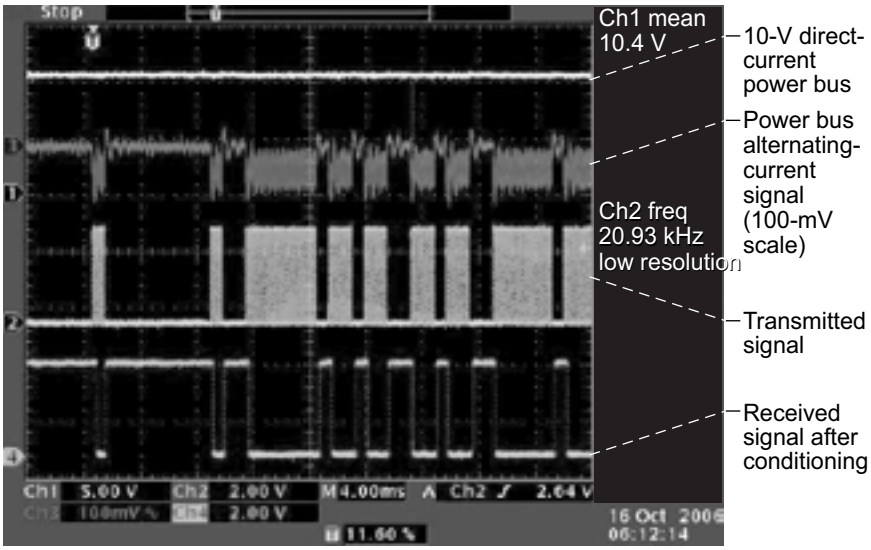


*Industrial temperature circuit (at room temperature).*

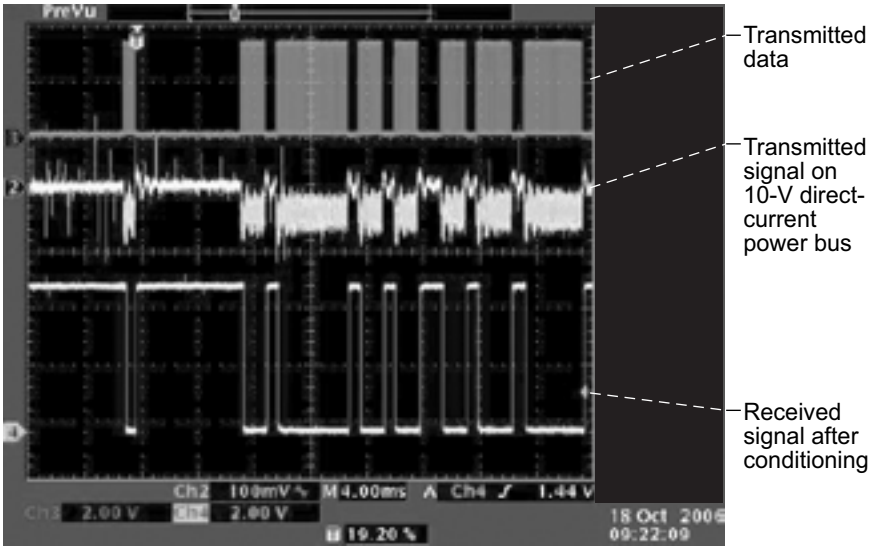


*High-temperature circuit (at room temperature).*

closing the loop internally while still communicating with a central controller. On-node sensor signal conditioning and actuation results in less bus bandwidth for the node, and less processing for the central controller. Many obstacles must be overcome to reach the goal of distributed engine control, including the insufficient availability of high-temperature electronic components and the complex parameters of the available components.

The flight electronics laboratory team in the NASA Glenn Research Center's Optical Instrumentation and NDE Branch is researching different approaches for enabling high-temperature smart nodes. One approach is to use commercially available high-temperature components and a capacitive coupling communication technique to transmit data on the power bus. This technique is being developed for a demonstration in Glenn's distributed engine control testbed.

The top figure demonstrates serial data being passed over a 10-V power line via a capacitive coupling technique and commercially available industrial temperature components. The bottom figure shows an analogous demonstration of the same technique using high-temperature electronic components, rated to 225 °C, or to 260 °C for short periods. This demonstration was done at room temperature using high-temperature semiconductors but with military temperature-range resistors and capacitors. The data are serial at 1.2 kbaud, transmitted with an 18.5-kHz carrier. This technique is scalable to higher baud rates representative of A, B, C, and D band communications. Because this is a bit-recessive technique, it could be used to implement a Controller Area Network (CAN) bus-based communication protocol.

The major advantage of this technique over commercially available power line transceiver systems is that it can be realized immediately for high-temperature and radiation-rich environments. Plans call for this communication technique to continue to be developed and tested at high temperatures and to be incorporated into an engine simulator testbed.

**Find out more about the research of Glenn's Optical Instrumentation & NDE Branch:**
http://www.grc.nasa.gov/WWW/OptInstr/

**Glenn contacts:**
Michael J. Krasowski, 216–433–3729, Michael.J.Krasowski@nasa.gov

Norman F. Prokop, 216–433–6718, Norman.F.Prokop@nasa.gov

Larry C. Greer, 216–433–8770, Lawrence.C.Greer@nasa.gov

**Authors:**
Michael J. Krasowski, Norman F. Prokop, Lawrence C. Greer, and Danny C. Spina

**Headquarters program office:**
Aeronautics Research Mission Directorate

**Programs/projects:**
Fundamental Aeronautics Subsonic Fixed Wing

# Flaw Resolution Improved by New Signal-Processing Approaches for Terahertz Data Obtained From Inspection of Space Shuttle External Tank Thermal Protection System Foam

Sprayed-on foam insulation covers the space shuttle external fuel tank and is necessary to prevent ice buildups as the shuttle sits awaiting liftoff with cryogenic propellants in the external tank. Flaws present in the foam can result in initiation sites for foam loss. Manually sprayed foam areas are especially prone to flaws. A major effort is underway at NASA to find and improve inspection methods to locate cracks, voids, delaminations (between the foam and the underlying tank, or between the foam and knitlines), and crushed areas of the foam in order to minimize foam debris release upon launch.

The latest external tank for the July 2006 shuttle launch (STS–121) had the protuberance air load ramp windshield removed to minimize large foam debris release upon launch. As a result, the highest priority areas to inspect are now the ice frost ramps, which prevent ice from forming on underlying aluminum brackets used to fasten fuel-pressurization lines and on a tray of electrical cables to the tank's exterior. It is impossible to completely prevent foam from coming off of the ramps during launch, but inspection methods can help locate damaged ramps prior to launch and also aid in the understanding of the conditions and flaws that cause foam release. (Future design changes also include possible removal of the ice frost ramp.)

Foam inspection methods in use and being researched for improvements at NASA include terahertz, microwave, shearography, and x-ray backscatter. Terahertz inspection in the reflection mode requiring access to only one side of a material has shown significant promise for the detection of voids and crushed foam. The schematic shows the overall operation of this method. Briefly, terahertz waves are electromagnetic waves with wavelengths on the order of 200 to 1000 μm (just shorter than those in the microwave domain). Electrically conducting materials such as metals reflect terahertz waves, whereas dielectric (nonconducting) nonpolar liquids, nonmetallic solids, and gases are transparent to terahertz energy. Reflections also occur off of interfaces, such as between a solid and air, where a dielectric discontinuity (difference in the indices of refraction) occurs. Thus, small reflections will occur off of voids in foam and

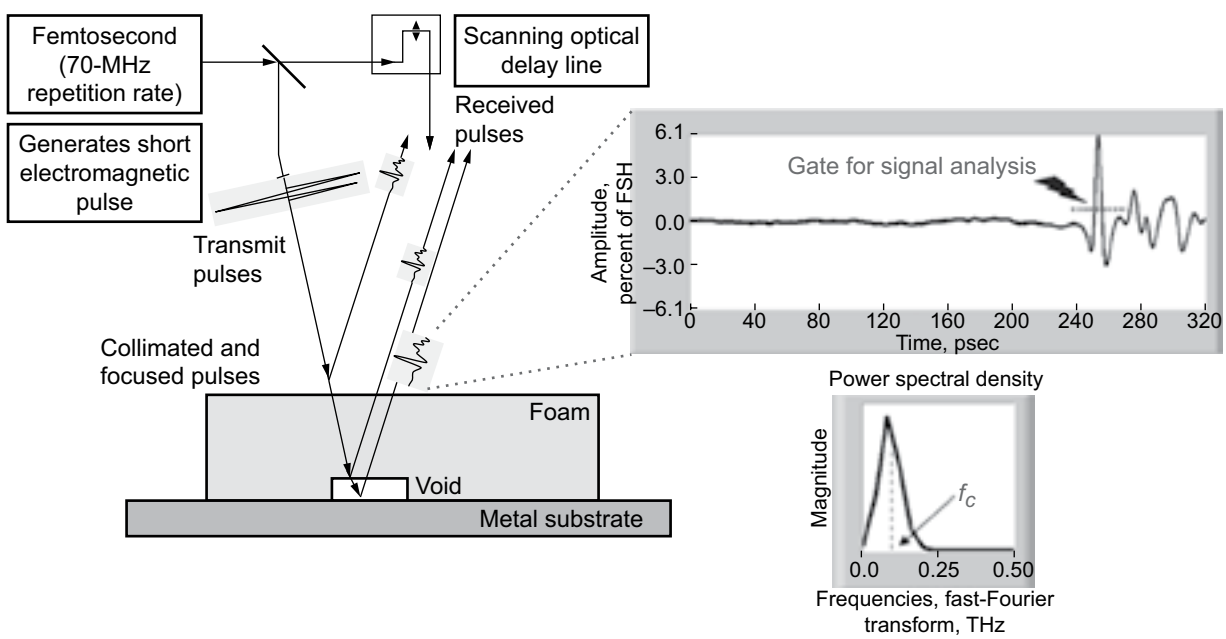


*Reflection-mode terahertz methodology. Reflections will be received off of the various interfaces. Reflection from metal will be the strongest. The horizontal dotted line over the large, initial portion of the wave shows the time gate of the echo typically used during signal processing. A sample power spectral density is shown with the centroid, $f_C$, denoted. FSH, full scale height.*

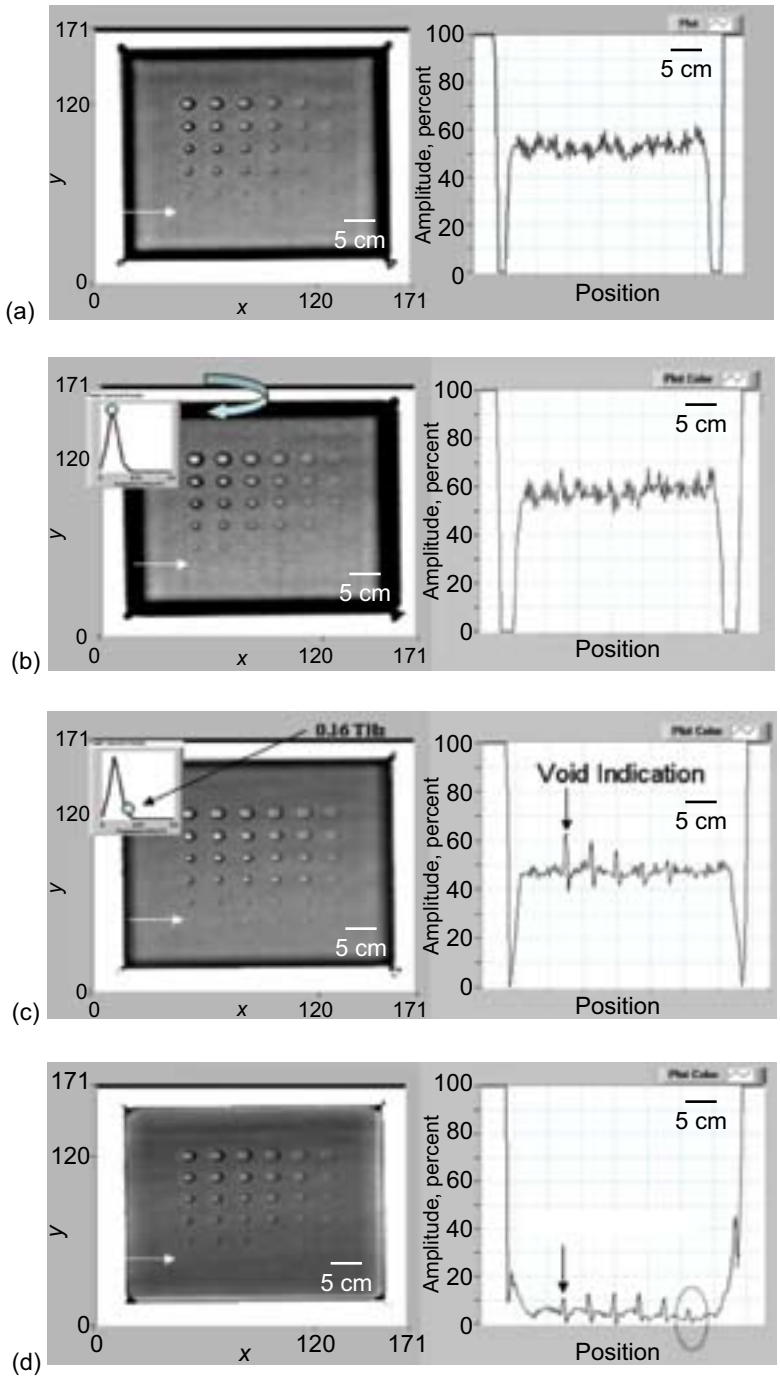


*Comparison of different terahertz images including line profiles (right side of figure) at the location of the bottom (smallest) row of voids. The voids are relatively deeper as one moves to the right in the image. (a) Time-domain peak-to-peak amplitude. (b) Power spectral density peak magnitude. (c) Power spectral density at 0.16 MHz. (d) Centroid, $f_C$, of the power spectral density.*

the signal transmitted through the void will have reduced signal amplitude. Significant time- and frequency-domain information is available in these reflection signals.

Currently applied signal-processing techniques for terahertz data are generally based on simple parameter extractions such as peak detection of the time-domain signal or the Fourier-transformed signal. The focus of this research effort is to develop signal analysis techniques that capitalize on all the information that is available in the terahertz signal to improve the resolution of flaws and differentiation of flaws from normal foam variations such as knit lines.

This past year, the multicenter effort focused particularly on the computation and image display of the centroid of the power spectral density for the reflections off of a metal substrate located beneath foam (the configuration of such a sample simulates the external tank configuration) for foam samples containing seeded voids. The centroid images were compared with those formed from traditional waveform parameters such as peak-to-peak amplitude (time-domain) and peak magnitude (frequency-domain). The centroid is reasonably simple and rapid computationally, and proved to significantly enhance flaw resolvability in foam samples containing seeded voids of various sizes and depths as shown in this figure.

The product of this study is a commercial-grade software package that is being used both by Michoud Assembly Facility and NASA Glenn Research Center personnel to analyze data and visualize terahertz (and ultrasonic) images. The software was developed by Glenn in cooperation with the NASA Langley Research Center, Michoud Assembly Facility, NASA Marshall Space Flight Center, and Cleveland State University.

**Glenn contact:**

Don Roth, 216–433–6017, Donald.J.Roth@nasa.gov

**Author:**
Dr. Don J. Roth

**Headquarters program office:**
NASA Engineering and Safety Center

**Programs/projects:**
NASA Engineering and Safety Center External Tank Thermal Protection System
Nondestructive Evaluation Super Problem Resolution Team

# Phase-Only Filtering Developed for Improved Particle Image Velocimetry Data Reduction

The standard approach in particle image velocimetry (PIV) data processing is to use fast Fourier transforms to obtain the cross correlation of two single-exposure subregions, where the location of the cross-correlation peak is representative of the most probable particle displacement across the subregion. This standard PIV processing technique is analogous to matched spatial filtering, a technique commonly used in optical correlators to perform the cross-correlation operation. Phase-only filtering is a well-known variation of matched spatial filtering which, when used to process PIV image data, yields correlation peaks that are narrower and up to an order of magnitude larger than those obtained using traditional PIV processing. Researchers at the NASA Glenn Research Center recently used this technique to improve PIV image processing.

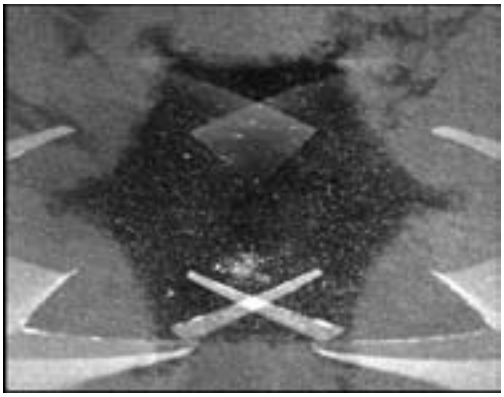

*PIV data from a chevron nozzle flow experiment where the stereo PIV system is configured for cross-stream measurements. The left and right camera views are overlapped to illustrate the flare light scattered off of the chevron tips.*

In addition to possessing desirable correlation plane features, phase-only filters provide superior performance in the presence of direct-current (dc) noise (or flare light from surfaces) in the correlation subregion. When PIV image subregions contaminated with surface flare light or high background noise levels are processed using phase-only filters, the correlation peak pertaining only to the particle displacement is readily detected above any signal stemming from the dc objects. Many of the PIV data collected in the jet noise facilities at Glenn are contaminated with flare light from the model, see the photograph, which leads to a loss of data in these regions (see the top plot on the next page). Phase-only filtering techniques developed at Glenn minimize the effect of the flare light and recover the complete velocity field (see the bottom plot).

**Bibliography**

Wernet, Mark P.: Symmetric Phase Only Filtering: A New Paradigm for DPIV Data Processing. Meas. Sci. Technol., vol. 16, no. 3, 2005, pp. 601–618.

Wernet, M.: Symmetric Phase Only Filtering for Improved DPIV Data Processing. AIAA–2006–0042, 2006.

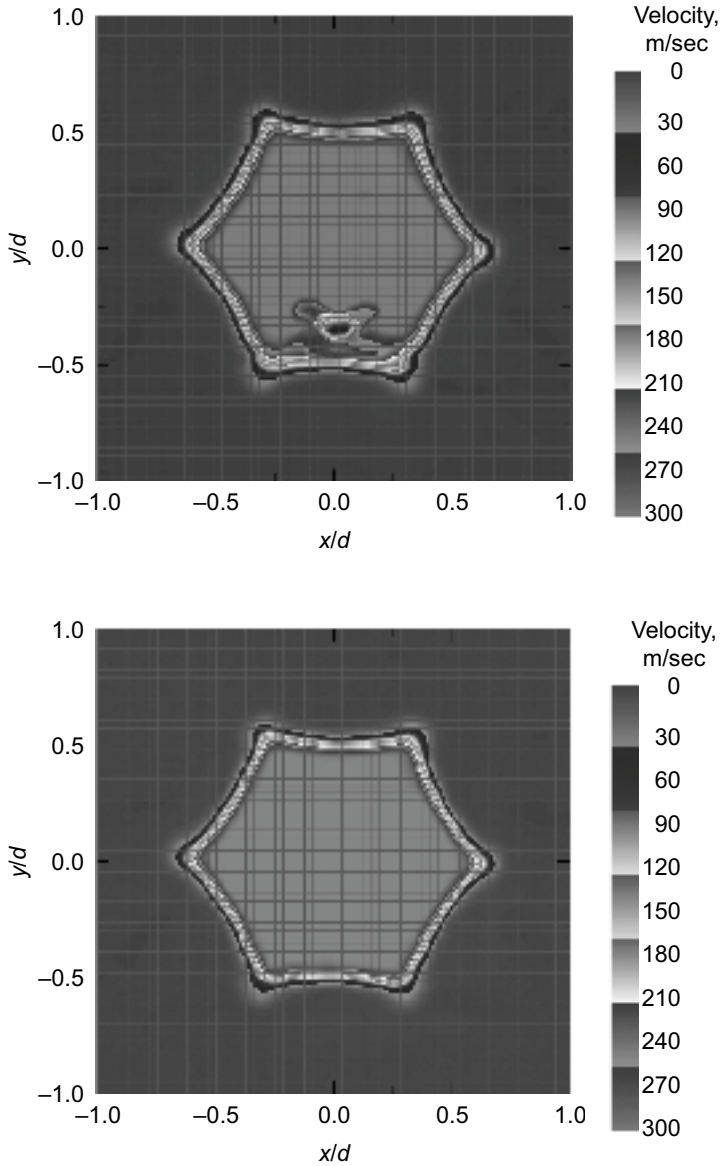


*Top: Ensemble averaged, three-dimensional velocity field where only the out-of-plane, w, component of velocity is plotted here as a color contour plot. The model flare light contaminated images were used to compute the three-component velocity field, resulting in the spurious velocities at the bottom of the nozzle flow field. Bottom: Phase-only filtering processing of the same image data yielded the true flow field, and no evidence of the model flare light contamination can be observed in the final result. This figure is shown in color in the online version of this article (http://www.grc.nasa.gov/WWW/RT/2006/RI/RIO-wernet.html).*

**Find out more about this research:**
http://www.grc.nasa.gov/WWW/OptInstr/planarvel.html

**Glenn contact:**
Dr. Mark P. Wernet, 216–433–3752, Mark.P.Wernet@nasa.gov

**Author:**
Dr. Mark P. Wernet

**Headquarters program office:**
Aeronautics Research Mission Directorate

**Programs/projects:**
Quiet Aircraft Technology, Constant Volume Combustion Cycle Engine

# Improved Modeling of Forward-Scattered Light From an Optically Trapped Particle Demonstrated

The NASA Glenn Research Center has identified photonic control (optical micromanipulation using optical tweezers) as a nonintrusive tool for manipulating nanoscopic and microscopic material, without contamination, into the required configurations for the fabrication of sensors that will be integrated into the intelligent engines of the future. A complete understanding of the forward-scattered light from optically trapped particles provides information about material in optical traps that is not directly observable. Such signatures measured from the forward-scattered light of a trapped particle can be used as a guide for particle manipulation and placement.

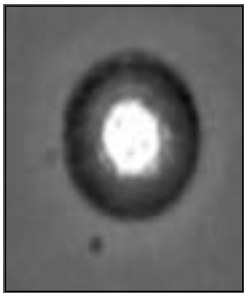

*Optically trapped 10-μm-diameter polystyrene microsphere.*

The NASA Glenn Research Center and Cleveland State University collaborated to compare two theoretical models of the forward scattered light plus the trapping beam light from an optically trapped polystyrene microsphere. The theoretical models were formulated at Cleveland State University, and experimental tests of those models were performed at Glenn. The predicted optical trapping properties of a gaussian beam in the liquid surrounding the particle were compared with that of a gaussian beam that was apertured and focused by a high-numerical-aperture oil-immersion microscope objective lens and aberrated by the interface between the coverslip and the water in the sample chamber (i.e., an apertured, focused, abbreviated (AFA) beam).

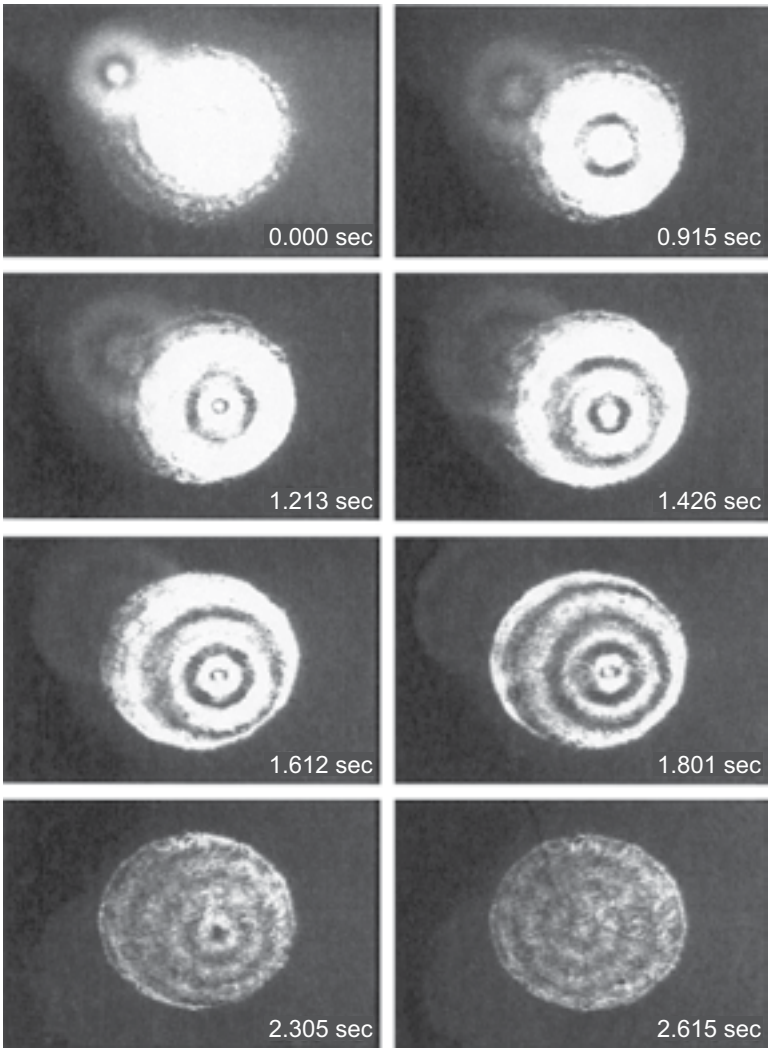


*Time-sequence series of eight photographs illustrating changes in the forward scattered light as a 10-μm-diameter particle is drawing into an optical trap, from 0.000 sec (before the sphere moves toward the trap) to 2.615 sec (when the sphere has come to rest in a stable trapping position).*

In the Glenn experiment, a downward-propagating laser beam was tightly focused by a 100× microscope objective lens to form an optical trap. The forward-scattered light from a 10-μm-diameter polystyrene latex sphere as it was drawn into the optical trap was projected onto a screen, recorded, and examined. It was found that before the sphere was drawn into the trap, the forward-scattered light initially showed a bright featureless spot. As the sphere was drawn into the trap, a series of concentric interference rings formed and appeared to propagate radially outward from the center of the pattern as the sphere moved into the trap. The number of concentric rings in the pattern increased and became dimmer as the focal waist of the beam moved inside the sphere. The AFA beam model

correctly predicted that six or seven bright and dark fringes would form as the sphere was drawn into the trap. The initial beam before trapping can be seen at 0.000 sec. Some of the changes in the interference fringes are seen from 0.915 to 2.305 sec. The dim set of interference fringes from the optically trapped particle can be seen at 2.615 sec.

Proper characterization and modeling of the forward-scattered light from an optically trapped object will greatly enhance NASA's ability to create unobtrusive sensors out of new nanoscale and microscale materials. Proper understanding of the signature of forward-scattered light allows for automation of assembly processes even when objects that are manipulated in the optical trap are not directly observable. Knowledge of the signature of the forward-scattered light of optically trapped objects will aid in characterizing the unobtrusive sensors of the future.

**Bibliography**

Lock, James A.; Wrbanek, Susan Y.; and Weiland, Kenneth E.: Scattering of a Tightly Focused Beam by an Optically Trapped Particle. Applied Optics, vol. 45, no. 15, 2006, pp. 3634–3645.

**Find out more about the research of Glenn's Optical Micromanipulation Lab:**
http://www.grc.nasa.gov/WWW/OptInstr/Nano_OpticalMicroManipulationLab.html

**Glenn contact:**
Susan Y. Wrbanek, 216–433–2006, Susan.Y.Wrbanek@nasa.gov

**Cleveland State University contact:**
Dr. James A. Lock, 216–687–2420, J.LOCK@csuohio.edu

**Authors:**
Susan Y. Wrbanek and Dr. James A. Lock

**Headquarters program office:**
Aeronautics Research Mission Directorate

**Programs/projects:**
Subsonic Fixed Wing

## Deep Reactive Ion Etching Process Optimized for Silicon Carbide Micromachining

Silicon carbide (SiC) has properties that make it a nearly ideal material for the creation of harsh-environment electronics and microelectromechanical systems (MEMS). The chemical inertness of SiC enhances its robust nature, but it makes it difficult to micromachine. The NASA Glenn Research Center has been investigating problems related to the bulk micromachining of single-crystal SiC by deep reactive ion etching (DRIE), including the formation of high-aspect-ratio structures (ref. 1) and the reduction of imperfections introduced by the DRIE process.

This photograph illustrates typical defects introduced when a circular well is etched into a SiC wafer to produce a pressure-sensing diaphragm. Although this process, which represented the state of the art for SiC DRIE in 2005 (ref. 2), generally provides sufficiently smooth etched surfaces, it introduces other significant nonidealities such as nonvertical sidewalls and microtrenching at the base of the sidewall. Microtrenching is a particularly serious defect for pressure sensors because the trench serves as a stress concentrator that weakens the diaphragm. This research effort developed an improved DRIE process that provides the required characteristics of smooth etched surfaces, vertical sidewalls, and minimal microtrenching, together with a high etch rate for cost-effective manufacturing (ref. 3).

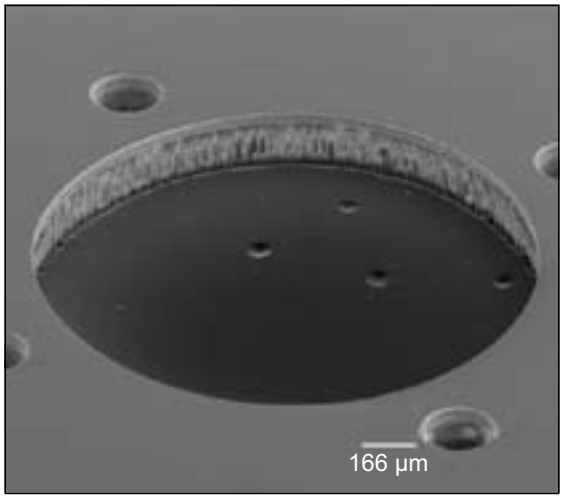


*Circular well (1 mm in diameter) etched to a depth of 245 μm using the prior state-of-the-art DRIE process. The structure shows typical defects for this process: that is, microtrenching at the base and the reentrant slope of the sidewalls (diameter of well increases with increasing depth).*

A parametric study was used to optimize the DRIE recipe by varying four important parameters: the temperature of the wafer chuck, the pressure within the chamber, and the concentrations of oxygen ($O_2$) and argon (Ar) in a mixture composed of $O_2$, Ar, and sulfur hexafluoride ($SF_6$). Sixteen etches were performed using all combinations of high and low values of each of the four parameters. This experiment was used to determine how microtrench depth, sidewall slope, surface roughness, and etch rate were affected by the key process parameters. Trenches and wells were etched to depths from 100 to 150 μm in single-crystal SiC specimens, which were then cross sectioned and examined using optical microscopy, scanning electron microscopy (SEM), and surface profilometry to characterize the etched structures.

The use of high radiofrequency powers (2500 W applied to the coil and 200 W applied to the platen) resulted in high etch rates (>0.5 μm/min) for all process conditions studied. Oxygen addition was found to be undesirable because it caused increased microtrenching, whereas high temperature was found to be beneficial because it reduced microtrenching. Sidewall slopes became more vertical, as desired, with increasing pressure; however, higher pressure was found to produce increased roughness. This roughness was reduced by using a gas mixture comprising Ar in addition to the principal etchant gas, $SF_6$.

This study enabled us to produce an optimized DRIE process that simultaneously provides minimal microtrenching, vertical sidewalls, and smooth etched surfaces. By using a high fraction of Ar (40 vol%) along with a high temperature (180 °C) and a high pressure (35 mT, or 4.67 Pa), we were able to optimize etch characteristics. The sidewall slope obtained was approximately 90°, with an etch rate of 0.7 μm/min and a surface roughness of 40 Å. The following photograph shows the results achieved using the optimized process. This research is ongoing, with plans for further studies in process repeatability and the characterization of pressure sensors that will be fabricated with this process.

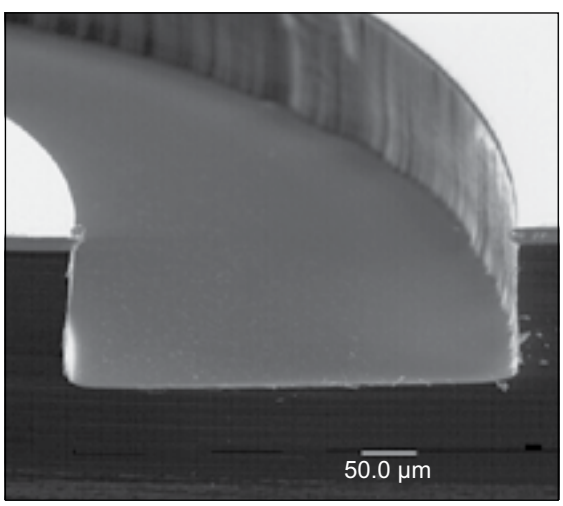


*Cross-sectional view of a portion of a 400-μm-wide ring-shaped well that was etched to a depth of 150 μm using the optimized DRIE process. The etched well has minimal microtrenching and has vertical sidewalls and smooth surfaces.*

**References**


1. Evans, Laura J.; and Beheim, Glenn M.: New Deep Reactive Ion Etching Process Developed for the Microfabrication of Silicon Carbide. Research & Technology 2004. NASA/TM—2005-213419, 2005. http://www.grc.nasa.gov/WWW/RT/2004/RI/RIS-evans.html
2. Beheim, Glenn M.; and Evans, Laura J.: Deep Reactive Ion Etching for Bulk Micromachining of Silicon Carbide. The MEMS Handbook, Second ed., vol. 2, Mohamed Gad-el-Hak, ed., CRC Press, Boca Raton, FL, 2006, pp. 8–1 to 8–15.
3. Beheim, Glenn M.; and Evans, Laura J.: Control of Trenching and Surface Roughness in Deep Reactive Ion Etched 4H and 6H SiC. M. Dudley, et al., eds., Mater. Res. Soc. Symp. Proc., vol. 911, Warrendale, PA, 2006, pp. 329–334.


**Find out more about silicon carbide electronics research at Glenn:**
http://www.grc.nasa.gov/WWW/SiC/SiC.html


**Glenn contacts:**
Laura J. Evans, 216–433–9845, Laura.J.Evans@nasa.gov

Dr. Glenn M. Beheim, 216–433–3847, Glenn.M.Beheim@nasa.gov

**Authors:**
Laura J. Evans and Dr. Glenn M. Beheim


**Headquarters program office:**
Aeronautics Research Mission Directorate

**Programs/projects:**
Subsonics Fixed Wing, Supersonics

# Small-Area, Fast-Response Heat Flux Sensor With Large Output Signal Developed

A small-area, thin-film heat flux sensor that has a large output signal and fast response in a flexible package has been developed at the NASA Glenn Research Center under a Technology Transfer Agreement with the Goodyear Tire & Rubber Company of Akron, Ohio. Heat flux is one of a number of parameters (in addition to pressure, temperature, flow, and others) of interest to engine designers and fluid dynamicists. All heat flux sensors operate by measuring the temperature difference across a thermal resistance. There are various designs of heat flux sensors, such as Gardon gauges, plug gauges, and thin-film thermocouple arrays. The thin-film designs have the advantage of high-frequency response and minimal flow disturbance.

Recently there has been a need for a sensor to measure the heat flux on the sidewalls and within the tread of a tire. These measurements would be on curved surfaces over an area that is smaller than the area of sensors currently available commercially. Thus, a design was developed that retains the fast response of the thin-film thermocouple sensors but that has a larger output and can be made smaller and in a flexible package. The photograph shows the sensor developed to fit in a tire tread.

The new sensor design consists of a resistor bridge fabricated onto a 0.25-mm- (0.010-in.-) thick polyester film. The temperature-sensitive element is sputter-deposited platinum, patterned and applied using a photolithography technique newly developed at Glenn, with line width and line spacing of approximately 60 μm. The variation of platinum's electrical resistance with temperature is well characterized.

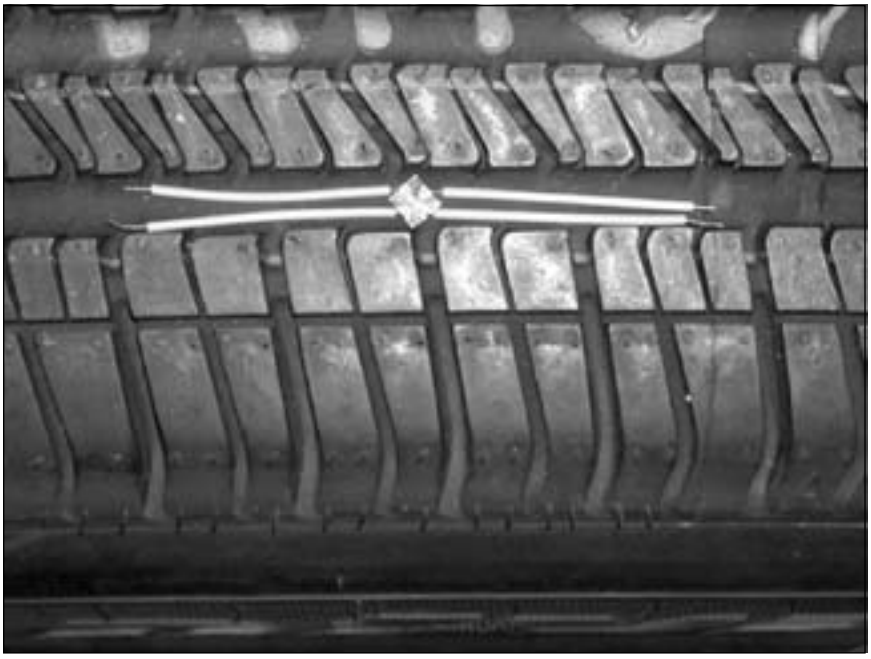

*Heat flux sensor developed at Glenn to fit in a tire tread.*

Thus, the ability to measure heat flux magnitude and direction was incorporated into a resistance bridge design fabricated using thin-film techniques to allow fast response. The result is a sensor that does not need the large area and stiff packaging required for the old thermopile design, and that does not have the low output of the thermopile design, but that has a response that is nearly as fast. The development of this sensor offers a new laboratory procedure to establish heat transfer coefficients for different regions of a tire. Testing at the Goodyear Tire & Rubber Technical Center (shown in the photograph on the next page) generated measured heat transfer coefficients that were within the range of values obtained from thermal finite element tire models previously reported in the literature. The experimentally measured temperatures from these data also agree well with the numerically generated values, thus verifying the models.

The new sensor can be used in components for process control, modeling validation, determination of cooling requirements, and general calorimetry in rocketry, aerospace, and automotive environments. One specific application is to enable thermal control in advanced multiuse extravehicular activity (EVA) pressure suits for future lunar missions. The heat flux sensor is small enough to allow measurement of the heat load on the thermal cooling system as well as the heat flux from various parts of the suit. The correlation of these parameters will give a more accurate estimate of the astronaut's metabolism and any external thermal loading and will permit a more rapid adjustment of the suit's cooling system.

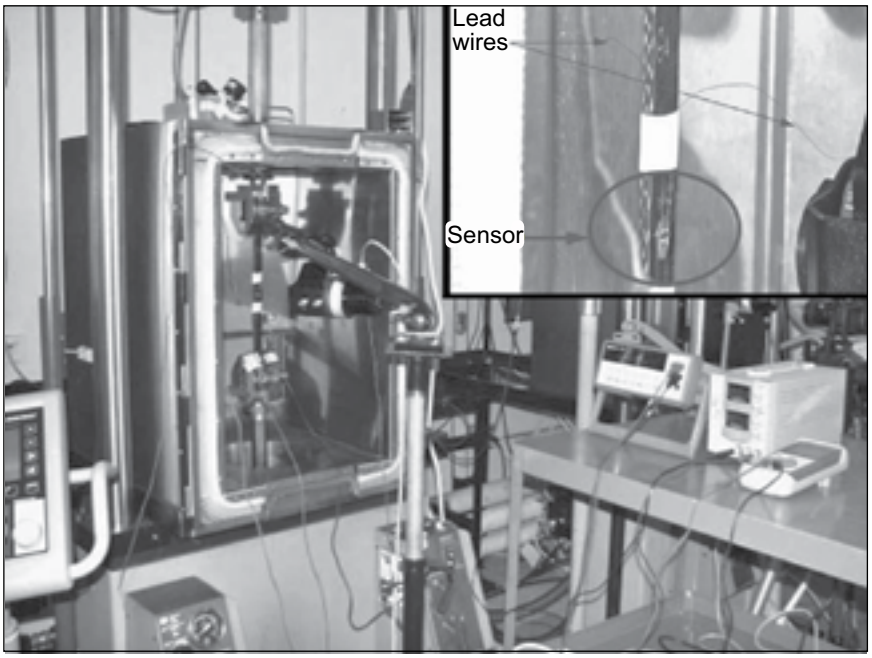


*Tests at the Goodyear Tire & Rubber Technical Center using the new heat flux sensor are validating numerical models of tire heat transfer. (Photograph courtesy of Goodyear Tire & Rubber Company; used with permission).*

**Find out more about this research at Glenn's Sensors and Electronics Branch:**
http://www.grc.nasa.gov/WWW/sensors/

**Glenn contacts:**
Gustave C. Fralick, 216–433–3645, Gustave.C.Fralick@nasa.gov

John D. Wrbanek, 216–433–2077, John.D.Wrbanek@nasa.gov

**Goodyear contact:**
Mahmoud C. Assaad, 330–796–8804, mahmoud.assaad@goodyear.com

**Authors:**
Gustave C. Fralick, John D. Wrbanek, José M. Gonzalez III, Charles A. Blaha, and Mahmoud C. Assaad

**Headquarters program office:**
Aeronautics Research Mission Directorate, Exploration Systems Mission Directorate

**Programs/projects:**
Fundamental Aeronautics, Advanced Extravehicular Systems

## Smart Leak-Detection Systems Being Matured for Crew Launch Vehicle

As NASA begins development of launch systems for space exploration, the need for space-ready technology that enables safe, automated, and autonomous operation is significant. One major safety system associated with the present space shuttle has been the leak-detection system that is meant to ensure that hazardous conditions do not occur. The space shuttle uses gases such as hydrogen and oxygen, and leaks of these gases can potentially result in explosive conditions. The present shuttle leak-detection system is based on mass spectrometers on the ground or sample bottles in flight. Although these shuttle systems provide significant information related to safety conditions, the shuttle systems have their limitations, especially in providing continuous, real-time information as the vehicle is launched. For a number of years, the NASA Glenn Research Center has been developing smart leak-detection systems (SLDSs) to augment ground systems and to provide real-time data for flight systems. This year, steps were taken to prepare these SLDSs for a possible Crew Launch Vehicle (CLV) application.

SLDSs are based on microsystems technology; that is, they are miniaturized systems fabricated using silicon semiconductor processing technology for minimal size, weight, and power consumption. The SLDS is composed of microsensors to detect leaks and supporting electronic hardware for data processing and temperature control. The approach has been to develop a smart "lick and stick" leak-detection system of near postage stamp size that could be applied wherever safety information is needed.

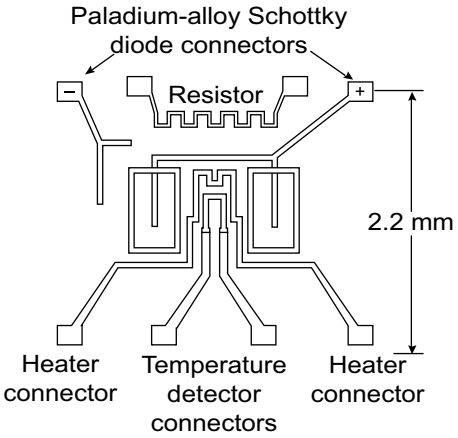


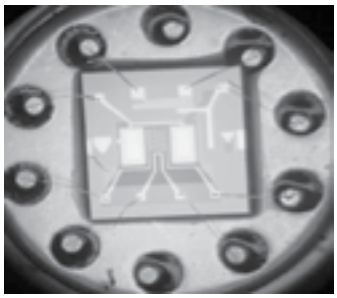

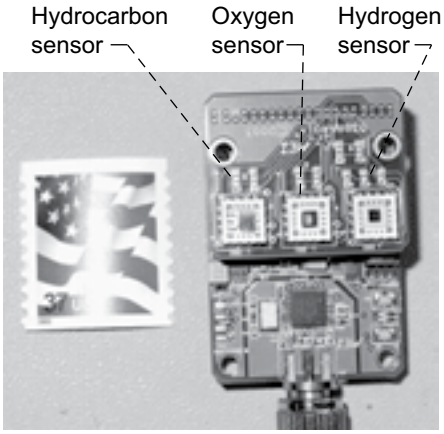


*Left: Silicon-based hydrogen sensor. The palladium (Pd) alloy Schottky diode (rectangular regions) resides symmetrically on either side of a heater and temperature detector. The Pd alloy resistor is included for high-concentration measurements. Center: Packaged sensor. Right: Prototype version of a lick-and-stick SLDS with hydrogen, hydrocarbon, and oxygen detection capabilities combined with supporting electronics.*

One example of an SLDS microsensor is the hydrogen sensor. The left figure shows the microfabricated hydrogen sensor design, and the center photograph shows a packaged sensor. The structure includes two different hydrogen-sensing elements (Schottky diode and resistor), a temperature detector, and a heater incorporated in the same silicon chip. The Schottky diode and resistor have different sensing mechanisms combining to allow hydrogen detection over a wide concentration range. Glenn has been involved in years of testing the sensor and developed the alloy used in the sensor structure. This hydrogen sensor has been demonstrated in the space shuttle, and it has qualified for an International Space Station criticality 1 function.

The right photograph shows a prototype SLDS that uses hydrogen, oxygen, and hydrocarbon sensors. A range of capabilities were built into this lick-and-stick system, including a microcontroller, signal conditioning and temperature control, wireless or wired communications, operation from a 3- to 5-V power source or battery, internal temperature and pressure measurement, and operation of up to three chemical sensors.

Glenn has led the efforts to turn this promising technology into a sensor system that can be integrated into the CLV. This year's SLDS activities involved testing and documentation to verify that the existing system has the basic capabilities to meet CLV application needs, especially concentrating on hydrogen- and oxygen-sensing capabilities. These efforts included Glenn involvement in the maturation of the oxygen sensor technology. Other efforts included verifying that space-qualifiable parts are being used and performing fault analysis on component parts to understand failure mechanisms.

Overall, this CLV work represents steps toward the implementation of "smart" system technology into NASA's Exploration program. As with the introduction of any new technology, challenges exist in showing benefits and gaining acceptance. However, given the future needs of space exploration systems, the introduction of smart system technology could be a significant enabler of the Vision for Space Exploration.

**Glenn contacts:**
Gary Hunter, 216–433–6459, Gary.W.Hunter@nasa.gov

Jennifer Xu, 216–433–6669, Jennifer.C.Xu@nasa.gov

Larry Oberle, 216–433–3647, Lawrence.G.Oberle@nasa.gov

**Authors:**
Dr. Gary W. Hunter and Dr. Jennifer C. Xu

**Headquarters program office:**
Constellation Project Office

**Programs/projects:**
Crew Launch Vehicle, Advanced Sensors Project

# Nanosensor Technology Tools Being Explored—Tools Advanced To Overcome Three Technical Barriers

Hidden fires, which can originate on aircraft in areas out of sight of the crew, are a significant aviation safety concern. An aircraft fire can spread quickly, and the crew may not be aware of its existence or location until the fire poses a safety hazard. One approach to address this problem is to place a number of sensors in the closed, hidden compartments where these fires may occur. By correlating the signal from these multiple sensors, a smart fire-detection system could both detect a fire and determine its location, allowing the crew to apply fire suppressant. To minimize the penalty to the vehicle operation, the sensors should not use wires or power from the vehicle, should wirelessly transmit their information, and should be in operation for years without maintenance. A significant challenge in realizing this vision is developing sensor technology that can detect a range of chemical species with near zero power consumption.

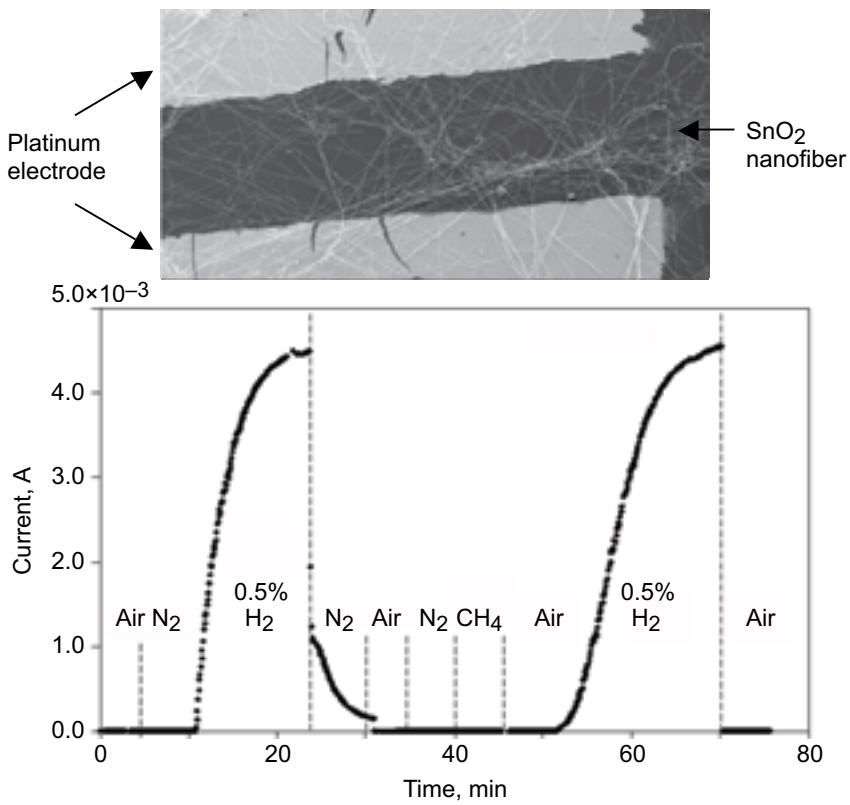


*Top: Bridging of electrospun tin oxide ($SnO_2$) nanofibers across electrodes. Bottom: Current response at 23 °C and 2 V of electrospun palladium- (Pd-) doped $SnO_2$ nanofibers to hydrogen ($H_2$) and methane ($CH_4$) in nitrogen ($N_2$) at room temperature.*

The approach being taken in this work at the NASA Glenn Research Center is to develop chemical sensors based on nanostructured oxide materials. Although layers of nanocrystals have shown significant potential for chemical-sensing applications and are used in present NASA-developed fire-detection sensors, the advantages of nanostructured oxide sensors—such as nanorods, nanofibers, nanoribbons, and nanotubes—are just beginning to be explored. The use of these nanostructures in sensors has the potential to produce significant gains in sensor performance. However, these gains must be demonstrated, and significant technical challenges remain before nanostructured oxides can be implemented routinely in sensing applications.

The major issues addressed in this work are associated with making workable sensors. Three technical barriers related to the application of nanostructures into sensor systems were addressed at Glenn: (1) improving contact of the nanostructured materials with electrodes in a microsensor structure, (2) controlling nanostructure crystallinity to allow control of the detection mechanism, and (3) widening the range of gases that can be detected by using different nanostructured materials. The major accomplishment of this year's work was the advancement of some of the tools necessary to overcome these barriers.

This figure shows an example of controlling the contact between the nanostructured material and the microstructure, where tin oxide nanofibers have been electrospun across the electrodes of a microstructure. Electrospinning is a process whereby a charged solution that is drawn from a capillary retains a

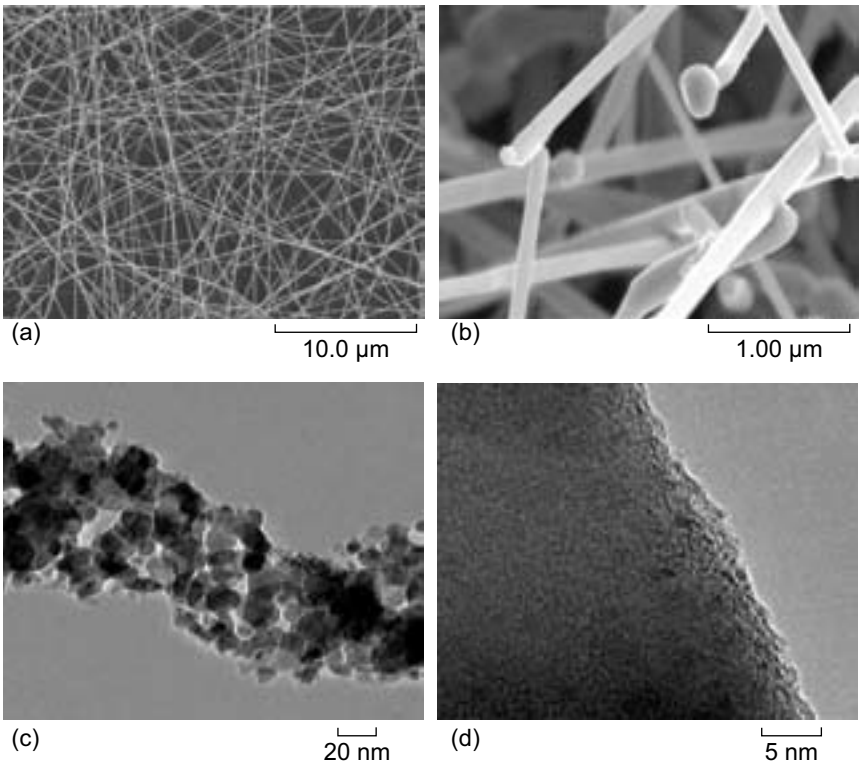


*Control of $SnO_2$ nanostructure fabrication. The different processing techniques result in very different crystal structures. (a) Scanning electron microscopy (SEM) of electrospun nanofibers. (b) SEM of TEC grown nanorods. (c) High-resolution transmission electron microscopy (HRTEM) of electrospun nanofibers. (d) HRTEM of TEC nanorods.*

**Glenn contacts:**
Gary Hunter, 216–433–6459, Gary.W.Hunter@nasa.gov

Randy Vander Wal, 216–433–9065, Randall.L.VanderWal@nasa.gov

Jennifer Xu, 216–433–6669, Jennifer.C.Xu@nasa.gov

Laura Evans, 216–433–9845, Laura.J.Evans@nasa.gov

**Authors:**
Dr. Gary W. Hunter and Dr. Jennifer C. Xu

**Headquarters program office:**
Aeronautics Research Missions Directorate

**Programs/projects:**
Aviation Safety, Director's Discretionary Fund

"threadlike" form while it is deposited on a grounded surface. The result is a nanofiber "spun" across electrode structures as seen in the photomicrograph on the preceding page. The resulting sensor, after treatment with a catalytic metal, is sensitive to hydrogen at room temperatures (as seen in the preceding plot). When the different fabrication techniques of electrospinning and thermal evaporation-condensation (TEC) are used, very different nanostructure materials can be formed (as illustrated in the photomicrographs on this page). Electrospinning and TEC produce very different crystal structures. The research approach is to tailor the sensing element nanostructure to achieve optimal selectivity and sensitivity.

Although this work demonstrates useful tools and techniques for further development, these are just the beginning steps toward the realization of repeatable, controlled sensor systems using oxide-based nanostructures and the realization of the range of new capabilities that these sensors might enable.

# High-Temperature Amplifier Based on a Silicon Carbide Metal-Semiconductor Field Effect Transistor and Ceramic Packaging Designed, Fabricated, and Electrically Operated at 500 °C

High-temperature semiconductor transistor electronics capable of prolonged 500 °C operation would enable important advancements in the sensing and control of combustion in jet engines, making them cleaner, safer, and more fuel-efficient. In addition, such electronics are keys to the long-term operation of scientific probes on or near the scorching 460 °C surface of Venus. Although there have been reports of short-term (less than 10 hr) transistor operation at 500 °C or above, much longer operating times are needed for these and other beneficial high-temperature electronics applications. Toward this end, the NASA Glenn Research Center has been pioneering silicon carbide (SiC) semiconductor transistors and ceramic packaging technology targeted for greatly prolonged operational durability at 500 °C. These efforts previously demonstrated high-temperature chip- and board-level packages for prolonged 500 °C operation (refs. 1 and 2) and 2000 hr of 500 °C operation of an SiC metal-semiconductor field effect transistor (MESFET) (refs. 3 and 4) based on high-temperature ohmic contact technology (ref. 5).

Building on this foundation, civil servants and Ohio Aerospace Institute (OAI) researchers at Glenn designed, fabricated, and electrically operated continuously at 500 °C for more than 600 hr a high-temperature amplifier circuit based on an SiC MESFET, epilayer resistors, and a ceramic packaging system. This is the first semiconductor-based amplifier to demonstrate stable continuous electrical operation in such a harsh high-temperature oxidizing air environment with excellent stability over such an extended period of time.

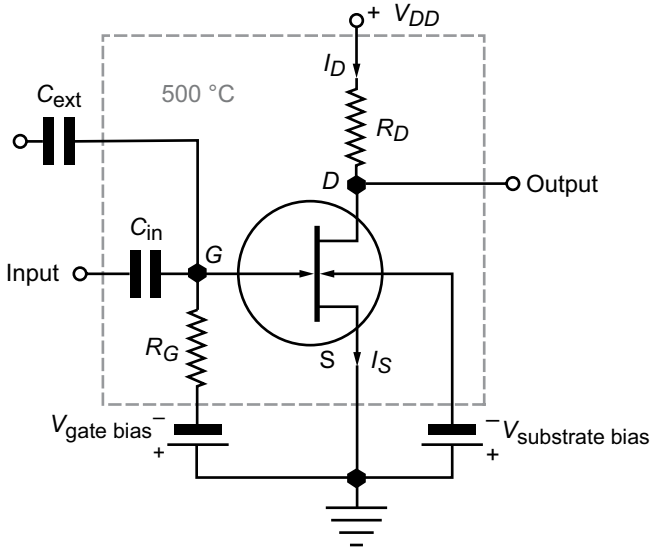


*Circuit diagram of a common-source amplifier circuit operated for more than 600 hr at 500 °C. The elements within the dotted box were operated in the 500 °C air-ambient oven; drain bias, $V_{DD}$ = 120 V; gate bias voltage, $V_{gate\ bias}$ = –9 V; substrate bias voltage, $V_{substrate\ bias}$ = –20 V; external coupling capacitor, $C_{ext}$ = 0.47 μF; gate resistance, $R_G$ = 150 kΩ; drain resistance, $R_D$ = 340 kΩ; drain current, $I_D$.*

The circuit schematic diagram shows the simple common-source amplifier circuit, which consists of an SiC MESFET, two SiC resistors, and a ceramic capacitor. The components inside the dotted lines of the diagram were packaged onto the ceramic high-temperature circuit board (see the photograph on the next page), which was operated at 500 °C inside an oven. The circuit board with components was subjected to 656 hr of unbiased 500 °C heat soaking prior to initiation of the 500 °C continuous electrical operation. For this initial low-frequency demonstration, an external (room temperature) coupling capacitor was used to obtain sufficient coupling of the input signal because the 500 °C onboard capacitor was not designed to support circuit operation at frequencies as low as ~100 Hz.

The final figure shows the input (1-V peak-to-peak amplitude) and output (7-V peak-to-peak) sine voltage waveforms measured during the 430th hour of continuous electrical operation at 500 °C. Circuit power supply biases were not changed throughout the 500 °C electrical test duration. The amplifier gain remained stable (near 7) for over 600 hr of continuous 500 °C electrical operation (over 1300 hr of total soak time at 500 °C). After this time period, amplifier gain degraded significantly because of thermal annealing of the MESFET gate contact (ref. 4). Modifying the design of the SiC transistor (changing from a metal-semiconductor gate junction to a p-type/n-type semiconductor gate junction) should eliminate this gradual degradation mechanism. Nevertheless, this demonstration of 500 °C durability of a transistor-based amplifier circuit represents an important step toward significantly expanding the operational envelope of sensor signal-processing electronics for harsh environments such as the high-temperature regions of combustion engines and the surface of Venus.

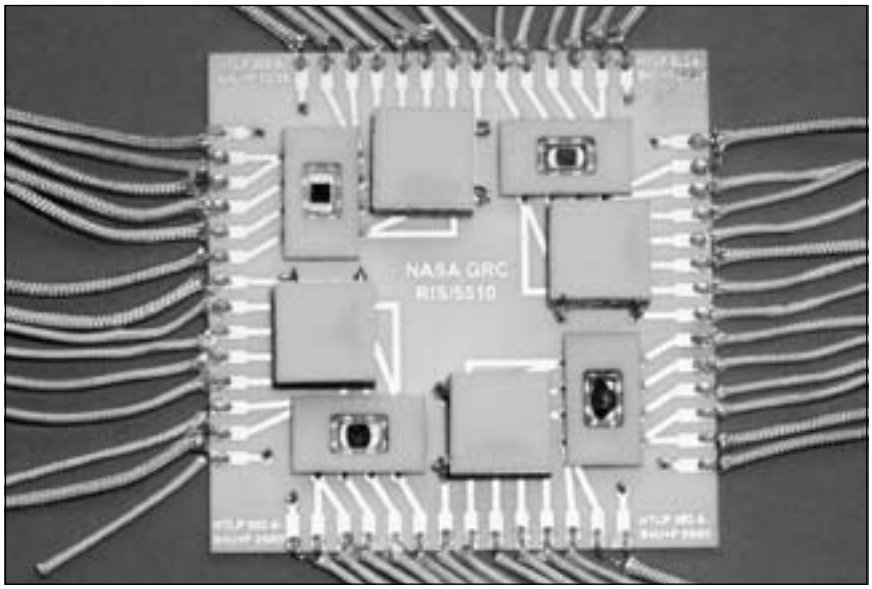


*Circuit-board assembly used for the long-duration 500 °C demonstration of the SiC transistor-based amplifier circuit.*

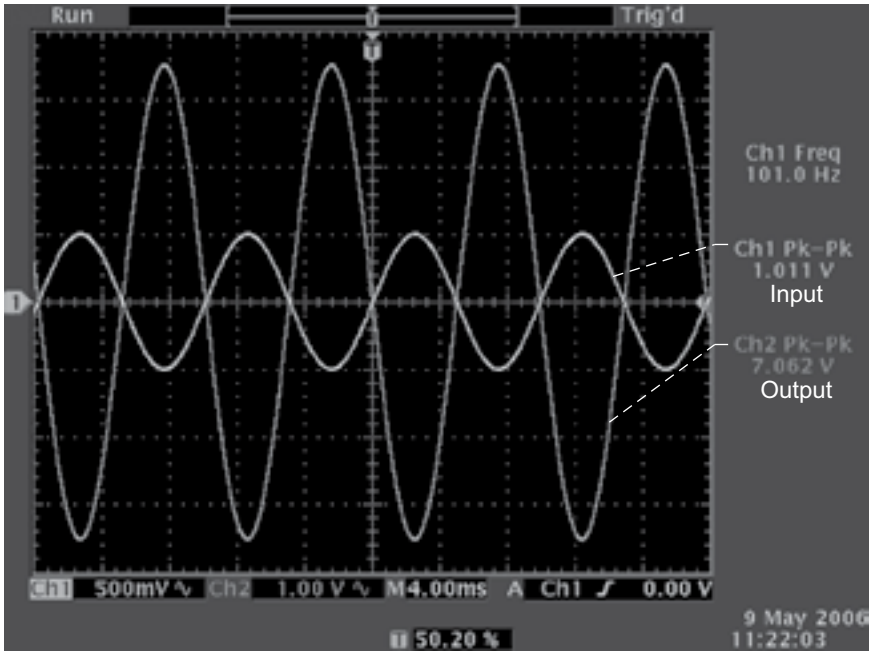


*Input (1-V peak-to-peak) and output (7-V peak-to-peak) sine waveforms recorded during the 430th hour of electrical operation of the amplifier stage at 500 °C.*

**References**

1. Chen, L.Y.; Spry, D.J.; and Neudeck, P.G.: Demonstration of 500 °C AC Amplifier Based on SiC MESFET and Ceramic Packaging. Proceedings 2006 IMAPS International High Temperature Electronics Conference, Santa Fe, NM, p. 240.
2. Chen, Liang-Yu: Ceramic Packages Designed, Fabricated, and Assembled for SiC Microsystems. Research & Technology 2002. NASA/TM—2003-211990, 2003, pp. 69–70. http://www.grc.nasa.gov/WWW/RT2002/5000/5510chen.html
3. Neudeck, Philip G., et al.: Nanometer Step Height Standard Chip Developed for Calibration of Scanning Probe Microscopy Instruments. Research & Technology 2005. NASA/TM—2006-214016, 2006, p. 55. http://www.grc.nasa.gov/WWW/RT/2005/RI/RIS-neudeck1.html
4. Neudeck, Philip G.: Packaged SiC Transistor Operated at 500 °C for 2000 hr in Oxidizing Air Ambient. Research & Technology 2005 NASA/TM—2006-214016, 2006, pp. 56–57. http://www.grc.nasa.gov/WWW/RT/2005/RI/RIS-neudeck1.html
5. Okojie, Robert S.: Thermally Stable Ohmic Contacts on Silicon Carbide Developed for High-Temperature Sensors and Electronics. Research & Technology 2000. NASA/TM—2001-210605, 2001, pp. 59–60. http://www.grc.nasa.gov/WWW/RT2000/5000/5510okojie.html

**Find out more about silicon carbide electronics research at Glenn:**
http://www.grc.nasa.gov/WWW/SiC/

**Glenn contacts:**
Dr. Philip G. Neudeck, 216–433–8902, Philip.G.Neudeck@nasa.gov

Dr. Robert S. Okojie, 216–433–6522, Robert.S.Okojie@nasa.gov

Dr. Glenn M. Beheim, 216–433–3847, Glenn.M.Beheim@nasa.gov

**Ohio Aerospace Institute (OAI) contacts:**
David J. Spry, 216–433–3361, David.J.Spry@nasa.gov; and

Dr. Liang-Yu Chen, 216–433–6458, Liangyu.Chen-1@nasa.gov

**Authors:**
Dr. Philip G. Neudeck and
Dr. Liang-Yu Chen

**Headquarters program office:**
Aeronautics Research Mission Directorate

**Programs/projects:**
Glennan Microsystems Initiative, Propulsion 21, Ultra Efficient Engine Technology, NASA Electronic Parts and Packaging

**Special recognition:**
This work was selected as one of the keynote presentations of the 2006 IMAPS High Temperature Electronics Conference held May 15 to 18 at Santa Fe, New Mexico.

# POWER AND ELECTRIC PROPULSION

## Closed-Cycle Hydrogen-Oxygen Proton-Exchange-Membrane Regenerative Fuel Cell Demonstrated at the NASA Glenn Research Center

The NASA Glenn Research Center has demonstrated the world's first fully closed cycle hydrogen-oxygen regenerative fuel cell (RFC). The RFC is an electrochemical system that collects and stores solar energy during the day then releases that energy at night, thus making the Sun's energy available all 24 hours. It consists of a dedicated hydrogen-oxygen fuel cell stack and an electrolyzer stack, the interconnecting plumbing and valves, cooling pumps, water transfer pumps, gas recirculation pumps, phase separators, storage tanks for oxygen ($O_2$) and hydrogen ($H_2$), heat exchangers, isolation valves, pressure regulators, vent and purge provisions (emergency only), instrumentation, and other components. It includes all the equipment required to (1) absorb electrical power from an outside source and store it as pressurized hydrogen and oxygen and (2) make electrical power from the stored gases, saving the product water for reuse during the next cycle. The Glenn RFC is a "brassboard" built mainly from off-the-shelf hardware components. It is used to

(1) Test fuel cells and fuel cell components under repeated closed-cycle operation (nothing escapes; everything is used over and over again).
(2) Simulate diurnal charge-discharge cycles.
(3) Observe long-term system performance and identify degradation and loss mechanisms.
(4) Develop safe and convenient operation and control strategies leading to the successful development of mission-capable, flight-weight, closed-cycle RFCs for space solar power.

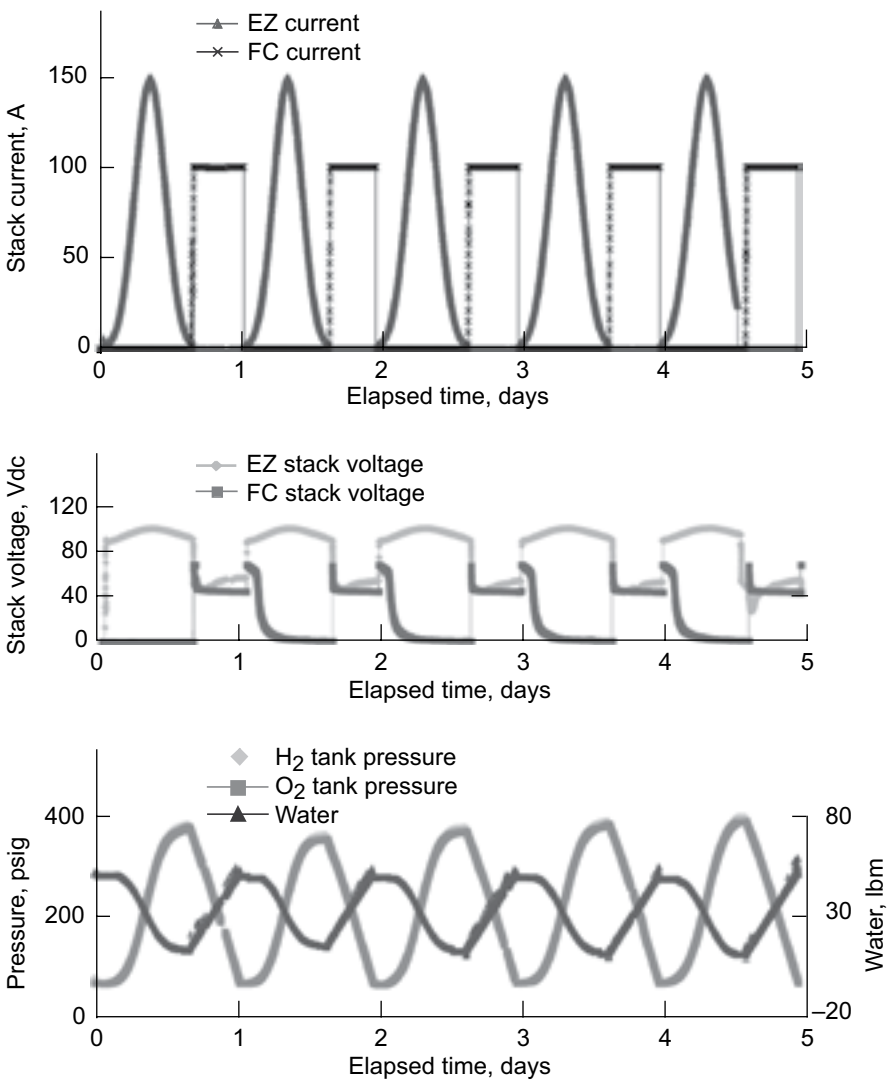


*Electrolyzer (EZ) and fuel cell (FC) currents and voltages, reactant flows, and balances measured during a 5-day continuous run.*

Construction was sponsored by the Environmental Research Aircraft and Sensor Technology (ERAST) project of the Flight Research Base Program. The ERAST charter included the development and demonstration of new technologies for unmanned aircraft that are suitable for Earth science, including RFC-equipped solar-electric aircraft with potentially unlimited endurance. Although ERAST was an aeronautics project, RFC energy storage is applicable to a wide variety of space and planetary surface missions in addition to high-altitude solar-electric flight; hence, there has been widespread interest throughout NASA to bring this technology to a flight demonstration.

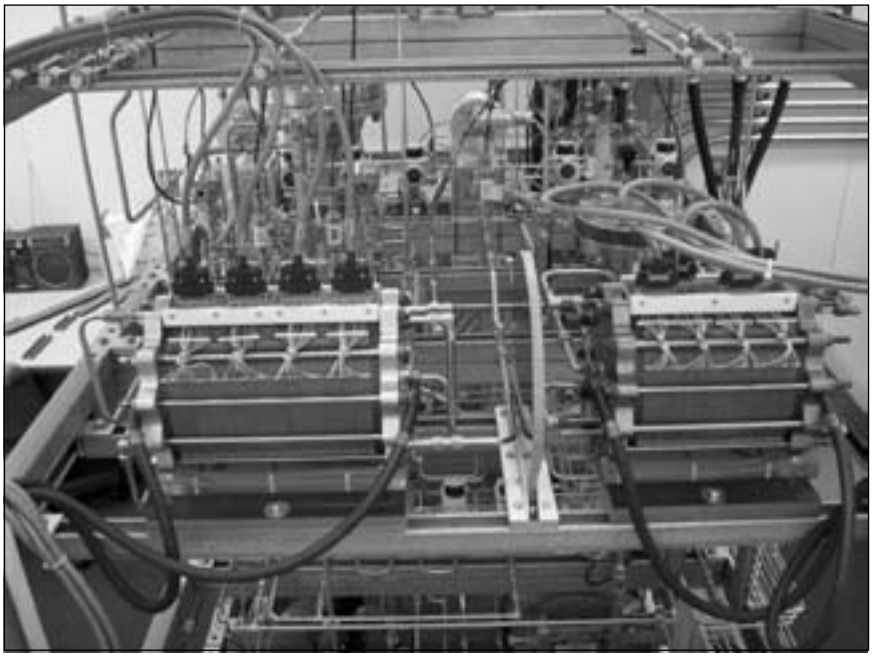

*RFC-integrated equipment assembly, with fuel cell and electrolyser stacks shown in the foreground.*

Leading up to a flight demonstration are several laboratory and full-scale demonstrations of key components and subsystems, including the coordinated operation of a hydrogen-oxygen fuel cell and electrolyzer as an energy storage system in a sealed, closed-loop environment (the venue provided by this brassboard RFC).

The Glenn RFC was built up over calendar years 2002 to 2003 and was operated as an end-to-end energy storage system for the first time in September 2003. Closed-cycle operation at full power operation was first demonstrated in June 2004. Multiple back-to-back contiguous cycles at full rated power, and round-trip efficiencies to 52 percent, were demonstrated in June 2005 (see the graphs on the preceding page).

During fiscal year 2006, the system underwent numerous modifications and internal improvements aimed at reducing parasitic power, heat loss, and noise signature; increasing functionality as an unattended automated energy-storage device, and increasing in-service reliability. Unattended operation was demonstrated in June 2006.

The Glenn RFC is the first fully closed cycle RFC ever demonstrated (the entire system is sealed: nothing enters or escapes the system other than electrical power and heat). The Glenn tests have demonstrated the RFC's potential as an energy-storage device for aerospace solar power systems such as solar electric aircraft, lunar and planetary surface installations, and system applications in any airless environment where minimum system weight is critical. Its development process has recently been slowed, but it continues on a path of risk reduction for the flight system NASA will eventually need for a manned lunar outpost.

The photograph shows the integrated equipment assembly at Glenn. The graphs on the preceding page show the electrolyser and fuel cell stack currents and voltages, reactant flows, and balances that were recorded during the June 2005, 5-day endurance run.

**Find out more about research at Glenn:**
http://www.nasa.gov/glenn/

**Glenn contact:**
David J. Bents, 216–433–6135,
David.J.Bents@nasa.gov

**Sierra Lobo, Inc., contact:**
Bei-Jiann Chang, 216–433–5095,
Beijiann.Chang-1@nasa.gov

**Gilcrest Electric & Supply Company contacts:**
Donald W. Johnson, 216–433–5075,
Donald.W.Johnson@nasa.gov

Christopher P. Garcia, 216–433–3933,
Christopher.P.Garcia@nasa.gov

**Analex Corporation contact:**
Ian J. Jakupca, 216–433–3853,
Ian.J.Jakupca@nasa.gov

**Authors:**
David J. Bents, Bei-Jiann Chang,
Donald W. Johnson, Christopher P. Garcia,
and Ian J. Jakupca

**Headquarters program office:**
Aeronautics Research Mission Directorate

**Programs/projects:**
Subsonic Fixed Wing, Exploration Technology, Constellation Systems

**Special recognition:**
NASA group achievement award for first-ever demonstration of hydrogen-oxygen regenerative fuel cell in a fully closed cycle operation

# Thermal Stability of Lithium Ion Cells Studied

The safety performance of lithium-ion (Li-ion) cells and batteries is critical to the successful implementation of this battery chemistry. The thermal abuse tolerance of the cells is a complex function of the interactions of the individual cell components at elevated temperatures. Complex reactions that generate heat, exothermic byproducts, and gas are the two main problems in Li-ion cells that lead to low abuse tolerance. Abuse conditions can result in uncontrollable chemical reactions that lead to thermal runaway. Cells should be designed so that, when they are exposed to extreme conditions (high temperature, short circuit, and overcharge), the battery cell fails gracefully. The NASA Glenn Research Center is using a variety of thermal safety analysis techniques to identify the nature and source of thermal instability in Li-ion batteries under various operational and abusive conditions. One type of study is called accelerating rate calorimetry.

*Sample bomb suspended from the top of the ARC. A thermocouple is attached to the bomb.*

An accelerating rate calorimeter (ARC, ref. 1) is an adiabatic calorimeter. Samples are loaded into titanium or hastelloy bombs suspended from the top of the calorimeter. A thermocouple is attached to the sample bomb to measure variation in temperature. A controller is programmed to increase the calorimeter's temperature via a predetermined profile. The sample temperature increases because of convection and conduction. If the sample undergoes chemical reactions that generate heat, the sample temperature will rise. If the self-heating rate is greater than the threshold level, then the ARC proceeds into the exotherm mode and the self-heating is followed until the rate falls below the detection limit or until the end-point temperature is reached. The adiabatic self-heating rate of the sample can be measured as a function of time and temperature.

Glenn performs experiments on commercial Li-ion cells and the key electrochemical components using the ARC (see the photographs). Experiments evaluating exothermic behaviors of electrolyte materials and anode and cathode materials at different states-of-charge are conducted.

*The blast enclosure and control rack of the ARC.*

An initial test to determine when self-heating would be detected in the ARC was performed using a 2-g electrolyte sample. The electrolyte sample, consisting of 1-M lithium hexafluorophosphate ($LiPF_6$) salt in 1:1 ethylene carbonate (EC):dimethyl carbonate (DMC) solvent, was contained in the sample bomb. A starting temperature of 40 °C, heating temperature of 5 °C/min, waiting time of 15 min, and slope sensitivity of 0.020 °C/min were used. The top and bottom graphs on the next page show temperature and pressure data plotted against time, and self-heating data plotted against the temperature profile for the electrolyte sample, respectively. The exothermic onset temperature for the electrolyte was 180 °C. After the initial electrolyte reactions, the self-heating rate increased in an almost linear mode before reaching a maximum at 265 °C. The second exotherm was detected at around 332 °C, with a pressure increase in both cases.

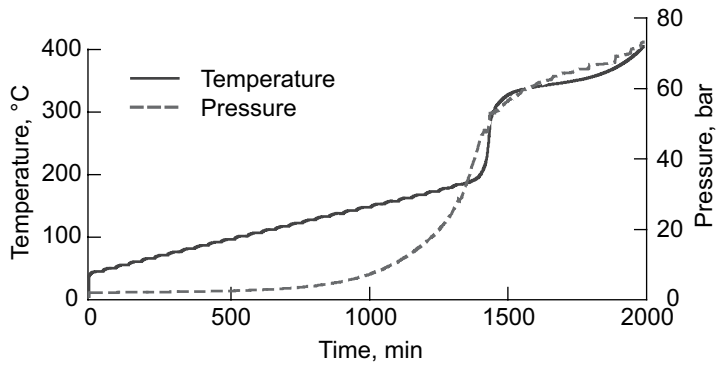


*Temperature and pressure data versus time for 1-M $LiPF_6$ in 1:1 EC: DMC electrolyte.*

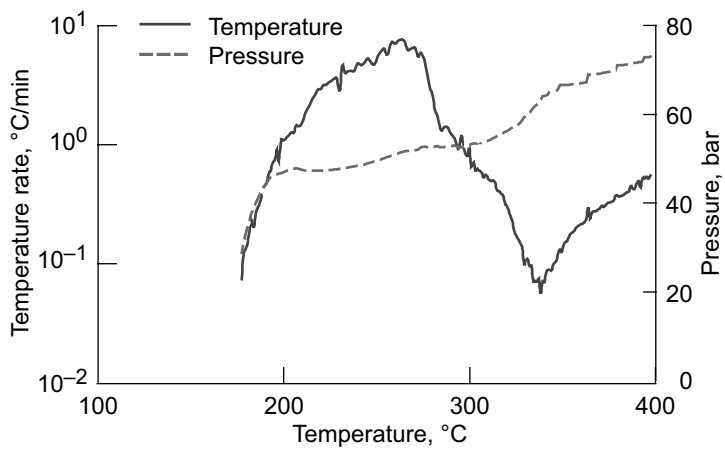


*Self-heating rate and pressure versus temperature for 1-M $LiPF_6$ in 1:1 EC:DMC electrolyte .*

In order to improve the safety of Li-ion cells, it is necessary to understand the thermal stability and heat generation from the decomposition and exothermic reactions of these cells. There is a need to study the role of the components on the initialization temperature of thermal runaway and relative heat generation. The use of calorimetric methods, such as the ARC, can provide this information and, therefore, will help alleviate thermal runaway and will result in safer Li-ion cell designs.

**Reference**

1. Townsend, D.I.; and Tou, J.C.: Thermal Hazard Evaluation by an Accelerating Rate Calorimeter. Thermochim. Acta, vol. 37, no. 1, 1980, pp. 1–30.

**Find out more about the research of Glenn's Electrochemistry Branch:**
http://www.grc.nasa.gov/WWW/Electrochemistry/

**Glenn contacts:**
Doris L. Britton, 216–433–5246, Doris.L.Britton@nasa.gov

Thomas B. Miller, 216–433–6300, Thomas.B.Miller@nasa.gov

Michelle A. Manzo, 216–433–5261, Michelle.A.Manzo@nasa.gov

**Authors:**
Doris L. Britton and Thomas B. Miller

**Headquarters program office:**
Exploration Systems Mission Directorate

**Programs/projects:**
Exploration Space-Rated Lithium-Ion Battery Task, Extravehicular Activities

# High-Altitude Long-Endurance Unmanned Air Vehicle Configurations Assessed

High-Altitude Long-Endurance (HALE) unmanned air vehicles have been the focus of significant research and development efforts for decades. The state of the art has been advanced to enable higher operational altitudes, longer durations with greater payloads, and increased autonomy. The desire to extend the endurance of these vehicles has led to research in solar-regenerative propulsion systems, which rely on a solar photovoltaic array coupled to an energy storage system. Solar-regenerative propulsion systems could theoretically propel air vehicles for many months.

An intercenter NASA study was performed to benchmark the performance potential of solar regenerative propulsion for operationally useful HALE missions and to quantify the technology improvements required, if any, to enable these missions. The secondary purpose, given a near-term technology-level assumption, was to examine several nonregenerative propulsion options to identify a preferred system concept for the study missions. The NASA Langley Research Center led the team, with participation from the NASA Ames Research Center, the NASA Dryden Flight Research Center, and the NASA Glenn Research Center.

An analysis of alternatives and a technology requirements study were conducted for two mission areas utilizing various types of HALE unmanned air vehicles. A hurricane science mission and a communications relay mission provided a set of vehicle requirements that were used to derive 16 potential HALE configurations, including heavier-than-air (HTA) and lighter-than-air (LTA) concepts with both consumable fuel and solar-regenerative propulsion systems.

Analysis proceeded in two phases. During phase I, the 16 potential solutions were analyzed, and the two leading consumable fuel configurations (one each from the HTA and LTA alternatives) were selected for the second phase of the study. One of the HTA solar-regenerative power system configurations was also

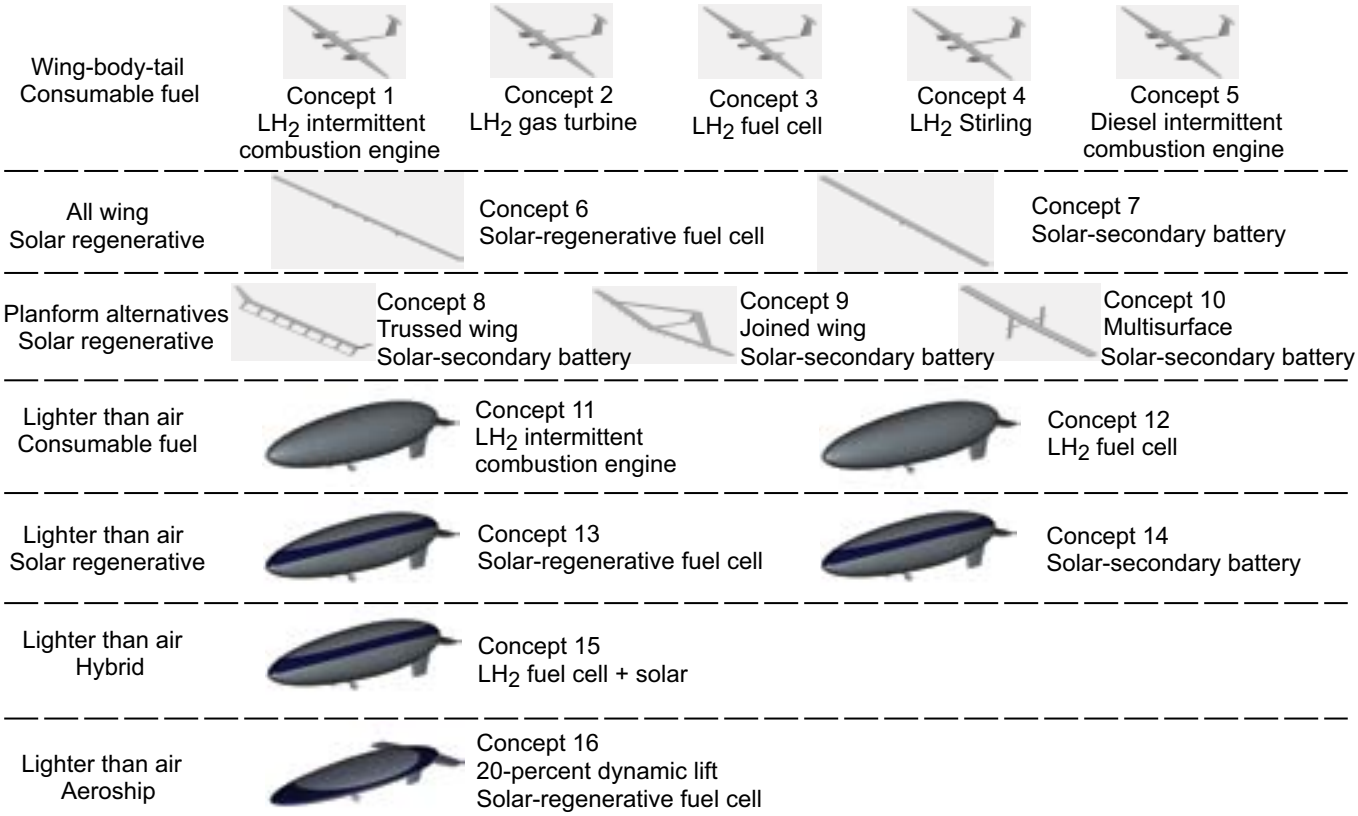


*HALE configurations considered in the analysis of alternatives. $LH_2$, liquid hydrogen.*

chosen for additional analysis. Phase II consisted of an operational analysis of the two consumable fuel configurations to derive the required fleet sizes and a life-cycle cost estimate for each potential fleet. An HTA diesel-fueled wing-body-tail configuration emerged as the preferred concept given near-term technology constraints. The cost-effectiveness analysis showed that simply maximizing vehicle endurance can be a suboptimum system solution. In addition, the solar-regenerative power system configuration was utilized to perform both a missions requirements study and a technology development study. Given near-term technology constraints, the solar-regenerative-powered vehicle was limited to operations during the long days and short nights found at higher latitudes during the summer months. Technology improvements are required in the energy-storage-system specific energy and the solar cell efficiency, along with airframe drag and mass reductions, to enable the solar-regenerative vehicle to meet the full mission requirements.

**Glenn contact:**
Lisa L. Kohout, 216–433–8004,
Lisa.L.Kohout@nasa.gov

**Power Computing Solution, Inc., contact:**
Paul C. Schmitz, 216–433–6174,
Paul.C.Schmitz@nasa.gov

**Authors:**
Lisa L. Kohout, Craig L. Nickol, and
Mark D. Guynn

**Headquarters program office:**
Aeronautics Research Mission Directorate

**Programs/projects:**
Fundamental Aeronautics Program,
Subsonic Fixed Wing Project

## NASA's Proton Exchange Membrane Fuel Cell Engineering Model Powerplant Evaluated

Recognizing the advantages of proton-exchange-membrane (PEM) fuel cell technology over existing alkaline fuel cell technology for space applications, NASA embarked on a 5-year PEM fuel cell powerplant development program in 2001. This program recently culminated with the delivery of a 7- to 10-kW engineering model (EM) to NASA for evaluation testing (see the photograph). NASA's 5-year program was conducted by the three-center NASA team of Glenn Research Center (lead), Johnson Space Center, and Kennedy Space Center. It was initially aimed at developing PEM fuel cell hardware for a reusable launch vehicle application, but more recently it shifted to applications supporting the NASA Exploration Program.

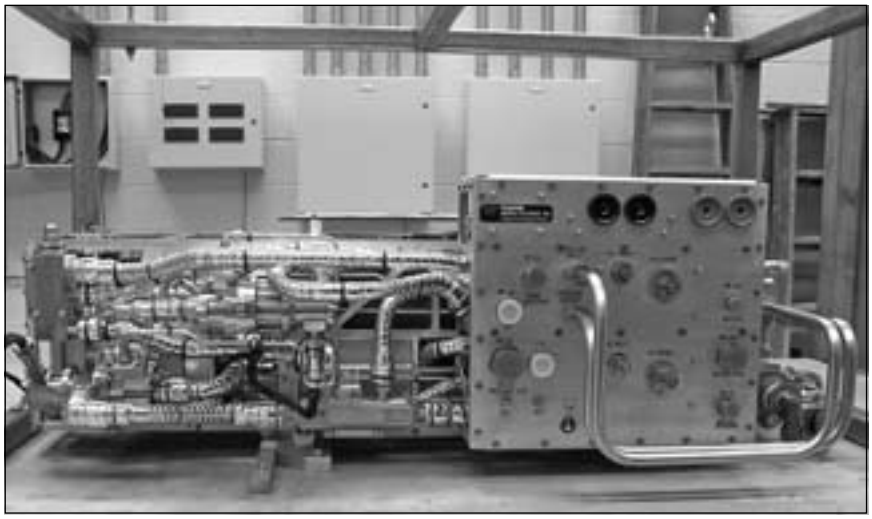

*PEM 7- to 10-kW EM fuel cell powerplant.*

KEY REQUIREMENTS AND GOALS FOR EM POWERPLANT

| Requirement | Goal |
|---|---|
| Nominal power, kW | 7 to 0 |
| Voltage regulation, percent | 30±10 |
| Voltage response time, sec | <0.2 |
| Operating life, hr | 10,000 |
| Operating temperature, °C | 60 to 80 |
| Operating pressure, kPa | <690 |
| Powerplant weight, kg | <140 |
| Powerplant volume, $m^3$ | <0.2 |

The first step in demonstrating the suitability of PEM fuel cell technology for space applications was evaluation testing of the 7- to 10-kW EM. The key requirements and goals for this powerplant are summarized in the table. As delivered to NASA, the EM powerplant met all of the program requirements and goals for power, voltage regulation, response time, operating temperature, operating

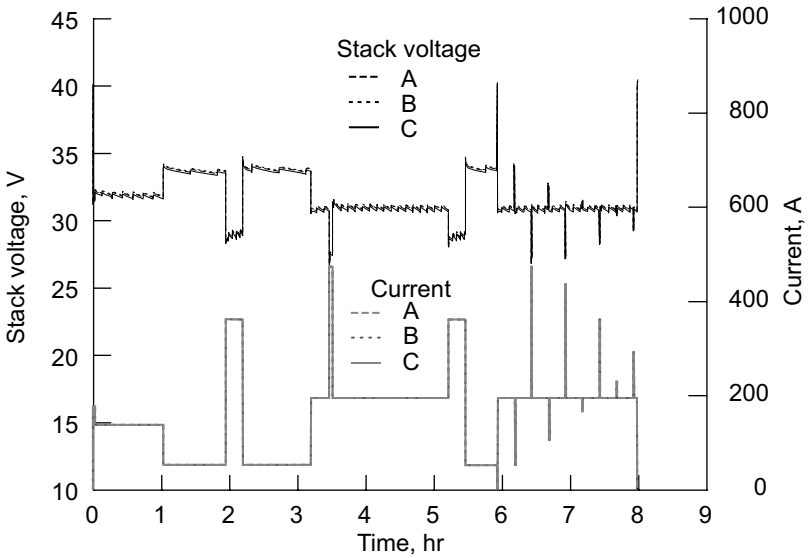


*Teledyne EM performance load profile test results.*

pressure, and powerplant volume. The powerplant weight was 25 percent in excess of the goal. Schedule and cost constraints prevented further reductions in balance-of-plant weight surrounding the fuel cell stack, which was the major contributor to the excess.

Initial evaluation tests, which were performed in Glenn's Fuel Cell Test Laboratory, consisted of a calibration series test, a rapid startup test, and a performance load profile. Mission profile, loss of coolant tests, and environmental performance tests are currently underway. The EM powerplant was tested in three different spatial orientations to evaluate gravitational effects on the overall performance of the fuel cell stack and supporting ancillaries.

Initial analysis of the test results to date has shown the EM powerplant performance to be largely independent of spatial orientation (see the graph to the left). The benchmark performance test also showed that the EM can achieve stable operation after experiencing large changes in the power load in less than a millisecond (see the following graphs). In addition, the EM powerplant's response times were evaluated under the rapid startup test; results indicate that the powerplant can deliver 50 percent of its rated capacity 5 sec after coming online with no preheating (see the graph on the next page).

Vibration and thermal vacuum testing are underway at Johnson. The final tests to be performed at Glenn are the mission profile and the loss-of-coolant test. The mission profile measures the EM powerplant performance over a continuous 240-hr power profile that is representative of future missions, and the loss-of-coolant test is used to evaluate the powerplant performance when a secondary cooling system external to the powerplant is interrupted. Testing is scheduled for completion in early 2007.

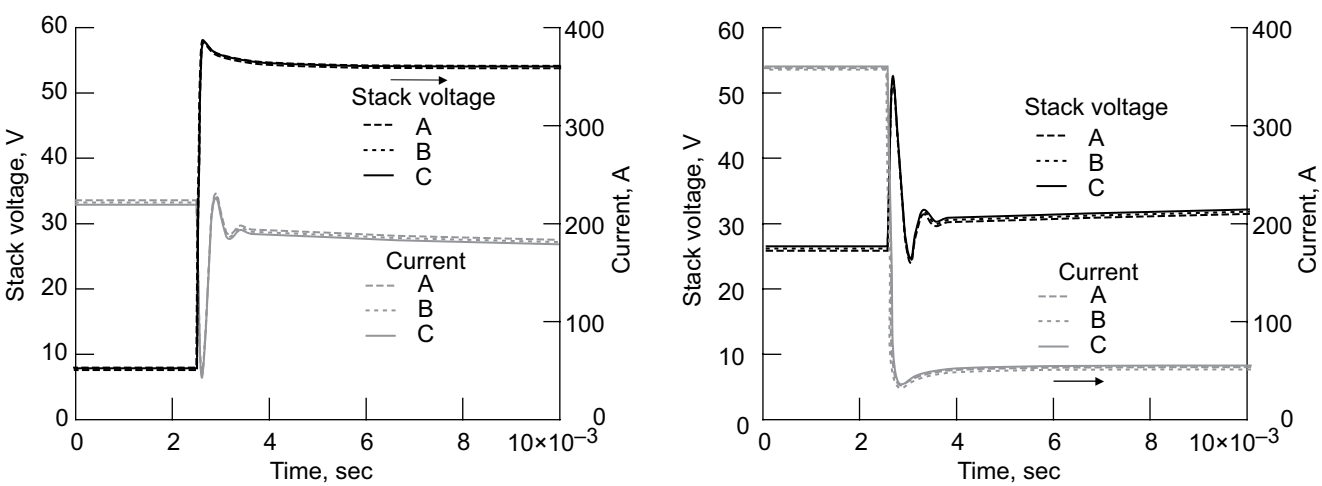


*Teledyne EM transient response to change in load. Left: Load increased from 51 to 357 A. Right: Load decreased from 357 to 51 A.*

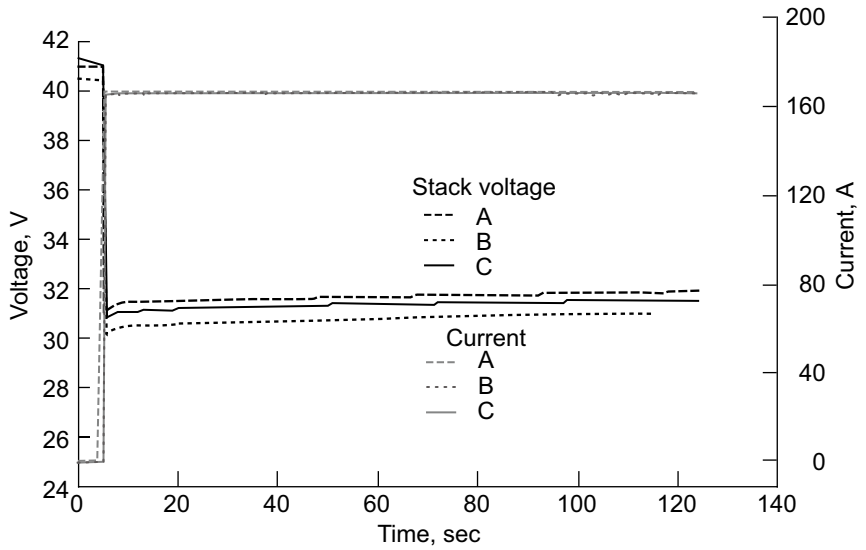


*Teledyne EM rapid startup test results; 50-percent capability 5 sec after start.*

**Find out more about this research:**

**Glenn's Electrochemistry Branch:**
http://www.grc.nasa.gov/WWW/Electrochemistry/

**Exploration Systems research at Glenn:**
http://exploration.grc.nasa.gov

**Glenn contacts:**
Dr. Patricia L. Loyselle, 216–433–2180, Patricia.L.Loyselle@nasa.gov

Mark A. Hoberecht, 216–433–5362, Mark.A.Hoberecht@nasa.gov

**Analex Corporation contact:**
Kevin P. Prokopius, 216–433–6137, Kevin.P.Prokopius@nasa.gov

**Authors:**
Kevin P. Prokopius, Mark A. Hoberecht, and Dr. Patricia L. Loyselle

**Headquarters program office:**
Exploration Systems Mission Directorate

**Programs/projects:**
Exploration Technology Development Program

## Lithium-Ion Cells From Multiple Vendors Demonstrated 10,000 Low-Earth-Orbit Cycles at Various Conditions

A Lithium-Ion Cell Low-Earth-Orbit Verification Test Program is being conducted by the NASA Glenn Research Center to assess the performance of lithium-ion (Li-ion) cells over a wide range of low-Earth-orbit (LEO) conditions. The data generated will be used to build an empirical model for Li-ion batteries. The goal of the modeling will be to develop a tool to predict the performance and cycle life of Li-ion batteries operating at a specified set of mission conditions. Using this tool, mission planners will be able to design operation points of the battery system while factoring in mission requirements and the expected life and performance of the batteries.

Test conditions were selected via a statistical design of experiments to span a range of feasible operational conditions for LEO aerospace applications. The variables under evaluation are temperature, depth-of-discharge (DOD), and end-of-charge voltage (EOCV). Four cells from each vendor are being LEO tested at each of 10 sets of test conditions. The LEO profile consists of a 90-min cycle: 55 min of charging, and 35 min of discharging. The required discharge (and charge) currents are calculated on the basis of the actual capacity of the cells.

The table on the next page shows the test matrix. As reflected in the table, test conditions for individual cells may vary slightly from the baseline test matrix depending upon the cell manufacturer's recommended operating conditions. In such instances, deviation from the baseline matrix to another controlled set of operating conditions will not perturb the statistical relationships because the alternate conditions fall within parameter ranges that are bounded by the baseline matrix.

Currently, cells from four cell manufacturers are undergoing life-cycle tests. The program has the flexibility to accommodate additional test articles

TEST CONDITIONS

| Temperature, °C | End-of-charge voltage, EOCV, V | Depth of discharge, DOD, percent |
|---|---|---|
| 30 | 4.05[c]/4.0[d] | 20 |
| 30 | 3.85 | 20 |
| 10 | 3.85 | 20 |
| 30 | 3.95 | 30 |
| 20 | 3.95 | 20 |
| 10 | 3.85 | 40[a]/35[b] |
| 20 | 3.85 | 30 |
| 30 | 3.85 | 40[a]/35[b] |
| 20 | 4.05[c]/4.0[d] | 40[a]/35[b] |
| 10 | 4.05[c]/4.0[d] | 30 |

[a]All vendors except Saft.
[b]Saft.
[c]All vendors except MSA.
[d]MSA.

as it progresses, so the tests are at various stages. Life cycling on the first sets of cells began in September 2004. These cells consisted of Saft 40-A-hr cells and Lithion 30-A-hr cells. In the past year, the test program expanded to include the evaluation of Mine Safety Appliances (MSA) 50-A-hr cells and ABSL (Power Solutions, Inc.) battery modules. The ABSL battery modules consist of commercial Sony hard carbon 18650 lithium-ion cells configured in series and parallel combinations to create nominal 14.4-V, 6-A-hr packs (four cells in series and four cells in parallel). The modules contain individual cell voltage monitors for data collection purposes, but charging and discharging is controlled on the module level. One module (four strings) is being tested at each of the 10 conditions. The figure shows the results of capacity characterization on cells from each vendor.

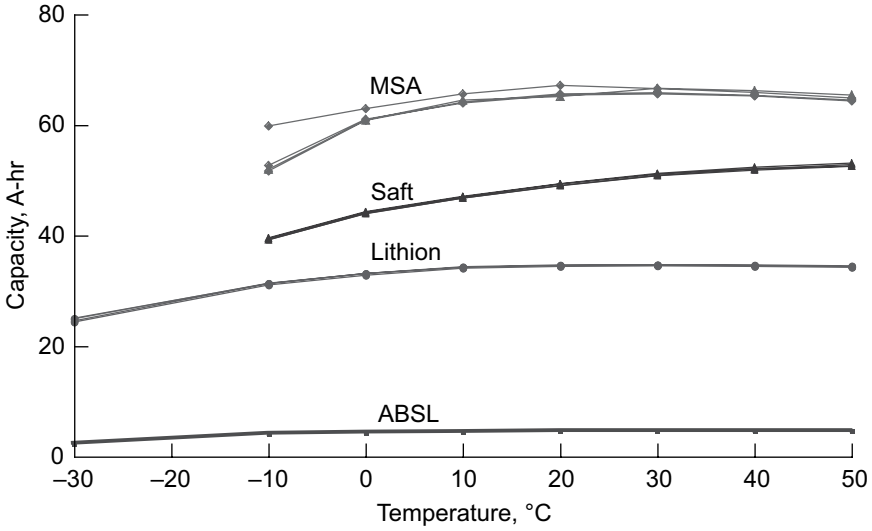


*Results of capacity characterization on ABSL modules and Lithion, MSA, and Saft cells at different temperatures.*

In fiscal year 2006, Saft and Lithion cells achieved over 10,000 cycles each, equivalent to about 20 months in LEO. Preliminary results were reported in references 1 and 2. Saft cells generally have a higher end-of-discharge voltage (EODV) than Lithion cells operating at the same conditions. Saft cells also have a lower EODV dispersion among cells operating at the same conditions. For both vendors, when cells are operating at the highest DOD, the EODV of the cells varies more than the EODV for the cells operating at the lower DODs. Also, as a cell's EODV gets lower and lower, operational capacity checks tend to have a more profound reconditioning effect on the cell. Upon return to LEO cycling, the cell tends to have a much higher EODV in comparison to the EODV before the capacity test.

Also in fiscal year 2006, ABSL modules accumulated approximately 3000 cycles. All 16 cells within each module are performing consistently and have shown very little EODV degradation. MSA cells will begin life cycling in October 2006. Actual capacity determination, open-circuit voltage stand, and capacity characterization at different temperatures have been performed on these cells thus far.

The life prediction and performance model for Li-ion cells in LEO will be built by analyzing the data statistically and performing regression analysis. Cells must be cycled to failure so that differences in performance trends that occur at different stages in the life of the cell can be observed and accurately modeled.

For this test program, a cell is considered to have failed once its discharge voltage reaches 3.0 V. By the end of fiscal year 2006, six cells had completed their life cycling by cycling to failure. All of these failures occurred in cells operating at the lowest EOCV and at the highest DOD for each vendor. Five of the six failures were in cells operating at 10 °C. The combination of the lowest EOCV, the highest DOD, and the lowest operating temperature (3.85-V EOCV, 35- or 40-percent DOD, and 10 °C) is considered to be the most

stressful set of conditions in the test matrix, therefore, it was not unexpected that these cells would fail the earliest. The sixth failed cell was operating at 30 °C. Five of the cells were Yardney cells, including the cell cycling at 30 °C. The sixth cell was a Saft cell. These early failures will begin to provide input for the life prediction and performance modeling.

Cell testing is being performed at the Naval Surface Warfare Center in Crane, Indiana, through an Interagency Agreement. Statistical analysis is being performed by Harold S. Haller & Co. under contract. Additional background on the program, results of the initial characterization, and preliminary life-cycling results of the Lithion and Saft cells are discussed in more detail in references 1 and 2.

**References**


1. McKissock, Barbara I., et al.: Preliminary Results of NASA Lithium-Ion Cell Verification Testing for Aerospace Applications. NASA/TM—2005-213995 (AIAA–2005–5561), 2005. http://gltrs.grc.nasa.gov/cgi-bin/GLTRS/browse.pl?2005/TM-2005-213995.html
2. McKissock, Barbara, et al.: Lithium-Ion Verification for Aerospace Applications. The 2nd International Symposium on Large Lithium-Ion Battery Technology and Applications (LLIBTA), Baltimore, MD, 2006.


**Find out more about the research of Glenn's Electrochemistry Branch:**
http://www.grc.nasa.gov/WWW/Electrochemistry/


**Glenn contact:**
Concha M. Reid, 216–433–8943, Concha.M.Reid@nasa.gov

**Author:**
Concha M. Reid


**Headquarters program office:**
Exploration Systems Mission Directorate

**Programs/projects:**
Space Rated Lithium-Ion Battery Task

## Hall Thruster Developed for Increased Mission Life

During 2006, researchers at the NASA Glenn Research Center successfully improved the lifetime capability of an electric propulsion technology currently under development to expand NASA's ability to conduct cost-capped deep-space robotic science missions. This benefit is due to the high fuel efficiency that can be achieved using electric propulsion. Although electric propulsion thrusters can achieve high specific impulse, a measure of fuel efficiency, these thrusters are capable of doing so only at low thrust levels. Therefore, in order to reach distant destinations within the solar system, it is necessary for electric propulsion thrusters to operate for thousands of hours. This requires the development of long-lasting electric propulsion thruster technologies.

These efforts are the responsibility of the In-Space Propulsion Technology Program, as part of NASA's Science Mission Directorate. The High Voltage Hall Accelerator (HIVHAC) development project is one such advanced development project that seeks to improve the lifetime capability of Hall thrusters, an electric propulsion technology currently used for stationkeeping of commercial Earth orbital satellites to enable deep-space NASA missions.

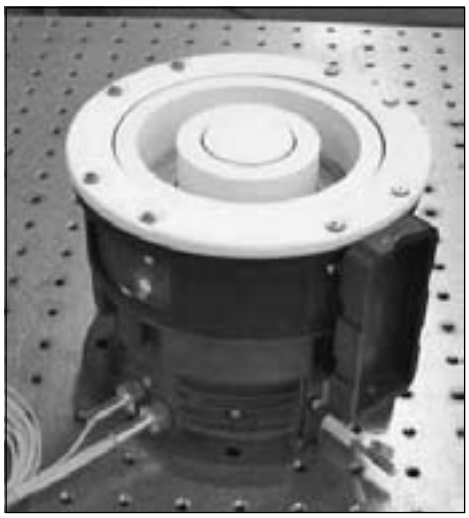

*7500-hr flight prototype high-voltage Hall accelerator.*

Recently the HIVHAC project was responsible for the design and fabrication of two new Hall thrusters: a flight prototype thruster designed and fabricated by a team from Glenn and the Aerojet Corporation (Redmond, WA) and a laboratory-model thruster designed and fabricated in-house. The flight prototype thruster was designed to enable operational lifetimes of greater than 7500 hr at specific impulses up to 2800 sec at a maximum power of 3.5 kW. The laboratory-model thruster was designed to provide an operational lifetime of greater than 15,000 hr at the same operating conditions as the flight prototype thruster. The twofold improvement in projected lifetime was achieved through the implementation of a breakthrough mechanical design innovation. Experimental validation of this innovation is planned for 2007.

*15,000-hr laboratory-model high-voltage Hall accelerator.*

**Glenn contacts:**
Dr. David H. Manzella, 216–977–7432, David.H.Manzella@nasa.gov

Dr. Hani Kamhawi, 216–977–7435, Hani.Kamhawi-1@nasa.gov

**Author:**
Dr. David H. Manzella

**Headquarters program office:**
In-Space Propulsion, Science Mission Directorate

**Programs/projects:**
Deep space robotic science exploration missions (Discovery, New Frontiers)

## Next-Generation Ion Propulsion System Development Program Achieved Major Goals: Prototype and Engineering Model Thruster Tested

The NASA Glenn Research Center is responsible for the development of NASA's Evolutionary Xenon Thruster (NEXT) ion propulsion system. The objective of the NEXT program is to advance next-generation ion propulsion technology to NASA Technology Readiness Level (TRL) 5, with significant progress towards TRL 6. This propulsion system design was selected to provide future NASA science missions with the greatest value in mission performance benefit at a low total development cost. Technology validation and mission analysis results earlier in this development program indicated that NEXT technologies could provide the expected benefits and that further development was warranted.

The NEXT ion propulsion system program accomplished a wide range of successful achievements in 2006. NASA's contractor for the thruster, Aerojet, delivered the first prototype model thruster (PM1) to Glenn in January. Performance acceptance testing demonstrated that PM1 meets performance requirements.

Thermal development testing of PM1 was conducted at the Jet Propulsion Laboratory (JPL), providing data critical to completion of the thruster thermal model. Qualification-level environmental testing—vibration testing of the thruster/gimbal assembly and thermal/vacuum testing of the thruster—is underway and planned to be completed by the end of the year.

As of September, a long-duration test of the NEXT Engineering Model-3 (EM–3) thruster had achieved over 6000 hr of operation at the full 7-kW power level—processing over 125 kg of

xenon propellant and demonstrating over $5x10^6$ N-sec of total impulse. All wear-related mechanisms remain within pretest projections. NASA's contractor for the power processor unit, L3-Com, completed the NEXT EM Power Processing Unit, with functional testing on a NEXT thruster planned prior to 2007. JPL performed vibration testing of the JPL/Swales Aerospace-produced NEXT gimbal with a thruster mass model, validating the structural design. In addition, a multithruster test was completed at the end of 2005, with an array of three active and one inactive NEXT EM thrusters, to address system and spacecraft integration questions. Analyses of the results indicate very little functional, operational, performance, and thermal interactions among the thrusters, providing confidence in modeling multithruster systems for future users. In addition, the test demonstrated multiple thruster operations off a single neutralizer, providing significant flexibility in system design and operation.

*NEXT multithruster test operations, with illuminated diagnostics probes.*

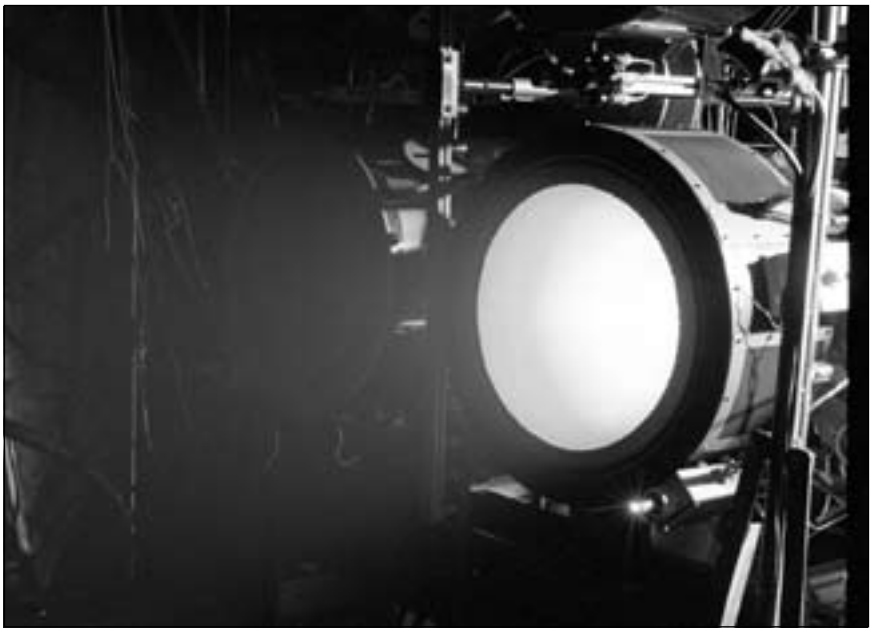

*NEXT PM1 thruster successfully completing performance acceptance test.*

**Find out more about Glenn's electric propulsion and ion thruster research:**
http://www.grc.nasa.gov/WWW/ep/

http://www.grc.nasa.gov/WWW/ion/

**Glenn contacts:**
Michael J. Patterson, 216–977–7481, Michael.J.Patterson@nasa.gov

George C. Soulas, 216–977–7419, George.C.Soulas@nasa.gov

**Authors:**
Michael J. Patterson and George C. Soulas

**Headquarters program office:**
Science Mission Directorate

**Programs/projects:**
NASA's Evolutionary Xenon Thruster

**Special recognition:**
2001 Turning Goals Into Reality Award, 2001 R&D 100 Award, NASA Invention of the Year, 2002 Hollow Cathode Assembly Award

# High-Temperature Titanium-Water Heat Pipes Built and Tested

Power-conversion systems for space power use a thermodynamic cycle to convert thermal energy from a heat source to electrical power. Radiators containing heat pipes are used to reject the waste heat from the thermodynamic cycle into space. The heat pipes serve two purposes. First, they transport and spread heat from the power-conversion system coolant loop into the radiator's large radiating surface. Second, they improve system reliability by decreasing the effect of micrometeoroid strikes on radiator performance in comparison to radiators using a fluid loop throughout the panel. The following photograph shows an example of such a panel. This small subscale panel was produced as a demonstration unit for NASA's Prometheus program and is currently undergoing thermal performance tests at the NASA Glenn Research Center. Full-size panels could be many square meters in size and utilize hundreds of heat pipes, depending on the size of the power-conversion system.

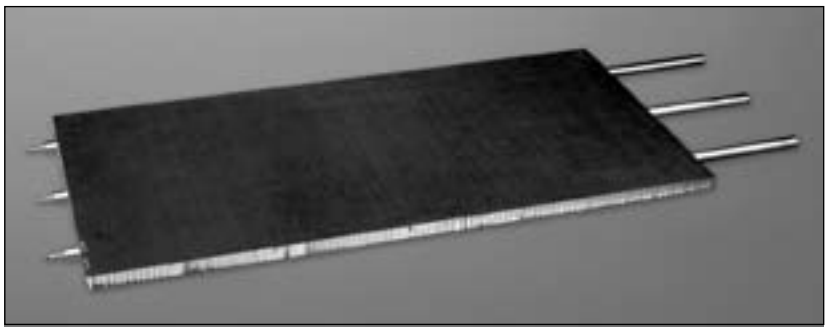

*Radiator demonstration unit panel.*

Although heat pipes using a copper envelope and water for the working fluid are commonly used for cooling low-temperature consumer electronics, large space-power-conversion systems require heat pipes capable of operating at much higher temperatures, between 350 and 500 K, for example. There had been little development of heat pipes in this temperature range. To determine the manufacturing capability and to gather operational data for heat pipes in this temperature range (often referred to as "intermediate temperature heat pipes"), Glenn tasked three heat pipe vendors to design, build, and deliver three heat pipes each of a design prototypic for a space-power-conversion system. Each vendor used heat pipe wicks of their own design. The heat pipes delivered to NASA use water as their working fluid and are constructed of commercially pure CP2 titanium tube, 1.27 cm in diameter by approximately 120 cm long.

The nine heat pipes are presently undergoing performance and life testing in Glenn's heat pipe laboratory as shown in the top right photograph. Power is supplied to the heat pipe through an electrically heated aluminum block clamped to the heat pipe's evaporator section. Heat is removed from the heat pipe condenser section through a gas gap calorimeter cooled by a commercial chiller. Heat pipe performance is measured via thermocouples attached along its length as well as heater and calorimeter instrumentation. Data logging and experiment control is accomplished using a computer running LabVIEW software (National Instruments Corporation).

*Glenn's heat pipe laboratory.*

The tests will provide performance data for use in radiator and power-conversion system analytic models, will verify predicted performance capability at temperatures from 350 to 500 K, and will use life tests to assess the ability of the heat pipes to perform reliably in a multiyear mission without significant performance degradation. Tests to date indicate that, depending upon the wick configuration, the heat pipes transport between 250 and 500 W while operating at 500 K.

**Find out more about the research of Glenn's Thermal Energy Conversion Branch:**
http://www.grc.nasa.gov/WWW/tmsb/

**Glenn contacts:**
Duane E. Beach, 216–433–6285, Duane.E.Beach@nasa.gov

Lee S. Mason, 216–977–7106, Lee.S.Mason@nasa.gov

**Author:**
Duane E. Beach

**Headquarters program office:**
Exploration Systems Mission Directorate

**Programs/projects:**
Prometheus/Fission Surface Power

# High-Power Alternator Testbed Results Reported

This year, the operating conditions of the Alternator Test Unit (ATU) were simulated, and its performance and interaction with various Lunar Surface Power System (LSPS) components were evaluated in the LSPS located at the NASA Glenn Research Center. Test results successfully demonstrated expected rectified user-load power quality during steady-state and transient conditions. They further demonstrated the ability of a high-power alternator control scheme based on parasitic loading of the alternator output to successfully regulate output bus voltage and alternator shaft speed. Information gained from this work could be used in the development and validation of analytical models used for performance prediction.

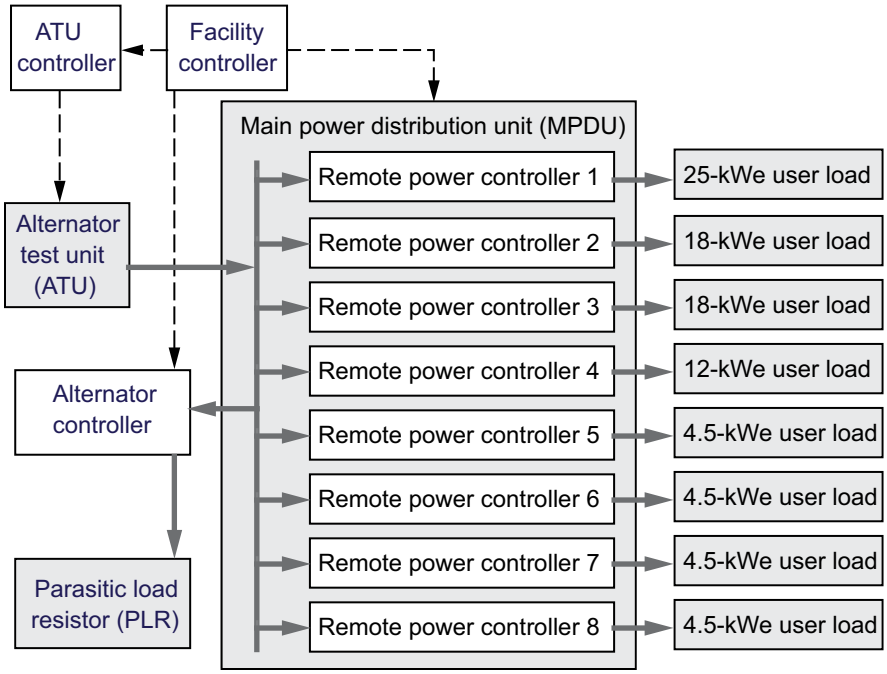


*Overall schematic of the Lunar Power System Facility (LPSF).*

*View of the ATU as installed in the LPSF at Glenn.*

The two primary objectives of the LSPS were to obtain test data to influence the power-conversion design and to assist in developing primary-power-quality specifications for an actual lunar fission surface power system. The main elements of the LSPS are a 50-kWe ATU, an alternator controller using a parasitic load, a main power distribution unit, and eight user loads. These elements are made of breadboard/brassboard components using readily available off-the-shelf hardware.

The ATU is the power supply for the LSPS. It is representative of the style of high-speed permanent magnet alternator that would be used on a Brayton power-conversion unit system. A variable-speed two-pole samarium cobalt permanent-magnet brushless motor drives the alternator in place of a Brayton cycle power system. The alternator is a six-pole permanent magnet alternator utilizing a Halbach array of samarium cobalt magnets. The ATU was operated at 35,000 rpm to a maximum of 50-kW three-phase power at 400-V rms line-to-line. A pressurized oil loop was used to lubricate and cool the individual shaft ball bearings and to cool the motor and alternator.

The alternator controller and parasitic load are designed to maintain a constant bus voltage and ATU shaft speed regardless of user loading. They do this by applying a parasitic load to the alternator output to maintain total load at the desired output voltage and speed. The alternator controller consists of two main circuits: (1) the power circuits including

the parasitic load elements and (2) the sensing circuits and feedback control loops sending the control signals to the power circuits.

All user loads received direct-current (DC) power through transformers and 12-pulse rectification of the main three-phase alternating-current (AC) bus power. The alternator operated at a power factor of 0.97. The rectified direct-current voltage measured at the loads showed around 0.5-percent ripple. Switching user loads on and off had very minimal impact on the DC power quality at other user loads, the AC bus voltage, and alternator shaft speed.

**Find out more about this research:**
**Glenn's Thermal Energy Conversion Branch:**
http://www.grc.nasa.gov/WWW/tmsb/

**Glenn's Advanced Electrical Systems Branch:**
http://www.grc.nasa.gov/WWW/5000/pep/electricsys/

**Glenn contacts:**
Arthur G. Birchenough, 216–433–6331,
Arthur.G.Birchenough@nasa.gov

Lee S. Mason, 216–977–7106,
Lee.S.Mason@nasa.gov

**Analex Corporation contact:**
David S. Hervol, 216–433–9624,
David.S.Hervol@nasa.gov

**Authors:**
Arthur G. Birchenough and David S. Hervol

**Headquarters program office:**
Exploration Systems Mission Directorate

**Programs/projects:**
Prometheus Power and Propulsion Program, Fission Surface Power

## Closed Brayton Power System Prototype Developed for Future Space Nuclear Power Applications

NASA is evaluating various power-conversion technologies for future space nuclear power system applications. One potential option is the closed Brayton cycle (CBC). CBC-based power conversion uses an inert gas working fluid (instead of air) and recirculates the fluid in a Brayton conversion loop. The Brayton loop consists of a heat source heat exchanger, turboalternator-compressor, recuperator, and gas cooler as shown in the top figure on the next page. The turbine and compressor are mounted on a single shaft with gas foil bearings. The heat source can be solar, fission, or radioisotope; however, this activity is focused on space fission power systems. The recuperator is a gas-to-gas heat exchanger that uses turbine exhaust to preheat the working fluid before it reenters the heat source. The gas cooler is a gas-to-liquid heat exchanger that transfers the Brayton waste heat to a radiator where it is rejected to space. The alternator provides three-phase alternating-current electrical power that can be modified as necessary via a power management and distribution subsystem.

A single heat source could serve multiple Brayton loops, precluding the possibility of single-point failures in the power-conversion subsystem. In the event that one of the Brayton units is shut down, the remaining units could continue to produce power. If the Brayton units share a common fluid-containment loop, there will be various interactions among the units that affect system operation and performance. Some of these interactions had been evaluated analytically. However, there had been no previous means to experimentally evaluate the operation of a multi-Brayton system with a common gas-containment loop.

In April 2006, the NASA Glenn Research Center awarded a contract to Barber Nichols (Arvada, CO) for the design, fabrication, and delivery of a dual-Brayton-unit power system with a common gas fluid loop coupled to an electrical resistance heater as shown in the bottom figure on the next page. The system is designed to produce approximately 30 kW with nitrogen working fluid at a turbine inlet temperature of 1000 K, a compressor inlet temperature of 315 K, and a compressor inlet pressure of 110 kPa. Waste heat is removed with a pumped-water

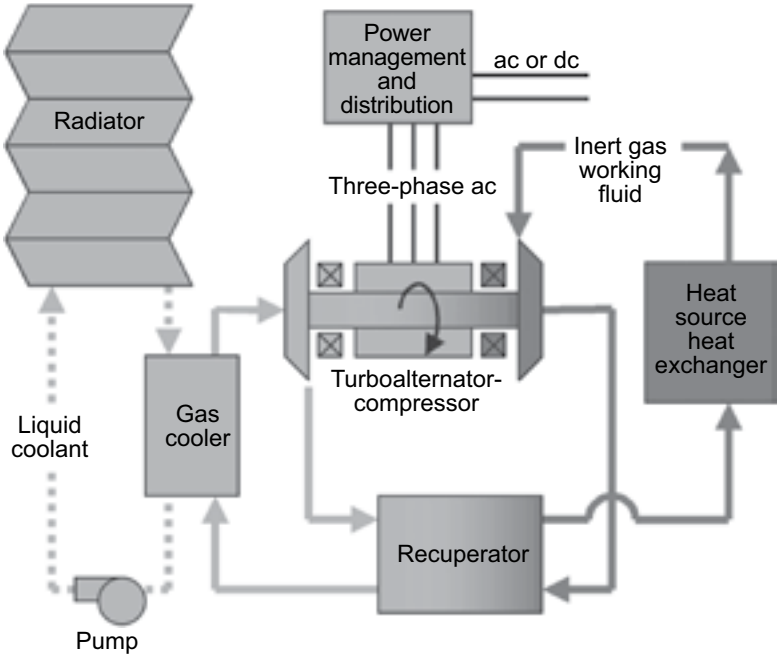


*Closed Brayton cycle.*

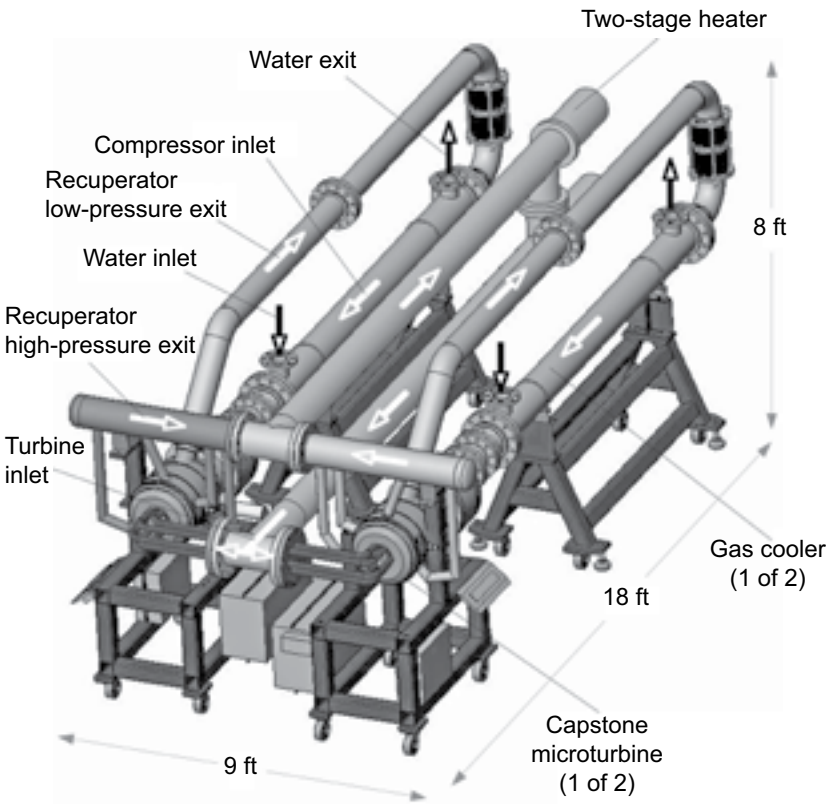


*Dual Brayton power system.*

cooling system. The Brayton system is designed for full-power operation with both turboalternator-compressor units at design speed or for partial power operation with either unit at operating speed and the remaining unit in standby. The overall system utilizes existing commercial components where available in order to reduce cost and minimize development schedule.

The system will be used as a laboratory testbed at Glenn to evaluate the performance and operational characteristics of closed Brayton power systems for future space power applications. The technical objectives include the development of operational control strategies; the investigation of design, off-design, and transient performance; and the validation of Government computer models.

As of February 2007, the system was in the final stages of assembly at Barber Nichols. All of the components had been acquired or fabricated. Initial acceptance testing is planned in late March prior to NASA delivery in April. In parallel with the contract, NASA has developed a detailed transient system model that will be used for pretest predictions. As a result of the testing, the analytical code will be experimentally validated to provide a more accurate and reliable model for future space Brayton design studies.

**Find out more about the research of Glenn's Thermal Energy Conversion Branch:**
http://www.grc.nasa.gov/WWW/tmsb/

**Glenn contacts:**
Lee S. Mason, 216–977–7106, Lee.S.Mason@nasa.gov

Harold F. Weaver, 216–433–8869, Harold.F.Weaver@nasa.gov

**Author:**
Lee S. Mason

**Headquarters program office:**
Exploration Systems Mission Directorate

**Programs/projects:**
Prometheus, Fission Surface Power

# Stirling Power Convertors Continued Extended Operation

The NASA Glenn Research Center has been supporting development of a Stirling Radioisotope Generator (SRG) by the Department of Energy (DOE), with Lockheed Martin Civil Space Systems (Valley Forge, PA) as the system integrator under contract to the DOE. The generator will utilize free-piston Stirling power-conversion technology to produce electrical power from a plutonium-238 heat source and will be capable of operation in deep space or in gaseous atmospheres such as on Mars. The first generator version was designed to produce 110 W from two Infinia Corp. convertors and was titled SRG110. The project has been redirected to increase efficiency and specific power by using Advanced Stirling Convertors (ASCs) from Sunpower, Inc. After this redirection, the generator title was changed to Advanced Stirling Radioisotope Generator (ASRG). Both Stirling power convertor designs make use of noncontacting, moving parts to eliminate wear mechanisms and enable long life.

Glenn has been supporting Lockheed Martin and the ASRG project by providing key data in the areas of performance enhancement and risk mitigation. Glenn tasks include extended-duration convertor testing, heater head life assessment, structural dynamics testing and analysis, organics assessment, and reliability analysis.

*Test setup of TDCs #15 and #16.*

The purpose of extended testing is to provide independent validation and verification of the conversion technology as well as to demonstrate life and reliability. To accomplish this, several convertors have been put on extended, around-the-clock operation. The Stirling research lab at Glenn comprises six test stands for in-air operation and one for thermal vacuum operation. Each test stand can maintain a pair of convertors in unattended mode. Five of the stands can sample the convertor working fluid via a residual gas analyzer and ultra-high-vacuum system. The gas analysis capability allows for the detection of contaminants entering the convertor working fluid, either through pressure vessel flange o-rings or by outgassing of internal components. Three pairs of flight-prototype convertors, known as Technology Demonstration Convertors (TDCs), have accumulated over 92,000 hr total of operation with no failures. These units, manufactured by Infinia Corp. are prototypes of the units intended for integration into the SRG110. TDCs #13 and #14 have accumulated 24,000 hr of operation, and TDCs #15 and #16 have accumulated 10,000 hr. TDCs #5 and #6 were set up in a thermal vacuum environment to simulate operation in deep space and have accumulated over 10,000 hr.

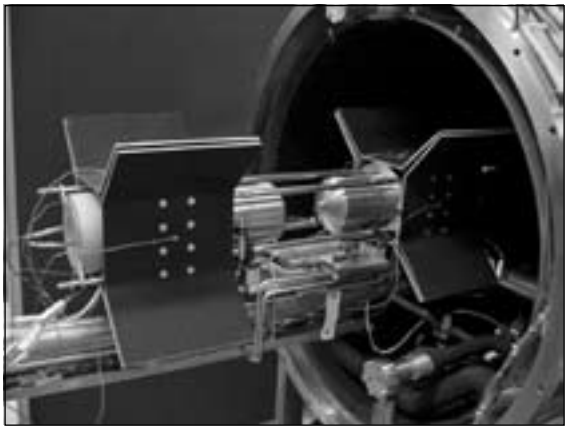

*TDCs #5 and #6 configured for thermal vacuum extended operation.*

Preparations have been made to begin extended operation of six Sunpower, Inc., ASC convertors in air and thermal vacuum environments. The ASC testing will support Lockheed Martin's development of the ASRG. This effort is supported by NASA's Science Mission Directorate, Radioisotope Power Systems.

TDC OPERATION SUMMARY

| TDC pair | Extended operation time, hr |
|---|---|
| #13 and #14 | 24,000 |
| #15 and #16 | 10,000 |
| #5 and #6 | 10,016 |

**Find out more about the research of Glenn's Thermal Energy Conversion Branch:**

http://www.grc.nasa.gov/WWW/tmsb/

**Glenn contact:**
Jeffrey G. Schreiber, 216–433–6144, Jeffrey.G.Schreiber@nasa.gov

**Author:**
Salvatore M. Oriti

**Headquarters program office:**
Science Mission Directorate

**Programs/projects:**
Radioisotope Power Systems, Advanced Stirling Radioisotope Generator

# Control Architecture Developed for Dual-Opposed Stirling Convertors With Active Power Factor Correction Controllers

An Advanced Stirling Radioisotope Generator using a pair of free-piston Stirling convertors is being developed to convert heat from a radioisotope source into electric power as a potential electric power source for NASA science or exploration missions. The Stirling convertor System Dynamic Model (SDM), developed at the NASA Glenn Research Center, provided a model that includes the Stirling cycle thermodynamics, heat flow, gas dynamics, mechanical dynamics, mounting dynamics, linear alternator, and controller. SDM has been used to answer many engineering questions during development of the power system.

The specification for the Stirling convertor power system being developed for NASA by the U.S. Department of Energy requires a pair of convertors to operate in synchronization at a power factor near unity. SDM simulations were performed to examine 10 candidate architectures and to determine which of the 10 could meet the operating requirements. All the configurations involved convertors in the dual-opposed configuration, controlled with active power factor correction (APFC) controller technology. The differences among the candidates included the number of controllers required (one or two), the electrical connections between the convertors (series, parallel, or isolated), and the thermodynamic configuration (isolated or combined working spaces). For the configurations involving isolated electrical output, different methods for synchronizing the two convertors were developed. Of the 10 configurations studied, stable operating modes were found for four. Three of the four had a common expansion space. One stable configuration was found for the dual-opposed convertors with separate working spaces. That connection architecture is being pursued in Glenn's controller development.

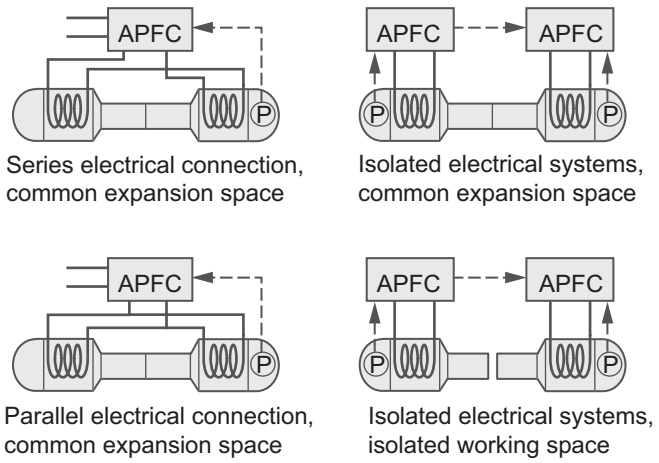


*Possible architectures for a dual-opposed Stirling convertor power system using APFC control technology.*

SDM was used to evaluate two methods of implementing this architecture. One method uses a frequency-control loop to synchronize the two isolated convertors. The other uses a phase control to accomplish the same result. The phase-control method is being implemented in Glenn's advanced controller. In August 2006, the phase-control loop implementation was used in the first successful parallel operation of electrically isolated, free-piston Stirling convertors. Two of Glenn's advanced controllers provided power factor correction of the convertors through the use of power electronics. The phase control kept the convertors synchronized, allowing the dynamic forces to be cancelled. SDM was an important tool in developing the controller systems being implemented in the advanced Stirling Radioisotope Generator and operating in Glenn's Stirling convertor test cells today. The Glenn SDM uses the Ansoft Simplorer 7.0 platform (Ansoft Corp.).

**Find out more about the research of Glenn's Thermal Energy Conversion Branch:**
http://www.grc.nasa.gov/WWW/tmsb/

**Sest, Inc., contacts:**
Dr. Edward J. Lewandowski,
216–433–5525,
Edward.J.Lewandowski@nasa.gov

Timothy F. Regan, 216–433–2086,
Timothy.F.Regan@nasa.gov

**Glenn contact:**
Jeffrey G. Schreiber, 216–433–6144,
Jeffrey.G.Schreiber@nasa.gov

**Authors:**
Dr. Edward J. Lewandowski and
Timothy F. Regan

**Headquarters program office:**
Science Mission Directorate

**Programs/projects:**
Radioisotope Power Systems, Advanced Stirling Radioisotope Generator

# Active Power Factor Correction Controller Achieved High-Power Operation of Dual Stirling Convertors

The free-piston Stirling power convertor is being considered as an advanced power-conversion technology for future deep-space missions requiring long-life radioisotope power systems. The NASA Glenn Research Center plays a critical role in developing advanced technologies to significantly improve the Stirling convertor. One of the key areas identified for technology development is the controller. The Glenn controller effort is focused on developing an active power factor correction (APFC) controller capable of dual-convertor operation. The APFC technology uses power electronics, which eliminates the tuning capacitors required for other control approaches, such as Zener-diode controllers. These capacitors add significant size, mass, and parts count to the system. Eliminating them will minimize volume and mass, which are critical parameters for space applications.

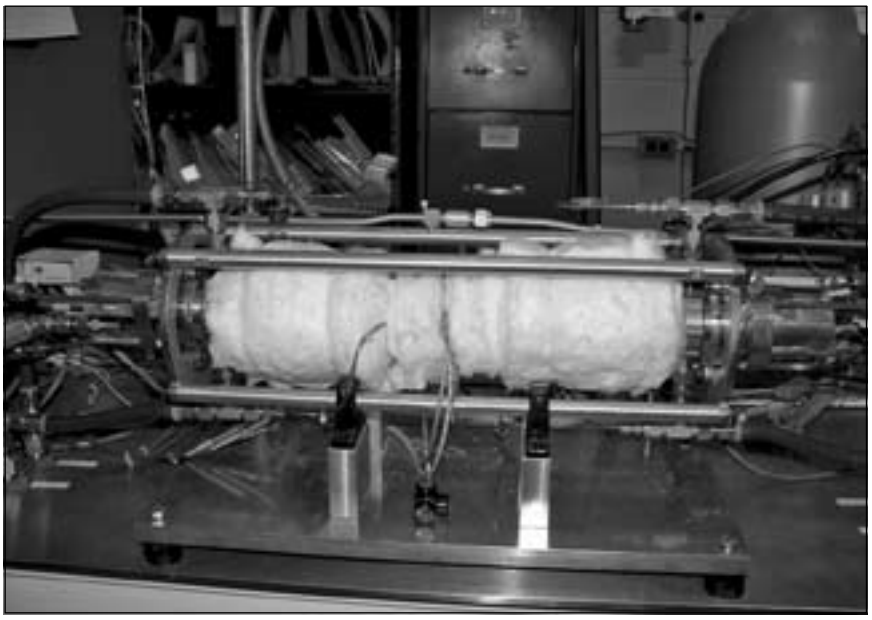

*Dual-opposed SBIR EE–35 Stirling convertors.*

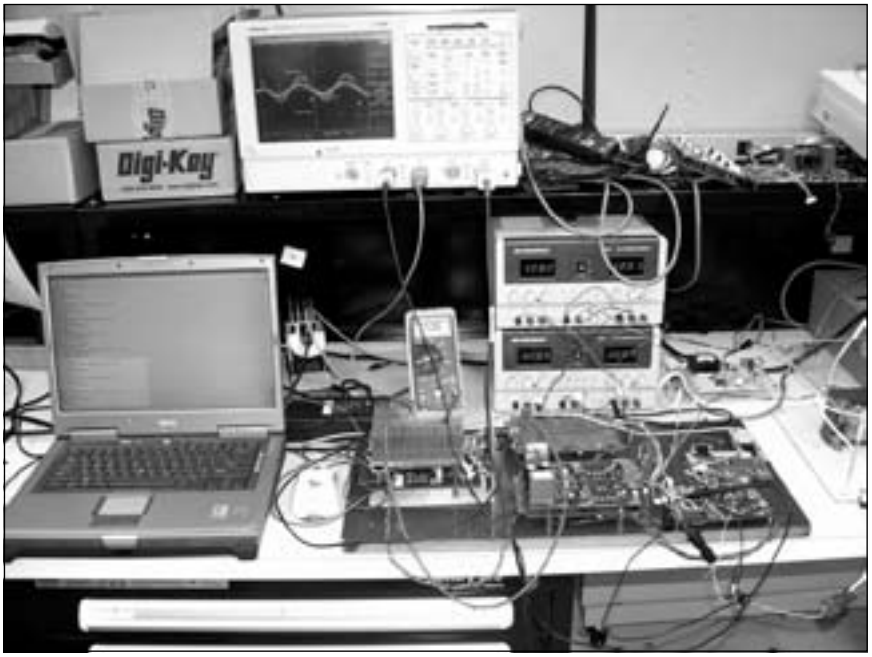


*Third-generation APFC controller prototype hardware.*

Glenn's in-house APFC controller development staff, in conjunction with engineers from Artic Slope Research Corporation (ASRC) and ZIN Technologies, began with a proof-of-concept unit designed to control a single Technology Demonstration Convertor from Infinia Corp. (Kennewick, WA). After successful operation of the APFC controller, modifications were made to include features such as startup capability and overload protection. The controller hardware and software were later tailored to operate EE–35 convertors and Advanced Stirling Convertors (ASCs) from Sunpower, Inc. (Athens, OH). Present-day development is focused on a third-generation prototype unit to validate the APFC controller as a viable control technology. The top photograph shows two EE–35 convertors in the dual-opposed configuration used for testing the APFC controller. The bottom photograph shows the third-generation prototype APFC control system.

High-power, synchronized operation of dual EE–35 convertors was achieved this year, along with successful startup of the convertors with the third-generation prototype module. These are significant steps in proving the APFC technology. Work will continue on the development and testing of a planned thermal vacuum unit, to be tested with ASCs in a thermal vacuum chamber.

**Find out more about the research of Glenn's Thermal Energy Conversion Branch:**
http://www.grc.nasa.gov/WWW/tmsb/

**Glenn contacts:**
Linda M. Taylor, 216–433–8478, Linda.M.Taylor@nasa.gov

Jeffrey G. Schreiber, 216–433–6144, Jeffrey.G.Schreiber@nasa.gov

**ASRC Corporation contact:**
Nuha S. Nawash, 216–433–3146, Nuha.S.Nawash@nasa.gov

**ZIN Technologies, Inc., contact:**
Scott S. Gerber, 216–433–5226, Scott.S.Gerber@nasa.gov

**Authors:**
Linda M. Taylor, Nuha S. Nawash, and Scott S. Gerber

**Headquarters program office:**
Science Mission Directorate

**Programs/projects:**
Radioisotope Power Systems, Advanced Stirling Radioisotope Generator

# Change in Solar Array Orientation Successfully Reduced *International Space Station* Propellant Usage

Although the *International Space Station* (ISS) flies in "space," it does not orbit completely outside the atmosphere. Even at 350-km altitude, the ISS passes through the tenuous upper reaches of the atmosphere, and this atmosphere in fact causes a minute amount of drag on the space station. In order to prevent the orbit from decaying, rocket engines on the ISS are used to "reboost" the station, maintaining its orbit. The solar arrays, which provide power for the ISS, are the largest elements causing this atmospheric drag on the ISS.

In 1991, Geoffrey A. Landis and Cheng-Yi Lu at the NASA Glenn Research Center (known then as the NASA Lewis Research Center) proposed a new method to orient the solar arrays on the ISS to reduce the drag they produce and, consequently, decrease the amount of propellant required to maintain the orbit. The concept was simple: orient the solar array to track the Sun while the ISS is in the illuminated part of the orbit (about 55 min per orbit), and then adjust the orientation so that the array is edge-on to the direction of flight ("feathered") during the eclipse period (about 36 min per orbit). The researchers calculated that this would reduce the propellant required to compensate for the drag of the solar arrays by 18.5 percent. They also suggested an operating mode, "beta-controlled," to decrease the drag area yet further: tracking the Sun in one axis, while flying with the solar arrays edge-on to the direction of flight, in effect "slicing" through the atmosphere like a knife. This mode of operation reduced the drag further, at the price of some decrease in power. Although the results were presented to the ISS power system group and published in the AIAA Journal of Propulsion and Power (ref. 1), the proposed fuel-saving orientation of the solar arrays was not implemented at the time because frequent shuttle flights to the ISS were anticipated to routinely supply drag makeup propellant, and the propellant savings were not expected to be worth the added complexity of operations.

*ISS in orbit in its configuration after the 2003 Columbia disaster and before the space shuttle return-to-flight missions of 2005 and 2006. The solar arrays can be seen as the largest drag area on the ISS.*

This situation changed after the *Space Shuttle Columbia* disaster. Routine access to the ISS was interrupted until the space shuttle return-to-flight

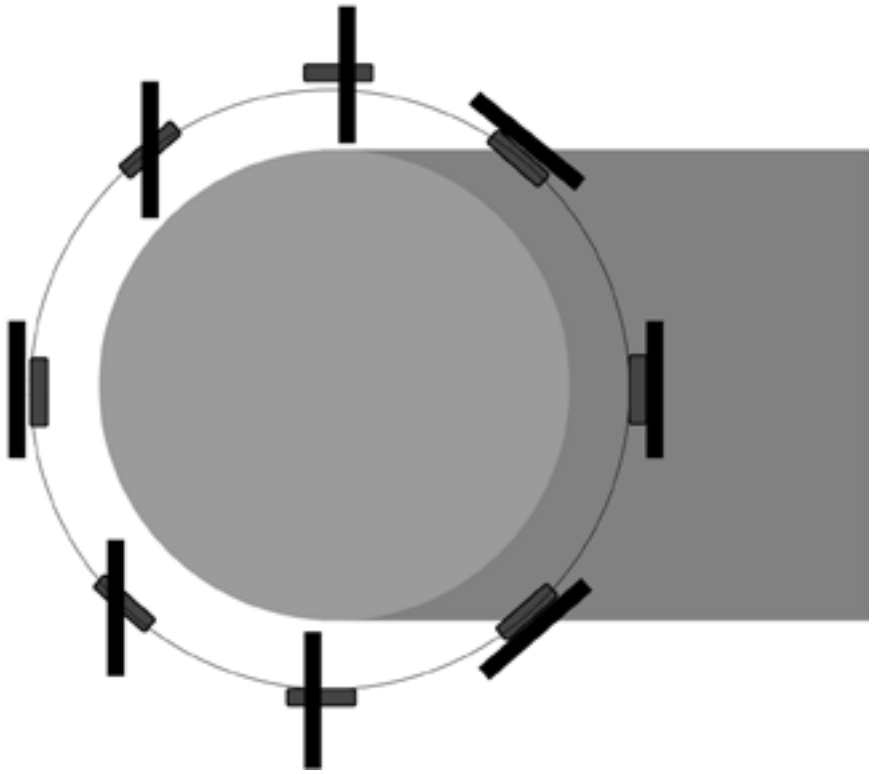

*The proposed orientation would face the solar arrays toward the Sun during the illuminated portion of the orbit and would turn them edge-on during the night (or "eclipse") portion of orbit.*

missions in late 2005 and in 2006, and the propellant to maintain circular orbit suddenly became a critical factor. Consequently, the new orientation concept of the arrays was reconsidered. Renamed the "eclipse drag reduction configuration," and tagged the "night-glider mode," the new mode of operation was implemented following the interruption of shuttle service to the ISS (ref. 2). This mode of operation has now been demonstrated, along with the "Sun-slicer" mode (similar to the beta-control mode proposed earlier). The new orientation method has been successfully demonstrated in over 3 years of operation and is now being used routinely. The results have been exceptional, and the lower fuel requirement has been one of the key factors in the continued operation of the ISS without frequent space shuttle support. According to Fortenberry et al., "Use of these techniques can reduce the atmospheric drag on the ISS as much as 25 percent, resulting in up to 1000 kilograms per year savings of propellant and allowing this unused *Progress* vehicle up-mass to be reprioritized to carry research payloads" (ref. 3).

**References**


1. Landis, Geoffrey A.; and Lu, Cheng-Yi: Solar Array Orientations for a Space Station in Low Earth Orbit. J. Propul. P., vol. 7, no. 1, 1991, pp. 123–125.
2. NASA Space Operation Mission Directorate: Station Without Shuttle. NASA Explores—Express Lessons and Online Resources, Nov. 18, 2004. http://www.nasaexplores.com/show2_articlea.php?id=04-070
3. Fortenberry, L., et al.: Continuing the Journey on the International Space Station. Int. Astronaut. Cong. Proc., vol. 3, 2003, pp. 669–705.



**Glenn contact:**
Dr. Geoffrey A. Landis, 216–433–2238, Geoffrey.A.Landis@nasa.gov

**Author:**
Dr. Geoffrey A. Landis.


**Headquarters program office:**
International Space Station

**Programs/projects:**
International Space Station

# Dust on Mars Solar Arrays Examined With Microscopic Imager

The Martian atmosphere contains a significant amount of suspended dust. Dust is known to settle out of the atmosphere onto exposed surfaces, causing surfaces to slowly turn a dusty yellow-orange. More disturbingly, as the dust settles, it coats the surface of solar arrays and reduces the amount of power produced on Mars.

Up until now, the obscuration of the solar arrays by dust has been seen by the change in color of the arrays, and the effect has been measured from the current output of the arrays, but the dust and sand deposited on the arrays have not been examined directly. In this work, we used the Microscopic Imager (MI) to examine the surface of the solar array on the Mars Exploration Rovers (MERs) *Spirit* and *Opportunity*.

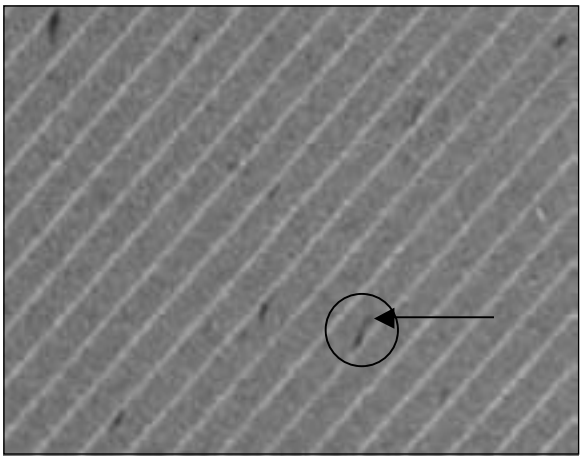

*Enlarged portion of a frame from the microscopic imager view of the dust-covered solar array on Spirit on sol 350, with an arrow showing one of the dark marks on the panel. Light-colored diagonal lines are the metallization pattern on the surface of the solar cell.*

The solar cells on the MERs are mounted on panels approximately 0.8 m above the ground. The MI is an instrument on the extendable Instrument Deployment Device on the rover, mounted below the deck and the solar arrays. This was not designed to inspect the solar arrays, but ground testing on the engineering model showed that it had sufficient freedom of motion to reach portions of three solar cells on the front edge of the rover deck. During the extended mission, images of these cells at MI resolution were made on both the *Spirit* and *Opportunity* solar arrays.

The preceding photograph shows an enlargement of a portion of one of the frames, taken after 350 Martian days (sols) on the surface of Mars. Dust-related features are evident. Before launch, the solar arrays were specular glass surfaces, covering a solar cell featuring parallel lines of metallization spaced at 0.625 mm on a dark cell surface. (These metallization lines are useful to show scale on the images.) After 11 months of exposure, the surface reflection is markedly diffuse in both the Panoramic camera (Pancam) and MI views. No clearly evident structure can be seen at MI resolution, with no visible aggregation or “fairy castle” structure. The dust coverage appears to be roughly uniform across the cells.

The size of particles suspended in the atmosphere at the MER sites has been estimated from optical scattering measurements to be approximately 1.5 μm. Since the MI has a resolution of 31 μm/pixel, it was not expected that any features would be visible at the resolution of the MI. Surprisingly, however, a distinct granularity is visible in the MI images. The top photograph on the next page shows an enlargement of one frame, with the contrast greatly enhanced to show detail. The fact that such details are visible is strong evidence that the deposits on the surface are significantly larger than the particles measured in the atmosphere by optical scattering. This could be either distinct larger particles, or conglomerate particles formed by agglomeration of micrometer-scale particles.

An additional feature of interest is the presence of dark streak marks on the surface, such as the one indicated with a circle in the photograph to the left. These marks vary in width from a few pixels for the smallest to roughly 0.25 mm for the larger marks, with lengths from 0.2 to 0.9 mm. We interpret these as streak marks in the dust coating, made by the impact of saltating sand grains as they bounce off the dust-coated surface, removing dust to reveal the dark surface of the solar cell beneath the glass.

In addition to the surfaces of the solar cells, one frame was taken at the edge of the solar cell, with the exposed solar-cell wiring. A portion of one of these frames is shown in the bottom photograph on the next page after 350 sols on Mars. The pockets formed by the wiring have accumulated a load of sand-sized particles, evidently brought to the rover deck by wind in a process known as saltation. The largest of these particles has a radius of ~150 μm. The number of particles seen trapped in this region increased during the mission. On Mars, the particle size most easily lifted by wind has been calculated to be that of fine sand, 80 to 100 μm in radius, consistent with the sizes of the particles seen on the deck.

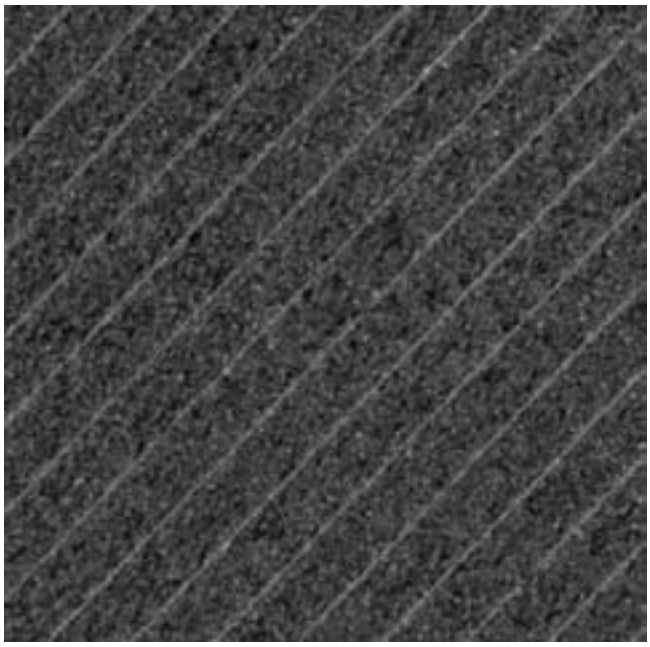

*Enlarged MI view of the Spirit solar array surface, with the contrast greatly enhanced to show features.*

The solar-scattering properties of dust that settles on solar arrays differ from those for atmospheric dust. We see evidence for a three-component particle distribution:

**(1) Atmospheric dust:** Primarily particles with a ~1- to 2-μm radius that stay suspended in the atmosphere for long periods
**(2) Settled dust:** Particles less than 10 μm in radius that are raised into the atmosphere by wind or dust-devil events but then settle out of the atmosphere
**(3) Saltating particles:** Particles with an 80- to 150-μm radius that move primarily by saltation

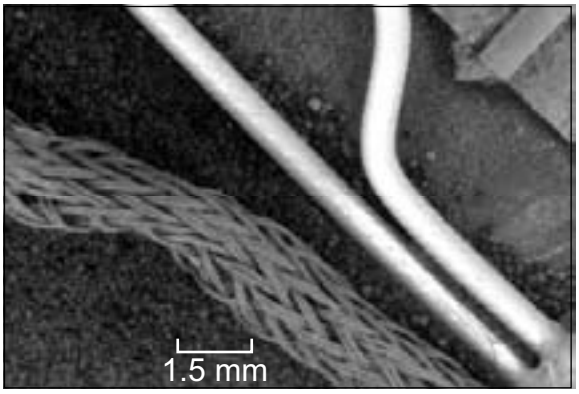


*MI image on sol 505 of the edge of one solar cell on Spirit with electrical wiring visible, showing sand grains accumulating at the edge of one panel on Spirit.*

**Bibliography**
Landis, G., et al.: Dust and Sand Deposition on the MER Solar Arrays as Viewed by the Microscopic Imager. Lunar and Planetary Science Conference XXXVII, Houston, TX, 2006.

**Glenn contact:**
Dr. Geoffrey A. Landis, 216–433–2238, Geoffrey.A.Landis@nasa.gov

**Author:**
Dr. Geoffrey A. Landis

**Headquarters program office:**
Office of Space Science

**Programs/projects:**
Mars Exploration

# Galium Arsenide on Silicon Advanced Photovoltaic Devices Flight Tested on the Exterior of the *International Space Station* as Part of the Materials International Space Station Experiment 5 (MISSE5)

Integration of III–V materials and devices on silicon substrates has demonstrated remarkable progress, due in large part to the development of low-dislocation-density (~$10^6$/cm$^2$), fully relaxed germanium (Ge) epitaxial films deposited on silicon (Si) substrates by researchers from the Massachusetts Institute of Technology (MIT). Transitioning III–V materials to Si substrates offers tremendous improvements in the size, mass, strength, and cost of high-efficiency III–V photovoltaics. Using these "virtual" Ge substrate materials, researchers from MIT, the Ohio State University (OSU), and the NASA Glenn Research Center have demonstrated the highest reported open-circuit voltage values for gallium-arsenide (GaAs) cells on Si to date. In addition, single-junction GaAs cells with efficiencies greater than 17-percent air mass zero (AM0) have been demonstrated.

This GaAs/Si technology was selected to participate in a flight experiment, Materials International Space Station 5 (MISSE5), developed by the Naval Research Laboratory and designed to test advanced photovoltaic technologies in the low-Earth-orbit (LEO) space environment. The MISSE5 payload was delivered to the International Space Station (ISS) on August 2005, and astronauts attached it to a handrail on the outer surface of the P6 truss (see the photograph). The test articles aboard MISSE5 were characterized along with their operating environment (temperature, Sun angle, etc.) each orbit, with the data telemetered to ground stations via the PCSAT2 portion of the MISSE5 spacecraft. MISSE5 was returned from the ISS to Earth in September 2006.

The flight data were analyzed to extract temperature coefficients for the device voltage and current as a function of temperature, angle of incidence, and Earth-Sun spacing, thereby allowing the flight data to be corrected back to ground measurement conditions. The analysis indicates that all test devices operated nominally and did not show any signs of degradation. Full postflight characterization is in progress. On-orbit temperature swings were lower than anticipated (~50 K) and were somewhat lower than those of the fully populated power panel (~80 K). The MISSE5 flight data confirm ground-based thermal cycling data, simulating 1 year in LEO (6000 thermal cycles of ±80 °C), which demonstrated that even though the GaAs/Si contained microcracks because of differences in thermal expansion coefficients, the device performance was stable.

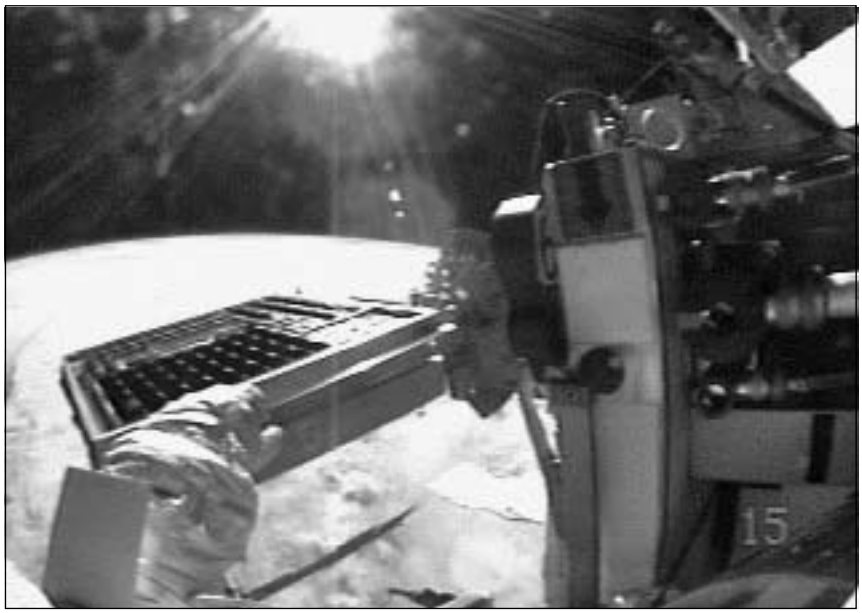


*MISSE5 shown being attached to the International Space Station (ISS).*

Recently, this development activity was extended to the demonstration of both lattice-matched (i.e., the cell-structure lattice is matched to the Ge final epilayer) and lattice-mismatched (LMM) tandem III–V devices on Si substrates. The LMM devices lack the microcracks normally found in thick GaAs epitaxial structures deposited on Si. Thermal cycle testing of these devices demonstrated that this crack-"free" characteristic is stable under normal LEO and geosynchronous-Earth-orbit thermal cycle environments. It appears that residual compressive strain resulting from the LMM structures being less than fully relaxed compensates for the tensile strain introduced by differences in thermal expansion coefficients between III–V materials and Si.

**Glenn contact:**
David M. Wilt, 216–433–6293, David.M.Wilt@nasa.gov

**Authors:**
David M. Wilt, Prof. Steven Ringel, and Prof. Eugene Fitzgerald

**Headquarters program office:**
Exploration Systems Mission Directorate

**Programs/projects:**
Constellation Systems

# Results From Scattered Atomic Oxygen Characterization Experiment Evaluated

Spacecraft materials in low Earth orbit (LEO) can be subjected to oxidative erosion from both direct and scattered atomic oxygen (AO). Scattered atomic oxygen AO is important for the assessment of the durability of polymers and metals that are not directly exposed to AO but may receive AO through secondary reflection processes, such as when apertures in the spacecraft surface allow LEO AO to enter into the interior of a spacecraft. Materials that receive such scattered AO may be compromised if their function depends on their structural, optical, or surface conductivity properties.

The Scattered Atomic Oxygen Characterization Experiment was proposed, designed, constructed, and analyzed by the NASA Glenn Research Center as part of our role as a world leader in understanding AO interactions with materials. The objective of this effort was to measure the scattered angular erosion characteristics of AO that is scattered from typical spacecraft surfaces. To make such measurements, a small AO scattering chamber was placed on the Materials International Space Station Experiment (MISSE) Passive Experiment Carrier 2 and exposed to LEO AO for almost 4 years as part of MISSE 1 and 2. The experiment (see the figure on this page) was flown in the Passive Experiment Carrier 2, tray 1, attached to the exterior of the International Space Station Quest Airlock. It consisted of a chamber with an aperture disk lid of Kapton H polyimide coated on the space-exposed surface with a thin, AO-durable, silicon dioxide ($SiO_2$) film. The aperture lid had a small hole in its center to allow AO to enter into the chamber and impact a base disk of aluminum. The AO that scattered from the aluminum base could react with the underside of the aperture lid, which was coated sporadically with microscopic sodium chloride (NaCl) particles.

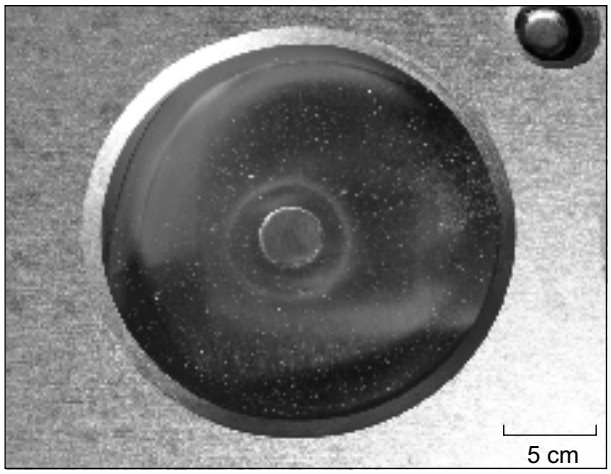


*Scattering chamber in experiment tray after retrieval.*

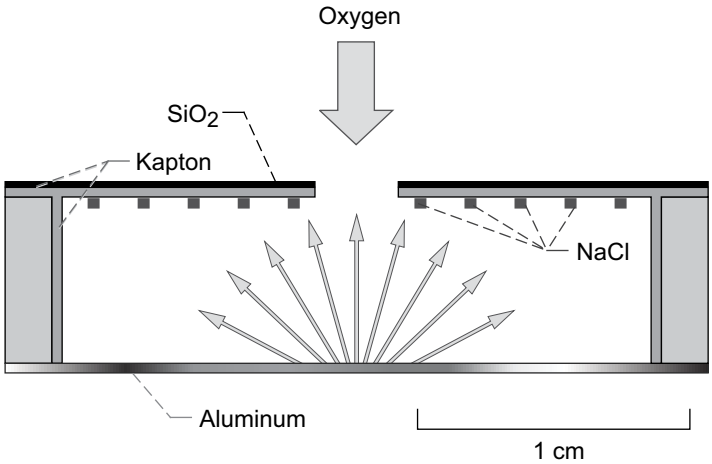


*Section view of scattering chamber.*

The erosion of the underside of the Kapton lid was sufficient to be able to use profilometry to measure the height of the buttes that remained after the salt particles were washed off. The erosion pattern indicated that a highly peaked flux of scattered AO occurred at an angle of approximately 45° from the incoming normal incidence on the aluminum base unlike that expected for simple cosine or Lambertian scattering (see the figure on the next page). Thus, very little atomic oxygen actually scattered in a specular direction as one might expect. The atomic oxygen that scattered was measured to have an effective erosion yield of $6.42\times10^{-25}$ $cm^3$/atom, which was a factor of 0.214 of that for direct impingement on Kapton H polyimide.

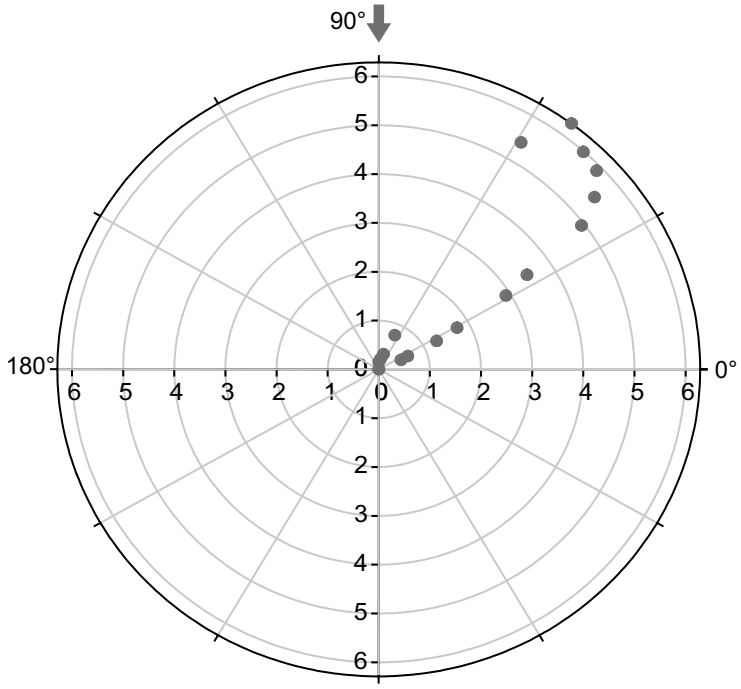


*Angular distribution of scattered atomic oxygen erosion rate on Kapton H polyimide relative to normal incident erosion rate.*

**Bibliography**
Banks, Bruce A.; de Groh, Kim K.; and Miller, Sharon K.: MISSE Scattered Atomic Oxygen Characterization Experiment. NASA/TM—2006-214355, 2006. http://gltrs.grc.nasa.gov/Citations.aspx?id=23

**Find out more about the research of Glenn's Electro-Physics Branch:**
http://www.grc.nasa.gov/WWW/epbranch/ephome.htm

**Glenn contacts:**
Bruce A. Banks, 216–433–2308, Bruce.A.Banks@nasa.gov

Kim K. de Groh, 216–433–2297, Kim.K.deGroh@nasa.gov

Sharon K. Miller, 216–433–2219, Sharon.K.Miller@nasa.gov

**Authors:**
Bruce A. Banks, Kim K. de Groh, and Sharon K. Miller

**Headquarters program office:**
Office of Safety and Mission Assurance

**Programs/projects:**
Exploration Systems, International Space Station

## Solar Effects on Tensile and Optical Properties of Hubble Space Telescope Silver-Teflon Insulation Investigated

The Hubble Space Telescope (HST) was launched on April 25, 1990, into low Earth orbit as the first mission of NASA's Great Observatories program. The HST was designed to be serviced on orbit to upgrade scientific capabilities. In December 1993, during the first servicing mission, the original power-generating solar arrays (SA–I) were replaced with a second set of arrays (SA–II). In March of 2002, after 8.25 years of space exposure, the second set of arrays were replaced with a third set during the fourth servicing mission, and the second set of arrays were brought back to Earth.

The majority of the HST is covered with thermal control materials, which passively control temperatures during orbit. These materials utilize back-surface-metallized Teflon FEP (i.e., DuPont, fluorinated ethylene propylene) as a space-facing layer because of the material's excellent optical properties (low solar absorptance and high thermal emittance). A section of the retrieved SA–II solar array drive arm (SADA) multilayer insulation (MLI) blanket was provided to the NASA Glenn Research Center so that environmental durability analyses of the top layer of silver-Teflon FEP (Ag-FEP, DuPont) could be conducted.

The MLI was wrapped completely around the SADA and, therefore, had solar- and anti-solar-facing surfaces (see the top photograph on the next page). The circular configuration of the insulation, along with the long-term

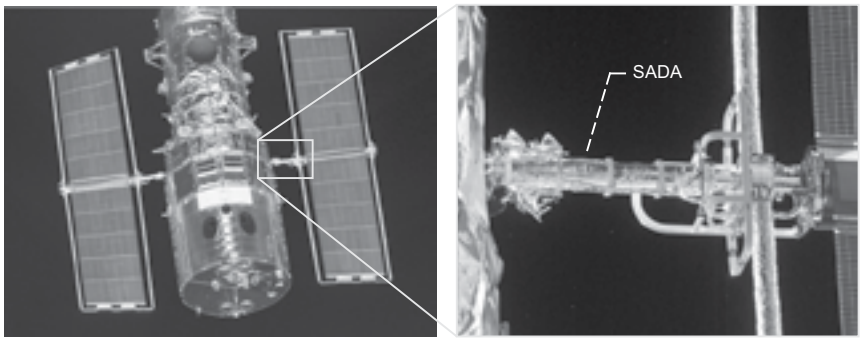


*HST photographed in December 1999 during the third servicing mission. Left: HST with SA–II. Right: Closeup of an MLI-covered SADA.*

space exposure, provided a unique opportunity to study solar radiation effects on the environmental degradation of Ag-FEP, a commonly used spacecraft thermal control material. Data obtained included tensile properties, solar absorptance, surface morphology, and chemistry.

A retrieved SA–II SADA MLI sample was provided by the European Space Agency (ESA) for this study. The following photograph shows the 36.9- by 9.1-cm sample. The sample's top layer was approximately 10 mil (0.25 mm) thick, consisting of a space-exposed 5-mil (127-μm) Teflon FEP (DuPont) layer coated on the backside with vapor-deposited-Ag and INCONEL (1500-Å-thick Ag layer and 275-Å-thick INCONEL layer). The FEP/Ag/INCONEL layer was adhered with 40-μm-thick 966 acrylic adhesive to a fiberglass cloth impregnated with polytetrafluoroethylene (PTFE). The MLI has 16 layers of double-sided aluminized-Kapton (50 μm thick) separated by Dacron (Invista, Inc.) netting and a bottom layer of PTFE-impregnated fiberglass cloth. All analyses were obtained from the top layer of insulation (FEP/Ag/INCONEL/adhesive/scrim), referred to as Ag-FEP. For this study, 0° was defined as the direct solar-facing surface (indicated as a line in the following photograph) and 180° was the anti-solar-facing surface, with 90° and 270° being solar-grazing surfaces.

The solar-facing surface of the SADA was found to be extremely embrittled and contained numerous through-the-thickness cracks. Tensile testing indicated that the solar-facing surface lost 60 percent of its mechanical strength and 90 percent of its elasticity, whereas the anti-solar-facing surface had ductility similar to that of pristine FEP. The solar absorptance $\alpha$ of both the solar-facing surface (0.155±0.032) and the anti-solar-facing surface (0.208±0.012) were found to be greater than that of pristine Ag-FEP (0.074). The figures on the next page are polar plots of elongation at failure and of solar absorptance versus solar angle.

A thermal model was developed to determine temperature versus solar angle for the insulation. Plotting elongation at failure versus temperature indicated a trend of increasing embrittlement for decreasing temperatures below –50 °C, appearing to correspond to a cold transition temperature, but this effect was not nearly as deteriorative as the solar-facing higher temperature exposures. These results indicate a very strong dependence of embrittlement on solar exposure, and temperature appears to play an important role.

Solar-facing and anti-solar-facing surfaces were microscopically textured, and locations of isolated contamination were present on the anti-solar surface, resulting in increased localized texturing. However, the overall texture was significantly more pronounced on the solar-facing surface, indicating a synergistic effect of combined solar exposure and increased heating with atomic oxygen erosion. The results indicate a very strong dependence

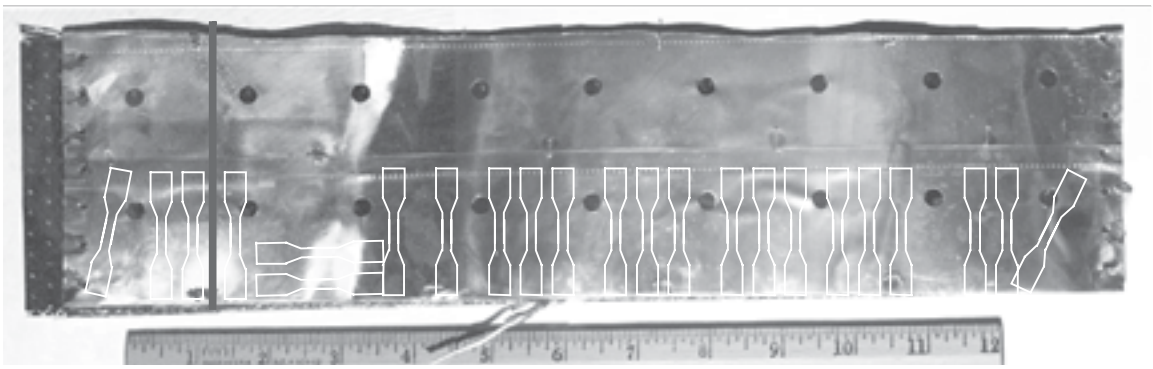

*The HST SADA MLI sample (the line indicates the solar-facing position, 0°).*

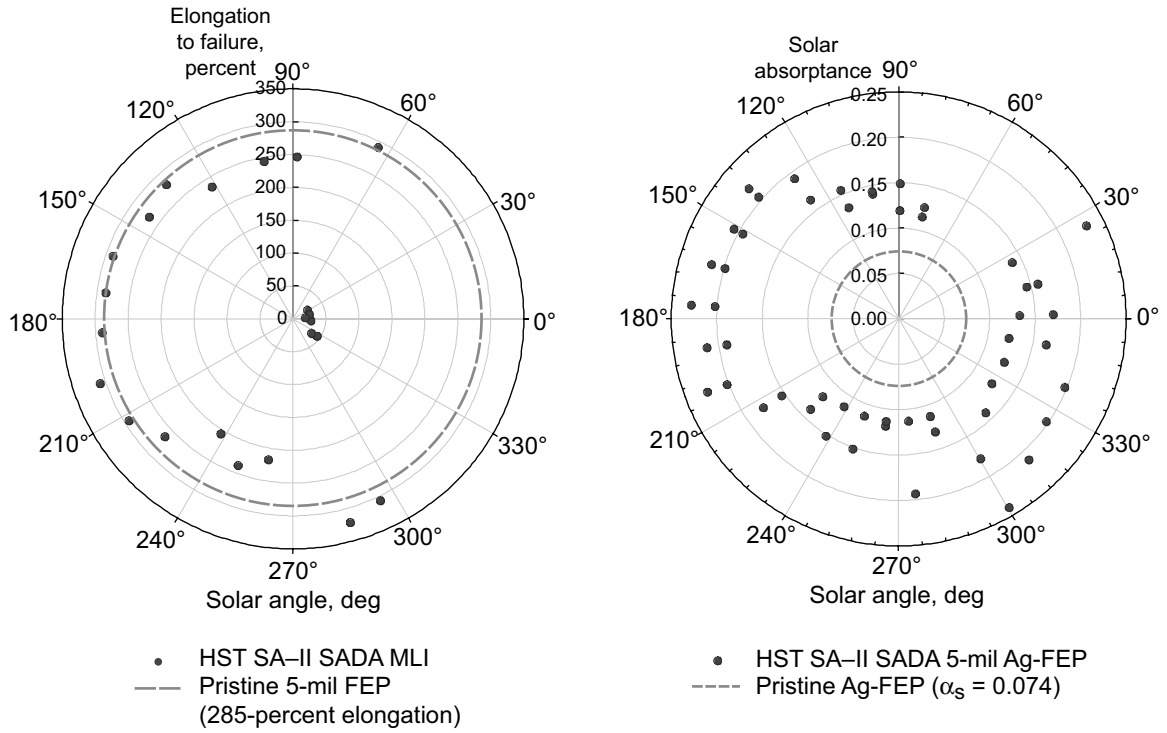


*Polar plots of the HST SADA Ag-FEP. Left: Percent elongation at failure versus solar angle. Right: Solar absorptance versus solar angle.*

of degradation, particularly embrittlement, upon solar exposure, with orbital thermal cycling having a significant effect. These results provide valuable information on space environmental degradation of Ag-FEP, particularly with respect to solar radiation and temperature effects on embrittlement.

**Find out more about the research of Glenn's Electro-Physics Branch:**
http://www.grc.nasa.gov/WWW/epbranch/ephome.htm

**Glenn contacts:**
Kim K. de Groh, 216–433–2297, Fax: 216–433–2221, Kim.K.deGroh@nasa.gov

Joyce A. Dever, 216–433–6294, Fax: 216–433–2221, Joyce.A.Dever@nasa.gov

Dr. Aaron Snyder, 419–621–3388, Fax: 419–621–3298, Aaron.Snyder-1@nasa.gov

**Authors:**
Kim K. de Groh, Joyce A. Dever,
Dr. Aaron Snyder, Sharon Kaminski,
Catherine E. McCarthy,
Allison L. Rapoport, and
Rochelle N. Rucker

**Headquarters program office:**
Science Mission Directorate

**Programs/projects:**
Hubble Space Telescope, International Space Station, Earth Observing Satellites, Crew Exploration Vehicle

# Optical and Mechanical Properties Determined of Polymer Film Samples Exposed on the Materials International Space Station Experiment (MISSE) 1 and 2

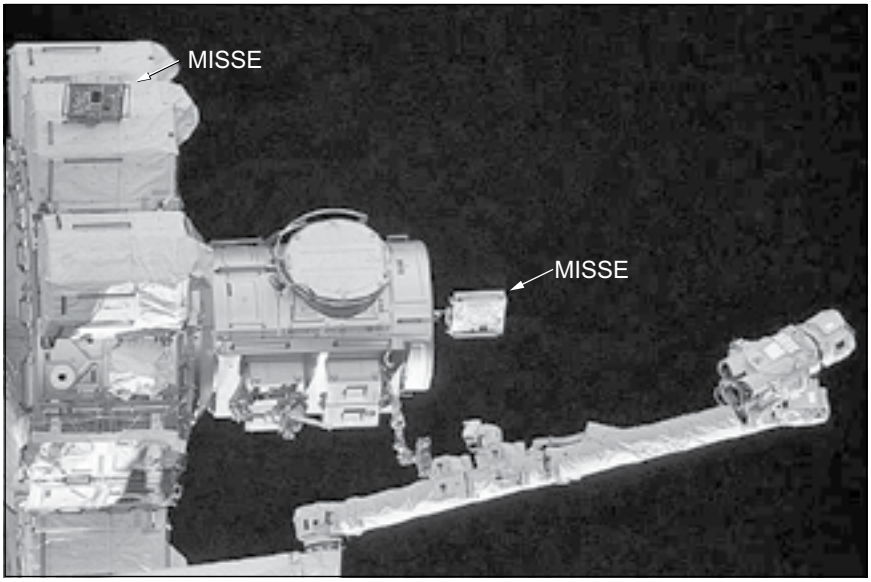


*MISSE 1 (upper left) and MISSE 2 (right) on the exterior of the ISS Quest Airlock.*

Polymer films used on spacecraft multilayer insulation, sunshields, and electrical wiring insulation and those proposed for use on advanced inflatable and deployable spacecraft structures are particularly vulnerable to the degrading effects of the space environment. The NASA Glenn Research Center developed the Polymer Film Thermal Control (PFTC) Experiment and the Gossamer Materials Experiment, which collectively included 31 samples flown as part of the Materials International Space Station Experiment (MISSE) on two passive experiment carriers (PECs) referred to as MISSE 1 and MISSE 2. The MISSE 1 and MISSE 2 PECs were deployed on the exterior of the International Space Station (ISS) on August 16, 2001, and were retrieved on July 30, 2005. Each of the suitcase-sized PECs contained two exposure faces, or "trays." When the PECs were deployed on the ISS, each PEC had one tray that was nominally exposed in the ram-facing direction and received atomic oxygen (AO) exposure and one tray that was nominally facing the wake direction and was intended to receive no AO.

The photograph shows the MISSE 1 and MISSE 2 PECs installed on the exterior of the ISS. Development of the PFTC and Gossamer Materials Experiments is described in detail in reference 1. Samples consisted of polymer films with or without front-side and/or back-side coatings. Polymers included polyimides Kapton HN (DuPont), Kapton H (DuPont), Kapton XC (DuPont), and Upilex-S (Ube Industries, Ltd.); fluorinated polyimide LaRC-CP1 (NASA); Teflon fluorinated

COATINGS USED ON POLYMER FILM SAMPLES ON PFTC AND GOSSAMER MATERIALS EXPERIMENTS

| Coating name | Description | Purpose |
|---|---|---|
| VDA | Vapor-deposited aluminum (~100 nm thick) | Back-side (second-surface) reflective layer |
| $SiO_x$-8% PTFE | Ion-beam co-sputter-deposited coating (~100 nm thick) from a sputter target consisting of silicon dioxide with a wedge of polytetrafluoroethylene (PTFE): 92 (vol% $SiO_x$ (where x = 2) and 8 vol% PTFE | Front-surface AO protective coating: PTFE provides increased flexibility over $SiO_x$ alone |
| $SiO_2/Al_2O_3/Ag/Al_2O_3$ (Ag composite) | Sputter-deposited layers of 550-nm $SiO_2$/2000-nm $Al_2O_3$/150-nm Ag/ 100-nm $Al_2O_3$ | Front-surface reflective coating: transparent oxide layers prevent degradation of silver |
| Ge | Sputter-deposited germanium coating (~50 nm thickness) | Conductive surface coating |
| ATO | Sputter deposited antimony tin oxide (~35 nm) | Transparent conductive surface coating |
| Ag/Nb | Sputter deposited silver (~135 nm thick) followed by a niobium layer (~30 nm thick) | Back-side (second-surface) reflective layer: niobium prevents degradation of silver |

ethylene propylene (FEP, DuPont); poly-p-phenylene polybensoxazole (PBO); and polyarylene ether benzimidazole TOR–LM (Triton Systems, Inc.). Coatings are described in the preceding table.

Following retrieval of MISSE 1 and MISSE 2, after approximately 4 years of space exposure, samples from the PFTC and Gossamer Materials Experiments were analyzed for changes in optical properties, mechanical properties, atomic oxygen erosion, and contamination. The samples flown on the PFTC and Gossamer Materials Experiments were analyzed during fiscal year 2006 both in-house at Glenn and through a contract with the University of Dayton Research Institute. Full details on the PFTC and Gossamer Materials Experiments exposure conditions, observations, and results are provided in reference 2, and results are briefly summarized here.

According to Kapton H erosion measurements, the AO-facing MISSE 2 PFTC Experiment tray experienced an atomic oxygen fluence of approximately $8.5\times10^{21}$ atoms/cm$^2$. The non-AO trays actually experienced some exposure to atomic oxygen because of maneuvers of the ISS during its mission. Erosion measurements of Kapton HN on the MISSE 2 non-AO-facing tray indicated an atomic oxygen fluence of approximately $2\times10^{20}$ atoms/cm$^2$. Contamination analysis of aluminum oxide witness

MECHANICAL PROPERTIES OF MISSE 1 PFTC AND GOSSAMER MATERIALS SAMPLES

| Sample description | Ultimate tensile strength, UTS, MPa | | | Elongation, percent | | |
|---|---|---|---|---|---|---|
| | Flight | Controls, average 2 | Loss, percent | Flight | Controls, average 2 | Loss, percent |
| AO-facing samples | | | | | | |
| $SiO_x$-8% PTFE/1-mil Upilex S/VDA | 210.5 | 330.2 | 36.2 | 4.1 | 12.6 | 67.5 |
| $SiO_x$-8% PTFE/5-mil FEP/VDA | 13.6 | 19.4 | 29.7 | 62.2 | 234.2 | 73.4 |
| Ag Composite/1-mil Kapton HN/VDA | 133.8 | 203.7 | 34.3 | 7.9 | 36.2 | 78.2 |
| Non-AO-facing samples | | | | | | |
| 2-mil FEP/VDA | 13.9 | 18.2 | 23.4 | 26.7 | 181.1 | 85.3 |
| 1-mil CP1/VDA | 88.9 | 87.4 | –1.8 | 6.7 | 7.9 | 14.6 |

SOLAR ABSORPTANCE AND THERMAL EMITTANCE OF MISSE 2 PFTC AND GOSSAMER MATERIALS SAMPLES

| Sample description | Solar absorptance, $\alpha$ | | | Thermal emittance, $\varepsilon$ | | |
|---|---|---|---|---|---|---|
| | Flight | Control | $\Delta\alpha$ | Flight | Control | $\Delta\varepsilon$ |
| AO-facing samples | | | | | | |
| $SiO_x$-8% PTFE/5 mil FEP/VDA | 0.139 | 0.149 | –0.010 | 0.858 | 0.862 | –0.004 |
| 5-mil FEP/VDA | .133 | .126 | .007 | .833 | .857 | –.024 |
| ATO/5-mil FEP/Ag/Nb | .083 | .087 | –.004 | .868 | .872 | –.004 |
| $SiO_x$-8% PTFE/1-mil Kapton HN/VDA | .368 | .361 | .007 | .699 | .698 | .001 |
| Ag composite/1-mil Kapton HN/VDA | .105 | .088 | .017 | .578 | .615 | –.037 |
| Ge/1-mil black Kapton/NOMEX (DuPont) scrim | .539 | .502 | .037 | .877 | .874 | .003 |
| $SiO_x$-8% PTFE/1-mil Upilex S/VDA | .509 | .464 | .045 | .751 | .690 | .061 |
| $SiO_x$-8% PTFE/1-mil CP1/VDA | .283 | .233 | .050 | .660 | .661 | –.001 |
| 1.5-mil TOR–LM (Triton Systems, Inc.) | .287 | .136 | .151 | (a) | (a) | (a) |
| Non-AO-facing samples | | | | | | |
| 2-mil FEP/VDA | 0.128 | 0.120 | 0.008 | 0.706 | 0.741 | –0.035 |
| 1-mil Kapton HN/VDA | .400 | .346 | .054 | .648 | .677 | –.029 |
| 1-mil Upilex S/VDA | .487 | .437 | .050 | .649 | .675 | –.026 |
| 1-mil CP1/VDA | .255 | .223 | .032 | .544 | .637 | –.093 |

[a]Not measured.

coupons indicated approximately 1-nm-thick silica contamination on the AO-facing MISSE 2 tray and greater than 10-nm-thick silica contamination (total contaminant thickness of 25 nm) on the non-AO-facing MISSE 2 tray.

Mechanical properties data and optical properties data for these experiments are provided in the tables on the preceding page. Sample descriptions in the tables indicate coating and polymer layers separated by a slash (/) in order from closest to farthest from the front, or space-facing, surface. Thickness of the polymer (as-manufactured) is indicated in the sample description.

The most significant degradation observed was for PBO film samples, which were completely degraded following the 4-year mission. This material was observed to have significant surface stress in its pristine condition, which may have played a role in its degradation. Mechanical properties data indicate that all exposed materials, except LaRC-CP1, experienced significantly reduced strength and elongation. The most significantly darkened polymer film was TOR–LM. Most other materials experienced low to moderate solar absorptance changes. Decreased emittance observed for the non-AO-facing polymer samples is evidence of the unplanned AO erosion. The results of the PFTC and Gossamer Materials Experiments are directly applicable to low-Earth-orbit spacecraft applications.

**References**

1. Dever, J.A., et al.: Exposure of Polymer Film Thermal Control Materials on the Materials International Space Station Experiment (MISSE). AIAA–2001–4924 (NASA/TM—2002-211363), 2001. http://gltrs.grc.nasa.gov/cgi-bin/GLTRS/browse.pl?2002/TM-2002-211363.html
2. Dever, Joyce A., et al.: Preliminary Analysis of Polymer Film Thermal Control and Gossamer Materials Experiments on MISSE 1 and MISSE 2. Presented at the 2006 MISSE Post-Retrieval Conference sponsored by the Air Force Research Laboratory, Orlando, FL, June 26–30, 2006. Abstract online: http://www.grc.nasa.gov/WWW/epbranch/other/SpaceDurabilitytitles.html#1

**Find out more about the research of Glenn's Electro-Physics Branch:**
http://www.grc.nasa.gov/WWW/epbranch/

**Glenn contacts:**
Joyce A. Dever, 216–433–6294, Joyce.A.Dever@nasa.gov

Sharon K. Miller, 216–433–2219, Sharon.K.Miller@nasa.gov

**Authors:**
Joyce A. Dever, Sharon K. Miller, Edward A. Sechkar, and Thomas N. Wittberg

**Headquarters program office:**
Exploration Systems

**Programs/projects:**
Crew Exploration Vehicle, International Space Station, Space Shuttle, Hubble Space Telescope

# Lunar Simulation Chamber Completed

NASA's Vision for Space Exploration calls for a return of humans to the Moon by no later than 2020. Reducing risk to astronaut safety and mission success will require technology development in a wide variety of areas. The exploration community is beginning to come to consensus with Apollo 17 astronaut Harrison Schmitt who recently declared, "Dust is the number one environmental problem on the Moon" (ref. 1). The Apollo record shows that dust caused a wide variety of problems for those missions including vision obscuration, false instrument readings, equipment clogging, radiator degradation, seal degradation, abrasion, and respiratory and eye irritation (ref. 2). Clearly, these are problems that must be understood and mitigated if humans are to establish a long-term presence on the Moon.

One source of the difficulties in understanding the interaction of lunar dust with sensitive surfaces (such as visors, radiators, and seals) in the lunar environment is that lunar dust has a structure unlike any dust on Earth, and the lunar environment is very different from any environment on Earth. This makes testing of components and systems that will be used on the Moon more difficult than one might suppose. For example, testing of radiator surfaces using real lunar dust in terrestrial lunar-simulation facilities suggested that a nylon bristle brush would be effective to remove dust from the Lunar Roving Vehicle battery radiators (ref. 3). However, in use on the actual lunar surface, the nylon bristle brushes were almost totally ineffective (ref. 4). This illustrates that there is more to accurately simulating the lunar environment than creating a good vacuum.

The Lunar Dust Adhesion Bell Jar (LDAB) was designed at the NASA Glenn Research Center to simulate the dusty lunar environment as accurately as possible. There are provisions to treat the dust by driving off absorbed water, thermal cycling the dust, exposing it to high-energy particles (simulating the solar wind) and ultraviolet light, and then applying a light coating of sieved dust to coupon-sized samples. These samples can then be further heated, cooled, and subjected to ultraviolet light. The LDAB also has a variety of diagnostic capabilities including residual gas analysis by mass spectroscopy, calorimetric measurements, and microscopic sample imaging. Capabilities to quantify the adhesive forces, lower the temperature to 40 K, and test mitigation techniques will be added in the coming year. It is expected that the LDAB will be a major asset in unraveling the web of interactions among the dust, the lunar environment, and spacecraft and that it will help to verify the effectiveness of various dust-mitigation strategies.

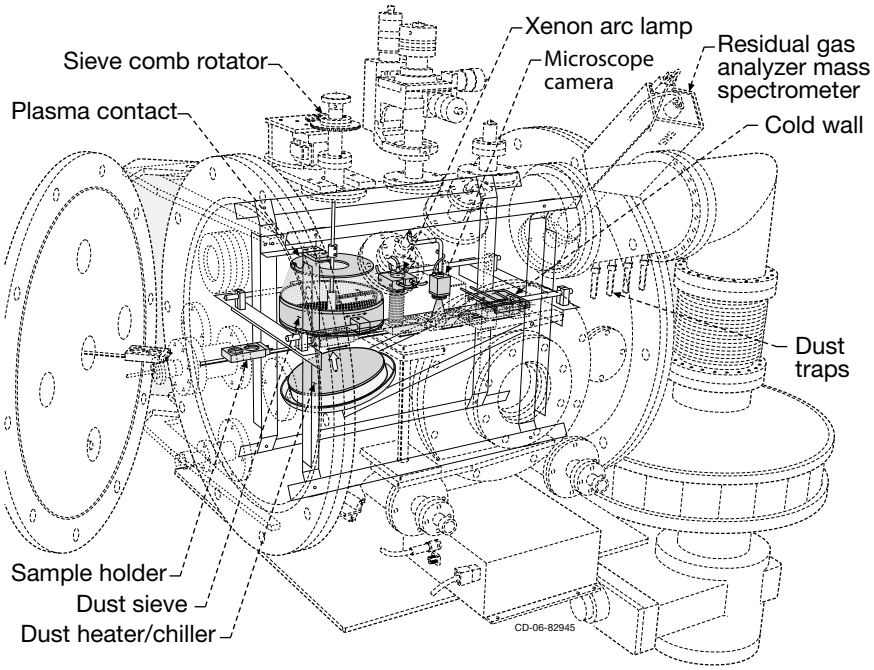


*Artist's cutaway drawing of the LDAB showing the principal features.*

**References**

1. Schmitt, Harrison: The Apollo Experience/Problems Encountered With Lunar Dust, Biological Effects of Lunar Dust Workshop, Sunnyvale, CA, 2005.
2. Gaier, James R.: The Effects of Lunar Dust on EVA Systems During the Apollo Missions, NASA/TM—2005-213610, 2005. http://gltrs.grc.nasa.gov/cgi-bin/GLTRS/browse.pl?2005/TM-2005-213610.html
3. Durkee, R.E.; Harris, R.S.; and Jacobs, S.: Lunar Dust Deposition Effects on the Solar Absorptance of Thermal Control Materials. AIAA Paper 71–479, 1971.
4. Saturn V Flight Working Group: Saturn V Launch Vehicle Flight Evaluation Report–AS–511, Apollo 16 Mission, MPR–SAT–FE–72–1 (NASA–TM–X–69535), 1972.

**Glenn contact:**
Dr. James R. Gaier, 216–433–6686, James.R.Gaier@nasa.gov

**Author:**
Dr. James R. Gaier

**Headquarters program office:**
Advanced Extravehicular Activity Systems

**Programs/projects:**
Lunar Surface Systems including Extravehicular Activity Systems, Lunar Surface Access Module, Lunar Habitat, and In Situ Resource Utilization

# *International Space Station* Experiment Used To Correlate Erosion Observed on Orbit for Coated Polymers to That Measured in Ground-Based Atomic Oxygen Facilities

Polymers exposed in the low-Earth-orbit (LEO) environment are subject to erosion by atomic oxygen that is present in the Earth's upper atmosphere through photodissociation of molecular oxygen by ultraviolet radiation from the Sun. The polymers typically fail in their performance earlier than their desired mission lifetime because of this erosion. Thus, protective coatings are used to slow or prevent the erosion from taking place. In order to determine how well protective coating candidates perform, they are often exposed in ground-based atomic oxygen facilities, where the sample turnaround time is shorter and less expensive than for actual flight testing. The difficulty in performing these tests is that there are no ground-based facilities that can exactly duplicate the space environment. The energy of the atomic oxygen arriving and/or the directionality of the arrival are not the same. Therefore, the question arises when performing ground-based atomic oxygen testing as to how long a protected polymer should be exposed to provide equivalent damage as that which would be observed in LEO. To provide an answer to this question, an experiment developed at the NASA Glenn Research Center was flown on the International Space Station as part of the Materials International Space Station Experiment (MISSE). Results of the experiment showed that for silicon-dioxide-coated Kapton, the erosion in ground-based atomic oxygen exposure facilities ranged from approximately 40 to 160 times greater than that observed in LEO, depending upon the type of ground facility exposure used.

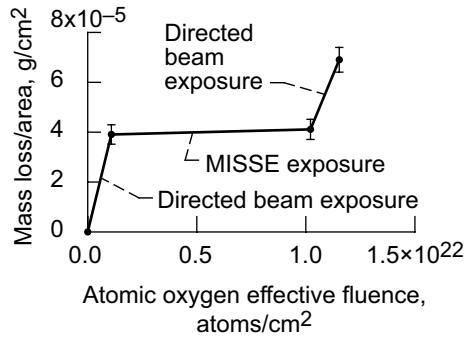


*Mass loss per unit area versus effective atomic oxygen fluence (dose) for samples exposed preflight in the atomic oxygen directed beam, exposed on orbit on MISSE, and exposed postflight in the atomic oxygen directed beam.*

The experiment consisted of two samples of Kapton HN (DuPont) polyimide film coated with approximately 1300 Å of silicon dioxide on both sides. One sample was exposed in a ground-based isotropic atomic oxygen plasma, and the other was exposed to an atomic oxygen directed beam. Both samples were carefully weighed prior to and after exposure to determine the amount of erosion that took place. Both samples were then flown on MISSE as part of a group of samples on the atomic-oxygen-facing side of the passive experiment carrier (PEC) 2 tray, which was mounted outside of the Quest Airlock. The photograph shows an astronaut with a PEC tray. After nearly 4 years on orbit, the samples were returned to Earth and again carefully weighed. The samples were then exposed to atomic oxygen in the facilities to which they had been exposed prior to flight to determine if the same mass loss resulted as had prior to flight. This was performed to verify that no damage occurred during flight that could have changed the erosion rate.

*Astronaut working with a MISSE PEC tray mounted on the International Space Station.*

The graph plots the mass loss per unit area versus effective atomic oxygen fluence (dose) for all three exposures for the atomic oxygen directed-beam-exposed sample. Results of the experiment show that the erosion for the directed-beam-exposed sample was approximately 160 times higher than that observed in LEO and that for the isotropic plasma was approximately 40 times higher than that observed in LEO, although the latter value

is probably higher because the number of defects had increased between preflight and postflight exposure, as evidence indicates. This experiment provided validation that ground-based atomic oxygen exposure facilities can provide meaningful durability data for coated polymers without conducting experiments to full mission fluence.

**Find out more about the research of Glenn's Electro-Physics Branch:**
http://www.grc.nasa.gov/WWW/epbranch/ephome.htm

**Glenn contacts:**
Sharon K. Miller, 216–433–2219, Sharon.K.Miller@nasa.gov

Bruce A. Banks, 216–433–2308, Bruce.A.Banks@nasa.gov

**Authors:**
Sharon K. Miller and Bruce A. Banks

**Headquarters program office:**
Office of Safety and Mission Assurance

**Programs/projects:**
Crew Exploration Vehicle, low-Earth-orbit satellites, International Space Station

## L-Band Global Positioning System Preamplifiers Space-Qualified for Low-Temperature Use Onboard the Space Shuttle

Electronics in space exploration missions such as Mars exploration rovers, lunar outposts, the James Webb Space Telescope, the Europa Orbiter, and deep-space probes need to operate reliably and efficiently under extreme cryogenic temperature conditions. Low-temperature electronics are also needed in the aerospace industry and the commercial sector in a wide range of applications that encompass advanced satellites, medical instrumentation, magnetic levitation, superconducting energy management and distribution, particle confinement and acceleration, and Antarctic missions. Besides surviving the hostile space environments, electronics capable of low-temperature operation would contribute to enhancing circuit performance, improving system reliability, extending lifetime, and reducing development and launch costs.

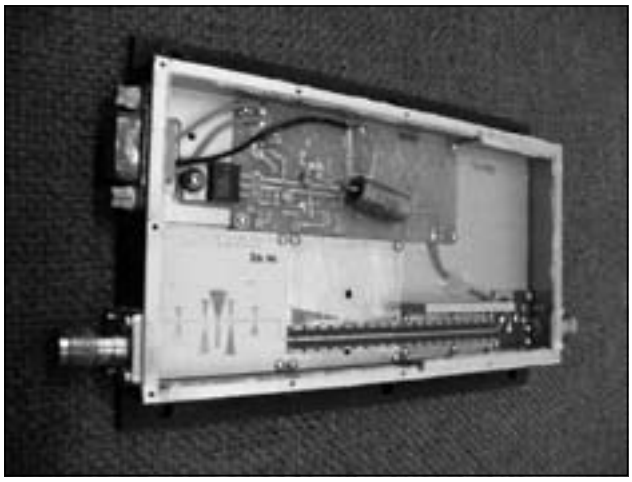

*Preamplifier unit with cover removed.*

The Low Temperature Electronics Program at the NASA Glenn Research Center focuses on the development and space-qualification of electronic parts and circuits for deployment in space exploration missions. The operational temperature range of electronic parts and circuits is greatly extended beyond the present range for industrial- and military-grade devices through the utilization of advanced materials, the application of new design techniques, and the exploitation of emerging technologies. Extensive evaluation of the developed parts and circuits is performed in-house under extreme temperatures and thermal cycling to space qualify these components and to establish their reliability.

The photograph shows one of four L-Band Global Positioning System (GPS) preamplifiers that were space-qualified at Glenn for use over an extended temperature range and thermal cycling between –85 and 93 °C. NASA planned to deploy these preamplifiers on the space shuttle, but there was a concern that these preamplifiers might

exceed their operational temperature limits because of the mounting configuration of the units on the shuttle's structure. Testing at Glenn showed that the preamplifiers were robust, operated well in the extended temperature range, and maintained good operation during and after thermal cycling. On the basis of testing at Glenn, NASA approved flying the preamplifiers in the extended temperature range. The preamplifiers have flown successfully on all space shuttle flights beginning with STS–114.

The research and development efforts in Glenn's Low Temperature Electronics Program are being performed through support from the NASA Electronic Parts and Packaging (NEPP) Program, and through collaboration with other Government agencies, industrial and aerospace companies, and academia. The program supports missions as well as technology development efforts at the NASA Johnson Space Center, NASA Goddard Space Flight Center, and the Jet Propulsion Laboratory.

**Find out more about the research of Glenn's Electro-Physics Branch:**
http://www.grc.nasa.gov/WWW/epbranch/ephome.htm

**Glenn contact:**
Richard L. Patterson, 216–433–8166,
Richard.Patterson@nasa.gov

**ASRC Corporation contact:**
Dr. Ahmad Hammoud, 216–433–8511,
Ahmad.Hammoud-1@nasa.gov

**Authors:**
Richard L. Patterson and
Dr. Ahmad Hammoud

**Headquarters program office:**
Shuttle Orbiter, Exploration Systems Missions Directorate

**Programs/projects:**
Lunar Landers, Mars Orbiters and Landers, James Web Space Telescope, Shuttle Orbiter Global Positioning System, NASA Electronic Parts and Packaging Program, and NASA Electronic Parts Assurance Group

## Trailing Edge Blowing Tested for Fan Blade Wake Management

The Acoustics Branch at the NASA Glenn Research Center conducts research to understand the mechanisms responsible for noise generation and assembles computational capability to predict and simulate the noise produced by aerospace systems. The results of these efforts are tools and technologies that allow products, such as aircraft, to have reduced noise emissions. Part of this effort involves the study of innovative noise-reduction technologies, at the fundamental level, to understand their effects on the entire system and to assess potential noise reductions.

One technology being studied is wake management using trailing edge blowing. When an airfoil, in this case a fan blade, slices through the air to generate the thrust that allows an aircraft to fly, wakes are created behind the airfoil much like those made by a boat in the water. These wakes travel downstream in the airflow and interact with downstream components, especially the downstream stationary airfoils called exit guide vanes. This wake-vane interaction generates one of the most significant noise sources in today's aircraft, being rivaled only by the exhaust jet noise.

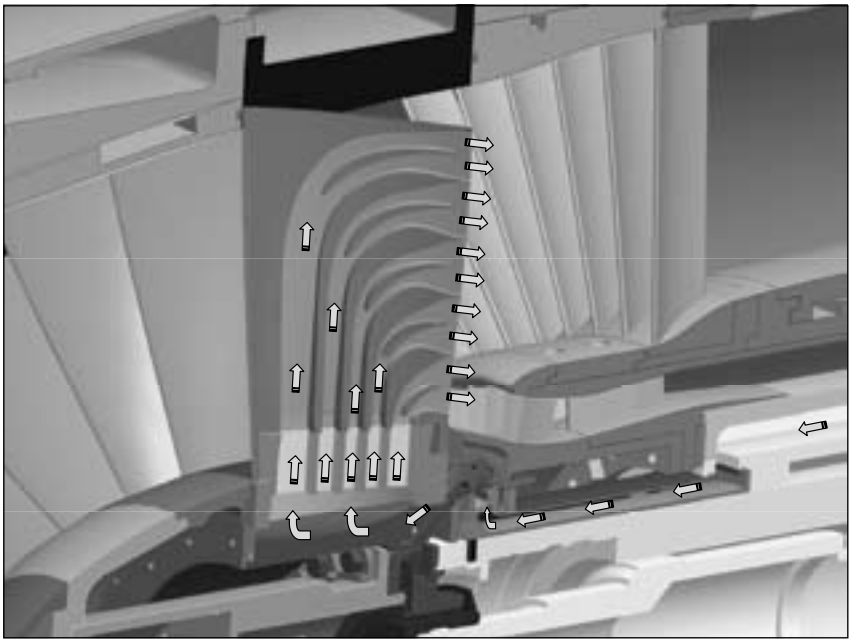

*Cross section of model showing path for air (the arrows represent airflow) injected through the fan blade and exiting the trailing edge, resulting in wake filling. This reduces downstream wake strength and turbulence where the wake encounters the exit guide vane, reducing a major noise source in turbofan engines.*

A fan with internal passages to carry air to the trailing edge and fill in the wakes was tested in a wind tunnel at Glenn, and acoustic, aerodynamic, and flow-field velocity data were acquired. Some operating configurations of this technology showed 2 dB of overall noise reduction—a meaningful reduction. Data inspection revealed details of how the technology works and possibly allows optimization of the injected flow to minimize system penalties. Computational aerodynamic and acoustic prediction tools were exercised using these data, and improvements in the codes may be implemented to better model advanced concepts.

The fan was designed using advanced three-dimensional computational tools to define the internal passages that carry air, efficiently and at specific flow rates, through the blade and to the trailing edge where it is injected into the flow stream. This fills the wake momentum deficit and reduces noise since the wake-vane interaction is lessened. The illustration shows the passages and injection at the trailing edge for wake filling.

The model was tested in Glenn's 9- by 15-ft acoustic test section, where the acoustic performance was measured using a traversing microphone, and performance and flow velocity data were acquired to determine the impact on system efficiency and to gain insight into the mechanics of the wake filling. Foremost, the data will be used to assess the potential viability of wake filling as a noise-reduction concept and to determine system impacts. The dataset also can be used for validating and improving analysis codes used to predict the

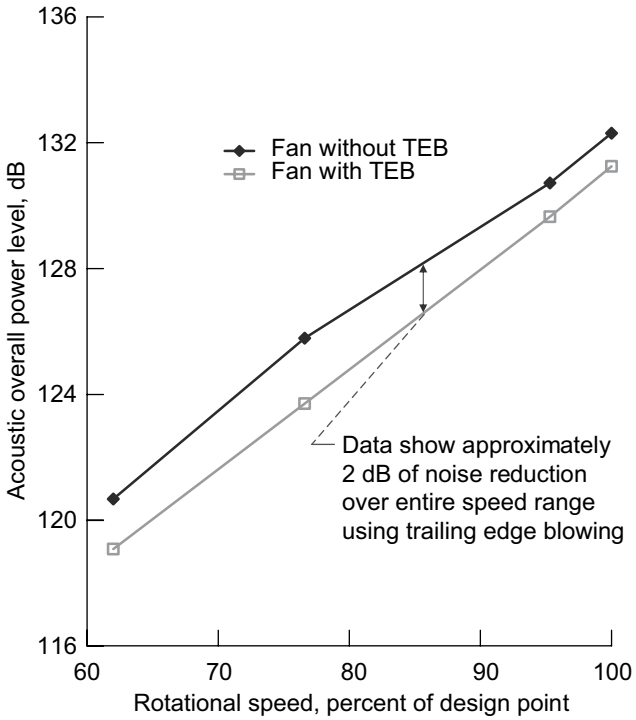


*The data show noise reduction using 2 percent of the fan flow injected along the trailing edge.*

performance of complex concepts. The data indicated reductions in tone noise (peaks), but more importantly, reductions were also observed at nearly all frequencies through 20 kHz for a substantial reduction in broadband noise. The graph shows the overall acoustic merit of the concept.

Together these tone and broadband reductions provide a 2-dB overall reduction, which is a significant reduction for the initial design iteration of the technology. In future efforts, NASA hopes to refine the concept and maximize the benefits while minimizing or eliminating overall system penalties.

**References**

1. Fite, E.; Woodward, R.; and Podboy, G.: Effect of Trailing Edge Flow Injection on Fan Noise and Aerodynamic Performance. AIAA–2006–2844, 2006.
2. Sutliff, D.L., et al.: Low-Speed Fan Noise Reduction With Trailing Edge Blowing. Int. J. Aeroacoustics, vol. 1, no. 3, 2002, pp. 275–305.
3. Halasz, C., et al.: Fan Flow Control for Noise Reduction Part 1: Advanced Trailing Edge Blowing Concepts. AIAA–2005–3025, 2005.

**Find out more about this research at Glenn's Acoustics Branch:**
http://www.grc.nasa.gov/WWW/Acoustics/

**Glenn contacts:**
E. Brian Fite, 216–433–3892, Eric.B.Fite@nasa.gov

Richard P. Woodward, 216–433–3923, Richard.P.Woodward@nasa.gov

Gary G. Podboy, 216–433–3916, Gary.G.Podboy@nasa.gov

**Author:**
E. Brian Fite

**Headquarters program office:**
Aeronautics Research Mission Directorate

**Programs/projects:**
Subsonic Fixed Wing

# New Procedure Created for Studying Core Noise

NASA's Aeronautics program is involved in engine test programs to identify dominate noise sources. Core noise is of interest since it becomes a significant contributor to the overall turbofan engine noise during takeoff or approach. A simple new procedure was created at the NASA Glenn Research Center that uses an aligned and unaligned coherence function to separate a mixture of "incoherent" noise, "coherent" noise, and tones so that noise components can be related to engine sources. The procedure provides a way to judge the significance of an aligned coherence-based function. Details are provided in references 1 to 3.

Data from a Pratt & Whitney PW4098 turbofan engine test are used to illustrate this technique. Instrumentation consisted of two pressure transducers in the combustor and four far-field microphones at 150 ft. Data were analyzed by using a periodogram averaging method to determine the amount of energy in a frequency band. The reciprocal of this band width is the sample segment length. If one calculates the coherence between a pressure transducer in the combustor and a far-field microphone, the two signals are completely out of synchronization since the analyzer only has the contents corresponding to the sample length, which is smaller than the propagation time for this test. The signals averaged do not include the combustor signal that was occurring when the noise left the engine.

This coherence is called the unaligned coherence. It measures the coherence of tones. Without tones, it has a value

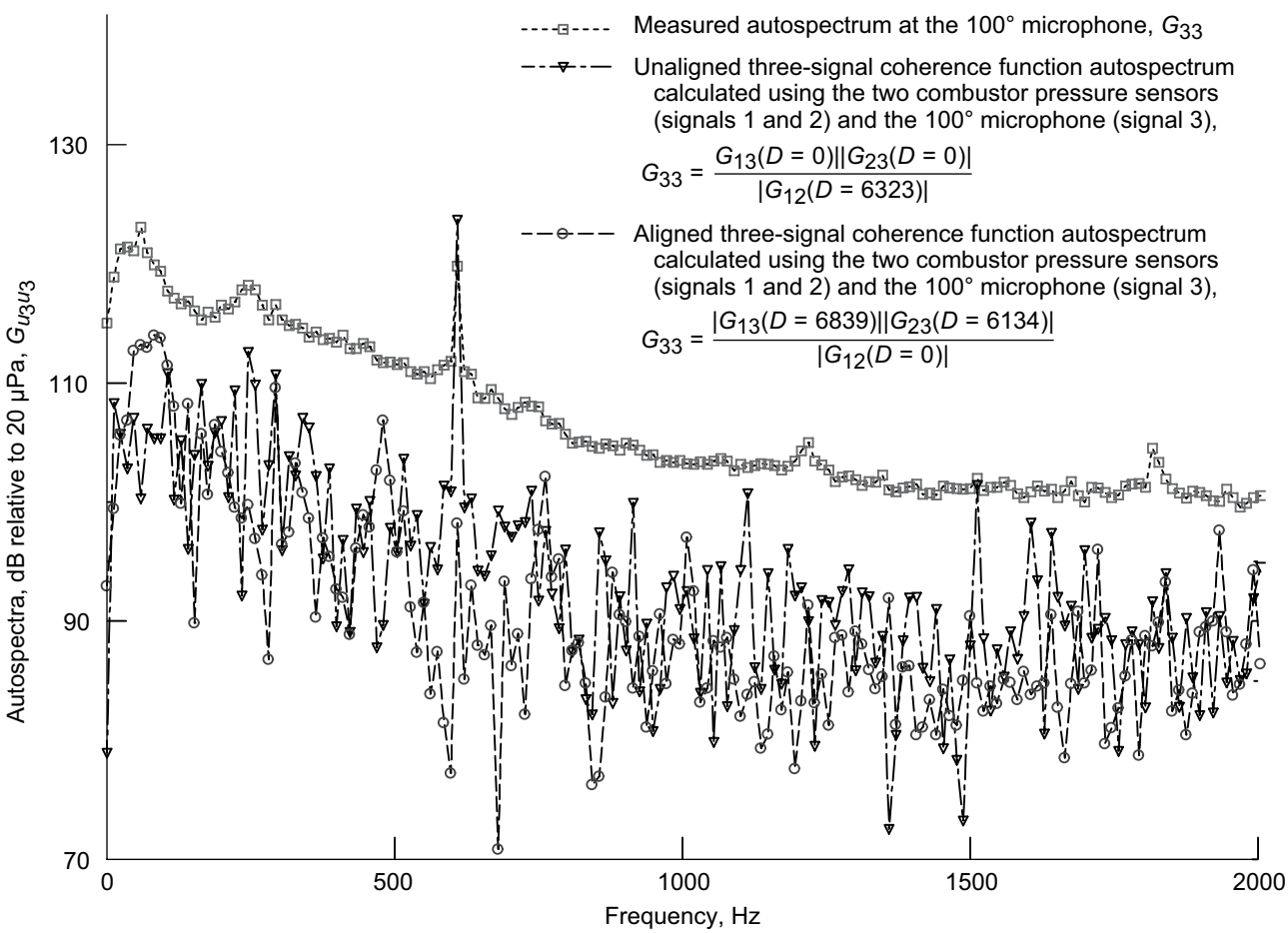


*Three-signal coherence technique using one far-field microphone at 100° and two internal combustor pressure sensors. Here D is the number of time steps that the signals are shifted to obtain alignment or misalignment. The time delay created by shifting the signal an amount D is $\tau = D/r$, where r is the sample rate in samples per second (r = 48,000).*

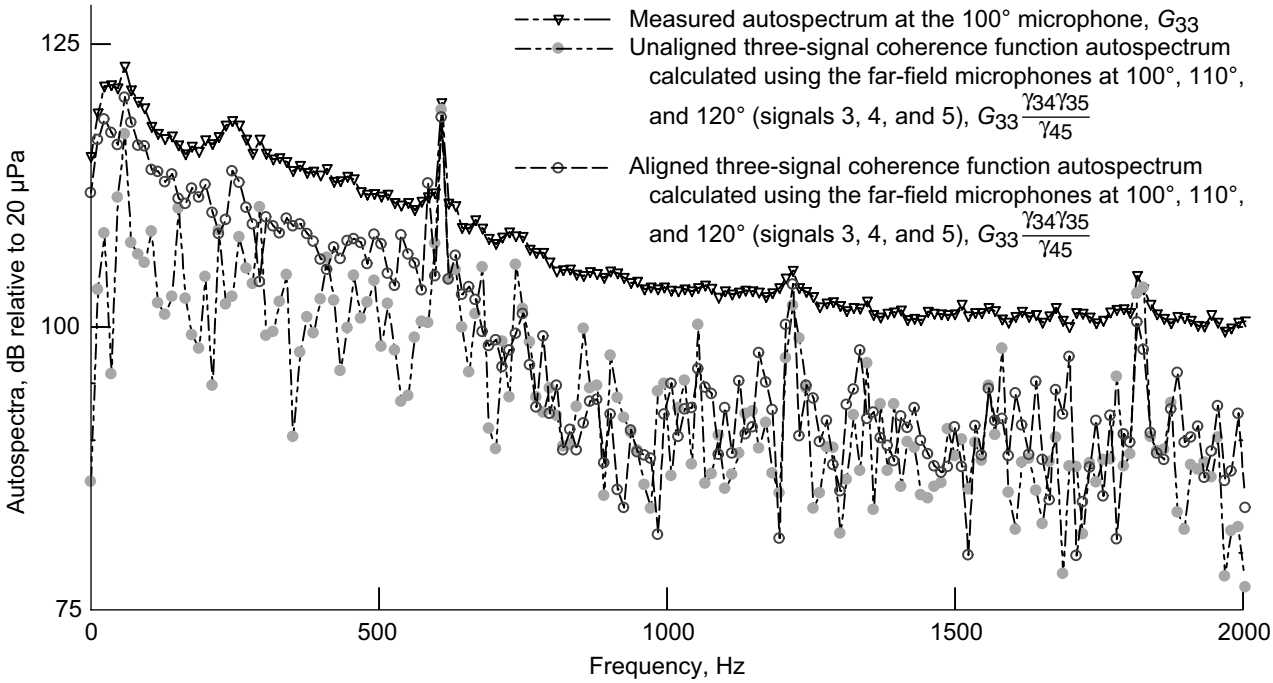


*Three-signal coherence technique using three far-field microphones.*

dependent on the number of segments averaged. An aligned far-field microphone signal must be created by the well-known procedure of time shifting the far-field time history forward by the time lag. The new procedure involves comparing functions calculated with the aligned and unaligned coherence so that one may judge their significance.

The figures illustrate the technique. Three-signal coherent power aligned and unaligned coherence functions calculated using a far-field microphone and two combustor transducers are shown in the figure on the preceding page. The small blip near 100 Hz in the aligned coherence rising above the unaligned coherence represents the correlated part of the total noise due to combustion. This blip is 9 dB below the total noise. Also note the presence of tones buried in the total noise. The separation of tones and broadband noise is also shown in the three-signal coherent power aligned and unaligned coherence functions created using three far-field microphones (see the figure on this page). The figure on the next page illustrates the two-signal aligned and unaligned coherent output power calculated using a combustor sensor and a far-field microphone. The small peak near 100 Hz is attributed to the presence of an $m = 0$ circumferential mode (i.e., the plane wave mode). This method lets one observe phenomena as low as 18 dB below the ordinary measured autospectrum.

The method confirms the presence of a coherent mode propagating from the combustor to the far field. It is being applied to turbofan engine acoustic data from Honeywell.

**References**

1. Faes, Luca, et al.: Surrogate Data Analysis for Assessing the Significance of the Coherence Function. IEEE Trans. Biomed. Engrg., vol. 51, no. 7, 2004.
2. Miles, Jeffrey Hilton: Aligned and Unaligned Coherence: A New Diagnostic Tool. NASA/TM—2006-214112 (AIAA–2006–0010), 2006. http://gltrs.grc.nasa.gov/Citations.aspx?id=68
3. Miles, Jeffrey Hilton: Restricted Modal Analysis Applied to Internal Annular Combustor Auto-Spectra and Cross-Spectra Measurements. AIAA J. (NASA/TM—2006-2143451, AIAA–2006–2581), vol. 45, no. 5, 2007. http://gltrs.grc.nasa.gov/Citations.aspx?id=12

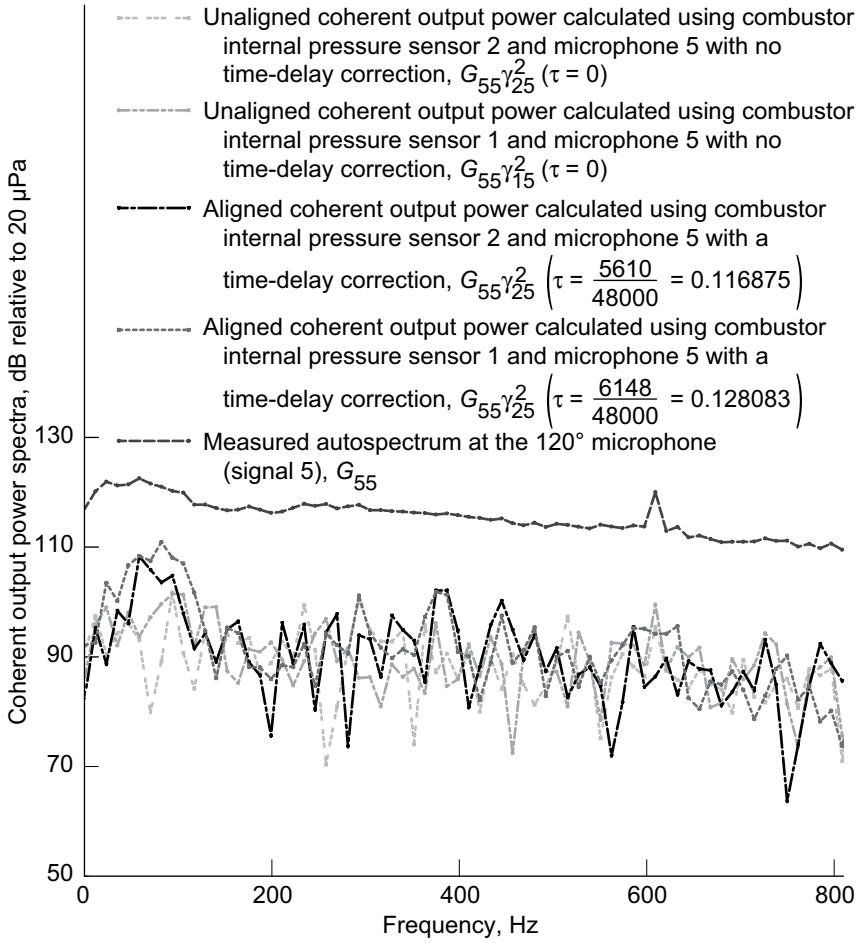


*Total sound power, aligned and unaligned coherent output power calculation for a test condition of 1622 rpm (corrected rotor speed, N1 corr)—using signal 1 (from the combustor pressure sensor 1 at 127° clockwise from top dead center viewed from the rear) and 5 (at 120°). This figure is shown in color in the online version of this article (http://www.grc.nasa.gov/WWW/RT/2006/RT/RTA-miles.html).*

**Find out more about this research at Glenn's Acoustics Branch:**
http://www.grc.nasa.gov/WWW/Acoustics/

**Glenn contact:**
Dr. Jeffrey Hilton Miles, 216–433–5909, Jeffrey.H.Miles@nasa,gov

**Author:**
Dr. Jeffrey Hilton Miles

**Headquarters program office:**
Aeronautics Research Mission Directorate

**Programs/projects:**
Subsonic Fixed Wing, Engine Validation
Noise Reduction Technologies

## Technique Improved for Measuring Noise Sources in a Supersonic Jet Via Two-Point Space-Time Correlations

A large component of the noise radiated by civilian and military aircraft is from the exhaust plumes of the gas turbine engines. For more than half a century, researchers have studied how to predict this noise from fundamental, physics-based principles (instead of using empiricism). A critical element in this effort is modeling the space-time correlation of the turbulent Reynolds stresses. So far, it has not been possible to directly measure this critical element from realistic high-velocity, high-temperature jets. In an effort to overcome this barrier, researchers at the NASA Glenn Research Center improved the molecular Rayleigh scattering technique to measure the space-time correlation of air-density fluctuations. This is the first step toward measuring these fluctuations in terms of density × velocity × velocity, which makes the full Reynolds stress term. The technique has been applied to unheated free jets from mach 0.9 to 1.8.

The optical setup consists of two laser beams crossing the jet plume in a vertical and a horizontal plane. Laser light scattered from each 1.06-mm-long beam

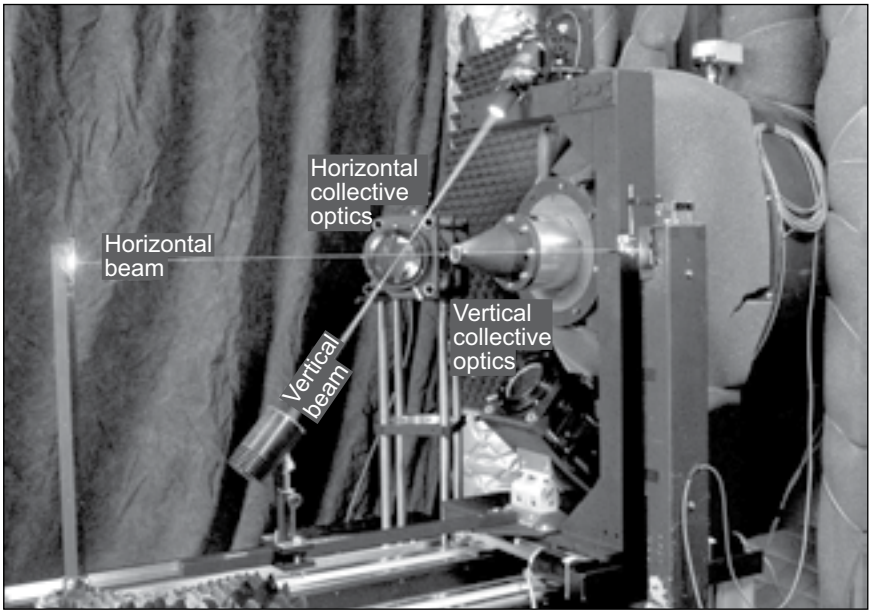


*Rayleigh scattering setup around a single-stream supersonic jet facility.*

was collected using two separate sets of lenses oriented 90° to the laser paths and was measured with photomultiplier tubes. The intensity of the scattered light was directly proportional to the air density. The beam path and the collection direction were designed for the next goal of simultaneously measuring density and velocity fluctuations from two different points in the jet.

The $k$-$\omega$ spectrum identifies the energy levels and the range of convective velocities associated with different frequency fluctuations. At any point, the $\omega/k$ ratio is a measure of this velocity. The turbulent fluctuations are convected by the jet flow; the overall inclination angle of each plot shows the average velocity. However, the spread at a given frequency $\omega$ shows

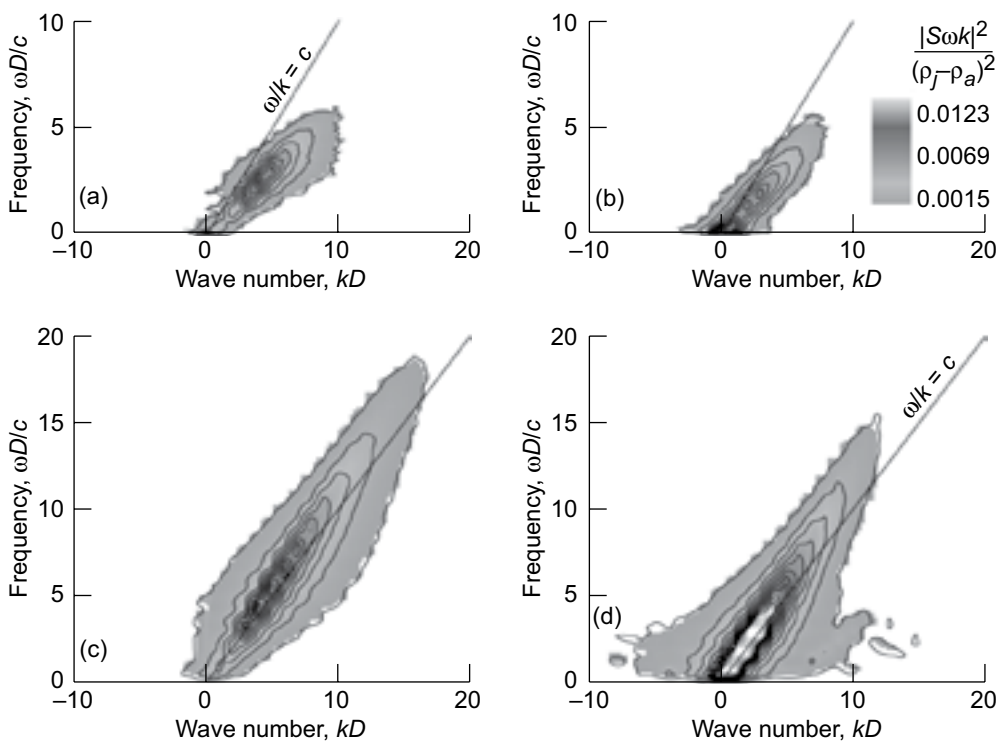


*Magnitude of the frequency-wave number ($k$-$\omega$) spectrum measured from the lip shear layer (left column) and the centerline (right column) of a subsonic (mach 0.95, $M_j$ = 0.95) and a supersonic ($M_j$ = 1.8) jet. The magnitude of each spectrum was normalized by the square of the difference between the jet density $\rho_j$ and the ambient density $\rho_a$. Here x is the distance downstream of the nozzle, D is the nozzle diameter, r is the radial distance, and S is the spectrum. The staircase-like appearance of the plots is reflective of the coarse wave number resolution achievable from the small jet. This figure is shown in color in the online version of this article (http://www.grc.nasa.gov/WWW/RT/2006/RT/RTA-panda.html). (a) $M_j$ = 0.95; fixed probe: x/D = 3, r/D = 0.5. (b) $M_j$ = 0.95; fixed probe: x/D = 7, r/D = 0.0. (c) $M_j$ = 1.8; fixed probe: x/D = 3, r/D = 0.5. (d) $M_j$ = 1.8; fixed probe: x/D = 10, r/D = 0.0.*

the dispersion of convection velocities. For the density fluctuations in the jet to become sound waves, they need to reach a velocity equal to or above the ambient speed of sound *c* (shown by a diagonal line in each plot). Therefore, the component of the *k*-ω spectrum lying left of the diagonal line is capable of radiating sound at different observer angles. Although most of the fluctuations in the subsonic mach 0.95 jet are incapable of radiating to the far field, the supersonic mach 1.8 jet shows a different scenario. With an average supersonic convective velocity, fluctuations in both the lip shear layer and the centerline of the jet are expected to radiate strongly, with peak radiation 25° to the jet axis. The low-frequency part of the spectra, more prominently from around the centerline, is found to radiate at all mach numbers. These data are expected to be valuable in validating various computational aeroacoustics codes.

**Bibliography**

Panda, Jayanta: Two Point Space-Time Correlation of Density Fluctuations Measured in High Velocity Free Jets. NASA/CR—2006-214222 (AIAA–2006–0006), 2006. http://gltrs.grc.nasa.gov/Citations.aspx?id=95

**Ohio Aerospace Institute (OAI) contact:**
Dr. Jayanta Panda, 216–433–8891, Jayanta.Panda-1@nasa.gov

**Glenn contact:**
Dr. James E. Bridges, 216–433–2693, James.E.Bridges@nasa.gov

**Author:**
Dr. Jayanta Panda

**Headquarters program office:**
Aeronautics Research Mission Directorate

**Programs/projects:**
Quiet Aircraft Technology, Subsonic Fixed Wing, Supersonics

## Planar Laser-Induced Fluorescence and Particle Imaging Velocimetry Used To Characterize a Baseline Nine-Point Lean Direct Injector for Comparison With National Combustor Code Results

Lean direct injection, conceived at the NASA Glenn Research Center, is representative of a new generation of turbine engine combustor injector concepts designed to rapidly mix air and fuel to create a stable combustion zone within a short distance from the injector in order to reduce the emission of oxides of nitrogen ($NO_x$). This injector concept was chosen as the primary test case for validating the National Combustion Code (NCC). To begin building a validation database, Glenn researchers tested a nine-point injector in an onsite flame tube combustor facility.

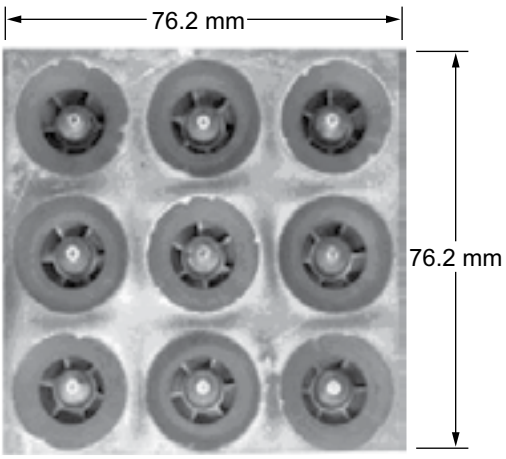


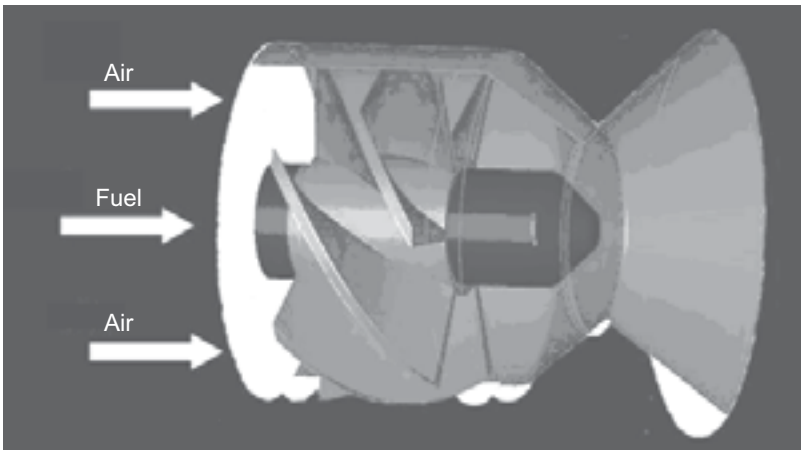


*Left: Nine-point LDI configuration tested at Glenn. The viewpoint is aft looking upstream. Right: Relative spatial positioning of the air swirler, fuel nozzle, and converging-diverging venturi for each injector element.*

The experimental hardware was the baseline nine-injector array shown in the view looking upstream in the photograph on the preceding page. Each injector element was the lean direct injector (LDI) shown in the illustration on the preceding page.

The nine-point injector was mounted in the optically accessible flame tube shown in the next illustration. A laser sheet passed through the top window. Cameras on each side imaged fluorescence (for planar laser-induced fluorescence (PLIF) measurements) or particle fields (for particle image velocimetry (PIV) or planar-light-scattering (PLS) measurements). The laser sheet and imaging apparatus were moved across the flow to gather data over the entire optically accessible volume. For PIV measurements, data also were gathered with the laser sheet passing through the side windows and the camera on top. Using appropriate laser wavelengths and filters, both hydroxyl radical (OH) and fuel PLIF were measured. For the PIV measurements, a high-pressure seeder seeded the flow with 0.3-μm-diameter aluminum oxide particles. Pairs of particle field images were used to determine the velocity field.

Three-dimensional species image maps showing the distribution of total fuel, OH, and liquid fuel were derived from PLIF and PLS data. Examples of these data are in the images at the top of the next page, which show views of fuel PLIF (left), OH PLIF (center), and PLS from fuel droplets (right) 7.5-mm downstream from the injector. The black circles indicate the position and diameter of each LDI venturi diffuser. The view is constrained by the window size so that only the central injector element is fully in view.

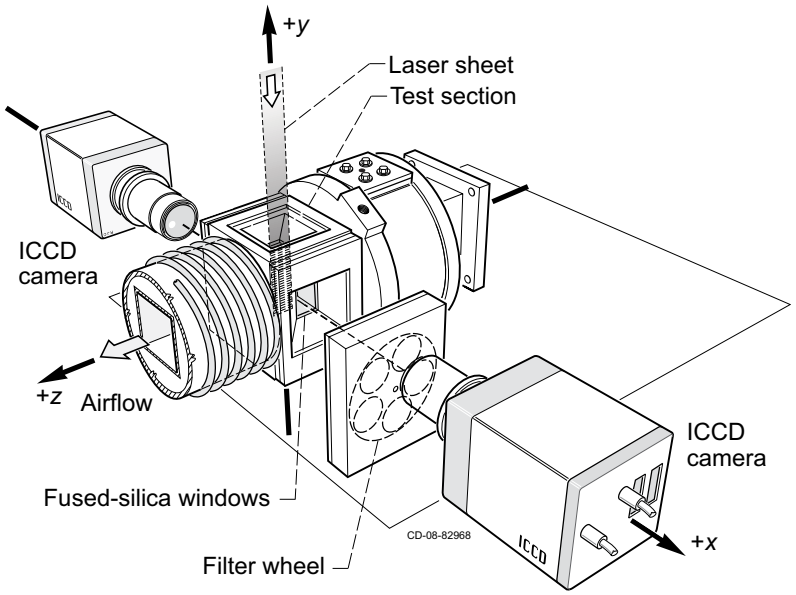


*Optically accessible flame tube and the relative orientation of the laser sheet and intensified charge-coupled device (ICCD) cameras to the test rig for a vertically applied laser sheet.*

In these images, we can see ringlike structures, particularly in the OH images; these give an indication of the size and position of the flame front at this location. Comparing the fuel PLIF (from liquid and vapor) and PLS (from liquid) images tells us whether the fuel is mostly liquid or vapor. In the top set of images, a significant portion of the fuel is in the liquid phase; whereas in the bottom set of images, which were acquired at a higher temperature, the fuel is almost completely vaporized.

As an example of the PIV results, the bottom figures on the next page compare experimentally and computationally derived axial air velocities under nonfueled, nonreacting conditions 6-mm downstream from the injector. The computations were obtained using a Reynolds averaged Navier-Stokes simulation. The square overlay on the computational result shows the region accessible by our PIV measurements. A comparison shows that the overall velocity field structure is similar. Finer experimental PIV grid spacing would likely bring out the fine structure observed in the computational results and improve the comparison.

**Bibliography**

Davoudzadeh, Farhad; Liu, Nan-Suey; and Moder, Jeffrey P.: Investigation of Swirling Air Flows Generated by Axial Swirlers in a Flame Tube. ASME Paper GT–2006–91300, 2006, pp. 891–902.

Tacina, Robert, et al.: Sector Tests of a Low-NOx, Lean-Direct-Injection: Multipoint Integrated Module Combustor Concept. ASME Paper GT–2002–30089, 2002, pp. 533–544.

Tacina, R.; Mao, C.; and Wey, C.: Experimental Investigation of a Multiplex Fuel Injector Module for Low Emission Combustors. AIAA–2003–0827, 2003.

Tacina, R.; Lee, P.; and Wey, C.: A Lean-Direct-Injection Combustor Using a 9 Point Swirl-Venturi Fuel Injector. XVII International Symposium on Air Breathing Engines (ISABE), ISABE–2005–1106, Munich, Germany, 2005.

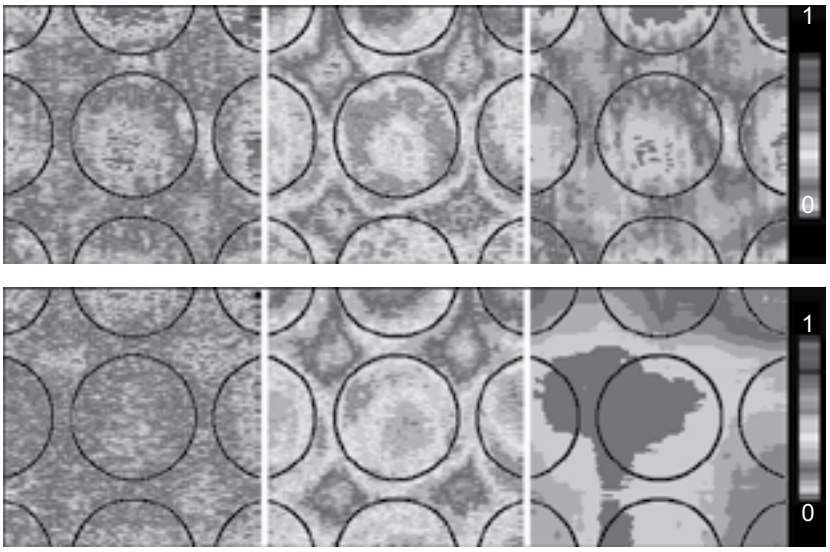


*End views 7.5 mm from the injector exit plane showing the species pattern of total fuel (left), OH (center), and liquid fuel (right). The field of view is the central 46- by 46-mm area. Each species is scaled independently. This figure is shown in color in the online version of this article (http://www.grc.nasa.gov/WWW/RT/2006/RT/RTB-anderson.html). Top: Inlet conditions: temperature, 617 K; pressure, 1030 kPa; equivalence ratio, 0.38. Bottom: Inlet conditions: temperature, 822 K; pressure, 1723 kPa; equivalence ratio, 0.41.*

**Find out more about this research:**

**Glenn's Optical Instrumentation & NDE Branch:**
http://www.grc.nasa.gov/WWW/OptInstr/AdvancedLaserDiag.html

**Glenn's Combustion Branch:**
http://www.grc.nasa.gov/WWW/combustion/

**Glenn contacts:**
Dr. Yolanda R. Hicks, 216–433–3410, Yolanda.R.Hicks@nasa.gov

Robert C. Anderson, 216–433–3643, Robert.C.Anderson@nasa.gov

**ASRC Corporation contact:**
Dr. Randy J. Locke, 216–433–6110, Randy.J.Locke@nasa.gov

**Authors:**
Robert C. Anderson, Dr. Yolanda R. Hicks, Dr. Randy J. Locke, and Changlie Wey

**Headquarters program office:**
Aeronautics Research Mission Directorate

**Program/projects:**
Subsonic Fixed Wing

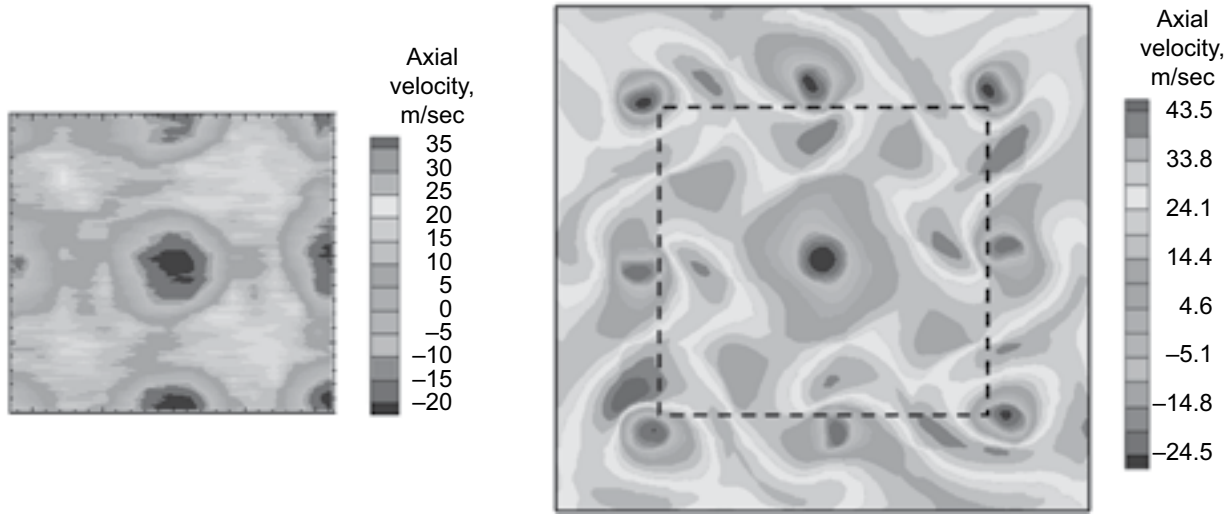


*Axial air velocities 6-mm downstream of the injector exit plane. This figure is shown in color in the online version of this article (http://www.grc.nasa.gov/WWW/RT/2006/RT/RTB-anderson.html). Left: Experimental PIV results. Inlet conditions: temperature, 617 K; pressure, 1030 kPa. Right: Computation. Inlet conditions: temperature, 822 K; pressure, 2740 kPa.*

# Fuel Injector-Mixer Concepts Examined for Kerosene and Diesel Fuel Reformer Applications Using Laser-Based Techniques

In conjunction with a program to develop low-emissions ground power and aircraft auxiliary power units, the NASA Glenn Research Center designed and built a facility to test fuel reformer concepts capable of providing 10-kWe power. NASA is investigating jet and diesel fuel reforming as a viable mechanism to generate hydrogen for solid oxide fuel cell (SOFC) operation. Jet-A and diesel fuels are being considered for fuel cell applications because they are relatively safe to handle, have high energy density, and have existing infrastructure.

In fuel reformation, a hydrogen-rich flow of syngas necessary for SOFC operation is created by catalytic reaction when a well-mixed, high-temperature flow of fuel, air, and sometimes steam impacts a catalyst. Three types of reforming processes are possible for fuels: catalytic partial oxidation (CPOX), autothermal reforming (ATR), and steam reforming (SR), depending on the amounts of steam and air used. Because reformer catalysts suffer degradation due to the buildup of carbon deposits and inadequate feed mixing and vaporization, nonuniform temperature distributions can result. A fuel injector system that fully vaporizes and mixes the reactants is critical to achieving optimal reforming performance.

A special feature of the NASA fuel reformer facility is an optically accessible test section (see the photograph), that allows researchers to obtain flow measurements to assess fuel injector mixing prior to entering the reformer. Diagnostics include flow-field visualization and quantitative measurements of velocity, fuel, and species distribution. Two methods are (1) particle image velocimetry (PIV) to acquire two-dimensional velocity field measurements and (2) Raman spectroscopy to determine the chemical species distribution across the flow field. The schematic drawing shows the region within the quartz cylinder that is probed by these methods.

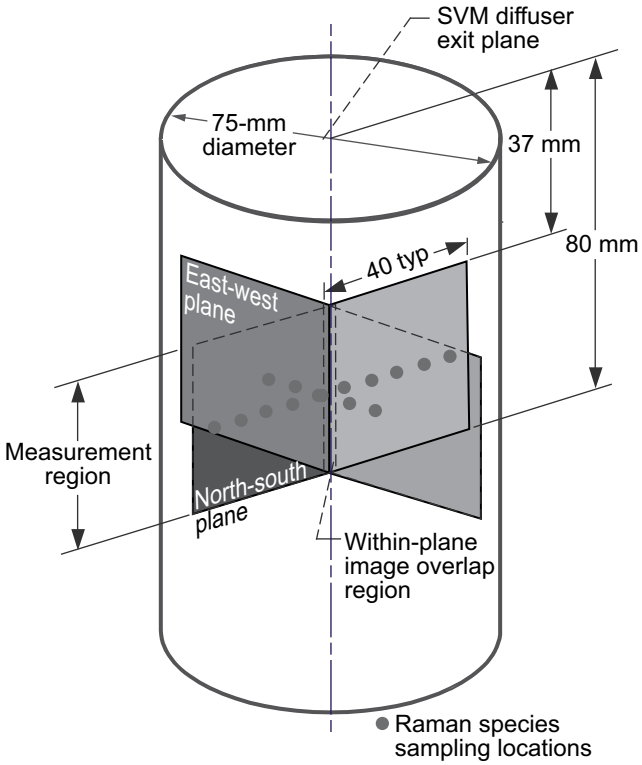


*Left: Optically accessible test section that includes the fuel injector-mixer concept being examined atop the quartz cylinder through which the mixing measurements are conducted. The fuel injector is mounted vertically with the flow downward. Right: Particle image velocimetry (PIV) laser sheet orientation and measurement region along with Raman sampling locations. Dimensions are in millimeters. SVM, swirl venturi mixer.*

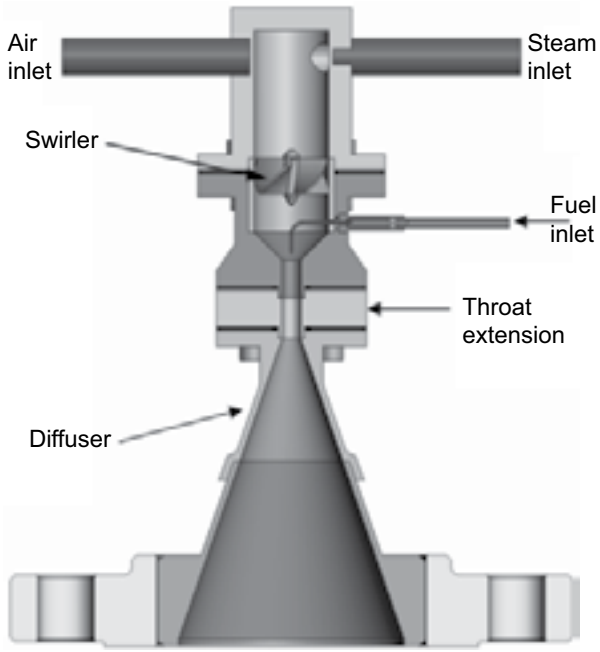


*Major fluidic components of the SVM. Flow passes from top to bottom.*

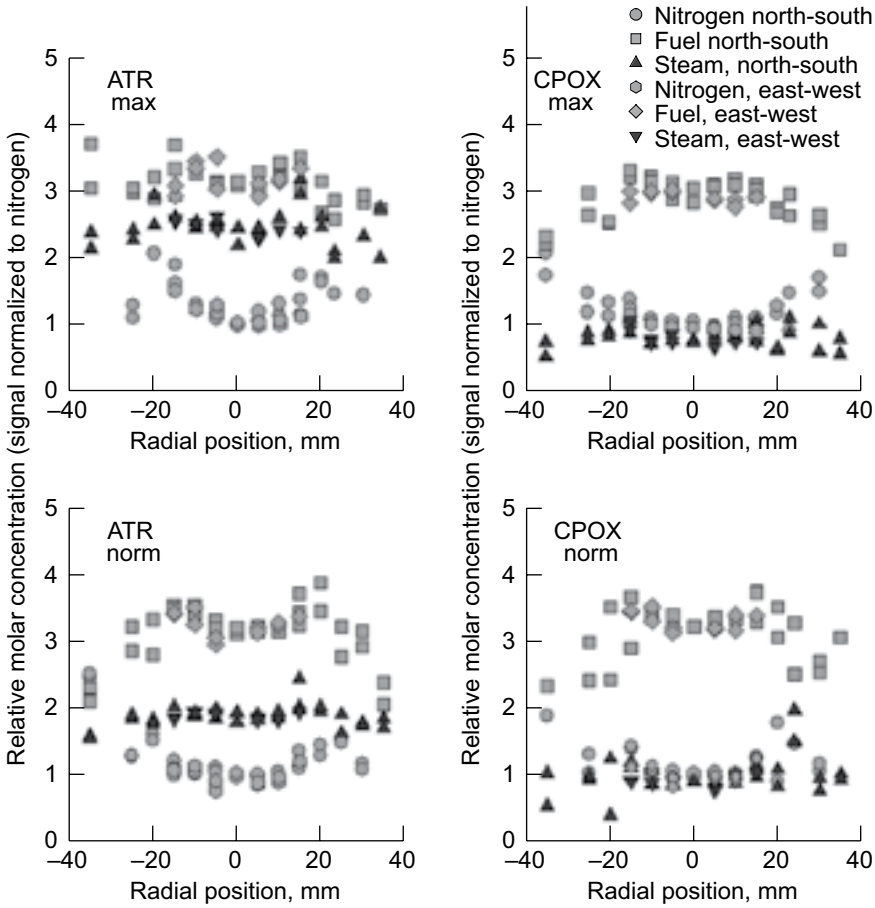


*Species profiles for one fuel injector configuration using two ATR and CPOX flow conditions.*

This schematic drawing shows a NASA-concept injector-mixer configuration. This swirl venturi mixer (SVM) concept provided a testbed for the parametric study of simple fluid elements whose combination leads to complex flow structure. These design elements include air/steam swirler angle, venturi throat size (diameter and length), and diffuser length and angle.

The final figures are examples of PIV and Raman results that show differences in species and velocity profiles. The Raman results show the differences between fuel loading for the same injector under two reforming processes and two flow rates. A flat, symmetric fuel profile is desired. The PIV results show distinct differences in velocity for different configurations of the SVM at the same flow conditions, with only one showing the desired uniform velocity profile across the flow field. This demonstrates that minor changes in fuel injector-mixer components can produce large differences in flow structure. These tests and others help to screen for the most suitable injector for a given reformer application and provide a database to help researchers understand the important parameters in injector design.

In addition to NASA concepts, Glenn has investigated several fuel atomization and mixing concepts using the new test facility in conjunction with private industry and the Department of Energy. These concepts include a gas-assisted simplex, a fuel-siphoning impingement injector, fuel preheating injection, piezoelectric injection, and fuel spray and venturis.

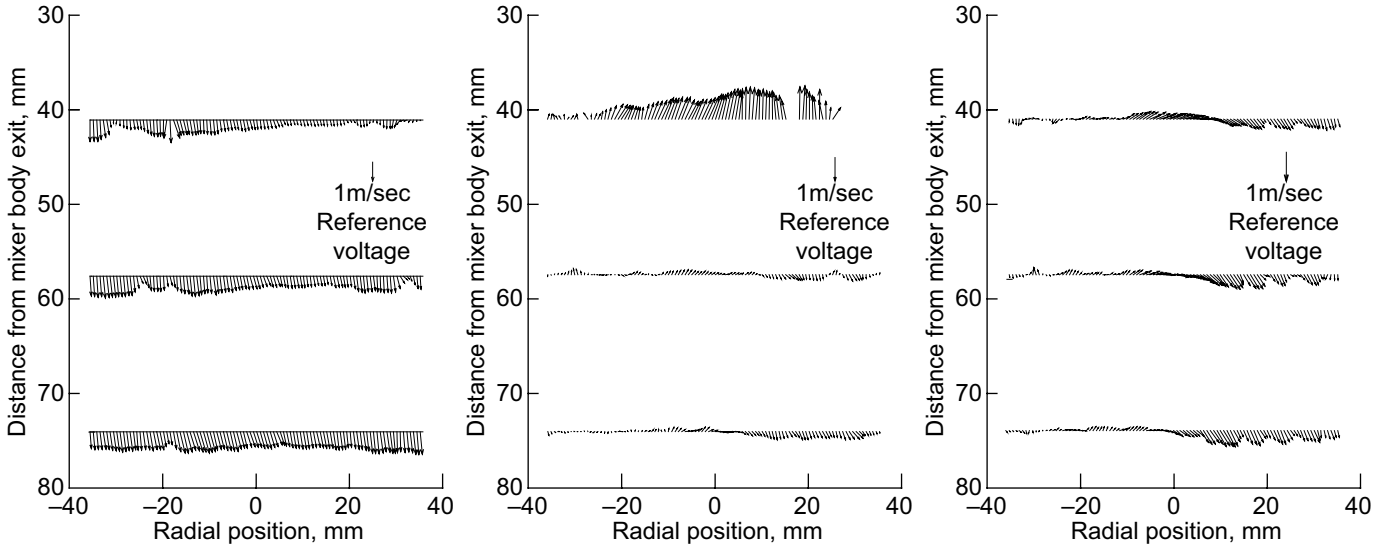


*Resultant two-dimensional velocity profiles for three fuel injector configurations at the same ATR flow conditions. Flow passes from top to bottom.*

**Bibliography**

Adrian, R.J.: Twenty Years of Particle Image Velocimetry. Exp. Fluids, vol. 39, no. 2, 2005, pp. 159–169.

Hicks, Y.; Locke, R.; and Yen, C.: Optical Evaluation of Fuel Injection and Mixing Processes in a 10 kW Fuel Reformer. AIAA–2006–2975, 2006.

Song, C.S.: Fuel Processing for Low-Temperature and High-Temperature Fuel Cells—Challenges, and Opportunities for Sustainable Development in the 21st Century. Catalysis Today, vol. 77, nos. 1–2, 2002, pp. 17–49.

Tacina, Robert, et al.: Experimental Performance of a Swirl-Venturi Fuel Mixer for a Fuel Cell Reformer. ASME Paper GT2006–90772, 2006, pp. 617–627.

**Find out more about this research:**

**Glenn's Combustion Branch:**
http://www.grc.nasa.gov/WWW/combustion/

**Advanced laser-based diagnostics for combustor research:**
http://www.grc.nasa.gov/WWW/OptInstr/AdvancedLaserDiag.html

**Glenn contact:**
Dr. Yolanda R. Hicks, 216–433–3410,
Yolanda.R.Hicks@nasa.gov

**ASRC Aerospace Corporation contact:**
Dr. Randy J. Locke, 216–433–6110,
Randy.J.Locke@nasa.gov

**University of Toledo contact:**
Judy Yen, 216–433–3626,
Chia.H.Yen@nasa.gov

**Authors:**
Dr. Yolanda R. Hicks, Chia H. Yen,
Robert C. Anderson, and
Dr. Randy J. Locke

**Headquarters program office:**
Aeronautics Research Mission Directorate

**Programs/projects:**
Subsonic Fixed Wing, Fuel Reforming

# Alternative Fuels Research Laboratory Being Designed and Constructed

Aircraft fuels will be changing in the near future, driven by a combination of environmental, operational, and safety-related concerns in an era of shrinking petroleum resources and growing air travel. The price of oil has increased dramatically from $30 per barrel in 2003 to over $70 per barrel in September 2006. As the price of oil remains high, other nonconventional fuels, such as those derived from coal or biomass may provide economically viable alternatives. Fuel composition can be tailored by the Fischer-Tropsch (F–T) synthesis and by operation conditions to improve engine combustor performance, improve fuel thermal stability, and reduce emissions. In phase I of the alternative fuels research at the NASA Glenn Research Center, we plan to test F–T synthesis processes with novel F–T catalysts and to study the effects of aircraft fuel composition on thermal stability and emissions.

Engineering design and construction of an alternative fuels research facility at Glenn was initiated in fiscal year 2006 with expected completion in the first quarter of fiscal year 2007 (see the figure on this page). This facility design includes three parallel bench-scale 1-liter autoclave F–T synthesis reactors (see the figure on the next page), gas feeds and reaction products handling, and synthesis product analysis. F–T catalyst performance evaluation and kinetic mechanism studies will be conducted at Glenn.

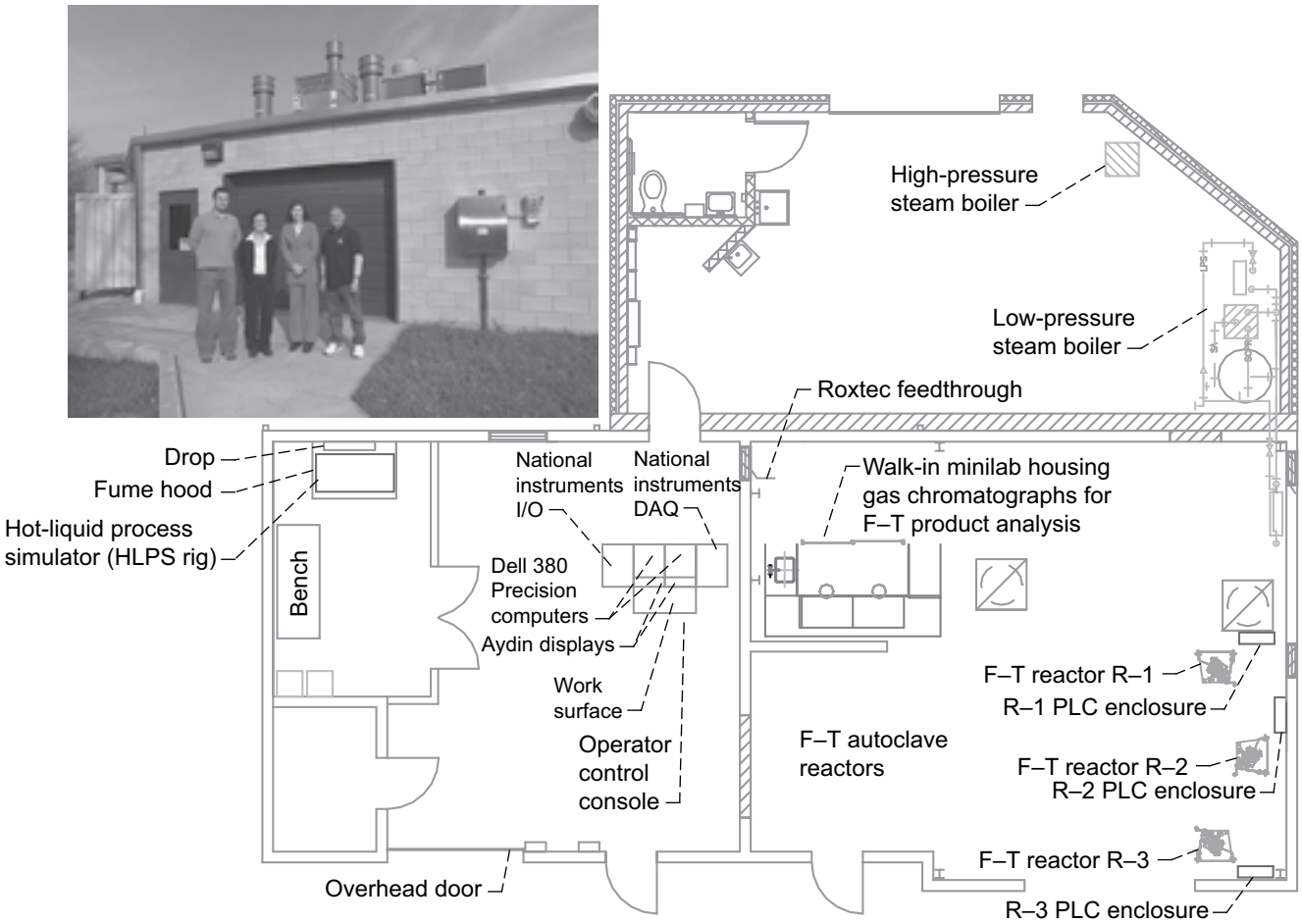


*Equipment plan for Glenn's Alternative Fuels Research Laboratory. I/O, input/output; DAQ, data acquisition.*

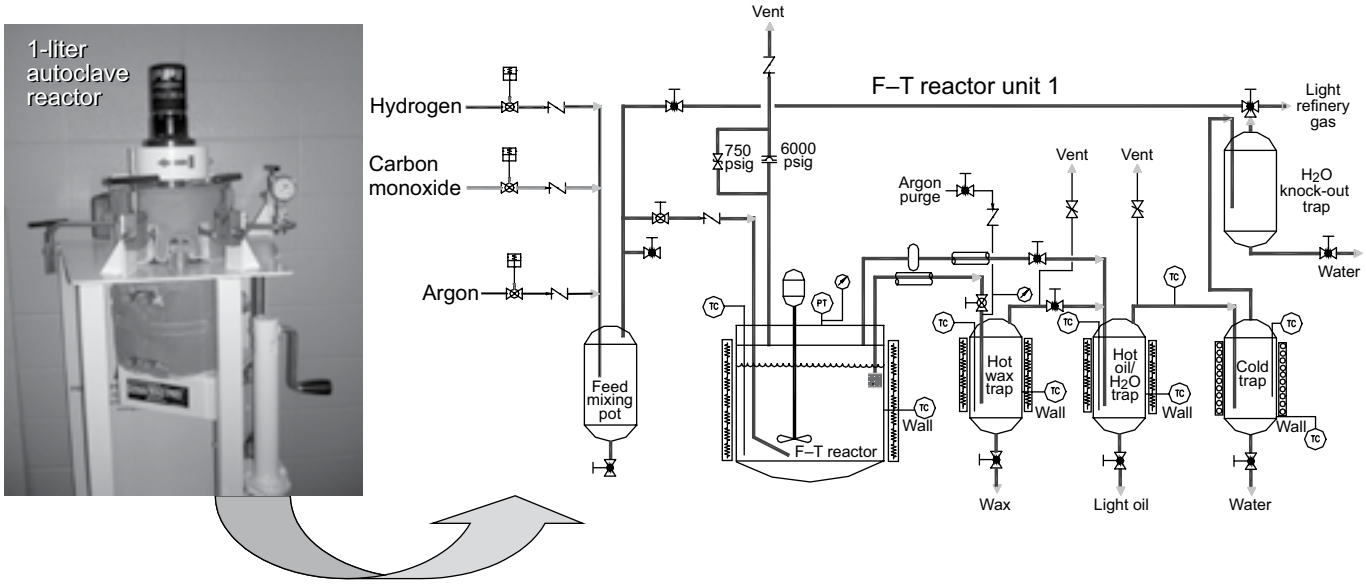


*F–T autoclave reactor system. TC, thermocouple; PT, pressure transducer.*

The compositions of alternative fuels differ from that of conventional petroleum-derived jet fuel because of the sources and processing of these fuels. Fuel composition differences affect emissions and chemical/physical properties. A comprehensive thermal stability study for alternative fuels will be included in the research to determine both oxidative and pyrolytic stability properties. Oxidative thermal stability is important in conventional engine performance, and pyrolytic stability is critical for future high-pressure, high-bypass-ratio engines.

The combustion performance of alternative fuels will also be studied to correlate emissions with fuel compositions. The overall program goal is to predict engine emissions according to fuel composition, combustor geometry, and operating conditions. Fundamental understanding of fuel composition effects on emissions and synthesis kinetics will guide future F–T catalyst development and F–T product upgrade technology to achieve more economical, efficient alternative fuels production.

**Find out more about the research of Glenn's Combustion Branch:**
http://www.grc.nasa.gov/WWW/combustion/

**Glenn contacts:**
Dr. Chi-Ming Lee, 216–433–3413,
Chi-Ming.Lee-1@nasa.gov

Thomas M. Tomsik, 216–977–7519,
Thomas.M.Tomsik@nasa.gov

Angela D. Surgenor, 216–433–3251,
Angela.D.Surgenor@nasa.gov

**University of Toledo contact:**
Judy Yen, 216–433–3626,
Chia.H.Yen@nasa.gov

**Authors:**
Dr. Chi-Ming Lee and Thomas M. Tomsik

**Headquarters program office:**
Aeronautics Research Mission Directorate

**Programs/projects:**
Fundamental Aeronautics, Subsonic Fixed Wing, Supersonics Fixed Wing

# End-to-End System Analysis Tool Developed for Studying Lunar In Situ Resource Utilization

The Vision for Space Exploration plans for eventual outposts on the lunar surface, requiring large amounts of mass launched from Earth. Each kilogram of oxygen or fuel produced on the Moon using lunar regolith or potential polar ice would reduce Earth launch mass by 5 to 8 kg. NASA is developing the architecture for lunar missions, and the benefits and requirements of a lunar-based in situ resource utilization (ISRU) system need to be quantified.

The interaction of components and subsystems will be critical to the overall design of this complex system. A team at the NASA Glenn Research Center has created a system-modeling tool to capture these interactions and to help understand optimization at the system level. The initial effort focused on the baseline concept of lunar regolith ISRU, which requires an excavation subsystem, a reaction subsystem, and an oxygen liquefaction subsystem, as shown in the following figure.

The excavation subsystem excavates and transports regolith to the reaction site. The subsystem model evaluates either a single roverlike vehicle or a combination of specialized vehicles, and it sizes the vehicles to successfully navigate the lunar soil.

The reaction subsystem converts the metal oxides in the regolith to water within the reactor and then converts the water to oxygen using an electrolyzer. The initial model assumes a fluidized bed batch reactor at 600 to 1000 °C using hydrogen to both fluidize and convert the oxides to water. The reactor is sized according to fluid-mechanics and chemical-reaction-rate requirements. Multiple reactors can be used in parallel to allow more time for reaction and heat-up of the regolith. The electrolyzer converts the water to hydrogen and oxygen, accounting for the thermodynamics and the electrical characteristics. Then the hydrogen is recycled back to the reactor, and the oxygen is sent to the liquefaction subsystem. Other components in the model include pumps and compressors, heat exchangers, and condensers.

The liquefaction subsystem model analyzes the power required to liquefy and maintain the liquid oxygen as well as the volume and mass of the tanks and cryocoolers.

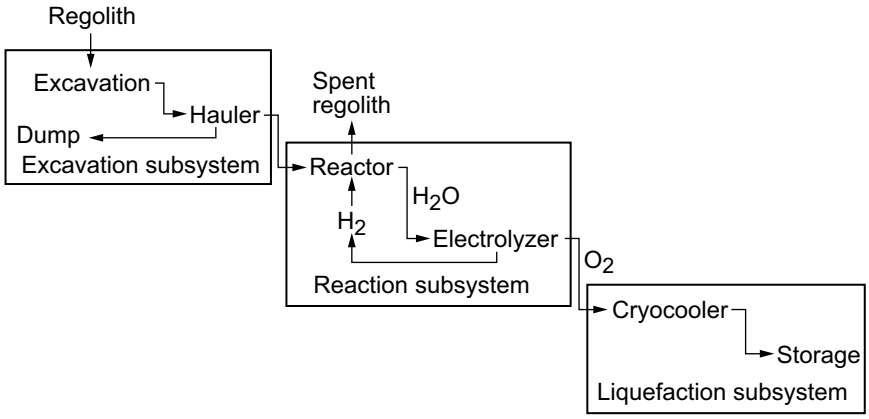


*Simplified lunar regolith ISRU system.*

At the system level, users can select which components are in the system and how these components will be arranged. This allows for great flexibility in both updating individual modules as new data become available and in incorporating entirely new components, such as alternative reactor processes. The optimization feature converges on the user-specified production rate while solving for a user-specified goal (such as minimum system mass) within sets of equality and inequality constraints.

The system model has produced both qualitative and quantitative results, and development continues. For example, the batch-based nature of the hydrogen reactor results in highly variable flow rates for downstream components. Operating with parallel reactors increases the reactor mass but reduces the overall system mass by 20 percent.

More quantitatively, parametric studies have been performed, such as varying the oxygen production level. The plot on the next page shows mass and power results for an equatorially located system where the regolith is heated via electrical power. Nuclear power has lower peak power demands because of 365-days-per-year operation, whereas solar power can operate only during daylight hours (about half time).

The system model is being refined with a focus on component and system validation. The goal is to be flexible in regards to other system approaches while maintaining consistent assumptions and an overall framework. This will enable a tool that can be used for tradeoff studies and in preparation for future hardware development.

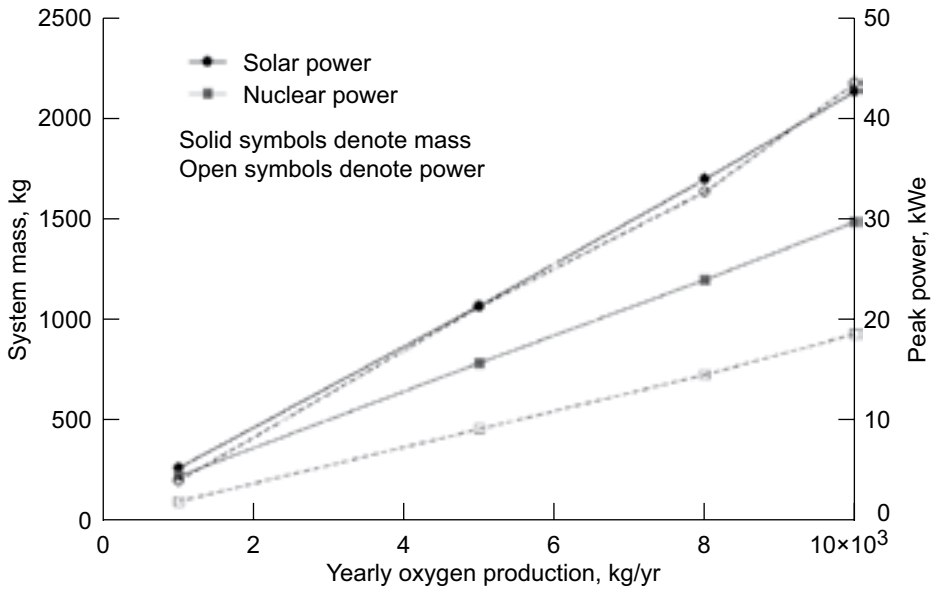


*Estimates of overall mass and peak power for different oxygen production levels for an equatorial lunar regolith ISRU system.*

**Glenn contacts:**
Diane Linne, 216–977–7512, Diane.L.Linne@nasa.gov

Joshua E. Freeh, 216–433–5014, Joshua.E.Freeh@nasa.gov

**Authors:**
Diane L. Linne, Joshua E. Freeh, Eric W. Faykus, Christopher A. Gallo, Robert D. Green, and Christopher J. Steffen

**Headquarters program office:**
Exploration Systems Mission Directorate

**Programs/projects:**
Constellation Systems, Exploration Technology Development Program

# Alternative Rotational Raman Thermometry Developed for Turbulent Combustion

Researchers from the Combustion Branch at the NASA Glenn Research Center and from the Ohio Aerospace Institute (OAI) have developed a novel optical technique for improved temperature measurements in high-pressure combustion environments. This new thermometry technique utilizes low-spectral-resolution pure-rotational spontaneous Raman scattering of nitrogen ($N_2$) and oxygen ($O_2$) to improve the accuracy of single-shot temperature measurements in turbulent combustion. This approach is especially useful in cases where the vibrational Raman signals are inadequate for a conventional temperature analysis.

According to spectral simulations (see the top graph on the next page) of low-resolution, pure rotational Raman scattering based on the theory from references 1 and 2, it is clear that the shape of the rotational $N_2$ spectrum becomes wider with an increase in temperature. This increase in width results from the fact that more rotational states with higher energies (longer wavelength at the Stokes side, shorter wavelength at the anti-Stokes side) are populated at higher temperatures as a result of the Boltzmann distribution. Thus, a measurement of the envelope bandwidth of the rotational spectrum can provide temperature information. The use of the low-resolution rotational bands permits an enhancement in the overall signal amplitude (because of a larger Raman cross section of rotational versus vibrational lines, and higher optical throughput resulting from the use of a wider optical slit), thereby decreasing the statistical uncertainty through a significant increase in the signal-to-noise ratio.

However, a challenge needs to be met for this strategy to be successful: the effects of spectral interferences from the rotational $O_2$ Raman spectrum must be compensated for. Since the rotational frequency of $O_2$ is very close to that of $N_2$, the rotational spectral band of $N_2$ and $O_2$ appears only as a single band combining the two spectra. This $O_2$ interference is

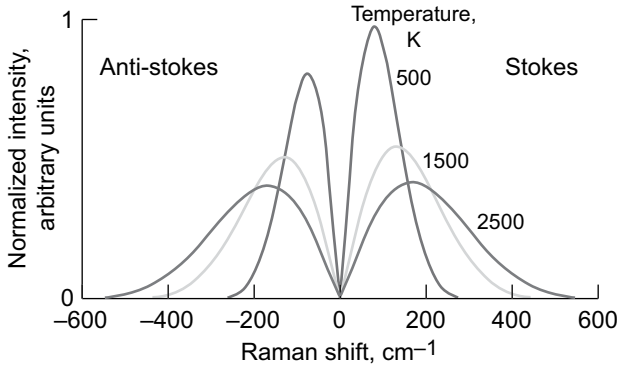


*Rotational Raman spectra at low resolution (35 cm$^{-1}$): calculated pure nitrogen spectra at different temperatures.*

unavoidable since any practical air-breathing combustion system essentially contains nitrogen and oxygen as the oxidizer. From the top graph, it is known that the overlapping causes a "narrowing" effect, in which the spectrum of the $N_2/O_2$ mixture shows a narrower envelope than that of the pure $N_2$ at the same temperature. To conveniently and effectively compensate for this spectral band narrowing because of the $O_2$ overlapping, we developed an algorithm based on the theoretically predicted spectral blending of the two individual species, adjusted by the relative concentrations of $N_2$ and $O_2$ obtained from the simultaneous vibrational Raman spectra (see the following graph).

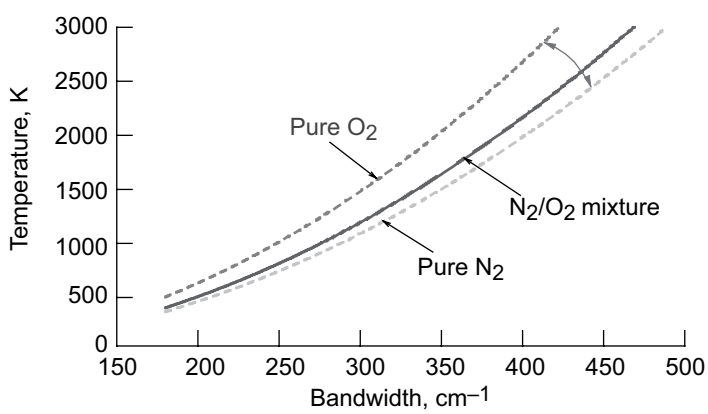


*Calculated correlations between the rotational-envelope bandwidth and the temperature of $N_2/O_2$ mixtures at 5 atm.*

An experimental verification of our method is given in the graph on the next page. For this test, a typical Raman-scattering spectroscopy apparatus (refs. 3 to 6) was used in a high-pressure gaseous calibration burner (refs. 7 to 9), which provided a steady flame that can be predicted using the assumption of chemical equilibrium. In this final graph, the flame temperatures derived from the present method are compared with the calculated adiabatic temperatures. An excellent agreement between the two over a range of equivalence ratios shows that the present flame thermometry is promising.

By using this new frequency-domain rotational Raman technique together with conventional vibrational scattering, we have demonstrated quantitative, spatially resolved, single-shot multiscalar measurements of temperature and fuel/oxidizer concentrations in a high-pressure turbulent methane-air flame. The technology described has been disclosed as a NASA New Invention and Technology (ref. 10). For a description of the application of this technique in flames, see reference 11.

**References**


1. Kojima, Jun; and Nguyen, Quang-Viet: Disclosure of Invention and New Technology (Including Software), Laser-Raman Spectral Analysis Software for Combustion Diagnostics. LEW–17769–1, 2004.
2. Kojima, J.; and Nguyen, Q.-V.: Quantitative Analysis on Spectral Interference of Spontaneous Raman Scattering in High-Pressure Fuel-Rich Hydrogen-Air Combustion. J. Quant. Spectrosc. Radiat. Transf., vol. 94, nos. 3–4, 2005, pp. 439–466.
3. Nguyen, Quang-Viet: Spontaneous Raman Scattering (SRS) System for Calibrating High-Pressure Flames Became Operational. Research & Technology 2002, NASA/TM—2003-211990, 2003, pp. 117–118. http://www.grc.nasa.gov/WWW/RT2002/5000/5830nguyen2.html
4. Kojima, J.; and Nguyen, Q.V.: Measurement and Simulation of Spontaneous Raman Scattering Spectra in High-Pressure, Fuel-Rich $H_2$-Air Flames. Meas. Sci. Tech., vol. 15, no. 3, 2004, pp. 565–580.
5. Nguyen, Quang-Viet; and Kojima, Jun: Transferable Calibration Standard Developed for Quantitative Raman Scattering Diagnostics in High-Pressure Flames. Research & Technology 2004, NASA/TM—2005-213419, 2005, pp. 170–172. http://www.grc.nasa.gov/WWW/RT/2004/RT/RTB-nguyen.html
6. Kojima, Jun; and Nguyen, Quang-Viet: Strategy for Multiscalar Raman Diagnostics in High-Pressure Hydrogen Flames. New Developments in Combustion Research, William J. Carey, ed., NOVA Science Publishers, New York, NY, 2006, pp. 227–256.

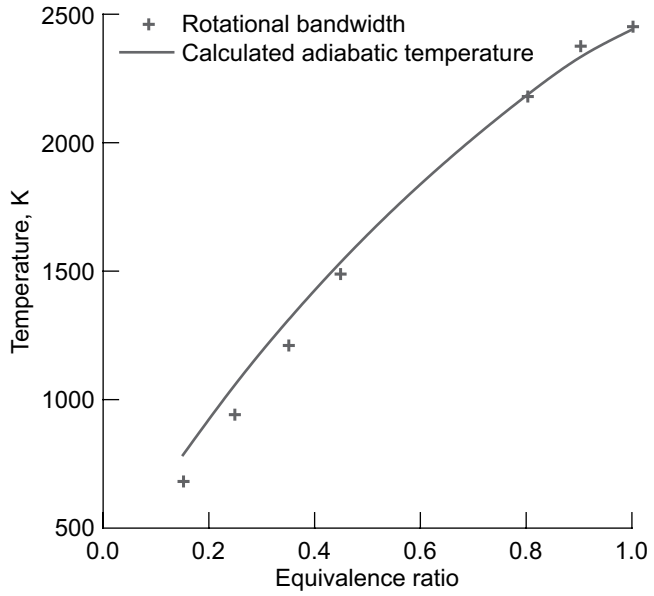


*Averaged flame temperatures determined by Raman thermometry in high-pressure (10-atm) lean hydrogen/air flames.*


7. Nguyen, Quang-Viet: High-Pressure Gaseous Burner (HPGB) Facility Became Operational. Research & Technology 2002, NASA/TM—2003-211990, 2003, pp. 116–117. http://www.grc.nasa.gov/WWW/RT2002/5000/5830nguyen1.html
8. Kojima, Jun; and Nguyen, Quang-Viet: Development of a High-Pressure Gaseous Burner for Calibrating Optical Diagnostic Techniques. NASA/TM—2003-212738, 2003. http://gltrs.grc.nasa.gov/cgi-bin/GLTRS/browse.pl?2003/TM-2003-212738.html
9. Nguyen, Q.V.: Disclosure of New Invention and Technology: Fully-Premixed Low-Emissions High-Pressure Multi-Fuel Burner. LEW–17786–1 (available for licensing Sept. 26, 2006), 2004.
10. Kojima, J.; and Nguyen, Q.–V.: Disclosure of New Invention and Technology: Frequency-Domain Method for Accurate Temperature Measurements in Hot Gases Using Low-Resolution Raman Spectroscopy. LEW–18100–1, 2006.
11. Nguyen, Quang-Viet; and Kojima, Jun N.: Quantitative, Single-Shot, Multi-scalar Measurements Demonstrated in a High-Pressure Swirl-Stabilized Turbulent Flame. Research & Technology 2006, NASA/TM—2007-214479, 2007, pp. 152–153. http://www.grc.nasa.gov/WWW/RT/2006/RT/RTB-nguyen2.html


**Find out more about Glenn's combustion diagnostics research:**
http://www.grc.nasa.gov/WWW/combustion/zDiag.htm


**Glenn contact:**
Dr. Quang-Viet Nguyen, 216–433–3574, Quang-Viet.Nguyen-1@nasa.gov

**Ohio Aerospace Institute (OAI) contact:**
Dr. Jun Kojima, 440–962–3095, Jun.N.Kojima@nasa.gov

**Authors:**
Dr. Quang-Viet Nguyen and
Dr. Jun N. Kojima


**Headquarters program office:**
Aeronautics Research Mission Directorate

**Programs/projects:**
Fundamental Aeronautics, Subsonic Fixed Wing, Supersonics

# Quantitative, Single-Shot, Multiscalar Measurements Demonstrated in a High-Pressure, Swirl-Stabilized Turbulent Flame

Understanding the physics of turbulence-chemistry interactions in practical low-emissions aircraft engine combustors, as well as accurately modeling and predicting their performance, is critical to the successful development of a new generation of aircraft engines that will have a low environmental impact on global air quality and climate change. With the increasing complexity of modern aircraft engines and their combustors, the traditional process of "cut-and-try" hardware testing is becoming prohibitively expensive. Thus, the development of aircraft engine computer simulations with predictive capabilities has become an economically driven need.

Before these predictive simulations can be used, they must be validated with careful comparisons with experiments. Researchers from the Combustion Branch of the NASA Glenn Research Center and from the Ohio Aerospace Institute (OAI) have made significant progress toward this goal by providing a data set for validating high-pressure turbulent flames. This data set is the first of its kind and provides a set of quantitative multiscalar data in a high-pressure, swirl-stabilized gaseous combustion using a time-resolved laser Raman diagnostics technique that was developed over the past 5 years (refs. 1 to 5).

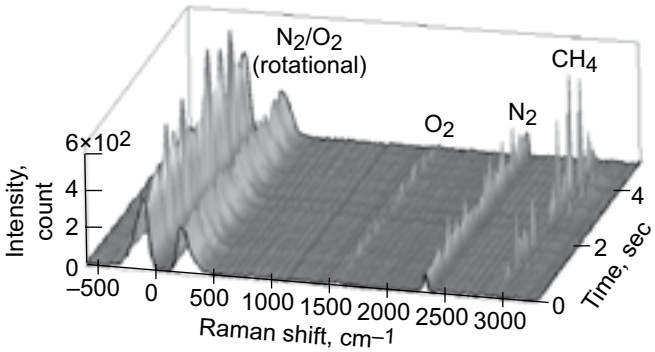


*A shot-to-shot (temporal) variation of spontaneous laser Raman-scattering spectra measured in a high-pressure (5-atm) swirl-flow methane-air non-premixed flame at a global equivalence ratio $\phi$ of 0.5.*

The preceding figure shows typical single-shot Raman spectral data acquired at a 10-Hz repetition rate by the Raman apparatus. Note the shot-to-shot variations in the Raman signal for each species—oxygen ($O_2$), nitrogen ($N_2$), and methane ($CH_4$)—indicating that the flame is highly turbulent and unsteady. From this single-shot data, we successfully determined the instantaneous temperatures of this turbulent flame with a precision of better than 3 percent by using a newly developed rotational bandwidth thermometry technique (which was also developed by the authors, ref. 6). The species concentrations were also determined from the vibrational bands in the same spectra with the aid of a quantitative calibration (ref. 7).

The results are shown in the figure on the next page—a histogram of the temperature measured in two regions of a turbulent flame. In the highly turbulent region of the flame, the data vary in temperature from 500 to 2500 K, whereas in the less-turbulent postflame region, the data have a smaller temperature variation and a lower averaged temperature. The figure also shows the scatter plots of $O_2$ and $CH_4$ concentrations versus temperature in the two different locations. This scatter-plot data of fuel and oxidizer mixing shows the profound effect of unsteadiness on turbulence-chemistry interactions.

These results are the first-ever quantitative multiscalar measurements that show details of the nature of turbulent mixing and its impact on chemical reactions in a realistic swirl-stabilized flame at elevated pressure. The data presented here permit comparison with models for code validation and provide critical insight into the performance of the fuel injector and the subsequent combustion process. For example, a significant amount of unmixed and unburned pockets of fuel (i.e., data points with temperatures lower than the ignition temperature and with higher concentrations of fuel) can be seen in the wide scatter of the data points, which indicates that incomplete combustion occurred locally around the edge of the flame.

Through spectroscopic data reductions and subsequent statistical analyses, the probability density functions of all the species and the temperatures can be derived as a function of mixture fraction, and this can be used to characterize the scalar structure of the turbulent flame. Such information from the multiscalar measurements will validate reacting computational fluid dynamics codes such as NASA's National Combustor Code (NCC) (ref. 8).

**References**


1. Kojima, Jun; and Nguyen, Quang-Viet: Disclosure of Invention and New Technology (Including Software), Laser-Raman Spectral Analysis Software for Combustion Diagnostics. LEW–17769–1, 2004.

2. Kojima, J.; and Nguyen, Q.-V.: Quantitative Analysis on Spectral Interference of Spontaneous Raman Scattering in High-Pressure Fuel-Rich Hydrogen-Air Combustion. J. Quant. Spectrosc. Radiat. Transf., vol. 94, nos. 3–4, 2005, pp. 439–466.
3. Nguyen, Quang-Viet: Spontaneous Raman Scattering (SRS) System for Calibrating High-Pressure Flames Became Operational. Research & Technology 2002, NASA/TM—2003-211990, 2003, pp. 117–118. http://www.grc.nasa.gov/WWW/RT2002/5000/5830nguyen2.html
4. Kojima, J.; and Nguyen, Q.V.: Measurement and Simulation of Spontaneous Raman Scattering Spectra in High-Pressure, Fuel-Rich $H_2$-Air Flames. Meas. Sci. Tech., vol. 15, no. 3, 2004, pp. 565–580.
5. Nguyen, Quang-Viet; and Kojima, Jun: Transferable Calibration Standard Developed for Quantitative Raman Scattering Diagnostics in High-Pressure Flames. Research & Technology 2004, NASA/TM—2005-213419, 2005, pp. 170–172. http://www.grc.nasa.gov/WWW/RT/2004/RT/RTB-nguyen.html
6. Nguyen, Quang-Viet; and Kojima, Jun N.: Alternative Rotational Raman Thermometry Developed for Turbulent Combustion. Research & Technology 2006, NASA/TM—2007-214479, 2007, pp. 149–151. http://www.grc.nasa.gov/WWW/RT/2006/RT/RTB-nguyen1.html
7. Kojima, Jun; and Nguyen, Quang-Viet: Strategy for Multiscalar Raman Diagnostics in High-Pressure Hydrogen Flames. New Developments in Combustion Research, William J. Carey, ed., NOVA Science Publishers, New York, NY, 2006, pp. 227–256.
8. Iannetti, A.: National Combustion Code Validated Against Lean Direct Injection Flow Field Data. Research & Technology 2002, NASA/TM—2003-211990, 2003, pp. 114–116. http://www.grc.nasa.gov/WWW/RT2002/5000/5830iannetti.html


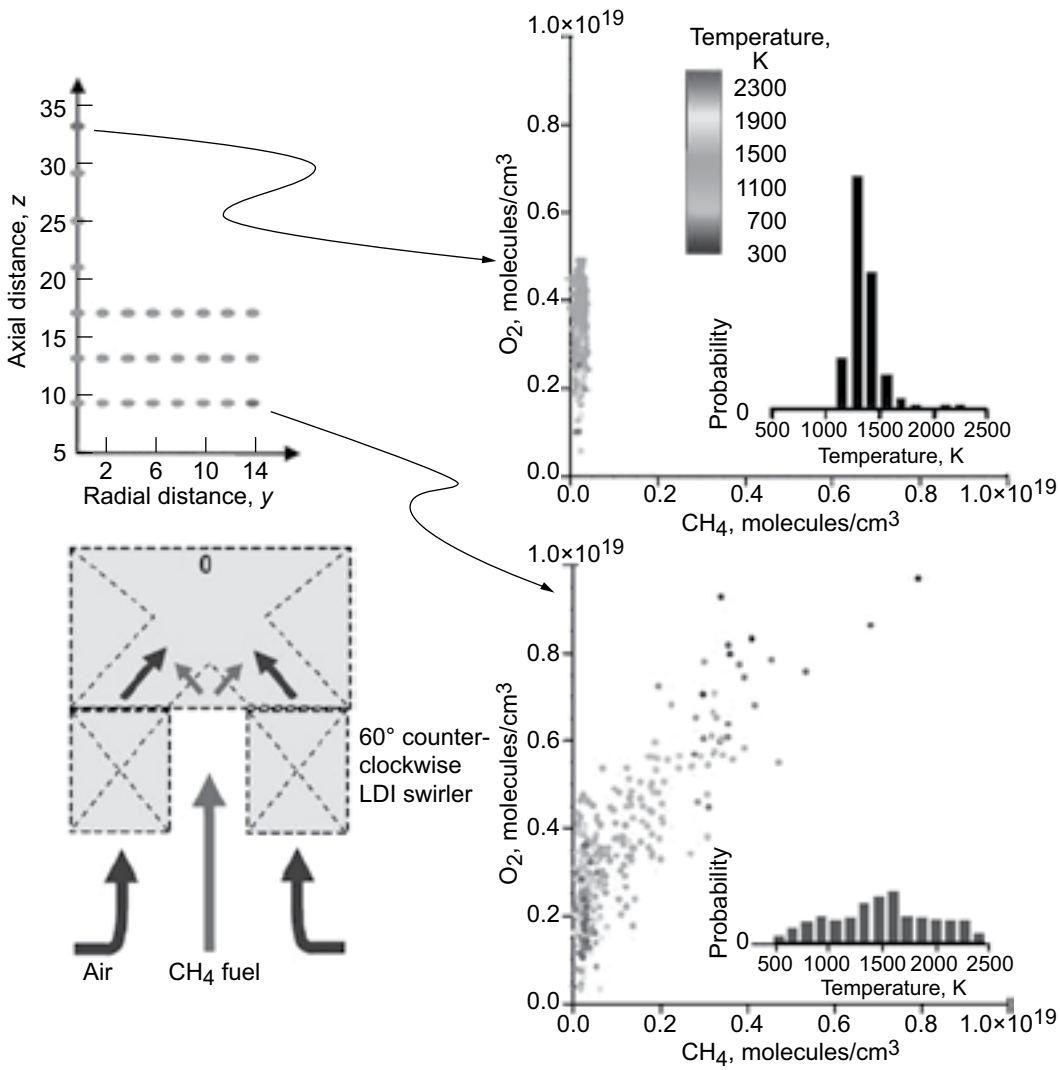


*Quantitative multiscalar data (fuel-oxidizer-temperature correlation) analyzed for single-shot measurement data in a high-pressure turbulent flame provided by a lean direct-injection (LDI) burner. This figure is shown in color in the online version of this article (http://www.grc.nasa.gov/WWW/RT/2006/RT/RTB-nguyen2.html).*

**Find out more about Glenn's combustion diagnostics research:**
http://www.grc.nasa.gov/WWW/combustion/zDiag.html


**Glenn contact:**
Dr. Quang-Viet Nguyen, 216–433–3574, Quang-Viet.Nguyen-1@nasa.gov

**Ohio Aerospace Institute (OAI) contact:**
Dr. Jun Kojima, 440–962–3095, Jun.N.Kojima@nasa.gov

**Authors:**
Dr. Quang-Viet Nguyen and Dr. Jun N. Kojima


**Headquarters program office:**
Aeronautics Research Mission Directorate

**Programs/projects:**
Fundamental Aeronautics, Subsonic Fixed Wing; Supersonics


**Special recognition:**
The data presented in this article were obtained with the aid of a technology developed by Dr. Nguyen (U.S. Patent 6,937,331, "High-speed electromechanical shutter for imaging spectrographs") that received an Exceptional Invention Award by the NASA Contributions and Inventions Board.

# High-Throughput Triple-Grating Spectrograph Developed for Nonintrusive Measurements of Combustion-Generated Plasmas

Researchers from the Combustion Branch of the NASA Glenn Research Center and from the Ohio Aerospace Institute (OAI) have developed and tested a novel high-throughput triple-grating spectrograph (TGS) for high-resolution, high-sensitivity, pure-rotational Raman and/or Thomson scattering spectroscopic studies. Rotational Raman scattering is the inelastic scattering of light from a molecule corresponding to the molecule's rotational quantum state and number density, and Thomson scattering is the inelastic scattering of light from electrons corresponding to the electron's translational temperature and density. By combining pure-rotational Raman and Thomson scattering with the gas-phase temperature, we can simultaneously measure the electron temperature and electron number density in aerospace engine combustion environments that contain low-temperature combustion plasmas.

In order to see the faint rotational-Raman and Thomson scattering over the intense background scattered stray light at the laser wavelength, we use a double-subtractive imaging spectrograph as a narrow-band (0.5-nm) notch filter with a $10^9$ optical rejection of the laser wavelength. In a double-subtractive imaging spectrograph, the first grating spectrograph disperses the light according to wavelength along a focal plane. An optical mask (an opaque strip), placed at the focal plane at a location corresponding to the excitation laser wavelength blocks the laser line; then a second grating spectrograph, arranged in mirrored geometry with respect to the first one, recombines the wavelength-dispersed light back to a single beam minus the laser wavelength. The width of the mask strip determines the notch filter width. The light from the double-subtractive spectrograph is then imaged into a third spectrograph to resolve and record the Raman/Thomson spectrum. Previous designs of double-subtractive spectrographs for studying Thomson scattering were described by van de Sande (ref. 1) and the references therein.

We have improved upon the relatively low throughput (optical aperture ratio of *f*/6) and bulky design in (ref. 1) with the compact (portable), all-transmissive design shown in the following figure. Our design utilizes custom-made volume-phase holographic (VPH) gratings and compact 35-mm camera lenses to realize a compact TGS with superlative optical throughput (*f*/2), high-resolution, and excellent imaging properties. The figure shows the current TGS design used with a linear 18-by-1 fiber-optic array that collects the Raman/Thomson signal scattered from an injection-seeded Q-switched Nd:YAG[1] laser. The spectrum is dispersed with a grating-prism (GRISM) spectrograph, and the signal is recorded using an intensified charge-coupled device (ICCD) camera.

The photograph on the next page shows the TGS setup. As can be seen from the optical breadboard with the 1-in. bolt-hole center, the TGS occupies less than 18 by 18 in. of space. The graph shows the pure-rotational Raman scattering

[1]Neodymium: yttrium aluminum garnet.

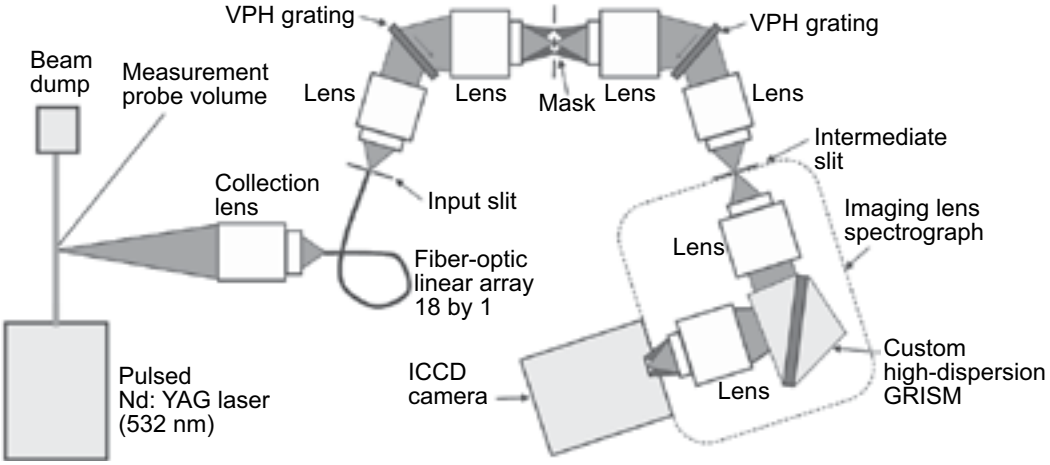


*TGS system showing the fiber-optic linear-array input for light collection, lenses, volume-phase holographic (VPH) gratings, optical mask, imaging spectrograph, and intensified charge-coupled device (ICCD) camera.*

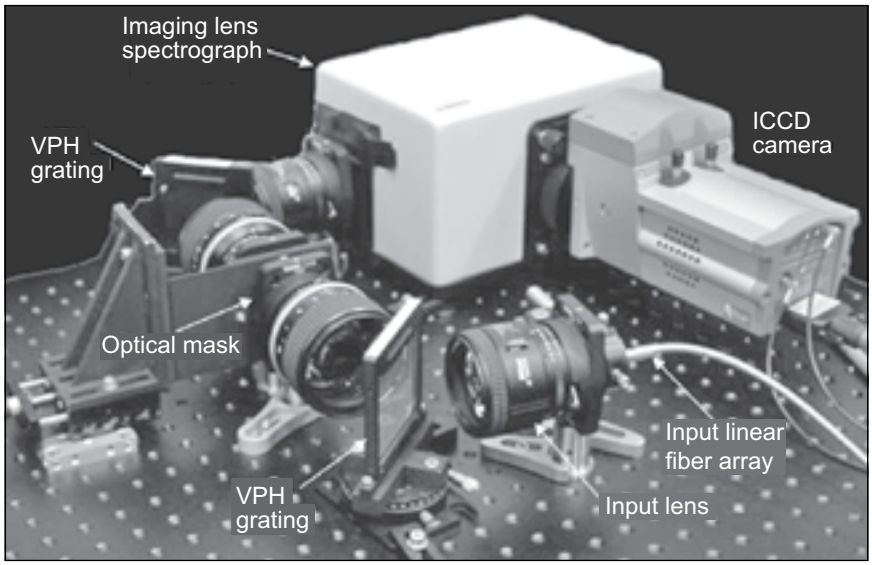


*TGS system as mounted on an optical breadboard with 1-in. bolt hole center spacing. Note that, on the lower left of the photograph, a translation stage for the mask permits wavelength tuning of the notch filter central wavelength.*

data of pure nitrogen ($N_2$) obtained with the TGS system (averaged over 200 laser shots). The individual rotational lines of $N_2$ starting from $J = 0$ (12-cm$^{-1}$ shift) can clearly be seen (here, $J$ is the rotational quantum number). The graph also shows the optical notch filter function (obtained using white light), which has a measured 0.52-nm (16-cm$^{-1}$) full-width at half-max (FWHM) notch. This permits spectral features as close as 8 cm$^{-1}$ to be observed and recorded. To the author's knowledge, this is the highest optical throughput *f*/2 imaging TGS system ever described.

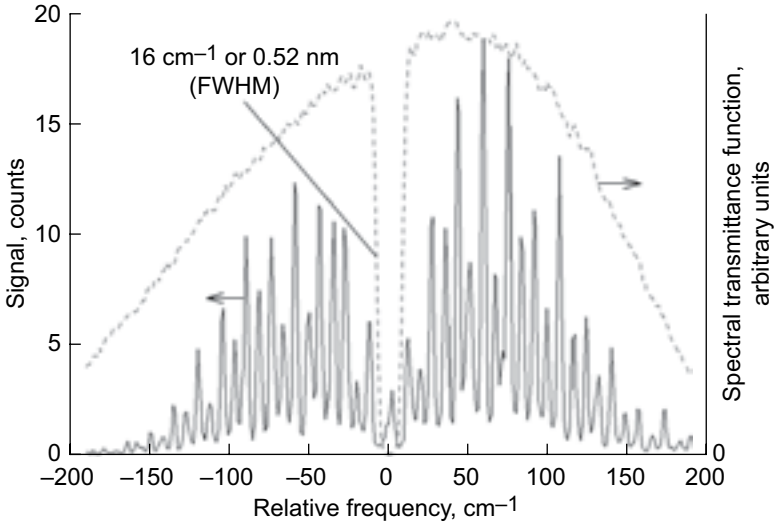


*200-shot average pure rotational Raman spectrum of $N_2$ superimposed with the transmission function from a white light source.*

**References**

1. van de Sande, Marcus Johannes: Laser Scattering on Low Temperature Plasmas. High Resolution and Stray Light Rejection. Ph.D. Thesis, Technische Univ. Eindhoven, The Netherlands, 2002.

**Find out more about the research of Glenn's Combustion Branch:**
http://www.grc.nasa.gov/WWW/combustion/zDiag.html

**Glenn contact:**
Dr. Quang-Viet Nguyen, 216–433–3574, Quang-Viet.Nguyen-1@nasa.gov

**Ohio Aerospace Institute (OAI) contact:**
Dr. Jun Kojima, 440–962–3095, Jun.N.Kojima@nasa.gov

**Authors:**
Dr. Quang-Viet Nguyen and
Dr. Jun N. Kojima

**Headquarters program office:**
Aeronautics Research Mission Directorate

**Programs/projects:**
Fundamental Aeronautics (Supersonics)

# Outer Planet Mining Vehicle Design Issues Identified and Analyzed

At the NASA Glenn Research Center, concepts and scenarios for the atmospheric mining of the outer planets were investigated (ref. 1). In 2006, atmospheric mining concepts first identified in 2005 were further refined to determine which concepts were the most promising. Although helium 3 (3He) is a primary product to be wrested from the atmosphere, hydrogen and other gases are also of great interest. These gases would be liquefied and used as fuels for either chemical rockets or other advanced propulsion concepts (rockets using fission or fusion energy, etc.). Three mining concepts were analyzed: atmospheric scoopers, cruisers, and balloons. The system complexity for these mining facilities in the atmospheres of Uranus and Neptune were assessed.

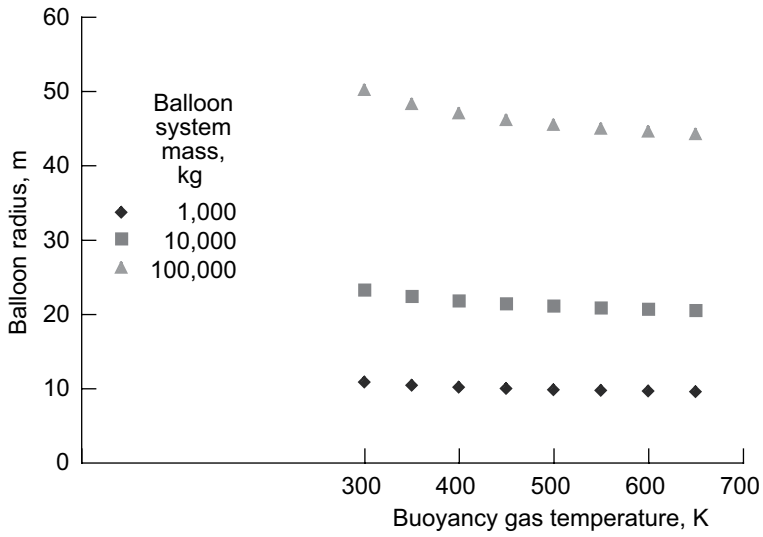


*Mining balloon radius versus buoyancy gas temperature. Temperature = 70 K in hydrogen environment with helium buoyancy gas.*

One sizing issue is balloon system mass and radius. Balloon-borne mining vehicles will likely require very large payloads. The preceding graph shows the overall size of the balloons. The balloon initial mass range is from 1000 to 100,000 kg. This initial mass includes the payload, balloon envelope, supporting onboard subsystems, and buoyancy gas. For payloads of 100,000 kg, the balloon radius is approximately 44 to 50 m. The graph on the next page shows the payload mass that can be supported. At very high gas temperatures—over 600 K—the balloon payload can be very high. At a buoyancy gas temperature of 600 K and an initial mass of 100,000 kg, the balloon payload can be 70,000 kg.

For outer planet mining, the following vehicles and facilities would be needed:

(1) Nuclear electric propulsion (NEP) interplanetary transfer vehicles
(2) Atmospheric mining vehicles
(3) Atmospheric to outer planet moon transfer vehicles (aerospacecraft)
(4) Outer planet orbital transfer vehicles (traveling between the moons, etc.)
(5) Factories to refurbish aerospacecraft and fuel capsules
(6) Storage facilities on the outer planet moon

For lunar mining, the following vehicles would be needed:

(1) Earth-to-Moon transfer vehicles
(2) Lunar landing and ascent vehicles
(3) Lunar surface mining vehicles
(4) Storage facilities on the Moon

In the near term for 3He mining, lunar regolith (dust and rock) mining might be more effective than outer planet atmospheric mining. However, from the number of maneuvers discussed in earlier research (ref. 2) and the number of spacecraft needed to allow the return of the 3He to Earth, it is not clear which option would be more effective. Even though the 3He reserves on Earth's Moon may be in the parts per billion range per ton of mined material, the deciding factor will likely be the effectiveness and reliability of factories for processing regolith versus that for factories processing atmospheric gases.

Mining outer planet atmospheres will require a small fleet of space and aerodynamic vehicles (or "aerospacecraft"). Options for balloons and atmospheric cruisers were assessed and found to be feasible for small and large mining missions. The technologies needed for quick trips to the outer solar systems may be 100-MWe-class nuclear-electric-propulsion interplanetary vehicles, lightweight mining systems, and highly

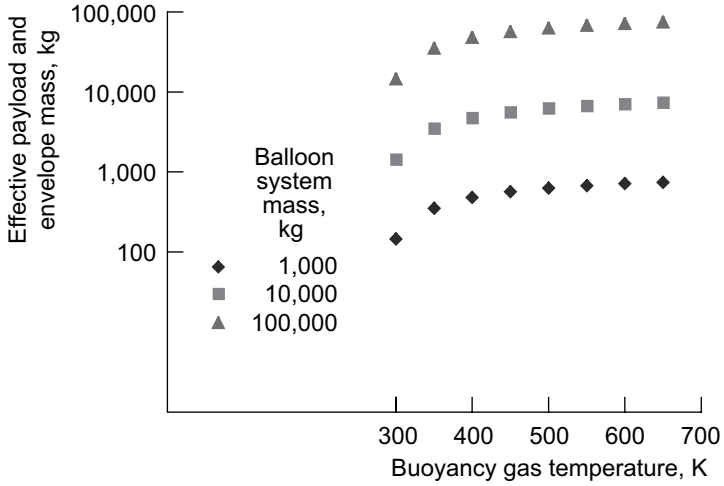


*Mining balloon effective payload mass versus buoyancy gas temperature. Temperature = 70 K in hydrogen environment with helium buoyancy gas.*

reliable autonomous aircraft, aerospacecraft, and balloon systems. On the basis of past estimates of 3He production from the outer planets and the apparent complexity of the mining systems, it seems that relatively small amounts of 3He will likely to be returned to Earth with such mining techniques. Using 3He at the factory's outer planet location might be the best use of the fuel.

**References**

1. Palaszewski, B.: Atmospheric Mining in the Outer Solar System: Vehicle Sizing Issues. AIAA–2006–5222, 2006.
2. Palaszewski, B.: Atmospheric Mining in the Outer Solar System. NASA/TM—2006-214122 (AIAA–2005–4319), 2006. http://gltrs.grc.nasa.gov/Citations.aspx?id=78

**Find out more about fuels and space propellants for reusable launch vehicles:**
http://sbir.grc.nasa.gov/launch/foctopsb.htm

**Glenn contact:**
Bryan Palaszewski, 216–977–7493,
Fax: 216–433–5802,
Bryan.A.Palaszewski@nasa.gov

**Author:**
Bryan A. Palaszewski

**Headquarters program office:**
Exploration Systems Mission Directorate

**Programs/projects:**
Nuclear propulsion, Supersonics, Subsonics, Hypersonics

## Aerospace Fuels Assessed for Future Aerospace Vehicles

From 2001 to 2006, as part of the Revolutionary Aeropropulsion Concepts project, gelled fuels and their derivatives were assessed for future aerospace vehicles at the NASA Glenn Research Center. Future fuels with higher energy may be needed for larger, more capable vehicle flying at supersonic and hypersonic speeds.

APPLICATIONS MATRIX: FUEL POSSIBILITIES FROM SUBSONIC FLIGHT TO SPACE FLIGHT

| Fuel or propellant type | Speed regime | | | |
|---|---|---|---|---|
| | Subsonic | Supersonic | Hypersonic | Space |
| Ungelled (neat) | √ | √ | √ | √ |
| Gelled | √ | √ | √ | √ |
| Metallized gelled | (a) | √, (a) | √ | √ |

[a]Atmospheric emissions and effects may preclude the use of metallized gelled fuels for high-volume subsonic and supersonic commercial aircraft traffic.

In 2006, studies were conducted of gelled fuels for a series of aerospace missions, including lunar, Mars, and missile propulsion. A matrix (see the table) was generated to illustrate the areas of application for gelled fuels. Both ungelled and gelled fuels would have broad applications over the full set of speed regimes: from subsonic flight to space flight.

Because they use metal particles, metallized gelled fuels would likely be used only in specialized subsonic and supersonic applications. For example, use in a small fleet of aircraft would be more likely than use in large fleets of commercial aircraft.

In addition, both hypersonic and space flight vehicles are excellent candidates for metallized gelled fuels. These vehicles are usually limited to smaller volumes, and the higher density of the metallized fuels will likely make a good performance match with these very high speed applications. The more the dense the fuel is, the easier it is to package the fuel tanks in the aerospace vehicle.

Historical reviews of the work with methane-fueled aircraft have been enlightening. The gelling of methane required a small fraction, about 1 wt%, of water to be added to the fuel. At liquid methane's cryogenic temperatures, the water becomes frozen particles in the fuel. Extensive design studies were conducted for using liquid methane on future airliners. The density of the fuel is lower than that of a liquid hydrocarbon such as jet fuel. Additional volume is generally needed for the cryogenic liquid fuels. Thus, typically the methane fuel tanks were integrated into a large fraction of the main aircraft fuselage rather than simply placing the fuel in the wing tanks. The advanced airliner was able to deliver performance that was very comparable to that of aircraft using tradition jet fuel (JP). These studies were used to direct new NASA studies of aerospace vehicles and led to a better direction for new gelled methane research.

Hypersonic and space flight vehicles also benefit from higher density cryogenic fuels. The use of gelled fuel could reduce the overall volume of a hypersonic vehicle, making room for added payload or allowing a smaller more compact vehicle to be created. Human Mars missions, in particular, would benefit from metallized gelled hydrogen fuel. An increase of payload mass of 20 to 33 percent over that of traditional oxygen/hydrogen-fueled rocket engines would be possible.

**Bibliography**

Carson, L.K., et al.: Study of Methane Fuel for Subsonic Transport Aircraft; Final Report. NASA CR–159320, 1980.

Harloff, Gary J.; and Berkowitz, Brian M.: HASA: Hypersonic Aerospace Sizing Analysis for the Preliminary Design of Aerospace Vehicles; Final Contractor Report. NASA CR–182226, 1988.

Kinoshita, Y., et al.: Studies on Methane-Fuel Ram Combustor for HST Combined Cycle Engine. Proceedings of the 11th International Symposium on Air Breathing Engines, ISABE 93–7080, vol. 2, 1993, pp. 822–830.

Palaszewski, Bryan A.: Metallized Propellants for the Human Exploration of Mars. NASA TP–3062, 1990.

Petley, Dennis H.; and Jones, Stuart C.: Thermal Management for a Mach 5 Cruise Aircraft Using Endothermic Fuel. AIAA–90–3284, 1990.

Sindt, C.F.; and Ludtke, P.R.: Characteristics of Slush and Boiling Methane and Methane Mixtures. Progress in Refrigeration Science and Technology, National Bureau of Standards, Contract Number NASA Order W–12893, vol. 1, AVI Publishing Co., Inc., Westport, CT, 1973, pp. 315–320.

Wall, E.M.V.: Investigation of the Suitability of Gelled Methane for Use in a Jet Engine. Final Report, 15 Jun. 1970–15 Feb. 1971, NASA CR–72876, 1971.

**Find out more about fuels and space propellants for reusable launch vehicles:**
http://sbir.grc.nasa.gov/launch/foctopsb.htm

**Glenn contact:**
Bryan Palaszewski, 216–977–7493,
Fax: 216–433–5802,
Bryan.A.Palaszewski@nasa.gov

**Author:**
Bryan A. Palaszewski

**Headquarters program office:**
Exploration Systems Mission Directorate,
Aeronautics Research Mission Directorate

**Programs/projects:**
Supersonics, Subsonics, Hypersonics,
Crew Exploration Vehicle

# Fuel-Injector Concepts Investigated in the Fuel-Reforming Injector Test Facility

The NASA Glenn Research Center's Fuel Reformer Injector Test facility (shown in the photograph) provides the means to perform catalytic fuel-reforming research, including the evaluation of feed-delivery systems and reforming catalysts. Fuel reforming converts hydrocarbon fuels into a hydrogen-rich syngas, also called reformate, which contains hydrogen ($H_2$), carbon monoxide (CO), carbon dioxide ($CO_2$), and traces of unreacted feeds. Reformate is an acceptable feed for a solid oxide fuel cell (SOFC) to produce electrical power. Fuel reforming requires steam and air co-feeds with the hydrocarbon fuels where feed-mixing characteristics are critical in achieving optimal reforming efficiency. Our research at Glenn focused on evaluating advanced fuel injector/mixer designs by measuring velocity and compositional profiles using nondestructive laser diagnostics. Various injector/mixer concepts have been ranked according to flow field uniformity and fuel distribution. Future plans are to conduct reforming experiments correlating injector/mixer designs with reforming catalysts under a set of protocol operating conditions, which will provide a better understanding of injector mixing and catalyst performance.

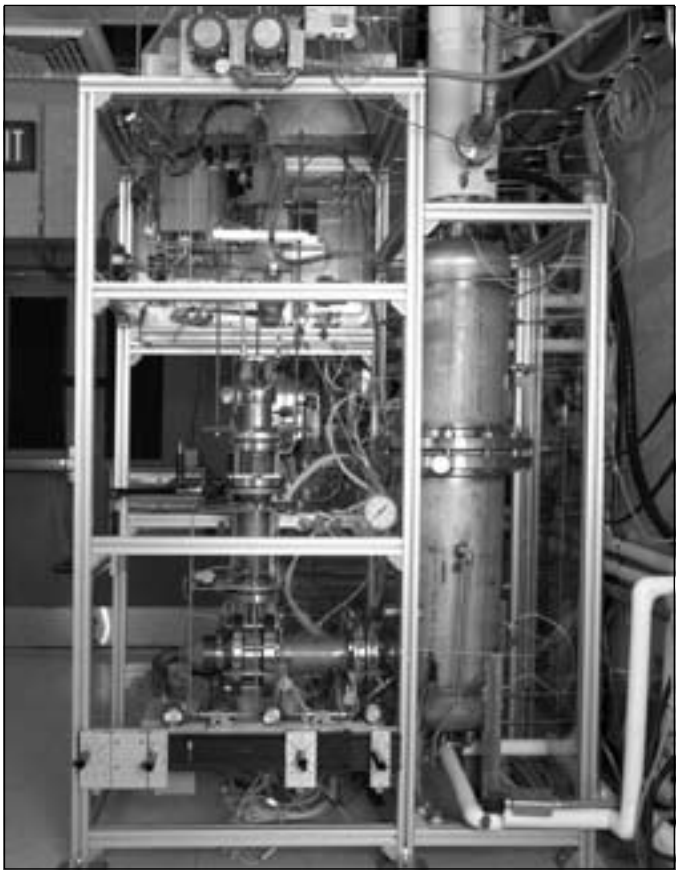

*Hardware setup of the Reformer Injector Test Rig containing a quartz window for laser diagnostics. This quartz window may be replaced with a reformer to produce syngas.*

The injector test facility can operate with liquid and vaporized hydrocarbon fuels and gaseous fuels, such as methane. We have tested injectors using commercial aviation Jet-A fuel, diesel, and gaseous methane. Liquid fuel was atomized and mixed with steam and/or air before being directed into a downstream quartz window or reformer.

This test facility was designed with the flexibility to operate in various reforming configurations including steam reforming (SR), autothermal reforming (ATR), and catalytic partial oxidation (CPOX), and to accommodate different catalyst types such as monolith, microlith, and catalyst pellets. The facility can handle reformate pressures up to 25 psig and a maximum outlet temperature of 1400 °F.

Characterization of reformer feed mixtures was accomplished by utilizing advanced laser diagnostic techniques including Raman spectroscopy and particle imaging velocimetry (PIV). These techniques revealed injector patternization, flow visualization, velocity contours, and fuel-air-steam mixing characteristics.

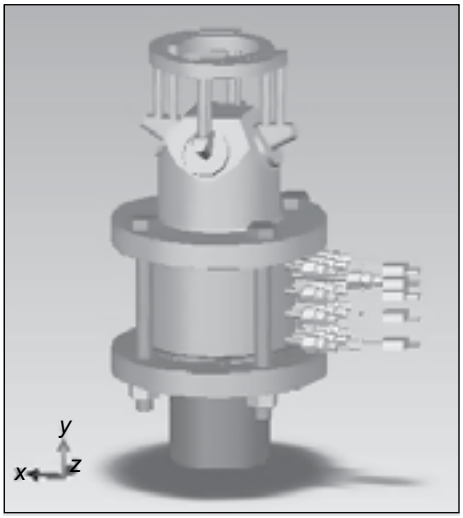


*Top: Three-dimensional model of the NASA-Goodrich impingement syphon injector. Center: Precision Combustion's ATR microlith reformer.*

The reformer test facility evaluated the following fuel-injector concepts:

- Goodrich impingement jet syphon (shown in the illustration on the preceding page) (fiscal year 2005, FY05)
- Goodrich gas-assisted simplex (FY05)
- Department of Energy multipoint impingement jet (FY05)
- Sun Valley cone mixer (FY05)
- NASA in-house swirl-venturi mixer (FY06)

The Goodrich gas-assisted simplex and NASA swirl-venturi mixer were ranked the best concepts with the most uniform velocity field and fuel distribution profile.

This test facility was also used in collaboration with Catacel Corp. (small business), the Department of Energy's Solid Energy Conversion Alliance program, and the Ohio Third Frontier Action Program with SOFC. For additional information on reforming catalysts and laser techniques used in Glenn's Injector Test Facility, please refer to the referenced articles.

**References**


1. Tomsik, Thomas M.: Catalytic Reforming Technologies Investigated for Hydrogen Production and Onboard Aerospace Power Generation. Research & Technology 2006, NASA/TM—2007-214479, 2007, pp. 171–172. http://www.grc.nasa.gov/WWW/RT/2006/RT/RTP-tomsik.html
2. Hicks, Yolanda R., et al.: Fuel Injector-Mixer Concepts Examined for Kerosene and Diesel Fuel Reformer Applications Using Laser-Based Techniques. Research & Technology 2006, NASA/TM—2007-214479, 2007, pp. 143–145. http://www.grc.nasa.gov/WWW/RT/2006/RT/RTB-hicks.html


**Find out more about the research of Glenn's Propulsion Systems Division:**
http://www.grc.nasa.gov/WWW/5000/propulsion/


**Glenn contacts:**
Angela D. Surgenor, 216–433–3251, Angela.D.Surgenor@nasa.gov

Thomas M. Tomsik, 216–977–7519, Thomas.M.Tomsik@nasa.gov

**University of Toledo contact:**
Judy Yen, 216–433–3626, Chia.H.Yen@nasa.gov

**Authors:**
Angela D. Surgenor and Chia H. Yen


**Headquarters program office:**
Aeronautics Research Mission Directorate

**Programs/projects:**
Subsonic Fixed Wing, Fuel Reforming

## Aerosol Microphysics in a Pressure-Reduction Chamber Predicted by Numerical Simulations

The NASA Glenn Research Center is currently engaged in characterizing the solid and volatile aerosol emissions from gas turbine combustors. A pressure-reduction chamber was fabricated at Glenn as a part of the aerosol sampling system, and a computational fluid dynamics code developed at Glenn was used to predict the evolution of the aerosol in the device.

To understand the impact of aircraft emissions on the environment, it is necessary to understand the formation and subsequent development of gaseous and aerosol emissions in the exhaust gas of jet engines. For gas and particle emissions to be measured accurately, the elevated pressure of the exhaust gas from the aircraft combustor must be brought down to the applicable range of the measuring devices.

A pressure reducer is a cylinderlike device that has an inlet tube at the top and an exit tube at the bottom. The schematic on the next page shows a typical pressure-reduction device. The portion of the inlet tube inside the pressure reducer may be expanded up to 5° to slow down the drop of the incoming pressure and temperature. In this study, the internal diameter (ID) of the inlet tube was 0.09 in., and the diameter at the exit of the inlet tube was 0.2646 in. because of

a 5° expansion. The gap distance was 2 in., the ID of the sample extraction tube was 0.34 in., and the diameter of the reducer was 3 in. The overall length of the domain that includes the inlet tube, the chamber, and the sample extraction tube was 35 in. (0.889 m). A chemistry mechanism having 29 species and 73 reactions was used, and the aerosol size distribution was divided into 12 bins. The size distribution of the soot particle was prescribed to be log-normal, with a median radius of 40 nm, modal widths of 1.5, and a total number density of $10^{13}$ particles/$m^3$.

Two cases are presented to show the chemical conversion and particle evolution in the device. The total pressures of the incoming gas were 65 and 255 psi, respectively. The total temperature was set to be 485 K for both cases. The exit pressure was set at 19.7 psi, and the pressure at the bleeding location was 14.7 psi. The wall temperature of the inlet tube entering the chamber was set to 477 K (400 °F); the rest of the wall was either at 450 K or was insulated. For the 65-psi case, the temperature was above 450 K from the inlet to the exit, hence the $H_2SO_4$-$H_2O$ droplets[1] could not be nucleated. For the 255-psi case, the temperature dropped to near 250 K at the end of the inlet tube. The distributions of $H_2SO_4$ mass fraction along the 0.018-in. line are shown in the following graph, which shows that the mass fraction increased in the straight portion of the inlet tube outside of the chamber region. This graph also indicates that the chamber had little influence on the evolution of $H_2SO_4$.

[1]Sulfuric acid-water droplets.

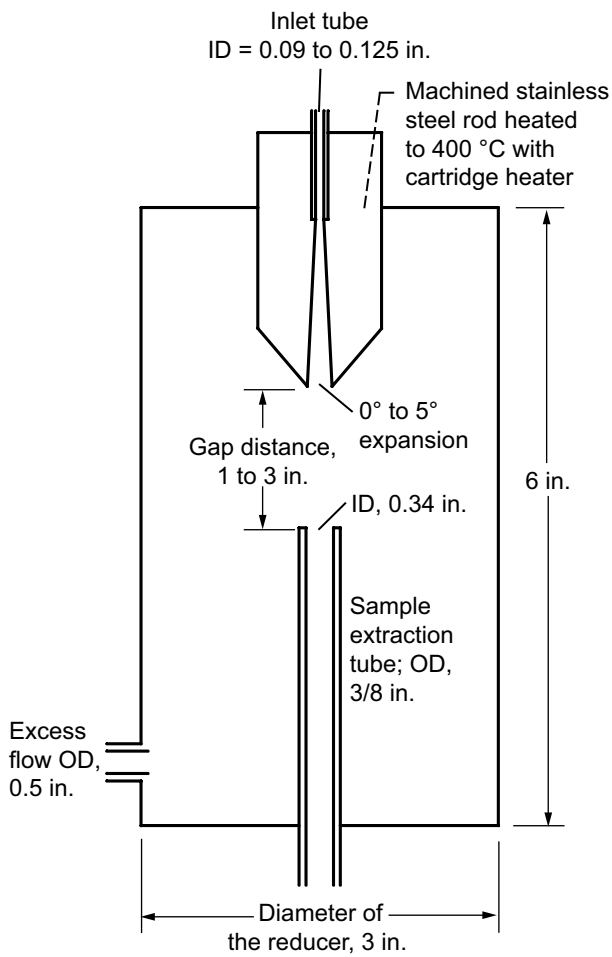


*Pressure-reduction chamber. OD, outside diameter of tube.*

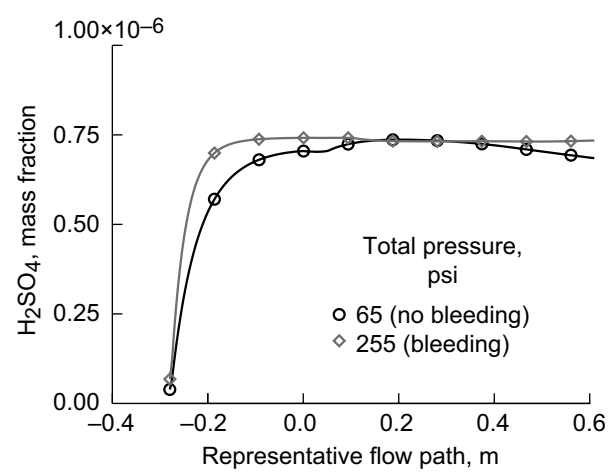


*$H_2SO_4$ distribution close to the centerline of the device (0.018 in. above the axis) for the 400 °F pressure-reduction chamber study.*

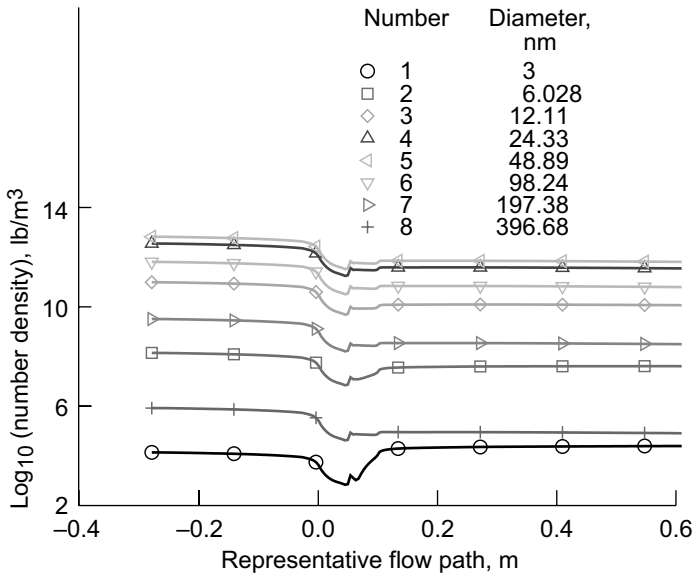


*Number density distribution of soot particles 0.018 in. above the axis for the 400 °F pressure-reduction chamber study.*

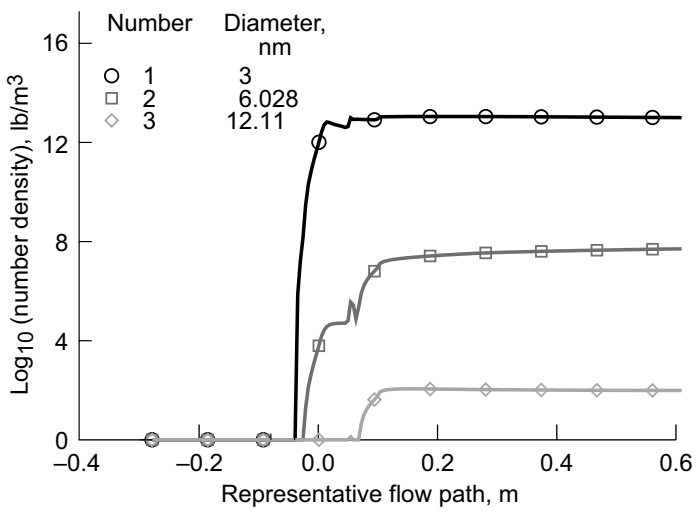


*Number density distribution of $H_2SO_4$-$H_2O$ droplets 0.018-in. above the axis for the 400 °F pressure-reduction chamber study.*

The top graph shows the number density distribution, in $\log_{10}$ scale, of the soot particles for the 255-psi case. The influence of the chamber on the size distribution of the soot particles is noticeable.

The bottom graph shows that the nucleation of $H_2SO_4$-$H_2O$ droplets is significant for the 255-psi case, so is the coagulation of droplets. Work to implement more aerosol microphysics models is in progress.

**Bibliography**

Wey, Thomas; and Liu, Nan-Suey: Modeling of Aerosols in Post-Combustor Flow Path and Sampling System. NASA/TM—2006-214397, 2006. http://gltrs.grc.nasa.gov/Citations.aspx?id=159

**Taitech, Inc. contact:**
Dr. Thomas Wey, 216–433–2934, Changju.T.Wey@nasa.gov

**Glenn contact:**
Dr. Nan-Suey Liu, 216–433–8722, Nan-Suey.Liu-1@nasa.gov

**Authors:**
Dr. Thomas Wey and Dr. Nan-Suey Liu

**Headquarters program office:**
Aeronautics Research Mission Directorate

**Programs/projects:**
Supersonic Project, Subsonic Fixed Wing Project

# Compressor Stability Model Developed

Jet engine compressors normally increase the pressure of the incoming air to high levels where combustion can occur efficiently. Occasionally disturbances in the incoming air can cause the compressor to lose pressure or stall, which can cause serious problems for the aircraft. Compressor stability, the ability of the compressor to resist stall, is very difficult to predict. In this work, a three-dimensional unsteady computer code called CSTALL was developed and used to investigate the stability of a transonic compressor stage.

CSTALL solves the unsteady inviscid (Euler) flow equations for the entire compressor, but rotor and stator blades are modeled using body force terms. This makes the code much faster than unsteady viscous (Navier-Stokes) codes but requires calibration of the body force model. A new formulation was developed at the NASA Glenn Research Center that allows the body force information to be calculated easily using a steady viscous code. Here, the SWIFT turbomachinery analysis code was used to analyze a transonic inlet stage for a core compressor called NASA stage 35 and to calculate calibration data for CSTALL.

CSTALL was first used in a two-dimensional throughflow mode to calculate the operating map for stage 35 and to estimate the stall point. The calculated operating map, stall point, and blade exit profiles agreed well with the original SWIFT calculations and experimental data. Calculated results with inlet radial distortion showed the expected loss of range.

CSTALL was then used in a three-dimensional mode to investigate inlet circumferential distortion over a 120° segment ahead of stage 35. The calculated operating map in the graph shows a loss in static pressure ratio that is comparable to experimental measurements. The bottom figure shows contours of computed axial velocity on a blade-to-blade surface near the tip of the compressor. To the right of the contour maps, the computational grid shows the locations of the rotor and stator. Steady calculations (top) show the low-velocity distorted flow ahead of the rotor. Stalled calculations (bottom) show unsteady rotating stall with two stall cells in the rotor and shock waves running upstream. The calculations predict recovery from stall when the exit pressure is reduced sufficiently.

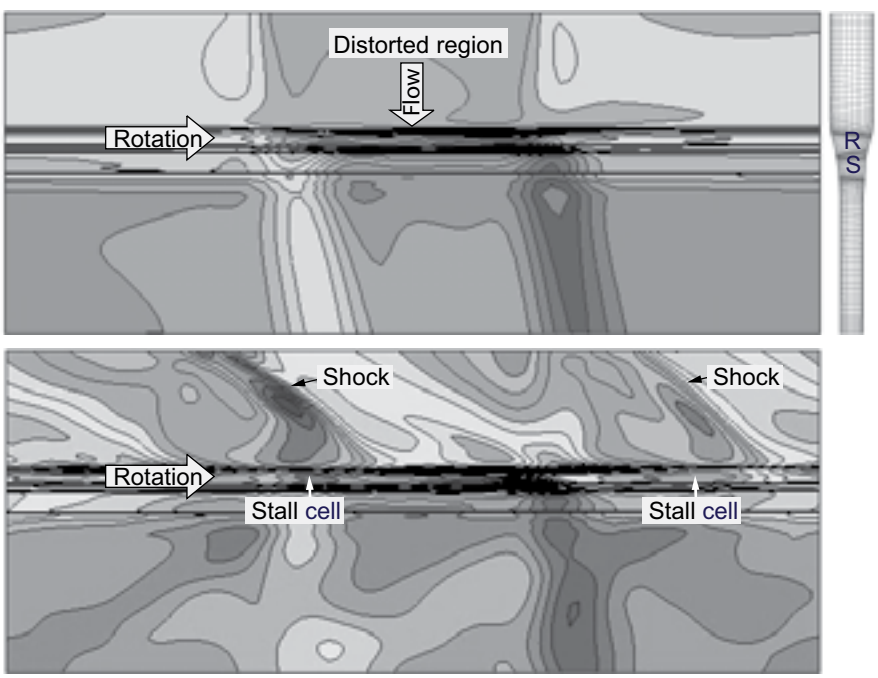


*Axial velocity contours on a blade-to-blade plane near the tip of a compressor stage. Right: Computational grid. Top: Steady flow with inlet distortion. Bottom: Unsteady rotating stall. This figure is shown in color in the online version of this article (http://www.grc.nasa.gov/WWW/RT/2006/RT/RTE-chima.html).*

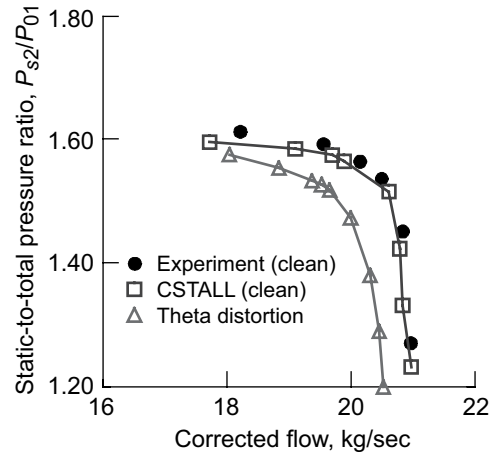


*Measured and calculated static-to-total pressure ratio for clean flow and flow with circumferential distortion.*

**Bibliography**
Chima, Rodrick V.: A Three-Dimensional Unsteady CFD Model of Compressor Stability. ASME Paper GT2006–90040 (NASA/TM—2006-214177), 2006. http://gltrs.grc.nasa.gov/Citations.aspx?id=73

**Find out more about computational fluid dynamics codes for turbomachinery:**
http://www.grc.nasa.gov/WWW/5810/rvc/

**Glenn contact:**
Dr. Rodrick V. Chima, 216–433–5919, Rodrick.V.Chima@nasa.gov

**Author:**
Dr. Rodrick V. Chima

**Headquarters program office:**
Aeronautics Research Mission Directorate

**Programs/projects:**
Intelligent Propulsion Systems Foundation Technology

# Baseline Inlet Tests Conducted for Supersonic Inlet Flow Control in a Partial Isentropic External Compression Inlet

Bleed has traditionally been used to improve the health of the boundary layer in supersonic aircraft engine inlets. However, the use of bleed adds mechanical complexity and increases the size of the inlet needed for a given engine mass flow requirement. Computational fluid dynamics (CFD) simulations in mixed compression inlets and small-scale shock-boundary layer interaction experimental and CFD results have shown that arrays of microdevices have the potential to reduce or eliminate the need for bleed. However, an inlet with microdevice arrays has not been tested in a wind tunnel. To provide baseline inlet data for a future inlet test with microdevices, researchers at the NASA Glenn Research Center tested a family of five external compression inlets in Glenn's 1- by 1-Foot Supersonic Wind Tunnel. These inlets had neither bleed nor microdevices. The tests were performed under the Fundamental Aeronautics program and a partially reimbursable Space Act Agreement with Gulfstream Aerospace Corporation.

The inlets tested, which were based on a design developed by Gulfstream Aerospace Corporation, included a partially isentropic compression surface. The external compression surface was the same for all five inlets; they differed only in the subsonic diffuser length and in the centerbody diameter at the aerodynamic interface plane (AIP). Two subsonic diffuser lengths and three centerbody diameters were studied. The three inlets with the long subsonic diffuser were made with all three AIP centerbody diameters; the two inlets with the short subsonic diffuser were made with only the largest and smallest AIP centerbody diameters.

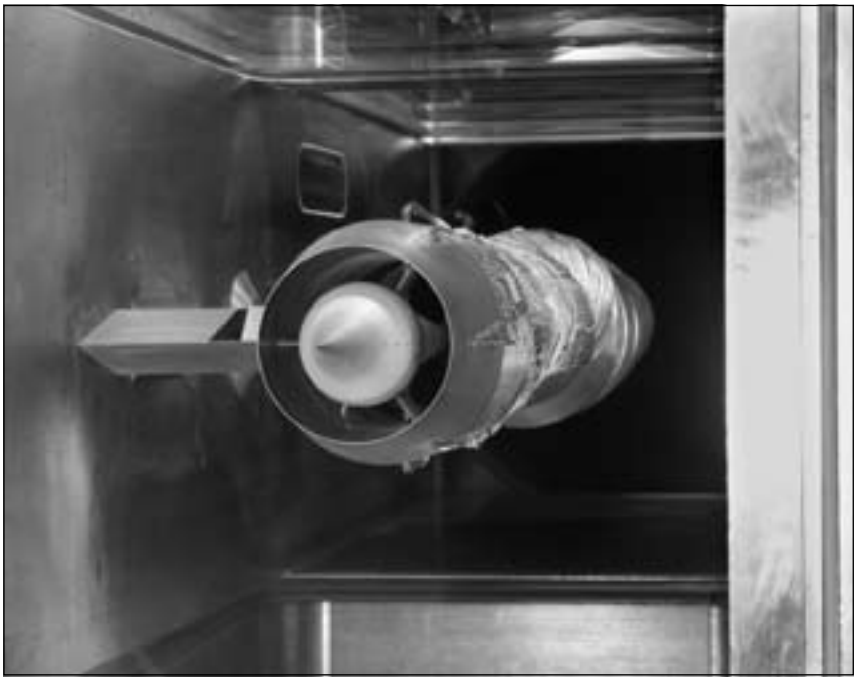

*Inlet installed in Glenn's 1- by 1-Foot Supersonic Wind Tunnel.*

All inlet testing was done at a tunnel mach number of 1.97. The experimental test results were compared with CFD calculations done by Glenn and Gulfstream Aerospace Corporation. The Wind code was used for Glenn's CFD calculations, and the Overflow code was used for Gulfstream's calculations. NASA and Gulfstream CFD results compared well with each other and with the experimental results.

The CFD and experimental results from Glenn's 1- by 1-Foot Supersonic Wind Tunnel will be used to determine which inlet design will be chosen for possible further study. In addition, a CFD study of this inlet may be done to determine the optimal location for an array of microramps. Then, a larger scale wind tunnel model may be tested in cooperation with Gulfstream Aerospace Corporation.

**Find out more about the research of Glenn's Inlet and Nozzle Branch:**
http://www.grc.nasa.gov/WWW/RTE/

**Glenn contacts:**
Dr. Kathleen M. Tacina, 216–433–6660, Kathleen.M.Tacina@nasa.gov

Stefanie M. Hirt, 216–433–6782, Stefanie.M.Hirt@nasa.gov

Bernhard H. Anderson, 216–433–5822, Bernhard.H.Anderson@nasa.gov

**Authors:**
Dr. Kathleen M. Tacina, Stefanie M. Hirt, Bernhard H. Anderson,
Dr. Jason M. Merret, Timothy R. Conners, and Donald C. Howe

**Headquarters program office:**
Aeronautics Research Mission Directorate

**Programs/projects:**
Fundamental Aeronautics, Space Act Agreement with Gulfstream

# Wind-US Code Updated

In October 2004, the NPARC (National Program for Application-Oriented Research in CFD) Alliance released Wind-US 1.0, the latest in its line of general-purpose, multizone, compressible flow solvers. Since then, several new features have been added, and existing capabilities have been improved, in preparation for the release of Wind-US 2.0 in 2007.

The unstructured grid solver, initially added in Wind-US 1.0, has been completely rewritten and has been incorporated at a lower level in the code structure. This allows more commonality between the structured and unstructured solvers, making the resulting code easier to maintain. More importantly, it is now easier to add new features that will apply to both types of grids. As a result, many of the capabilities that could only be used with structured grids in Wind-US 1.0 can now also be used with unstructured grids.

An empirical model that simulates the effects of an array of vortex generators was incorporated into Wind-US for applications on structured grids. The model enables the effects of vortex generators to be simulated without defining the details of the geometry within the grid, making it practical for researchers to evaluate multiple combinations of vortex generator arrangements.

The model determines the strength of each vortex on the basis of the generator chord length, height, and angle of incidence with the incoming flow, as well as on the incoming flow velocity and boundary layer thickness. The generators must be located at a coupled interface boundary between two zones.

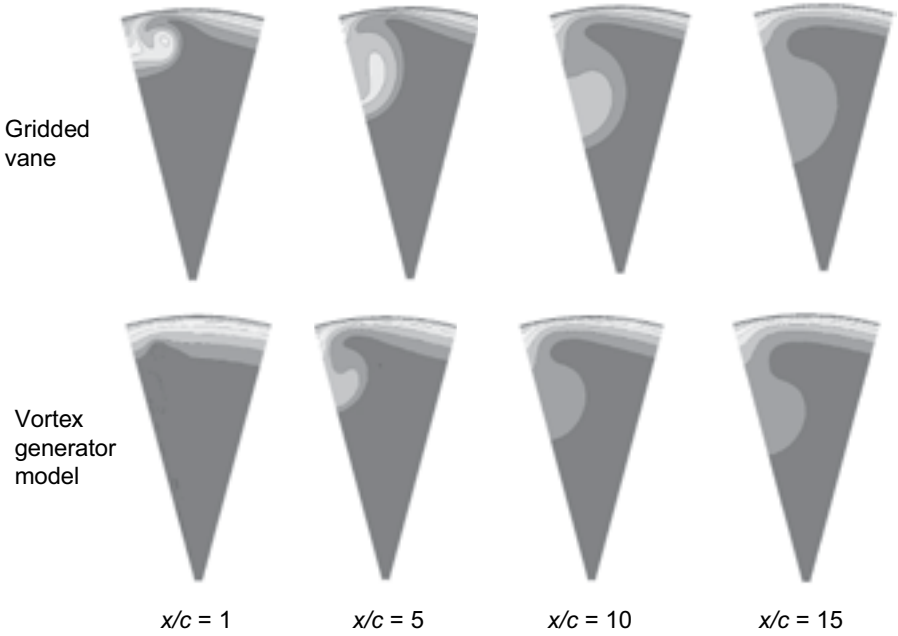


*Comparison of results for fully resolved and modeled vortex generators at 1, 5, 10, and 15 chord lengths downstream of the generator tip.*

A discontinuous change in secondary velocity is applied across the interface to simulate the vortices produced by the generators. Computed mach contours for flow in a circular duct with vortex generators are shown in the figure.

Work is also ongoing to improve the turbulence models available for use with the structured solver in Wind-US. Modifications have been made to the two-equation shear stress transport model to incorporate laminar-turbulent transition capability. For high-speed flows, a new compressible flow solution procedure has been formulated for the explicit algebraic Reynolds stress model. Both models are currently being evaluated for benchmark flow problems.

Enhancements have been made to the postprocessing tool, CFPOST, to allow users to more readily extract turbulence information from the solution file. The new output variables include the individual turbulent stresses and the ability to normalize values using appropriate near-wall scaling.

The NPARC Alliance is a formal partnership between the NASA Glenn Research Center and the Air Force Arnold Engineering Development Center, with additional significant involvement by the Boeing Company's Phantom Works Group, whose mission is to provide an applications-oriented computational fluid dynamics (CFD) system primarily for aerospace flow simulation.

All NPARC Alliance software is available free to U.S.-owned companies, public and private universities, and government agencies, for use by U.S. citizens and resident aliens. Instructions for obtaining the code are available at the NPARC Alliance homepage, or from the NPARC Alliance User Support team.

**Find out more about this research:**

**NPARC Alliance:**
http://web.arnold.af.mil/nparc/

**Wind-US Version 1.0 documentation:**
http://www.grc.nasa.gov/WWW/winddocs/

**CFD verification and validation (NPARC Alliance):**
http://www.grc.nasa.gov/WWW/wind/valid/

**Glenn contacts:**
Dr. Charles E. Towne, 216–433–5851, Charles.E.Towne@nasa.gov

Dr. Nicholas J. Georgiadis, 216–433–3958, Nicholas.J.Georgiadis@nasa.gov

**Author:**
Dr. Charles E. Towne

**Headquarters program office:**
Aeronautics Research Mission Directorate

**Programs/projects:**
Fundamental Aeronautics, Subsonic Fixed Wing, Supersonics, Hypersonics

**Special recognition:**
1999 NASA Software of the Year Honorable Mention, 2004 NASA Software Release Award

# Effect of Wedge-Shaped Deflectors on the Flow Field of a High-Bypass-Ratio Nozzle Studied

Stricter regulations on aircraft noise have led to numerous studies addressing jet noise reduction. One technique, developed at the University of California, Irvine, during research supported in part by a NASA grant, involves the use of a "wedge" to deflect and redistribute the flow from an engine exhaust. The wedge deflects the bypass (fan) stream sideways and downward so that a thick low-speed layer is formed underneath. When this is achieved, less noise is heard on the ground. In-house experiments at the NASA Glenn Research Center with larger scale nozzles confirmed the noise reduction, and computational studies indicated that the thrust penalty was modest.

The present experiment was conducted to further study the effect. It was done in collaboration with Rebecca Shupe of University of California, Irvine, who was at Glenn under a Graduate Student Researcher Program fellowship. The objectives were to (1) investigate the effect of the shape and placement of the wedge, (2) obtain detailed flow-field data including turbulent stresses, and (3) study the effect in the presence of a pylon structure.

The nozzle used in the study is shown in the photograph. Two crossed hot-wire probes, used for the measurements, can be seen on the right. The results pertain to cold flow with a primary jet velocity $U_p$ of 215 ft/sec and a secondary-to-primary velocity ratio $U_s/U_p$ of 0.7. The fan nozzle diameter $D_f$ is 2.1 in. A wedge placed in the fan stream is shown in the left schematic drawing on the next page. The wedge could be placed externally as shown or internally within the fan nozzle. The right schematic drawing shows the nozzle together with an internal wedge and a pylon structure. Flow fields for various configurations were surveyed in detail.

*Nozzle and hot-wire probes.*

A key result is shown in the final figure (bottom of the next page), which compares the effects of two internal wedges, without the pylon. The contours on the left show the mean velocity distribution on a cross-sectional plane located four fan diameters downstream from the end of the center plug. Without the wedge, the contours are circular and concentric. Both wedges deflected the flow downward, resulting in a "pear-shaped" distribution, but wedge 2 produced a stronger

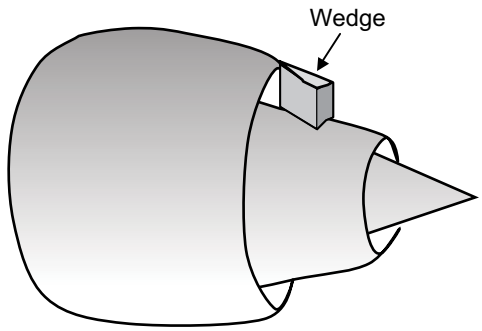


*Wedge placed externally in the fan stream.*

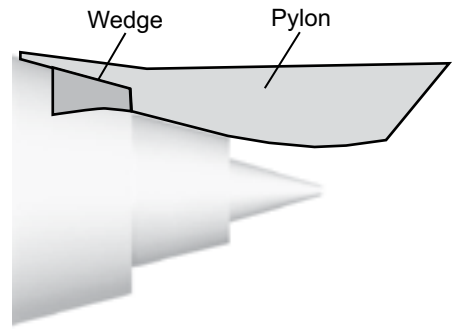


*Nozzle with an internal wedge and pylon structure.*

effect. Corresponding turbulence intensity distributions on the axial plane are shown on the right. In either case, turbulence is low on the underside, commensurate with lower noise heard on that side. Clearly, turbulence was suppressed more by wedge 2, which, therefore, has promise for better noise reduction. Compared with wedge 1, wedge 2 has the same base width but is shorter in length. The sidewalls are different. These differences produced significantly different effects on the flow field. Therefore, the geometry of the internal wedge, which is an integral part of the pylon structure in practice, might play a key role in fan flow deflection and the resultant noise reduction.

**Glenn contacts:**
Khairul Zaman, 216–433–5888, Khairul.B.Zaman@nasa.gov

Mary Jo Long-Davis, 216–433–8708, Mary.J.Long-Davis@nasa.gov

**Author:**
Dr. Khairul B. Zaman

**Headquarters program office:**
Aeronautics Research Mission Directorate

**Programs/projects:**
Subsonic Fixed Wing, Supersonics projects

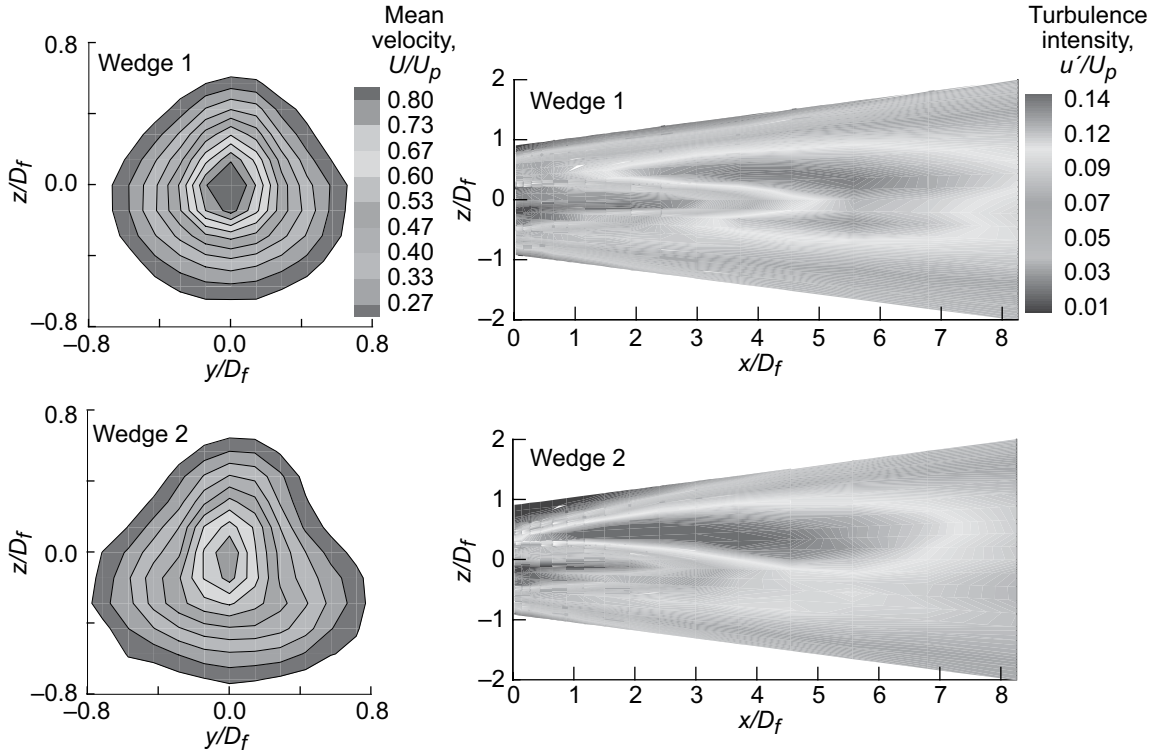


*Flow-field survey results for two internal wedge configurations. On the left are mean-velocity distributions on a cross-sectional plane at four fan diameters downstream from the end of the center plug ($x = 4D_f$). On the right are turbulence-intensity distributions on an axial plane ($y = 0$). This figure is shown in color in the online version of this article (http://www.grc.nasa.gov/WWW/RT/2006/RT/RTE-zaman.html).*

# SmaggIce 2D Version 2.0: Capabilities Added for the Interactive Grid Generation of Iced Airfoils

The Surface Modeling and Grid Generation for Iced Airfoils (SmaggIce) toolkit was recently expanded with additional capabilities. Version 2.0, the latest release, now accommodates multi-element as well as single-element airfoils for computational studies of icing effects. This suite of tools developed at the NASA Glenn Research Center is designed to help researchers and engineers study the effects of ice accretion on airfoil performance, which is difficult to do with other software packages because of the complexity of ice shapes. Using SmaggIce to simulate flow over an iced airfoil will also help to reduce the cost of performing flight and wind-tunnel tests for certifying aircraft in natural and simulated icing conditions. The graphical interface of SmaggIce is shown in the following figure, with an example grid created for a multi-element iced airfoil.

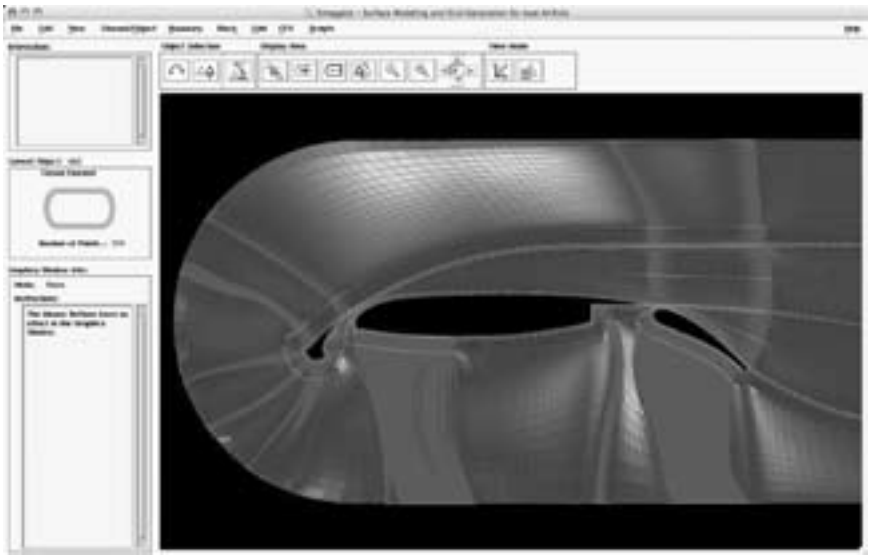

*SmaggIce main window. This figure is shown in color in the online version of this article (http://www.grc.nasa.gov/WWW/RT/2006/RT/RTI-kreeger.html).*

Ice shapes pose difficulty in generating the good-quality grids that are essential for predicting ice-induced complex flow. SmaggIce is used to prepare two-dimensional cross sections of iced airfoils for computational fluid dynamics analysis. This includes three broad phases of study—ice shape characterization, grid generation, and aerodynamic flow solution. Many tools are uniquely tailored for ice, including dividing the flow domain into blocks to set up the grid structure prior to grid generation, making changes to the grid-density distribution, and merging and smoothing multiblock grids. The use of a thin, tightly controlled block that wraps around the iced airfoil is an example of a unique feature available for handling difficult ice geometries. This feature is shown in the figure on the next page.

SmaggIce also provides tools to rapidly quantify ice-shape characteristics (such as horn height, angle, and location) and calculate integrated ice area, allowing researchers to examine their effect on aerodynamic performance. SmaggIce allows users to specify the size and location of simple, primitive ice shapes for parametric study. It includes tools that examine input data for possible errors (such as tangling introduced during data acquisition) and allows the user to smooth ice shapes to desired levels for computational fluid dynamics analysis. The shapes of block edges can be changed with control points by representing the edges as nonuniform rational B-spline curves. The density and distribution of points over the iced airfoil can be controlled to streamline the interactive grid-generation process.

Blocking and grid generation for multi-element airfoils required a number of additional supporting capabilities. Version 2.0 automatically creates blocks that connect and fill in the space between elements of a multi-element airfoil. In addition, the capability to divide blocks arbitrarily between opposite edges and to merge blocks was added to the block-modification tools. SmaggIce provides the tools needed to create high-quality grids for aerodynamic simulation of iced airfoils.

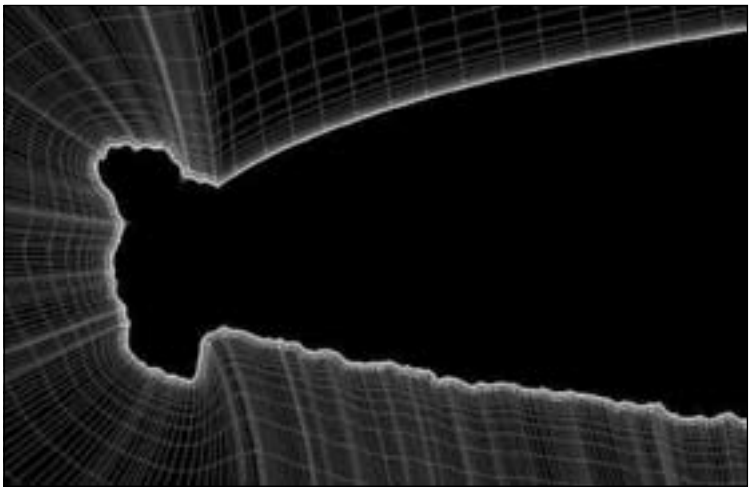

*Unique features for handling ice geometries. This figure is shown in color in the online version of this article (http://www.grc.nasa.gov/WWW/RT/2006/RT/RTI.kreeger.html).*

**Find out more about SmaggIce:**
http://icebox-esn.grc.nasa.gov/design/smaggice.html

**Glenn contacts:**
Richard E. Kreeger, 216–433–8766, Richard.E.Kreeger@nasa.gov

Mary B. Vickerman, 216–433–5067, Mary.B.Vickerman@nasa.gov

**Authors:**
Richard E. Kreeger and Mary B. Vickerman

**Headquarters program office:**
Aeronautics Research Mission Directorate

**Programs/projects:**
Aviation Safety

## Liquid Acquisition Devices Evaluated

Propellant management devices can be utilized within a propellant tank in space to deliver single-phase fluid to an engine in low gravity. One type of propellant management device, a liquid acquisition device (LAD) uses capillary flow and surface tension for acquiring liquid.

Capillary-flow LADs have been well characterized for storable (noncryogenic) propellants. More recently, there has been an interest in developing LADs for a variety of cryogenic applications. A screen-channel capillary flow LAD (see the figure to the right) consisting of multiple channels located close to the tank wall is of interest because it can perform in a variety of gravitational environments. The portion of the channel facing the tank wall is covered with a tightly woven screen. Propellant surface tension and wicking in screen pores ensures vapor-free propellant delivery.

*Notional view of four screen-channel LADs installed inside a propellant tank. The open area on the screen channels is covered with a tight mesh screen.*

A number of screen weaves can be used in LAD channels. The weave pattern and number of wires per inch in each direction determine the geometry of the screen pores. For example, a 200 by 1400 mesh Dutch twill screen has 200 shute and 1400 warp wires per square inch, and each shute wire travels over two warp wires before going under a warp wire. The geometry of the pore and the surface tension of the fluid determine the “bubble point”—the differential pressure across the screen that overcomes the surface tension

of the liquid on the screen. A high bubble point (fine screen mesh) is desirable to ensure single-phase liquid delivery and good wicking of fluid into the screen pores. Fine-mesh screens, however, exhibit a larger pressure drop during outflow. The total pressure loss in the system must be less than the bubble-point pressure to prevent vapor ingestion.

Recently completed research yielded data for LAD bubble-point values in isopropyl alcohol (IPA), liquid nitrogen ($LN_2$), and liquid oxygen ($LO_2$) for stainless steel Dutch twill screens with mesh sizes of 325 by 2300 and 200 by 1400. Screen channel outflow data also are reported for the screen with a mesh size of 200 by 1400.

The scanning electron micrograph to the right shows a 325-by-2300 mesh screen. Testing was conducted over a 2-year period in NASA Glenn Research Center's Cryogenic Components Lab in a small-scale fuel test stand designed for component screening. IPA and $LN_2$ testing was completed in 2004. During 2005, $LO_2$-compatible piping was installed at the facility, and $LO_2$ LAD testing was completed in 2006. The following photograph shows the LAD screen test hardware installed in the cryogenic dewar in the test facility.

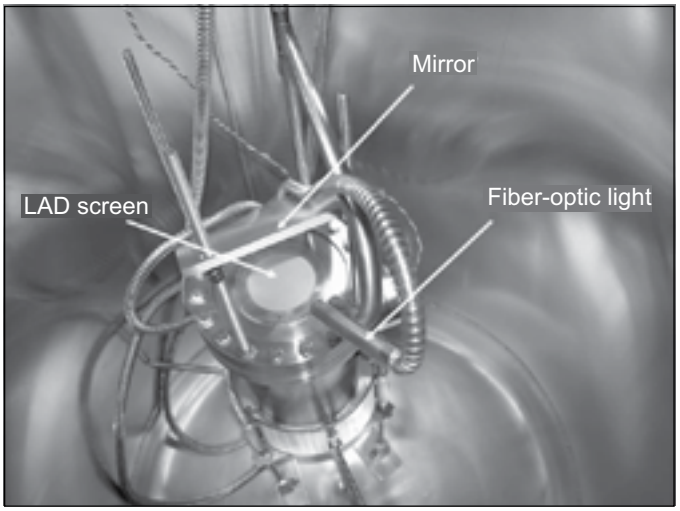


*LAD test article installed inside the cryogenic dewar.*

Observed bubble-point values for IPA, $LN_2$, and $LO_2$ were consistent with pretest predictions. The pressure drop across the screen during outflow tests correlated well with predicted values. Data were consistent, repeatable, and predictable for the fluids tested. Predictions were valid for saturated liquid at its normal boiling point. In the simple model used to predict bubble point, surface tension scaling fairly accurately predicted experimental bubble-point values.

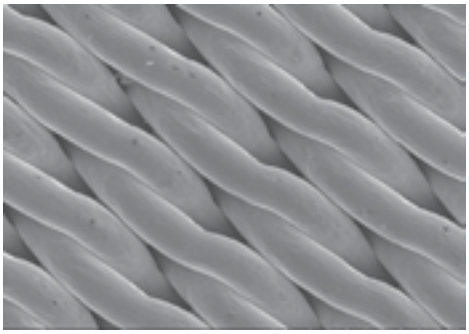


*Sample 200-by-1400 mesh screen.*

In addition to continuing to analyze the collected data, we plan to collect more fundamental data on various fluids (including liquid methane) and to evaluate LAD screens under varying levels of system pressure and degrees of liquid subcooling. Further analytical model development is planned, as well as evaluating the effects of heat trapped within LAD channels to ensure that fluid stored within the LAD channel remains in a single phase.

**ASRC Aerospace Corporation contact:**
John M. Jurns, 216–977–7416,
John.M.Jurns@nasa.gov

**Glenn contact:**
Maureen T. Kudlac, 216–977–7476,
Maureen.T.Kudlac@nasa.gov

**Authors:**
John M. Jurns and Maureen T. Kudlac

**Headquarters program office:**
Exploration Systems Mission Directorate

**Programs/projects:**
Explorations Systems Research and Technology program, Exploration Technology Development program, in-space cryogenic depots, main engine/reaction control propellant systems for a cryogenic version of the CEV

# Catalytic Reforming Technologies Investigated for Hydrogen Production and Onboard Aerospace Power Generation

Catalytic reforming technologies are being studied by the NASA Glenn Research Center for future commercial aerospace implementation. The fuel-processing application supports the onboard generation of auxiliary power, combustor emissions reduction, and propulsive thrust in more-electric aircraft architectures. For simplicity, an aviation fuel-cell-based power system utilizes Jet-A fuel as the feed to the fuel processor. The reformer catalytically converts the liquid Jet-A hydrocarbon into a synthesis gas rich in hydrogen ($H_2$) and carbon monoxide (CO); when integrated with solid oxide fuel cell (SOFC) power systems, electrical power is generated at high conversion efficiencies (exceeding 50 percent).

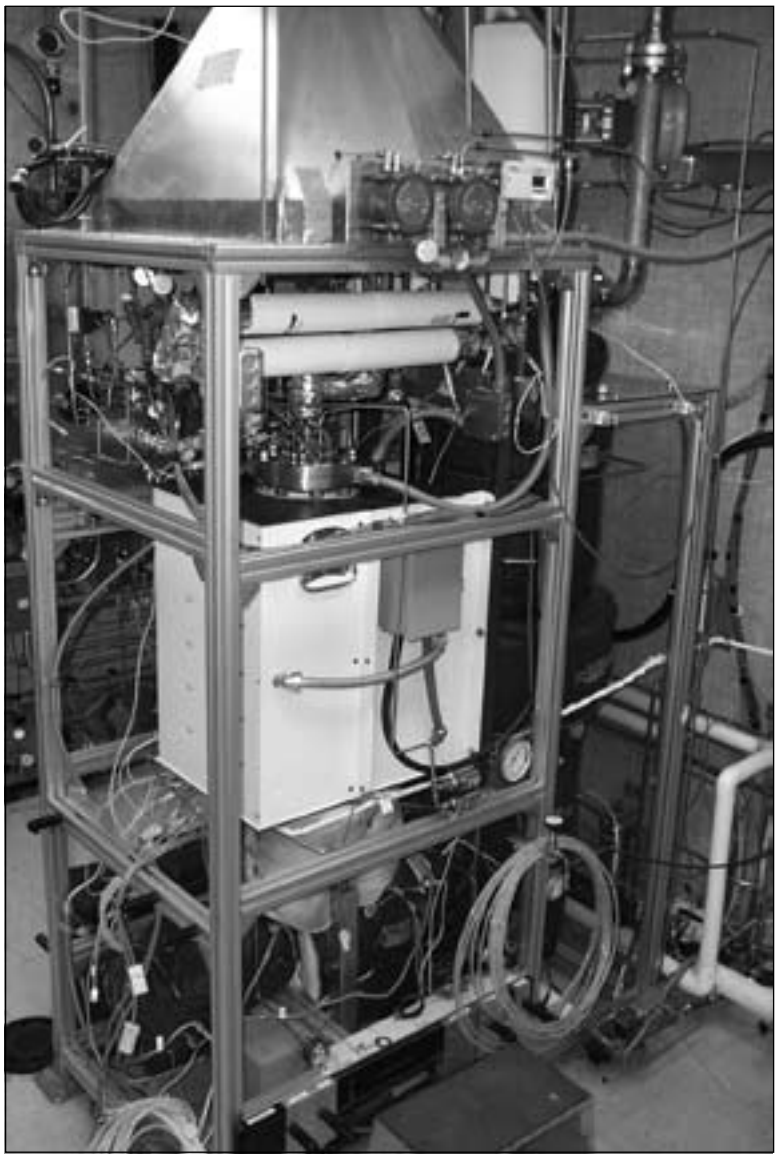

*Reformer reactor test equipment installation.*

The high-temperature synthesis gas can directly feed the SOFC stack where onboard electrical power and waste heat are produced. The reformer reactor technology for deployment with onboard aircraft systems must be compact and lightweight with long-term durability. Monolithic reforming catalysts offer high surface-to-volume ratios, are known to have high relative activity, are durable at extreme temperatures, are resistant to vibration affects, and produce very low pressure drop.

During one series of fuel-processing experiments, the autothermal reforming (ATR) of Jet-A fuel was examined in a small (0.05-kWe) microreactor test apparatus. Six monolith catalyst materials were selected to assess relative catalyst performance under atmospheric pressure ATR conditions. The reforming of Jet-A fuel occurred at a steam-to-carbon ($H_2O$:C) ratio of 3.5 and an oxygen-to-carbon ($O_2$:C) ratio of 0.36 provided from the reactant air feed. The average reformer efficiencies for the six test catalysts ranged from 75 to 83 percent at a constant gas-hourly space velocity (GHSV) of 12,000 $hr^{-1}$. The corresponding hydrocarbon conversion efficiency data varied from 86 to 95 percent at reformer reaction temperatures between 750 and 830 °C.

As a follow-on investigation, the two ATR catalysts that had demonstrated the best performance were tested for durability during a 1000-hr life study at similar reactor conditions. Test results showed that the first catalyst stopped working prematurely after 570 hr time on-stream (TOS) via a rapid deactivation decline. The second catalyst survived the target durability test period of 1030 hr TOS. However, its performance efficiency was observed to slowly decay from 81 percent initially to 54 percent at end-of-run. During all reforming test protocols, the

composition of the product gas, the volumetric flow rate of the product gas at standard conditions, and the temperatures of the catalyst were determined as a function of the control operating variables.

Similar experimental fuel reforming studies were conducted under catalytic partial oxidation conditions, where the reforming reaction was run exothermically, resulting in excess heat generated by the combustion of air. Attempts were made during these experiments to differentiate the effects on reformer catalyst performance that were due to the sulfur content of the Jet-A fuel. The maximum sulfur content was 1500 $ppm_w$; fuel blends with sulfur content below 300 $ppm_w$ significantly improved catalyst performance.

Consequently, fuel desulfurization processes were investigated during the program year for potential onboard use. For example, the high-temperature desulfurization adsorption of reformate gas with mixed oxide adsorbents was evaluated and tested by Tufts University under a NASA Research Grant.

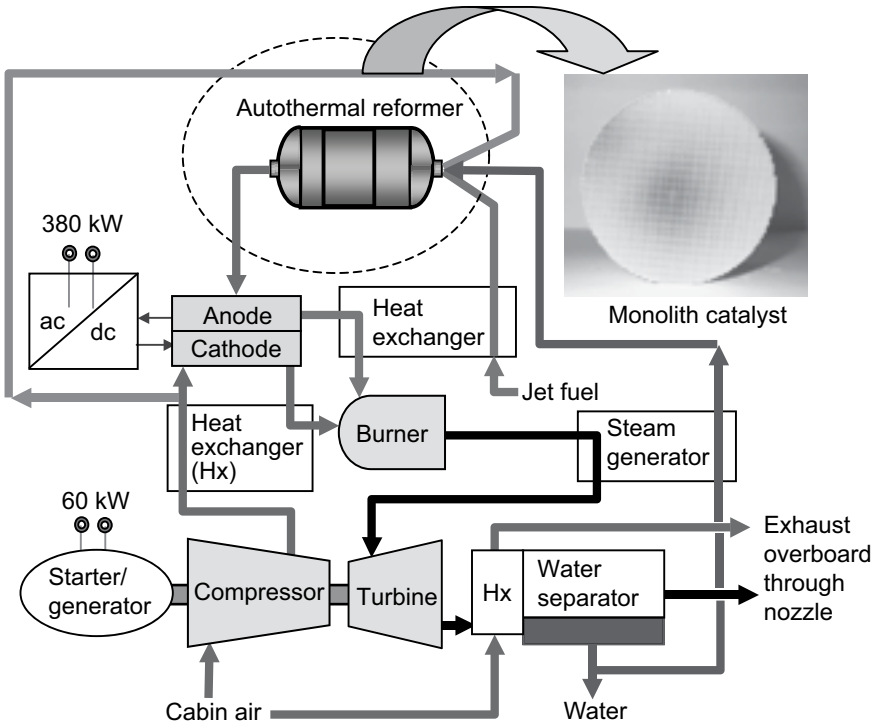


*SOFC hybrid power cycle with ATR.*

Further catalyst development work and long-term testing will be necessary to more thoroughly understand the observed catalyst deactivation mechanisms and to identify more robust formulations for the efficient ATR of jet fuels.

**Bibliography**


Tomsik, Thomas M.; and Yen, Judy C.H.: Bench-Scale Monolith Autothermal Reformer Catalyst Screening Evaluations in a Micro-Reactor With Jet-A Fuel. NASA/TM—2006-214254, 2006. http://gltrs.grc.nasa.gov/Citations.aspx?id=119

Peterson, A., et al.: Optimization of Swirler-Venturi Mixer Geometry Fuel Reformer Application. AIAA–2005–5556, 2005.


**Find out more about the research of Glenn's Propulsion Systems Division:**
http://www.grc.nasa.gov/WWW/5000/propulsion/


**Glenn contacts:**
Thomas M. Tomsik, 216–977–7519, Thomas.M.Tomsik@nasa.gov

Angela D. Surgenor, 216–433–3251, Angela.D.Surgenor@nasa.gov

**University of Toledo contact:**
Judy Yen, 216–433–3626, Chia.H.Yen@nasa.gov

**Author:**
Thomas M. Tomsik


**Headquarters program office:**
Aeronautics Research Mission Directorate

**Programs/projects:**
Subsonic Fixed Wing, Fuel Reforming

# Low-Gravity Gauging Concept Extended to Cryogenic Propellants

The pressure, volume, temperature (PVT) method of liquid quantity gauging in low gravity is based on calculations assuming conservation of pressurant gas within the propellant tank and the pressurant supply bottle (such as depicted in the figure to the right). This method is currently used to gauge the remaining amounts of storable propellants onboard the space shuttle's orbital maneuvering system and on Earth-orbiting communications satellites. There is interest in applying this method to cryogenic propellant tanks since it requires minimal additional hardware or instrumentation. An initial in-house study of PVT gauging of cryogenic propellants was completed at the NASA Glenn Research Center.

To use PVT with cryogenic fluids, a noncondensable pressurant gas (helium) is required. With cryogens, there will be a significant amount of propellant vapor mixed with the pressurant gas in the tank ullage. This condition, along with the high sensitivity of a cryogenic propellant's vapor pressure to temperature, makes the PVT method susceptible to substantially greater measurement uncertainty than is the case with less volatile propellants. A preliminary uncertainty analysis was applied to example cases of liquid hydrogen and liquid oxygen tanks. Calculations indicate that the PVT method will be feasible for liquid oxygen. Acceptable accuracy will be more difficult to obtain with liquid hydrogen.

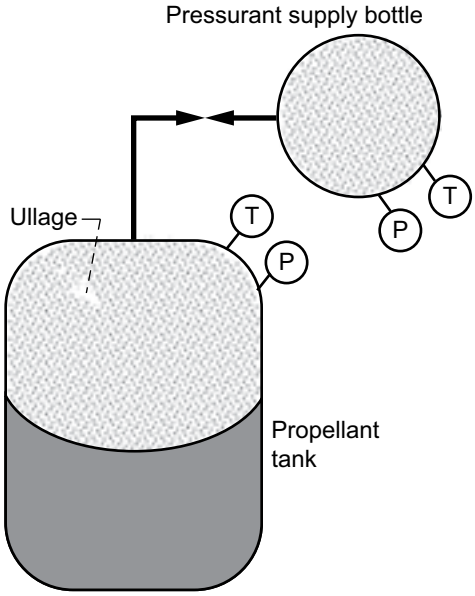


*Basic PVT gauging hardware configuration with instrumentation.*

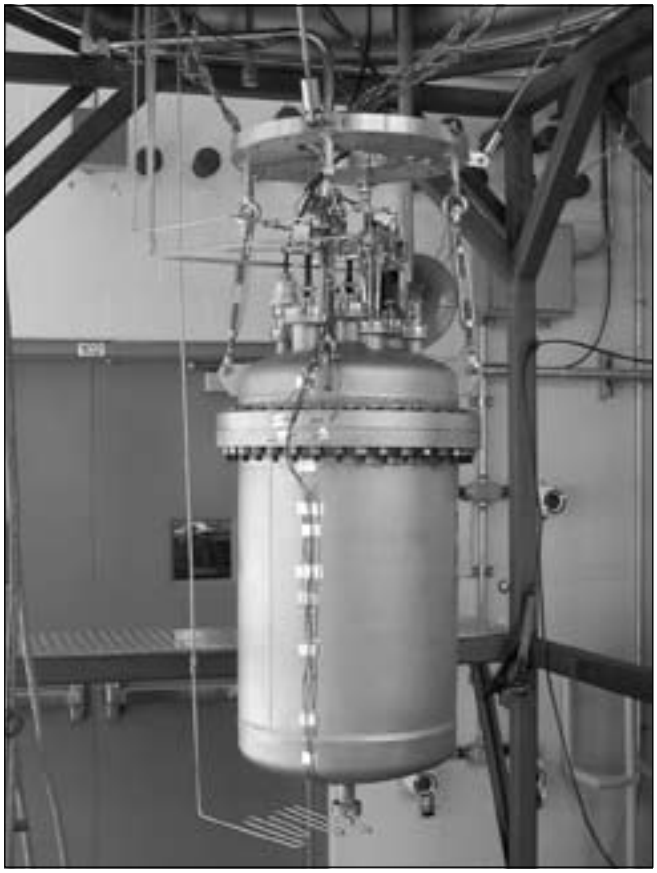

*Assembled test tank prior to installation of thermal insulation.*

PVT gauging experiments were conducted in a 0.16-$m^3$ liquid nitrogen tank (shown in the photograph) pressurized with ambient temperature helium in a normal-gravity environment. Liquid nitrogen was used as a simulant fluid for liquid oxygen. Gauging data were collected at nominal tank fill levels of 80, 50, and 20 percent and at nominal tank pressures of 0.3, 1.0, and 1.7 MPa. The test tank was equipped with a liquid pump and spray manifold to circulate and mix the fluid contents and therefore create near-isothermal conditions throughout the tank. Silicon-diode sensors were distributed throughout the tank to monitor temperatures. Close-spaced arrays of silicon-diode point sensors were utilized to precisely detect the liquid level at the nominal 80-, 50-, and 20-percent fill levels. The tests simulated the cryogenic tank-side conditions only; helium mass added to the tank was measured by gas flowmeters instead of using pressure and temperature measurements from a dedicated helium supply bottle.

Results show that helium solubility in the liquid propellant should be accounted for in PVT gauging calculations. Gauging results from the PVT method agreed with the reference liquid level measurements to within 3 percent and were in excellent agreement with predicted results from the uncertainty analysis. Work is underway at Glenn to conduct larger-scale PVT tests with liquid oxygen and liquid hydrogen in a 1.6-$m^3$ tank pressurized by a cryogenic temperature helium supply bottle.

**References**


1. Van Dresar, N.T.: An Uncertainty Analysis of the PVT Gauging Method Applied to Sub-Critical Cryogenic Propellant Tanks. Cryog., vol. 44, nos. 6–8, 2004, pp. 515–523.
2. Van Dresar, N.T.: PVT Gauging With Liquid Nitrogen. Cryog., vol. 46, nos. 2–3, 2006, pp. 118–125.



**Glenn contacts:**
Dr. Neil T. Van Dresar, 216–977–7533, Neil.T.VanDresar@nasa.gov

Dr. Gregory A. Zimmerli, 216–433–6577, Gregory.A.Zimmerli@nasa.gov

Michael L. Meyer, 216–977–7492, Michael.L.Meyer@nasa.gov

**Author:**
Dr. Neil T. Van Dresar


**Headquarters program office:**
Exploration Systems Mission Directorate

**Programs/projects:**
CEV, Constellation Systems, Exploration Technology Development Program

## Liquid Oxygen-Liquid Methane Ignition Demonstrated for Application to Reaction Control Engines

A workhorse liquid-oxygen/liquid-methane ($LOX/LCH_4$) ignition system was recently tested in NASA Glenn Research Center's Research Combustion Laboratory. The igniter was an in-house design used to evaluate the ignition processes for $LOX/LCH_4$. The tests examined the flammability of $LOX/LCH_4$ over a range of oxidizer-to-fuel mixture ratios. In addition, ignition pulses were accumulated to examine hardware durability: 1377 individual ignition pulses were successfully demonstrated.

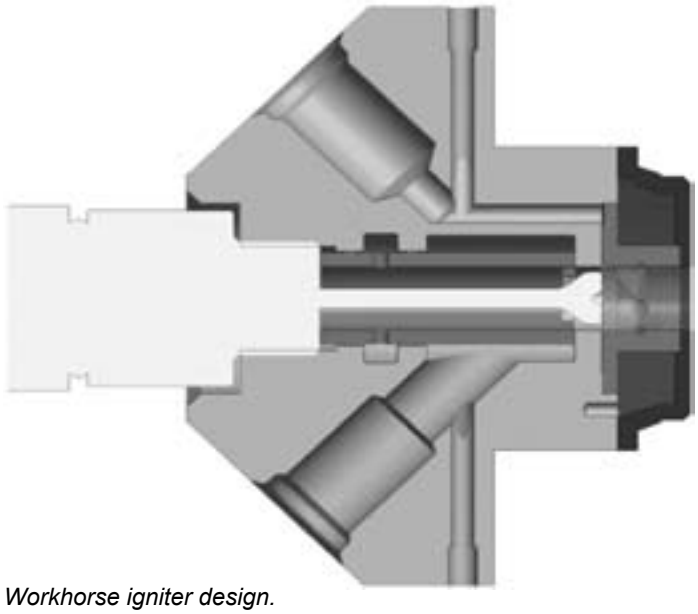

*Workhorse igniter design.*

Glenn's Workhorse igniter was designed around a bluff-body-tipped sparkplug (see the drawing). The exciter unit for the spark plug delivered 200 sparks/sec at 20 kV and 70 to 150 mJ. Design flow rates were in the 10-lbf thrust class. The igniter used three separate propellant feed lines, two for the fuel and one for the oxidizer. LOX was injected with four doublets in the annulus behind the bluff body on the spark plug tip and was excited by the spark. One fuel line injected fuel with four doublets just downstream of the spark plug tip to provide an oxidizer-rich core flow, while the second fuel line injected fuel with tangential swirl to supply film-cooling flow to the chamber wall and an overall fuel-rich torch. The core mixture ratio ranged between 10 and 22, and the overall mixture ratio was between 1.1 and 2.0. Both mixture ratios were selected because their flame temperatures are compatible with conventional materials. Propellant mass flow was controlled by cavitating venturis.

*Ignition plume shown in the video monitor.*

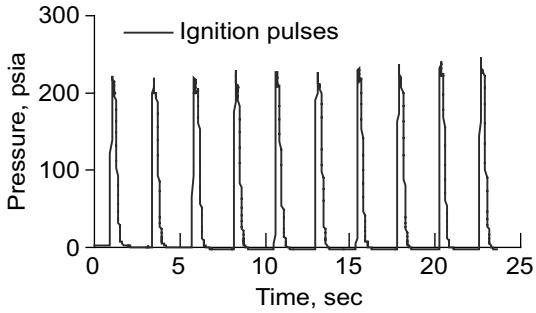


*Pressure trace from pulse train.*

Injector element pressure drops were designed to accommodate the desired propellant mass flows as saturated vapor as well as saturated liquid.

The LOX/$LCH_4$ igniter was tested in Glenn's RCL–21, a rocket test stand that can simulate an altitude of 100,000 ft (10 torr, or 0.2 psia). A liquid nitrogen cooling system was used to condense gaseous oxygen and gaseous methane in small propellant tanks. The cooling lines extended from the tanks to the igniter inlet valves to help ensure that the propellants remained in a liquid state up to the igniter manifold. An additional cooling line was used to cool the igniter body to simulate operating conditions in the cold soak of space.

Performance testing was designed to evaluate the effect of mixture ratio variations on the ignition process. A typical ignition reproduced from the video monitor is shown in the photograph. Single-pulse, 0.5-sec tests were conducted. Results indicated that ignition was possible across the entire range of mixture ratios tested with the igniter body at ambient temperatures.

Another objective was to accumulate ignition pulses to gauge the expected lifetime of the igniter components and valves as well as the repeatability of the ignition pulses. A 0.25-sec pulse was used so that a large number of pulses could be put on the igniter. During these tests, the igniter was operated in multiple pulse strings at a 10-percent duty cycle. The graph is a typical chamber pressure trace showing 10 pulses. The ignition pulse repeatability varied slightly over the course of testing because fluctuations in propellant inlet conditions led to slight variations in the propellant flow rates. This series of tests was halted after the igniter spark plug ceramic insulator failed.

**Glenn contacts:**
Dr. Steven J. Schneider, 216–977–7484, Steven.J.Schneider@nasa.gov

Jeremy W. John, 216–433–6199, Jeremy.W.John@nasa.gov

**Authors:**
Dr. Steven J. Schneider, Jeremy W. John, Joseph G. Zoeckler, Lynn A. Arrington, Jason C. Wendell, and Dale M. Diedrick

**Headquarters program office:**
Exploration Systems Mission Directorate

**Programs/projects:**
Propulsion and Cryogenics Advanced Development project, Reaction Control Engine

# Noninvasive Laser Doppler Flowmetry Used To Measure In Vivo Blood Flow in Distal Fingertips

Extravehicular activity (EVA) suits are designed to protect astronauts exposed to the low temperatures, low pressures, and lack of oxygen in space. Astronauts engaged in extravehicular activities have reported discomfort in their fingertips. The precise cause of this discomfort is not known, but is speculated to be reduced blood flow to the fingertips. Therefore, there is a critical need for monitoring blood circulation in astronaut extremities during missions. The data collected could be used to develop better countermeasures to help the astronauts avoid further discomfort and perhaps injury to their fingers during EVA. One way to quantify blood circulation is to measure the hemodynamics of the capillaries in the fingertips. Laser Doppler flowmetry (LDF) technology has significant potential for this purpose.

*Prototype LDF sensor.*

LDF is a noninvasive technique that allows the flux of moving red blood cells (RBCs) to be measured in the microvasculature of a tissue (e.g., in a fingertip). The technique is based on the Doppler effect, which describes the frequency shift that a wave undergoes when emitted from an object that is moving away from or toward an observer. Laser light scattered by moving particles, such as RBCs, is shifted in frequency by amounts proportional to the speeds of the particles. This scattered light is optically mixed with a reference signal and is detected by a photodetector. The detected signal is then analyzed to obtain the LDF parameters (speed, volume, and flow).

The goal of this work is to develop a miniaturized LDF system for portable use during EVAs, with a fiber-optic probe that could be outfitted in an astronaut's glove. As a first step, a prototype LDF system (see the photograph) for the measurement of blood flow in the capillaries of the distal fingertip was developed. A laser source with a wavelength of 780 nm and an output power of 5 mW is used to transmit the light through an optical fiber to the fingertip probe. Scattered light is collected into a second fiber that transmits the light to the detector. The detected light signal is acquired with an NI–DAQ card (National Instruments Corporation data-acquisition card), and the LDF calculations are made with a LabVIEW (National Instruments Corporation's Laboratory Virtual Instrumentation Engineering Workbench) program.

Ground-based experiments were performed on volunteer subjects by measuring the blood flow while increasing the pressure in the arm using a pressure cuff or by cooling the fingertip.[1] The results showed good linearity in all measured parameters. A typical data set is shown in the graphs. When the

[1]This work was done under an approved NASA Johnson Space Center institutional review board.

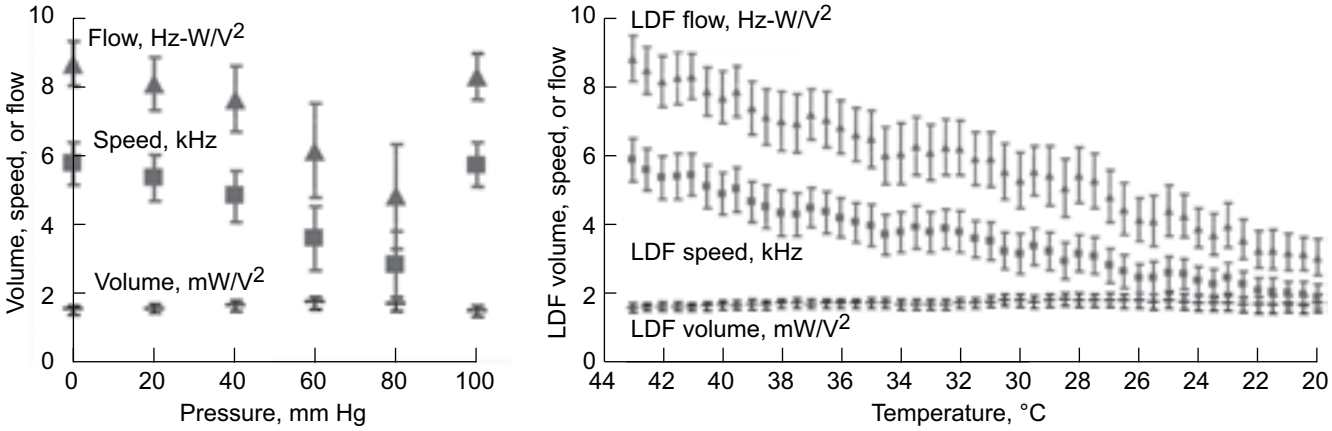


*Ground-based experiment results.*

pressure in the arm was increased from 0- to 80-mm mercury, the LDF volume increased by 11.6 percent, the LDF speed decreased by 50.4 percent, and the LDF flow decreased by 44.3 percent. When the fingertip was cooled from 43 to 20 °C, the LDF volume increased by 9 percent, the LDF speed decreased by 68.1 percent, and the LDF flow decreased by 65.7 percent. Further work is being done to integrate the probe into an astronaut's glove and to miniaturize the LDF instrument to the size of a wrist watch, as shown in the following photographs.

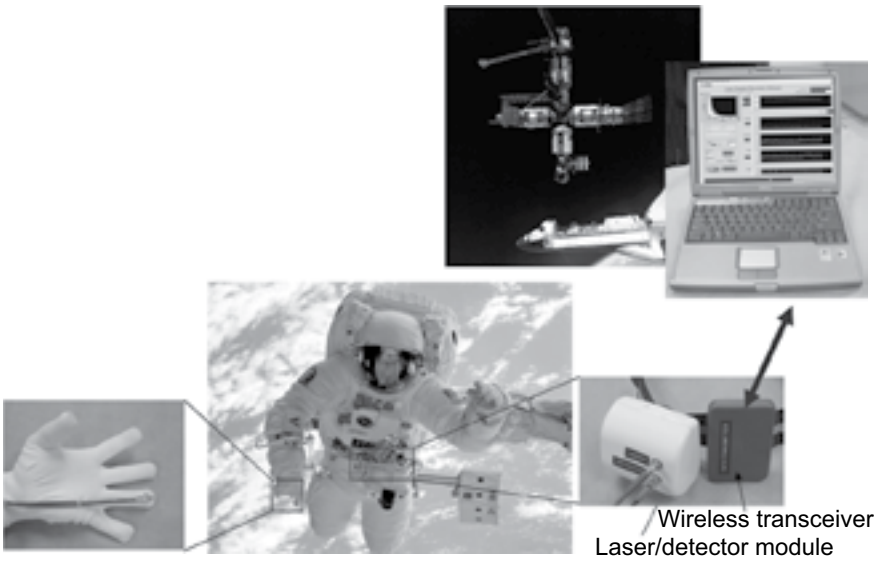


*Future design of miniaturized LDF system.*

**Find out more about Glenn's microgravity combustion science research:**
http://microgravity.grc.nasa.gov/combustion/

**Glenn contact:**
Rafat R. Ansari, 216–433–5008, Rafat.R.Ansari@nasa.gov

**Authors:**
Rafat R. Ansari, Ph.D.;
Kwang I. Suh, Ph.D.; and
Jeffrey A. Jones, M.D.

**Headquarters program office:**
Exploration Systems Mission Directorate

**Programs/projects:**
Advanced Capabilities Human Research Program

## Enzyme-Linked Immunosorbent-Assay-Based Optical Biosensors Investigated for Exploration Applications

With the advent of the Vision for Space Exploration, there is an immediate need for sensitive biosensors that can be used for spacecraft environmental monitoring (air and water). Optical biosensors have significant potential in this regard, since a given target species (antigen) can be captured by a bound antibody and this capture event can be detected via fluorescence emission. Recent efforts at the NASA Glenn Research Center have focused on increasing the sensitivity of a certain class of optical biosensors, namely enzyme-linked immunosorbent assay (ELISA)-based biosensors, for space exploration applications.

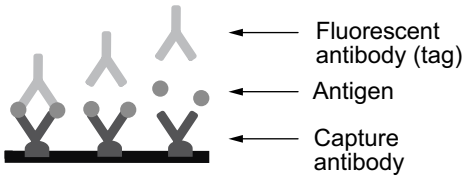


*ELISA sensing mechanism.*

ELISA-based biosensors have proven to be accurate in detecting a wide variety of antigens (ref. 1). In the sandwich ELISA biosensor (see the sketch), a given antibody (the capture antibody) is bound to the substrate. In the presence of an antigen, a complex is formed. If a second fluorescently labeled antigen-specific antibody is introduced and binds to the antigen, the sandwich is complete and the target antigen can be identified by fluorescence detection. The sensitivity of such capture-based biosensors can be dramatically improved by increasing the substrate surface-area-to-volume ratio (ref. 2).

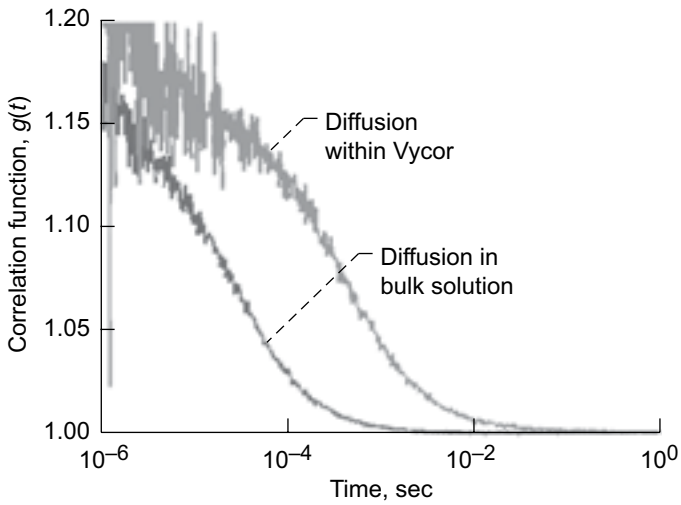


*Fluorescence correlation data of Rhodamine 6G in methyl alcohol (MeOH).*

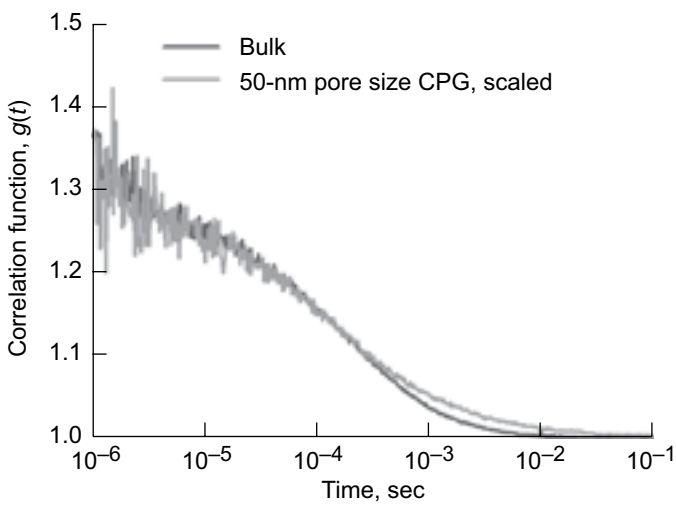


*Fluorescence correlation data of FITC-labeled antibody in bulk solution and within the 50-nm pore size CPG; $D_t$(bulk) ~ 16$D_t$(50-nm CPG).*

Because of their high surface-area-to-volume ratio, porous glasses are prime candidates as biosensor substrates. Two particular candidate materials are Vycor porous glass (Corning Incorporated, Vycor glass code 7930), which has a 4-nm pore size and a surface-area-to-volume ratio of 375 $m^{-1}$, and controlled-porosity glass (CPG), which has surface-area-to-volume ratios of 16 and 8 $m^{-1}$, respectively, for 50-nm and 100-nm pore-size samples. Before these substrates can be utilized effectively, however, the effect of the nanoscale pore structure on molecular diffusion needs to be understood.

Accordingly, two-photon excitation fluorescence correlation spectroscopy was used to examine the microscale diffusion of biomolecules within the candidate materials. The experimental correlation data were fit to theoretical functional forms, and the diffusion timescales were calculated. These results within the substrate were then compared with those in bulk solution to determine the effect of the confining geometry on the diffusion timescales.

To quantify the effects of confinement, we examined the diffusion of a simple fluorophore, Rhodamine 6G, in the Vycor sample. Results are illustrated in the top graph for the diffusion of Rhodamine 6G in both Vycor and bulk solution. The correlation data fit the three-dimensional diffusion model very well. From the data, it was determined that the diffusion timescale within Vycor is 13 to 14 times slower than in the bulk solution. In addition, the diffusion of fluorescein isothiocyanate (FITC)-labeled antibodies (a complex molecule) was also studied. Studies were only performed in the CPG, since the pore size (4 nm) of the Vycor substrate was prohibitively small. In this case, the diffusion timescale $D_t$ in the 50-nm CPG was determined to be 16 times slower than in the bulk solution (bottom graph), whereas the timescale in the 100-nm CPG was roughly 8 times slower than in the bulk solution.

These studies have examined the diffusion of simple and complex molecules in nanoporous substrate materials, demonstrating that the confined geometry results in longer diffusion times (slower diffusion) in comparison to that in bulk solution. However, the reduction in diffusion speed is not so great that the throughput of an operational sensor would be compromised. Considering the significant increase in sensing surface area (and the resulting increase in detection sensitivity), ELISA-based biosensors utilizing nanoporous glass substrates hold great promise for exploration.

**References**

1. Tailt, C.R., et al.: A Portable Array Biosensor for Detecting Multiple Analytes in Complex Samples. Microb. Ecol., vol. 47, no. 2, 2004, pp. 175–185.
2. Ganesh, N.; Block, I.D.; and Cunningham, B.T.: Near Ultraviolet-Wavelength Photonic-Crystal Biosensor With Enhanced Surface-to-Bulk Sensitivity Ratio. Appl. Phys. Lett., vol. 89, no. 2, 2006.

**Glenn contacts:**
Marius Asipauskas, 216–433–8778, Marius.Asipauskas-1@nasa.gov

Dr. Gregory A. Zimmerli, 216–433–6577, Greg.Zimmerli@nasa.gov

Dr. David G. Fischer, 216–433–6379, DGFischer@nasa.gov

**Authors:**
Marius Asipauskas,
Dr. Gregory A. Zimmerli, and
Dr. David G. Fischer

**Headquarters program office:**
Exploration Systems Mission Directorate

**Programs/projects:**
Human Research Program

# Microvascular Remodeling Analysis Developed for Advances in Human Health

Protecting astronaut health in the harsh microgravity space environment is fundamental to the NASA Vision for Space Exploration. Many health risks, including numerous cardiovascular alterations (CVAs) worsen as space flight is prolonged. Major Earth-based pathologies, such as impaired wound healing, cancer, blindness in diabetes, and certain types of heart disease are also characterized by important microvascular changes or remodeling. Our overall goal is to use research on Earth-based microvascular physiology and pathologies to develop new, improved quantitative measures for assessing and mitigating bioastronautic risk factors. To survive, every cell in the human body must reside in close proximity (≤200 μm) to a (microvascular) capillary blood vessel for necessary oxygen, metabolic, and fluid exchange. Because of this metabolic complexity, microgravity CVAs include highly networked risk factors such as adverse fluid shifts to the upper body, hematologic and wound-healing impairments, immunosuppression, and orthostatic intolerance (ref. 1).

In collaboration with the Cole Eye Institute and Department of Cell Biology, Lerner Research Institute, Cleveland Clinic Foundation (CCF), current research goals at the NASA Glenn Research Center include (1) intravital particle imaging velocimetry (PIV) of blood flow as illustrated in the left figure on the next page, (2) application of novel fractal-based methods for improved microvascular analysis and diagnosis of human retinal disease, (3) evaluation of new therapeutics to regulate pathological vascular/lymphatic remodeling and fluid leakage, and (4) development of the Glenn fractal-based VESGEN (VESsel GENeration for blood vessel images) software analysis of microvascular remodeling.

Microvascular remodeling is difficult to analyze because the human cardiovascular system is a complex, three-dimensional, treelike structure embedded in opaque tissue. Imaging technologies such as magnetic resonance imaging (MRI) and Doppler ultrasound are currently unable to visualize small blood vessels such as arterioles and capillaries. We use the two-dimensional, optically accessible microvasculature of an avian experimental model (quail embryos) as an experimental testbed to develop new methods for analyzing microvascular remodeling and blood flow. Methods developed in this experimental testbed have been extended successfully to the analysis of human retinal disease (see the figure on the last page of this article and ref. 2) and the critical microvascular remodeling component of tumor progression in genetically engineered murine cancer models (ref. 3).

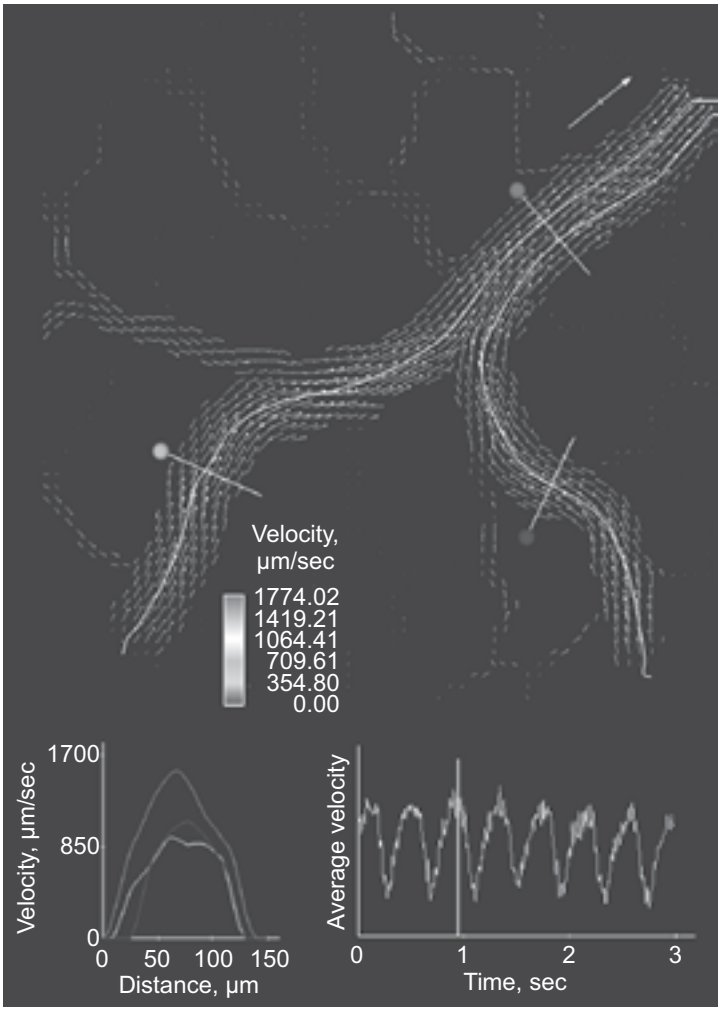


*PIV of multigenerational microvascular blood flow in vivo. Top: A representative vector plot illustrates the velocity flow field produced by PIV analysis of blood flow in the collecting veins of an avian embryonic model. By the color scale, blood flows slowly through the smallest vessels (capillaries, the site of oxygen and other gaseous exchanges). Blood flow increases considerably as blood is collected into successively larger, converging venules and veins. Two solid (white) lines in the veins display streamlines calculated for red blood cells, which serve as the tracking particles. This figure is shown in color in the online version of this document (http://www.grc.nasa.gov/WWW/RT/2006/RU/RUB-parsons.html). Bottom left: Velocity profile. In the larger blood vessels, velocity profiles of the three cross-sectional cuts in the top plot are laminar and approximately parabolic. Bottom right: Spatial average of velocity versus time. Pulsatility of the blood flow results from the pumping cycles of the beating heart. The average blood flow velocity is therefore cyclic.*

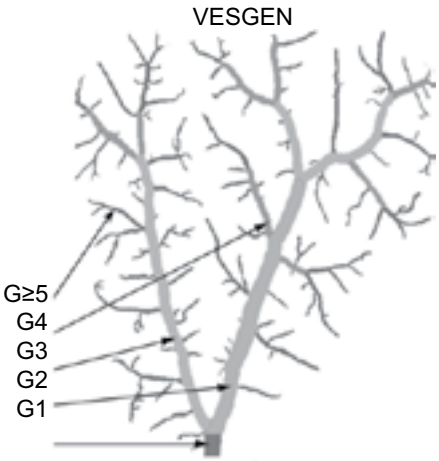


*VESGEN software development. Digitized images of blood vessels are analyzed by computerized fractal-based mathematics to quantify morphological changes in vessel branching generations G1 to G≥5.*

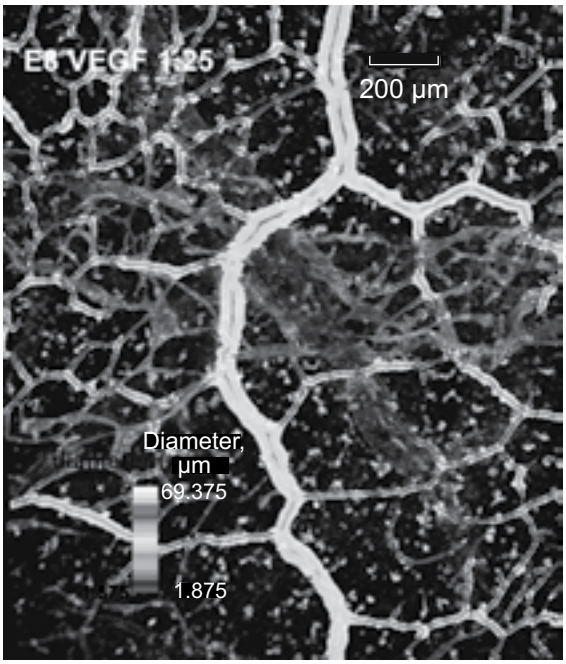


*Novel euclidean distance mapping (EDM) of microvascular networks. Lymphatic vessels with pseudocolored skeletons that are proportional to vessel thickness as shown by color scale bar are overlaid onto the confocal fluorescence image (ref. 4). This figure is shown in color in the online version of this document (http://www.grc.nasa.gov/WWW/RT/2006/RU/RUB-parsons.html).*

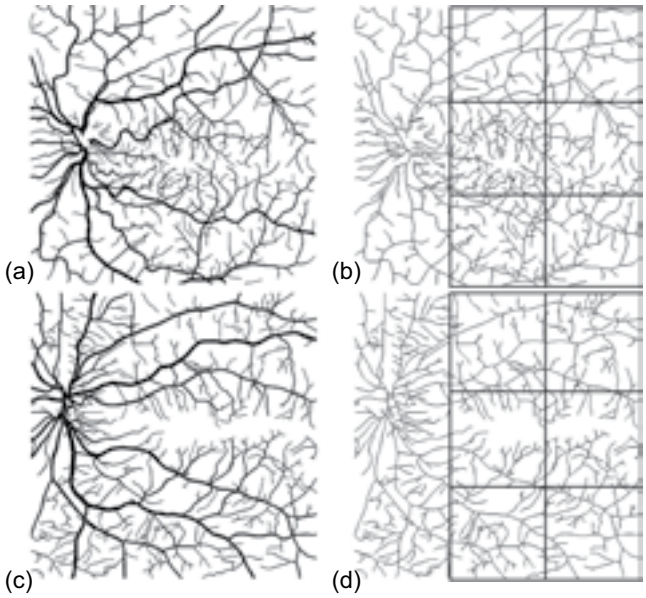


*Fractal analysis of pathological remodeling in the human retina. Using fractal-based methods first developed in the avian chorioallantoic membrane (CAM), we extract and quantify vascular patterns from ophthalmic clinical images of normal retinas (a), as linearized in (b), compared with retinas diagnosed with diabetic retinopathy, (c) and (d), as now funded by the National Institutes of Health (NIH). Note the loss of blood vessels in the central boxed region of the diabetic retina (d) in comparison with the normal retina (b).*

**References**

1. NASA Research Yields Insights Into Aging. NASA Space Research, Exploration Systems Mission Directorate, vol. 3, no. 4, Fall 2004, p. 6.
2. Avakian, A., et al.: Fractal Analysis of Region-Based Vascular Change in the Normal and Non-Proliferative Diabetic Retina. Curr. Eye Res., vol. 24, no. 4, 2002, pp. 274–280.
3. Parsons-Wingerter, P., et al.: Uniform Overexpression and Rapid Accessibility of $alpha_5$beta Integrin on Blood Vessels in Tumors. Amer. J. Pathol., vol. 167, no. 1, 2005, pp. 193–211.
4. Parsons-Wingerter, P., et al.: The $VEGF_{165}$-Induced Phenotypic Switch From Increased Vessel Density to Increased Vessel Diameter and Increased Endothelial NOS Activity. Microvasc. Res., vol. 72, no. 3, 2006, pp. 91–100.

**Bibliography**

McKay, T., et al.: Intravital PIV of Blood Flow as a Function of Microvessel Generational Branching. SPIE Great Lakes Photonics Symposium, Aerospace Applications Session, Dayton OH, 2006.

Parsons-Wingerter, P.A.; McKay, T.L.; and DiCorleto, P.E.: VEGF–A Induces Reorganization of the Lymphatic Tree Into Homogeneous Networks. A Special Transatlantic Meeting of The Microcirculatory Society, Inc., and The British Microcirculation Society, Paper OC28, Durham NH, 2005.

Parsons-Wingerter, P., et al.: Lymphangiogenesis by Blind-Ended Vessel Sprouting Is Concurrent With Hemangiogenesis by Vascular Splitting. Anat. Rec., vol. 288A, no. 3, 2006, pp. 233–287.

Parsons-Wingerter, P., et al.: $VEGF_{165}$-Dependent Switch From Increased Vessel Density to Increased Vessel Diameter and Increased Endothelial NOS Activity. FASEB J., vol. 20, no. 4, 2006, pp. A708–A709.

**Glenn contacts:**

Dr. Patricia Parsons-Wingerter, 216–433–8796, Patricia.A.Parsons-wingerter@nasa.gov

Dr. John M. Sankovic, 216–977–7429, John.M.Sankovic@nasa.gov

**Author:**

Patricia A. Parsons-Wingerter, Ph.D.

**Programs/projects:**

Glenn IR&D, Human Research Program, National Eye Institute/National Institutes of Health

**Special recognition:**

An R01 Independent Principal Investigator grant (Vascular Remodeling and Effects of Angiogenic Inhibition in Diabetic Retinopathy) was awarded to Dr. Parsons to fund a 2-year collaboration with the Cole Eye Institute, Cleveland Clinic Foundation.

# Smoke-Detection Model Developed for the Destiny Laboratory on the *International Space Station*

As part of NASA Glenn Research Center's program in spacecraft fire prevention, detection, and suppression, a numerical model of the ventilation flows in the Destiny laboratory (U.S. segment) of the *International Space Station* (ISS) was developed. This model facilitates the evaluation of smoke-detector performance, location options, and fire-suppression strategies. The ISS has the means to detect, isolate, and extinguish fires in all locations where this capability may be needed. Fire is detected by smoke detectors in the racks with internal airflow, smoke detectors at the ventilation return air ducts, and by the crew's sense of smell or other senses. The open area of Destiny is covered by two smoke detectors—one forward-port, the other aft-starboard; both are situated near ventilation return ducts.

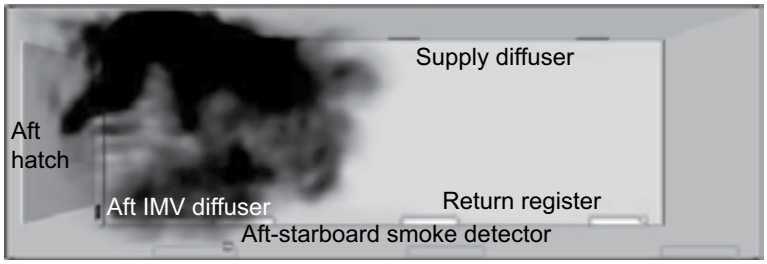


*Smokeview program showing smoke source on the aft-starboard wall of Destiny (condition 2).*

The Fire Dynamics Simulator (FDS) is a computational fluid dynamics model of thermally induced fluid flow that focuses on smoke and heat transport from fires. Smokeview is a three-dimensional visualization program that displays the results of an FDS simulation. These programs were used to determine the smoke density and smoke-detector alarm time for a smoke source in Destiny. The preceding figure shows a Smokeview snapshot of Destiny with an aft-starboard smoke source.

The cabin dimensions, vent locations, and flow rates were obtained from ISS documentation and from conversations with ISS Environmental Control and Life Support System personnel. The smoke source was located along the center of an integrated standard payload rack within the cabin. An aft circumferential profile was constructed by moving the smoke source around the cabin along the four walls. The six air-supply diffusers and ventilation return ducts within the cabin are positioned such that the flow is across the ceiling and down the port wall, establishing a rotational flow pattern (counterclockwise facing forward). Two intermodule ventilation (IMV) diffusers (one aft-port, the other forward-starboard) direct flow along the floor in the forward and aft directions. Three different conditions were investigated: (1) cabin ventilation with aft and forward IMV flow and no cabin obstructions, (2) cabin ventilation with aft IMV flow and no cabin obstructions, and (3) cabin ventilation with aft IMV flow and cabin obstructions (estimated using ISS photographs and located in the aft area of the lab). Condition 1 produced the most symmetric flow, having both IMV diffusers active: one blowing forward, the other aft, in addition to the rotational flow from the supply diffusers. Deactivating the forward IMV produced a fast stream on the port floor, directing flow toward the forward smoke detector. Adding obstructions disturbed the flow field and made the model more realistic.

The bar chart (next page) displays smoke-detector alarm time and location for an aft radial profile. For a smoke source located on the starboard wall, eliminating forward IMV flow increased the detection time by 89 percent and changed the detection location. Adding obstructions increased the time 34 percent more. Moving the source to the ceiling displayed similar trends. Removing forward IMV flow increased detection time by 133 percent, and adding obstructions an additional 9 percent. A smoke source on the port wall had the overall lowest detection time. A 31-percent decrease resulted from turning off the forward IMV flow, and adding obstructions increased the detection time by 21 percent. The lowest detection time (15.3 sec) was obtained when both aft and forward IMV were used and the source was on the floor. It also had the largest increase (414 percent) with just aft IMV flow. Detection time decreased 44 percent when obstructions were added. Overall, the addition of obstructions or moderate changes in the ventilation flow can have significant effects on the time required to detect a fire. Careful modeling of the flow in future spacecraft is needed to ensure rapid fire detection.

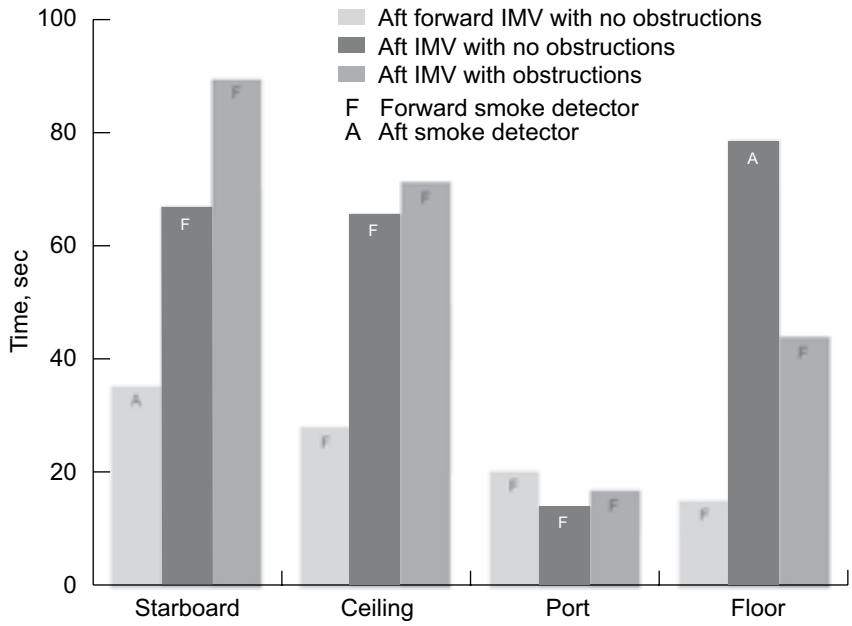


*Results of aft radial smoke source profile showing time and location to first smoke detector alarm.*

**Find out more about Glenn's micro-gravity combustion research:**
http://microgravity.grc.nasa.gov/combustion/

**Glenn contacts:**
John E. Brooker, 216–433–6543, John.E.Brooker@nasa.gov

Dr. David L. Urban, 216–433–2835, David.L.Urban@nasa.gov

**Authors:**
John E. Brooker and Dr. David L. Urban

**Headquarters program office:**
Exploration Systems Mission Directorate

**Programs/projects:**
Advanced Capabilities, Fire Prevention, Detection, and Suppression

## Portable Unit for Metabolic Analysis Benchmarked for Measuring Human Metabolic Activity

The objective of the Portable Unit for Metabolic Analysis (PUMA) project is to develop a prototype portable device that will measure human metabolic activity. PUMA provides highly time resolved measurements (relative to human respiration rate) of temperature, pressure, flow rate, and oxygen and carbon dioxide partial pressure. The pressure, temperature, and flow measurements use existing commercial off-the-shelf (COTS) technology repackaged into a device suitable for measuring human metabolic activity. The oxygen partial pressure ($O_2$) measurement system is a modification of a COTS technology that uses the fluorescence quenching properties of oxygen. The carbon dioxide partial pressure ($CO_2$) measurement system utilizes the strong and relatively unique infrared absorption characteristics of the carbon dioxide molecule to measure its concentration. The latter two measurements do not involve COTS technology, but rely on well-established physical principles for their measurement. All measurements occur at the mask (close to the mouth) and are time resolved so that both an instantaneous and integrated signal history is possible during inhalation and exhalation. This time resolution enables not only highly accurate breath-by-breath analysis but also within-breath analysis.

The photograph (next page) shows the most recent PUMA unit (PUMA3). The PUMA3 avionics box fits into a small backpack for use during varied exercise activities. PUMA3 connects wirelessly (via Bluetooth) to a laptop computer for data storage and analysis. The power source for the unit is a COTS camcorder battery.

The graph shows carbon dioxide ($CO_2$) and oxygen ($O_2$) partial pressures and volumetric flow rate for a brief period of time. The remote computer integrates these data to determine metabolic quantities such as the volumetric consumption of $O_2$ and the volumetric production of $CO_2$.

*PUMA3 unit. The avionics box fits into a small backpack and is suitable for use in varied activities. The data transfer wirelessly to a laptop computer for analysis and storage via Bluetooth.*

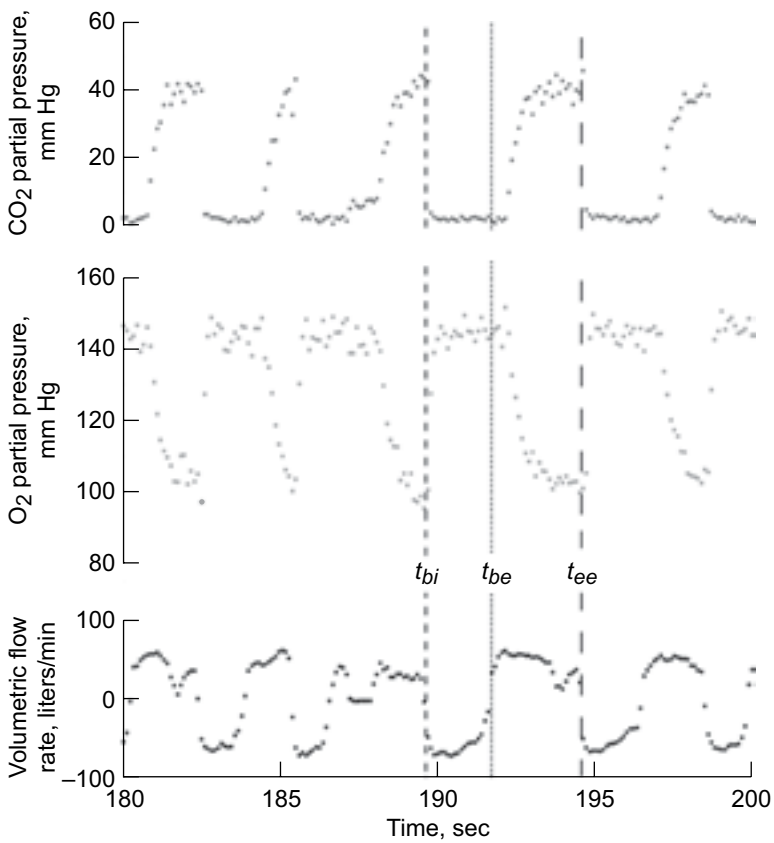


*Typical raw data output of $CO_2$ (top) and $O_2$ (middle) partial pressure and volumetric flow rate (positive flow rate corresponds to exhalation, negative flow rate to inhalation) from PUMA. The vertical lines correspond to the beginning of an inhalation, $t_{bi}$, the beginning of an exhalation, $t_{be}$, and the end of an exhalation, $t_{ee}$.*

The PUMA team (which is composed of NASA Glenn Research Center researchers) conducted human subject tests in May 2004 and November 2005 at Glenn's fitness center. Subsequent tests at the University Hospital Health System pediatric cardiology lab and the NASA Johnson Space Center exercise physiology lab benchmarked the performance against commercial metabolic carts. Future testing will further verify the performance to make accurate metabolic measurements and will include utilizing PUMA to measure the metabolic costs of varied crew functions during simulated extravehicular activities.


**Glenn contact:**
Daniel L. Dietrich, 216–433–8759, Daniel.L.Dietrich@nasa.gov

**Authors:**
Daniel L. Dietrich, Jeffrey R. Juergens, Michael J. Lewis, Michael J. Lichter, and John W. Easton


**Headquarters program office:**
Human Systems Research and Technology, Human Research Program

**Programs/projects:**
Human Research Program, Constellation Program, Extravehicular Activity project, International Space Station Program

# Distribution of Micrometer and Submicrometer Content of the Lunar Regolith Measured

The first quantitative measurements of the fine (20 μm to 200 nm) and ultrafine (200 to 10 nm) components of lunar regolith (refs. 1 and 2) were made by the NASA Glenn Research Center and Professor Da-Ren Chen at the University of Washington (St. Louis, MO) under grant NAG3–2625. The size distributions were measured by gas-phase dispersal and analysis with aerosol measurement techniques. This provided direct evaluation of the transport diameters, in contrast to indirect sizing by light-scattering or two-dimensional projections of high-magnification images. The results demonstrate considerable particle populations in these size regimes, of significant importance to continued lunar exploration.

Concerns over the particulate environment emerged early in Apollo, and a variety of problems were observed. These included the degradation of spacesuit materials, compromised performance of sample return box vacuum seals, off-nominal performance of thermal emissive surfaces, and crew observations of ocular and respiratory irritation (ref. 3).

Numerous approaches are available to measure small particulates. Here, aerodynamic diameters were measured directly, utilizing a differential mobility analyzer (SMPS, TSI, Inc., ref. 4) with a Condensate Particle Counter (CPC) for the ultrafines and an Aerodynamic Particle Sizer (APS, TSI, Inc., ref. 4) for the fines.

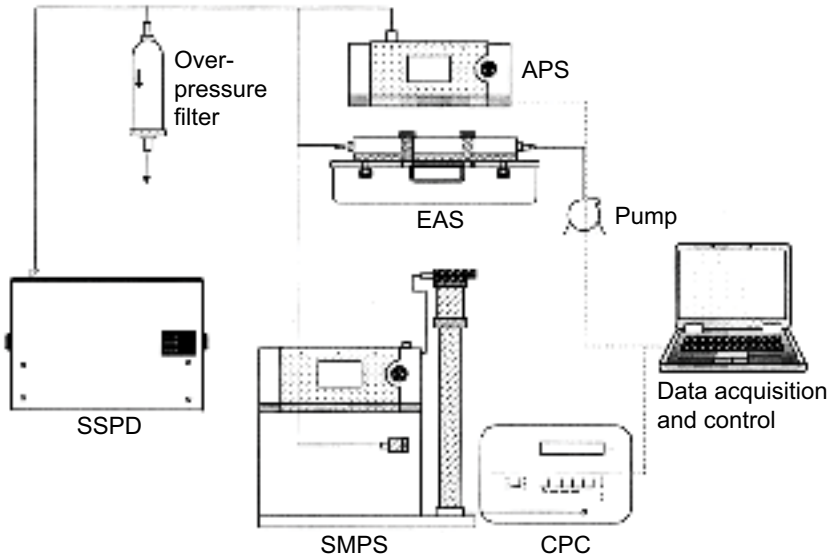


*Experimental configuration for particle size distribution measurements.*

Two samples of surface regolith were analyzed: the first was manually collected by Neil Armstrong (Apollo 11); the second deposited on the surface of the lunar rover and was subsequently collected by Harrison Schmitt (Apollo 17). Both samples were mechanically sieved at 20-μm before analysis. The schematic diagram shows the apparatus used for these measurements. A Small Sample Particle Disperser (SSPD, TSI. Inc.) using a high shear orifice aerosolized and deagglomerated the sample. The sample stream was directed in parallel to an Electrostatic Aerosol Sampler (EAS) to validate deagglomeration and to elucidate shape factors using electron microscopy.

Because the SMPS and APS instruments performed different physical measurements and afforded differing sensitivities and bin widths, merging the data as a single, continuous particle size distribution required careful calibration and matching at the boundaries between measurement ranges. Numerous reference materials were examined to ensure that this was implemented properly.

The most notable observation (see the graphs on the next page) was the considerable submicrometer population, the first reported quantitative measurement of ultrafine content in lunar regolith. The observed bimodal distributions displayed peaks at approximately 1.1 to 1.2 μm and 85 to 90 nm. The maxima occurred at slightly larger sizes in the first sample, which also exhibited more fines. The error bars for each size bin were calculated directly from the data. The comparatively larger fluctuations in the ultrafines are attributable to the small sample sizes involved (order of 100 mg) and to the scanned nature of the SMPS.

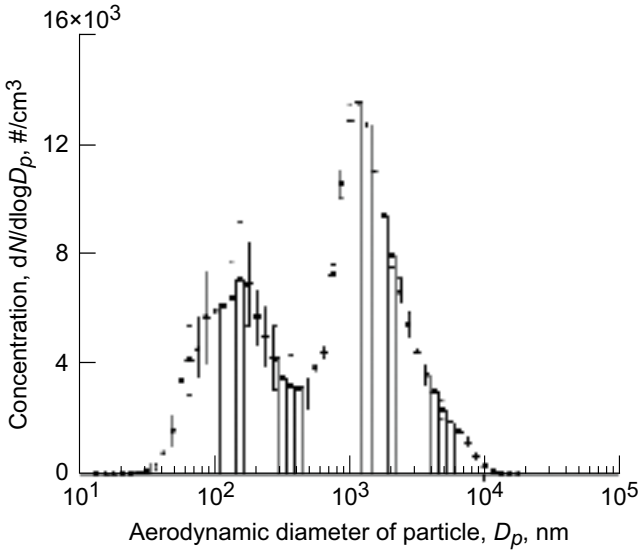


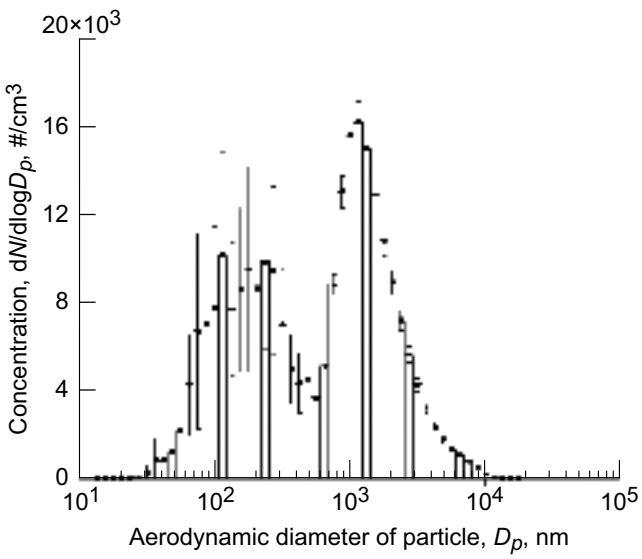


*Measured particle size distribution functions of surface regolith samples. N, number of particles. Top: First sample—Apollo 11. Bottom: Second sample—Apollo 17.*

*Typical particle shape in supermicron regime.*

Electron microscopy analysis of the EAS grids demonstrated that a random sample with several hundred particles had only two agglomerate structures. It is not known whether the structures were fused together by lunar surface processes or from insufficient shear forces in the SSPD, but the infrequency of these chains tends to rule out the latter.

Electron microscopy was also used to relate the aerodynamic diameters to the true particle dimensions, since shape factors influence aerodynamic properties. The images do not reveal complex or rodlike features that would result in significant departures between the aerodynamic and physical dimensions.

**References**


1. Greenberg, Paul: Nanoparticulates on the Moon and Mars. 2nd International Symposium on Nanotechnology and Occupational Health; Minneapolis, MN, 2005.
2. Greenberg, Paul: Sensor Development for the Detection and Characterization of Lunar Dust. Report of the Space Resources Roundtable VII: LEAG Conference on Lunar Exploration, League City, TX, 2005, p. 57.
3. Gaier, James R.: The Effects of Lunar Dust on EVA Systems During the Apollo Missions. NASA/TM—2005-213610, 2005. http://gltrs.grc.nasa.gov/cgi-bin/GLTRS/browse.pl?2005/TM-2005-213610.html
4. Baron, Paul A.; and Willeke, Klaus: Aerosol Measurements: Principles, Techniques, and Applications. 2nd ed., John Wiley & Sons, New York, NY, 2001.



**Glenn contact:**
Paul S. Greenberg, 216–433–3621, Paul.S.Greenberg@nasa.gov

**Authors:**
Paul S. Greenberg and
Prof. Da-Ren Chen


**Headquarters Program Office:**
Exploration Technology and Development Program

**Program/projects:**
Crew Exploration Vehicle, Constellation Systems

# Experimental Rig Built and Used To Investigate Supercritical Water Oxidation for Solid Waste Management and Water Reclamation Systems

Future space exploration missions will require advanced systems to efficiently handle and recycle a variety of waste streams. Super Critical Water Oxidation (SCWO)—one technology under consideration—processes waste materials mixed in a water slurry at temperatures and pressures above the critical point of water (374 °C and 22.1 MPa). At these conditions, there are no distinctions between the liquid and vapor phases, and most gases and organic contaminants in the waste stream become completely miscible in water. Reaction rates are no longer limited by the slow diffusion rates of reactants across phase boundaries, and the overall oxidation efficiency increases substantially.

In one waste-management system envisioned by NASA for extended space missions, organic materials in the waste stream (e.g., biowastes, papers, and plastics) would serve as the fuel source for the SCWO reactions. This technology converts all carbon-based wastes to carbon dioxide ($CO_2$) and can efficiently remove small organic molecules (e.g., methanol and acetic acid) from waste streams, which often proves to be difficult with conventional methods.

Successfully used in many commercial applications, SCWO (1) has very high conversion rates (e.g., residence times of seconds or less); (2) requires minimal preprocessing of waste feed streams; (3) has conversion efficiencies that can approach 99.999 percent; and (4) has clean, well-characterized product streams of $CO_2$, $N_2$, water, and to the extent inorganic material is included in the feed stream, residual precipitates (salts) and metal oxides.

Traditionally, SCWO reactions have been considered to be “flameless,” low-temperature oxidation reactions; however, it has been shown that, under certain conditions, hydrothermal flames can develop suddenly. The inception of flames and their stability are highly dependent on the presence of gravitationally induced buoyant forces. Without proper control, excessive temperatures from these flames would damage unprotected surfaces, such as reactor walls and fluid injection nozzles, and could result in undesirable combustion products. Consequently, a comprehensive approach to environmental testing and evaluation will be required for any SCWO-based system. At the NASA Glenn Research Center, this technology is being advanced through a series of normal-gravity and reduced-gravity tests to identify potential problems, offer mitigating design solutions, and assist in identifying and assessing advanced SCWO design concepts.

In fiscal year 2006, an experimental test rig was built at Glenn for investigating a number of these problems. In addition to operating in normal gravity, the rig can be operated in Glenn’s Zero Gravity Research Facility (which provides 5.2 sec of 0g, refs. 1 and 2). This facility comprises a 480-ml high-pressure reactor vessel and supporting equipment for studying a wide range of SCWO reactions in either a constant-pressure (continuous-flow reactor) or constant-volume (batch reactor) mode.

*The SCWO test facility is designed to be operated in Glenn’s 5.2-sec drop tower to study buoyancy effects on “spontaneous flaming” and injector design.*

Results from two tests in the new rig, using an aqueous mixture of 10 vol% methanol ($CH_3OH$) oxidized by air, have shown a total conversion of 98 percent in approximately 24 sec. These tests showed that without normal-gravity buoyant forces, significant differences in temperature uniformity and temperature transients occurred during and immediately following the reaction (ref. 2).

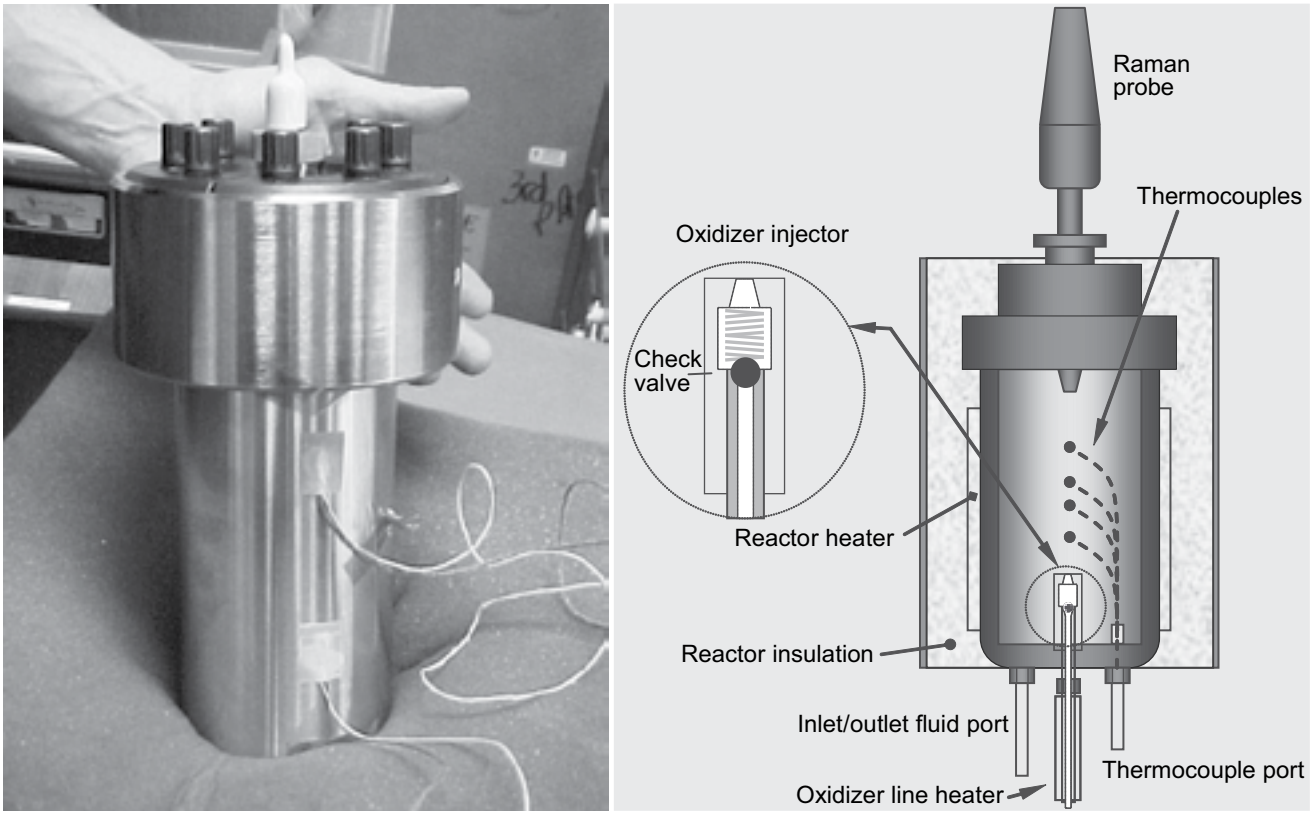


*The SCWO reactor is constructed from Hastelloy C–276 and has an internal volume of 480 cm$^3$. The vessel has been ASME certified for a maximum allowable working pressure of 40.7 MPa at 550 °C. Four thermocouples and a Raman probe are inserted into the reactor to provide near real-time measurements of reactant concentrations. In this test configuration, the oxidizer is injected axially into the reactor vessel once the supercritical conditions are attained.*

**References**

1. Hicks, M.C., et al.: Gravity Effects on Premixed and Diffusion-Limited Supercritical Water Oxidation. 2005 Transactions Journal of Aerospace, SAE Technical Paper Document No. 2005–01–3036, 2005.
2. Hicks, Michael C., et al.: Diffusion Limited Supercritical Water Oxidation (SCWO) in Microgravity Environments. SAE Technical Paper Document No. 2006–01–2132, 2006.

**Glenn contact:**
Michael C. Hicks, 216–433–6576, Michael.C.Hicks@nasa.gov

**National Center for Space Exploration Research contact:**
Uday G. Hegde, 216–433–8744, Uday.G.Hegde@nasa.gov

**Authors:**
Michael C. Hicks and Dr. Uday G. Hegde

**Headquarters program office:**
Exploration Systems Mission Directorate

**Programs/projects:**
Advanced Capabilities, Exploration Life Support

# Narrow Channel Apparatus Used To Simulate Low-Gravity Flames on Earth

One of the most distinguishing characteristics of flames or fires in normal gravity is the strong upward buoyant convection that carries away both heat and combustion products and brings fresh air to the flame. In partial (e.g., lunar) gravity or microgravity, these flows are reduced. Thus on a spacecraft, the ventilation system or crew movement is often the dominant driver of the flow. This slow-flow regime of combustion, which is difficult to study in normal gravity, can be dangerous to the crew and spacecraft. As anyone who has fanned or blown on an incipient fire knows, airflow can have a huge impact on whether a fire erupts or not.

A new apparatus was developed at the NASA Glenn Research Center to try to mimic the flow conditions found in partial-gravity or microgravity to allow flammability screening of materials to be used in space. This is especially relevant as NASA prepares to return to the Moon, since much remains unknown about fire dangers in partial gravity or the lower pressure, higher oxygen level atmospheres being planned for these missions.

The apparatus consists of a narrow channel, approximately 1 cm tall by 36 cm wide by 46 cm long, with the sample material to be tested held parallel between the metal bottom and the quartz top. The quartz top plate serves as a window to observe the flame and also dramatically reduces the buoyant convection by eliminating a path for hot gases to rise. After passing through an inlet plenum, a slow flow of air is directed across the sample at velocities typical of spacecraft ventilation systems (~10 cm/sec). Ignition of the material is achieved at one end using a hot wire energized for a few seconds. A video camera is used to record the flame as it spreads across the sample. Gas mass-flow controllers vary the flow velocity in the channel, allowing researchers to find the flow conditions where the flame can no longer propagate.

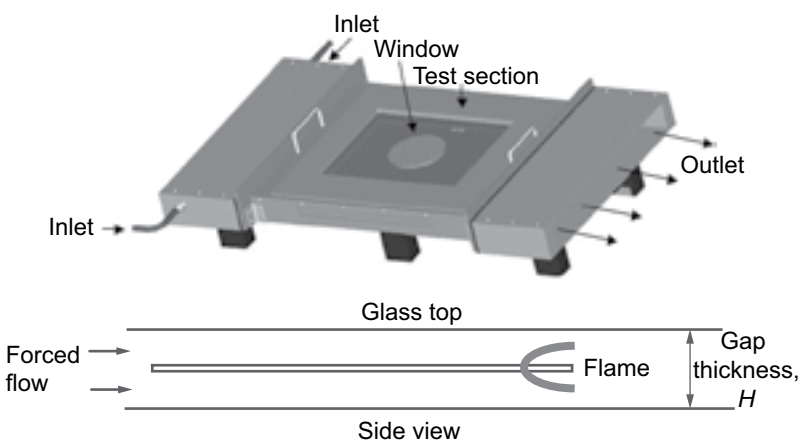


*Narrow Channel Apparatus used to simulate partial-gravity or microgravity flame conditions for material flammability screening.*

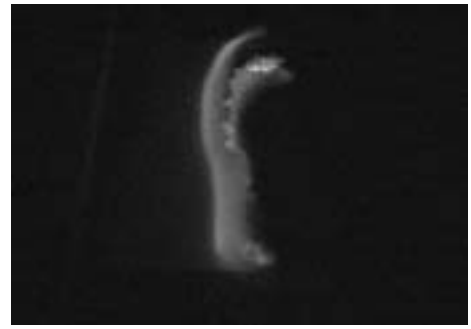

*A flame in Glenn's Narrow Channel Apparatus. This figure is shown in color in the online version of this article (http://www.grc.nasa.gov/WWW/RT/2006/RU/RUC-olson1.html).*

Experiments using filter paper as the fuel were conducted in the apparatus to determine the flame spread rate for various flow velocities and channel heights. A few comparison tests were performed in true microgravity in Glenn's Zero Gravity Research Facility using a similar apparatus. Though more tests are needed, the preliminary results showed good agreement between the Narrow Channel Apparatus and the Zero Gravity Research Facility results. Flames in the Narrow Channel Apparatus were mostly or all blue, like microgravity flames, and were unlike the traditional yellow, sooty flames found when paper burns in normal gravity. In addition, the rate at which the paper was consumed was similar in both the Narrow Channel Apparatus and the Zero Gravity Research Facility.

These results show that narrow channel testing, with further refinements, may become one of the tests NASA conducts to determine a material's suitability for use in space. The current NASA screening test does not consider the effect of gravity or provide quantitative data that can be used to assess actual fire dangers. Narrow channel testing can mimic in normal gravity some important aspects of microgravity combustion without the expense and/or short time durations of flight experiments or drop facilities.

**Bibliography**
Olson, S.L.; Miller, F.J.; and Wichman, I.S.: Characterizing Fingering Flamelets Using the Logistic Model. Combustion, Theory and Modeling, vol. 10, no. 2, 2006, pp. 323–347.

Wichman, I.S., et al.: A Buoyancy-Suppressing Apparatus for Materials Flammability Assessment in Reduced Gravity Applications. Presented at the Central States Section Meeting of the United States Section of the Combustion Institute, Fundamentals & Applications, Cleveland, OH, 2006.

**Glenn contact:**
Dr. Sandra L. Olson, 216–433–2859, Sandra.L.Olson@nasa.gov

**National Center for Space Exploration Research contact:**
Dr. Fletcher J. Miller, 216–433–8845, Fletcher.J.Miller@nasa.gov

**Authors:**
Dr. Sandra L. Olson, Dr. Fletcher J. Miller, and Indrek S. Wichman

**Headquarters program office:**
Exploration Systems Missions Directorate

**Programs/projects:**
Advanced Capabilities/Fire Prevention, Detection, and Suppression

**Special recognition:**
A journal cover photo of our work appeared on Combustion Theory and Modeling in April 2006.

# Equivalent Low Stretch Apparatus Developed for Testing Flammability

NASA is working to develop (or extend) a normal-gravity test (or set of tests) that can be used to screen materials for use in space exploration environments. One candidate test method uses the Equivalent Low Stretch Apparatus (ELSA). In this test, gravity effects are minimized by burning the material in a ceiling fire configuration, so the hot air cannot rise. The “stretch”—the velocity gradient near the fuel surface—is created by an air jet blowing up toward the fuel surface. Stretch is varied by varying the air jet velocity.

Developed at the NASA Glenn Research Center, ELSA is a modified version of the standard cone calorimeter test method. It uses an oven coil wound into an open-tipped cone shape to radiatively heat a fuel sample up to its ignition temperature. In ELSA, the cone is underneath the sample, with the air jet blowing through the center of the cone.

Because ignition delay times are shorter at lower stretch (or lower g), the normal cone calorimeter test overestimates the ignition time in microgravity, lunar gravity, and Martian gravity. To date, ELSA data with multiple fuels have confirmed that ELSA can simulate key features of the flammability behavior of low-stretch materials. Comparison with available low-gravity data is good.

The critical heat flux necessary for ignition decreases with stretch rate (or g level). At zero stretch, any heat flux that is just slightly more than the experimental heat losses, such as radiation from the surface, is sufficient to ignite the material. The heat flux needed for ignition is lowest in microgravity.

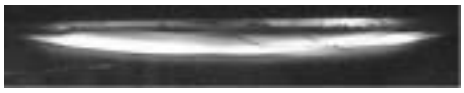

*Flame shortly after ignition of a fuel sample in ELSA. The flame is beneath the fuel sample. This figure is shown in color in the online version of this article (http://www.grc.nasa.gov/WWW/RT/2006/RU/RUC-olson2.html).*

Regression rates (burning rates) for polymethyl methacrylate (PMMA, or Plexiglas—Rohm and Haas Company) increase with heat flux and stretch rate, but the low-stretch flame with external radiation is very fuel rich, and nearly an order of magnitude more CO is produced (1000 ppm) than in the normal cone configuration.

These results suggest that the current standard cone calorimeter test used to evaluate materials for use in spacecraft (NASA–STD–6001, test 2) overestimates the ignition times and underestimates the toxic products in a reduced-gravity environment.

**Bibliography**

Olson, S.L., et al.: An Earth-Based Equivalent Low Stretch Apparatus for Material Flammability Assessment in Microgravity and Extraterrestrial Environments. Proceedings of the Combustion Institute, vol. 30, issue 2, 2005, pp. 2335–2343.

Olson, S.L.; Beeson, H.; and Haas, J.P.: Experimental Demonstration of an Earth-Based Equivalent Low Stretch Apparatus to Assess Material Flammability for Microgravity & Extraterrestrial Fire-Safety Applications. The 3rd Joint Meeting of the U.S. Sections of The Combustion Institute, Chicago, IL, 2003.

**Find out more about this research:**

**Glenn's Spacecraft Fire Safety program:**
http://microgravity.grc.nasa.gov/life/firesafe.html

**ELSA video:**
http://exploration.grc.nasa.gov/combustion/web/vid_elsa.htm

**Glenn contact:**
Dr. Sandra L. Olson, 216–433–2859, Sandra.L.Olson@nasa.gov

**Authors:**
Dr. Sandra L. Olson and Dr. Harold Beeson

**Headquarters program office:**
Exploration Systems Mission Directorate

**Programs/projects:**
Fire Prevention, Detection, and Suppression

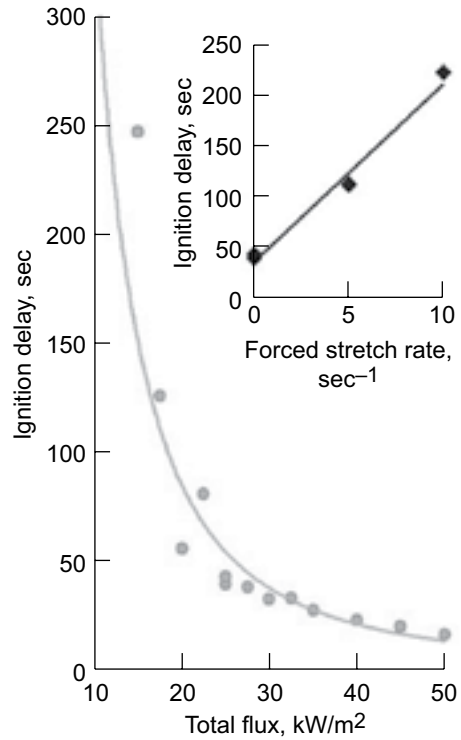


*Ignition delay for Kydex 100 decreases with increasing heat flux, as shown here. In the inset, ignition delay decreases at lower stretch rate (i.e., lower gravity) at 25 kW/m$^2$.*

## Gravitational Effects Evaluated in Swirl-Stabilized Fluidized Bed

A fluidized bed reactor was developed in-house at the NASA Glenn Research Center for use in reduced-gravity environments for space exploration applications such as life support and in situ resource utilization. On Earth, fluidized particle beds are established through the balance of an upward fluid flow (and its resultant drag force) and gravity's downward pull on the bed particles. In the novel reactor concept, a swirling flow was used to stabilize a radial fluidized bed in microgravity experiments conducted in Glenn's 2.2 Second Drop Tower. Specifically, the fluidized bed was formed through a balance of the radial drag (from an inward flow) and apparent centrifugal forces acting on the bed particles. Gravitational settling dominated the particle behavior in comparison normal-gravity tests.

Fluidized bed reactors are advantageous in chemical processing for reasons including rapid mixing, liquidlike behavior, resistance to temperature fluctuations, and high heat and mass transfer rates. Given these benefits, NASA had begun evaluating such reactors for filtration, the reduction of lunar regolith to produce oxygen, and the pyrolysis or incineration of solid waste to recover valuable resources during long-duration outpost missions. However, the function of these reactors in reduced-gravity environments had generally not been evaluated.

In the cylindrical reactor concept developed at Glenn, the air (or other fluid) is tangentially injected at the reactor wall and is exhausted through a porous tube out the ends of the reactor. This configuration creates an inwardly swirling flow with a zone of low axial and radial velocity along the reactor wall between the injection ports. In the experiments conducted, two injection ports were symmetrically located at each end of the

*Numerical simulation of the flow field within the reactor, illustrating the region of low axial and radial velocity along the reactor wall and between the two injection ports (top center of figure), where the particle bed is stabilized in microgravity.*

reactor vessel (which was internally 9.2 cm in length and 10 cm in diameter). A fluidized bed of zirconium silicate particles (which were nominally 0.2 to 0.3 mm) was stabilized in microgravity experiments. The same airflow conditions, where the apparent centrifugal and gravitational accelerations were of similar order, were insufficient to maintain the radial bed in normal Earth gravity. As expected from the numerical simulation of the gas flow, the microgravity particle bed formed at the middle of the reactor length because of the stagnation region at the symmetry plane. With increasing particle loads, the bed was observed to spread axially toward the ends of the reactor. The exploratory study of this reactor concept has been completed.

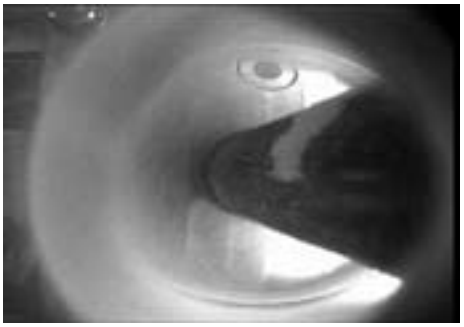

*Microgravity end-view photograph showing the white swirl-fluidized particle bed along the reactor wall, while the center of the reactor is nearly particle free.*

**Bibliography**

Stocker, D., et al.: Effects of Gravity on Swirl-Stabilized Fluidized Beds. AIAA–2006–1136, 2006.

**Glenn contacts:**
Dennis P. Stocker, 216–433–2166, Dennis.P.Stocker@nasa.gov

John E. Brooker, 216–433–6543, John.E.Brooker@nasa.gov

**Authors:**
Dennis P. Stocker, John E. Brooker, and Dr. Uday G. Hegde

**Headquarters program office:**
Exploration Systems Mission Directorate

**Programs/projects:**
Exploration Systems

# Durable Coating Technology Tested for Lunar Dust Protection and Mitigation

Special coatings are being developed and tested by the NASA Glenn Research Center in collaboration with the Cleveland State University to contend with the effects of dust on the lunar surface. These coatings potentially have wide applicability ranging from the prevention of dust buildup on solar arrays and radiator surfaces to the protection of extravehicular activity space suit fabrics and visors. They need to be durable and functional based on the application.

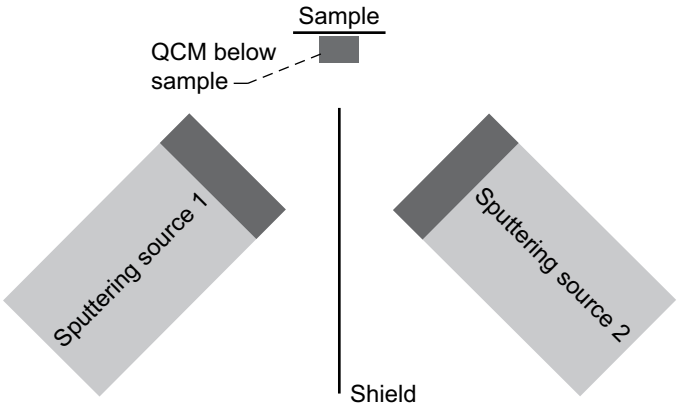


*Planview of two-source radiofrequency magnetron sputter system for fast prototyping of mixed or doped coatings. QCM, quartz-crystal microbalance.*

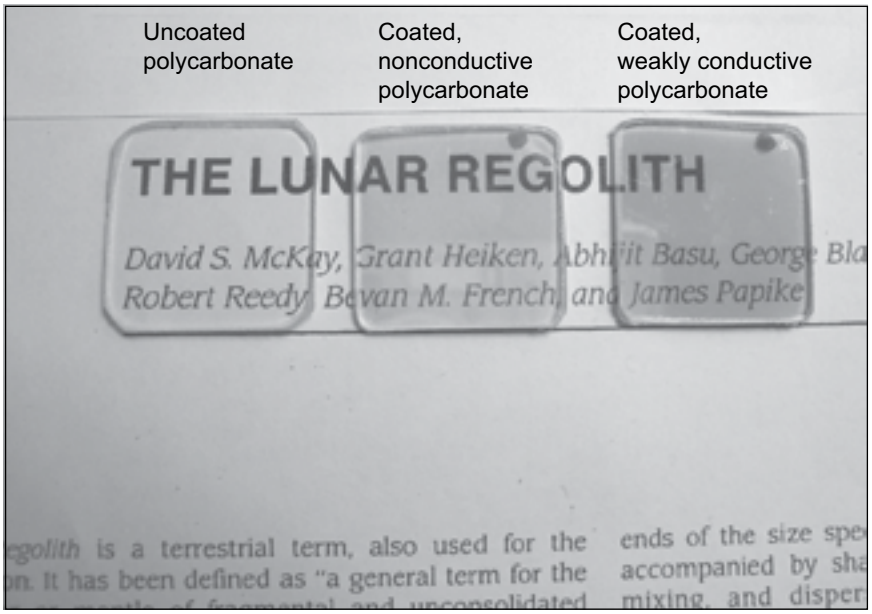


*Coated and uncoated polycarbonate sample coupons. This figure is shown in color in the online version of this article (http://www.grc.nasa.gov/WWW/RT/2006/RU/RUF-agui.html).*

One particular initial focus is on transparent coatings. Conventional transparent coatings are specialized for transmission (antireflective) or are made scratch resistant. The current coating development also aims at making transparent coatings that are slightly conductive to reduce the electrostatic attraction of dust particles, in particular lunar dust particles.

We have started preparing coatings approximately 80 nm thick on room-temperature glass and polycarbonate substrates using the radiofrequency magnetron sputtering technique shown in the sketch (ref. 1). The film material consists of a mixture of titanium dioxide ($TiO_2$) and excess titanium (Ti). The $TiO_2$ produces a hard transparent film, whereas the Ti makes the film slightly conductive. The photograph shows representative coated and uncoated samples. The coating produces a slightly bluish tint but provides adequate transparency. A coating with high conductivity is not desirable since it can produce electrical shorting problems. Other standard and exotic coating materials are being investigated to provide the best compromise between transparency, conductivity, and durability.

The lunar environment includes exposure to ultraviolet solar radiation and abrasive dust that can be harsh on materials. The coatings will be checked for changes in electrical properties under prolonged ultraviolet light exposure. We have also started conducting a series of environmental tests that simulate the exposure of coated samples to dust under relevant conditions, beginning with abrasion tests using lunar stimulant materials (a close lunar dust reproduction).

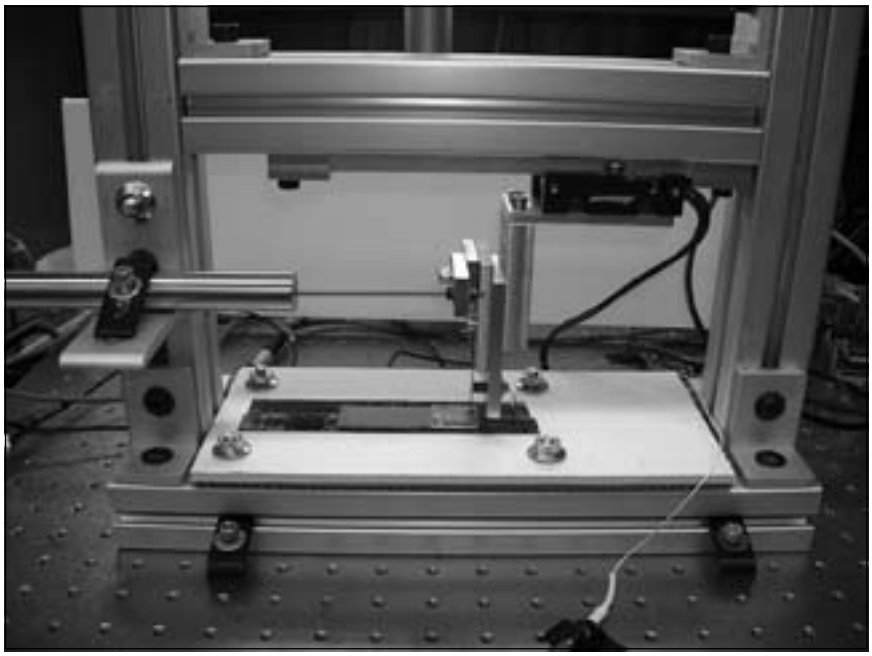

*Abrasion testing device.*

A custom abrasion testing device (shown in this photograph) was developed for this purpose. The device was designed for small sample coupons, 1-in.-square coupons in this case, and allowed for a range of frictional contact pressures, from very low contact pressures. It also provided a way to control and quantify the total amount of abrasion. Also importantly, a lunar stimulant known as JSC–1 was used to prepare an abrasive medium substrate for these tests. A series of abrasion tests at light contact pressures showed that these coatings can tolerate this degree of dust abrasion and that the coatings attracted less dust during the abrasion process than did the corresponding uncoated samples. In addition, we expect that these coatings can be commercialized for applications in harsh environments such as desert and cold weather operations.

**References**

1. Agui, J.H., et al.: Durable Coating Technology for Lunar Dust Protection and Mitigation. 2006 Transactions Journal of Aerospace, SAE Technical Paper Document No. 2006–01–2205, 2006.

**Glenn contact:**
Dr. Juan H. Agui, 216–433–5409,
Juan.H.Agui@nasa.gov

**Authors:**
Dr. Juan H. Agui and
Prof. Paul Hambourger

**Headquarters program office:**
Exploration Systems Mission Directorate

**Programs/projects:**
Advance Extravehicular Activity, Lunar Surface Access Module

# Porous-Media-Based Condensing Heat Exchanger Investigated for Space Systems

Temperature and humidity control using condensing heat exchangers in microgravity requires condensation and separation of liquid from the airstream. Current technology employs a fin-and-plate heat exchanger followed by a centrifugal separator. A layered porous media-based condensing heat exchanger where capillary suction is used to imbibe and selectively remove the condensed water from a flowing airstream provides an attractive alternative to current designs. A conceptual design of such a system using a porous flat-plate with embedded cooling tubes proposed by researchers at the NASA Glenn Research Center is presented in reference 1. The critical elements of a concept are (1) condensation of vapor from the airstream on the chilled porous substrate, (2) absorption and retention of the condensate in the porous substrate, and (3) selective removal of the condensate from the porous substrate in the presence of air under reduced-gravity to microgravity conditions. The basic feasibility issues associated with the three elements were successfully resolved in laboratory tests at Glenn, and they are summarized here.

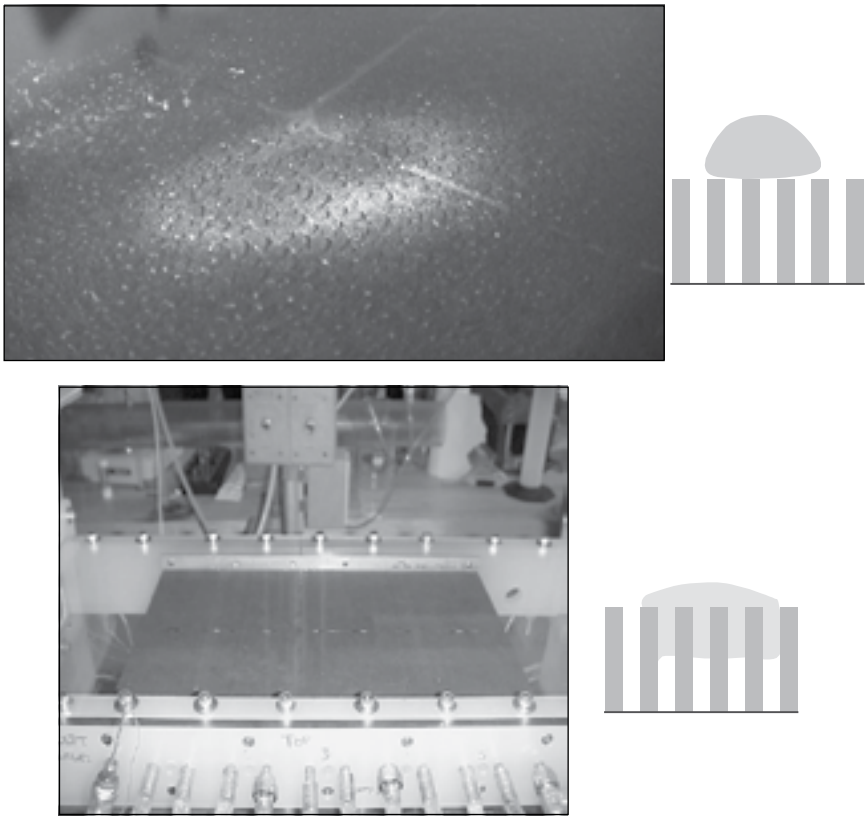

*Top: Condensation on a nonwetting porous graphite substrate: Condensate beads up. Bottom: Condensation on a treated wetting porous graphite substrate: Condensate is imbibed immediately.*

Initial tests with an untreated porous graphite as the condensing substrate showed that condensate tends to bead up on the surface and does not imbibe immediately into the unsaturated porous medium as shown in the top photograph. To overcome this problem, we developed a clay-based treatment to enhance the wettability of graphite with water. The treated material was completely wetting, and the condensate imbibed into the pores immediately (bottom photograph).

In tests in which condensate removal was turned off, the condensate did not drip until the overall saturation reached approximately 45 percent in the graphite substrate (see the graph on the next page). When condensate was removed at a steady rate, liquid saturation levels as high as 80 percent were observed without dripping or liquid layer formation. Details of heat transfer analysis and experimental measurements of moisture condensation are presented in references 2 and 3. Further tests were conducted with a composite porous system composed of porous graphite block and porous ceramic tubes to demonstrate the selective phase separation aspect of the design under controlled saturation of the porous substrate in a terrestrial environment. It was demonstrated that the liquid phase could be preferentially separated from the unsaturated porous graphite block as proposed (ref. 4).

The results of this investigation should help in the design of a passive, porous media-based condensing heat exchanger capable of gravity-independent operation. It applies to the *International Space Station* and all advanced manned missions, a lunar habitat, Mars habitat, and Mars transit vehicle for temperature and humidity control.

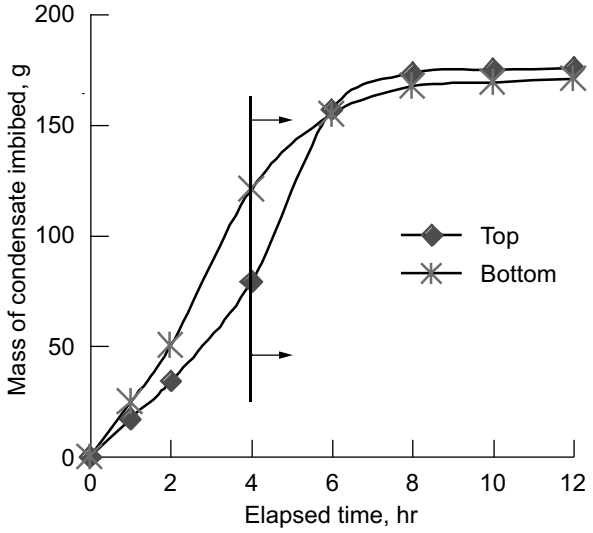


*Condensate mass imbibed as a function of time in each half of the porous substrate.*

**References**


1. Hasan, Mohammad M., et al.: Conceptual Design of a Condensing Heat Exchanger for Space Systems Using Porous Media. NASA/TM—2006-214130, 2006. http://gltrs.grc.nasa.gov/Citations.aspx?id=81
2. Balasubramaniam, R., et al.: Analysis of Heat and Mass Transfer During Condensation Over a Porous Substrate. Interdisciplinary Transport Phenomena in the Space Sciences, S.S. Sadhal, ed., Annals of the New York Academy of Sciences, Blackwell Publishing, vol. 1077, 2006, pp. 459–470.
3. Nayagam, Vedha, et al.: A Porous Media-Based Heat Exchanger: Experimental Measurements of Moisture Condensation. SAE Technical Paper Document No. 2006–01–2037, 2006.
4. Khan, Lutful; and Hasan, Mohammad: Porous Media Based Phase Separation in Condensing Heat Exchanger for Space Systems. SAE Technical Paper Document No. 2006–01–2275, 2006.


**Find out more about microgravity fluid physics research at Glenn:**
http://exploration.grc.nasa.gov/life/legacy_fluid.html


**Glenn contact:**
Dr. M.M. Hasan, 216–977–7494, Mohammad.M.Hasan@nasa.gov

**National Center for Space Exploration Research contact:**
Dr. Vedha Nayagam, 216–433–8702, Vedha.Nayagam@nasa.gov

**Authors:**
Dr. Mohammad M. Hasan and Dr. Vedha Nayagam


**Headquarters program office:**
Exploration Systems Mission Directorate

**Programs/projects:**
Advanced Life Support Systems, Humidity and Temperature Control for the International Space Station, Crew Exploration Vehicle, Lunar and Martian Missions, extravehicular activities

# MATERIALS AND STRUCTURES

## Long-Term Creep Resistance of a Cast Superalloy Investigated

Nickel-based superalloys represent the current state-of-the-art for many high-temperature, nonnuclear, power-generation applications. However, these superalloys have not been tested in creep at the combination of high temperatures and very long service times anticipated in space nuclear power generation. A baseline Brayton power-generation cycle would employ a superalloy impeller having significant centrifugal stresses at temperatures up to 1200 K for durations exceeding several years in a working environment of a helium-xenon inert gas mixture (refs. 1 and 2). Designers of this impeller need to know the creep resistance of potential impeller materials at realistic temperatures, stresses, and environments.

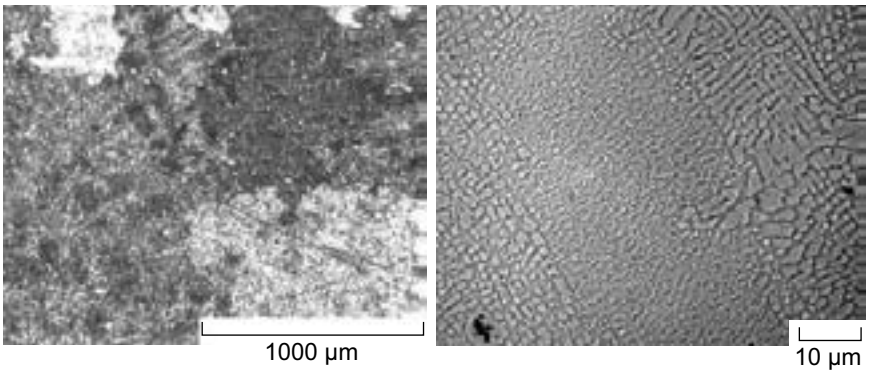


*MAR–M 247LC microstructure. Left: Coarse grain size. Right: Varying y' size.*

MAR–M 247LC is a representative of the cast superalloys currently used in impellers and rotors where the hub and blades are cast as a single unit, and was selected for the present evaluations at the NASA Glenn Research Center. Most creep tests were performed in air using conventional, uniaxial-lever-arm constant-load creep frames with resistance-heating furnaces and shoulder-mounted extensometers. However, two tests were run in a specialized creep-testing machine, where the specimens were sealed within environmental chambers containing inert helium gas of 99.999-percent purity held slightly above atmospheric pressure. All creep tests were performed according to the ASTM E139 standard.

The cast MAR–M 247LC had irregular, very coarse grains with widths near 700 μm and lengths near 800 to 12,000 μm. The grains were often longer in the direction of primary dendrite growth (see the photomicrographs). The microstructure was predominated by about 65 to 70 vol% of $Ni_3Al$-type ordered intermetallic $\gamma'$ precipitates in a face-centered cubic $\gamma$ matrix, with minor MC and $M_{23}C_6$ carbides. The sizes of the $\gamma'$ precipitates varied from about 0.4 μm at dendrite cores to 3.0 μm between dendrites, because of dendritic growth within grains.

Creep tests in air were designed to determine allowable creep stresses for 980, 1090, and 1200 K that would give 1-percent creep in 10 years of service, a typical goal for this application. This service goal represented a target strain rate of 0.1 percent/year. Creep strain rate to 0.2-percent creep is shown versus stress in the following graph. Stresses of about 475, 150, and 70 MPa were estimated to achieve the target strain rate at 980, 1090, and 1200 K, respectively. Additional creep tests and analyses are necessary, but a preliminary creep analysis using current test results indicates quite good potential for an impeller fabricated of MAR–M 247LC to meet Brayton-cycle requirements, for maximum temperatures to 1200 K (ref. 3).

Tests to estimate the effects of air versus inert environments on creep resistance were also initiated. The results of single tests in air at 1-atm pressure and in helium at slightly above 1 atm at 1090 and 1200 K are compared in the graphs on the next page. Creep progressed as fast or even faster in helium than in air at 1090 and 1200 K. The creep tests in air reasonably approximate response in helium to low creep strain levels near

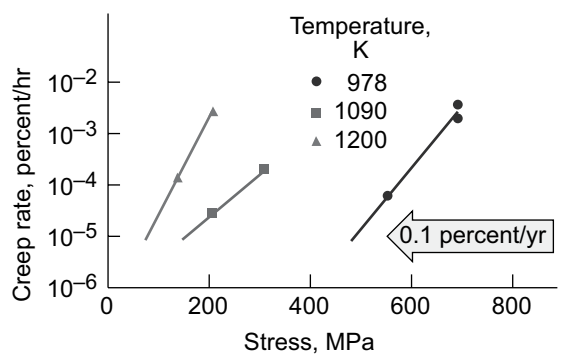


*Creep stress versus strain rate for MAR–M 247LC, showing estimated stresses necessary to achieve a maximum strain rate of 0.1 percent per year.*

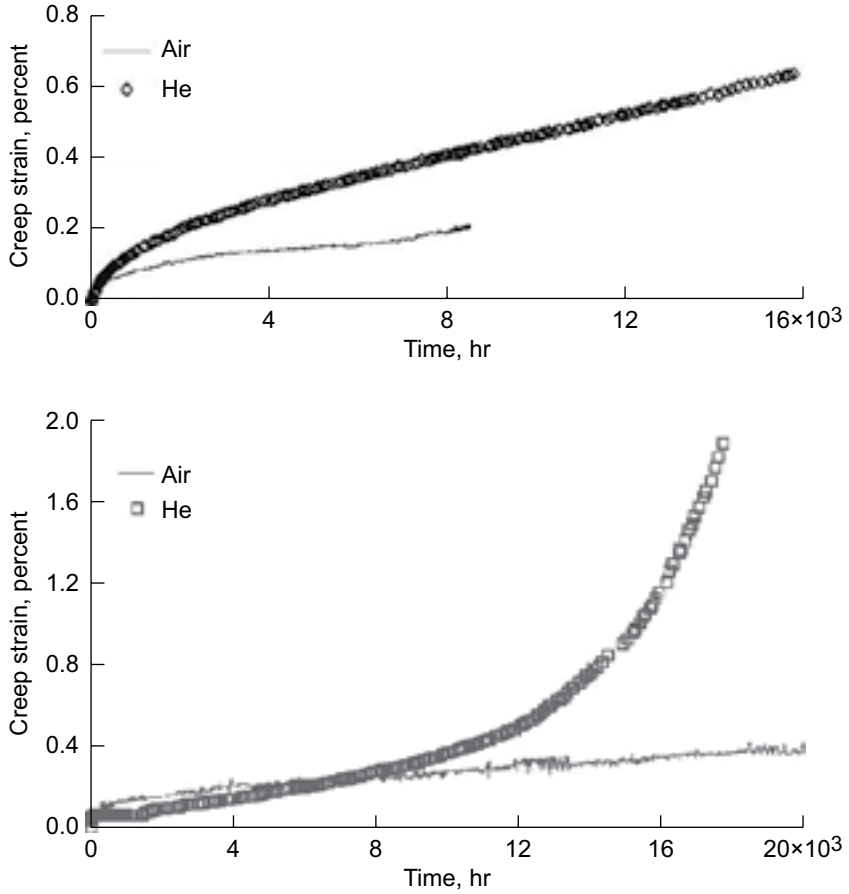


*Comparison of creep response in air versus helium. Top: 1090 K. Bottom: 1200 K.*

0.1 percent, but not at high strains. More tests are needed for confirmation, but this suggests that there may be no improvement in creep resistance due to the inert environment (ref. 4).

**References**


1. Mason, Lee S.: A Power Conversion Concept for the Jupiter Icy Moons Orbiter. J. Propul. P., vol. 20, no. 5, 2005, pp. 902–910.
2. Barrett, Michael J.: Expectations of Closed-Brayton-Cycle Heat Exchangers in Nuclear Space Power Systems. J. Propul. P., vol. 21, no. 1, 2005, pp. 152–157.
3. Gayda, John; and Gabb, Timothy: Two Dimensional Viscoelastic Stress Analysis of a Prototypical JIMO Turbine Wheel. NASA/TM—2005-213650, 2005.
4. Ammon, R.L.; Eisenstatt, L.R.; and Yatsko, G.O.: Creep Rupture Behavior of Selected Turbine Materials in Air, Ultra-High Purity Helium, and Simulated Closed Cycle Brayton Helium Working Fluids. J. Eng. Power, vol. 103, no. 2, 1981, pp. 331–337.


**Find out more about the research of Glenn's Materials Division:**
http://www.grc.nasa.gov/WWW/MDWeb/


**Glenn contacts:**
Tim Gabb, 216–433–3272, Timothy.P.Gabb@nasa.gov

John Gayda, 216–433–3273, John.Gayda-1@nasa.gov

**Authors:**
Dr. Timothy P. Gabb, Dr. John Gayda, and Dr. Cheryl L. Bowman


**Headquarters program office:**
Exploration Systems Mission Directorate

**Programs/projects:**
Prometheus, Fission Surface Power

# Low-Density, Creep-Resistant Superalloys Developed for Turbine Blades

The most demanding conditions in an aircraft turbine engine are in the high-pressure turbine rotor, and a stringent set of requirements are placed on the materials used in that application. The requirements include a balance of creep resistance, temperature capability, environmental resistance, and damage tolerance. In today's engines, blade performance and durability are achieved through advanced nickel-base superalloys combined with sophisticated internal cooling schemes and thermal barrier coatings.

The NASA Glenn Research Center undertook a program to further improve the turbine engine thrust-to-weight ratio by developing new turbine blade alloys with higher creep resistance and reduced densities in comparison to those of current production superalloys. Alloy density has a significant impact because reducing the turbine blade weight through lower alloy densities enables reductions in the design weight of other parts throughout the turbine rotor, including the disk, hub, and shaft, as well as supporting structures in the engine. This cascading effect traditionally results in a total engine weight savings of 8 to 10 times the blade weight savings, translating into reduced fuel consumption and reduced emissions.

The new nickel-base alloys represent a major departure from previous alloy design practices used in industry for single-crystal superalloys. Advances in past superalloy development for turbine blade applications have been accomplished with continued increases in the refractory metal content, which significantly increase alloy density. High alloy densities have limited the use of the advanced superalloys to specialized applications.

The technical challenge in this new effort was to identify specific alloying additions to the nickel base that would provide both high-temperature creep strength and density reductions. Engineering judgment was first used to identify three new superalloy compositions and four key elements to vary over a new range of concentrations. A design-of-experiments methodology was adopted to minimize the number of alloys that would need to be cast, yet still produce models with good predictive capabilities over the full range of compositions for subsequent optimization and balance-of-property tradeoffs.

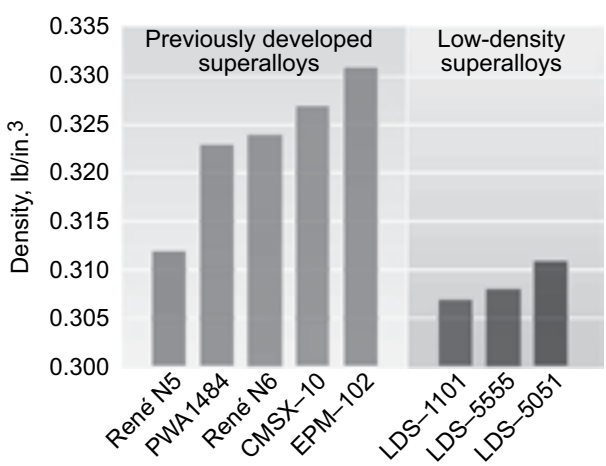


*Measured densities of new low-density superalloys compared with previously developed superalloys. The most creep resistant, low-density alloys are shown here for comparison.*

Based on the computational analysis, 12 alloys were cast for initial screening tests, which included the determination of density, microstructural stability, and oxidation resistance. The measured densities of 11 of the 12 alloys in the design space were significantly lower than those of superalloys previously developed by industry. A range of microstructural stability was observed over the design space, which was a desirable outcome for optimization and property tradeoffs in subsequent casting rounds. A range of cyclic oxidation behavior was observed over the design space, with several alloys approaching or exceeding the excellent oxidation resistance of second-generation superalloys after 200 cycles at 2012 °F.

Regression analyses of the alloy responses were then performed to determine the influence of specific elements on the measured properties and to predict compositions optimized for density, stability, and oxidation resistance for subsequent casting rounds. These regression models were used to downselect the alloys for casting into single crystals to characterize the high-temperature creep resistance at 1800 and 2000 °F. The elevated-temperature creep resistance of the new alloys was demonstrated to significantly exceed those of second-generation superalloys that are currently used in production. Furthermore, the low-density alloys had specific creep strengths that met or exceeded those of third- and fourth-generation alloys. The strongest new alloys also had low densities, stable microstructures, good oxidation resistance, and damage tolerance.

Future plans include fatigue testing, burner rig testing, castability checks, and coating compatibility tests to further develop the commercialization potential of these new superalloys. Further optimization of alloy compositions is being pursued with additional castings to produce a suite of alloys for tailoring to specific applications.

**Glenn contacts:**
Dr. Rebecca A. MacKay, 216–433–3269, Rebecca.A.MacKay@nasa.gov
Dr. Michael V. Nathal, 216–433–9516, Michael.V.Nathal@nasa.gov

**Authors:**
Dr. Rebecca A. MacKay, Dr. Timothy P. Gabb, Dr. James L. Smialek, and Dr. Michael V. Nathal

**Headquarters program office:**
Aeronautics Research Mission Directorate

**Programs/projects:**
Subsonic Fixed Wing Project

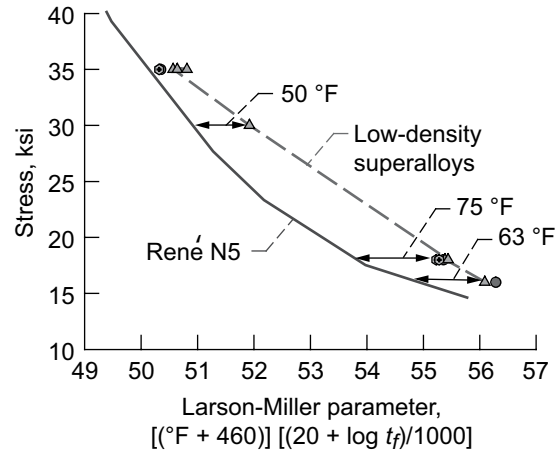


*The new low-density alloys significantly improved creep resistance and metal temperature capability in comparison to a current-production superalloy (René N5). The data are plotted using a Larson-Miller parameter, which allows test data generated at different temperatures to be compared on a single plot.*

## Compatibility of Titanium With Liquid-Metal NaK (78 wt% Potassium/ 22 wt% Sodium) Evaluated

Designs of space nuclear power systems under consideration specify liquid-metal cooling for the nuclear reactor and heat-rejection loops. NaK—a high-thermal-conductivity eutectic mixture of 78 wt% potassium (K) with the balance sodium (Na)—is one candidate under consideration for use as the heat transfer fluid. As part of the Prometheus Nuclear Power and Propulsion project, the NASA Glenn Research Center initiated an experimental program to examine the compatibility of titanium with NaK. Candidate materials for the ducting were identified, and a literature review indicated that stainless steel and titanium may have very good resistance to NaK. A reasonable understanding of the compatibility for stainless steel has been done in support of land-based nuclear systems, but relatively little compatibility information is available for titanium. Titanium would be the preferred material for space applications because of its lower density. This study developed test techniques and determined the compatibility of NaK with commercial-purity (CP2) titanium.

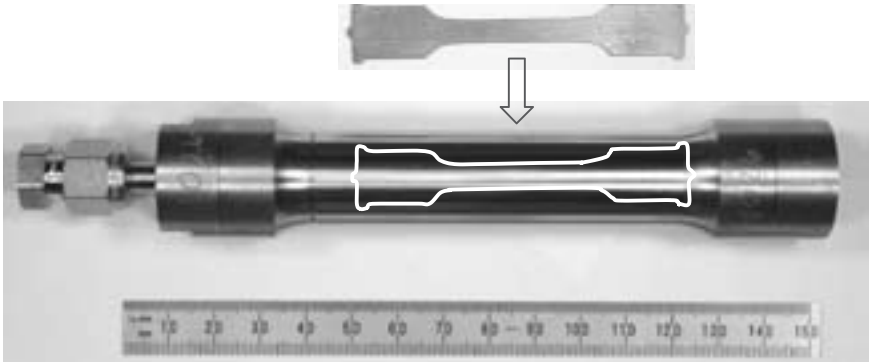

*Typical capsule design and tensile specimen used to evaluate the compatibility of NaK with titanium.*

Sealed capsules containing a small tensile specimen, both made of titanium, were filled with about 12 g of NaK, sufficient to completely immerse the titanium tensile specimen. The BASF Company (Evans City, PA), a major supplier of NaK alkali metals in the United States, filled

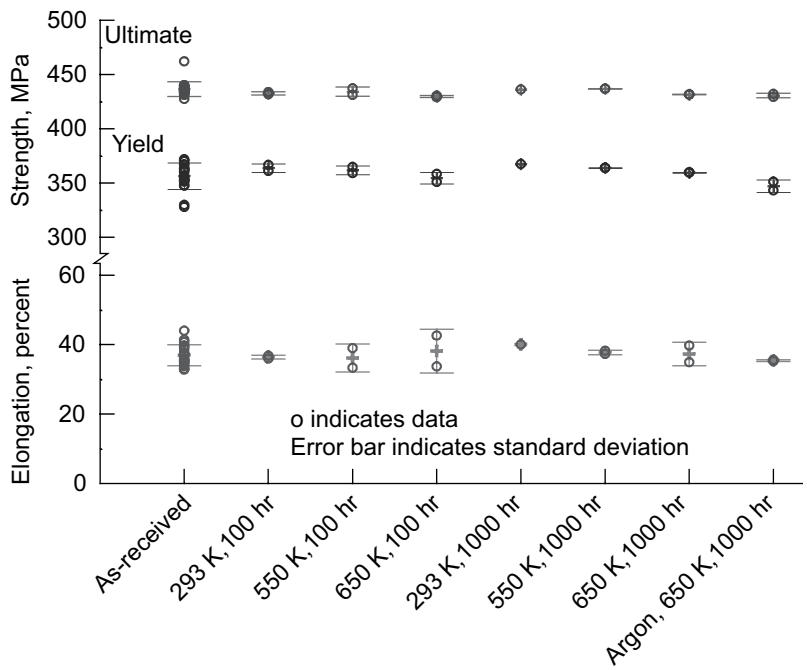


*No significant mechanical property difference was observed in the titanium tensile specimens after the 100- and 1000-hr exposures to NaK at 550 and 650 K.*

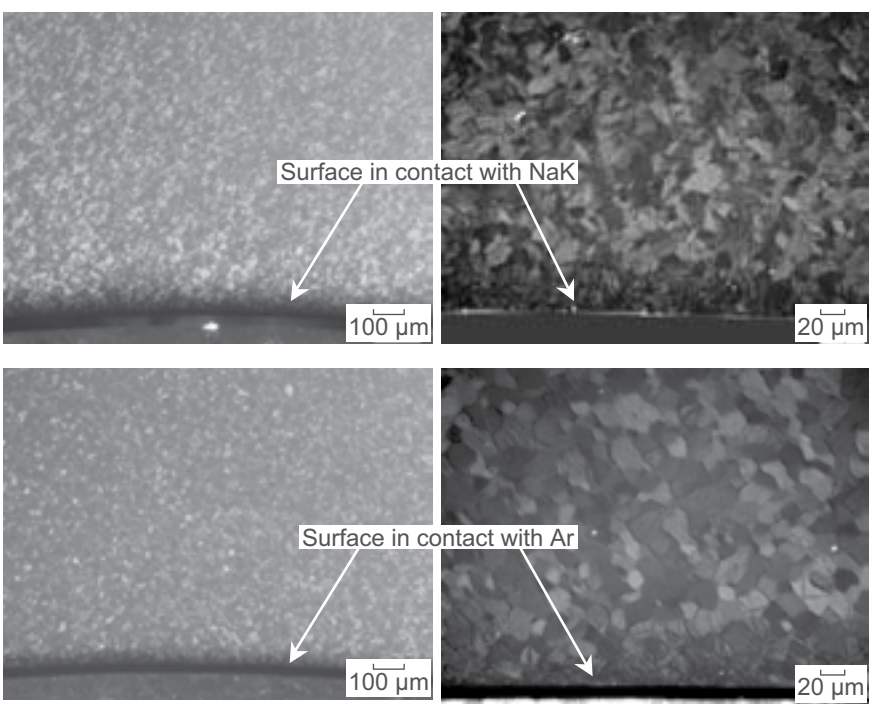


*Optical microscopy images of cross sections of capsules exposed to NaK and to argon for 1000 hr at 650 K show no signs of pitting or crevice corrosion. Top: Exposure to NaK. Bottom: Exposure to argon.*

and emptied the capsules and reacted and quenched the NaK. The capsule components were assembled by electron beam welding since this method is performed in a vacuum, which minimizes the possibility of contamination and produces very consistent welds. Evaluations were conducted at 550 and 650 K (277 and 377 °C) for up to 1000 hr. Additional capsules were evacuated and filled with argon, sealed, and then exposed to 650 K for various times to differentiate whether temperature or NaK exposure was responsible should any strength loss occur. Longer exposures, up to 15,000 hr, are in progress.

After the various exposures, the changes in weight of the immersed tensile specimen, the tensile strength, the amount of titanium dissolution into the NaK, and any evidence of chemical attack of the exposed capsule surfaces by optical and scanning electron microscopy were determined. CP2 titanium exposed to NaK at temperatures to either 550 or 650 K for up to 1000 hr showed no significant differences in weight, mechanical properties, or dissolved titanium levels.

Metallography showed surfaces that were largely similar to the as-machined condition, and cross-sectional observations did not show any signs of pitting or crevice corrosion after the 1000-hr exposure at either 550 or 650 K. The 1000-hr results indicated that CP2 is a suitable ducting material candidate for NaK heat-exchanger systems, but longer exposure times, which are in progress, need to be evaluated to confirm this conclusion.

**Bibliography**

ASM International Handbook Committee: Metals Handbook. Ninth ed., Vol. 13, table 20, 1985, p. 687.

Foust, O.J., ed.: Sodium-NaK Engineering Handbook. Vol. V, Sodium Purification, Materials, Heaters, Coolers, and Radiators, Gordon and Breach, New York, NY, 1972.

Godard, Hugh P., et al.: The Corrosion of Light Metals. Titanium, R.L. Kane, ed., The Corrosion Monograph Series, John Wiley & Sons, New York, NY, 1967.

Jackson, Carey B., et al.: Liquid-Metals Handbook—Sodium (NaK) Supplement. Third ed., Atomic Energy Commission, Washington, DC, 1955.

**Find out more about the research of Glenn's Materials Division:**
http://www.grc.nasa.gov/WWW/MDWeb/

**University of Toledo contact:**
Dr. Ivan E. Locci, 216–433–5009, Ivan.E.Locci@nasa.gov

**Glenn contacts:**
Dr. John Gayda, 216–433–3273, John.Gayda-1@nasa.gov

Dereck F. Johnson, 216–433–5038, Dereck.F.Johnson@nasa.gov

Dr. Cheryl L. Bowman, 216–433–8462, Cheryl.L.Bowman@nasa.gov

**Authors:**
William S. Loewenthal, Dr. Ivan E. Locci, Dr. John Gayda, Dereck F. Johnson, and Dr. Cheryl L. Bowman

**Headquarters program office:**
Exploration Systems Missions Directorate

**Programs/projects:**
Project Prometheus

## GRCop-84 Tubing Produced Using Optimized Production Methods

Tubular main combustion chambers (MCCs) have been used for many years as an alternative to milled wall liners, such as the one used in the Space Shuttle Main Engine. Examples of prior and current engines to use tubular designs are the Douglas PGM–17 "Thor" missile (ref. 1) first deployed in September 1958, the Pratt & Whitney RL–60 engine (ref. 2), and the Pratt & Whitney Advanced Expander Combustor developed under the Integrated High Payoff Rocket Propulsion Technology initiative (ref. 3). Tubular liner designs, such as the one shown in this photograph, offer the potential for considerable increases in rocket engine life over conventional milled channel liners (ref. 4). Additional benefits in tubular liner performance and life could be gained from utilizing the advanced copper alloy GRCop-84, recently developed by the NASA Glenn Research Center, which has a balance of improved strength and temperature capability combined with high thermal conductivity in comparison to competing alloys. Prior efforts to draw GRCop-84 into tubing successfully demonstrated feasibility, but the manufacturing methods were not suitable for large-scale production. Therefore, Glenn undertook an effort with LeFiell Manufacturing of Sante Fe Springs, California, to improve the production.

*Example of tubular combustion chamber liner, which consists of multiple, contoured tubes running along the length of the liner. (Courtesy of Pratt & Whitney Rocketdyne.)*

The first step was to eliminate gun drilling of small-diameter solid bars to make the starting stock. Instead, 300 lb of powder were consolidated into a large solid cylinder, a small hole was gun drilled into the cylinder, and the cylinder was extruded through a die and over a mandrel to produce 15 m (45 ft) of tubular starting stock. This change increased the yield by approximately 50 percent. The second step was to maximize the amount of reduction prior

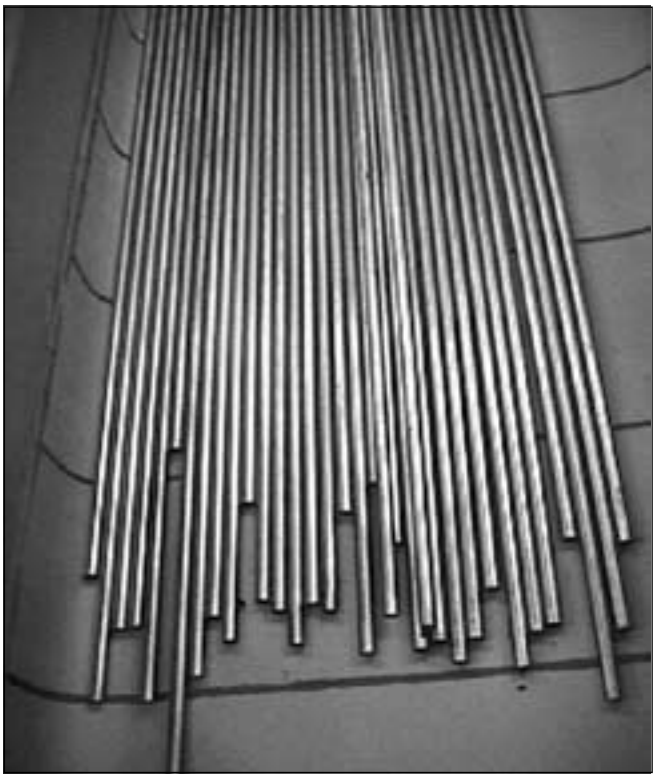

*Finished 9.5-mm OD by 1.0-mm wall GRCop-84 tubing.*

to annealing and to minimize the required annealing temperature. A design of experiments was conducted with three drawing reductions and three annealing temperatures as the independent variables. Room-temperature tensile properties were used to establish any difference in tubing after drawing to 9.5-mm (0.375-in.) outside diameter (OD) by 1.0-mm (0.040-in.) wall. The results indicated that GRCop-84 exhibits a wide processing window with all three annealing temperatures and two of the drawing reductions resulting in tubing with statistically identical tensile properties. The third and most aggressive drawing reduction resulted in failure of the tubes during drawing because of tensile overload and was abandoned. From the remaining conditions, the optimum processing parameters were selected.

To validate the optimized production parameters, over 330 m (1100 ft) of 9.5-mm OD by 1.0-mm wall GRCop-84 tubing was produced. A portion of the finished tubing is shown in the preceding photograph. The optimized conditions required approximately one-third fewer drawing steps than the original drawing conditions did and reduced the annealing temperature by 200 °C (360 °F). Along with the improved starting stock, these changes will result in large cost and time savings for GRCop-84 tubing. Further details can be found in reference 5.

**References**


1. Sutton, George P.: Rocket Propulsion Elements: An Introduction to the Engineering of Rockets. Fifth ed., John Wiley & Sons, New York, NY, 1986.
2. Bullock, J.; Santiago J.; and Popp, M.: RL60 Demonstrator Engine Design, Manufacturing, and Test. AIAA–2003–4489, 2003.
3. Cooley, C.; Fentress, S.; and Jennings, T.: Hot Firing of a Full Scale Copper Tubular Combustion Chamber. AFRL–PR–ED–TP–2002–078, 2002.
4. Jankovsky, R.S., et al.: Structurally Compliant Rocket Engine Combustion Chamber—Experimental and Analytical Validation. J. Spacecr. Rockets, vol. 32, no. 4, 1995, pp. 645–652.
5. Ellis, David L., et al.: Drawing of GRCop-84 Tubing. NASA/TM—2006-214223, 2006. Available from the Center for AeroSpace Information.



**Glenn contact:**
Dr. David Ellis, 216–433–8736, David.L.Ellis@nasa.gov

**LeFiell Manufacturing contact:**
Steve Cummings, 800–451–5971, scummings@lefiell.com

**Author:**
Dr. David L. Ellis


**Headquarters program office:**
Constellation Program Office

**Programs/projects:**
Crew Exploration Vehicle, Constellation Systems

# Nickel Chromium Aluminum Yttrium (NiCrAlY) Overlay Coatings Successfully Deposited on GRCop-84 Subscale Combustion Chamber Liners

GRCop-84 (Cu-8 at.% Cr-4 at.% Nb)[1] advanced copper alloy is a candidate for combustion chamber liners and nozzles in reusable launch vehicles. Many of the properties of this alloy have been shown to be far superior to those of conventional copper alloys, such as NARloy-Z (ref. 1). Despite this considerable advantage, GRCop-84 will suffer from environmental degradation depending on the rocket fuel utilized. In a liquid-hydrogen ($LH_2$)/liquid-oxygen ($LO_2$) rocket engine, copper alloys undergo repeated cycles of oxidation of the copper matrix and subsequent reduction of the copper oxide resulting in "blanching" (ref. 2). Blanching results in increased surface roughness and poor heat-transfer capabilities, local hot spots, decreased engine performance, and premature failure of the liner material. This environmental degradation, coupled with thermomechanical stresses, creep, and high thermal gradients, can severely distort the cooling channels, leading to liner failure (ref. 3).

Protective coatings on a GRCop-84 substrate can minimize or eliminate many of these problems and extend the life of the combustion liner (ref. 3). Therefore, the NASA Glenn Research Center is developing advanced overlay coatings technology for GRCop-84 liners.

Four techniques were considered: (1) vacuum plasma spray (VPS), (2) Kinetic Metallization (KM) spray, (3) cold spray (CS), and (4) ionic fusion (IF). Coatings deposited by IF spalled during thermal cyclic furnace tests, and IF was dropped from consideration. Although CuCrAl top coats[2] were successfully deposited by CS, insufficient funds were available to advance the process. VPS and KM were optimized for depositing NiCrAlY top coats[3] on GRCop-84 substrates using suitable bond coats with the final objective of proof-of-concept demonstration trials on subscale liners.

VPS involves melting coating powders in a low-pressure plasma flame, then splat cooling the molten droplets as they hit the substrate. KM is a near-room-temperature process conducted in an open environment using a helium carrier gas to transport powder particles (accelerated to very high subsonic velocities) to the substrate surface, where they are welded to each other and the substrate by adiabatic deformation.

NiCrAlY coating deposition of GRCop-84 substrates by VPS is difficult since GRCop-84 has high thermal conductivity, has a lower melting point than NiCrAlY, and is reactive to residual oxygen in the spray chamber. These factors influence the coating-to-substrate bond strength. In addition, differences in the thermophysical and mechanical properties of the top and bond coats and GRCop-84 lead to residual stresses that can debond the coating.

The process was scaled up in stages, starting with test coupons 12.5 mm in diameter for thermal cyclic testing in furnaces. Next, specially designed GRCop-84 specimens (152 by 102 mm) with machined water-cooling channels were sprayed with a NiCrAlY top coat using either a Cu-8%Cr or a Cu-8%Cr-1%Al bond coat. The coatings were exposed to a hydrogen-oxygen combustion flame with a heat flux of ~3.4 $MW/m^2$ to evaluate their ability to remain on the substrates (see the following photograph). These coatings performed very well after forty 180-sec cycles, for a total cumulative time of 2 hr.

The third stage consisted of coating subscale liners that had a ~90-mm throat diameter, ~155-mm end diameters, and ~228-mm length. The photographs on the next page show subscale liners coated with a NiCrAlY top coat by VPS and KM. These studies demonstrate that overlay NiCrAlY coatings can be successfully deposited by either technique. The coated subscale liners were successfully machined by a commercial vendor without coating spallation.

*Quick Access Rocket Exhaust (QARE) rig testing of a NiCrAlY-coated GRCop-84 water-cooled specimen at a heat flux of about 3.4 $MW/m^2$.*

[1]Copper chromium niobium.

[2]Copper chromium aluminum top coats.

[3]Nickel chromium aluminum yttrium top coats.

*KM and VPS NiCrAlY-coated GRCop-84 subscale liners showing the machined inner coated surfaces and the exterior cooling channels.*

**References**


1. Ellis, David L.; and Michal, Gary M.: Mechanical and Thermal Properties of Two Cu-Cr-Nb Alloys and NARloy-Z. NASA CR–198529, 1996. http://gltrs.grc.nasa.gov/cgi-bin/GLTRS/browse.pl?1996/CR-198529.html
2. Morgan, Deena B.; and Kobayashi, A.C.: Main Chamber Combustion and Cooling Technology Study; Final Report. NASA CR–184345, 1989. Available from the Center for AeroSpace Information.
3. Quentmeyer, R.J.: Experimental Fatigue Life Investigation of Cylindrical Thrust Chambers. NASA TM–X–73665, 1977.



**Glenn contacts:**
Dr. Sai V. Raj, 216–433–8195, Sai.V.Raj@nasa.gov

Dr. James A. Nesbitt, 216–433–3275, James.A.Nesbitt@nasa.gov

**Author:**
Dr. Sai V. Raj


**Headquarters program office:**
Exploration Systems Mission Directorate

**Programs/projects:**
Constellation Systems, Hypersonics

# Fiber Architecture Used To Increase the Matrix Cracking Stress of Silicon Carbide (SiC)/SiC Ceramic Composites for Propulsion and Power Applications

NASA Glenn Research Center-developed silicon carbide (SiC)/SiC ceramic matrix composites (CMCs) reinforced by two-dimensional woven fabrics of Sylramic-iBN SiC fiber tows are considered to be state-of-the-art structural materials for reusable propulsion and power components operating for long times in high-temperature (1200 to 1500 °C) oxidizing environments (ref. 1). Recently, under a Glenn Independent Research and Development program, the use of alternate fiber architectures was investigated with the goals of understanding and increasing the matrix cracking stress (MCS) of these Si-based CMCs. The MCS is an important design parameter because life-limiting oxidation mechanisms occur when through-the-thickness matrix cracks allow oxygen ingress into the CMC microstructure. In addition, matrix cracks degrade the high thermal conductivity of these CMCs, which is needed to reduce thermal stresses. Thus, improving MCS can increase material design allowables and/or safety margins.

The two concepts behind using alternate fiber architectures to increase MCS are (1) to reduce intrinsic stresses on the matrix by increasing the volume fraction of fiber tows in the key high-stress direction, for example, in the radial direction of a rotating turbine blade, and (2) to reduce the effective stress concentration of those matrix flaws that are related to the size of fiber tows that are perpendicular to the high-stress direction. Thus, as part of this research effort at Glenn, a variety of SiC/SiC flat panels were fabricated with slurry-cast melt-infiltrated matrices and with architectures that would take advantage of these two concepts. To compare against the standard NASA two-dimensional woven melt-infiltrated SiC/SiC system (N24A system in ref. 1), these panels were fabricated with two-dimensional woven (ref. 2), two-dimensional triaxially braided, three-dimensional orthogonal (ref. 3), and angle-interlock architectures with lower and higher fiber fractions $f_x$ along the in-plane test direction $x$, and with smaller and larger effective tow areas $A_{yz}$ perpendicular to that direction.

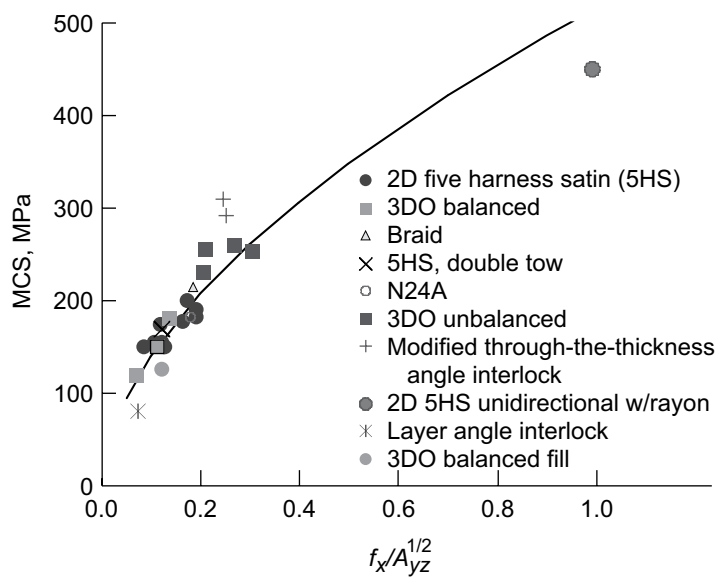


*MCS, as-determined by acoustic emission, versus parameter $P = f_x / A_{yz}^{1/2}$. 2D, two-dimensional; 3DO, three-dimensional orthogonal.*

The graph shows the MCS for the various panels as a function of parameter $P = f_x/A_{yz}^{1/2}$, which is a combined measure of both improvement concepts. These stresses were measured by the occurrence of acoustic emission, which has been shown to be an excellent method for determining matrix cracking in melt-infiltrated SiC/SiC CMC (ref. 2). It is evident that as the parameter $P$ increased, the onset of through-the-thickness matrix cracking occurred at an increased stress level. The MCS for the two-dimensional N24A SiC/SiC composite system was approximately 175 MPa (solid data point). However, composites with higher fiber volume fractions and smaller tow areas exhibited improvements in MCS ranging from 30 to over 100 percent. The relationships that govern matrix cracking for these different architectures are currently being refined at Glenn. However, this general result gives designers of CMC propulsion and power components a good sense of what is feasible and what tradeoffs in stress allowables would have to be made if one uses alternate fiber architectures.

**References**


1. DiCarlo, J.A., et al.: SiC/SiC Composites for 1200 °C and Above. Handbook of Ceramics Composites. Ch. 4, Kluwer Academic Publishers, Boston, MA, 2005, pp. 77–98.
2. Morscher, G.N.: Stress-Dependent Matrix Cracking in 2D Woven SiC-Fiber Reinforced Melt-Infiltrated SiC Matrix Composites. Comp. Sci. T., vol. 64, no. 9, 2004, pp. 1311–1319.

3. Morscher, G.N.; Yun, Hee Mann; and DiCarlo, J.A.: Matrix Cracking in 3D Orthogonal Melt-Infiltrated SiC/SiC Composites With Various Z-Fiber Types. J. Am. Ceram. Soc., vol. 88, no. 1, 2005, pp. 146–153.

**Ohio Aerospace Institute (OAI) contact:**
Dr. Gregory N. Morscher, 216–433–5512, Gregory.N.Morscher@nasa.gov

**Glenn contact:**
J. Douglas Kiser, 216–433–3247, James.D.Kiser@nasa.gov

**Authors:**
Dr. Gregory N. Morscher, J. Douglas Kiser, Dr. James A. DiCarlo, and Dr. Hee Mann Yun

**Headquarters program office:**
Aeronautics Research Mission Directorate

**Programs/projects:**
Independent Research and Development

# Physics-Based Models Developed for Predicting Creep Effects in Silicon Carbide (SiC)/SiC Composite Components

The N24A ceramic composite system, which was developed at the NASA Glenn Research Center, has a silicon-containing silicon carbon (SiC) matrix reinforced by boron nitride (BN) -coated Sylramic-iBN SiC fibers (also developed at Glenn). It is considered to be one of the state-of-the-art SiC/SiC structural materials for reusable propulsion and power components operating for long times in oxidizing environments up to 1315 °C, or 2400 °F (ref. 1). Recently Glenn also developed SiC/SiC systems (N26 series) with improved silicon-free matrices and BN-based fiber coatings that increase the SiC/SiC temperature capability to 1450 °C, or 2640 °F (ref. 2). Even so, all of these systems display measurable creep within their upper-use temperature ranges and at stresses well below the levels where matrix cracks occur. Since this creep behavior can cause adverse residual stress development in an SiC/SiC component, in-house studies were recently initiated under a Glenn Internal Research and Development program to develop physics-based analytical and finite element models that can predict the effects of creep on important composite design properties, such as matrix cracking strength.

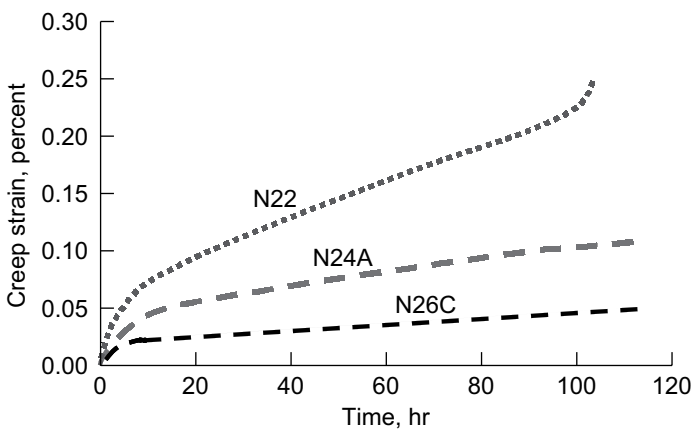


*Typical in-plane tensile creep curves in the primary fiber direction for some advanced Glenn-developed two-dimensional 0/90-balanced SiC/SiC panels in 2400 °F air at 15 ksi. These systems have been labeled by the prefix N for NASA, followed by their approximate upper-temperature capability in degrees Fahrenheit divided by 100 (e.g., N22, N24, and N26), with suffix letters A, B, and C to indicate their generation.*

The initial creep modeling approach assumes that (1) physics-based creep mechanisms in the SiC/SiC composites are generally the same as those observed at NASA within the SiC fibers as well as in other Si-based monolithic ceramics: that is, a combination of time-dependent

anelastic (recoverable) and viscoelastic (nonrecoverable) creep strain components; (2) below the matrix cracking stress, both creep strain components vary linearly with stress (tension and compression); (3) temperature effects (activation energies) on the creep strain components are the same as those measured for SiC fibers; and (4) composite creep strain with a primary and secondary stage (see the graph on the preceding page) can be analytically fit to a four-parameter mechanical analog model (ref. 3).

Although little, if any, composite creep data exist for stresses off the primary fiber direction, one can make initial assumptions for the directional behavior using composite and monolithic SiC creep theories. Then for finite element analyses, directional four-parameter models can be developed to generate stress-relaxation Prony series for input into commercial design codes such as ANSYS. This, in turn, should allow prediction of creep effects in SiC/SiC components that will be subjected to stress and temperature gradients. Glenn is currently working to develop these capabilities by generating the missing creep data and by doing preliminary finite element analyses to evaluate the degree of residual stress development in highly stressed sections of potential SiC/SiC components, such as within the leading edge of an internally cooled SiC/SiC turbine airfoil.

**References**


1. DiCarlo, J.A., et al.: SiC/SiC Composites for 1200 °C and Above. Handbook of Ceramics Composites, Ch. 4, Kluwer Academic Publishers, Boston, MA, 2005, pp. 77–98.
2. DiCarlo, James A.; Yun, Hee Mann; and Bhatt, Ramakrishna T.: Advanced SiC/SiC Ceramic Composite Systems Developed for High-Temperature Structural Applications. Research & Technology 2005, NASA/TM—2006-214016, 2006, pp. 120–121. http://www.grc.nasa.gov/WWW/RT/2005/RX/RX16-dicarlo.html
3. Lang, J.; and DiCarlo, J.: Modeling Creep Effects in Advanced SiC/SiC Composites. Proceedings of the 30th Annual Conference on Ceramics, Materials and Structures, CMC Materials, Cape Canaveral/Cocoa Beach, FL, Jan. 23–26, 2006. Available from Zeta Associates Inc. (http://www.zai.com).



**Glenn contact:**
Dr. James A. DiCarlo, 216–433–5514, James.A.DiCarlo@nasa.gov

**Authors:**
Dr. James A. DiCarlo and Dr. Jerry Lang


**Headquarters program office:**
Aeronautics Research Mission DIrectorate

**Programs/projects:**
Independent Research and Development

## Thermal- and Environmental-Barrier-Coated Silicon Nitride Vanes Tested in NASA Glenn's High Pressure Burner Rig

An advanced multicomponent hafnia ($HfO_2$) and rare-earth-doped mullite/silicate thermal- and environmental-barrier coating (T/EBC) system was developed for high-temperature silicon nitride ($Si_3N_4$) turbine vane applications (refs. 1 to 3). The coating systems, along with a 2600 °F (1427 °C) -capable ceramic bond coat, showed improved water-vapor resistance and high-temperature dynamic rupture strength for AS800 and SN282 $Si_3N_4$ substrates (refs. 2 and 3). The current research effort at the NASA Glenn Research Center was focused on testing and demonstrating the T/EBC-coated $Si_3N_4$ vane durability, improving the robustness of the coating processing of complex-shaped components, and providing vital design data for coating technology development.

The coating systems for the component demonstration consisted of a low-expansion $HfO_2$ top coat, a rare-earth-doped mullite and/or ytterbium silicate ($Yb_2SiO_5$) environmental barrier coating system, and a multicomponent $HfO_2$-based bondcoat. Two types of coated nozzle vanes (Honeywell Engines of Phoenix, Arizona) were used for the High Pressure Burner Rig demonstrations at temperatures up to 2700 °F (1482 °C). The coating systems were deposited onto AS 800 $Si_3N_4$ nozzle vanes using room-temperature plasma spray. The total T/EBC thickness was about 127 to 180 μm (0.005 to 0.007 in.).

The top photograph on the next page shows the High Pressure Burner Rig and the AS800 $Si_3N_4$ vane testing

configurations. Single- and triple-vane test fixtures were designed and fabricated for the larger-sized and miniature-sized vanes for the burner rig tests, respectively, as shown in center and bottom photographs. The burner rig temperature conditions were characterized for the vane test fixture configurations. The following graph illustrates the flame gas temperatures as a function of fuel/air ratio and the location for the triple-vane test configuration. All vane tests were conducted under 6-atm pressure and 30-m/sec combustion gas velocity for up to 50 hot hours at the maximum gas temperature of 1632 °C (2970 °F). The vane temperature was monitored using a pyrometer and then fully modeled for the temperature distributions using finite element analysis (FEA) methods.

The three-dimensional plot on the next page shows the FEA-modeled temperature distribution for a vane test at the gas temperature of 1632 °C (2970 °F). It can be seen that the nozzle vane leading-edge temperature reached approximately 2700 °F (1482 °C). The vane leading-edge, which experienced the highest temperature and gas velocity (and thus also the highest stresses), generally showed more coating recession and damage accumulations. A tested vane is shown in the photograph on the next page. Durability of the coated-ceramic vane has been demonstrated for 50 hr at temperatures up to 2700 °F (1482 °C), providing essential coating design experience for silicon-based ceramic component systems. The advanced T/EBCs show great promise toward achieving the component performance goals for future advanced turbine engines.

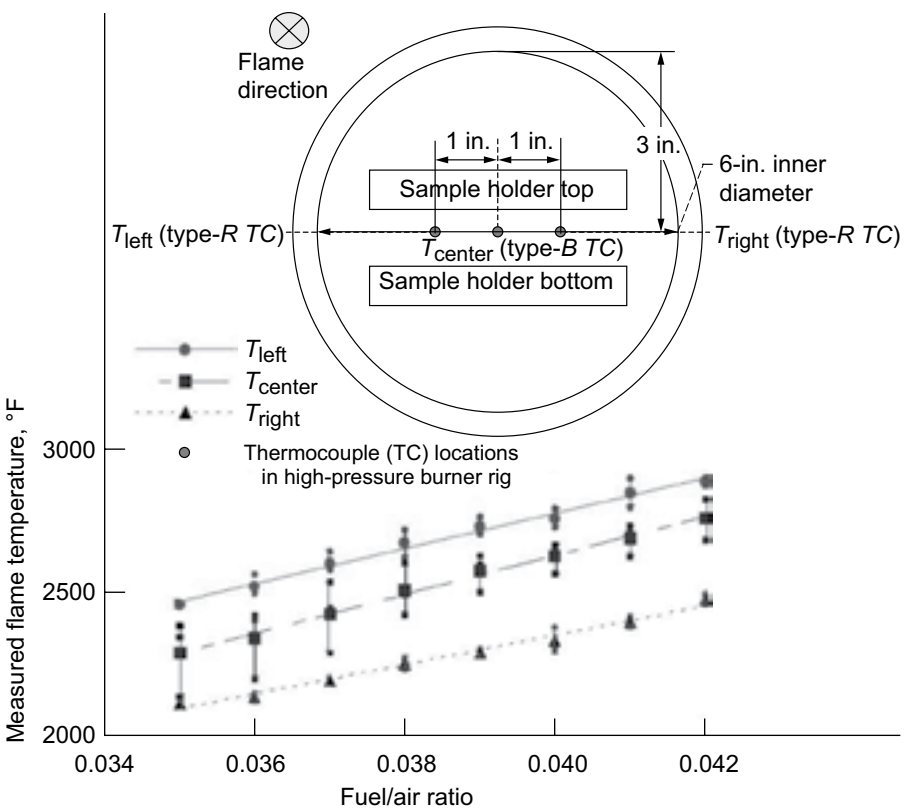


*Flame gas temperature distributions. T, temperature.*

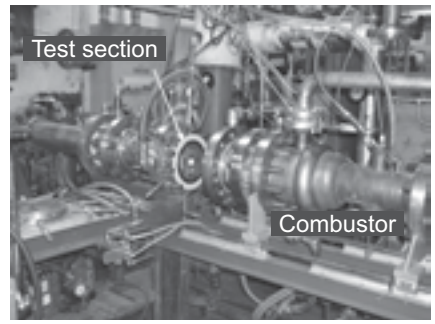


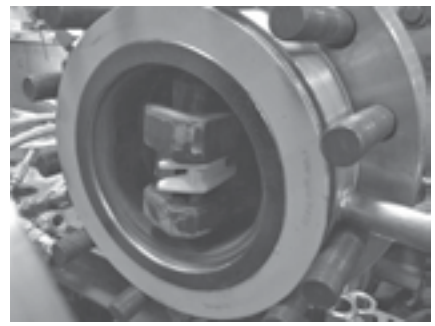

*High Pressure Burner Rig and test configurations for $Si_3N_4$ nozzle vane demonstrations. Top: High Pressure Burner Rig at Glenn. Center: Single-vane testing configuration for the larger-sized $Si_3N_4$ vane components. Bottom: A triple-vane testing configuration for the miniature-sized $Si_3N_4$ vane components.*

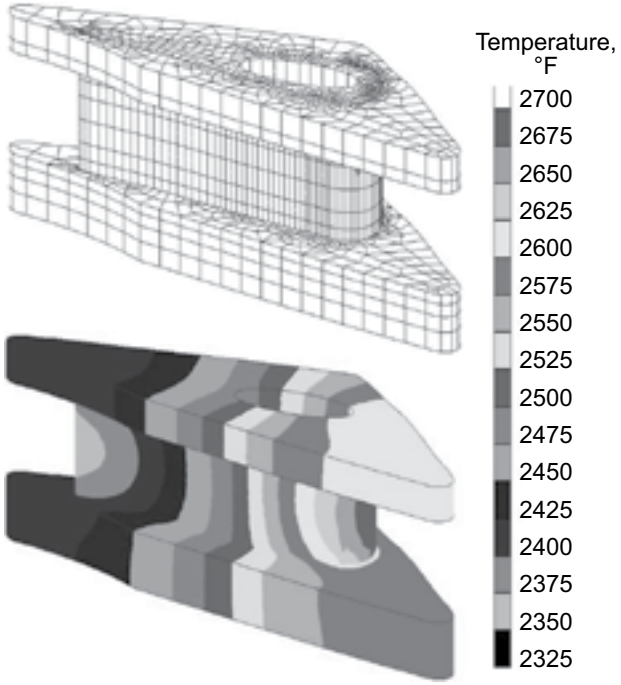


*FEM temperature distribution of the $Si_3N_4$ vane. This figure is shown in color in the online version of this article (http://www.grc.nasa.gov/WWW/RT/2006/RX/RX08D-zhu.html).*

*Tested $Si_3N_4$ vane.*

**References**

1. Zhu, Dongming: Multifunctionally Graded Environmental Barrier Coatings for Silicon-Based Ceramic Components. U.S. Provisional Patent Application Serial No. 60/712,605, filed Aug. 26, 2006.
2. Zhu, Dongming; Choi, Sung R.; and Robinson, Raymond C.: Advanced Testing and Performance Evaluation of Environmental Barrier Coatings. Presented at the Environmental Barrier Coatings Workshop, Nashville, TN, 2005.
3. Choi, Sung R.; Zhu, Dongming; and Bhatt, Ramakrishna T.: Life-Limiting Properties of Uncoated and Environmental-Barrier Coated Silicon Nitride at Higher Temperature. Ceram. Eng. Sci. Proc., vol. 27, issue 3, 2006.

**Glenn contact:**
Dr. Dongming Zhu, 216–433–5422, Dongming.Zhu-1@nasa.gov

**Authors:**
Dr. Dongming Zhu, Robert T. Pastel, Dennis S. Fox, Dr. Louis J. Ghosn,
Dr. Robert A. Miller, Dr. James L. Smialek, and Raymond Craig Robinson

**Headquarters program office:**
Aeronautics Research Mission Directorate

**Programs/projects:**
Fundamental Aeronautics Program, Supersonics Project

# Current Limits for High-Temperature Nickel-Titanium-Based Shape-Memory Alloys Defined

One of the most effective ways to increase the performance, reduce the noise and emissions, and improve the overall efficiency of subsonic to hypersonic aircraft is to replace various static structures with adaptive or reconfigurable components. Designs for everything from adaptive inlets, nozzles, flaps, and other control surfaces, to variable-geometry chevrons, reconfigurable blades, and active hinges for the operation of various doors and panels have been developed. However, enabling such dramatic design changes requires the use of high-energy-density functional materials such as shape-memory alloys (SMAs).

The most viable SMAs have been based on binary nickel titanium (NiTi), but this class of SMA has a very low temperature capability, generally in the range of –100 to 80 °C. Many of the envisioned applications in aeronautics require SMAs that have temperature capability far in excess of this level but that can still generate significant work output. Alloying additions including palladium (Pd), platinum (Pt), gold (Au), halfnium (Hf), and zirconium (Zr) have been shown to increase the transformation temperatures for NiTiX alloys, but to date, almost all research on high-temperature SMA (HTSMA) behavior has been performed under stress-free conditions. The mere exhibition of shape-memory behavior at elevated temperature is not sufficient for evaluating the potential of these materials, especially when the primary application calls for integration of the HTSMA within adaptive structures or as a component in a solid-state actuator (ref. 1). Instead, work output (or the ability of the material to recover strain against some biasing force) is the most important property for screening the viability of different alloys. Because such data do not exist in the open literature, load-bias testing was performed at the NASA Glenn Research Center to quantify the work output of several HTSMA systems (e.g., NiTiPd, NiTiPt, and NiTiAu) over a wide range of temperatures. The load-bias testing consisted of constant-load, strain-temperature tests, where the load was applied to the sample at room temperature and then held constant as the sample was heated and cooled through the transformation regime (for details, see ref. 1).

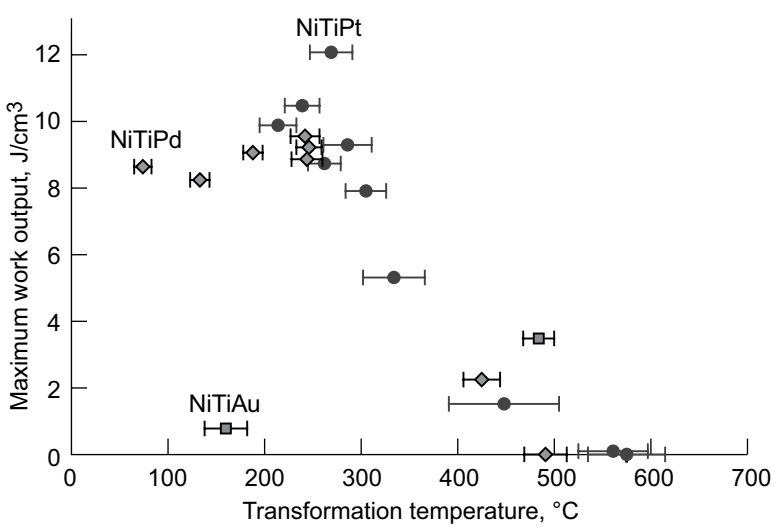


*Maximum work output and transformation temperature range ($M_f$ to $A_f$) for various NiTiPt, NiTiPd, and NiTiAu alloys. Each data point represents a unique alloy. In general, work output drops off appreciably for alloys with transformation temperatures above 300 °C, although a second generation of alloys is being developed for use at higher temperatures.*

The graph summarizes the data generated during this survey. Each data point represents a unique alloy composition with the maximum work output plotted (for details on many individual alloys in the figure, see ref. 2). The bars surrounding each data point indicate the full temperature range of the transformation from the martensite finish temperature $M_f$ to the austenite finish temperature $A_f$ for each alloy. For active control of a component using SMAs, the environmental temperature must be below this transformation temperature range, whereas passive control of an actuator would require the environmental temperature to pass through this temperature range. Consistent work output of between 8 and 11 J/cm$^3$ was achieved for alloys with potential operating capability between 100 and approximately 300 °C. To put this level of work output into perspective, 10 J/cm$^3$ is roughly equivalent to the work performed by a piece of wire 0.04 in. in diameter by 25 in. long lifting an attached 110-lb weight a distance of 0.5 in.

For alloys with transformation temperatures above 300 °C, the work output drops off appreciably. To address this issue, Glenn researchers are currently developing a new generation of advanced SMAs with significantly improved properties for use at higher temperatures.

**References**

1. Noebe, Ronald, et al.: Properties and Potential of Two (Ni,Pt)Ti Alloys for Use as High-Temperature Actuator Materials. Proc. SPIE Int. Soc. Opt. Eng., vol. 5761, 2005, pp. 364–375.
2. Padula, S.: Challenges and Progress in the Development of High-Temperature Shape Memory Alloys Based on NiTiX Compositions for High-Force Actuator Applications. SMST 2006: Proceedings of the International Conference on Shape Memory and Superelastic Technologies, ASM International, Metals Park, OH, 2006.

**Glenn contacts:**

Dr. Ronald D. Noebe, 216–433–2093, Ronald.D.Noebe@nasa.gov

Dr. Santo A. Padula II, 216–433–9375, Santo.A.Padula@nasa.gov

**Authors:**

Dr. Ronald D. Noebe, Glen S. Bigelow, Dr. Santo A. Padula II, and Darrell J. Gaydosh

**Headquarters program office:**

Aeronautics Research Mission Directorate

**Programs/projects:**

Independent Research and Development, Quiet Aircraft Technology, Propulsion 21

# Electrical and Piezoelectric Properties of Piezoelectric Ceramics Measured at High Temperatures

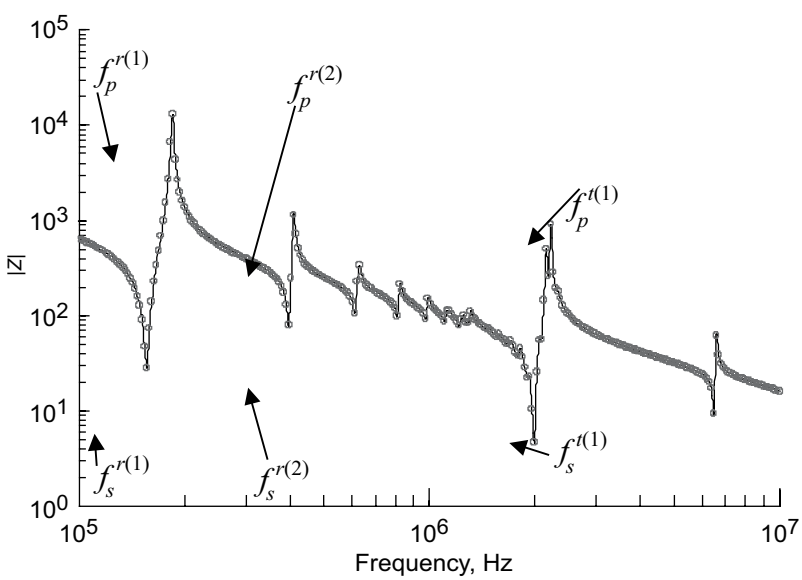


*Absolute impedance Z versus frequency for $Pb(Zr_xTi_{1-x})O_{3-\delta}$ (Navy Type II; Pb, lead; Zr, zirconium; Ti, titanium; O, oxygen). All communication and control programs between the computer and its peripherals were written in the LabVIEW 7.1 language. The controller receives the temperature set-points from the personal computer using the iTools program (Object Linking and Embedding for Process Control) server option. The frequencies were detected by a network analyzer within the frequency range of 10 kHz to 10 MHz.*

A smart-structure system can be defined as a system that can sense the external stimulus and respond to that stimulus quickly through a control system. Unique features of these systems will provide innovative capabilities and improvements in future aeronautics and space vehicle systems. NASA has been interested in piezoelectric materials as actuators and sensors for vibration control, shape control of aeronautical structures, noise reduction, adaptive flow control, and active combustion control. One emerging need is for high-temperature piezoelectric materials that function above 200 °C. There are techniques to measure the dielectric properties of piezoceramic materials to determine the Curie point. However, there are no existing test capabilities for measuring piezoelectric coupling coefficients at high temperatures. To assess the high-temperature performance of piezoelectric materials, researchers at the NASA Glenn Research Center designed and fabricated an experimental apparatus

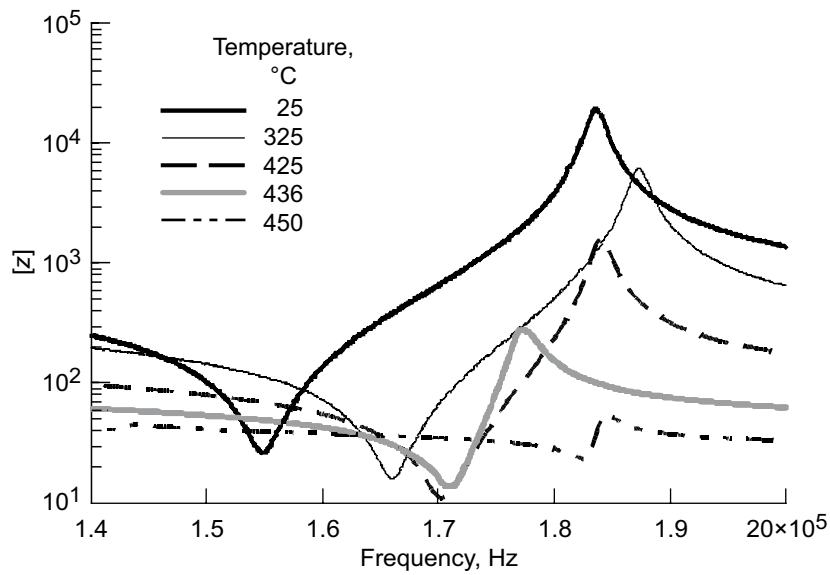


*First radial mode frequency shift with respect to temperature for $Pb(Zr_xTi_{1-x})O_{3-\delta}$ (Navy Type II). The resonance frequency shift was measured at 4 °C increments for wide range of $Pb(Zr_xTi_{1-x})O_{3-\delta}$ samples that were engineered at the morphotropic phase boundary.*

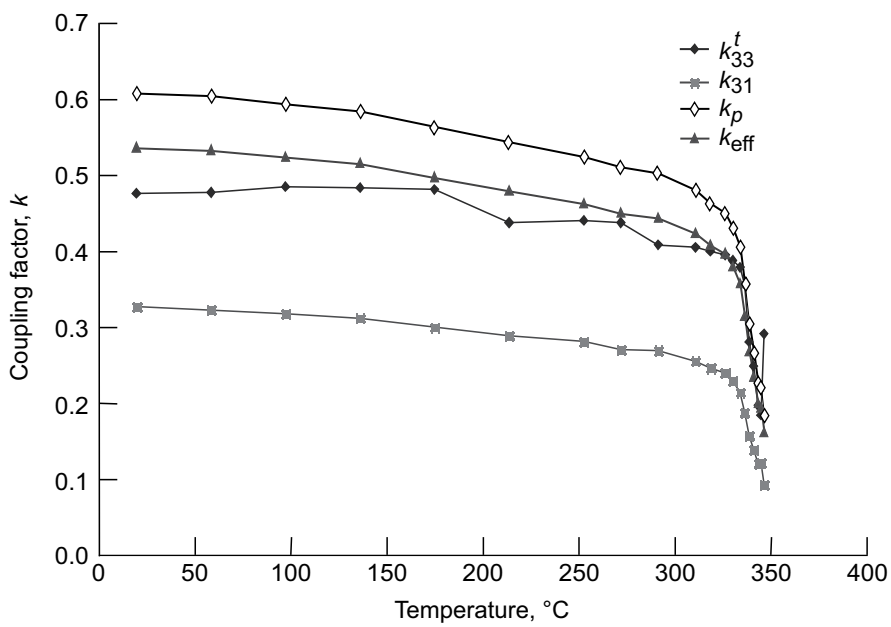


*Planar coupling factor, $k_p$, effective coupling factor, $k_{eff}$, and thickness-extensional mode coupling factor $k_{33}^t$, determined using a combination of Newton's Law, constitutive equations, and Maxwell equations, as a function of temperature.*

to measure piezoelectric properties. We also developed a benchmark test procedure using resonant analysis that is not addressed in an IEEE standard, and we measured the piezoelectric properties of a commercial lead zirconate titanate (PZT) piezoelectric disc as a function of temperature.

The elastic properties $C_{ijkl}^E$, piezoelectric coefficients $e_{kij}$ and $\varepsilon_k^S$, dielectric properties, and electromechanical coupling factors were determined as a function of temperature. These coefficients of the constitutive equations define the operating envelope in a temperature and frequency paradigm for radial and thickness mode vibrations. The graph on the preceding page shows the location of resonant and antiresonant frequencies for PZT at room temperature. The measured resonant $f_s$ and antiresonant frequency $f_p$ pairs correspond to different vibration modes, $f_p^{r(1)}, f_s^{r(1)}, f_p^{r(2)}, f_s^{r(2)}, f_p^{t(1)}, f_s^{t(1)}$, where the superscript $r(i)$ refers to the first and second ($i = 1, 2$) resonant frequencies of the radial mode and the superscript $t(1)$ refers to the first thickness mode resonant frequency.

A representative spectrum for the shifts in resonant frequencies as a function of temperature is shown in the top graph. The trend between antiresonant and resonant frequencies of a vibration mode with temperature helps to predict the behavior of the coupling factors and permittivity. The temperature-dependent piezoelectric coefficient $d_{33}$ decreased with temperature. The coupling factor $k_{33}$ was found to be relatively constant to 200 °C and to exhibit slight temperature dependence above 200 °C. The temperature sensitivity for both the piezoelectric coefficient and the electromechanical coupling factor were very small; the slopes $\Delta d_{31}^T / d_{31}^T$ and $\Delta k_{33} / k_{33}$ were found to be 0.01 and –0.07, respectively, in the range of 120 to 200 °C.

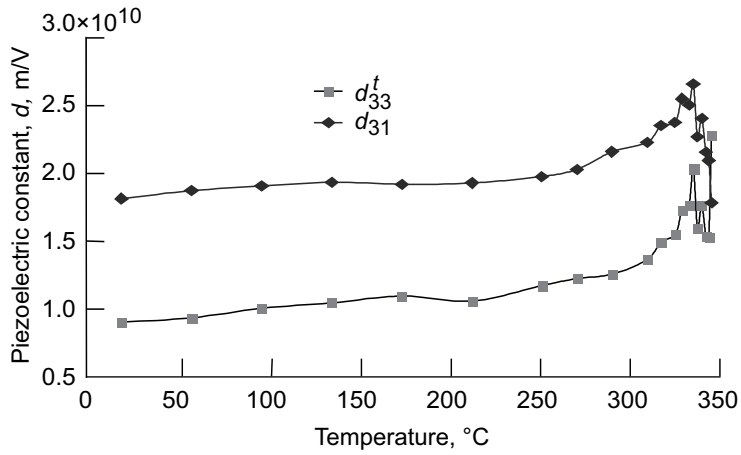


*Thickness extensional mode piezoelectric constant, $d_{33}^t$, and extensional mode piezoelectric constant, $d_{31}$, as a function of temperature.*

**Case Western Reserve University contact:**
Dr. Ali Sayir, 216–433–6254, Ali.Sayir-1@ nasa.gov

**Glenn contact:**
Dr. Frederick W. Dynys, 216–433–2404, Frederick.W.Dynys@nasa.gov

**Authors:**
Dr. Ali Sayir, Dr. Frederick W. Dynys, Zoltan Gubinyi, and Dr. Celal Batur

**Headquarters program office:**
Aeronautics Fundamentals

**Programs/projects:**
Subsonic Fixed Wing

Glenn researchers developed a high-temperature measurement system to measure piezoelectric properties. In the present investigation, commercial PZT ceramics were examined under weak alternating electric fields. Then, an exact temperature use of these materials could be estimated by the current measurement system. This technique will organize and populate databases that describe the piezoelectric properties and facilitate the assessment of new piezoelectric materials that are currently being developed for higher temperature applications.

## Multifunctional, Foam Core, Ceramic Matrix Composite Integrated Structures Developed

The NASA Glenn Research Center has developed a family of ceramic composite sandwich materials composed of a ceramic foam core between two ceramic composite face sheets. These materials are being investigated as multifunctional, integrated structures (see the top photograph on the next page). The face sheet reinforcement may be a ceramic fiber or a hybridized fabric woven with a ceramic and a carbon fiber. Choice of fibers and weave architectures permits the thermal expansion of the face sheet to be tailored to that of the core. Selection of fiber reinforcements enables a large design space within which thermal and elastic properties of the face sheet can be varied. Control of core properties—including strut thicknesses and pore sizes and spacings—and control of the face-sheet-to-core thickness determine the elastic and thermal properties of the integrated structure.

The core can serve as thermal insulation, as a cooling path, or as an acoustic insulator. High-thermal-conductivity fibers can be incorporated in the face sheet to enhance heat transfer and dissipation. Thus, the core can provide thermal insulation (see the graph on the next page) as well as impact absorption capabilities (see the bottom photograph). Analytical modeling of constituents and structural response has been complemented by empirical measurements of face sheet

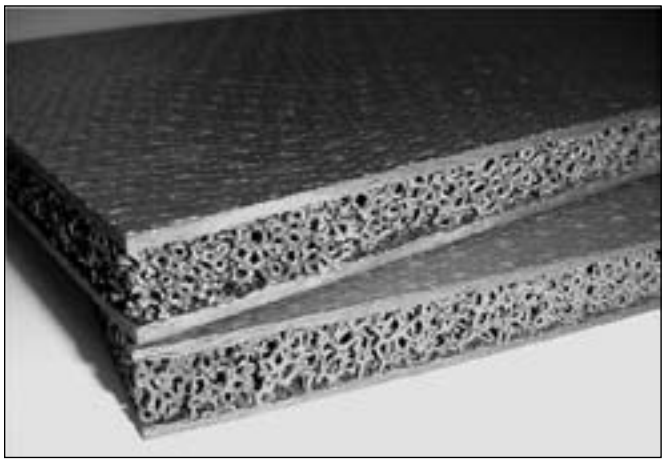

*Multifunctional, ceramic matrix composite/foam core sandwich structure.*

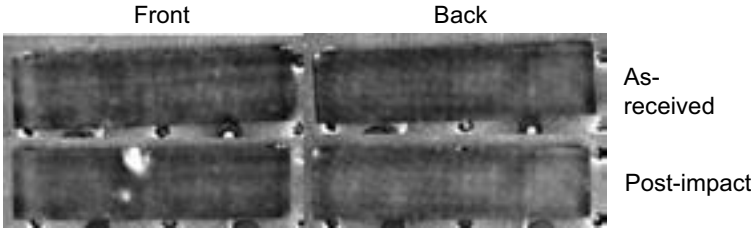


*Impact response to a 0.4-mm test particle fired at 7 km/sec illustrates only a small impact on the face sheet with no delamination and no damage to the back structure.*

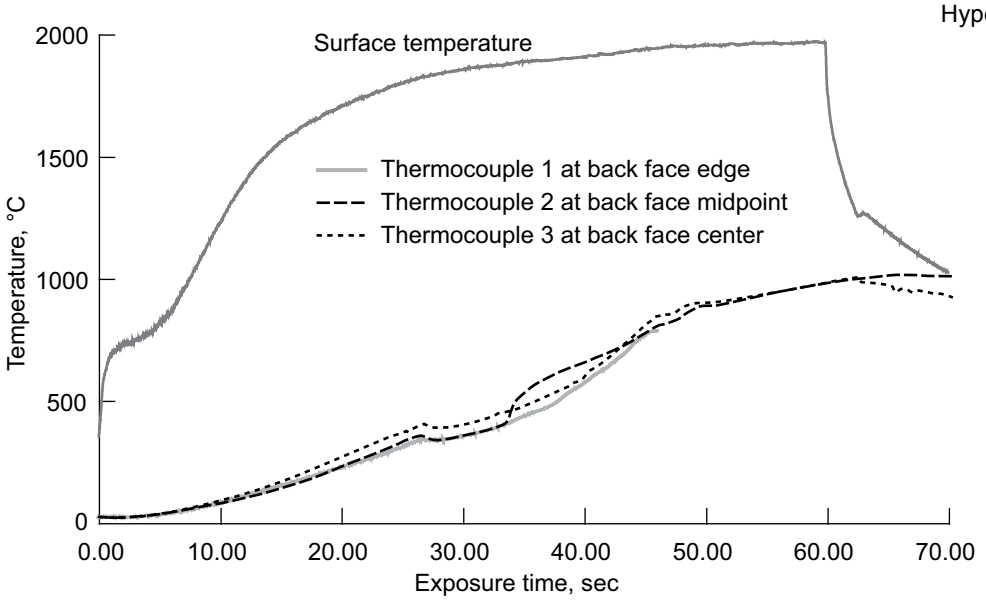


*Thermal response to a heat flux of 150 W/cm$^2$ illustrates thermal insulation capability.*

and foam core structure properties. During fiscal year 2006, Glenn demonstrated thermal protection capabilities and impact resistance using a baseline geometry and set of constituents. Additional analysis, fabrication, and testing are expected to optimize the structure for a variety of multifunctional applications. Recent analysis has shown the advantage of the choice of ceramic fiber in increasing stiffness, minimizing matrix cracking, and increasing proportional limit.

**Glenn contacts:**
Dr. Frances I. Hurwitz, 216–433–5503, Frances.I.Hurwitz@nasa.gov

Dr. Roy M. Sullivan, 216–433–3249, Roy.M.Sullivan@nasa.gov

**Univ. of Toledo contact:**
Dr. Subodh K. Mital, 216–433–3261, Subodh.K.Mital@nasa.gov

**Connecticut Reserve Technologies (CRT) contact:**
Joe Palko, 216–433–5551, Joseph.L.Palko@nasa.gov

**Authors:**
Dr. Frances I. Hurwitz, Dr. Subodh K. Mital, Joseph L. Palko, and Dr. Roy M. Sullivan

**Headquarters program office:**
Fundamental Aeronautics

**Programs/projects:**
Hypersonics, Supersonics

# Moisture-Induced Hydrogen Embrittlement of the Alumina-Metal Interface Demonstrated

Alumina scales are widely used in high-temperature aerospace material systems for their slow-growing and adherent protective behavior on MCrAl-based alloys.[1] Although their performance is optimized for alloys with reactive element dopants (Y, Zr, Hf)[2] and/or extremely low (<1 ppmw)[3] levels of sulfur impurity, additional secondary spallation phenomena have been occasionally observed. Tremendous thermal expansion mismatch stresses up to 4 GPa are developed immediately upon cooldown from oxidation at 1100 °C. But delayed spallation under ambient constant stress conditions is often observed. The same is true for the technologically important thermal barrier coating (TBC). Here delayed failure is often referred to as the "weekend effect," "cold spallation," or "desktop spallation." These effects are believed to be caused by exposure to moisture, or moisture-induced delayed spallation (MIDS), see the following figure. However, the atomistics of the process have remained elusive.

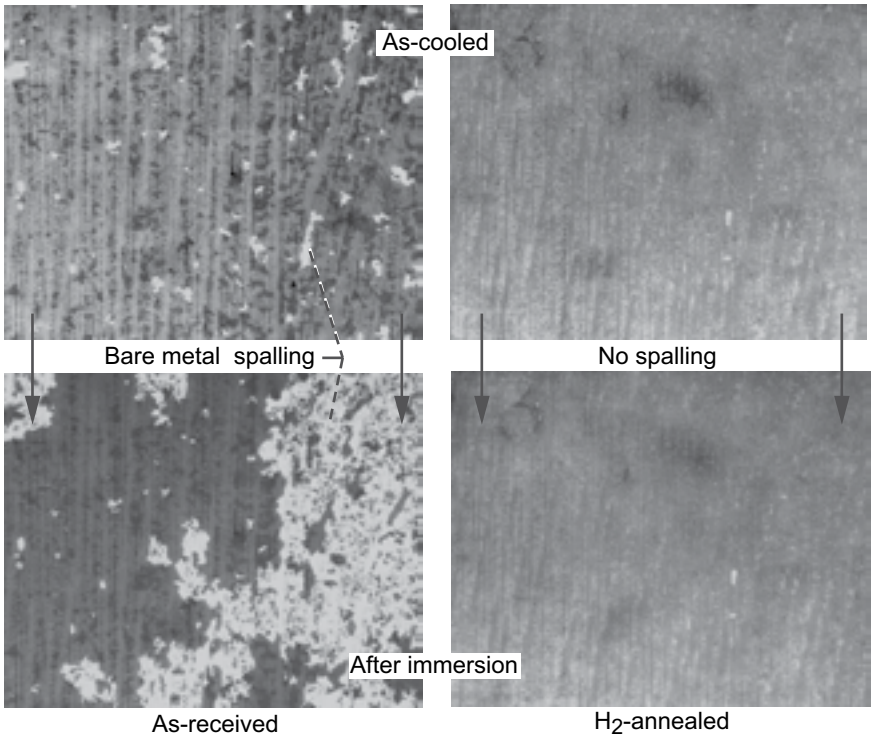


*Effect of water immersion on alumina scale spallation for René N5+Y that had been oxidized at 1150 °C for 1000 1-hr cycles. The right side was hydrogen annealed at 1250 °C for 100 hr to remove sulfur and carbon before oxidation; the left side was not.*

Initial theories have related this phenomenon to moisture-assisted crack growth in bulk ceramics, including alumina ($Al_2O_3$). Here $H_2O$ reacts chemically with the oxide at the highly stressed region of the crack tip, causing only slow crack growth under a static load, referred to as "corrosion fatigue." Another intriguing possibility is analogous to moisture-induced hydrogen embrittlement of intermetallic compounds, most notably $Ni_3Al$ and FeAl. Indeed, earlier work using standard cathodic hydrogen charging had embrittled $Ni_3Al$. Accordingly, researchers at the NASA Glenn Research Center used the same electrolytic recipe for cathodic charging a preoxidized René N5+Y superalloy for interfacial embrittlement. We found that, by monitoring current for every 0.1-V increment, a relatively intact scale could be cathodically removed at –2.0 V and at less than 1 mA (see the top figure on the next page).

We conclude that cathodic hydrogen embrittlement of the scale-metal interface occurred. By analogy to the intermetallics case, we propose that moisture-induced delayed spallation arises from hydrogen embrittlement of the scale metal interface (see the bottom figure on the next page). Here reaction of water with aluminum from the alloy produces aluminum hydroxide and frees hydrogen to diffuse down the oxide-metal interface, encouraged by the biaxial tensile stress state under the scale. This interfacial weakening is consistent with fundamental studies that predict decreased $Al_2O_3$–Ni bond strengths due to hydrogen, with a negative synergy in the presence of sulfur.

[1] Alloys containing chromium and aluminum.
[2] Yttrium, zirconium, or halfnium.
[3] Parts per million by weight.

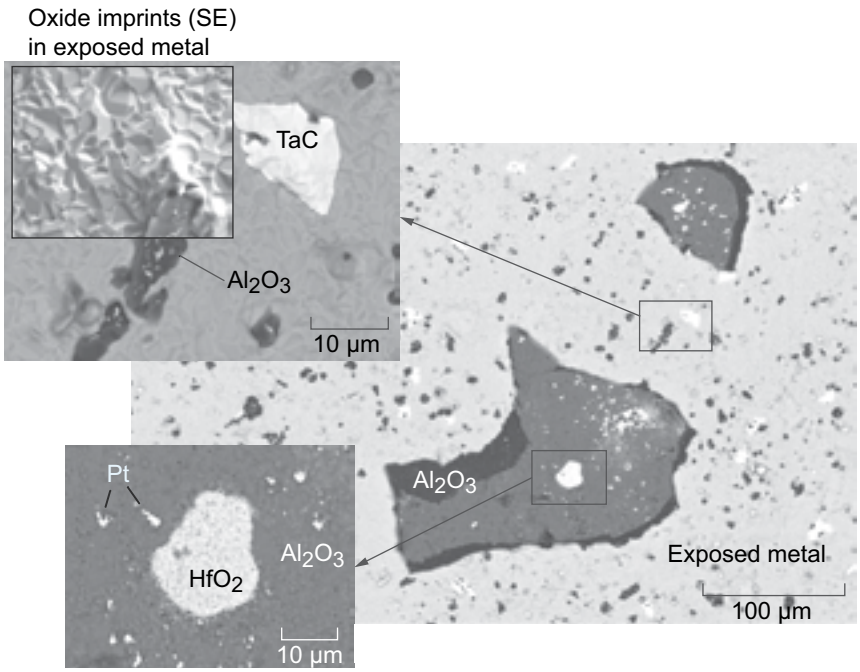


*Exposed bare metal surface after cathodic descaling of René N5. Montage of scanning electron microscope, backscattered electron, and secondary electron imaging micrographs showing oxide grain imprints in metal, residual alumina particles and plates, internal tantalum carbide (TaC), and external halfnium dioxide ($HfO_2$) (polarized at –2.0 V and <1 mA in 1N sulfuric acid ($H_2SO_4$) for 1 hr, preoxidized at 1150 °C for 1000 cycles).*

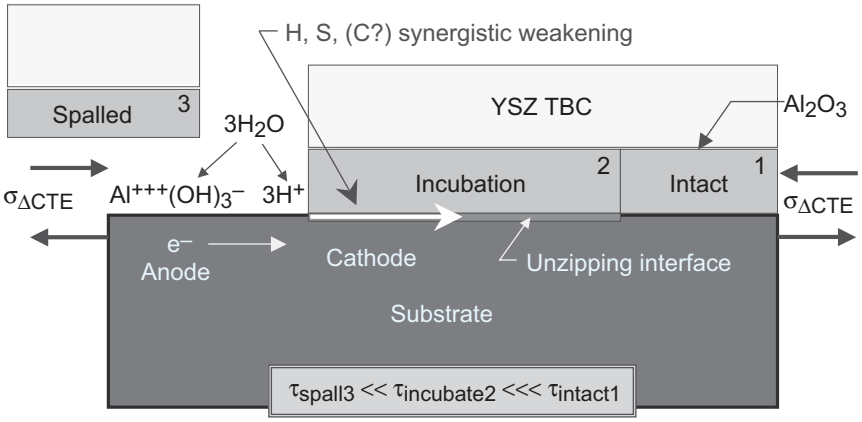


*MIDS of alumina scales due to interfacial hydrogen embrittlement. Moisture from ambient air reacts with aluminum in the alloy to form $Al(OH)_3$ and H, which is then attracted by biaxial tension to diffuse into the alloy. After sufficient incubation time for hydrogen diffusion, a scale segment (and TBC) may detach under the large counterbalanced biaxial compressive stress; $\sigma_{CTE}$, thermal expansion mismatch stress; YSZ, yttria stabilized zirconia; $\tau$, event duration.*

**Bibliography**

Smialek, James L.: Moisture-Induced Delayed Spallation and Interfacial Hydrogen Embrittlement of Alumina Scales. JOM (NASA/TM—2005-214030), vol. 58, no. 1, 2006, pp. 29–35. http://gltrs.grc.nasa.gov/cgi-bin/GLTRS/browse.pl?2005/TM-2005-214030.html

**Find out more about the research of Glenn's Durability and Protective Coatings Branch:**
http://www.grc.nasa.gov/WWW/EDB/

**Glenn contact:**
James L. Smialek, 216–433–5500, James.L.Smialek@nasa.gov

**Author:**
Dr. James L. Smialek

**Headquarters program office:**
Aeronautic Research Mission Directorate

**Programs/projects:**
Subsonic Fixed Wing

# New Burner-Rig-Based Erosion Test With High-Temperature (>2200 °F) Capability Developed

Particulate erosion of high-temperature gas engine turbine materials may now be studied at the NASA Glenn Research Center using a new burner-rig-based erosion rig developed and built by researchers in Glenn's Materials and Structures Division. This is one of very few available systems in the country with the capability to study high-temperature turbine section material as well as lower temperature compressor section materials. The heart of the rig is a burner rig torch with a mach-1-capable nozzle of 19.05-mm (0.75-in.) internal diameter, whose design was based on American Society of Mechanical Engineers (ASME) flow nozzle guidelines. Powders are injected into the combustor section of the erosion rig through an injection port fed from a commercial powder feeder. A dust-collection system and a powerful room exhauster capture and remove the particles after they strike the test specimen. To date, testing has focused on either 25.4-mm- (1.0-in.-) or 50.8-mm- (2-in.-) diameter test specimens, oriented perpendicular to the burner axis, although many other specimen geometries and orientations are feasible. The photographs show the rig and closeup front and back views of a specimen in test.

The need for high temperature requires that test specimens be located within the hottest region of the gas jet, a region close to the nozzle exit called the potential core. Since the potential core is only a few inches long, the erodent particles fed into the burner combustor section must accelerate to high velocity in a distance of just a few inches. To ensure that high particle velocities could be achieved, researchers used a commercial computational fluid dynamics code to calculate gas and particle velocities for erosion rig temperatures and pressures of interest. It was determined that spherical alumina particles 50 μm in diameter (a typical laboratory erodent) injected into the erosion rig could achieve the high velocities required for meaningful testing. Specifically, the predicted centerline particle velocities were over 200 m/sec at 3 in. from the nozzle at mach 0.7 and were over 100 m/sec at 3 in. from the nozzle at mach 0.3. In either case, a representative degradation mode with sufficient damage would be expected, thereby providing an excellent testing capability for evaluating the erosion resistance of materials. The model will be backed by experimental verification and adjusted accordingly.

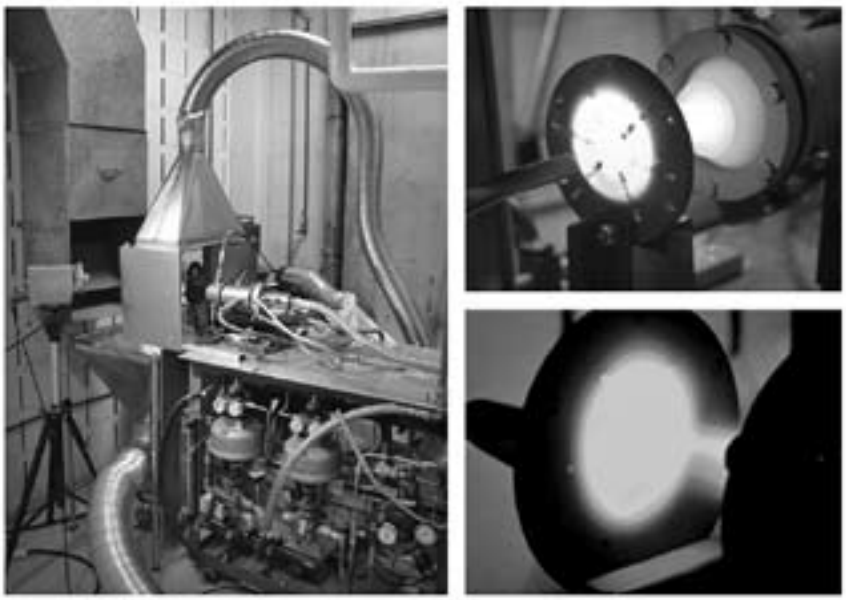

*Glenn's new high-temperature erosion rig. Left: Erosion rig. Right: Closeup front (top) and back (bottom) views of a specimen being tested in the rig.*

**Glenn contact:**
Dr. Robert A. Miller, 216–433–3298,
Robert.A.Miller@nasa.gov

**Authors:**
Dr. Robert A. Miller,
Dr. Maria A. Kuczmarski,
Dr. Dongming Zhu, and Michael D. Cuy

**Headquarters program office:**
Aeronautics Research Mission Directorate

**Programs/projects:**
Fundamental Aeronautics Program,
Subsonic Rotary Wing Project

# Photocured Polyimides Developed

Diels-Alder cycloadditions have often been utilized in polymer synthesis as an alternative to condensation reactions. These methods are attractive for use in the preparation of high-performance polymers, such as polyimides, because they utilize monomers that have less environmental, health, and safety risks. In addition, they have the potential to be adapted to low-cost processing techniques. Future NASA human and robotic exploration missions will require polymers and adhesives that can be cured in ambient space environments for in-space repairs; large deployable, rigidizable arrays; and inflatable habitats and rovers. On Earth, lower cure temperatures are desirable to reduce tooling costs and processing-induced thermal stresses. In addition, thermal processing conditions may be too severe to use with certain functional groups, such as nonlinear optically active or antimicrobial units. For these reasons, researchers from the NASA Glenn Research Center and the Ohio Aerospace Institute (OAI) have been pursuing the development of high-performance polymers that can be cured at low temperatures with ultraviolet radiation.

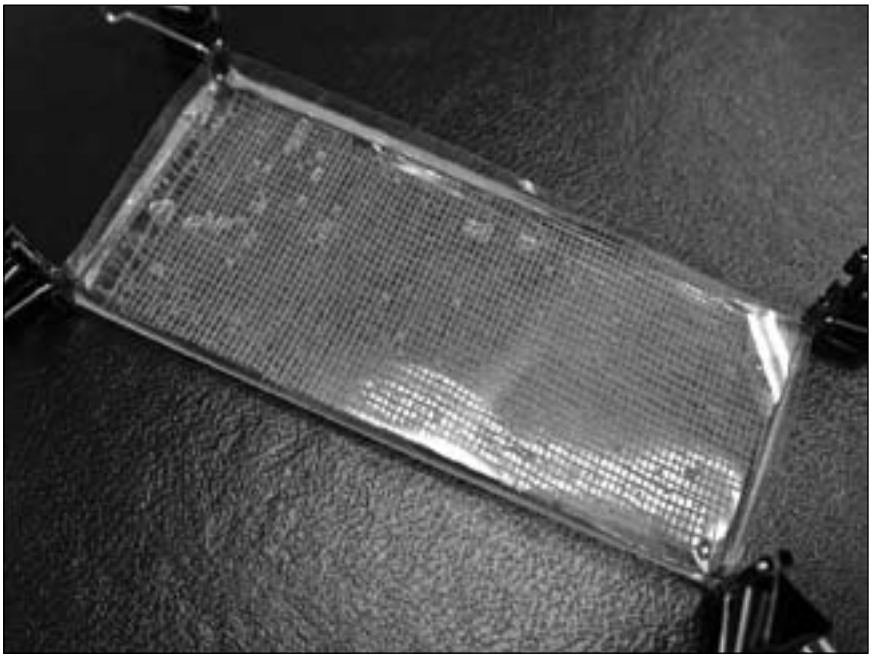

*Photocured polyimide composite.*

Our approach to exploiting Diels-Alder cycloaddition reactions has focused on bis(o-quinodimethanes), which are generated in situ by a classical photochemical reaction: the photoenolization of o-methylphenyl ketones. Recently, we designed and synthesized a new system based on the results of our previous work. Here, a bis(o-methylbenzophenone) diene (**1**) was prepared with an ethylene oxide subunit to increase the flexibility of the resulting polymer. The dienophile (**2**) was chosen to include maleimide units to limit competing reactions and an ethylene oxide chain to improve solubility. Interestingly, (**1**) is a viscous oil at room temperature, allowing the photoactive blend to be film cast with or without solvent. The latter makes use of (**1**) to dissolve (**2**), creating a photoactive gel. Initial studies indicate that the resulting polyimide thin films have high glass-transition temperatures $T_g$'s and are fairly strong, flexible, and elastometric. In addition, polymerization was complete in the presence of oxygen, suggesting improved reaction rates. This is likely due to the inherently high concentration of a solventless system.

Additional studies on the properties and applications of the photoactive monomer solution were carried out by Advanced Coatings International (ACI). ACI successfully prepared polyimide coatings, bulk polymer materials, and composite materials. Initial tests in rigidizable arrays indicated that photocurable polymers based on the photoenolization of *o*-methylphenyl ketones have significant potential for this application.

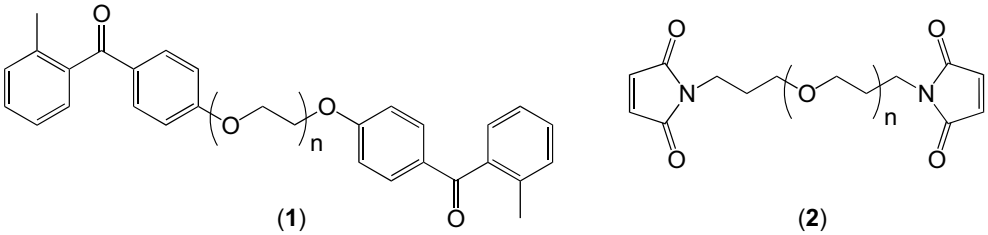


*Structures of novel o-methylbenzophenone (1) and dienophile (2).*

**Find out more about the research of Glenn's Polymer Branch:**
http://www.grc.nasa.gov/WWW/5000/MaterialsStructures/polymers/

**Glenn contact:**
Dr. Michael A. Meador, 216–433–9518, Michael.A.Meador@nasa.gov

**Ohio Aerospace Institute (OAI) contact:**
Dr. Daniel S. Tyson, 216–433–3187, Daniel.S.Tyson@nasa.gov

**Authors:**
Dr. Michael A. Meador, Dr. Daniel S. Tyson, and Dr. Faysal Ilhan

**Headquarters program office:**
Aeronautics Research Mission Directorate

**Programs/projects:**
Vehicle Systems, Exploration Systems

# High Glass Transition Temperature, Low-Melt Viscosity Polyimides Developed for Resin Transfer Molding

Polyimide/carbon-fiber composites have been used as lightweight materials in high-service-temperature aerospace components for decades. Most notably, the PMR–15 polyimide was successfully utilized as a replacement for titanium in composite ducts for military aircraft engines, resulting in a 30-percent cost savings and 12-percent weight savings. Processing of PMR–15 into aerospace components is costly because of a combination of labor-intensive manufacturing methods and the need to employ engineering controls to protect those working with PMR–15 prepregs from exposure to methylene dianiline, a known mutagen. To address safety concerns and to reduce manufacturing labor and costs, researchers in the NASA Glenn Research Center's Polymers Branch are focusing current research efforts on developing low-melt viscosity polyimide resins that are adaptable to low-cost resin transfer molding (RTM) or resin infusion (RI) processes. The RTM process can be easily automated to lower the processing labor and costs, and it is commonly used in industry for fabricating epoxy and bismaleimide (BMI) composites for applications seeing temperatures as high as 177 and 232 °C, respectively.

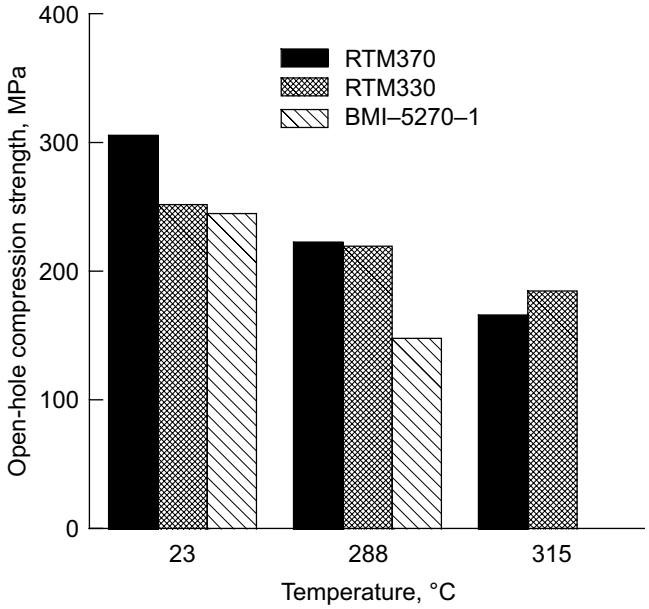


*Open-hole compression strength of RTM370 and RTM330 versus that of BMI–5270–1.*

Two new polyimide resins with low-melt viscosities (10 to 30 poise) and high glass transition temperatures ($T_g$ = 330 to 370 °C) were recently developed for RTM applications. These two polyimide resins are based on asymmetrical 2,3,3',4'-biphenyl dianhydride (a-BPDA) and 3,4'-oxydianiline (designated as RTM370) and 3,3'-methylene dianiline (designated as RTM330) and are both endcapped with 4-phenylethynylphthalic anhydride. Carbon fiber (T–650–35) composites were prepared from these resins using the RTM process by injecting the resin

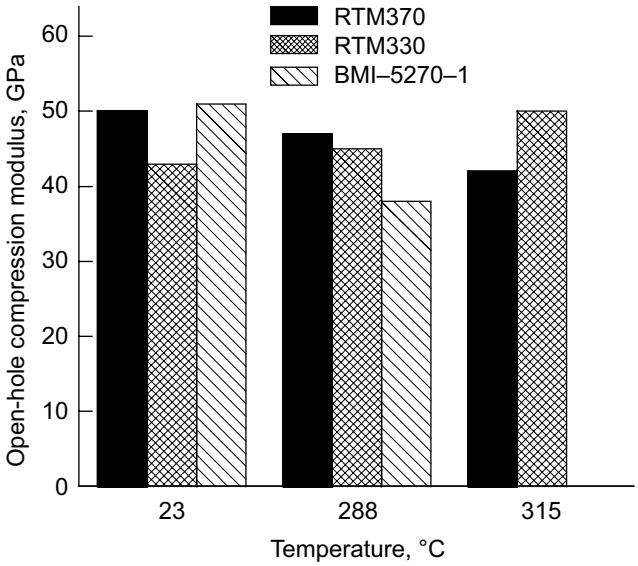


*Open-hole compression modulus of RTM370 and RTM330 versus that of BMI–5270–1.*

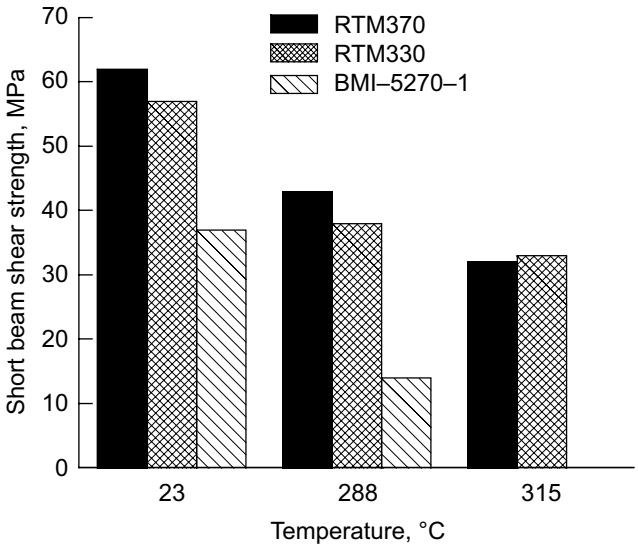


*Short beam shear strength of RTM370 and RTM330 versus that of BMI–5270–1.*

at 260 to 280 °C (30-60 min pot life) and curing the resin-infused preform at 370 °C. RTM370 and RTM330 composites both displayed very good property retention at temperatures up to 315 °C, well exceeding the performance of commercially available RTM resins, such as 5270–1 BMI. RTM370 and RTM330 exhibited excellent open-hole compressive strength and retained 73 and 87 percent (see the figure on the preceding page) of their room temperature properties at 288 °C while maintaining most of their compressive modulus (see the top figure on this page). Furthermore, RTM370 and RTM330 also retained 69 and 67 percent of their initial short-beam shear strength at 288 °C, respectively (see the final figure). These results suggest that both of these resins hold promise for use in the production of cost-effective aerospace components for use at temperatures as high as 288 °C.

**Glenn contact:**
Dr. Kathy Chuang, 216–433–3227, Kathy.Chuang@grc.nasa.gov

**Author:**
Dr. Kathy Chuang

**Headquarters program office:**
Aeronautics Research Mission Directorate

**Programs/projects:**
Glenn Alliance for Technology Exchange: Supersonics

# Reaction Zones Associated With Joining Nickel-Based Superalloys to Titanium Investigated

Future power systems for spacecraft and lunar surface systems will likely have a strong dependence on nuclear power. The design of a space nuclear powerplant involves integrating the major subsystems of the reactor, the power-conversion system, and the heat-rejection system. Optimum material choices for subsystems and between subsystems can vary significantly depending on the design. A heat-rejection system made of titanium could be integrated to a power-conversion system made of superalloys or stainless steels. The transition and stability of the joined dissimilar materials are critical points in the overall system and key factors in determining life and performance. This work describes preliminary investigations by researchers from the NASA Glenn Research Center and the University of Toledo to join a commercial, wrought superalloy, HASTELLOY X (HX), to a widely used titanium alloy, Ti-6Al-4V (titanium-6 wt% aluminum-4 wt% vanadium).

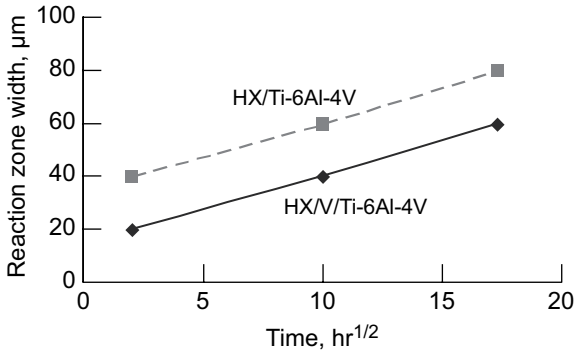


*Interdiffusion reaction zone widths for HX/Ti-6Al-4V diffusion couples with and without a V interlayer after annealing at 1150 K.*

Titanium alloys, a lightweight alternative to stainless steels, are used extensively in aeronautic applications. In space power applications, replacing some stainless steel components with titanium alloys could reduce the overall mass of the spacecraft. However, the use of titanium alloys in a space power system requires understanding the limitations of joint formation and temperature stability. Fusion welding can be problematic because of the reactive nature of titanium and the increased potential formation of brittle intermetallic compounds. A few previous attempts to join Ti or Ti-alloys to superalloys through explosive bonding, brazing, and diffusion welding (with or without thin interlayers of other metals to minimize the formation of deleterious brittle intermetallic phases) have been reported in the literature (refs. 1 to 3).

In this investigation, joints between the superalloy and titanium alloy were produced by hot pressing small coupons of each material for 4 hr at 1150 K (877 °C). An exploratory 70-µm-thick V foil interlayer was inserted between the two dissimilar alloys in one of the couples prior to hot pressing. After the initial bond was formed, the "diffusion couple" was annealed in an ultra-high-purity argon atmosphere for 100 and 300 hr at 1150 K to accelerate the diffusion process. The table shows the diffusion couples that were formed as well as the temperatures and anneal times. The diffusion-affected region of the bond was subsequently examined by scanning electron microscopy, and the couples were also examined for compositional variations.

DIFFUSION COUPLES AND ANNEALING TIMES

| Diffusion couple | Annealing time at 1150 K, hr | | |
|---|---|---|---|
| HX/Ti-6Al-4V | 4 | 100 | 300 |
| HX/V/Ti-6Al-4V | 4 | 100 | 300 |

For the HX/V/Ti-6Al-4V system, the reaction zone was narrower than for the couple without the V interlayer.

A single diffusion layer formed at the HX/V interface in the reaction zone of the HX/V/Ti-6V-4Al couple. Conversely, multiple phase layers developed in the reaction zone of the HX/Ti-6V-4Al couple. Elemental maps (next page) show the distribution of Ti and Ni in the two diffusion couples after annealing 300 hr at 1150 K. At this accelerated exposure temperature, minimal elemental intermixing occurred in the HX/V/Ti-6Al-4V system, but extensive diffusion of Ti and Ni occurred in the HX/Ti-6Al-4V system.

In summary, although traditional welding of nickel to titanium alloys is problematic, nickel-based alloys can be joined to Ti alloys by nonfusion techniques, and the addition of a V interlayer may minimize the formation of deleterious, brittle intermetallic phases in a superalloy/Ti-alloy dissimilar metal joint.

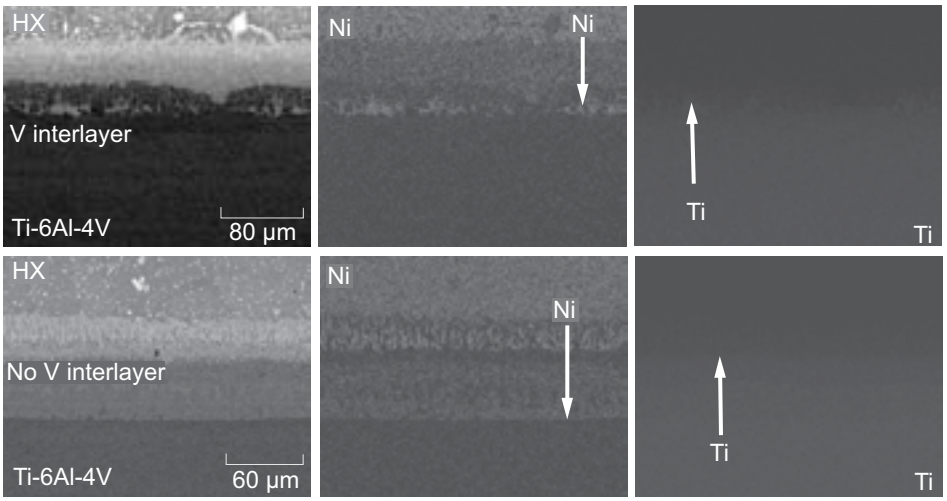


*Electron microscopy images and elemental maps for Ni and Ti for HX/V/Ti-6Al-4V and HX/Ti-6Al-4V diffusion couples after hot pressing for 300 hr at 1150 K, showing different depths of Ni and Ti diffusion with or without the V interlayer.*

**References**

1. Schwartz, M.M.: Fabrication of Dissimilar Metal Joints Containing Reactive and Refractory Metals. Weld. Res. Counc. Bull., no. 210, 1975.
2. Banker, J.G.; and Linse, V.D.: Explosion Welds Between Titanium and Dissimilar Metals. Advances in the Science and Technology of Titanium Alloy Processing. International Symposium on Advances in the Science and Technology of Titanium Alloy Processing at the 125th TMS Annual Meeting and Exhibition, Anaheim, CA, 1996, pp. 539–547.
3. Bykovskii, O.G., et al.: Effect of the Composition of Initial Materials on the Formation and Properties of Spot Welded Joints Between Titanium Alloys and Steel and Nickel. Weld. Int. (Translation 774), vol. 4, no. 4, 1990, pp. 300–302.

**Find out more about the research of Glenn's Structures and Material Division:**
http://www.grc.nasa.gov/WWW/5000/MaterialsStructures/

**University of Toledo contact:**
Dr. Ivan E. Locci, 216–433–5009, Ivan.E.Locci@nasa.gov

**Glenn contacts:**
Dr. James A. Nesbitt, 216–433–3275, James.A.Nesbitt@nasa.gov

Frank J. Ritzert, 216–433–8199, Frank.Ritzert@nasa.gov

Dr. Cheryl L. Bowman, 216–433–8462, Cheryl.L.Bowman@nasa.gov

**Authors:**
Dr. Ivan E. Locci, Dr. James A. Nesbitt, Frank J. Ritzert, and Dr. Cheryl L. Bowman

**Headquarters program office:**
Exploration Systems Mission Directorate

**Programs/projects:**
Project Prometheus

# Diffusion Bonding of Silicon Carbide to Silicon Carbide Developed for a Lean Direct Injector Application

Silicon carbide (SiC)-based ceramics are enabling materials for a number of high-temperature and high-performance technical applications. Monolithic SiC-based ceramics are being used as heating elements, ceramic armor, and mirror and optical components for space applications. In addition, SiC-based composites are being developed for aerospace and ground-based propulsion and hot-structure airframe systems and for hot-structure fusion reactor applications. SiC offers favorable properties such as high strength, high-temperature capability, and corrosion resistance. However, many of the potential applications require complex-shaped components that are difficult and expensive to manufacture. Joining of simple-shaped ceramics offers a cost-effective method for manufacturing large, complex-shaped components.

For specific applications, some joint fabrication methods may be more suitable than others depending on the application requirements and the properties of the materials used to form the joints. In many of the processing methods, high temperatures and applied stresses are required to form the joint. Some starting materials and designs cannot take such conditions. Other joining approaches, which do not require high stresses and high temperatures, often result in joints that are brittle, have low strength, or are unstable at high temperatures. However, one such application that is well suited for high-temperature, high-stress processing is a lean direct injector that is formed by joining flat SiC laminate disks. In this application, etched SiC laminates can be used to create intricate, interlaced passages that speed up fuel-air mixing to allow for lean-burning and ultralow emissions. The joining requirements for such an application are the ability to bond relatively large geometries (i.e., 4-in.-diameter disks), leak-free operation, high strength, and chemical stability. To develop joining technology that could meet these requirements, NASA and U.S. Army researchers at the NASA Glenn Research Center used hot pressing to investigate the diffusion bonding of SiC to SiC.

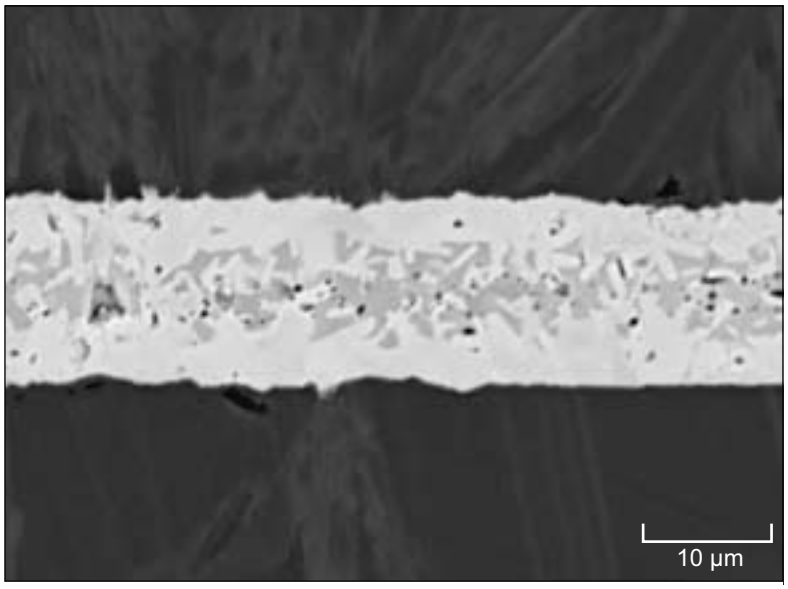


*Cross section of the joined SiC substrates. The diffusion bond, located across the middle of the figure, has two phases (gray and light gray). The SiC substrates (black) are above and below the bond.*

SiC joining technology was developed in the Fundamental Aeronautics Program. Titanium (Ti) interlayers were used to form diffusion bonds between chemically vapor deposited (CVD) SiC substrates. The titanium interlayers consisted of either physically vapor deposited (PVD) Ti interlayers or alloyed Ti foil. Microstructural analysis revealed that the diffusion bonds were well adhered to the SiC substrates. No delaminations were observed between the SiC layers. The best diffusion bonds were obtained when PVD Ti coatings were used as interlayers between the SiC laminates (see the photomicrograph). The bonds were uniform, they formed preferred phases, and they did not contain microcracking. Preliminary tensile tests show that the bond strength is well beyond the requirements of a proposed injector application. The initial results suggest that diffusion bonding is a good process for fabricating a laminated injector component. Future analysis and subcomponent tests are planned to confirm that the diffusion bonds are leak free, strong, and stable at elevated temperatures.

**Bibliography**


Halbig, Michael C., et al.: Diffusion Bonding of Silicon Carbide Ceramics Using Titanium Interlayers. Ceram. Eng. Sci. Proc., vol. 27, no. 2, 2006, pp. 133–143.



**U.S. Army Research Laboratory at Glenn contact:**
Michael C. Halbig, 216–433–2651, Michael.Halbig@nasa.gov

**Glenn contact:**
J. Douglas Kiser, 216–433–3247, James.D.Kiser@nasa.gov

**Authors:**
Michael C. Halbig, Dr. Mrityunjay Singh, Tarah P. Shpargel, and J. Douglas Kiser


**Headquarters program office:**
Aeronautics Research Mission DIrectorate

**Programs/projects:**
Fundamental Aeronautics Program, Subsonics Fixed Wing Project, Supersonics Project

# Adhesive Joining of Titanium to Carbon-Carbon Composite and Foam Structures Demonstrated

Robust brazing and integration technologies are critically needed for the assembly of heat-rejection system components for lunar and other space exploration systems. Under the auspices of the Prometheus program, over 20 adhesive candidate materials were explored by researchers from the NASA Glenn Research Center and the Ohio Aerospace Institute (OAI) to ascertain their viability for joining titanium (Ti) tubes to carbon-fiber-reinforced carbon (C–C) composite and/or carbon foam structures. On the basis of the initial bonding strength of Ti to C–C composites and microstructural analysis to assess the effectiveness of the bonding, nine adhesives were selected for mechanical testing of joints. Mechanical tests were performed using a butt-strap tensile (BST) lap shear test. Two coupons of Ti were joined to a P120 (carbon fiber produced by Cytec Industries) two-dimensional woven C–C composite strap section as shown in the sketch. Shear failure tests were performed on as-bonded specimens, specimens that were subjected to a liquid nitrogen soak for 15 min, and specimens that were subjected to a heat treatment of 530 K for 24 hr. Specimens that showed the best promise were then tested to failure at an elevated temperature (270 °C). The graph shows the tensile results.

The failure location dictated the shear strength (see the graph). In other words, if failure occurred within the outer ply of the C–C, the shear strengths were high. However, if failure occurred between the epoxy and Ti or C–C, indicating poor adhesion, then shear strengths were low. Failure within the epoxy fell between the above two extremes. The three adhesives that showed the best strengths for all three room-temperature test conditions were chosen for testing at 270 °C. We found that all three systems showed that strength at 270 °C was significantly less than at room temperature. The best systems, with shear strengths of approximately 2 MPa, were the two adhesives with aluminum nitride (AlN) as a filler material: CM–122 and EP45HTAN (epoxy made by Master Bond Inc.). However, 270 °C-tested specimens failed at the interface between the Ti and epoxy or C–C and epoxy.

So that the feasibility of joining structures similar to that envisioned for the heat-rejection application could be demonstrated, Ti tube, POCO foam (POCO Graphite), and C–C composite sandwich structures were fabricated (see the photograph on the next page). The specimens were tested in tension and in shear. In all cases, failure occurred within the POCO foam—not at either of the epoxy joints. The failure loads were commensurate with the shear strengths of the foam itself, which indicates that the weak point in the structure is the foam and not the adhesive, thus demonstrating the viability of the adhesive joining approach. The loads applied to the structure indicate that the Ti-tube, POCO foam joint could withstand stresses greater than 3.6 MPa in shear and 2.2 MPa in tension. This is based on the simple force over area. The joint itself showed no indication of failing at those applied loads.

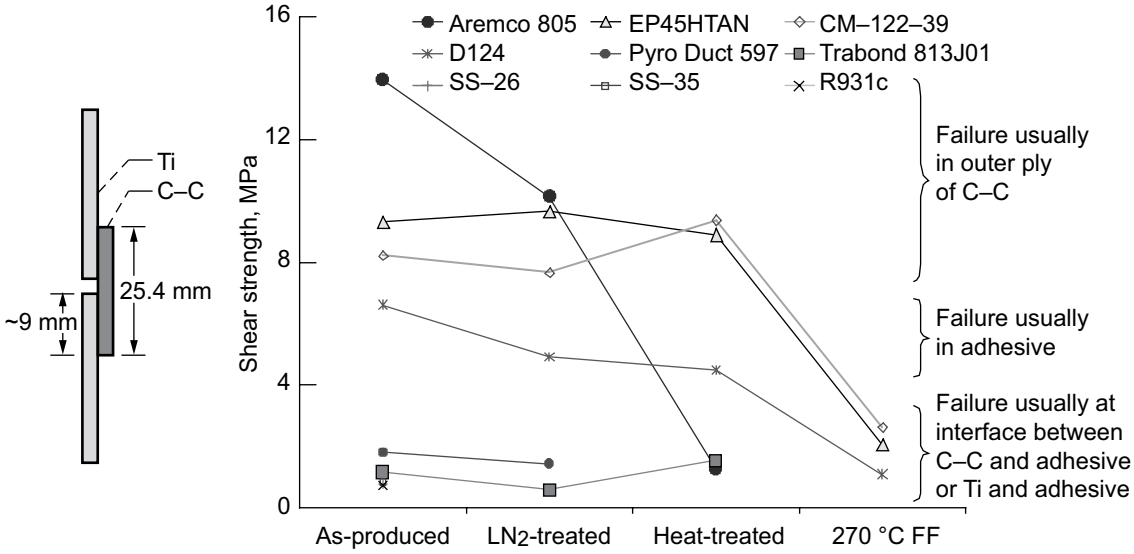


*BST test. Left: Schematic. Right: Results from BST test on different adhesively joined systems. Aremco 805 and Pyro Duct 597 are epoxies made by Aremco Products, Inc.; D124 and R931C are epoxies made by TRA–CON, Inc.; SS–26 and SS–35 are epoxies made by Silicone Solutions; TRA–BOND 813J01 is an epoxy made by TRA–CON, Inc.; FF is fast fracture; $LN_2$ is liquid nitrogen.*

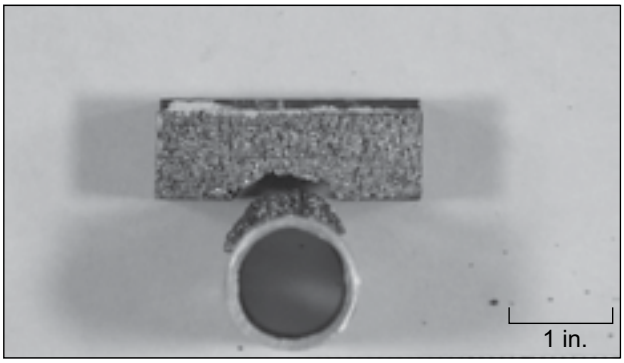


*Ti tube, POCO foam, K1100 2D 5HS plate structure (Amoco/Cytec Industries K1100 fiber, two-dimensional, five-harness satin fiber) joined with CM–122 epoxy after shear failure. Failure occurred in the foam and not at the joint.*

**Bibliography**
Cerny, Jennifer; and Morscher, Gregory: Adhesive Bonding of Titanium to Carbon-Carbon Composites for Heat Rejection Systems. Ceram. Eng. Sci. Proc., vol. 27, no. 2, 2006, pp. 125–132.

**Ohio Aerospace Institute (OAI) contact:**
Dr. Gregory N. Morscher, 216–433–5512, Gregory.N.Morscher@nasa.gov

**Glenn contact:**
Dr. Mrityunjay Singh, 216–433–8883, Mrityunjay.Singh-1@nasa.gov

**Authors:**
Dr. Gregory N. Morscher,
Dr. Mrityunjay Singh, and Jennifer Cerny

**Headquarters program office:**
Exploration Systems Mission Directorate

**Programs/projects:**
Prometheus

## Effect of Processing Conditions on Chemical Makeup of Di-Isocyanate Crosslinked Silica Aerogels Studied

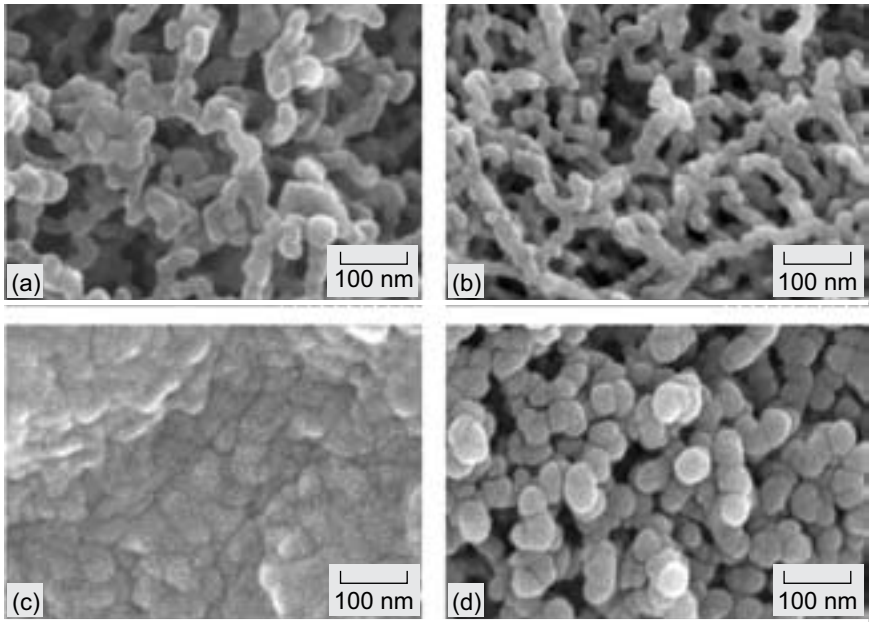


*Scanning electron micrographs of aerogels comparing no washings, (a) and (c); four washings, (b) and (d); low concentrations of silane, water, and polymer, (a) and (b); and low concentration of silane but high concentrations of water and polymer, (c) and (d).*

Because of their low density and high mesoporosity, sol-gel-derived silica aerogels are attractive candidates for many unique thermal, optical, catalytic, and chemical applications (ref. 1). However, their inherent fragility has restricted their use. Researchers at the NASA Glenn Research Center previously reported crosslinking the mesoporous silica structure of an aerogel with polymers such as polyureas (refs. 2 to 4) and epoxies (ref. 5). These materials have very high specific strength in comparison to that of uncrosslinked aerogels with only a small effect on density. Thus, they may be enabling for future space exploration missions as well as advanced aeropropulsion systems that demand lighter weight, robust, dual-purpose materials for insulation, radiation protection, and/or the structural elements of habitats, rovers, astronaut suits, and cryotanks.

Although density is a prime predictor of the strength and thermal conductivity

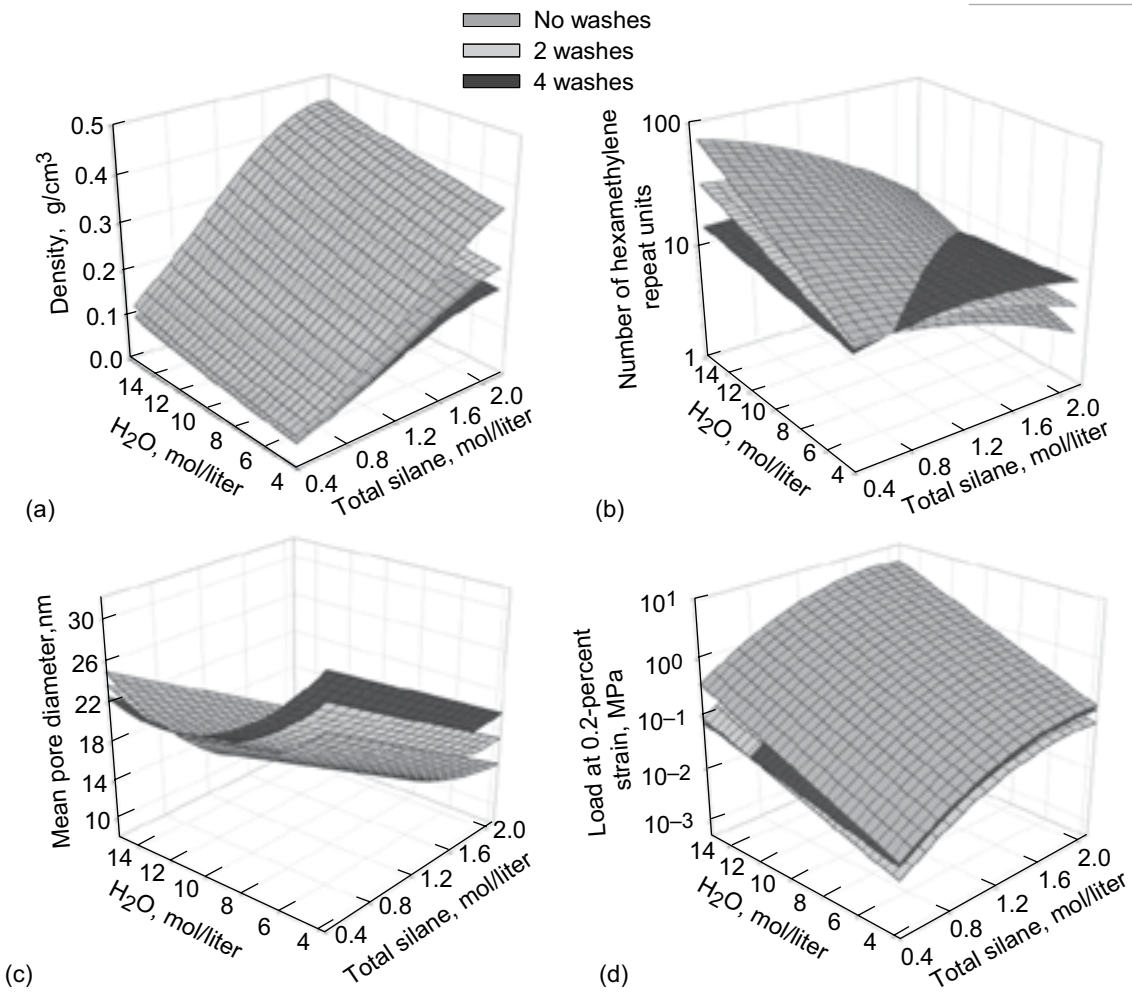


*Slices of the response surface models plotted versus total silane and water concentration with di-isocyanate held constant at the lowest concentration. (a) Density. (b) Polymer repeat units. (c) Average pore diameter. (d) Offset yield strength.*

of aerogels, previous studies indicated that varying the silica backbone and size of the polymer crosslink independently can give rise to combinations of properties unpredictable from density alone. For use as a multifunctional insulation/structural material, such as in a cryotank, Glenn researchers wished to optimize the strength of aerogels while reducing density and thermal conductivity as much as possible. The effects of four processing parameters for producing di-isocyanate crosslinked aerogel were examined using statistical experimental design methodology to reduce the number of experiments and to allow computation of empirical models describing the relationship between the four variables and resulting properties.

The photomicrographs on the preceding page show aerogel monoliths from the study at some of the extreme values of the four variables. It is evident, by comparing an aerogel with no washings (a) to that with four washings (b), that the number of washings is less critical when low values of polymer and water are employed: (a) and (b) are very similar. Other properties of the monoliths in (a) and (b) are also very similar (8 to 10 repeat units of isocyanate in the crosslink, porosity of >94 percent, and mechanical properties). However, at high values of water and polymer, no washings (c) produced a monolith with very low porosity, whereas four washings (d) resulted in a porosity of 90 percent. Note that the difference in properties and morphology of (b) and (d) are due entirely to the increased size of the crosslink in (d) (7 times as many repeat units) since both start with the same silane concentration.

Some of the properties measured and modeled in this study are plotted in the preceding graphs, where di-isocyanate concentration is held constant at the lowest value studied. In general, mechanical properties, such as offset yield strength at 0.2-percent strain (d) increase as density (a) increases. Other properties, such as size of the crosslink (b) or mean pore size (c), are at a maximum when density

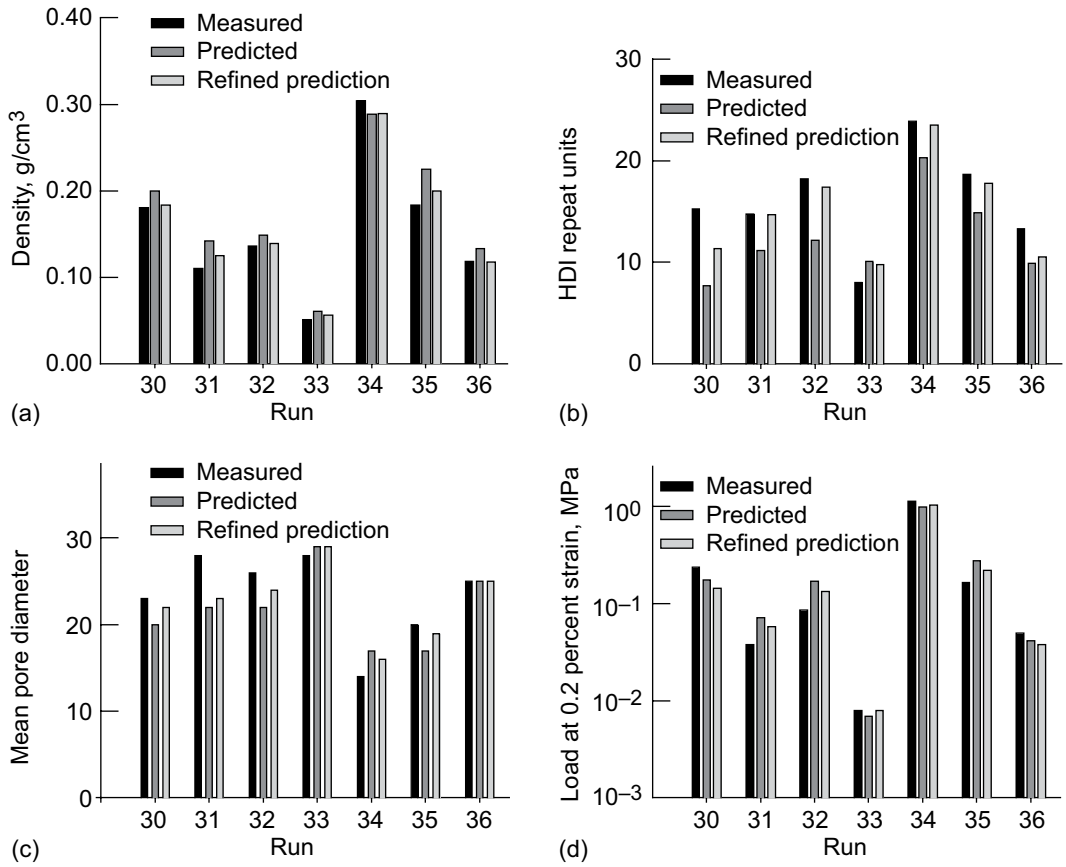


*Predicted and measured properties of polymer crosslinked aerogel optima from the experimental design. New runs were added to the original data to refine the models. HDI indicates hexamethylene di-isocyanate, the basic unit in the polymer crosslink.*

is minimized. These types of models provide the ability to dial in a property for a particular application, for example, the minimum density aerogel with a desired mechanical strength.

To assess the validity of the models and test their ability to accurately predict aerogel properties, seven additional monoliths were produced, corresponding to model-generated optima for certain responses, and their properties were measured and compared with the predicted values. Some of these are shown in the bar charts for the same properties as in the preceding graphs. More of the results from this study are reported in reference 6.

**References**


1. Morris, C.A., et al.: Silica Sol as a Nanoglue: Flexible Synthesis of Composite Aerogels. SCI, vol. 284, 1999, pp. 622–624.
2. Leventis, N., et al.: Nanoengineering Strong Silica Aerogels. Nano Letters, vol. 2, no. 9, 2002, pp. 957–960.
3. Zhang, Guohui, et al.: Isocyanate-Crosslinked Silica Aerogel Monoliths: Preparation and Characterization. J. Non-Cryst. Solids, vol. 350, 2004, pp. 152–164.
4. Capadona, Lynn A., et al.: Flexible, Low-Density Polymer Crosslinked Silica Aerogels. Polymer, vol. 47, 2006, pp. 5754–5761.
5. Meador, Mary Ann B., et al.: Cross-Linking Amine-Modified Silica Aerogels With Epoxies: Mechanically Strong Lightweight Porous. Chem. Mater., vol. 17, no. 5, 2005, pp. 1085–1098.
6. Meador, Mary Ann B., et al.: Structure-Property Relationships in Porous 3D Nanostructures as a Function of Preparation Conditions: Isocyanate Cross-Linked Silica Aerogels. Chem. Mater., vol. 19, no. 9, 2007, pp. 2247–2260.



**Glenn contacts:**
Dr. Mary Ann B. Meador, 216–433–3221, Maryann.Meador@nasa.gov

Dr. Lynn A. Capadona; 216–433–5013, Lynn.A.Capadona@nasa.gov

**Authors:**
Dr. Mary Ann B. Meador,
Dr. Lynn A. Capadona, and
Dr. Nicholas Leventis


**Headquarters program office:**
Aeronautics Research Mission Directorate

**Programs/projects:**
Fundamental Aeronautics (subsonics fixed wing and subsonics rotary wing), Exploration Systems Research & Technology, Advanced Extravehicular Activity Project

# X-Aerogel Processing Time Reduced by One-Pot Synthesis

Polymer crosslinked aerogels have generated tremendous interest as multifunctional materials because of their superior mechanical properties in comparison to traditional silica aerogels (refs. 1 to 3). The high degree of porosity makes them attractive candidates as insulation for extreme environments, whereas their ability to bear load makes the materials amenable to applications requiring insulation as part of a load-bearing structure. One significant drawback to these materials is their method of production, a lengthy process requiring multiple steps and about 15 days to fully complete. Despite their promising properties, application of the polymer crosslinked aerogels in future space missions depends on simplification of this process.

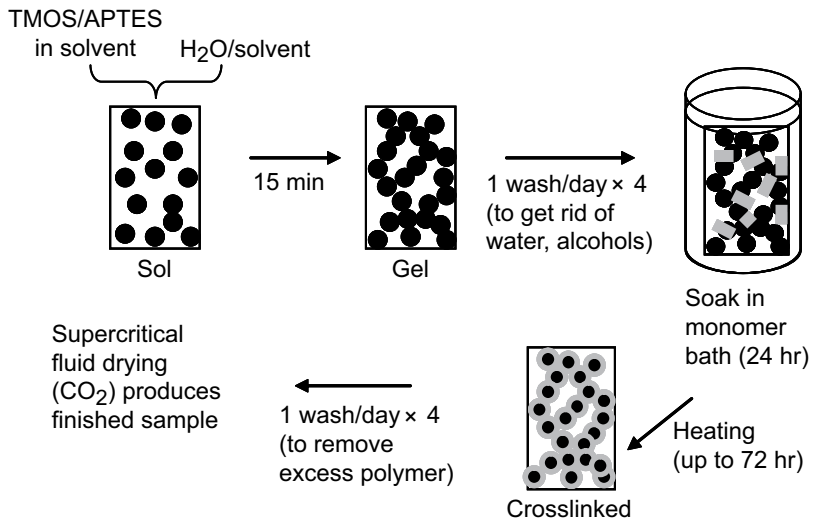


*Traditional method to prepare crosslinked aerogels. Each wash step takes 24 hr, and heating to crosslink can take as long as 72 hr. It takes approximately 1 liter of solvent to prepare one ~20-ml cylindrical monolith.*

The top figure demonstrates the traditional manner in which crosslinked aerogels are prepared. The gel is produced after the hydrolysis and condensation of common silica precursors tetramethyl orthosilicate and 3-aminopropyltriethoxysilane (TMOS and APTES) and is subject to several washing steps. Polymer crosslinking is introduced as a secondary step, requiring a nonstoichiometrically controlled soaking process where polymer precursors diffuse through the aerogels' porous network and await reaction with heat. This is largely dependent on the cross-sectional area of the monolith, making larger pieces somewhat more difficult to crosslink in this manner. Finally, the crosslinked aerogel is washed four more times in preparation for supercritical fluid extraction of the solvent. The overall process is very effective for making reproducible polymer crosslinked aerogel monoliths; however, it is not very efficient.

An alternative reaction scheme is under development at the NASA Glenn Research Center in which the precursors for crosslinking are included in the sol at the start (see the next figure). This simplifies the process to only a few steps, eliminating most of the time-consuming

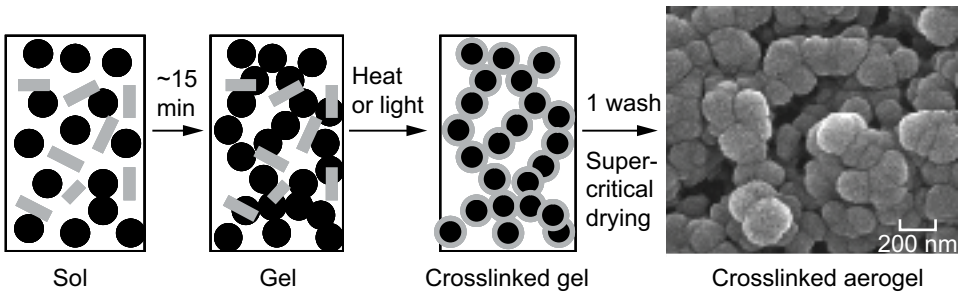


*One-pot synthesis of crosslinked aerogels. Gray constituents indicate prepolymers in the sol that are inert to gelation. Once the gel is formed, it can be reacted to initiate crosslinking. After one wash, which removes any unreacted components, the monolith, whose scanning electron microscopy (SEM) image is shown here, was supercritically dried and demonstrated nanoscale morphology similar to that of the well-characterized multistep-prepared crosslinked aerogels.*

wash steps and totally eliminating diffusion-driven crosslinking. When the polymer precursors are added in this manner, the gelation continues as normal. After a brief aging period, the gel is ready to be crosslinked. Depending on the type of crosslinking mechanism, the monoliths might be heated to start a chain growth reaction or be exposed to ultraviolet light to begin a radical polymerization reaction. In either case, not only does the one-pot method produce crosslinked aerogels in many fewer steps, but more control of stoichiometry and uniformity of the crosslinked gels is possible since diffusion-driven crosslinking is eliminated.

For this one-pot synthesis to proceed effectively, the polymer precursors must remain inert to gelation by either being introduced as a co-reacting agent with the oxide gel like an acrylate-modified siliane, or as a soluble monomer or oligomer that does not interfere with gelation, such as a bismaleimide; both of which we have demonstrated. As seen in this photograph, the one-pot-created isocyanate crosslinked aerogels look very similar to the traditionally prepared monoliths.

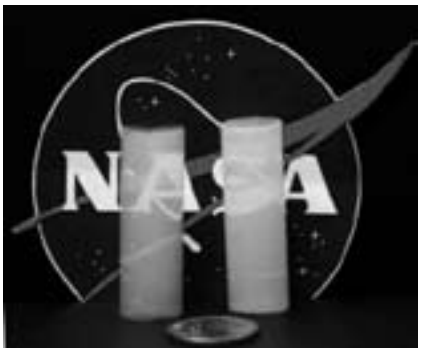


*Visual comparison of aerogels, showing similar diameters and moderate transparency. Left: One-pot-processed isocyanate crosslinked aerogel. Right: Traditionally processed version.*

Ongoing work involves full development of the factors contributing to the one-pot process, such as aging time, reaction times, optimal stoichiometric conditions, and optimum combinations of reaction initiator in cases where appropriate. A patent application for this new technology has been filed.

**References**


1. Capadona, Lynn A., et al.: Flexible, Low-Density Polymer Crosslinked Silica Aerogels. Polymer, vol. 47, no. 16, 2006, pp. 5754–5761.
2. Katti, A., et al.: Chemical, Physical, and Mechanical Characterization of Isocyanate Cross-Linked Amine-Modified Silica Aerogels. Chem. Mater., vol. 18, no. 2, 2006, pp. 285–296.
3. Meador, Mary Ann B., et al.: Cross-Linking Amine-Modified Silica Aerogels With Epoxies: Mechanically Strong Lightweight Porous Materials. Chem. Mater., vol. 17, no. 5, 2005, pp. 1085–1098.



**Glenn contacts:**
Dr. Lynn A. Capadona, 216–433–5013, Lynn.A.Capadona@nasa.gov

Dr. Mary Ann B. Meador, 216–433–3221, Maryann.Meador@nasa.gov

**Authors:**
Dr. Lynn A. Capadona and Dr. Mary Ann B. Meador


**Headquarters program office:**
Exploration Systems Mission Directorate

**Programs/projects:**
Advanced Extravehicular Activity

# Computer Simulation Developed for Modeling the Thermal Conductivity of Silica Aerogels

Aerogels are low-density materials whose low thermal conductivity make them of interest for aerospace applications where lightweight insulation is needed. Aerogels typically consist of nanoscale particles of porous amorphous silica, connected by “bridges” to form “pearl necklace” structures. The gels are highly porous and appear to exhibit a fractal structure, so that conventional methods for modeling the thermal conductivity are of limited utility. The NASA Glenn Research Center has developed, in-house, a model for predicting gel thermal conductivity that incorporates a model for the structure of gel clusters and a means for computing thermal conduction on such a cluster.

Gel structure was modeled using a modified version of the Diffusion Limited Cluster Aggregation (DLCA) scheme, which produced clusters that appear qualitatively similar to observed gels, as shown in the graph to the right. Quantitatively, the low-density model gels exhibited a fractal dimensionality of about 1.8, consistent with experimental observation. Higher-density model gels exhibited a larger fractal dimension and a fractal-to-compact transition at larger length scales, again as observed experimentally.

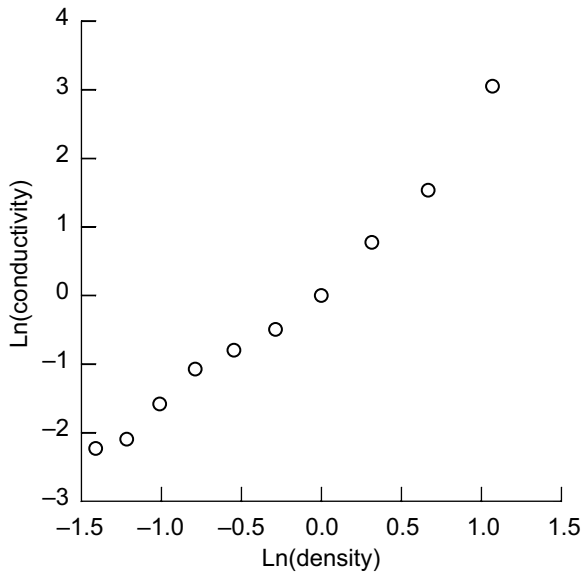


*Low-density aerogel model cluster from the DLCA computer simulation. Fractal dimension is approximately 1.75.*

The thermal conductivity of model DLCA clusters was computed by noting the formal similarity of the equations governing thermal and electrical conduction in source-free regions and by adapting methodology developed to compute the electrical conductivity of a random resistor network. In this model, each particle is represented by a node at its center and is connected to other nodes via thermal conductances that represent the combined conductance of the particle and an interconnecting bridge. The functional form of the conductance was computed analytically, with a prefactor representing the thermal conductivity of the particle material. Node temperatures were computed under Dirichlet boundary conditions, and the thermal conductivity was computed using the electrical analog mentioned earlier. The thermal conductivity of the model gels was found to depend strongly on the density (and therefore on the fractal dimensionality), exhibiting a power-law scaling (see ref. 1 for details).

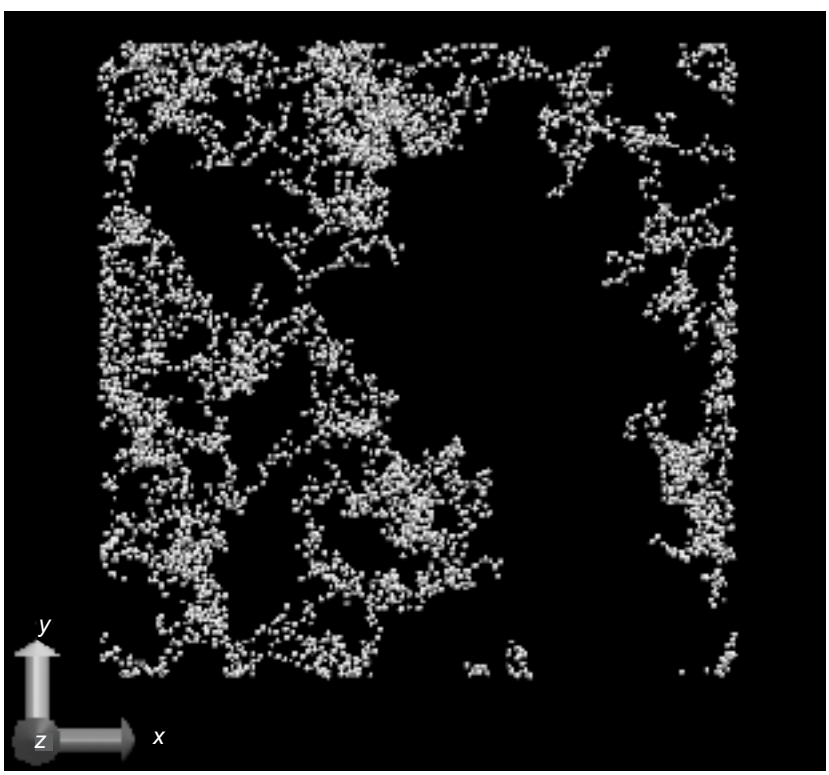


*Dependence of thermal conductivity as a function of density and of the ratio of gas-to-gel conductivity.*

The model was extended to include gaseous thermal conduction across the gel pores. A grid of “gas nodes” was superimposed on the cluster of gel particle nodes, and conductances between gas nodes and between a gas node and a

gel node were defined. Typically, the thermal conductivity of the gel particle material is about two orders of magnitude larger than that of air in the pores, for example. With gel-to-gas conductivity ratios in this range, the combined gel/gas thermal conductivity was found to exhibit a scaling exponent in the experimentally observed range of 1.2 to 1.8 (see the bottom figure on the preceding page). Details are given in reference 2.

**References**


1. Good, Brian S.: Structure and Thermal Conductivity of Silica Aerogels From Computer Simulations. 2005 Fall Proceedings of the Materials Research Society. The Hydrogen Cycle—Generation, Storage and Fuel Cells, MRS Proceedings, vol. 885, MRS 0885–A09–35, 2005.
2. Good, Brian: Thermal Conductivity of Silica Aerogels From Computer Simulations. Abstract ID: BAPS.2006.MAR.J1.204, Session J1, Poster Session II. Presented at the 2006 American Physical Society March Meeting, Baltimore, MD, 2006. http://meetings.aps.org/link/BAPS.2006.MAR.J1.204



**Glenn contact:**
Dr. Brian S. Good, 216–433–6296, Brian.S.Good@nasa.gov

**Author:**
Dr. Brian S. Good


**Headquarters program office:**
Exploration Systems Mission Directorate

**Programs/projects:**
Advanced Extravehicular Activity

## Carbon-Nanofiber-Reinforced Polymer Crosslinked Aerogels Studied

Silica aerogels are attractive candidates for a variety of NASA applications because of their lightweight structure, high surface area, and low thermal conductivity. Because silica aerogels are fragile, their use has been limited to protected, temperature-extreme environments, such as battery insulation for Mars surface rovers. However, advances over the last several years at the NASA Glenn Research Center have led to significant enhancements in mechanical durability as a result of polymer crosslinking the silica aerogel network (refs. 1 to 3). Recently, the incorporation of nanoscale fillers, such as carbon nanofibers, into the crosslinked aerogel matrix was demonstrated. The addition of these fillers can be advantageous since they may enhance not only the mechanical properties of the aerogel but other material properties, such as electrical conductivity or catalytic activity.

The Pyrograf-III (Applied Sciences, Inc.) nanofiber (top micrograph) was chosen for several reasons, primarily because the surface functionalization with alcohol provided good chemical compatibility with the existing processes. In addition, other properties unique to carbon nanotubes can be realized by substituting nanofibers that are easier to produce and are more cost effective. For certain applications, nanofiber-integrated crosslinked aerogels can simultaneously enhance the electrical conductivity and the mechanical reinforcement of the silica matrix. Other benefits include improved high-energy storage and decreased radiative heat transfer (due to the black color), both of which are desirable properties for efficient solar energy collection material.

Using a statistical design methodology, Glenn researchers produced 19 samples, with approximately two-thirds containing fiber in varying amounts according to the total silane component of the gel mixture. The

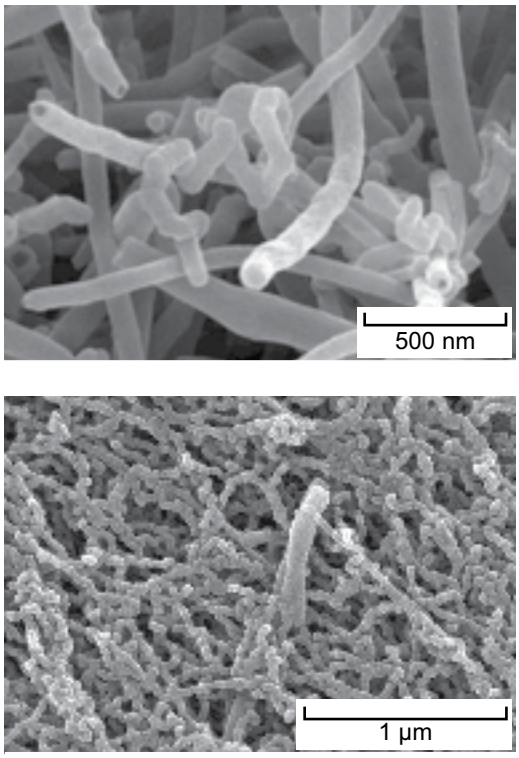


*Scanning electron micrographs of carbon nanofibers. Top: As-received. Bottom: As integrated into the crosslinked aerogel matrix.*

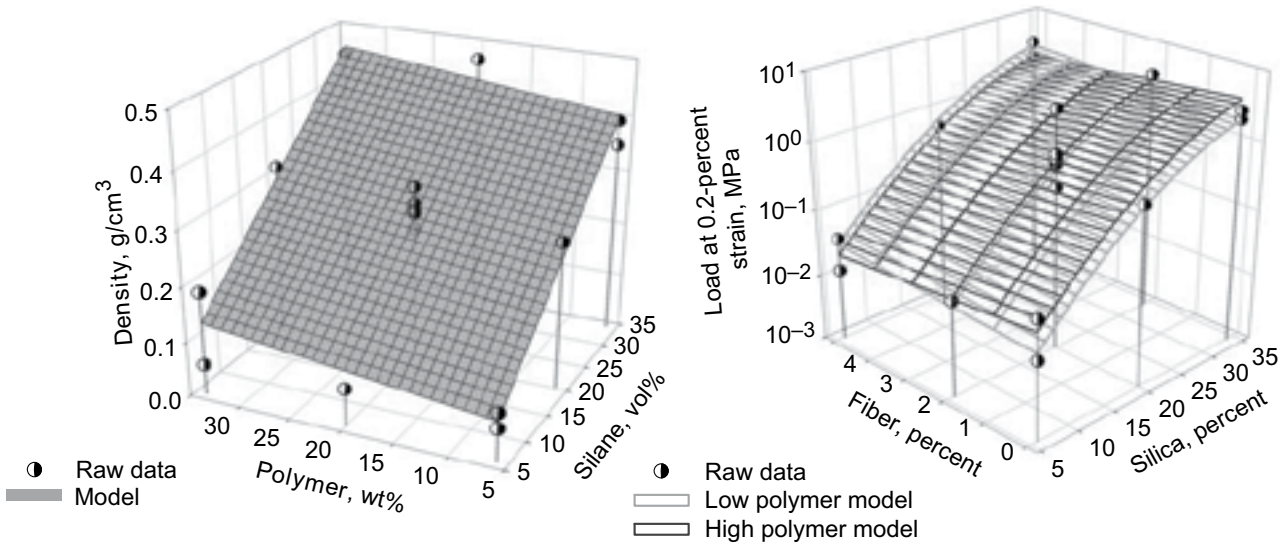


*Response surface models. All raw data points for the 19 samples measured are also displayed on the surfaces. Left: Density. Right: Yield stress for low and high polymer models. There is no clear effect resulting from carbon fiber addition. This figure is shown in color in the online version of this article (http://www.grc.nasa.gov/WWW/RT/2006/RX/RX22P-capadona2.html).*

bottom micrograph on the preceding page shows the successful integration of carbon fiber into the silica-polymer matrix on the nanoscale. Empirical models were derived for several macroscopic properties from data from the 19 samples using multiple linear regression and incorporating only highly statistically significant terms. Interestingly, the response surface model for density shown in the left plot demonstrates that the addition of carbon fiber has no significant effect. In fact, the only drivers for density at the levels studied are total silane and polymer concentrations. The lack of effect on density with fiber addition could be ideal, since properties may be changed without the addition of weight, a premium for most NASA missions.

The effect of carbon fiber incorporation on the mechanical properties of the crosslinked aerogels is still under investigation; however, initial results show that it has little effect on the yield stress. The right plot shows the model for the load at 0.2-percent strain for both the low and high polymer cases, noting that the other significant variables are fiber content (percent) and total silane. The load values through the fiber range studied are very similar. However, before crosslinking, the fiber-containing gels are easier to handle without damaging them, especially at low density, indicating that the materials' green strength is improved by the fiber addition. Further tests of this new material are being developed to accurately capture the perceived improvements. We also plan to look in greater detail at the dispersion of the fibers into the matrix, as this is a common problem with carbon nanotubes (ref. 4) and with nanofibers by extension. This problem often requires purification and functionalization to avoid fiber agglomeration. Other properties being examined are specific compressive strength, Young's modulus, and electrical and thermal conductivities.

**References**

1. Capadona, L.A., et al.: Flexible, Low-Density Polymer Crosslinked Silica Aerogels. Polymer, vol. 47, no. 16, 2006, pp. 5754–5761.
2. Katti, A., et al.: Chemical, Physical, and Mechanical Characterization of Isocyanate Cross-Linked Amine-Modified Silica Aerogels. Chemistry of Materials, vol. 18, no. 2, 2006, pp. 285–296.
3. Meador, Mary Ann B., et al.: Cross-Linking Amine-Modified Silica Aerogels With Epoxies: Mechanically Strong Lightweight Porous Materials. Chem. Mater., vol. 17, no. 5, 2005, pp. 1085–1098.
4. Sun, Y.P., et al.: Functionalized Carbon Nanotubes: Properties and Applications. Acc. Chem. Res., vol. 35, no. 12, 2002, pp. 1096–1104.

**Glenn contacts:**
Dr. Lynn A. Capadona, 216–433–5013, Lynn.A.Capadona@nasa.gov

Dr. Mary Ann B. Meador, 216–433–3221, Maryann.Meador@nasa.gov

**Authors:**
Dr. Lynn A. Capadona,
Dr. Mary Ann B. Meador, and
Stephanie L. Vivod

**Headquarters program office:**
Innovative Partnerships Office

**Programs/projects:**
Glenn Alliance for Technology Exchange

# Mechanical Strength and Physical Properties of Functionalized Graphene-Epoxy Nanocomposites Studied

Expanded graphite has attracted considerable attention as a nanoscale filler in composite materials. This interest stems from a combination of factors including high aspect ratio, nanometer scale, organic compatibility, and low cost. In addition, the conjugated structure of the graphene sheet imparts both thermal and electrical conductivity to the matrix resin.

However, although numerous publications cite improvements in the modulus and electrical conductivity of expanded graphite-filled composites, there are often reports of poor mechanical properties. This primarily results from incomplete exfoliation of expanded graphite in a polymer matrix and, thus, poor dispersion of the filler. Improved results were observed by using graphite that had been oxidized to produce graphite oxide (GO). The GO was then split into individual graphene sheets through a rapid expansion process (ref. 1). Most of the particles were smaller than 1 μm in the lateral dimensions. Because of the presence of residual epoxide and hydroxide sites, this material was referred to as a functionalized graphene sheet (FGS). The FGS used in this study was prepared by researchers at Princeton University.

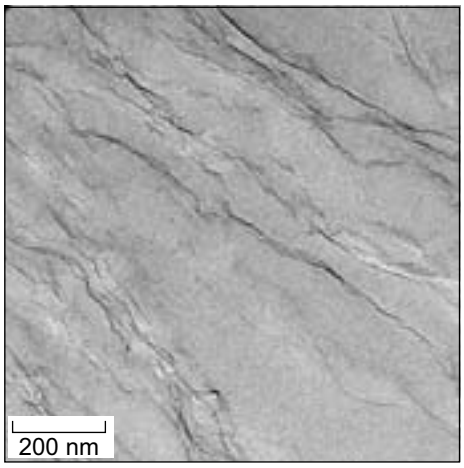


*Transmission electron microscopy image of epoxy composite with 0.50-wt% as-received FGS.*

The FGS dispersed well in an epoxy matrix without the need for additional functionalization, as evidenced by the uniform dispersion displayed in the transmission electron microscopy image. This was attributed to the presence of residual epoxy and hydroxy sites on the graphene sheets.

Despite some of the mechanical property improvements expected by the incorporation of nanoscale fillers, dispersion of a rigid nanoparticle in a resin matrix often reduces the toughness of the system, as has been observed with phyllosilicate-reinforced nanocomposites (ref. 2). The toughness of the FGS-epoxy nanocomposites was measured as the energy required to break the tensile specimens (see the table). This value was calculated by the area under the load displacement curve following tensile tests.

FRACTURE TOUGHNESS OF EPOXY–FGS NANOCOMPOSITES

| FGS sample loading, wt% | Energy to break, N-m | | |
|---|---|---|---|
| | Unmodified FGS | Carbon 18 ($^{18}C$) -modified FGS | 10-percent excess amine in epoxy formulation |
| 0 | 0.875±0.27 | 0.875±0.27 | 0.314±0.11 |
| .10 | .914±0.18 | .724±0.11 | .981±0.02 |
| .25 | .898±0.10 | .725±0.06 | .804±0.11 |
| .50 | 1.000±0.10 | .395±0.19 | 1.015±0.56 |

Nanocomposites prepared with 10-percent excess amine in the epoxy displayed a significant increase in toughness over that of the comparable neat resin, also containing excess amine. This is due to two possible mechanisms: better interfacial bonding and optimized epoxy amine ratios in the composite formulation. Covalent bonding between excess amine and the graphene would strengthen the filler-matrix interface. In addition, without excess amine the surface epoxides on the FGS unbalance the optimum stoichiometry of the epoxy reactions. Addition of excess amines actually contributes to returning the epoxy matrix properties to their optimal values; however, 10-percent excess amine may not be the appropriate amount.

The FGS-reinforced resin nanocomposites displayed up to a 40-percent reduction in the coefficient of thermal expansion. Addition of the rigid particles resulted in restricted polymer chain motion near the particle interface and, therefore, an enhanced dimensional stability (ref. 3).

These results suggest that FGS-epoxy nanocomposites could be suitable materials for use in cryogenic propellant tanks. Reduced resin CTE and improved toughness are desirable for this application since they can help to mitigate thermal-cycling-induced microcracking, which has been a major impediment to the use of composites in cryotanks.

This work was performed by the NASA Glenn Research Center in collaboration with Professors Ilhan Aksay and Robert Prud'homme, as well as Dr. Douglas Adamson at Princeton University, supported from the NASA University Research, Engineering, and Technology Institute on BioInspired Materials (BIMat) under Award No. NCC–1–02037.

**References**

1. Schniepp, Hannes C., et al.: Functionalized Single Graphene Sheets Derived From Splitting Graphite Oxide. J. Phys. Chem. B, vol. 110, no. 17, 2006, pp. 8535–8539.
2. Balakrishnan, S., et al.: The Influence of Clay and Elastomer Concentration on the Morphology and Fracture Energy of Preformed Acrylic Rubber Dispersed Clay Filled Epoxy Nanocomposites. Polymer, vol. 46, issue 25, 2005, pp. 11255–11262.
3. Yasmin, Asma; and Daniel, Isaac M.: Mechanical and Thermal Properties of Graphite Platelet/Epoxy Composites. Polymer, vol. 45, issue 24, 2004, pp. 8211–8219.

**Glenn contact:**
Sandi G. Miller, 216–433–8489, Sandi.G.Miller@nasa.gov

**Princeton contact:**
Dr. Ilhan Aksay, 609–258–4393, iaksay@Princeton.edu

**Authors:**
Sandi G. Miller, Dr. Michael A. Meador, Dr. Ilhan Aksay, and Robert K. Prud'homme

**Headquarters program office:**
Aeronautics Research Mission Directorate

**Programs/projects:**
Subsonics Fixed Wing

## Photo-Oxidation of Single-Walled Carbon Nanotubes Examined

The addition of functional groups to single-wall carbon nanotubes (SWNTs) has been a topic of investigation because it makes the tubes easy to disperse and, in some cases, partially soluble in organic solvents (refs. 1 to 8). Oxygen groups have been observed on the SWNTs after treatment in acidic solutions such as nitric acid, hydrochloric acid, or sulfuric acid (refs. 9 to 12). These reagents are used mainly to remove metal impurities left on the SWNTs after synthesis. Carbon nanotubes are functionalized with oxygen groups during purification, but afterward, most of these functional groups are removed at the last step—heating the tubes to higher than 500 °C. To restore the oxygen groups, the SWNTs must be treated once again with acid, but the continued exposure of SWNTs to acid may affect their properties.

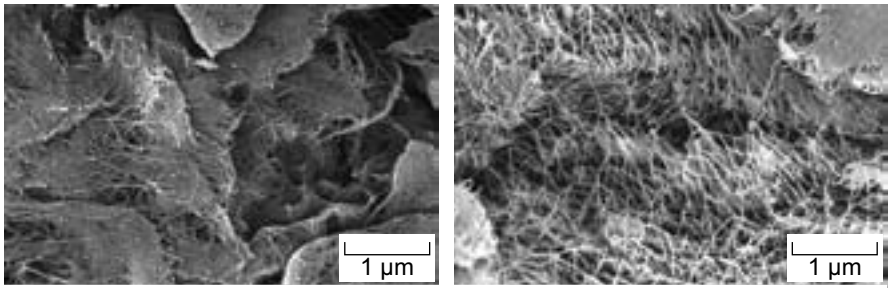


*Scanning electron micrographs of SWNTs. Left: Before photo-oxidation. Right: After photo-oxidation.*

Photo-oxidation is a convenient way to induce the attachment of oxygen groups on the surface of SWNTs. This technique was reported by Savage and others using multiwalled carbon nanotube (MWNT) films. They demonstrated by thermopower measurements that when MWNT films are exposed to ultraviolet light and oxygen at the same time, the tubes oxidize (ref. 13). In the current effort at the NASA Glenn Research Center, SWNTs in an oxygenated solution of dimethylformamide (DMF) were exposed to a

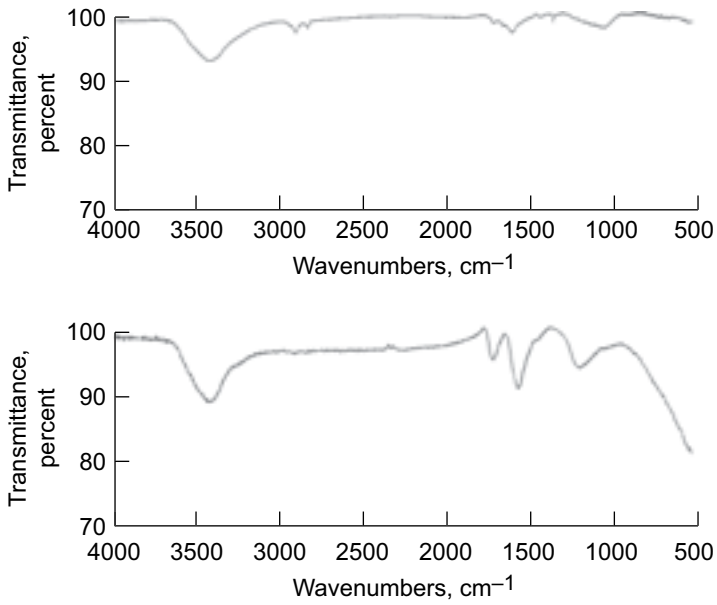


*FTIR spectra of SWNTs. Top: Before photo-oxidation. Bottom: After photo-oxidation.*

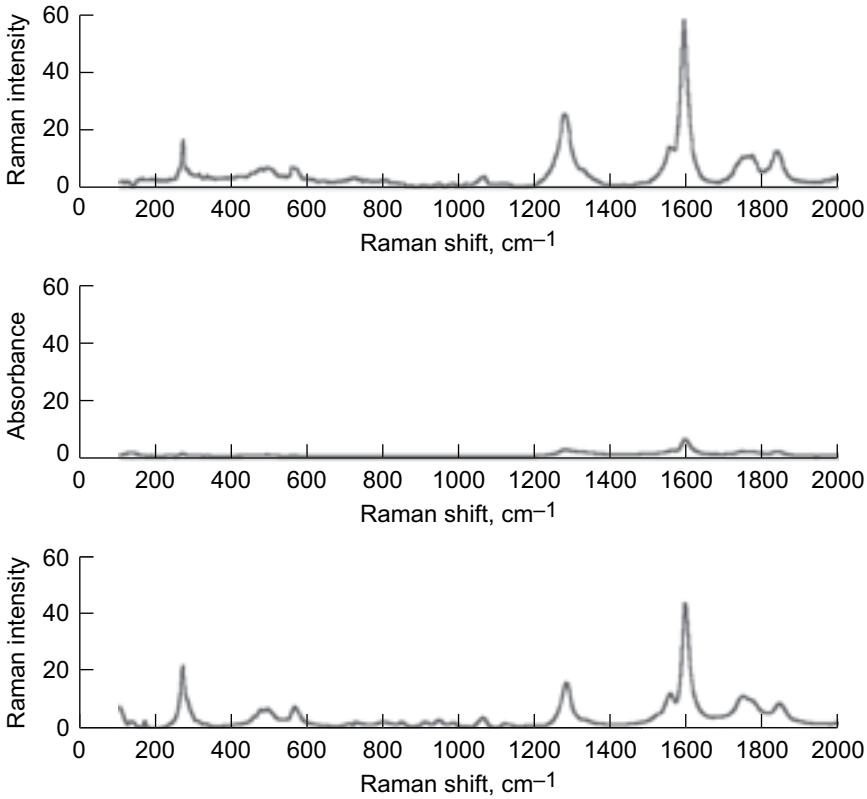


*Raman spectra of SWNTs. Top: Raman intensity before photo-oxidation. Center: Absorbance. Bottom: Raman intensity after photo-oxidation.*

source of ultraviolet light (450 W) overnight. The process involved continuous oxygenation of the DMF solution of the SWNTs. Researchers characterized the SWNTs after the oxygenation. The scanning electron micrographs on the preceding page show the SWNTs before and after photo-oxidation, indicating that the quality of the SWNTs was conserved after treatment.

Analytical characterizations of the SWNTs indicated the presence of oxygen groups. Fourier-transform infrared (FTIR) spectra show the SWNTs before and after photo-oxidation. The dispersion of the SWNTs in polar solvents was enhanced because of the additional oxygen groups on the tubes. The FTIR spectra of the photo-oxidized SWNTs show increases in the bands characteristic of carboxylic, carboxylate, and ester groups.

The oxygen functional groups can be removed from the carbon nanotubes by annealing the tubes. This was confirmed by Raman spectroscopy, where the intensity of the characteristic bands of SWNTs tends to decrease in the presence of oxygen groups. However, the intensity is recovered after the tubes are annealed. This recovery indicates that the functional groups on the tubes are substantially reduced or completely eliminated. This behavior is another essential confirmation of the theoretical studies of Savage et al., suggesting that the mechanism that takes place during the photo-induced oxidation of carbon nanotubes is chemisorption (ref. 13).

Oxygen-functionalized SWNTs can serve as anchor precursors for SWNTs with further functionalization, especially when the reaction needs to be carried out in polar solvent media. By taking advantage of the capacity for carbon nanotubes to be functionalized by photo-oxidation, Glenn researchers have eliminated the use of strong acids and have significantly minimized further damage to the tubes.

**References**


1. Chen, Jian, et al.: Solution Properties of Single-Walled Carbon Nanotubes. SCI, vol. 282, 1998, pp. 95–98.
2. Riggs, Jason E., et al.: Strong Luminescence of Solubilized Carbon Nanotubes. J. Am. Chem. Soc., vol. 122, no. 24, 2000, pp. 5879–5880.
3. Boul, P.J., et al.: Reversible Sidewall Functionalization of Buckytubes. Chem. Phys. Lett., vol. 310, issues 3–4, 1999, pp. 367–372.
4. Bahr, J.L., et al.: Functionalization of Carbon Nanotubes by Electrochemical Reduction of Aryl Diazonium Salts: A Bucky Paper Electrode. J. Am. Chem. Soc., vol. 123, no. 27, 2001, pp. 6536–6542.
5. Bahr, J.L., et al.: Dissolution of Small Diameter Single-Wall Carbon Nanotubes in Organic Solvents? Chem. Commun., vol. 2, 2001, pp. 193–194.
6. Sun, Y.; Wilson, S.R.; and Schuster, D.I.: High Dissolution and Strong Light Emission of Carbon Nanotubes in Aromatic Amine Solvents. J. Am. Chem. Soc., vol. 123, no. 22, 2001, pp. 5348–5349.
7. Georgakilas, V., et al.: Organic Functionalization of Carbon Nanotubes. J. Am. Chem. Soc., vol. 124, no. 5, 2002, pp. 760–761.
8. Bandyopadhyaya, R., et al.: Stabilization of Individual Carbon Nanotubes in Aqueous Solutions. Nano Letters, vol. 2, no. 1, 2002, pp. 25–28.
9. Chiang, I.W., et al.: Purification and Characterization of Single-Wall Carbon Nanotubes. J. Phys. Chem. B, vol. 105, no. 6, 2001, pp. 1157–1161.
10. Chiang, I.W., et al.: Purification and Characterization of Single-Wall Carbon Nanotubes (SWNTs) Obtained From the Gas-Phase Decomposition of CO (HiPco Process). J. Phys. Chem. B, vol. 105, no. 35, 2001, pp. 8297–8301.
11. Bond, A.M.; Miao, W.J.; and Raston, C.L.: Mercury (II) Immobilized on Carbon Nanotubes: Synthesis, Characterization, and Redox Properties. Langmuir, vol. 16, no. 14, 2000, pp. 6004–6012.
12. Hiura, H.; Ebbesen, T.W.; and Tanigaki, K.: Opening and Purification of Carbon Nanotubes in High Yields. Advanced Materials, vol. 7, no. 3, 1995, pp. 275–276.
13. Savage, T., et al.: Photoinduced Oxidation of Carbon Nanotubes. J. Phys. Condens. Matter, vol. 15, no. 35, 2003, pp. 5915–5921.


**Find out more about the research of Glenn's Polymers Branch:**
http://www.grc.nasa.gov/WWW/5000/MaterialsStructures/polymers/


**Glenn contacts:**
Dr. Marisabel Lebron-Colon, 216–433–2292, Marisabel.Lebron-Colon-1@nasa.gov

Dr. Michael A. Meador, 216–433–9518, Michael.A.Meador@nasa.gov

**Authors:**
Dr. Marisabel Lebron-Colon and Dr. Michael A. Meador


**Headquarters program office:**
Aerospace Research Mission Directorate

**Programs/projects:**
Low Emissions Alternative Power Project, Alternate Energy Foundation Technologies

# Boron Nitride Nanotubes Demonstrated as Solid-State Hydrogen Storage Media

Fuel cell systems with accompanying hydrogen storage requirements may be critical for several of NASA's anticipated space missions, such as lunar and Mars bases. Solid-state storage mechanisms offer a greater degree of safety for human-tended missions or even Earth-based consumer products. Nanotubes based on graphene sheets (carbon nanotubes, CNTs, and boron nitride nanotubes, BNNTs) are attractive as hydrogen storage materials because of their low weight, potential for high degree of hydrogen adsorption, and high strength. In-house research funded by NASA Glenn Research Center's Independent Research and Development program was aimed at developing hydrogen storage systems based on BNNTs. Hydrogen sorption characteristics were evaluated by thermogravimetric analysis techniques. Results indicated that, even in an unrefined state, BNNT demonstrated hydrogen sorption similar to that for other promising solid-state storage candidates of about 3 wt%. However, these results were obtained for much more reasonable pressure-temperature combinations than for many other competing systems.

Adsorption results (shown in this graph) with as-produced BNNT and CNT materials indicate nearly 3.0 mass% for BNNT versus 1.0 mass% for CNT. Although not fully optimized or even cleaned of catalyst material and debris, the hydrogen mass adsorbed for mixed-phase BNNT was similar to that found for lithium borohydride ($LiBH_4$), a promising current candidate for hydrogen storage. The complex metal hydride class of materials required high operating temperatures and pressures to perform similarly. Commercial solid-state hydrogen storage units utilizing nickel hydrides also operate in this adsorption range but have problems with reversibility. Finally, the BNNT hydrogen uptake was fully reversible, an important consideration for storage. The CNT material was not fully reversible.

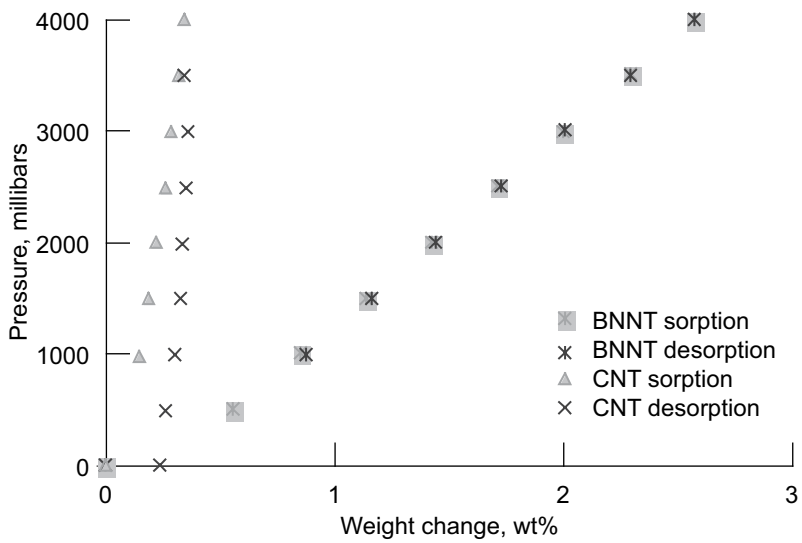


*Hydrogen sorption data for BNNT and CNT at 20 °C.*

Desorption began at only 70 °C, barely warm water temperatures, and continued more rapidly with increasing temperature to 500 °C. These are very modest temperatures in comparison with those of complex metal hydrides, which must adsorb hydrogen at cryogenic temperatures and desorb at temperatures in excess of 700 °C. For the case of BNNT, desorption rates can be "tuned" for a variable draw rate by altering desorption temperatures. In addition, adsorption in BNNT could be accomplished at room temperatures rather than requiring cryogenic temperatures. Finally, it was noted that hexagonal BN did not adsorb hydrogen. Significantly, 50 vol% of the starting material examined in the Higen unit was hexagonal BN by volume. The remaining 50 vol% was BNNT, which did adsorb hydrogen. Because BNNT has only one-half the density of hexagonal BN, BNNT was actually a minority phase by weight and yet the material performed equal to the state-of-the-art commercial product. This suggests that significant improvements in hydrogen adsorption are possible through a combination of improving the purity of the BNNT product and extending the temperature range into cryogenic temperatures.

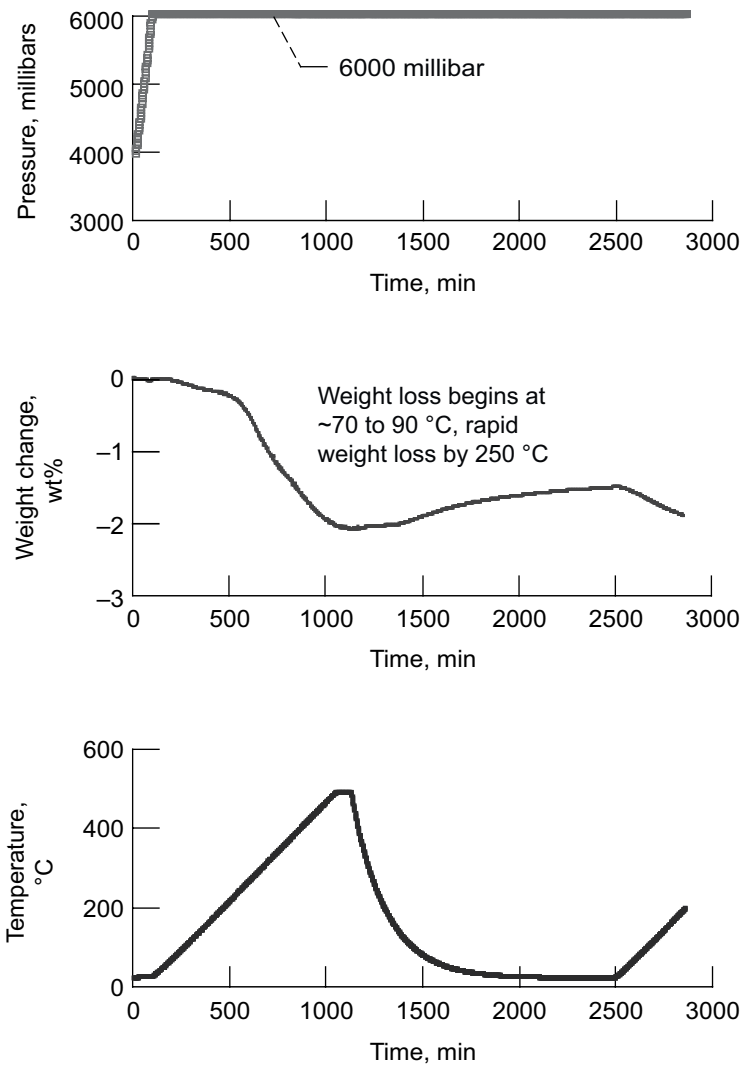


*Hydrogen desorption data for BNNT.*

**Glenn contact:**
Janet B. Hurst, 216–433–3286, Janet.B.Hurst@nasa.gov

**Author:**
Janet B. Hurst

**Programs/projects:**
Independent Research and Development

# Water Electrolysis and Regenerative Tests Conducted on NASA Glenn Solid Oxide Cell Demonstrated High Efficiency

Because of their high energy efficiency, solid oxide fuel cells (SOFCs) are expected to impact both terrestrial and aerospace industries. NASA has recently been investigating reversible SOFCs or regenerative fuel cells (RFCs) for their many applications, including UAVs and for water electrolysis for lunar missions.

RFCs can operate over temperatures from 600 to 1000 °C. Higher temperatures favor regenerative operation, requiring less energy to perform electrolysis, resulting in higher electrochemical efficiency. Most SOFC designs use a metal plate with gas channels to connect the ceramic cells in series. The metal/ceramic bond makes them difficult to seal, and the metal limits operation to lower temperatures. This prevents conventional SOFCs from meeting NASA's challenging specific power density (kilowatts per kilogram) requirements.

To achieve a fourfold to fivefold increase in specific power density of 1.0 kW/kg, the NASA Glenn Research Center developed a novel cell design by adapting a special ceramic fabrication technique. The Glenn design, called a bielectrode supported cell (BSC), see the illustration, has low volume and low weight. The metal interconnects are removed, replaced by a thin ceramic interconnect, and gas flow channels are incorporated into the yttria-stabilized zirconia (YSZ) electrode supports. The use of all ceramic materials enables operation at high temperatures and makes hermetic ceramic-to-ceramic seals possible.

The BSC fuel cell design is particularly suited to regenerative (reversible) operation. The photomicrograph shows a "unitized" block of cells fabricated with a single firing step. The graph on the next page shows regenerative test results for a single BSC cell with excellent efficiency. The cell was operated from 0.4 to 1.0 V in fuel cell (FC) mode and then from 1.0 to 1.6 V in electrolysis (EL) mode. A smooth transition from FC mode on the right side (positive current density) to the EL mode on the left (negative current density) is evident. The cell was tested with three levels of $H_2O$ in the hydrogen ($H_2$) feed gas: 11, 25, and 50 vol%. The voltage increases sharply and current is limited at 11 and 25 vol% $H_2O$ because the cell has consumed the available $H_2O$ and it is starved. The regenerative efficiency is the ratio of the power generated in fuel cell mode to the power required to perform electrolysis ($P_{FC}/P_{EL}$). The majority of the testing was performed at 850 °C to compare Glenn's data with data in the literature at similar conditions. Recently published data report efficiencies from 83 to 85 percent (refs. 1 and 2), comparable to but lower than Glenn's efficiencies of 89 to 93 percent.

RFCs are being considered for immediate applications to extend the missions of UAVs from 2 to 3 days to 90 days. Using a single tank of water, they would operate in EL mode using solar power during the day and operate in FC mode during the night.

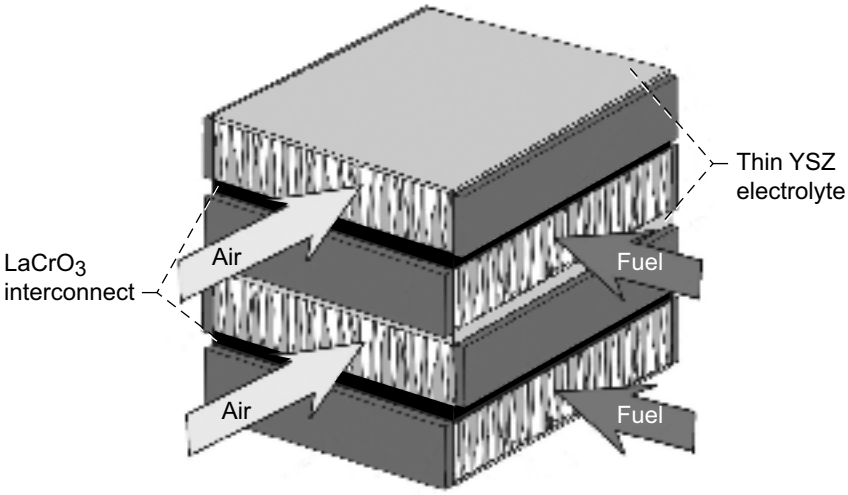


*BSC cross-flow stack. $LaCrO_3$, lanthanum chromite. This figure is shown in color in the online version of this article (http://www.grc.nasa.gov/WWW/RT/2006/RX/RX26C-cable.html).*

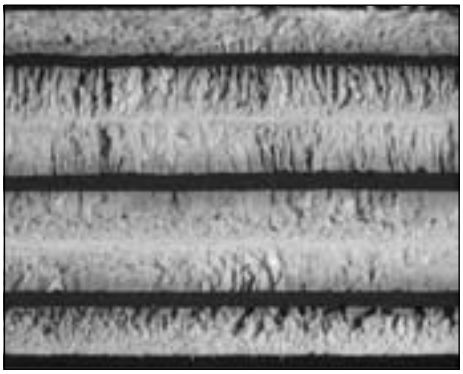

*Multilayer, unitized BSC stack of two complete repeat units. The gray layers are the YSZ cells with the thin, lighter colored electrolyte in the center; the $LaCrO_3$ interconnect layers are black. This figure is shown in color in the online version of this article (http://www.grc.nasa.gov/WWW/RT/2006/RX/RX26C-cable.html).*

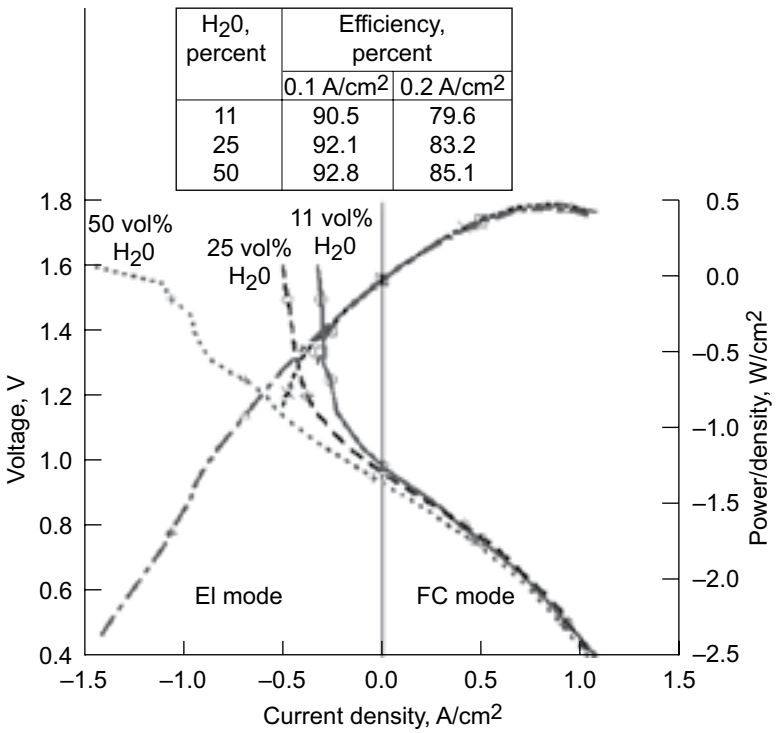


| $H_20$, percent | Efficiency, percent | |
|---|---|---|
| | 0.1 A/cm$^2$ | 0.2 A/cm$^2$ |
| 11 | 90.5 | 79.6 |
| 25 | 92.1 | 83.2 |
| 50 | 92.8 | 85.1 |

*BSC performance in EL mode. Voltage increases sharply and current density is limited at 11 and 25 vol% $H_2O$, indicating $H_2O$ starvation.*

**References**

1. Hickey, Darren, et al.: Optimization and Demonstration of a Solid Oxide Regenerative Fuel Cell System. PESOD, vol. PV 2005–07, 2005, pp. 285–294.
2. Herring, J., et al.: Hydrogen Production Through High-Temperature Electrolysis in a Solid Oxide Cell. The Second Information Exchange Meeting on Nuclear Production of Hydrogen, Argonne National Laboratory, Argonne, IL, 2004, pp. 183–200.

**University of Toledo contact:**
Dr. Thomas L. Cable, 216–433–5897, Thomas.L.Cable@nasa.gov

**Glenn contact:**
Dr. Serene C. Farmer, 216–433–3289, Serene.C.Farmer@nasa.gov

**Authors:**
Dr. Thomas Cable, John A. Setlock, and Dr. Serene Farmer

**Headquarters program office:**
Fundamental Aeronautics

**Programs/projects:**
Subsonic Fixed Wing

## Protonic-Conducting Ceramic Films Fabricated Using Pulsed Laser Deposition

Achieving high protonic conductivity with thermodynamic stability is considered to be a key problem for high-temperature protonic-conducting (HTPC) materials for electrochemical applications. Applications include fuel cells, gas sensors, gas purification systems, and steam electrolyzers that will provide economic and ecological benefits. HTPC materials for hydrogen separation at high temperatures are $A^{2+}B^{4+}O_3^{2-}$ materials that have the Perovskite structure. A trivalent cation ($M^{3+}$) substitution is needed at the $B^{4+}$ site to introduce oxygen vacancies to promote proton transport. An example of such a material is $BaCe_{0.85}Y_{0.15}O_3$.[1] There are considerable technological challenges related to the processing of HTPC materials. The high melting point and multi-cation chemistry of HTPC ceramics create difficulties in material processing. The presence of secondary phases and grain-boundary interfaces are detrimental to the protonic conduction and environmental stability of polycrystalline HTPC materials.

The hydrogen permeation rate for HTPC materials is inversely proportional to membrane thickness. Thus, reducing HTPC membrane thickness is a practical way to enhance the hydrogen permeation rate or reduce the operating temperature. For the fabrication of thin HTPC membranes (≥25-μm-thick), the membranes have to be supported with porous structures that provide mechanical strength. Successful fabrication of inexpensive membranes by solid-state sintering methods is hindered by processing temperatures, exceeding 1500 °C, which cause a reaction

[1]Ba, barium; Ce, cesium (0.85 percent); Y, yttrium (0.15 mol%); O, oxygen.

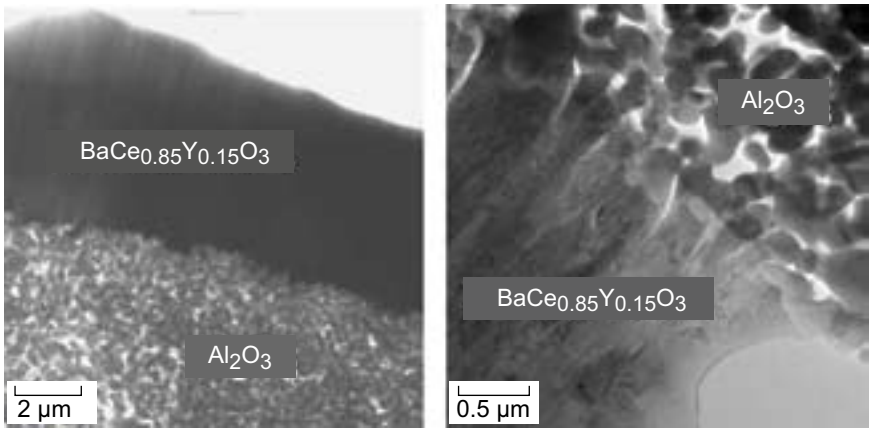


*Microstructure of $BaCe_{0.85}Y_{0.15}O_3$ film deposited at 800 °C on porous $Al_2O_3$ substrate.*

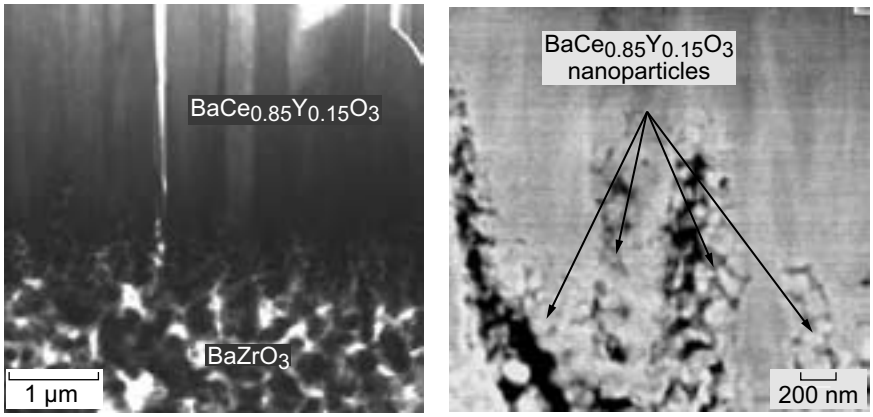


*Microstructure of $BaCe_{0.85}Y_{0.15}O_3$ film deposited at 600 °C on porous $BaZrO_3$ substrate.*

between the substrate and HTPC membrane. This study at the NASA Glenn Research Center investigated the feasibility of using pulsed laser deposition (PLD) to deposit thin films of HTPC material on porous substrates.

Thin films of $BaCe_{0.85}Y_{0.15}O_3$ were deposited onto porous alumina ($Al_2O_3$) and barium zirconate ($BaZrO_3$) substrates at temperatures of 600 to 1000 °C, as shown in the transmission electron micrographs. The transmission electron microscopy (TEM) reveals oriented nanocrystalline films with columnar growth morphology. Results show that physical vapor deposition can be used to fabricate dense films at low temperatures. Dense films are formed by the impingement of growing columnar $BaCe_{0.85}Y_{0.15}O_3$ grains. Results show direct nucleation and growth of $BaCe_{0.85}Y_{0.15}O_3$ on $Al_2O_3$ particles. Expected epitaxial growth between $BaCe_{0.85}Y_{0.15}O_3$ and $BaZrO_3$ did not occur. The columnar $BaCe_{0.85}Y_{0.15}O_3$ grains originate from nucleated $BaCe_{0.85}Y_{0.15}O_3$ nanoparticles; $BaCe_{0.85}Y_{0.15}O_3$ nanoparticles coated the $BaZrO_3$ particles. Because of crystal symmetry mismatch, $BaCe_{0.85}Y_{0.15}O_3$ films grown on $Al_2O_3$ substrate exhibit a high concentration of growth defects that affect protonic conduction.

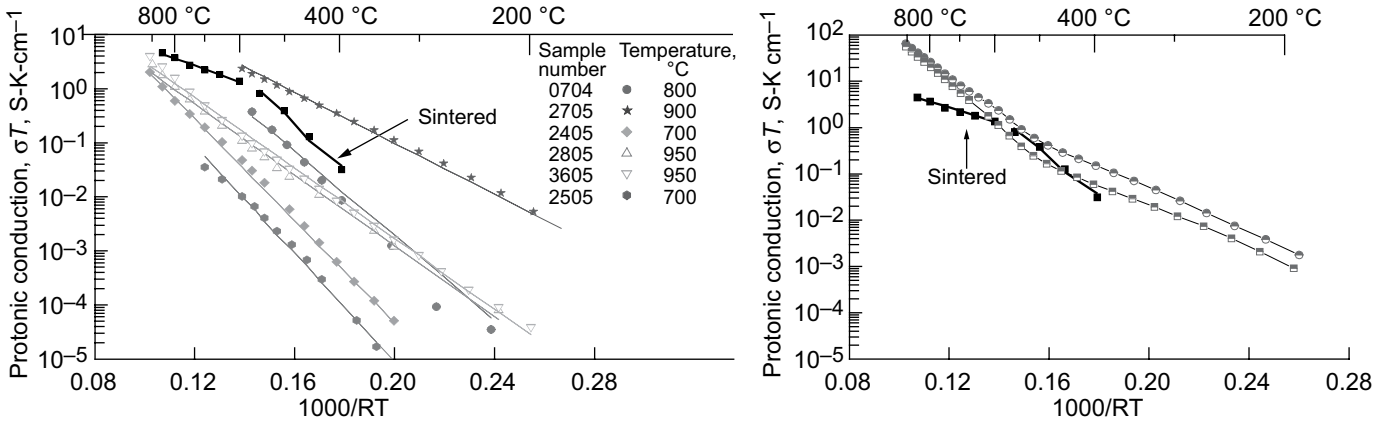


*Arrhenius plots of protonic conduction for $BaCe_{0.85}Y_{0.15}O_3$ films deposited at different temperatures on $Al_2O_3$ and $BaZrO_3$ substrates.*

Protonic conduction for both substrates was measured parallel to the substrate surface by impedance spectroscopy: protonic conductivity of a sintered 2-mm-thick $BaCe_{0.85}Y_{0.15}O_3$ specimen was used as a reference sample (see the Arrhenius plots on the preceding page). $BaCe_{0.85}Y_{0.15}O_3$ films fabricated on $BaZrO_3$ exhibit a high protonic conductance that is greater than the reference sample and exhibit a small dependence on processing conditions. In contrast, $BaCe_{0.85}Y_{0.15}O_3$ films fabricated on $Al_2O_3$ have a large dependence on processing conditions and exhibit protonic conduction that is generally less than in the reference sample. Matching the crystal symmetry between the substrate and film is important for achieving high conducting films.

Low-temperature fabrication of thin-film HTPC membranes on porous substrates can be achieved by physical vapor deposition. Crystal symmetry between the film and substrate is important in achieving highly protonic conducting films.

**Find out more about Glenn's ceramics research:**
http://www.grc.nasa.gov/WWW/5000/MaterialsStructures/ceramics/

**Glenn contacts:**
Dr. Frederick W. Dynys, 216–433–2404, Frederick.W.Dynys@nasa.gov

Dr. Ali Sayir, 216–433–6254, Ali.Sayir-1@nasa,gov

**Authors:**
Dr. Frederick W. Dynys and Dr. Ali Sayir

**Headquarters program office:**
Independent Research and Development

**Programs/projects:**
Space Power

## Novel Polymers Synthesized for High-Temperature Use in Proton Exchange Membrane Fuel Cells

Proton exchange membrane (PEM) fuel cells have been the focus of considerable research to find efficient low-emission power-generation devices for stationary uninterruptible power sources, residential power, portable devices, and alternatives to internal combustion engines. Furthermore, NASA has an interest in fuel cells for space exploration, space suits, and unmanned air vehicles. The current state-of-the-art membranes used in fuel cells are perfluorinated sulfonic acid membranes, such as Nafion, made by DuPont. Nafion shows excellent thermal and mechanical stability, as well as high proton conductivity when hydrated. The good low-temperature proton conductivity of Nafion is believed to be due to phase separation between the hydrophobic perfluorinated backbone and the hydrophilic sulfonic acid groups, with protons being carried by water between the hydrophilic regions. The hydrated sulfonic acid aggregates form channels through which water carries protons. However, Nafion membranes become much less conductive above 80 °C because the membrane is dehydrated.

It would be advantageous to operate PEM fuel cells at temperatures above 100 °C for several reasons, such as enhancement of electrode reaction kinetics, higher tolerance toward carbon monoxide poisoning of the catalyst, reduced electrode flooding, and greater system efficiency. However, at these higher temperatures the fuel cell would have to be operated under high pressure, or water would have to be replaced with a less volatile proton carrier. Protic ionic liquids (ILs) are one potential replacement for water in fuel cell membranes. ILs are nonvolatile and nonflammable, making them an ideal candidate for use in high-temperature operations.

The NASA Glenn Research Center recently synthesized a series of polymers that contain rigid sulfonated aromatic backbones that are crosslinked with diamine-terminated poly(ethylene oxide) (PEO) oligomers as potential host materials for IL-doped membranes. The purpose of the aromatic backbone is to provide mechanical strength to the polymer film, which is further reinforced by crosslinking. The PEO oligomers enable the film to swell in the presence of solvent to aid the IL imbibing

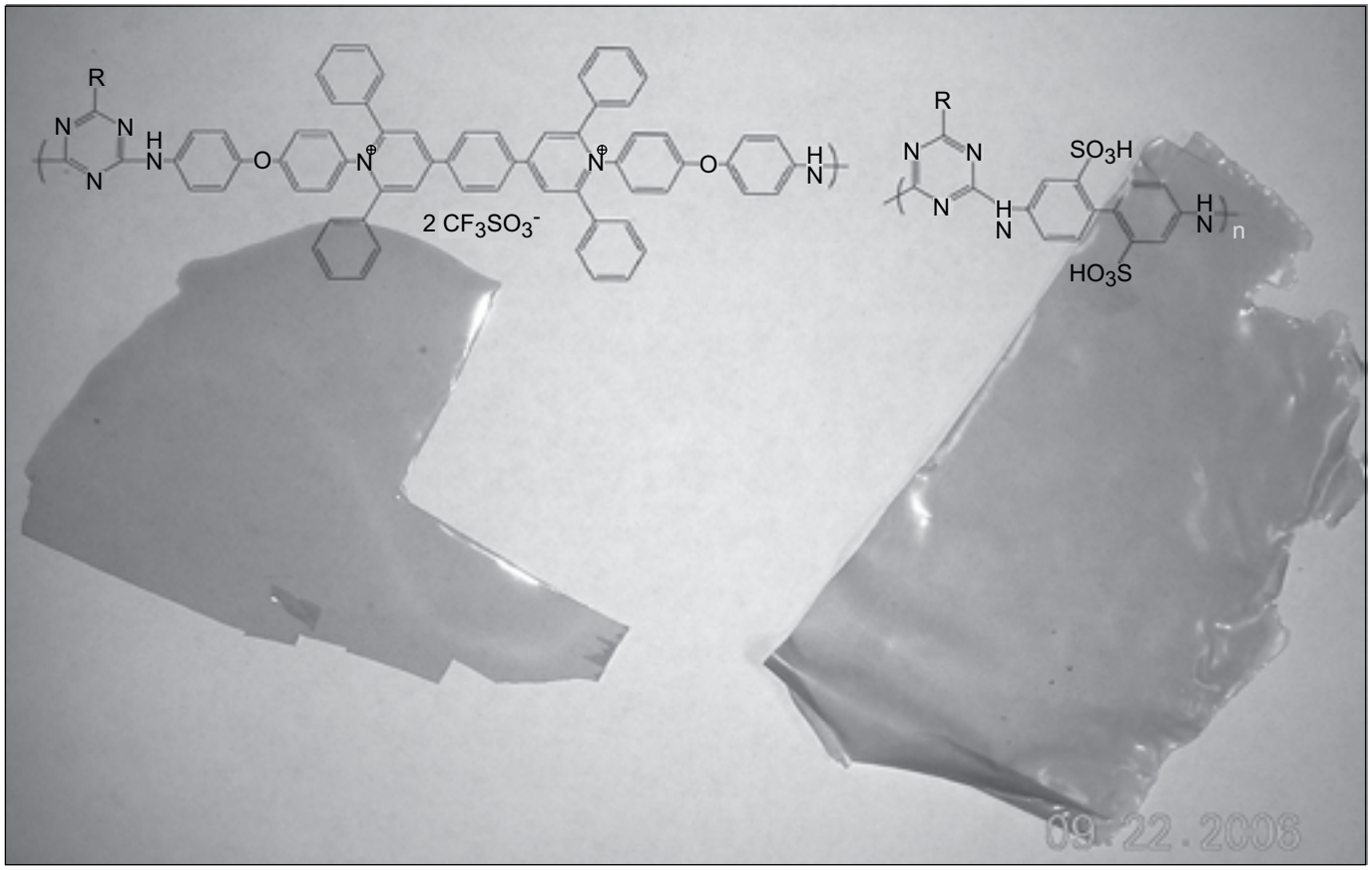


*Polymer films made from hydrophobic (left) and hydrophilic (right) monomers.*

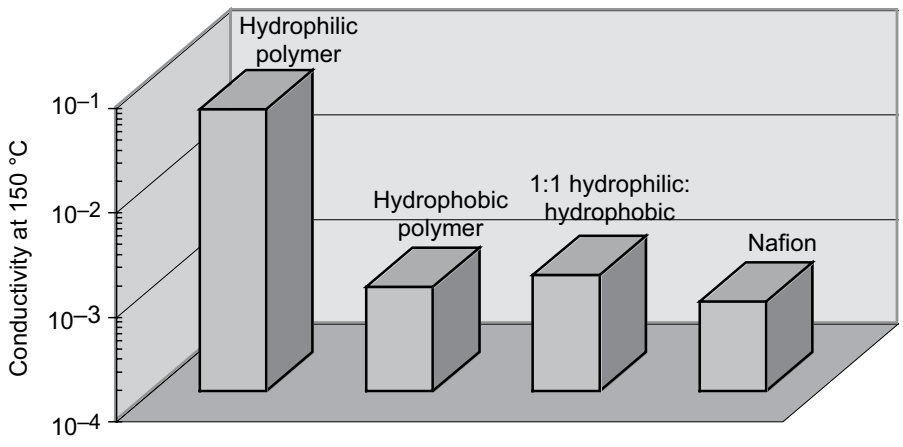


*Conductivity at 150 °C for various polymer films imbibed with ILs.*

process. The volatile solvent can then be removed so that the film can shrink and trap the IL. In addition, to better suit humidified conditions, researchers from Glenn and the Ohio Aerospace Institute (OAI) designed a hydrophobic aromatic polymer backbone with a high affinity for ILs. Poly(pyridinium triflate)s were chosen for this purpose since, like imidazolium-based ionic liquids, the polymer contains charged heterocyclic rings with perfluorinated sulfonate counterions. The photograph shows films made from these polymers.

This bar chart shows that, when imbibed with IL, the hydrophilic polymer has a conductivity almost two orders of magnitude higher than that of Nafion imbibed with the same IL at 150 °C. When the hydrophilic unit was replaced with a hydrophobic one, the water uptake decreased from 187 to 10 percent, while the conductivity was still higher than that of Nafion at 150 °C.

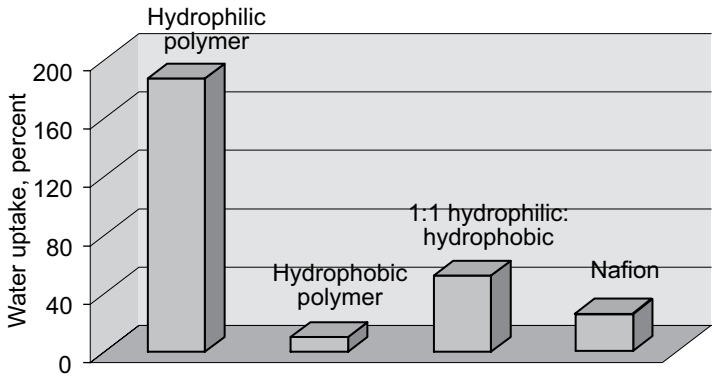


*Water uptake of various polymer films made for this study.*

**Find out more about the research of Glenn's Polymers Branch:**
http://www.grc.nasa.gov/WWW/5000/MaterialsStructures/polymers/

**Ohio Aerospace Institute (OAI) contact:**
Dr. Dean M. Tigelaar, 216–433–3667, Dean.M.Tigelaar@nasa.gov

**Author:**
Dr. Dean M. Tigelaar

**Headquarters program office:**
Aeronautics Mission Research Directorate

**Programs/projects:**
Subsonics Fixed Wing

**Bibliography**
Tigelaar, Dean M., et al.: Study of the Incorporation of Protic Ionic Liquids Into Hydrophilic and Hydrophobic Rigid-Rod Elastomeric Polymers. Polymer, vol. 47, no. 12, 2006, pp. 4269–4275.

# Novel Polymer Membranes Synthesized for Lithium Batteries Doped With Ionic Liquids

Rechargeable lithium-polymer batteries offer several advantages over their liquid and gel electrolyte counterparts, particularly in terms of safety. Typical lithium ion batteries contain volatile and flammable solvents in the conducting medium. A short circuit can cause localized heating that can create a fire. This is a particular concern for batteries that are used for human-rated space applications. One way to avoid this problem is to replace the liquid with a solid polymer that can conduct lithium ions. The polymer used most often is poly(ethylene oxide) (PEO). The use of PEO would also be advantageous because lithium metal anodes could be used instead of the normally used graphite intercalation anodes, increasing the potential power density. Unfortunately, PEO and its derivatives have yet to reach a lithium ion conductivity sufficient for practical use. Polymer electrolytes appear to have reached an upper conductivity limit[1] of $10^{-4}$ S/cm, but at least $10^{-3}$ S/cm is needed. Furthermore, PEO has poor mechanical properties at higher operating temperatures.

The NASA Glenn Research Center had previously synthesized a series of hyperbranched polymer electrolytes that contain PEO-based oligomers that were connected via a triazine linkage. The polymers were crosslinked via a sol-gel technique to improve their dimensional stability. When doped with lithium salts, these polymers were strong, flexible, thermally and mechanically stable up to high temperatures, and completely amorphous over the required temperature range. These polymers have room-temperature conductivities up to $4\times10^{-5}$ S/cm, which is still too low for practical

[1]Limit of $10^{-4}$ siemens per container.

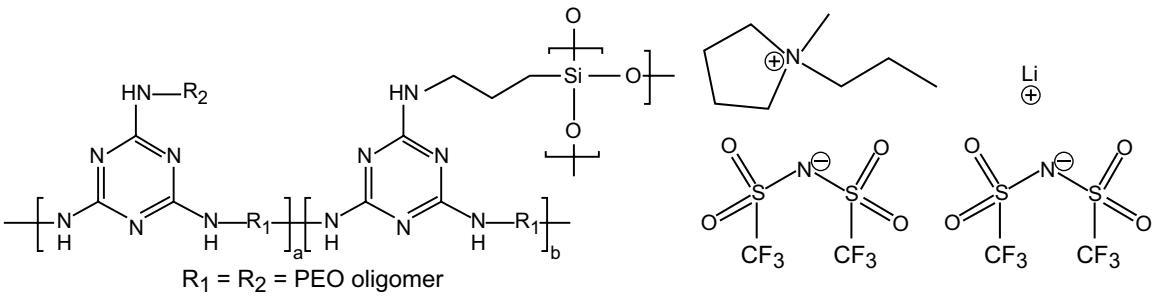


*Chemical structure of the polymer, IL, and lithium salt that make the polymer electrolyte.*

use. Recently, researchers from Glenn and the Ohio Aerospace Institute (OAI) greatly increased the conductivity by adding room-temperature ionic liquids (ILs). ILs are made from an asymmetric organic cation and a bulky anion with a highly delocalized charge to minimize packing. ILs are both nonvolatile and nonflammable, thereby maintaining the safety advantages of the solid polymer electrolyte while adding a conductive liquid component.

The addition of only 30 wt% IL increased the conductivity by over an order of magnitude. Conductivity further increased as more IL was added. The hyperbranched polymer films are now capable of holding over 150 wt% IL, with the highest conductivity being $8.8\times10^{-4}$ S/cm at ambient temperatures. Furthermore, these films maintain their mechanical properties even at such high IL loadings.

**Find out more about the research of Glenn's Polymers Branch:**
http://www.grc.nasa.gov/WWW/5000/MaterialsStructures/polymers/

**Glenn contact:**
Dr. Mary Ann Meador, 216–433–3221, Maryann.Meador-1@nasa.gov

**Ohio Aerospace Institute (OAI) contact:**
Dr. Dean M. Tigelaar, 216–433–3667, Dean.M.Tigelaar@nasa.gov

**Authors:**
Dr. Dean M. Tigelaar, Dr. Mary Ann B. Meador, and William R. Bennett

**Headquarters program office:**
Exploration Systems Mission Directorate

**Programs/projects:**
Advanced Battery Program

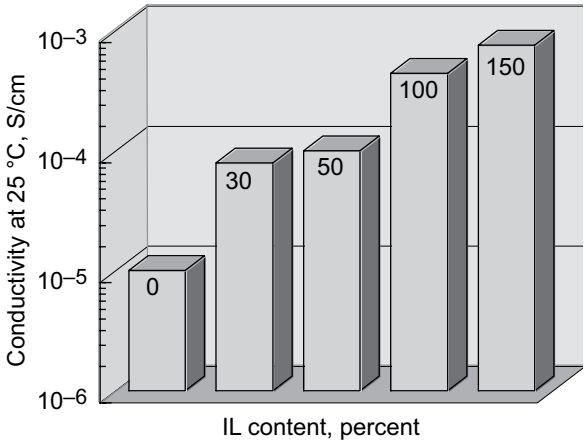


*Room-temperature conductivity of several polymer electrolytes as a function of IL content.*

# High-Temperature Regenerator Developed and Demonstrated for a High-Temperature Stirling Convertor

The Department of Energy (DOE) and NASA have identified Stirling Radioisotope Generators (SRGs) as a candidate power system for use on long-duration, deep-space science missions and Mars rovers (ref. 1). One development planned for an upgraded SRG (known as the ASRG) is to increase efficiency by increasing the overall operating temperature of the system. However, increasing the operating temperature of the convertor puts increased demands on all hot-end parts, including the regenerator. To meet these needs, researchers at the NASA Glenn Research Center developed and demonstrated a high-temperature regenerator.

*Fecralloy (UKEA) regenerator developed for the Advanced Stirling Convertor Program.*

The regenerator consists of a sintered compact of very fine random fibers that form a structure which is approximately 90-vol% porous. The purpose of the regenerator is to increase the efficiency of the convertor by storing and releasing thermal energy to the working gas during the Stirling cycle. Two problems have historically plagued sintered-fiber-type regenerators: surface contamination and fiber shedding. Any compromise of the surface (by oxidation for example) degrades the performance of the regenerator. The other major failure mode is from release of the fibers into the convertor. These fibers can shed for a number of reasons, but the primary cause is from improper processing. The release of fibers can be catastrophic if they find their way into one of the many tight clearances between the moving parts of the convertor.

Historically, the regenerator has been fabricated from stainless steel. Shedding has always been an issue with the sintered fiber design, but surface degradation was of secondary concern because of the relatively low temperatures (650 °C or lower). However, with the higher temperatures used in the advanced Stirling designs, both shedding and oxidation have become serious concerns.

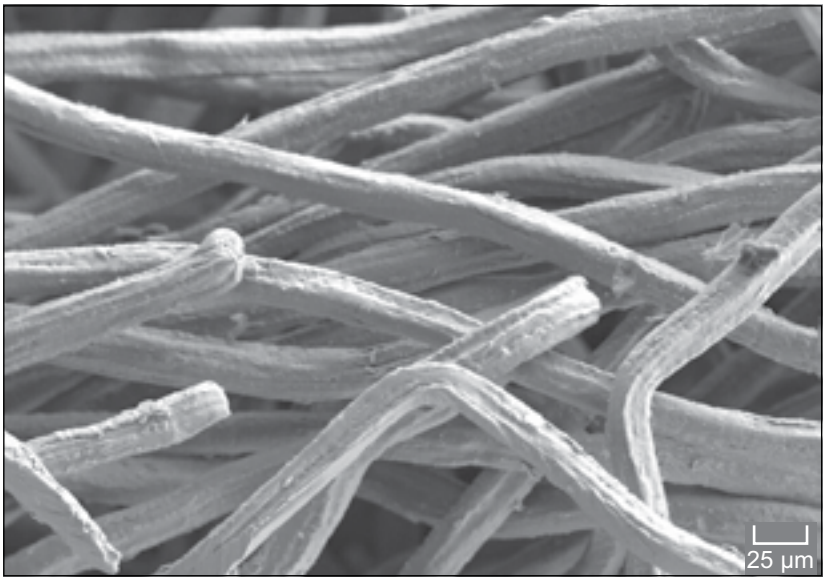


*Micrograph showing the fiber structure of the regenerator.*

An extensive examination of Stirling convertors that had been in operation for extended periods of time revealed that oxidation had indeed occurred. A material selection program identified Fecralloy as an alternative regenerator material. Stainless steel regenerators are consumed in just a few hundred hours at 850 °C, but Fecralloy regenerators show a stable structure even after 5000 hr.

A comprehensive process development study also was performed, with the primary goal of producing a regenerator with increased resistance to fiber shedding. The processing method that was eventually developed included both optimized thermomechanical processing as well as postmachining cleaning methods to remove any liberated fibers. In the end, the new material and techniques have all but eliminated the fiber-shedding problem that plagued past designs of both stainless and Fecralloy regenerators.

Success of this program was confirmed by the adoption of these regenerators by members of the industry team, which included the Department of Energy, Lockheed Martin, Rocketdyne, and Sunpower Inc. To date, Glenn has supplied over 50 regenerators to the advanced Stirling development effort. The regenerator design and fabrication procedure have proven to be so successful that Sunpower has decided to incorporate them into their commercial systems. Glenn recently hosted representatives of Sunpower for a 2-day training course. Glenn continues to provide technical support to Sunpower as they develop in-house capabilities to produce these regenerators and incorporate them into both present and future Government and commercial applications.

**Reference**


1. Thieme, Lanny G.; and Schreiber, Jeffrey G.: Advanced Technology Development for Stirling Convertors. Space Technology and Applications International Forum—STAIF 2004, Mohamed S. El-Genk, ed., AIP Conf. Proc., vol. 699, 2004, pp. 432–439.


**Find out more about this research:**

**Glenn's Advanced Metallics Branch:**
http://www.grc.nasa.gov/WWW/AdvMet/webpage/

**Glenn's Thermal Energy Conversion Branch:**
http://www.grc.nasa.gov/WWW/tmsb/

**Glenn's Power & Propulsion Office:**
http://space-power.grc.nasa.gov/ppo/


**Glenn contact:**
Dr. Randy R. Bowman, 216–433–3205, Randy.R.Bowman@nasa.gov

**Author:**
Dr. Randy R. Bowman


**Headquarters program office:**
Science Mission Directorate

**Programs/projects:**
Radioisotope Power System Project

## Structural Benchmark Testing Completed for 110-W Stirling Radioisotope Generator Heater Head Life Prediction

A year-long final phase of structural benchmark testing was completed at the NASA Glenn Research Center for a critical component of the 110-W Stirling Radioisotope Generator (SRG110). Durability testing of this heater head concluded for two test articles under prototypical environmental conditions: Glenn's special-purpose test rigs subjected the specimens to design operating temperatures and pressure. Under these conditions, creep deformation was the primary life-limiting damage mechanism. The experimental data supported the development of an analytical life-prediction methodology (ref. 1).

The SRG110 was developed to provide electric power for multimission uses, including possible future long-duration deep-space missions, Mars rovers, or lunar applications (refs. 2 and 3). For these applications, the heater head component must endure high temperature at low stress for a long time. It is designed to minimize the effects of material creep—a gradual increase over time in the pressure vessel diameter that could result in reduced system performance if the heater head is not properly designed.

Because the heater head is subjected to a biaxial stress state, Glenn researchers developed a benchmark test setup (see the top photograph on the next page) to experimentally evaluate the response to this specific stress condition. The final test phase was performed at prototypical stresses and temperatures, and the high scatter of very small magnitude creep strains was integrated over time to produce high-quality averaged creep strains and rates. For the two test articles, results showed median creep behavior at or near the predictions based on extrapolation of earlier uniaxial creep tests on the Inconel 718 material of construction. However, unexpected moderate to high anisotropy in creep rates was measured around the circumference of the test article gauge area. This observation is the subject for future investigation.

The heater head test rigs are located at the Mechanics and Life Prediction Branch's Structural Benchmark Test Facility. The test stand (see the bottom photograph) includes two independently operated test rigs with argon pressurization systems, induction power supplies, and a data-acquisition and control system to safely conduct tests and record results.

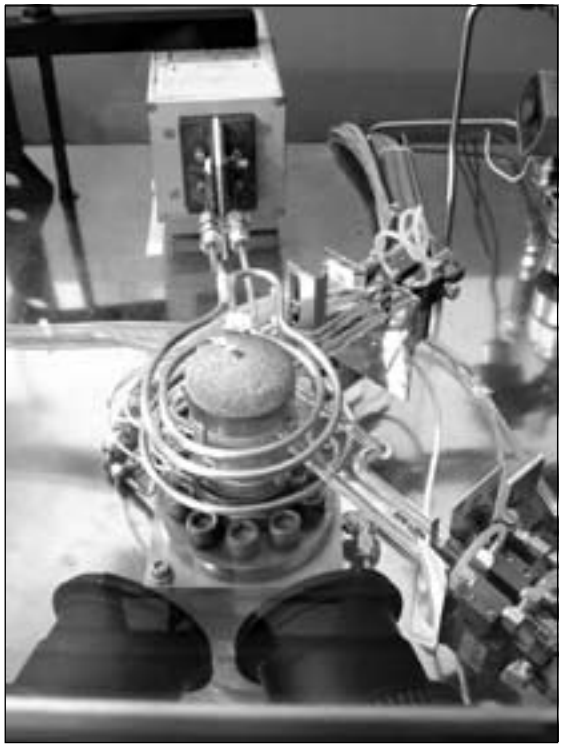

*A 12-month test of a heater head test article at 650 °C (1200 °F); the induction heater and diametral extensometers are visible.*

The benchmark testing was performed in collaboration with Glenn's Thermal Energy Conversion Branch as part of a Glenn in-house project supporting the development of the SRG110. NASA's Science Mission Directorate provided funding for this effort. The overall SRG110 project was managed by the Department of Energy. Lockheed Martin and Infinia Corporation developed the SRG110 for the Department of Energy. Glenn provided supporting technology development for the SRG110, independent verification and validation testing, and advanced technology efforts.

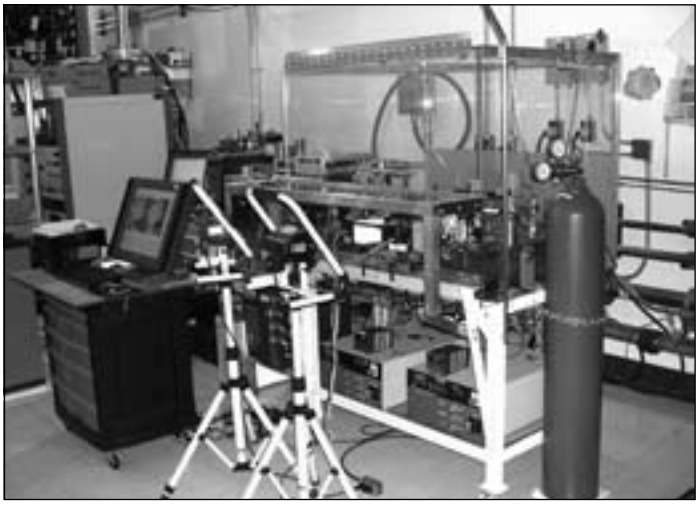

*The heater head structural benchmark test stand includes two independent test rigs on one bench.*

**References**


1. Halford, Gary R., et al.: Structural Analyses of Stirling Power Convertor Heater Head for Long-Term Reliability, Durability, and Performance. NASA/TM—2002-211327, 2002. http://gltrs.grc.nasa.gov/cgi-bin/GLTRS/browse.pl?2002/TM-2002-211327.html
2. Schreiber, J.: Developmental Considerations on the Free-Piston Stirling Power Convertor for Use in Space. AIAA–2006–4015, 2006.
3. Thieme, Lanny G.; and Schreiber, Jeffrey G.: Supporting Development for the Stirling Radioisotope Generator and Advanced Stirling Technology Development at NASA Glenn Research Center. NASA/TM—2005-213628 (AIP Conf. Proc., vol. 746, 2005, pp. 674–681), 2005. http://gltrs.grc.nasa.gov/cgi-bin/GLTRS/browse.pl?2005/TM-2005-213409.html


**Find out more about this research:**

**Glenn's Thermal Energy Conversion Branch:**
http://www.grc.nasa.gov/WWW/tmsb/

**Glenn's Power & In-Space Propulsion Division:**
http://www.grc.nasa.gov/WWW/5000/pep/

**Glenn's Mechanics and Life Prediction Branch:**
http://www.grc.nasa.gov/WWW/LPB/

**NASA Glenn Research Center:**
http://www.nasa.gov/glenn/


**Glenn contact:**
David L. Krause, 216–433–5465, David.L.Krause@nasa.gov

**Ohio Aerospace Institute (OAI) contact:**
Dr. Sreeramesh Kalluri, 216–433–6727, Sreeramesh.Kalluri-1@nasa.gov

**Authors:**
David L. Krause and
Dr. Sreeramesh Kalluri


**Headquarters program office:**
Science Mission Directorate

**Programs/projects:**
Nuclear Power Radioisotope System Development, Stirling Radioisotope Generator 110

# Novel Cascade Technique Developed for Accelerated Testing of Advanced Stirling Convertor Heater Heads

A Stirling radioisotope power system is being developed for potential use on NASA missions, including deep-space missions, Mars rovers, and lunar applications (ref. 1). Advanced Stirling convertors would provide substantial performance and mass benefits for these long-duration missions of up to 17 years. In the current design of the Advanced Stirling Radioisotope Generator, the heater head component of the Advanced Stirling Convertor (ASC) is fabricated from INCONEL 718, whereas another version is being developed with a MAR–M 247 (Lockheed Martin) heater head (refs. 2 and 3). The MAR–M 247 material allows increased hot-end temperatures of up to 850 °C (1560 °F), thus increasing efficiency and specific power.

For the long life required, a structurally significant limit for the ASC heater head is creep deformation induced under low stress levels at high material temperatures. Conventional investigations of creep rely on experimental results from uniaxial specimens, and much creep information is available for both materials. However, very little experimental data is available that directly applies to the atypical thin walls, specific microstructures, and low stress levels. In addition, the geometry and loading conditions apply a multiaxial stress state on the part, far from the conditions of uniaxial testing. For these reasons, benchmark testing was developed to accurately assess durability of the heater head. Because testing at prototypical stress requires many months to obtain creep data, initial accelerated creep testing is planned. The results will be used to calibrate deterministic and probabilistic analytical creep models of the heater head.

Previous short-term heater head creep tests relied on increased internal pressure to accelerate creep deformation (ref. 4). Safety considerations limited the maximum acceleration because of hazards associated with potential rupture under high pneumatic pressures. In addition, the method produced only one experimental stress-temperature condition for each test. Addressing these issues, the NASA Glenn Research Center developed a “cascade” test procedure. Cascade testing is so called because of the cascade of experimental creep rates produced by a single test article over a wide range of stresses at the temperature of interest. It subjects a large volume of material amenable to creep measurement by using an inductively heated susceptor to create uniform temperature over a major portion of the test article tapered wall (see the following figure). In this way, internal pressure creates a large multiaxial stress range at the desired temperature.

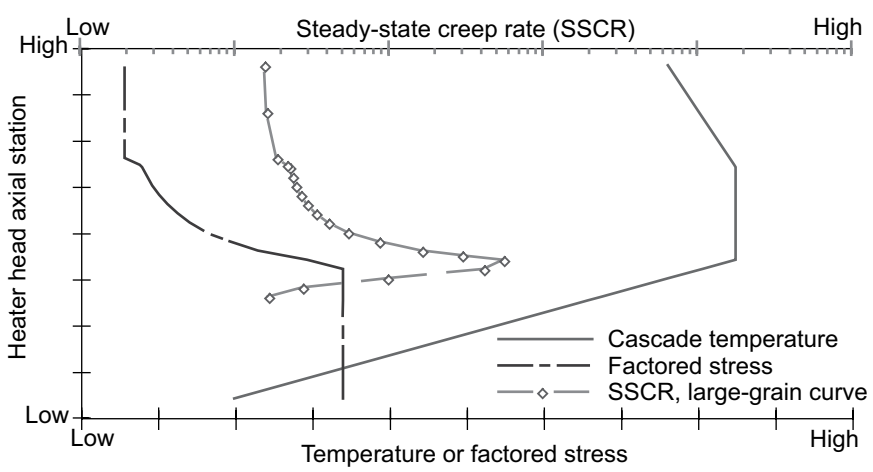


*Conceptual creep rate response is shown for cascade testing of a heater head test article.*

The cascade test rig is currently being assembled, with the first test results expected in early 2007. The rig (see the figure on the next page), which is located at the Structural Benchmark Test Facility, includes an argon pressurization system, the induction power supply, diametral extensometers and laser micrometers for strain measurement, and a data-acquisition and control system to safely conduct tests and record results.

Under NASA’s Science/Nuclear Power Radioisotope System Development project, the Department of Energy is developing high-efficiency Stirling power systems with Glenn and the Lockheed Martin Corporation (Valley Forge, PA). Sunpower Inc. (Athens, OH) is developing the ASC under a NASA Research Announcement (NRA) award. Glenn manages the NRA project and is providing supporting technology development for the Stirling convertor and the overall generator. The benchmark testing is being performed in collaboration with Glenn’s Thermal Energy Conversion Branch as part of this effort.

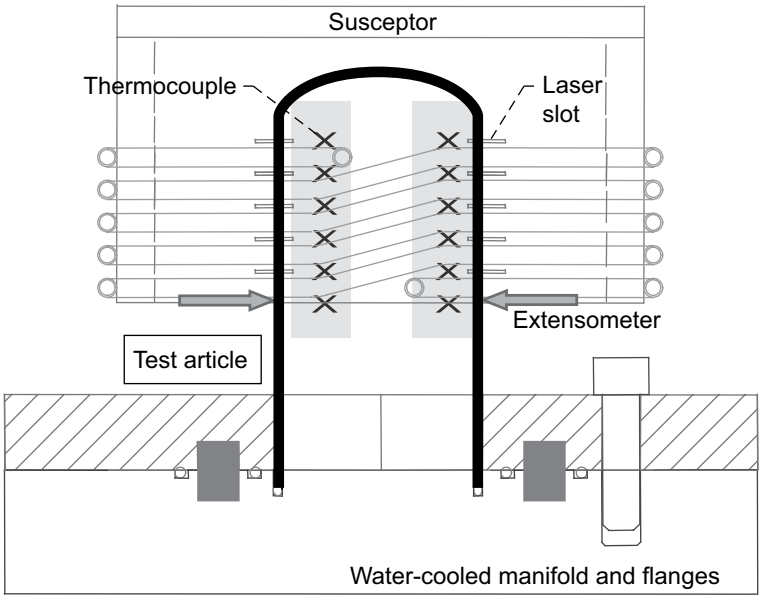


*Cascade test apparatus for applying heat and measuring creep strains on a heater head test article.*

**References**

1. Schreiber, J.: Developmental Considerations on the Free-Piston Stirling Power Convertor for Use in Space. AIAA–2006–4015, 2006.
2. Chan, Jack; Wood, J. Gary; and Schreiber, Jeffrey G.: Development of Advanced Stirling Radioisotope Generator for Space Exploration. Space Technology and Applications International Forum—STAIF 2007, Mohamed S. El-Genk, ed., AIP Conf. Proc., vol. 880, 2007, pp. 615–623.
3. Wood, J. Gary, et al.: Advanced Stirling Convertor Update. Space Technology and Applications International Forum—STAIF 2006, Mohamed El-Genk, ed., AIP Conf. Proc., vol. 813, 2006, pp. 640–652.
4. Krause, David L.; and Kantzos, Pete T.: Accelerated Life Structural Benchmark Testing for a Stirling Convertor Heater Head. Space Technology and Applications International Forum—STAIF–2006, Mohamed S. El-Genk, ed., AIP Conf. Proc., vol. 813, 2006, pp. 623–630.

**Find out more about this research:**

**Glenn's Thermal Energy Conversion Branch:**
http://www.grc.nasa.gov/WWW/tmsb/

**Glenn's Power & In-Space Propulsion Division:**
http://www.grc.nasa.gov/WWW/5000/pep/

**Glenn's Mechanics and Life Prediction Branch:**
http://www.grc.nasa.gov/WWW/LPB/

**NASA Glenn Research Center:**
http://www.nasa.gov/glenn/

**Glenn contacts:**
David L. Krause, 216–433–5465, David.L.Krause@nasa.gov

Dr. Randy R. Bowman, 216–433–3205, Randy.R.Bowman@nasa.gov

**Ohio Aerospace Institute contact:**
Dr. Sreeramesh Kalluri, 216–433–6727, Sreeramesh.Kalluri-1@nasa.gov

**Authors:**
David L. Krause, Dr. Sreeramesh Kalluri, and Dr. Randy R. Bowman

**Headquarters program office:**
Science Mission Directorate

**Programs/projects:**
Nuclear Power Radioisotope System Development, Advanced Stirling Radioisotope Generator

# Organics Evaluated for Advanced Stirling Convertor

Organic materials are an essential part of Stirling Radioisotope Generator (SRG) convertor construction as adhesives, potting compounds, wire insulation, lubrication coatings, bobbins, bumpers, insulators, thread lockers, or fasteners. Most space mission applications that can utilize SRGs (Mars rovers, deep-space, and lunar surface power) will have long lifetime requirements—in some cases more than 14 years. Thus, the performance, durability, and reliability of those organics should be critically evaluated in every possible material-process-fabrication-service environment relation. As in earlier efforts (refs. 1 to 5), a systematic and extensive evaluation was conducted for various organic materials used in Advanced Stirling Convertors (ASC) that are being developed by Sunpower under NASA Research Announcement funding as highly efficient and lower mass convertors. The key objective of this study was to evaluate, validate, and recommend organics for use in Sunpower's ASC.

Initially, this effort focused on the primary epoxy, Hysol EA9394 (Loctite, Henkel Co.), currently used in the ASC for bonding magnets and lamination stacks and for potting the linear alternator coil. This epoxy can be cured at room temperature and maintains good bond strength at temperatures up to 177 °C, thereby meeting mission requirements. However, its cure kinetics and their effects on bonding—which are needed for optimizing cure conditions and evaluating long-term thermal-mechanical stability and outgassing behavior—were not well understood. Cure kinetics studies were completed on this resin and a time-temperature-transformation (TTT) diagram was constructed (see the graph) using samples cured in folded aluminum foil to simulate the actual magnet bonding conditions. A two-step cure cycle was suggested on the basis of the TTT diagram: for example, an initial cure at a lower temperature, such as 24 hr at either 25 or 66 °C, followed by treatment at a higher temperature, preferably 85 °C, to drive the cure to completion. However, input from the outgassing and bond strength evaluations should be factored into the final selection of the cure cycle.

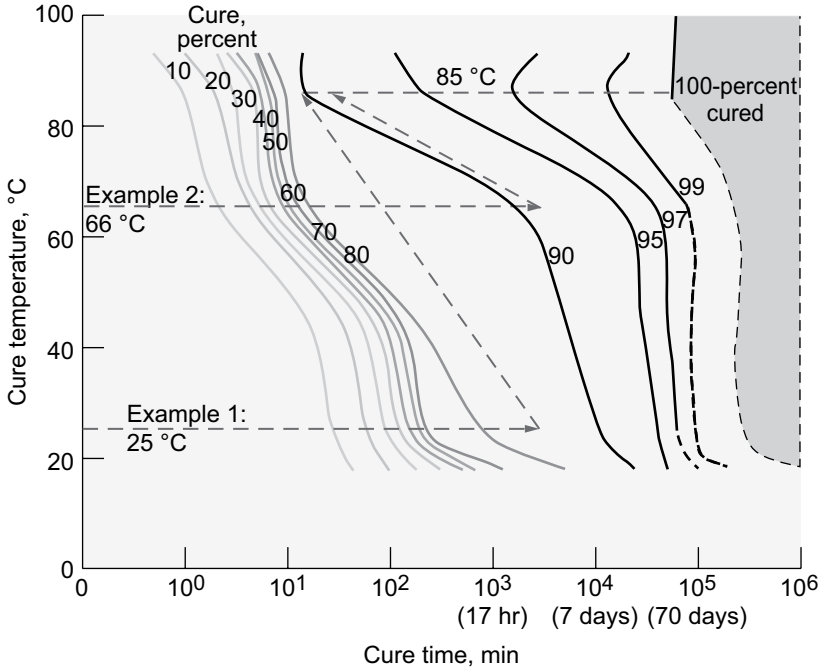


*TTT diagram for Hysol EA9394 epoxy.*

The outgassing potential of these organic materials was evaluated using a methodology based on weight loss measurements by thermogravimetric analysis (TGA) in both temperature ramp and isothermal modes. This method is indirect and involves semiquantitative properties, but it is practical and has the potential to be standardized. The accuracy and reproducibility of this technique were improved by normalizing the weight changes to the total amount of potential outgassing phase in the material. Various processing variables, such as degree of cure, volume/thickness and sealing, cure temperature, and mixing ratio are being investigated.

Long-term aging studies on other candidate epoxies, including high-temperature epoxy, Supreme 10HT (Master Bond Inc.), and room-temperature epoxy, Scotch-Weld 2216 B/A Gray (3M), had been initiated (see the photograph on the next page) under the SRG110 project. These tests will continue, and the Hysol EA9394 will be added to the test. Aging tests are being run in high-purity helium at the convertor design pressure and maximum expected temperature. Tests of 1/3, 1, and 3 years are planned, to enable the projection of bond life. Samples will be characterized after each test period. Other key milestones include (1) determining component-scale bond strength, mechanical integrity, and thermal stability of magnet epoxy bonding in collaboration with Cincinnati Testing Laboratories, (2) completing a long-term aging test on Hysol EA9394, and (3) completing evaluation of organics radiation resistance.

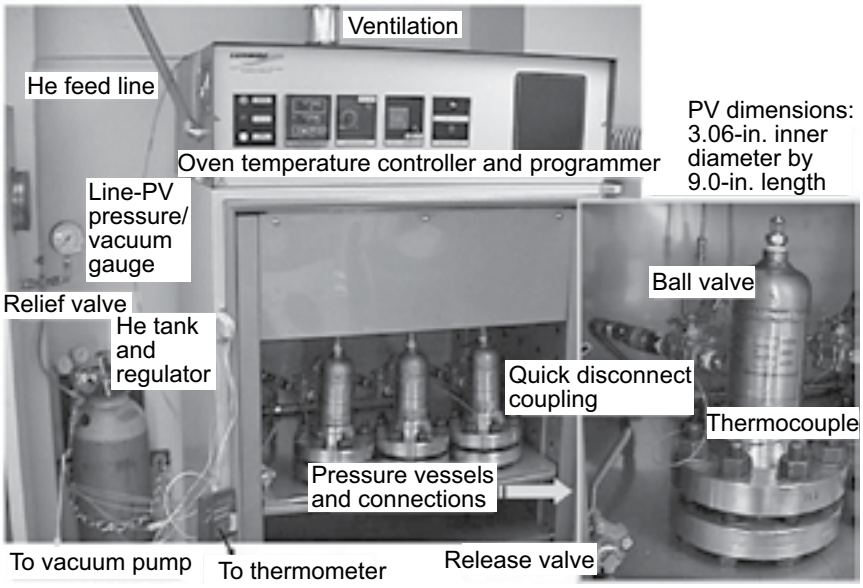


*Test facility for long-term in-service simulation aging of epoxy adhesives. PV, pressure vessel; He, helium.*

**References**

1. Thieme, Lanny G.; and Schreiber, Jeffrey G.: Supporting Development for the Stirling Radioisotope Generator and Advanced Stirling Technology Development at NASA Glenn Research Center. NASA/TM—2005-213628 (AIP Conf. Proc., vol. 746, 2005, pp. 674–681), 2005. http://gltrs.grc.nasa.gov/cgi-bin/GLTRS/browse.pl?2005/TM-2005-213628.html
2. Schreiber, J.: Developmental Considerations on the Free-Piston Stirling Power Convertor for Use in Space. AIAA–2006–4015, 2006.

**Find out more about this research:**

**Glenn's Polymers Branch**
http://www.grc.nasa.gov/WWW/MDWeb/5150/Polymers.html

**Glenn's Thermal Energy Conversion Branch:**
http://www.grc.nasa.gov/WWW/tmsb/

**Stirling Radioisotope Generator research at Glenn:**
http://www.grc.nasa.gov/WWW/tmsb/stirling.html

**Sunpower Inc.:**
http://www.sunpower.com

**Cincinnati Testing Laboratories, Inc.:**
http://www.cintestlabs.com

**Ohio Aerospace Institute (OAI) contact:**
Dr. E. Eugene Shin, 216–433–2544, Euy-Sik.E.Shin@nasa.gov

**Glenn contacts:**
Dr. James K. Sutter, 216–433–3226, James.K.Sutter@nasa.gov

Lanny G. Thieme, 216–433–6119, Lanny.G.Thieme@nasa.gov

**Authors:**
Dr. E. Eugene Shin, Dr. James K. Sutter, and Lanny G. Thieme

**Headquarters program office:**
NASA Science Mission Directorate

**Programs/projects:**
Prometheus, Radioisotope Power Systems; Advanced Stirling Radioisotope Generator; Affordable Fission Surface Power

# Sublimation Suppression Coatings Evaluated for Advanced Thermoelectric Materials

Skutterudite-based thermoelectrics are currently being considered for use in the next-generation Radioisotope Thermoelectric Generators (RTGs). Compositions[1] of interest include $CeFe_3RuSb_{11}$ (p-type) and $CoSb_3$. The goal for the segmented multicouple design is to achieve a conversion efficiency of greater than 10 percent to increase specific power for future science missions. The antimony present in the skutterudite-based materials is vulnerable to sublimation during the mission life of over 10 years at elevated temperatures, and this antimony loss will degrade RTG efficiency over the mission life. In a joint program between the NASA Glenn Research Center and the Jet Propulsion Laboratory, collaborative work was initiated to develop oxide-based coatings for deposition directly onto skutterudite.

Thermal expansion coefficients measured at Glenn were $13\times10^{-6}$/K and $11\times10^{-6}$/K for p-type ($CeFe_3RuSb_{11}$) and n-type ($CoSb_3$) legs, respectively. Oxides that exhibit similar thermal expansion behavior to the n- and p-type skutterudite legs were chosen as candidate coating materials. Ion-beam-assisted deposition, magnetron sputtering, and pulse laser deposition were evaluated as potential coating techniques. Coatings were deposited on substrates that were heated from room temperature to 750 °C, with thicknesses ranging from 0.5 to 2 μm. Coated coupons were tested under severe conditions of 700 °C for 1 week in an argon/5 vol% hydrogen environment. The microstructures of the coupons were evaluated for coating failure and antimony loss. The photograph shows a successful magnesium aluminum oxide ($MgAl_2O_4$) coating on an n-type leg. The coated surface shows no significant depletion of antimony, whereas the uncoated surfaces show significant antimony depletion. This study identified both alumina ($Al_2O_3$) and $MgAl_2O_4$ as promising candidate materials to suppress antimony sublimation at 700 °C for the n-legs and at 600 °C for the p-legs. The sublimation suppression coating development program is continuing for other advanced thermoelectric materials that contain volatile components.


**Glenn contacts:**
Dr. Frederick W. Dynys, 216–433–2404, Frederick.W.Dynys@nasa.gov

Dr. Michael V. Nathal, 216–433–9516, Michael.V.Nathal@nasa.gov

Dr. James A. Nesbitt, 216–433–3275, James.A.Nesbitt@nasa.gov

Dr. Elizabeth J. Opila, 216–433–8904, Elizabeth.J.Opila@nasa.gov

**Case Western Reserve University contact:**
Dr. Ali Sayir, 216–433–6254, Ali.Sayir-1@nasa.gov

**Authors:**
Dr. Frederick W. Dynys,
Dr. Michael V. Nathal,
Dr. James A. Nesbitt,
Dr. Elizabeth J. Opila, and Dr. Ali Sayir


**Headquarters program office:**
Science Division, Radioisotope Power Systems

**Programs/projects:**
Advanced Thermoelectric Converter Technology

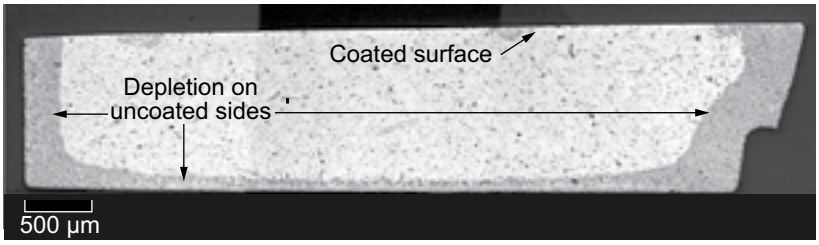


*Optical image of a $MgAl_2O_4$ coated n-type skutterudite tested at 700 °C in argon/5 vol% hydrogen for 1 week.*

[1]Ce, cerium; Fe, iron; Ru, ruthenium; Sb, antimony; Co, cobalt.

# Reliable Manufacturing Process Developed for Magnetic Materials Used in Hall Thrusters

An advanced soft magnetic material, Hiperco 50A (Carpenter Technology Corp.), was selected for use in the fabrication of the magnetic circuit for a Hall thruster developed under the High Voltage Hall Accelerator (HIVHAC) development project. Hiperco 50A is an ordered Fe-48Co-2V alloy[1] that has a high magnetic saturation limit and permeability, which are derived from a plot of the magnetic induction output (*B*) as a function of the magnetic field strength input (*H*). Weight and size reduction, critical for space applications, can be achieved by utilizing high magnetic saturation materials since the required magnetic force can be achieved with a lower weight component.

Initial magnetic testing on Hiperco 50A test rings produced excellent magnetic properties that were used for the design and construction of a prototype Hall thruster. However, the prototype thruster's magnetic circuit did not perform as predicted, and it was determined that the Hiperco 50A material did not have the same magnetic properties as the initial test rings. Similar poor magnetic performance was noted in a parallel program at a NASA contractor. Therefore, an in-house study at the NASA Glenn Research Center was undertaken to understand the sources for the disparity between the initial magnetic test rings and the underperforming material used in the components.

Metallographic examination of the initial Hiperco 50A magnetic test rings showed small, irregular grains, on the order of 20 μm in diameter, in the unannealed condition. Upon annealing, the grains recrystallized and grew to an average diameter of 90 μm. Grain growth also occurred in the underperforming material during the anneal; however, scanning electron microscopy revealed both very small grains and subgrains in the structure, indicative of incomplete recrystallization. It is known that the magnetic properties of FeCo-2V depend on the grain size after heat treatment, with large, stress-free grains producing better magnetic properties (ref. 1). Tracing the processing history of different materials disclosed that the initial Hiperco 50A, with the optimum magnetic properties, had undergone both forging and rolling, whereas the underperforming material was only forged. It was theorized that the forged and rolled material was more extensively worked, enabling easier recrystallization and grain growth during heat treatment.

To confirm this hypothesis plus determine the appropriate processing window for future components, a deformation study was undertaken to determine the effect of processing parameters on the microstructure of Hiperco 50A after annealing. Using the results of the study, processing parameters were determined that produced a microstructure similar to that of the initial Hiperco 50A rings. Extrusion was selected as the manufacturing method to both produce the required shape and impart sufficient deformation into the material. Several bars of Hiperco 50A were manufactured by extrusion with the new processing parameters,

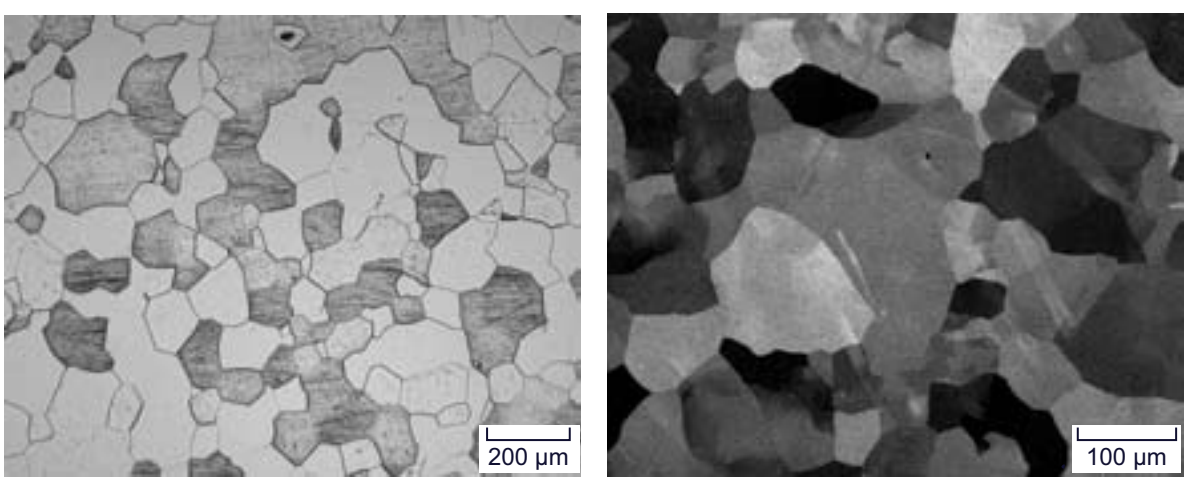


*Left: Optical micrograph of annealed magnetic rings. Right: Scanning electron micrograph of underperforming Hiperco 50A.*

[1]50 wt% iron, 48% cobalt, 2 wt% vanadium.

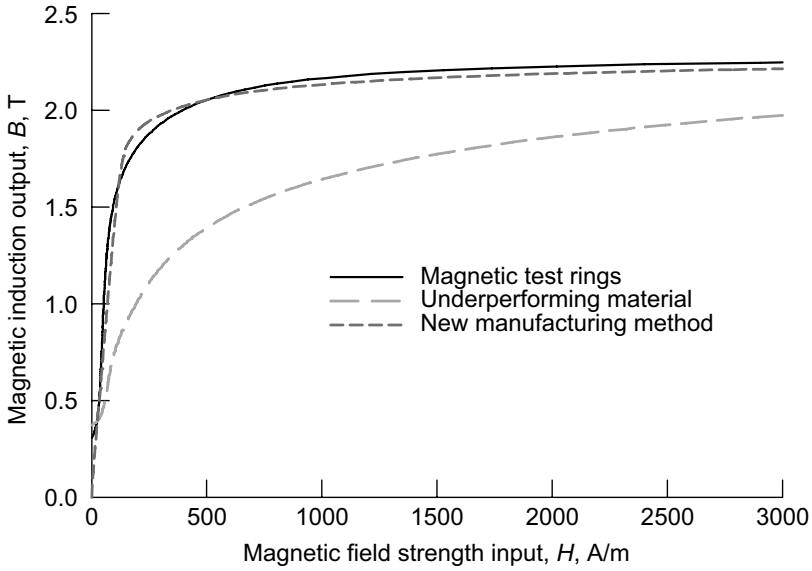


*Magnetic performance of initial test rings, underperforming Hiperco 50A, and material produced via the new processing method.*

and the magnetic properties of the extruded and heat-treated material were equivalent to those of the initial rings. Utilizing the new manufacturing method, Glenn has fabricated two thruster pole pieces from extruded and annealed Hiperco 50A.

The optical micrograph of the annealed magnetic rings (left on the preceding page) shows large, stress-free grains, which gave optimum magnetic properties. Small grains and/or subgrains were visible by scanning electron microscopy (right) in the underperfoming Hiperco 50A. These resulted in poor magnetic properties. The new processing method utilizing extrusion has consistently produced large, stress-free grains with good magnetic properties.

**Reference**

1. Standard Specification for Wrought Iron-Cobalt High Magnetic Saturation Alloys. ASTM A801–04, ASTM, West Conshohocken, PA, 2007.

**Glenn contacts:**
Susan L. Draper, 216–433–3257, Susan.L.Draper@nasa.gov

Dr. David H. Manzella, 216–977–7432, David.H.Manzella@nasa.gov

**Authors:**
Susan L.Draper and Dr. David H. Manzella

**Headquarters program office:**
Science Mission Directorate

**Programs/projects:**
In-Space Propulsion

## Applicability of Fracture Mechanics to Foams Examined

The primary purpose of the foam on the space shuttle's external tank (ET) is to provide thermal insulation. Although the foam has been successful in this function, it has not been without problems. Since the beginning of the shuttle program, bits of foam have been released during ascent. Early in the program, this was deemed only a minimal problem. However, since the catastrophic loss of the *Space Shuttle Columbia*, which was determined to be caused by a piece of foam debris, understanding foam shedding mechanisms has become of paramount importance. A considerable amount of money and effort have been expended in characterizing the structural properties of the foam, improving analysis methods for predicting foam stresses, and improving methods for predicting foam cracking. As part of this effort, the Mechanics and Lifing Branch at the NASA Glenn Research Center has been requested by the ET Program Office at the NASA Marshall Space Flight Center to help improve the thermostructural models for the foam.

Foam cracking has been modeled using linear elastic fracture mechanics (LEFM). However, LEFM was developed for use on monolithic materials. Since foam is a cellular structure, it is not known if LEFM is applicable to this material. To better understand this issue, a series of fracture studies were conducted on foam. A commercially available polystyrene foam was used since large amounts of the ET foams were not available. The polystyrene is a closed-cell foam having a density and cell dimensions very similar to those of the polyurethane ET

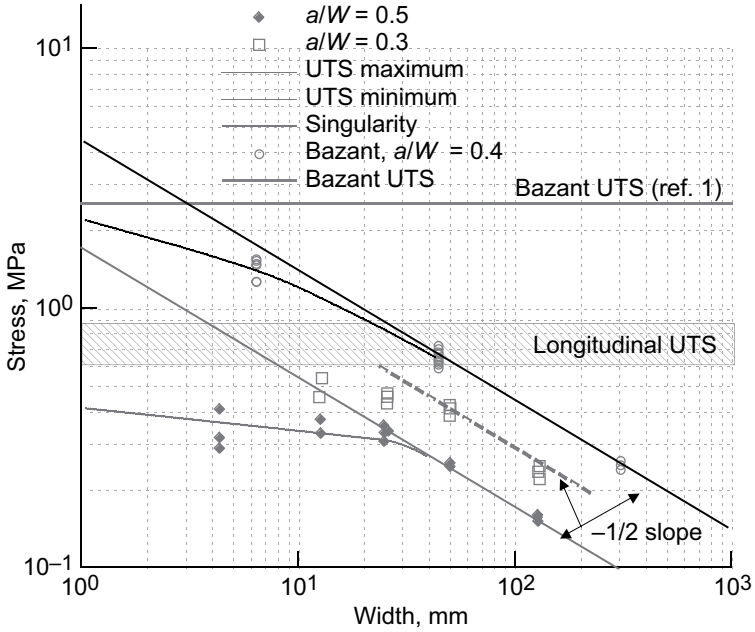


*Fracture data for polystyrene foam showing the deviation from a slope of –1/2 for small specimens indicating the breakdown of fracture mechanics. UTS, ultimate tensile strength.*

foams. Fracture tests were conducted on notched samples of various sizes with the goal being to see if there is a size affect on the fracture stress. Following the approach of Bazant (ref. 1), fracture tests were performed for two different ratios of crack length to width *a*/*W*. The results showed that there is a specimen size below which LEFM no longer applies (see the graph). This agrees with the results shown by Bazant. In addition, the damage zone $r_p$ in front of the crack tip was measured and found to be large (several millimeters in diameter). On the basis of general fracture mechanics guidelines, the critical specimen dimensions would have to be large (>$25r_p$), much larger than the specimens used in this study.

We conclude that LEFM does not apply to polystyrene foams below certain critical dimensions and that foam samples need to be much larger than one would originally think. Future work will determine whether similar statements can be made for the polyurethane foams used on the ET.

**Reference**

1. Bazant, Z.P., et al.: Size Effect and Asymptotic Matching Analysis of Fracture of Closed-Cell Polymeric Foam. Int. J. Solids Struct., vol. 40, no. 25, 2003, pp. 7197–7217.

**Find out more about the research of Glenn's Life Prediction Branch:**
http://www.grc.nasa.gov/WWW/LPB/

**Glenn contacts:**
Dr. Bradley A. Lerch, 216–433–5522, Bradley.A.Lerch@nasa.gov

Dr. Roy M. Sullivan, 216–433–3249, Roy.M.Sullivan@nasa.gov

**Ohio Aerospace Institute (OAI) contact:**
Dr. John C. Thesken, 216–433–3012, John.C.Thesken@nasa.gov

**Authors:**
Dr. Bradley A. Lerch, Dr. Roy M. Sullivan, and Dr. John C. Thesken

**Headquarters program office:**
Space Operations Mission Directorate

**Programs/projects:**
Space Shuttle

# Framework Developed for Performing Multiscale Stochastic Progressive Failure Analysis of Composite Structures

The Integrated Multiscale Micromechanics Analysis Code (ImMAC) Software Suite developed by the NASA Glenn Research Center and the Ohio Aerospace Institute (OAI) consists of three components for the design and analysis of composite structures: (1) the Micromechanics Analysis Code with Generalized Method of Cells (MAC/GMC) performs rapid, standalone analysis of composite materials and laminates based on non-finite-element analysis (non-FEA) micromechanics methods (ref. 1); (2) the Finite Element Analysis—Micromechanics Analysis Code (FEAMAC) couples the efficient micromechanics capabilities of MAC/GMC with the ABAQUS finite element code (ABAQUS, Inc.) for multiscale analysis of composite structures; and (3) HyperMAC couples the MAC/GMC micromechanics capabilities with the HyperSizer stiffened structural optimization software (ref. 2).

FEAMAC has enabled multiscale stochastic progressive failure analysis of composite structures. It uses the generalized method of cells (GMC) micromechanics approach to model the local composite material behavior at the integration points within each finite element of a composite structure via the ABAQUS user-definable subroutines. GMC localizes to the level of the fiber and matrix constituent materials and thus enables the use of arbitrary nonlinear constitutive, damage, and life models (many of which are provided by MAC/GMC) for each monolithic constituent phase throughout the composite structure. This circumvents the need for the development and characterization of effective anisotropic constitutive models for the composite materials within the structure, which can be difficult in the presence of material nonlinearity. Furthermore, GMC provides access to the constituent-level stresses and strains throughout the structure, enabling the use of fiber- and matrix-scale failure and damage-evolution criteria. The well-documented computational efficiency of the GMC micromechanics approach (as compared with the finite element micromechanics approach, for example; refs. 3 and 4) permits the tractability of coupled structural FEA-micromechanics problems.

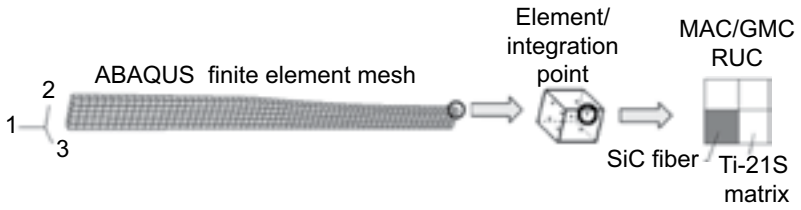


*ABAQUS finite-element mesh of a dogbone specimen and MAC/GMC repeating unit cell (RUC) operating at each integration point.*

The figures show an application of the developed modeling framework to the stochastic progressive failure analysis of a longitudinally reinforced SiC/Ti-21S composite[1] dogbone specimen. A standard finite element mesh was employed, but the MAC/GMC micromechanics repeating unit cell was operative at each integration point in each element. The material input data thus became the material properties of the SiC fiber and Ti-21S matrix constituents. In this example, a deterministic viscoplastic model was employed to represent the Ti-21S matrix and a stochastic strength model was employed for the SiC fibers. The statistical strength properties for the fibers within each element were assigned randomly over the mesh geometry such that they sum to the vendor-supplied fiber strength histogram.

This process enables the failure initiation location, as well as the failure progression, to be random, rather than occurring at the highest stress riser. This is illustrated in the figure on the next page, which plots the fiber damage at different times during a simulated tensile test on the composite specimen. Fiber failure initiated within the specimen gauge section and then arrested. Fiber failure then initiated at another location in the gauge section and also arrested. Finally, failure progressed through the specimen (indicating final failure) at the first failure initiation location.

Deterministic simulations, and those that do not randomize the fiber failure properties over the specimen geometry, predict failure to initiate at the highest stress riser in the specimen, which is at the bottom of the transition region to the gauge section (above the predicted

[1]Silicon carbide, 15-wt% molybdenum, 2.7-wt% niobium, 3-wt% aluminum, 0.2-wt% silicon.

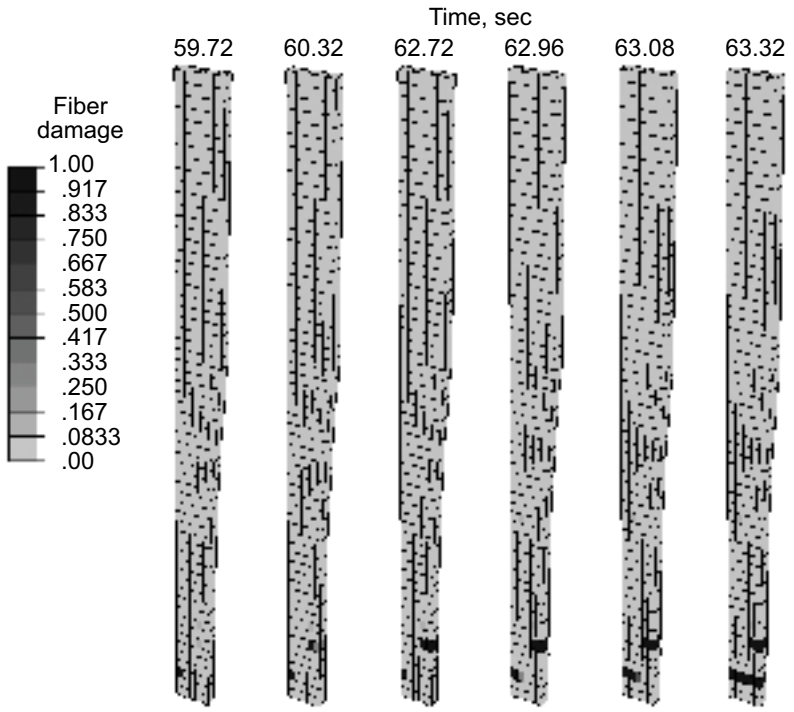


*Local fiber damage fraction as a function of time as fiber failure progresses within a longitudinal 33 wt% SiC/Ti-21S specimen with spatially distributed fiber strength statistics.*

failure location shown). Correctly accounting for the stochastic nature of the failure initiation location is important because real structures fail in this manner. For example, in experimental tensile tests, SiC/Ti-21S specimens, like those modeled, repeatedly failed within the gauge section, not at the bottom of the transition region.

**References**

1. Bednarcyk, Brett A.; and Arnold, Steven M.: MAC/GMC 4.0 User's Manual: Keywords Manual; Volume 2. NASA/TM—2002-212077/VOL2, 2002. http://gltrs.grc.nasa.gov/cgi-bin/GLTRS/browse.pl?2002/TM-2002-212077-VOL2.html
2. HyperSizer Structural Sizing Software. Collier Research Corp., Hampton, VA, 2005.
3. Wilt, T.E.: On the Finite Element Implementation of the Generalized Method of Cells Micromechanics Constitutive Model. NASA CR–195451, 1995. http://gltrs.grc.nasa.gov/cgi-bin/GLTRS/browse.pl?1995/CR-195451.html
4. Pindera, M.-J.; and Bednarcyk, B.A.: An Efficient Implementation of the Generalized Method of Cells for Unidirectional, Multi-Phased Composites With Complex Microstructures. Composites, vol. 30B, no. 1, 1999, pp. 87–105.

**Find out more about this research:**

**ImMAC (Integrated multiscale Micromechanics Analysis Code) Software Suite:**
http://www.grc.nasa.gov/WWW/LPB/mac/

**HyperSizer product profiles:**
http://www.hypersizer.com/Products/products.htm

**Ohio Aerospace Institute (OAI) contact:**
Dr. Brett A. Bednarcyk, 216–433–2012, Brett.A.Bednarcyk@nasa.gov

**Glenn contact:**
Dr. Steven M. Arnold, 216–433–3334, Steven.M.Arnold@nasa.gov

**Authors:**
Dr. Brett A. Bednarcyk and
Dr. Steven M. Arnold

**Headquarters program office:**
Aeronautics Research Mission Directorate

**Programs/projects:**
Integrated Vehicle Health Management

# Level of Risk in an Optimal Design Solution Quantified by a Stochastic Calculation

A stochastic design methodology was developed by researchers from the NASA Glenn Research Center and the Ohio Aerospace Institute (OAI) to optimize components of an airframe structure. Uncertainties were accommodated as distribution functions for the design load, strength, and elastic property of the material, whereas failure mode was specified as a function of the risk level *p*. The Monte Carlo technique and the fast probability integrator (FPI) of the Numerical Evaluation of Stochastic Structures Under Stress (NESSUS) code were used as the probabilistic analysis tools, and Glenn's design testbed CometBoards was used as the optimizer. The stochastic design method generated the optimum solution and weight of an airframe component as a function of risk level *p* (see the following graph). The center (corresponding to a 50-percent probability of success, or $p = 0.5$) of this inverted S-shaped graph corresponded to the deterministic solution. Weight increased for reliability that exceeded 50 percent. Weight decreased when the reliability was compromised. In other words, a design can be selected depending on the level of risk acceptable to the situation. Performance was satisfactory for the Monte Carlo technique and the FPI as well as for normal, lognormal, and Weibull distribution functions.

Stochastic optimization was illustrated considering the ninth web or rib of an airframe stabilizer as an example. The web was about 100 in. long, 12 in. wide, and 0.072 in. thick. It was discretized by a finite-element model with quadrilateral and triangular elements. The magnitude of the applied loads had a mean value of 33 lbf with a wide variation of 400 lbf. The maximum von Mises stress for the initial design was 3227 psi, with a maximum displacement of 0.0415 in. Stochastic optimum solutions are depicted in the graph. The weight was reduced to 3.2 lbf from the initial weight of 9 lbf for a 50-percent risk level ($p = 0.50$). The weight was increased by 12 percent when probability of success was increased by 20 percent, from $p = 0.5$ to $p = 0.7$, and vice versa. The figures on the next page depict the von Mises stresses for $p = 0.5$ and $p = 0.7$, respectively. The designs were limited by the active displacement constraint. The stress was reduced by 12 percent when the probability of risk of failure was increased to 70 percent from its nominal 50-percent value.

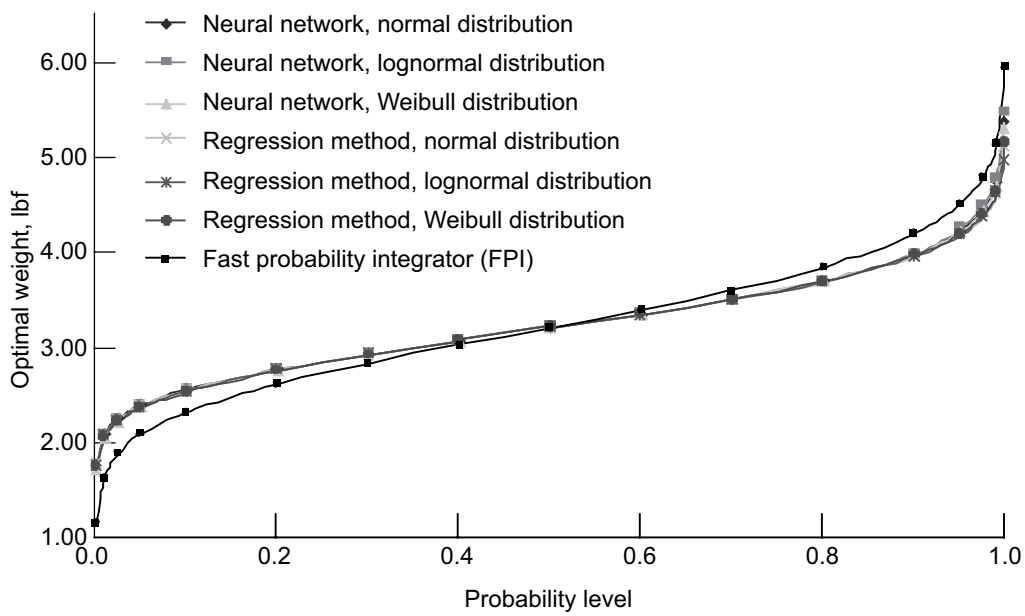


*Inverted S graph for optimum weight versus probability level. This figure is shown in color in the online version of this article (http://www.grc.nasa.gov/WWW/RT/2006/RX/RX38S-patnaik.html).*

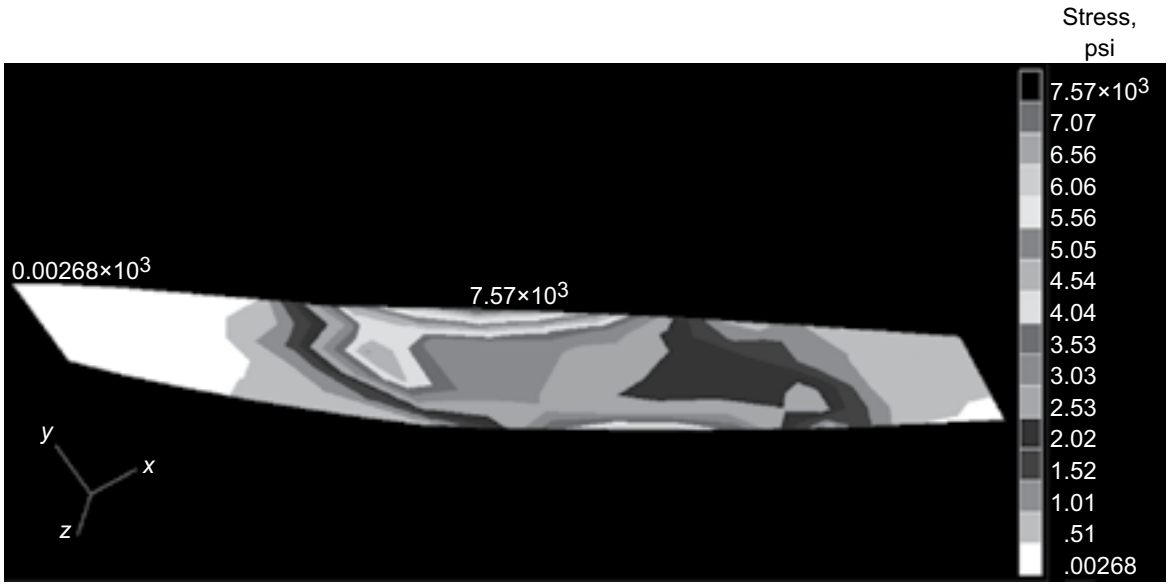


*Stress distribution for deterministic design (p = 0.5). This figure is shown in color in the online version of this article (http://www.grc.nasa.gov/WWW/RT/2006/RX/RX38S-patnaik.html).*

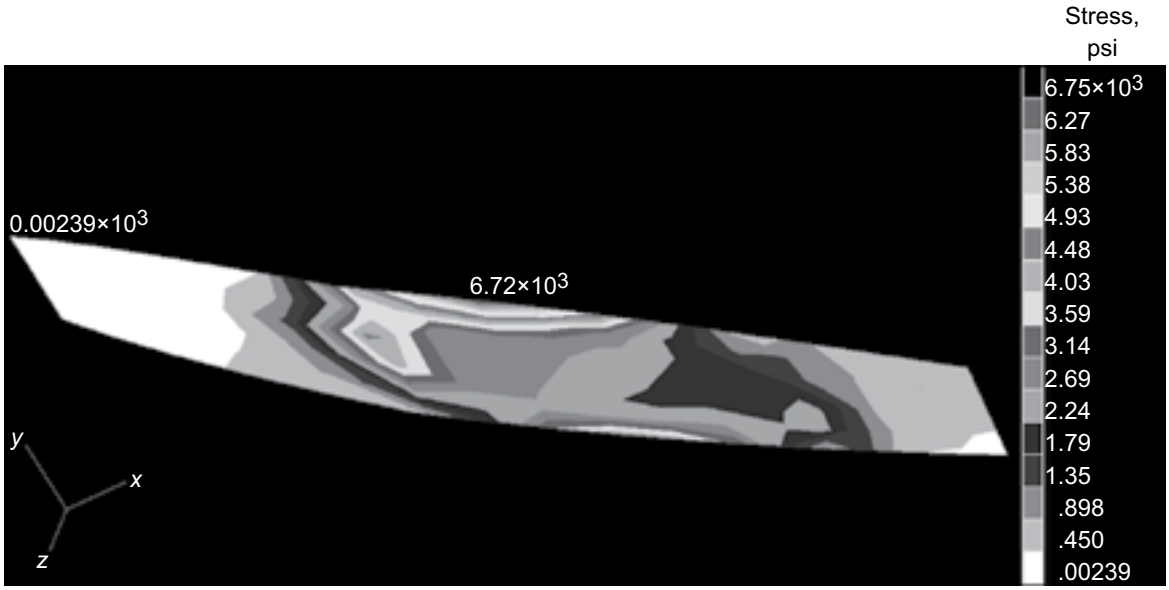


*Stress distribution with reduced probability of failure (p = 0.7). This figure is shown in color in the online version of this article (http://www.grc.nasa.gov/WWW/RT/2006/RX/RX38S-patnaik.html).*

**Bibliography**

Tenable Network Security, Inc.: Nessus 3.0, Advanced User Guide, rev. 8, 2007. http://www.nessus.org/documentation/nessus_3.0_advanced_user_guide.pdf

Guptill, James D., et al.: CometBoards Users Manual. NASA TM–4537, 1996. http://gltrs.grc.nasa.gov/cgi-bin/GLTRS/browse.pl?1996/TM-4537.html

**Glenn contacts:**

Dr. Shantaram S. Pai, 216–433–3255, Shantaram.S.Pai@nasa.gov

Dale A. Hopkins, 216–433–3260, Dale.A.Hopkins@nasa.gov

**Authors:**

Dr. Surya N. Patnaik, Dr. Shantaram S. Pai, and Dale A. Hopkins

**Headquarters program office:**

Aeronautics Research Mission Directorate

**Programs/projects:**

Ultra Safe, Ultra-Efficient Engine Technology Program, High Speed Research

# Multiaxial Failure Response of Nuclear Grade Graphite Predicted With Ceramics Analysis Reliability Evaluation of Structures/Life (CARES/*Life*) Software

There is a renewed interest in nuclear energy because nuclear powerplants generate zero greenhouse gas emissions and new reactor technologies may enable hydrogen co-generation (for the hydrogen economy). At present, 10 countries have agreed to cooperate on the development of the fourth-generation (Gen IV) nuclear energy system in order to help meet the world's growing energy needs. The expectation is that these Gen IV reactors will be gas cooled and run at high temperature (up to 950 °C) using graphite (instead of water) as the moderator material. The ultimate goal of the initiative is to develop a system that is sustainable, economical, safe, reliable, and resistant to proliferation (ref. 1). NASA has complementary interest in this endeavor with regards to the development of lunar surface power generation and nuclear propulsion for interplanetary missions.

One important area of investigation and subsequent design standards development (ASME Boiler and Pressure Vessel Code) for graphite core structures involves the testing, qualifying, and design methodology for new material grades of nuclear graphite. Graphite is a brittle material or quasi-brittle material, and brittle materials require a design methodology that is different from ductile materials (such as metals). Brittle materials do not exhibit plastic deformation and show wide scatter in strength because of the variable nature of intrinsic microscopic flaws. The Ceramics Analysis and Reliability Evaluation of Structures/Life (CARES/*Life*) software was developed at the NASA Glenn Research Center to predict the statistical reliability of brittle materials.

*Graphite multiaxial specimen. The specimen is loaded with various combinations of pulling (tensile stress) and internal pressurization (hoop stress).*

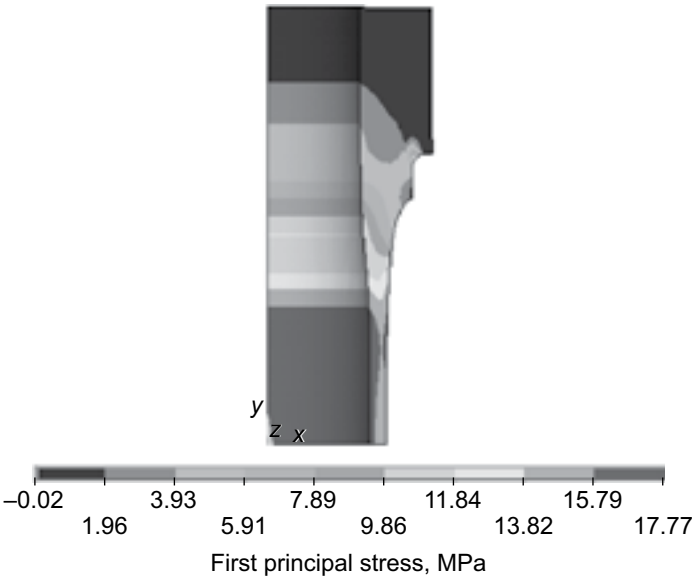


*ANSYS finite-element analysis of a graphite specimen under a combined axial tensile load and pressurization load. Minimum stress, 0.021377 MPa; maximum stress, 17.771 MPa. This figure is shown in color in the online version of this article (http://www.grc.nasa.gov/WWW/RT/2006/RX/RX39L-nemeth.html).*

The figures show CARES/*Life* results predicting the multiaxial strength (the strength from various combinations of applied loads) of the IG–110 grade of graphite specimens originally tested at Oak Ridge National Laboratory. The photograph shows a graphite specimen outside of its loading rig. The specimen is loaded to fracture with various combinations of axial loading (tensile or compressive) and internal pressurization.

The plot to the left shows the first principal stress from an ANSYS (ANSYS, Inc.) finite-element analysis of the specimen under a combined axial tensile load and pressurization load. The graphs on the next page show CARES/*Life* failure predictions for two different multiaxial failure theories. CARES/*Life* uses the results from finite-element analysis to make the predictions. The left graph shows the predictions using the more traditional Principle of Independent Action (PIA) model, which uses the combined

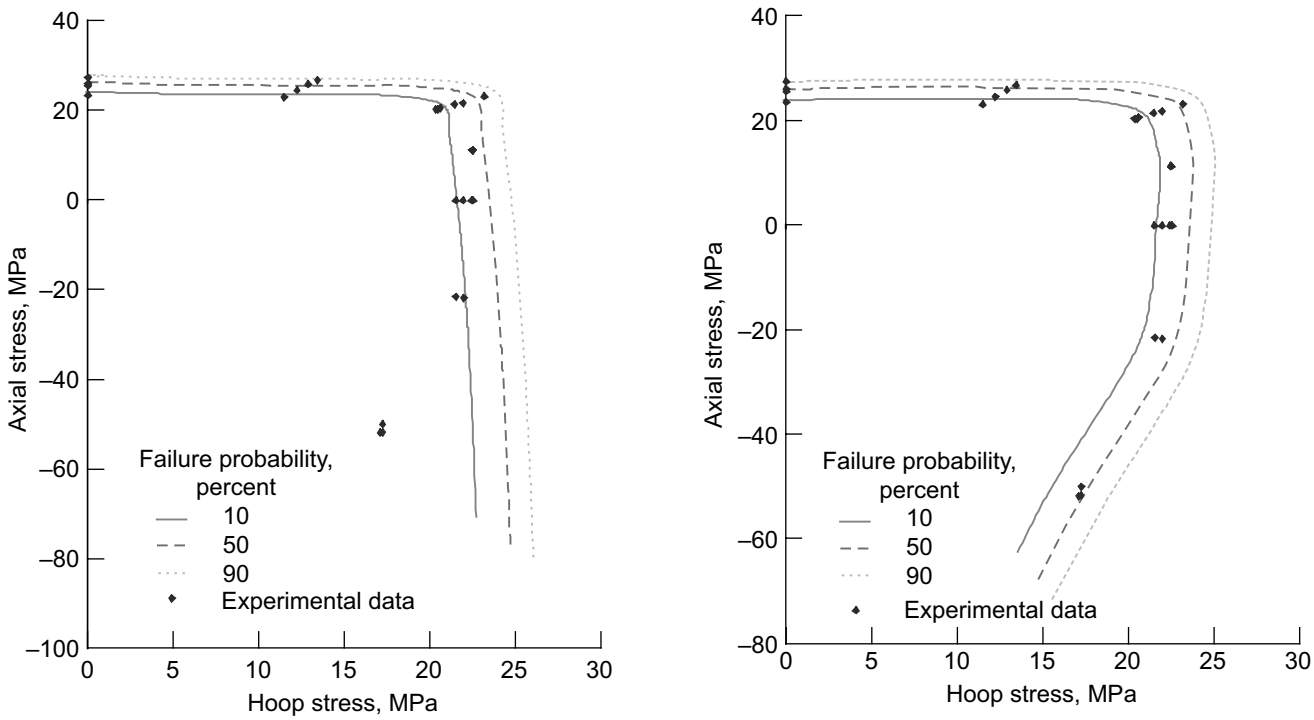


*Failure envelope at 10-, 50-, and 90-percent levels of failure probability. Left: PIA theory. Right: Batdorf theory for a shearing stress sensitivity, C, of 1.2.*

action of the principal stresses. The right graph shows the predictions from the more sophisticated Batdorf multiaxial theory, which uses linear elastic fracture mechanics combined with the random orientation of microcracks to predict the multiaxial failure response. Clearly, the Batdorf multiaxial theory provides more accurate predictions of the multiaxial failure response for all combinations of tensile and compressive stresses.

**References**

1. U.S. DOE Nuclear Energy Research Advisory Committee: A Technology Roadmap for Generation IV Nuclear Energy Systems. GIF–002–00, Dec. 2002.
2. Nemeth, Noel N., et al.: Predicting the Reliability of Ceramics Under Transient Loads and Temperatures With CARES/Life. Probabilistic Aspects of Life Prediction, ASTM STP–1450, W. Steven Johnson and Ben M. Hillberry, eds., ASTM International, West Conshohocken, PA, 2004.

**Glenn contacts:**
Noel N. Nemeth, 216–433–3215, Noel.N.Nemeth@nasa.gov

John P. Gyekenyesi, 216–433–3210, John.P.Gyekenyesi@nasa.gov

**Authors:**
Noel N. Nemeth, Steven Sookdeo, and Dr. John P. Gyekenyesi

**Headquarters program office:**
Exploration Systems Mission Directorate

**Programs/projects:**
Prometheus, Constellation Systems, Exploration Systems Research & Technology

# Composite Gyroscope Momentum Wheels Optimized

Although the nonterrestrial applications for gyroscopes demand an optimized, lightweight, and low-volume design, the momentum wheel design has not typically been optimized. For example, heritage designs have predominantly used a standard operating rotational speed of 6000 rpm, despite the fact that higher speeds might provide significantly improved mass and volume efficiency (ref. 1). Also, designs are often based on one material, chosen a priori, and on the performance of a finite-element stress analysis to determine the minimum margin under operating conditions (ref. 2). Clearly, this approach is overconservative and does not make use of the efficiency that could be provided through design and material selection. For example, a 22- to 60-percent savings of package volume or a 15- to 48-percent savings of mass could be realized, depending on the required momentum, with lower momentum rotors having higher savings.

To investigate these benefits, the Naval Research Laboratory solicited researchers from the NASA Glenn Research Center and the Ohio Aerospace Institute (OAI) to perform an analytical stress analysis, applicable to both composite (anisotropic) and metallic (isotropic) gyroscope momentum wheels. The stress analysis was combined with an anisotropic failure criterion to enable the failure (rupture) prediction of the momentum wheel due to angular velocity and gimbal maneuver loading. A factor of safety was incorporated, and a sizing (optimization) procedure was developed and implemented in a computer code.

The following plot compares the optimum momentum wheel designs for four materials considered—graphite/epoxy (Gr/Ep) polymer matrix composite (PMC), SiC/Ti metal matrix composite (MMC), AerMet 100, and stainless steel—for an equally weighted performance index (which accounts for both mass and volume efficiency) versus inner-to-outer-radius ratio $X$ in the case of an $H$ = 1700 ft-lbf-sec momentum wheel with an out-of-plane thickness $t$ of 1 in. A factor of safety of 2 was employed, and the momentum wheels were sized to ultimate strength. This figure shows that the stainless steel design is inferior over the entire range of $X$ values. At lower $X$ values (below 0.4), the remaining three materials are comparable in terms of performance index. As the value of $X$ increased, the PMC's performance index increased much more rapidly than those of the other materials and reached a maximum value that is approximately 75-percent higher than that of the MMC and AerMet 100. This is due to the PMC's extremely low density. The PMC reached its optimum design at $X$ = 0.81, whereas the other three materials reached their optimum designs at $X$ = 0.74.

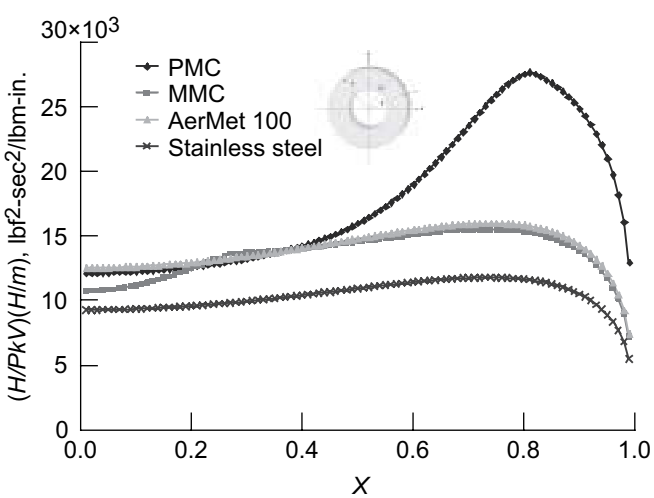


*Comparison of the equally weighted performance index as a function of inner-to-outer-radius ratio, X (= a/b) for the Gr/Ep PMC, SiC/Ti MMC, AerMet 100, and stainless steel for t = 1 in. and H = 1700 ft-lbf-sec.*

From the log-log plot on the next page of $H$ per unit package volume ($H/PkV$) versus $H$ per unit mass $(H/m)$ for the previous four materials and four angular momentums (95, 325, 700, and 1700 ft-lb-sec) with an out-of-plane thickness of 1 in., it is clear that the PMC provides the best design (as measured by this performance index) given equal weight to both mass and volume: that is, using a –1 line of slope. Also plotted on this figure is a –2.7 line of slope that intersects an extreme point of both the PMC and AerMet 100 curves. This indicates that in order for the AerMet 100 material design to be competitive with the PMC material design, the package volume must be 2.7 times more important than mass to the design of the gyroscope momentum wheel. Using such a performance index enables designers to quantify the required tradeoff space. More details can be found in reference 3.

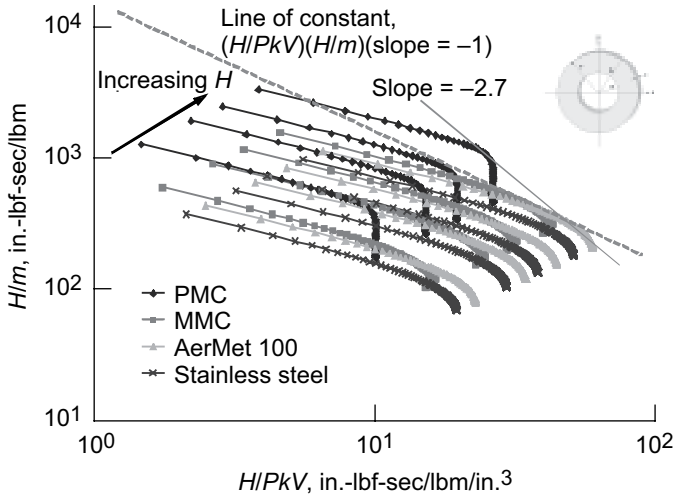


*Comparison of angular momentum per unit mass as a function of angular momentum per unit package volume for Gr/Ep PMC, SiC/Ti MMC, AerMet 100, and stainless steel for t = 1 in. and various values of H.*

**References**

1. Davis, Porter: Momentum System Concepts and Trades for the New Class of Smaller Lower Cost Satellites. Proceedings of the 29th Annual AAS Rocky Mountain Guidance and Control Conference, AAS 06–23, vol. 125, Breckenridge, CO, 2006, pp. 13–24.
2. Monaco, Anthony: Stress Analysis of the ISSA/CMG Flywheel (P/N 5181280). International Space Station Alpha, Control Moment Gyroscope, rev. B. NASA Document 5461508–MT, 1995.
3. Bednarcyk, B.; and Arnold, S.: Design and Optimization of Composite Gyroscope Momentum Wheels. AIAA–2007–2293, 2007.

**Glenn contact:**
Dr. Steven M. Arnold, 216–433–3334, Steven.M.Arnold@nasa.gov

**Ohio Aerospace Institute (OAI) contact:**
Dr. Brett A. Bednarcyk, 216–433–2012, Brett.A.Bednarcyk@nasa.gov

**Authors:**
Dr. Steven M. Arnold and Dr. Brett A. Bednarcyk

**Headquarters program office:**
Aeronautics Research Mission Directorate

**Programs/projects:**
Space Act Agreement 3–873, Advanced Control Momentum Gyroscope Study

# Computationally Efficient Blade Mistuning Analysis Codes Studied for Mistuned Bladed Disk Analysis: Subset of Nominal Modes (SNM) and Fundamental Mistuning Model (FMM)

A novel reduced-order modeling approach was studied at the NASA Glenn Research Center, called the subset of nominal modes (SNM) and the fundamental mistuning model (FMM). The model is based on two simple concepts. First, the mode shapes of the tuned system and the mistuned system span the same displacement space. As a result, the mistuned modes can be determined as a weighted sum of the nominal tuned modes, which are generated efficiently using a cyclic symmetric finite-element model (FEM). Second, only the modes with natural frequencies near that of the mode of interest, or of the excitation, contribute significantly to the response. Thus, only a relatively small subset of the nominal tuned system modes is needed to accurately calculate the forced response.

The input data are relatively easy to generate. For example, only a finite-element analysis of a single-blade disk sector is needed to generate the tuned system modes as input to SNM. In addition, since only nominal modes are used as a basis for the representation, it is necessary to determine the motion-dependent aeroelastic forces only for these modes.

As the number of degrees of freedom in the SNM model increases, the results from a mistuned system calculation converge to the exact solution. Consequently, the accuracy of the SNM model can be checked by observing how the results converge as more degrees of freedom are used. This is especially important in bladed disks with a large number of degrees of freedom in the FEM since it is difficult to run a finite-element analysis of a full mistuned bladed disk as a benchmark. A geometrically mistuned benchmark was developed that matches the data fairly well, as shown in the following graphs. The theory underlying the SNM approach is documented in references 1 and 2.

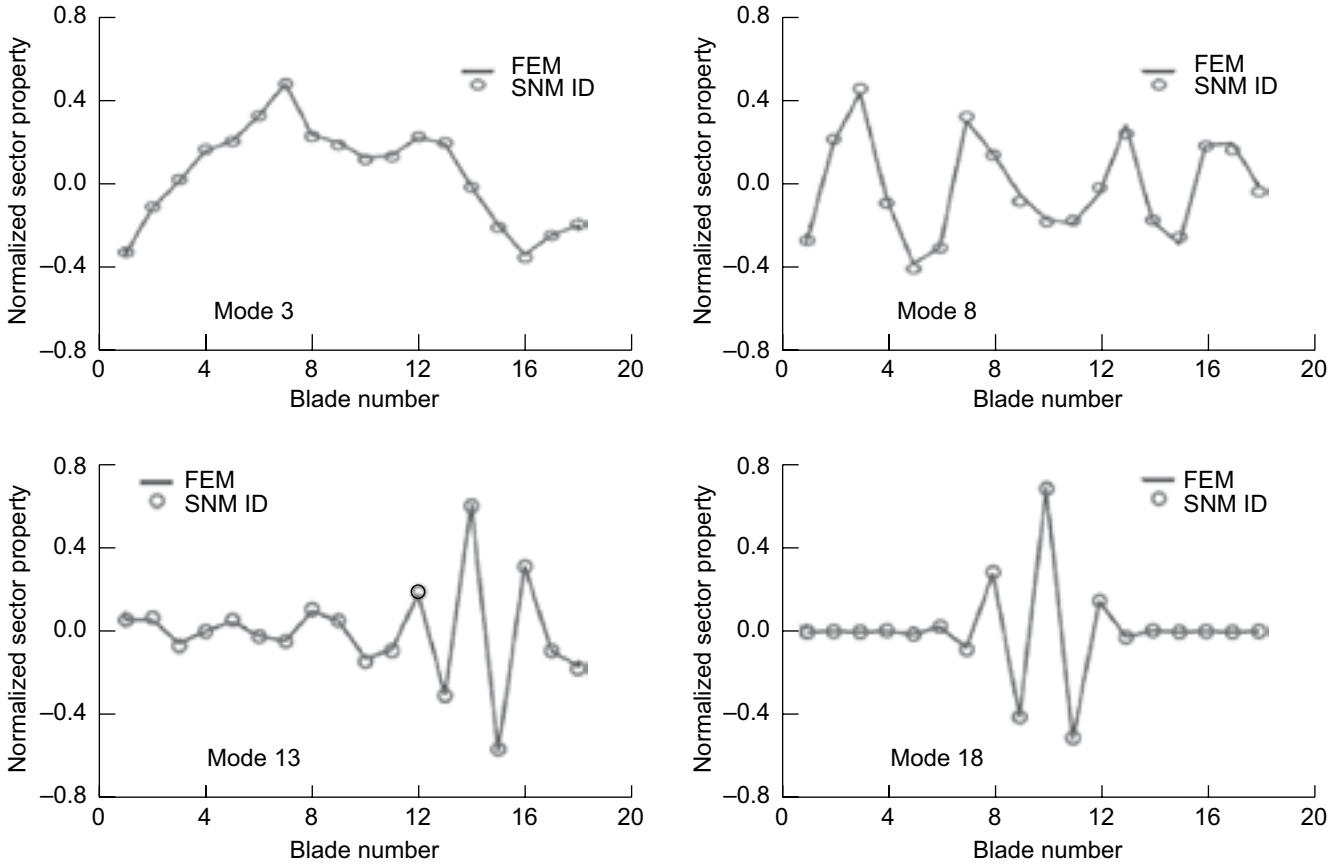


*Mistuned modes comparisons. SNM ID is the SNM identification.*

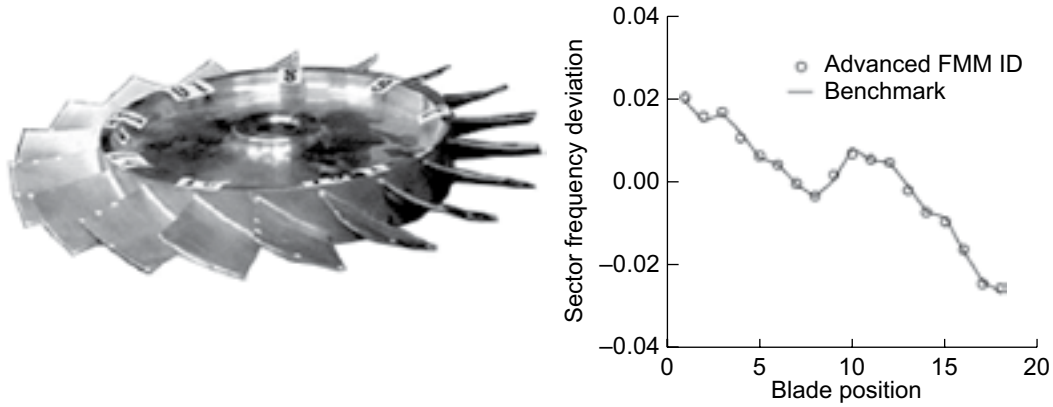


*Experimental verification of blade frequency deviations.*

The completely experiment based FMM method is a simplification of the SNM and is designed for use in isolated families of modes such as first bending and first torsion. One of the advantages of this approach is that it reduces the mistuning problem to its most basic elements. As a result, FMM requires a minimum number of input parameters and is extremely easy to use. The simplification also makes FMM extremely efficient. The complete FMM formulation was presented in reference 3 and then later revised to allow for a more flexible disk (ref. 4). The FMM method was verified experimentally as shown in the preceding figure.

**References**

1. Yang, M.-T.; and Griffin, J.H.: A Reduced Order Model of Mistuning Using a Subset of Nominal Modes. ASME J. Eng. Gas Turbines Power, vol. 123, no. 4, 2001, pp. 893–900.
2. Yang, M.–T.; and Griffin, J.H.: A Reduced Order Approach for the Vibration of Mistuned Bladed Disk Assemblies. J. Eng. Gas Turbines Power, vol. 119, no. 1, 1997, pp. 161–167.
3. Feiner, D.M.; and Griffin, J.H.: A Fundamental Model of Mistuning for a Single Family of Modes. J. Turbomach., vol. 124, no. 4, 2002, pp. 597–605.
4. Feiner, D.M.; and Griffin, J.H.: Mistuning Identification of Bladed Disks Using a Fundamental Mistuning Model—Part I: Theory. ASME J. Turbomach., vol. 126, no. 1, 2004, pp. 150–158.
5. Feiner, D.M.; and Griffin, J.H.: A Fundamental Model of Mistuning for a Single Family of Modes. J. Turbomach., vol. 124, no. 4, 2002, pp. 597–605.

**Glenn contact:**
Dr. James B. Min, 216–433–2587, James.B.Min@nasa.gov

**Author:**
Dr. James B. Min

**Headquarters program office:**
Aeronautics Research Mission Directorate

**Programs/projects:**
Aviation Safety, Crew Exploration Vehicle, Constellation Systems

# Turbo-Reduce Code Used To Predict Blade Stress Levels Directly From Reduced-Order Vibration Models of Mistuned Bladed Disks

The forced vibration amplitudes of bladed disks can increase dramatically because of small, random discrepancies among the blades, referred to as "mistuning." Blade mistuning can lead to significant durability and reliability problems in turbine engines. Finite element models (FEMs) are used to analyze bladed disk designs and assess the effects of mistuning. From a finite-element analysis (FEA) of vibration, the displacement and the stress state can be obtained at all degrees of freedom and finite elements. However, because industrial bladed disk FEMs usually have very many degrees of freedom, traditional FEA can be prohibitively expensive. To address this problem, researchers developed a variety of techniques (refs. 1 to 6) for constructing and analyzing FEM-based reduced-order models (ROMs). Although ROMs can solve the vibration response quickly and accurately relative to FEA, they are typically formulated in terms of modal and physical displacement variables for the bladed disk, whereas the primary variable of interest for durability and reliability studies is stress. For blade and/or disk stress levels, the displacements predicted by the ROM analysis can be projected back to finite-element coordinates and then postprocessed via FEA (ref. 4). However, this can be cumbersome and expensive, especially if this process needs to be repeated many times for a Monte Carlo simulation. To take full advantage of the ROM technique, it would be better to predict the increase in stress levels due to mistuning directly from the ROM.

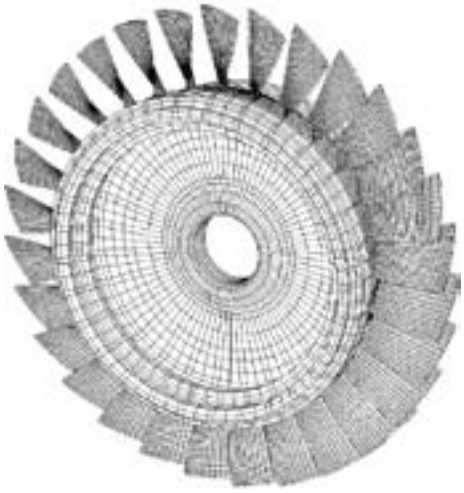

*Finite-element mesh for an industrial rotor.*

In this work, researchers at the NASA Glenn Research Center and University of Michigan proposed three normalized stress indicators (NSIs) as ROM-based measures of the level of blade stress in a mistuned bladed disk. All three can be calculated directly from the displacements obtained from ROM results, without an expensive FEA of stress.

The first NSI is formulated in terms of the Euclidean norm of the physical blade displacement vector, the second in terms of modal amplitudes, and the third in terms of blade strain energy. The FEM of an industrial rotor (preceding figure) with 29 blades was used to test the three proposed NSIs. Blade mistuning was implemented by varying Young's modulus in the finite elements of the blades, and 50 randomly mistuned systems were obtained.

The largest peak von Mises stress in each blade during a period of oscillation was calculated using the complex stress state for the finite-element centers obtained from the FEA. The results for the second and third flexural bending mode (2F and 3F) regions are shown in the left and right graphs, respectively, on the next page. Although all indicators underestimate the stress level (left graphs), the NSI based on the Euclidean norm is a better stress approximation than the other two NSIs. The data points in the right graphs are considerably more scattered than in the left graphs, especially for small NSI values, but the general trend is that the NSIs overestimate the blade stress level slightly. All three of the proposed NSIs show good agreement with the normalized largest von Mises stress.

The final graph shows that the results obtained with the FEM-based NSI and the ROM-based NSI match very well, and that they are in good agreement with the direct FEA stress calculation across the frequency range. Although all three NSIs showed good accuracy, the computational cost of the second NSI is significantly lower than the other two, especially when more than one dominant blade mode is present in a frequency range.

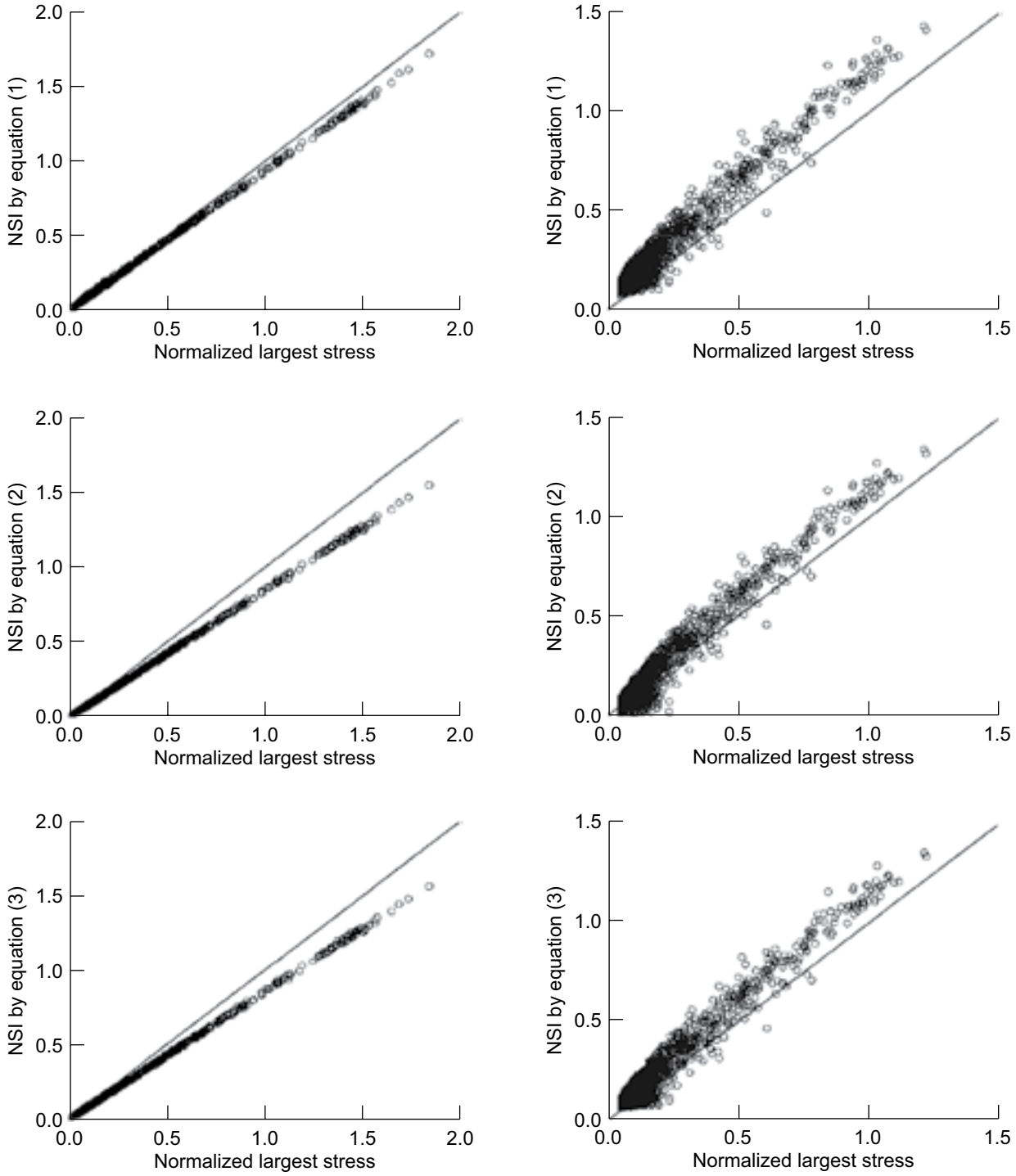


*Performance of normalized stress indicators for second (left) and third (right) flexural mode region. Top: Using Euclidean norm. Center: Using modal displacement. Bottom: Using strain energy.*

**References**

1. Castanier, M.P.; Óttarsson, G.; and Pierre, C.: A Reduced-Order Modeling Technique for Mistuned Bladed Disks. ASME J. Vib. Acoust. Trans. ASME, vol. 119, no. 3, 1997, pp. 439–447.
2. Yang, M.-T.; and Griffin, J.H.: A Reduced Order Approach for the Vibration of Mistuned Bladed Disk Assemblies. J. Eng. Gas Turbines Power, vol. 119, no. 1, 1997, pp. 161–167.
3. Yang, M.-T.; and Griffin, J.H.: A Reduced Order Model of Mistuning Using a Subset of Nominal System Modes. J. Eng. Gas Turbines Power, vol. 123, no. 4, 2001, pp. 893–900.
4. Bladh, R., et al.: Dynamic Response Predictions for a Mistuned Industrial Turbomachinery Rotor Using Reduced Order Modeling. J. Eng. Gas Turbines Power, vol. 124, no. 2, 2002, pp. 311–324.
5. Petrov, E.P.; Sanliturk, K.Y.; and Ewins, D.J.: A New Method for Dynamic Analysis of Mistuned Bladed Disks Based on the Exact Relationship Between Tuned and Mistuned Systems. ASME J. Eng. Gas Turbines Power, vol. 124, no. 3, 2002, pp. 586–597.
6. Lim, S., et al.: A Compact, Generalized Component Mode Mistuning Representation for Modeling Bladed Disk Vibration. AIAA–2003–1545, 2003.

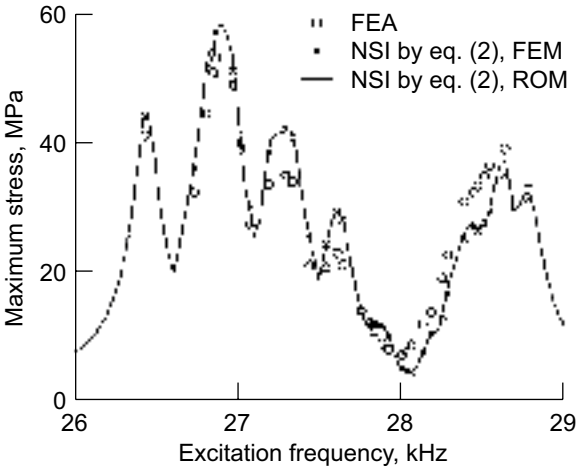


*Mistuned forced response in the 26- to 29-kHz frequency range, where the seventh cantilevered-blade mode is dominant.*

**Glenn contact:**
Dr. James B. Min, 216–433–2587, James.B.Min@nasa.gov

**Author:**
Dr. James B. Min

**Headquarters program office:**
Aeronautics Research Mission Directorate

**Programs/projects:**
Aviation Safety, Crew Exploration Vehicle, Constellation Systems

## Preliminary Tests Showed That Turbomachinery Blade Damping Coatings Are Effective

Excessive vibration of engine components causes high-cycle fatigue (HCF), shortening life. This leads to increased design and maintenance costs and can also lead to component failure. Newer high-performance engine designs have higher blade loading with lower inherent damping, resulting in increased resonant stresses. For example, recent turbomachinery designs include integrally bladed rotors (IBRs), where the disk and blades are manufactured together as a single component. IBRs have lower cost and weight and better performance; however, they lack the frictional damping that occurs at the attachment of a blade to the disk. Some airfoil shapes have a lower aspect ratio, leading to more complex modes that can be excited within the operating speed range. These higher-order modes have even lower damping and are less responsive to traditional damping treatments, such as platform friction dampers.

Designing damping treatments for rotating blades in an extreme engine environment is problematic. Temperatures can be very high, and centrifugal accelerations for rotor blades are on the order of tens of thousands of g's. A damping treatment must not affect the aerodynamics of the blade; therefore, it must be internal to the blade, out of the air stream, or applied to the blade surface in a thin layer. Many blades are very thin, making an internal damper difficult to

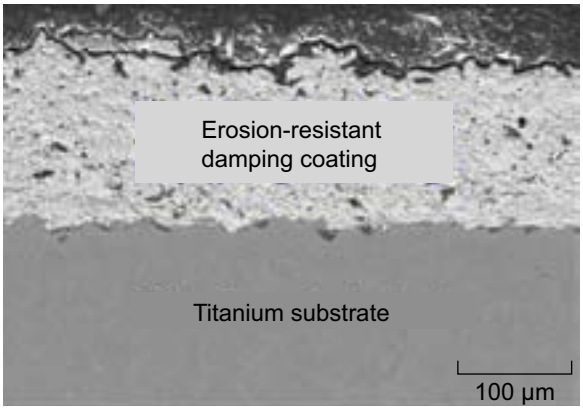


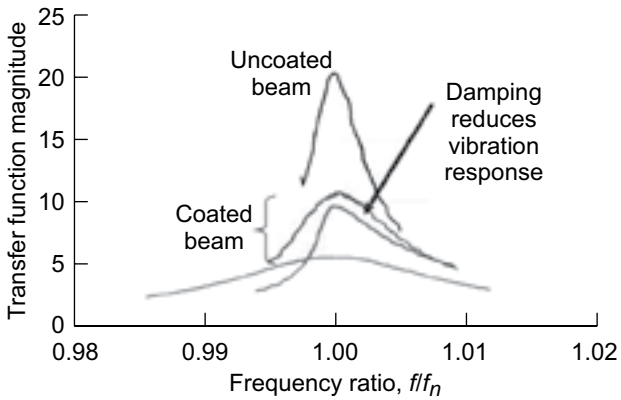


*Top: Damping coating microstructure. Bottom: Second bending mode stress reduction; $f/f_n$, ratio of forcing frequency to resonance frequency.*

implement. It is very challenging to design damping that can withstand the harsh engine environment and still be cost-effective and easily manufactured.

Researchers in the Structures and Mechanics Branch and the Durability and Protective Coatings Branch at the NASA Glenn Research Center are collaborating to develop air-plasma-sprayed damping coatings. Typically these coatings are used as environmental barrier coatings (EBCs) or thermal barrier coatings (TBCs). EBCs and TBCs are designed to function in the extreme engine environment and, since they are applied in a thin layer, do not adversely affect the blade's aerodynamics. Damping is believed to originate from friction within the coating microstructure (see the photomicrograph) and is nonlinear with strain.

Initial testing has begun to determine the effect of two different coatings on the bending vibration stresses in small titanium beams. The first coating is an yttria-stabilized-zirconia formulation—a ceramic TBC—and the second coating is a tungsten-carbide-cobalt formulation—an erosion-resistant coating. Each coating was sprayed onto an 8- by 0.75- by 0.092-in. beam in 0.005- or 0.013-in. thicknesses. The beams were then vibration tested at room temperature to determine the damping coefficient at various strain levels and for different bending modes. Preliminary test results have been encouraging, showing that the resonant stress can be reduced by as much as 75-percent, depending on the coating thickness and bending mode (see the graph).

**Glenn contacts:**
Robert Miller, 216–433–3298, Robert.A.Miller@nasa.gov

QuynhGiao Nguyen, 216–433–6073, Quynhgiao.N.Nguyen@nasa.gov

**Authors:**
Dr. Kirsten P. Duffy, Dr. Robert A. Miller, and QuynhGiao N. Nguyen

**Headquarters program office:**
Fundamental Aeronautics Program

**Programs/projects:**
Subsonic Fixed Wing

# New Turbulence and Transition Models Implemented Into Turbomachinery Aeroelastic Analysis Code

Advanced turbulence and transition models have been implemented into NASA Glenn Research Center's TURBO code (Reynolds-Averaged Navier-Stokes solver) to improve and extend its capability of modeling turbomachinery flows. This will enable better prediction of steady and unsteady loads on fan and compressor blades at on-design and off-design operating conditions. As a result, aeroelastic vibrations and high-cycle fatigue failures in gas turbine engine blades will be better predicted and avoided over a wider range of operating conditions. Avoidance of aeroelastic blade vibrations and fatigue failures will improve the safety and reliability of aircraft propulsion systems.

As the flow goes over blade surfaces, boundary layers are formed that may be laminar, transitional, or turbulent. The accurate modeling of these flow regimes is necessary for an accurate prediction of steady and unsteady loads on the blade. When a turbomachinery blade row operates at off-design conditions, the angle of incidence of the flow can be quite large, resulting in separation of the flow away from the surface over a portion of the blade. Numerical modeling of separated flows is very challenging and requires accurate modeling of transition and turbulence. Prior to the current work, the TURBO code required the user to prescribe a transition location on the blade surface at which the flow model was abruptly changed from laminar to turbulent. In reality, the flow goes through a transition region in which the flow is neither laminar nor fully turbulent. As a result of the current work, the TURBO code now includes the capability to calculate a transition onset location and to calculate a modified turbulent viscosity based on a transition model. The transition model now implemented into the TURBO code is the Solomon-Walker-Gostelow model, and the turbulent eddy viscosity is now modeled using the Spalart-Allmaras turbulence model.

The TURBO code with the improved modeling capability described here was used to model flow through Glenn's Transonic Flutter Cascade (ref. 1). Calculations were carried out at low and high flow incidence angles at which experimental data were previously acquired by Glenn researchers. For the high-incidence condition, the new turbulence and transition modeling capability clearly showed an improved flowfield prediction. In particular, the pressure plateau noted in the experimental data, and not correctly modeled with the assumption of fully turbulent flow, was captured well with the new modeling capability.

The research work described here was performed under a grant to Dr. Vincent R. Capece (University of Kentucky, Paducah, KY) and Dr. Max F. Platzer (Naval Postgraduate School, Monterey, CA). This work was supported by the Ultra-Efficient Engine Technology Project, Dr. Robert J. Shaw, manager.

**Reference**

1. Whitlow, D., et al.: Navier-Stokes Computations of the Flow Through the NASA–GRC Transonic Flutter Cascade. AIAA–2006–4455, 2006.

**Glenn contacts:**
Dr. James B. Min, 216–433–2587, James.B.Min@nasa.gov

Dr. Milind A. Bakhle, 216–433–6037, Milind.A.Bakhle@nasa.gov

**University of Kentucky contact:**
Dr. Vincent R. Capece, 270–534–3123, vcapece@engr.uky.edu

**Naval Postgraduate School contact (currently at AeroHydro Research & Technology Associates):**
Dr. Max F. Platzer, 831–521–0587, platzer@ahrta.com

**Authors:**
Dr. Milind A. Bakhle, Darryl Whitlow, Dr. Vincent R. Capece, Dr. Kevin D. Jones, and Dr. Max F. Platzer

**Headquarters program office:**
Aeronautics Research Mission Directorate

**Programs/projects:**
Ultra-Efficient Engine Technology

# Hybrid Pulse Detonation Engine Turbine Blades Analyzed

A hybrid aircraft engine, where a combustion chamber with multiple detonation tubes precedes a turbine stage, is being studied at the NASA Glenn Research Center. These engines, known as pulse detonation engines (PDEs), operate with constant-volume combustion, rather than the constant-pressure combustion that is currently used in gas turbine engines, and have been predicted to be more efficient than current aeronautical propulsion systems. However, the structural integrity of the turbine blades for PDEs needs to assessed.

High-momentum fluid exiting from the detonation tubes results in large input pressure fluctuations for the downstream turbine rotor blades. These fluctuations may excite the natural modes of the blades, resulting in multiple resonance conditions. Forced vibration at or near these resonant conditions is the primary contributing factor to high-cycle fatigue (HCF) failures. In order for the design to operate safely, the turbine must avoid all the resonant conditions. However, it may not be possible to avoid these multiple engine-order crossings in a hybrid-PDE turbine, so the magnitude of the stresses and displacements must be predicted at multiple resonant conditions to ensure safe operation.

The objectives of this study were to predict the unsteady aeroelastic response on the turbine rotor blades and assess the safety of the rotor blades. To accomplish this, researchers used a finite-volume-based Navier-Stokes solver developed at Mississippi State University (MSU–TURBO) to calculate the flow field around the turbine stage. The unsteady solution is an improved model in which the detonation tubes are included as part of the computational domain. The solution was written in blocks, and a postprocessor assembled the parts of the blocks that make up the rotor grid.

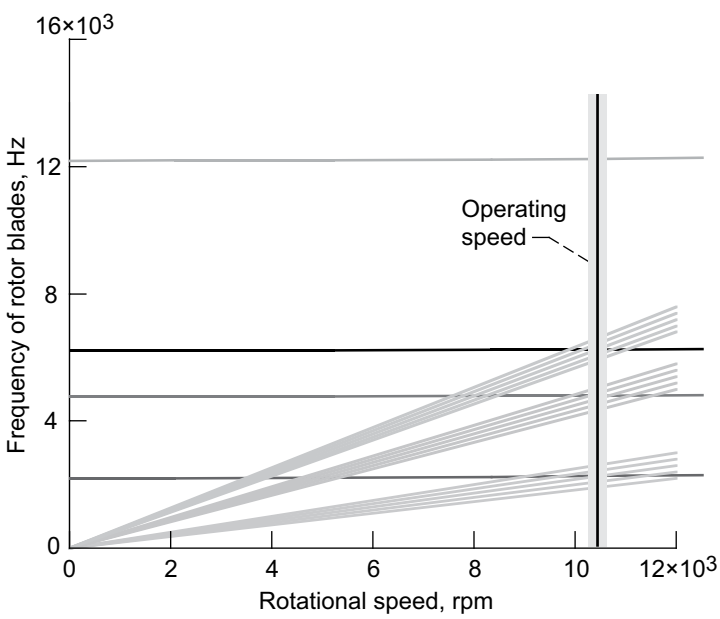


*Campbell diagram showing multiple engine orders close to the first, second, and third modes.*

The unsteady pressures were Fourier analyzed to obtain the frequencies and the magnitudes of the corresponding mean, and the unsteady pressures. The pressures were then converted to grid nodal forces for use by the structural analysis program.

A free-vibration analysis used ANSYS structural analysis software (ANSYS, Inc.) to obtain the mode shapes and modal frequencies of the rotor blade at six rotating speeds, resulting in the following Campbell diagram. The diagram plots the modal frequencies with rotational speed, for various engine orders, modified for a PDE application. It indicates that the response has to be analyzed near the first three modal frequencies for multiple engine orders at the rotor operating speed. The mode superposition method was used to predict the structural response. Six modes were used in the modal summation, and the analysis was repeated with various values of structural damping.

The graph on the next page shows the response and stress obtained with varying damping for the loading condition corresponding to the 36th engine order. The response obtained at 6170 Hz, close to the third-mode frequency, is shown. Just 0.3-percent damping reduced the stresses and blade displacements by about 75 percent. This amount of damping is typically present in rotor blades because of the friction at the blade root-disk interface. The analysis showed that flightweight turbine blades can be built to survive the pulse detonation loadings in a hybrid PDE engine.

The present study was performed under a NASA grant to University of Toledo researchers in collaboration with Glenn researchers. This work was supported by the Low-Emissions, Alternative Power Project, under the Constant Volume Combustion Cycle Engine subproject, Leo Burkardt, manager.

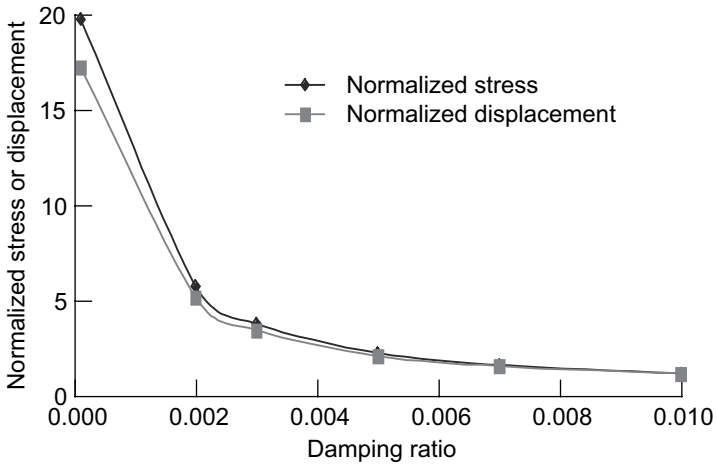


*Normalized response and stress variation with damping for engine order 36.*

**University of Toledo contact:**
Dr. T.S.R. Reddy, 216–433–6083, Tondapu.S.Reddy@nasa.gov

**Glenn contacts:**
Dr. James B. Min, 216–433–2587, James.B.Min@nasa.gov

Dr. Milind A. Bakhle, 216–433–6037, Milind.A.Bakhle@nasa.gov

George L. Stefko, 216–433–3920, George.L.Stefko@nasa.gov

**Authors:**
Dr. T.S.R. Reddy, Dr. James B. Min, Dr. Milind A. Bakhle, George L. Stefko, and Dr. Dale E. VanZante

**Headquarters program office:**
Aeronautics Research Mission Directorate

**Programs/projects:**
Low-Emissions, Alternative Power Project, Constant Volume Combustion Cycle Engine subproject

## Power Electronics for Switched-Reluctance Motor Improved

The NASA Glenn Research Center conducts aeronautics research on improving the fuel efficiency and reducing the noise and emissions of aircraft engines. Glenn researchers are considering the use of a hybrid drive with propulsors driven by electrical motors and primary power provided by a turbogenerator or fuel cell that could burn traditional fuel or hydrogen. A hybrid drive may be more efficient with lower emissions than a typical aircraft engine; however, the mass penalty is too high when standard electrical motors and drives are used.

Glenn's Structural Mechanics and Dynamics branch has begun research in increasing the power-to-mass ratio (specific power) of several types of motors for consideration in different size categories of aircraft. The cryogenic switched-reluctance motor (cryo-SRM) described by Brown et al. (refs. 1 to 4) has experimentally demonstrated higher specific power than any other SRM we are aware of, most recently exceeding 7 hp/lb-EM (horsepower per pound of electromagnetic weight). The enhanced motor coil design and the increased current capability of the power electronics were the source of these improvements.

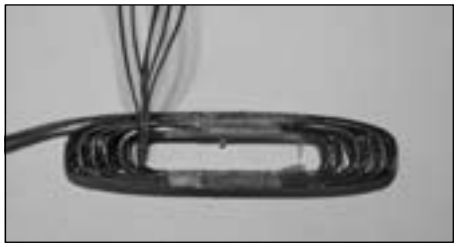

*Front view of "self-finned" coil for cryogenic switched-reluctance motor stator showing a six-layer coil with space between the end turns.*

The cryo-SRM coils are designed to carry maximum current by increasing heat transfer through the use of a finned end-turn design. The coils are wound so that each layer of end turns forms

a passage several wire diameters wide for cryogenic fluid to pass through; as the cryogen passes through the coil, it boils and carries heat away. This design allows an 18-gauge copper wire to carry approximately 70 $A_{rms}$, which equates to a 100-A-peak square current waveform for the SRM motor. Initially our coil design was four layers thick with 80 turns, which provided 8000 A-turn capacity. Improvements in winding methods resulted in a progression to a six-layer, 18-turn coil with six parallel conductors. The improved coil has a capacity of 10,800 A turns, with 35 percent more copper and 1/20th of the inductance. These changes allow the motor to be run at higher field strengths and allow the current to be switched more quickly, resulting in a current waveform that is much closer to ideal (square). These improvements result in a higher generated torque at high shaft speeds and hence to an increased power-to-mass ratio.

The drive power electronics, switching at 20 kHz, were also enhanced. Initially a 2.5-kW pulse-width-modulated drive capable of 170 V and 15 A continuous was used on each coil. Several more iterations resulted in a pair of inverters specially configured to drive an SRM motor, a capacitive direct-current bus filter, and a custom analog control circuit to power each coil. This 126-kW system, switching at 20 kHz, is capable of 300 V and 420 A continuous. We have been unable to test the limits of this system because we have reached our dynamometer capability, but we are developing new test procedures to allow higher speed operation. Future work in the power electronics area is planned to support a second-generation SRM motor that is designed to operate at higher specific power than the present motor.

**References**


1. Brown, Gerald V.: Cryogenic Electric Motor Tested. Research & Technology 2003, NASA/TM—2004-212729, 2004, pp. 162–163. http://www.grc.nasa.gov/WWW/RT/2003/5000/5930brown.html
2. Brown, Gerald V.; and Siebert, Mark W.: Switched-Reluctance Cryogenic Motor Tested and Upgraded. Research & Technology 2004, NASA /TM—2005-213419, 2005, pp. 137–139. http://www.grc.nasa.gov/WWW/RT/2004/RS/RS14S-brown.html
3. Brown, Gerald V., et al.: Performance of Switched-Reluctance Cryogenic Motor Tripled. Research & Technology 2005, NASA/TM—2006-214016, 2006, p. 166. http://www.grc.nasa.gov/WWW/RT/2005/RX/RX50S-brown.html
4. Brown, Gerald V., et al.: Specific Power of Cryogenic Motor Increased 50 Percent. Research & Technology 2006, NASA/TM—2007-214479, 2007, pp. 281–282. http://www.grc.nasa.gov/WWW/RT/2006/RX/RX51S-brown.html



**Glenn contacts:**
Gerald V. Brown, 216–433–6047, Gerald.V.Brown@nasa.gov

Jeffrey J. Trudell, 216–433–5303, Jeffrey.J.Trudell@nasa.gov

**University of Toledo contact:**
Ralph H. Jansen, 216–433–6038, Ralph.H.Jansen@nasa.gov

**Sierra Lobo, Inc. (SLI) contact:**
Timothy P. Dever, 216–433–2384, Timothy.P.Dever@nasa.gov

**Authors:**
Ralph H. Jansen, Dr. Gerald V. Brown, Timothy P. Dever, and Jeffrey J. Trudell


**Headquarters program office:**
Aeronautics Research Mission Directorate

**Programs/projects:**
Propulsion and Power, Vehicle Systems Program, Revolutionary Aeropropulsion Concepts, Alternate Energy Foundation Technologies, Subsonic Propulsion

# Self-Levitated Switched-Reluctance Motor Demonstrated Successfully at Low Temperatures for Non-Combustion-Based Propulsion

The NASA Glenn Research Center has developed and successfully demonstrated a self-levitated motor control technology for a 12–8 (12 poles in the stator and 8 poles in the rotor) switched-reluctance motor operating in liquid nitrogen (boiling point, 77 K (–196 °C, or –321 °F)). This year, Glenn's Bearingless Motor Control Team pushed previous disciplinary limits of electromagnetic controller technique by extending the state-of-the-art bearingless motor (see the photograph) operating at liquid nitrogen for high-specific-power applications. The motor was levitated even in its nonlinear region of magnetic saturation, which is believed to be a world first for the motor type.

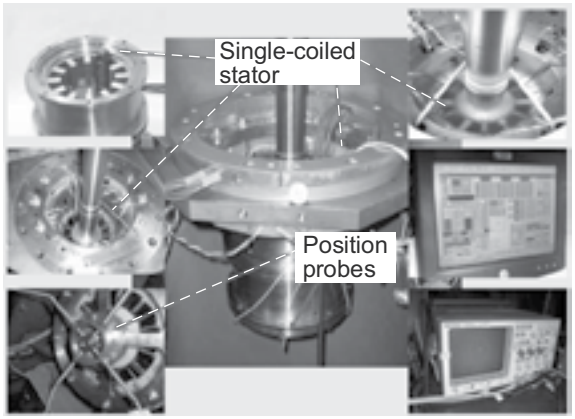


*Glenn's bearingless, cryogenic switched-reluctance motor.*

Early in fiscal year 2006, the Bearingless Motor Team demonstrated self-levitation of the motor at room temperature by limiting the coil currents to the linear region to avoid magnetic saturation as the first step of the study. The present work demonstrated self-levitation well into the fully saturated magnetic region where a super-high-power-density motor operates. The team developed two innovative features in hardware and software. First, the motor does not have separate coils for motor action and magnetic bearing action, but only motor coils as in a conventional motor configuration. Second, because it does not use a mathematical plant model, this simple observation-based controller avoids mathematical complexity and can be implemented in real-time at much higher rotor speeds. The following figures show the rotor orbit within the backup bearing clearance circle at rotor speeds to 4000 rpm, with the maximum available current for the existing amplifier.

These unique features can significantly reduce controller design time and overall system weight by eliminating separate mechanical or magnetic bearing systems and the associated plumbing and electrical subsystems. Furthermore, they drastically improve overall system efficiency (increasing net power) and reliability because of the simple architecture that needs no additional magnetic bearing system. This noncontact rotor bearing system operating at extremely low temperature is an enabling technology for future NASA missions in space exploration. In addition, this pioneering research can help bring to reality an all-electric, quiet, pollution-free aircraft propulsion system. This work is in support of the Noncombustion Based Propulsion Project.

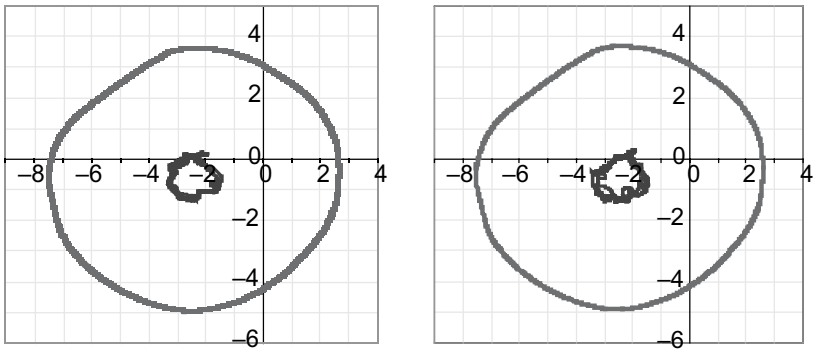


*Rotor orbits within backup bearing clearance circle. Left: 20 A at 4000 rpm. Right: 22 A at 4000 rpm.*

**Glenn contacts:**
Benjamin B. Choi, 216–433–6040, Benjamin.B.Choi@nasa.gov

Gerald V. Brown, 216–433–6047, Gerald.V.Brown@nasa.gov

**Authors:**
Dr. Benjamin B. Choi and Mark W. Siebert

**Headquarters program office:**
Aeronautics Research Mission Directorate

**Programs/projects:**
Noncombustion Based Propulsion Project, Propulsion and Power, Alternate Energy Foundation Technologies

# Electrical Model Developed To Predict Blade Tip Drive Rig Performance

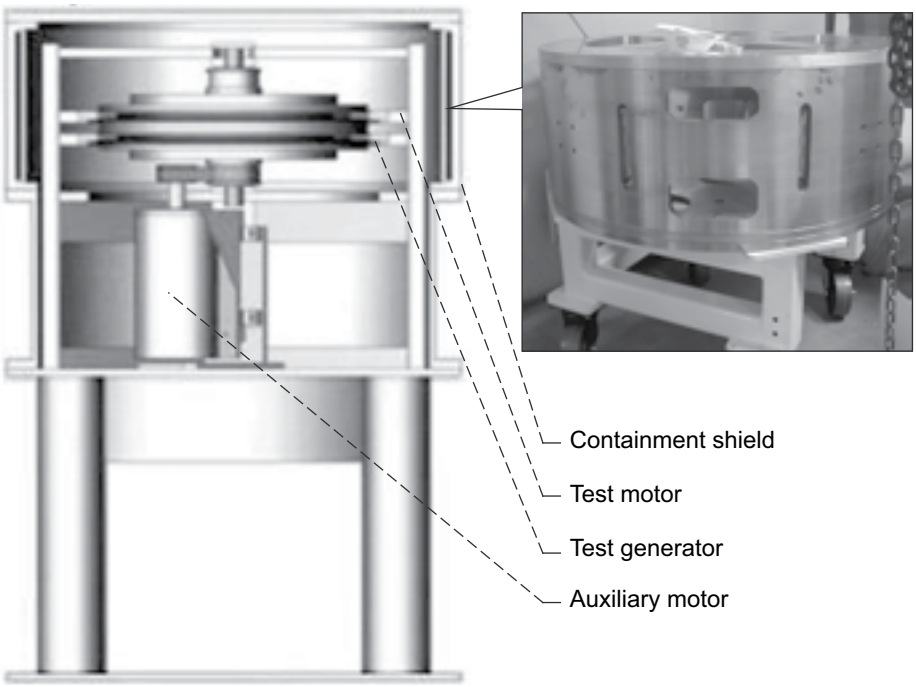


*Blade tip drive test rig.*

Electric motors for helicopter tail drives must have very high specific power. An effective technique for raising specific power is to locate the motor on the periphery of the tail drive fan. The NASA Glenn Research Center has been developing an axial motor/generator rig to develop technology and analysis methods for possible future application on helicopters that may utilize high-speed tip-drive motors and generators that would replace the tail rotor drive shaft.

This rig was designed by Glenn and is being tested by Texas A&M University at their spin pit facility (see the photograph). The rig being developed has an integral generator and motor on a shaft that is driven by an auxiliary conventional motor. The rig has the advantage that it does not need an external power supply for the test motor. Also, the speed of the rig is controlled by the auxiliary motor speed control. The test generator produces the current to drive the test motor, and the test motor and auxiliary motor produce the torque to drive the generator. The stator torques are measured with a load cell, and the mechanical indexing of the generator stator is used to set the phase of the current to the motor stator. The motor and the generator electromagnetic forces (EMFs) are set by shimming the magnet gaps that enclose the stators.

The coil resistances, mutual inductances, and current capacity have been measured. The induced EMF measurements of the generator and motor have been made at low tip speed (mach 0.15). The rig has been run to full current levels (150 A) and at half speed (mach 0.5). Some of these results were reported in reference 1.

To guide upgrades in stator coil geometry and to validate analysis methods that can be extended to flight test motors, a model was developed to predict the motor/generator performance. Some of the predicted results are shown in the graph on the next page, which shows that the motor might produce 600 kW at mach 0.90. The motor was designed to operate at mach 1.2 from a strength aspect, but there are thermal issues, both aero and electrical, that could limit its power. Motor tests are being made to verify this model.

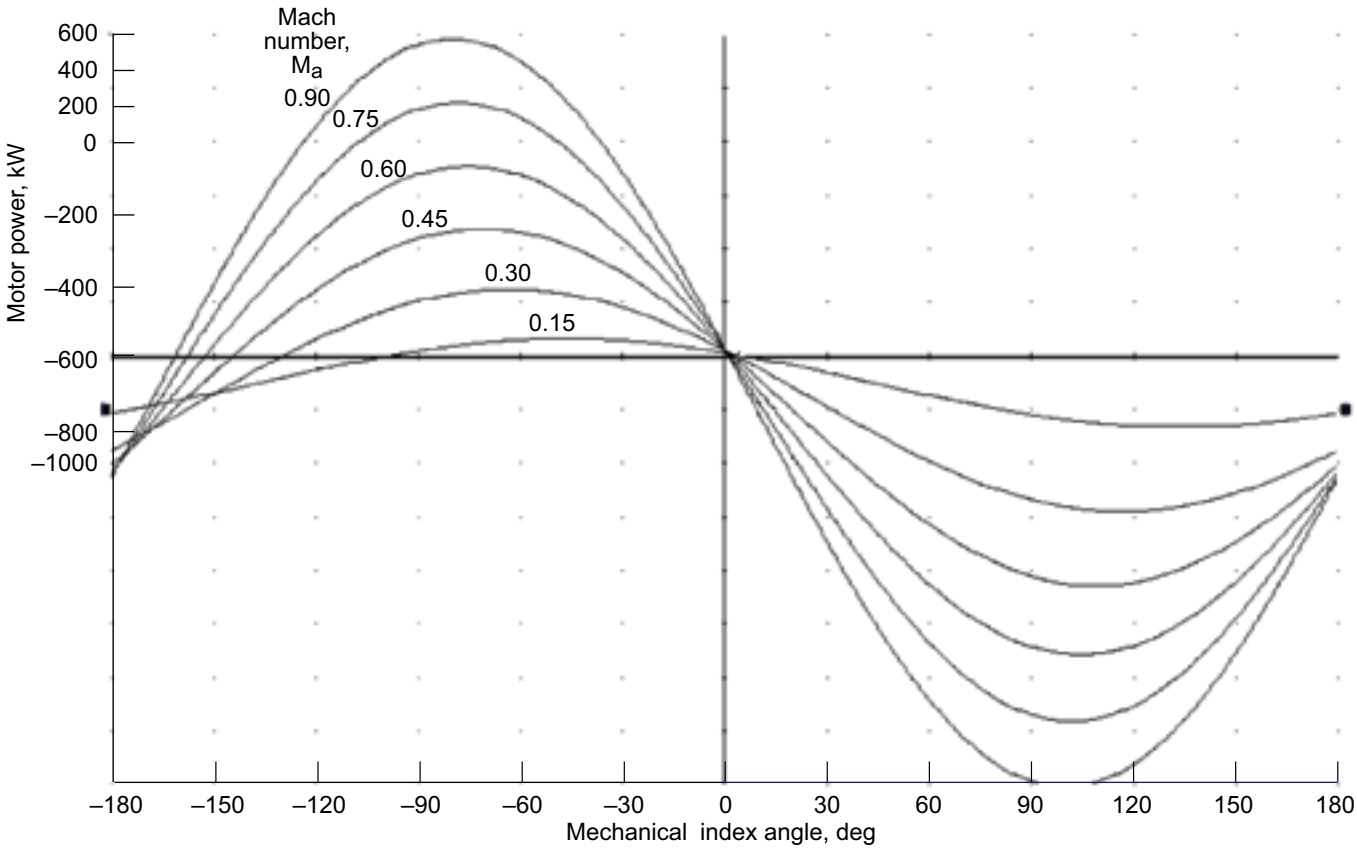


$$P = \mathrm{Re}\left(\frac{(4.43)^2}{0.067}\left(\frac{M_a}{0.15}\right)^2\left(\frac{(48.8)}{(43.4)}e^{-i\Delta\varphi} - 1\right)\begin{bmatrix} i \\ (1-i)/2 \\ -i \\ (1+i)/2 \end{bmatrix}^T \left([1] + i\left(\frac{1600\,\pi}{0.067}\right)\left(\frac{M_a}{0.15}\right)\begin{bmatrix} 11.4 & 4.6 & 2.4 & 0.095 \\ 4.6 & 11.4 & 4.6 & 2.4 \\ 2.4 & 4.6 & 11.4 & 4.6 \\ 0.095 & 2.4 & 4.6 & 11.4 \end{bmatrix}\right)^{-1} \begin{bmatrix} 1 \\ (1+i)/2 \\ i \\ (1-i)/2 \end{bmatrix}\right)$$

*Motor power versus mechanical index angle for a series of mach numbers from 0.15 to 0.90. Power, P, is the product of the magnitude of the current, the magnitude of the motor EMF, and the cosine of the angle between them—which is equal to the real part of the complex expression, Re. Mach number, $M_a$, is the ratio of the blade peripheral or tip speed to the standard speed of sound.*

**Reference**


1. Dibua, Imoukhuede Tim Odion: Development of a High Power Density Motor for Aircraft Propulsion. Master's Thesis, Texas A&M University, College Station, TX, 2007. http://handle.tamu.edu/1969.1/4933


**Glenn contacts:**


Albert F. Kascak, 216–433–6024, Albert.F.Kascak@nasa.gov

Jeffrey J. Trudell, 216–433–5303, Jeffrey.J.Trudell@nasa.gov


**Authors:**


Albert F. Kascak and Jeffrey J. Trudell


**Headquarters program office:**

Aeronautics Research Mission Directorate

**Programs/projects:**

Propulsion and Power, Vehicle Systems Program, Revolutionary Aeropropulsion Concepts, Alternate Energy Foundation Technologies, Subsonic Propulsion

# Room-Temperature Bearingless Electric Motor Technology Demonstrated for Future NASA and Aerospace Missions

The NASA Glenn Research Center has been developing high-power-density motors (refs. 1 and 2) for possible use for NASA and aerospace missions. One design would use turbogenerators to develop electric power for motors that rotate a hydrogen-fueled aircraft's propulsive fans or propellers. If hydrogen was carried as a liquid, it could provide essentially free refrigeration to cool electric motor windings before being used as fuel. Recently, we demonstrated improved performance of a switched-reluctance motor, stemming mainly from cryogenic operation and coil design, surpassing (we believe) previous specific torque and specific tangential force records for the motor type. We anticipate further increases in motor specific power from upgrades to electric power conditioning and coil windings.

However, cryogenic operation at higher rotational speeds markedly shortens the life of mechanical rolling element bearings. Even without cryogenics, conventional bearing life may be limited at the high speeds possible with switched-reluctance motors. Thus, a non-contact rotor-bearing system is a crucial technology for demonstrating the practical feasibility of using this high-power-density motor. During the last decade, a variety of bearingless motors were introduced, including permanent magnet, induction, and reluctance types. The switched-reluctance motor is a favored candidate for future airborne systems because it has inherent fault tolerance and has rotor robustness and reliability at high rotational speeds (no coil windings on the rotor).

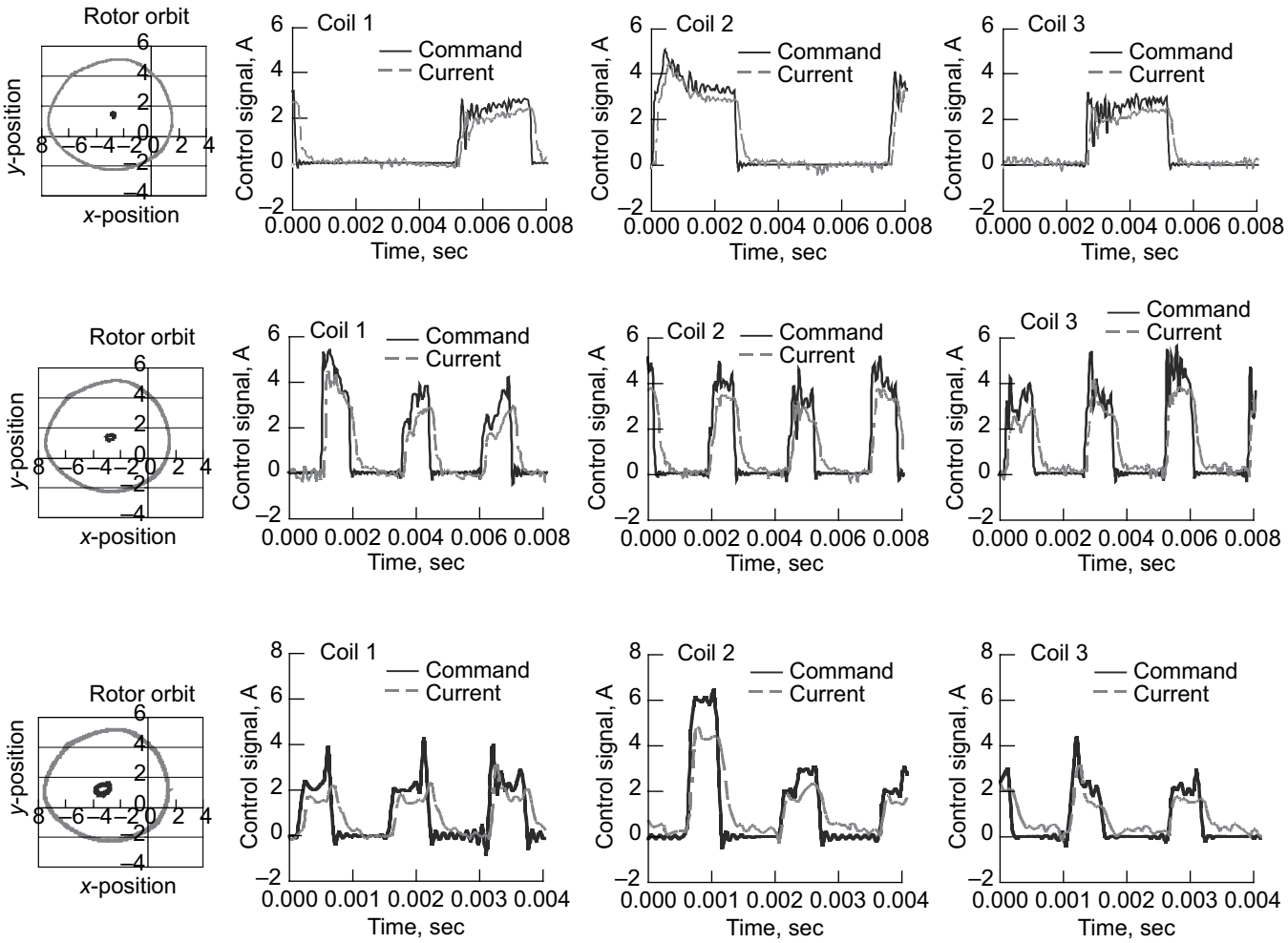


*Rotor orbit within backup bearing clearance circle, command signals, and actual currents of different coils. Top: 1000 rpm. Center: 2000 rpm. Bottom: 5000 rpm.*

Since the switched-reluctance motor has a doubly salient[1] structure, an exact analytical expression for its plant model cannot be obtained. Numerous authors have addressed this problem with solutions using the Maxwell stress tensor, the finite-element method (FEM), a flux tube, and so forth. In 2001, Takemoto et al. published a successful controller demonstration of a 12–8 (12 poles in the stator and 8 poles in the rotor) bearingless switched-reluctance motor up to 2500 rpm (ref. 3). They developed a much simplified mathematical expression of the radial bearing force equation based on results of FEM analysis to express fringing fluxes and neglect magnetic saturation. However, they added a separate magnetic bearing coil winding to each stator pole motor winding for the rotor levitation.

Glenn's Self-Levitation Team began by describing a model-based controller, mainly following the procedure developed by Takemoto et al., but modifying the controller somewhat on the basis of some three-dimensional finite-element results. The resulting controller was successfully demonstrated experimentally. Then, we demonstrated a much simpler observation-based proportional-derivative controller for levitation, which does not require any mathematical plant models and is advantageous at high motor speeds because it is less computationally intensive. However, the demonstration was at room temperature with the coil currents limited to the linear region to avoid magnetic saturation.

We ran the motor from 0 to 6500 rpm (maximum allowable speed at that time) with small rotor orbits. The graphs on the preceding page show the experimental rotor orbit (within the backup bearing clearance circle), the command signal from the controller, and the actual current applied to the pulse-width-modulated amplifier for each phase. The rotor was quite stable and stayed within less than 10 percent of the backup bearing clearance (±10 mils). The required levitation current was less than 10 percent of the motoring current.

This technology could significantly reduce overall system weight and increase system reliability and specific net power, preparing the way for an all-electric, quiet, pollution-free aircraft propulsion system. This work is supported by the Noncombustion Based Propulsion Project.

**References**


1. Brown, Gerald V.; and Siebert, Mark W.: Switched-Reluctance Cryogenic Motor Tested and Upgraded. Research & Technology 2004, NASA/TM—2005-213419, 2005, pp. 137–139. http://www.grc.nasa.gov/WWW/RT/2004/RS/RS14S-brown.html
2. Brown, G.V., et al.: NASA Glenn Research Center Program in High Power Density Motors for Aeropropulsion. NASA/TM—2005-213800 (ARL–MR–0628), 2005. http://gltrs.grc.nasa.gov/cgi-bin/GLTRS/browse.pl?2005/TM-2005-213800.html
3. Takemoto, Masatsuga, et al.: A Design and Characteristic of Switched Reluctance Type Bearingless Motors. Proceedings of the 4th International Symposium on Magnetic Suspension Technology. NASA/CP—1998-207654, 1998, pp. 49–63.


[1]A switched-reluctance motor has a salient (tooth-shaped) stator and rotor.


**Glenn contacts:**
Benjamin B. Choi, 216–433–6040, Benjamin.B.Choi@nasa.gov

Gerald V. Brown, 216–433–6047, Gerald.V.Brown@nasa.gov

**Authors:**
Dr. Benjamin B. Choi and Mark W. Siebert


**Headquarters program office:**
Aeronautics Research Mission Directorate

**Programs/projects:**
Noncombustion Based Propulsion Project, Propulsion and Power, Alternate Energy Foundation Technologies

# Specific Power of Cryogenic Motor Increased 50 Percent

Electric motors for aircraft must have very high specific power, and the most effective technique for raising specific power is cryogenic cooling. The NASA Glenn Research Center has been developing cryogenic switched-reluctance motor technology and analysis methods in-house for possible future application on aircraft that may utilize liquid hydrogen fuel. Motor coil current capacity measurements and locked-rotor torque measurements have been made to guide a series of upgrades in coil geometry and power electronics and to validate analysis methods that can be extended from our present liquid-nitrogen-cooled motors to liquid-hydrogen-cooled motors. Motor power tests have also been made with a progression of coil configurations, power electronics capacities, and motor speed. These results were reported previously (refs. 1 to 3).

We reported in reference 3 that the specific power of a switched-reluctance motor was tripled to 3.5 hp/lb-EM (horsepower per pounds electromagnetic), or 5.8 kW/kg-EM, from the previous report (ref. 2). That specific power number was somewhat underreported; with appropriate drag corrections, it was 4.6 hp/lb-EM (7.6 kW/kg-EM) produced at 12,000 rpm. Improvements in the motor windings and power electronics upgrades (described in ref. 4) have increased the specific power to 7.1 hp/lb-EM (11.7 kW/kg-EM) at 19,000 rpm. This specific power is 50-percent higher than that produced by switched-reluctance motors operating at room temperature or above. The dynamometer-measured shaft-power output, projected to the full motor and corrected appropriately for bearing and fluid drag, was 126 hp (94 kW). The motor has an EM weight (i.e., the weight of the magnetic core laminations and the copper windings) of 18 lb (8.2 kg). With a factor of 1.5 to convert from an EM weight to a total weight, the specific power would be 4.7 hp/lb-total (7.7 kW/kg-total).

*Switched-reluctance motor stator showing a variety of coils with "self-finned" construction for enhanced heat rejection.*

This testbed switched-reluctance motor with copper windings is operated in liquid nitrogen at current densities, specific torque, specific force, and specific power much higher than would be possible at room temperature. The stator and windings of the motor are shown in the photograph. The recent tests demonstrated the development of the magnetic forces and torques at higher speed than in previous tests, and the increased performance is the result of lower coil inductance, higher power electronics voltage and current capacity, and higher motor shaft speed. The low-speed specific torque of the motor reached 3.1 ft-lb/lb-EM (9.2 N-m/kg-EM), and the specific torque at maximum power was 2.1 ft-lb/lb-EM (6.3 N-m/kg-EM). These are at least twice the best specific torque numbers produced by switched-reluctance motors operating at room temperature or above.

To reduce the cost of power electronics, we energized the coils on only 2 of the 12 stator poles for the high-power tests. The reported results are the projections of those test results to the entire motor. Electric motors are often capable of significant overloads for short times. We must perform further testing to assure that steady-state performance has been obtained.

Further improvements will involve careful equalization of the inductances and mutual inductances of paralleled coils on each pole, a further reduction in coil inductance, and still higher power electronics capacity. A further 50-percent increase in specific power is possible from these improvements, plus operation nearer the calculated safe rotor structural limit of 30,000 rpm.

**References**

1. Brown, Gerald V.: Cryogenic Electric Motor Tested. Research & Technology 2003, NASA/TM—2004-212729, 2004, pp. 162–163. http://www.grc.nasa.gov/WWW/RT/2003/5000/5930brown.html
2. Brown, Gerald V.; and Siebert, Mark W.: Switched-Reluctance Cryogenic Motor Tested and Upgraded. Research & Technology 2004, NASA /TM—2005-213419, 2005, pp. 137–139. http://www.grc.nasa.gov/WWW/RT/2004/RS/RS14S-brown.html
3. Brown, Gerald V., et al.: Performance of Switched-Reluctance Cryogenic Motor Tripled. Research & Technology 2005, NASA/TM—2006-214016, 2006, p. 166. http://www.grc.nasa.gov/WWW/RT/2005/RX/RX50S-brown.html
4. Jansen, Ralph H., et al.: Power Electronics for Switched Reluctance Motor Improved, Research & Technology 2006, NASA/TM—2007-214479, 2007, p. 274–275. http://www.grc.nasa.gov/WWW/RT/2006/RX/RX47S-jansen.html

**Glenn contacts:**
Gerald V. Brown, 216–433–6047, Gerald.V.Brown@nasa.gov

Jeffrey J. Trudell, 216–433–5303, Jeffrey.J.Trudell@nasa.gov

**University of Toledo contact:**
Ralph H. Jansen, 216–433–6038, Ralph.H.Jansen@nasa.gov

**Sierra Lobo, Inc., contact:**
Timothy P. Dever, 216–433–2384, Timothy.P.Dever@nasa.gov

**Authors:**
Dr. Gerald V. Brown, Ralph H. Jansen, Timothy P. Dever, Dr. Aleksandr S. Nagorny, and Jeffrey J. Trudell

**Headquarters program office:**
Aeronautics Research Mission Directorate

**Programs/projects:**
Propulsion and Power, Vehicle Systems Program, Revolutionary Aeropropulsion Concepts, Alternate Energy Foundation Technologies, Subsonic Propulsion

## Magnesium Diboride Superconducting Coils Evaluated for Electric Aircraft Propulsion

The NASA Glenn Research Center investigated the possibility of using turbogenerators to produce electric power to drive electric motors to turn the propulsive fans or propellers of aircraft. The recent development of magnesium diboride ($MgB_2$) superconducting wires makes possible the potential for superconducting coils that weigh much less than any other metal or ceramic superconducting coils in applications cooled to 20 K, the temperature of liquid hydrogen.

*$MgB_2$ coil fabricated for a compression test. The compression plates and nylon bag used for epoxy impregnation are also shown.*

$MgB_2$ rotor coil segments were fabricated and tested by Hyper Tech Research, Inc., as part of a NASA Small Business Innovation Research contract to determine if satisfactory critical current density at high field will satisfy the requirements of aircraft motors cooled to 20 K. A rotor coil segment, shown in this photograph, underwent compression testing, with the results shown in the graph on the next page. The $MgB_2$ coil windings survived a force that would have been generated from the rotor operating at 15,000 rpm.

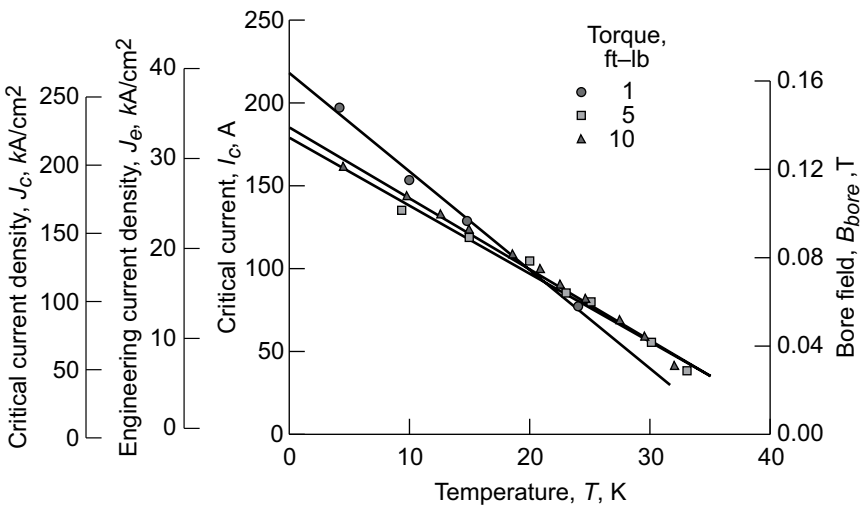


*Critical current, critical current density, engineering current density, and bore field versus temperature test results of three compression tests of a racetrack coil segment. Curves were linearly interpolated.*

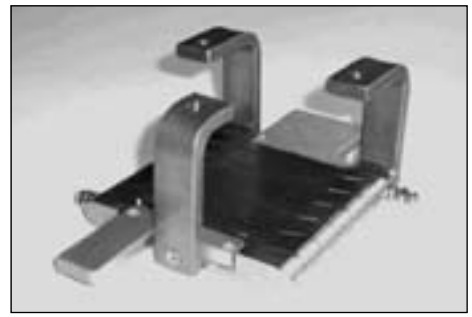

*$MgB_2$ stator coil segment with copper lead terminals and L-shaped support brackets attached.*

Hyper Tech Research, Inc., also designed, fabricated, and tested a representative alternating-current (ac) stator soil segment (see the photograph on this page). The present wire configurations are estimated to have acceptable levels of loss for 50-Hz, 20-K operation. An ac stator would significantly improve efficiency as well as power density. Methods have been identified to increase operation to 500 Hz, but these will require further wire development to reduce wire filament diameter without an impact on performance.

Complete $MgB_2$ rotor coil packs will be fabricated during 2007. The complete coil packs are designed to function in a 2-MW superconducting ac generator and could be tested by Glenn under realistic loads and cooling in the liquid hydrogen electric motor testbed, part of Glenn's Small Multi-Purpose Research Facility (SMiRF).

**Glenn contact:**
Jeffrey J. Trudell, 216–433–5303, Jeffrey.J.Trudell@nasa.gov

**Hyper Tech Research, Inc., contacts:**
Michael Tomsic, 614–481–8050, ext. 105, mtomsic@hypertechresearch.com

Matt Rindfleish, 614–481–8050, ext. 109, mrindfleisch@hypertechresearch.com

**Author:**
Jeffrey J. Trudell

**Headquarters program office:**
Aeronautics Research Mission Directorate

**Programs/projects:**
Propulsion and Power, Vehicle Systems Program, Revolutionary Aeropropulsion Concepts, Alternate Energy Foundation Technologies, Subsonic Propulsion

# Novel Bearingless Switched-Reluctance Motor Characterized by One-Dimensional Electromagnetic Radial Force Equations

A bearingless switched-reluctance motor (BSRM) has the combined characteristics of a switched-reluctance motor and a magnetic bearing. The BSRM developed by the NASA Glenn Research Center (refs. 1 and 2) incorporates a hybrid rotor configuration wherein a cylindrical-shaped portion of the rotor is used for levitation and a scalloped section is used for rotation. The asymmetric geometry of the rotor engenders a complex three-dimensional magnetic field topology in and around the rotor and would require complex mathematical analysis to completely describe the radial magnetic field affecting the rotor. However, we began our analysis with a one-dimensional approach, in an effort to reduce the mathematical complexity of the electromagnetic radial force derivation, and we found that it provided a good prediction of the forces. Each rotor segment (circular lamination stack and castellated lamination stack) was treated as an independent entity, and accordingly, the general one-dimensional radial electromagnetic force equation,

$$F = \frac{\mathrm{d}w(x)}{\mathrm{d}g(x)} = -\frac{A_o}{2\mu_o}\frac{\mathrm{d}}{\mathrm{d}x}\ [B^2(x)g(x)] \qquad (1)$$

was developed for each rotor segment. The function $w(x)$ represents the magnetic energy stored in the gap $g(x)$ between the stator and a rotor segment; $A_o$ is the common cross-sectional area between the stator and rotor pole; $\mu_o$ is the permeability of free space; and $B(x)$ is the magnetic field function. Determining a suitable mathematical form of the $B(x)$ function was critical in obtaining the correct electromagnetic radial force impinging on the hybrid rotor. The electromagnetic radial forces on each rotor segment were subsequently summed to obtain the total *levitation* magnetic radial force on the rotor. The analysis was done with the nonrotating rotor poles aligned with the appropriate stator poles to achieve the maximum levitated electromagnetic radial force loads on the rotor. Two magnetic circuit geometries, approximating the complex topology of the electromagnetic fields existing in and around the hybrid rotor, were employed in formulating the electromagnetic radial force equations.

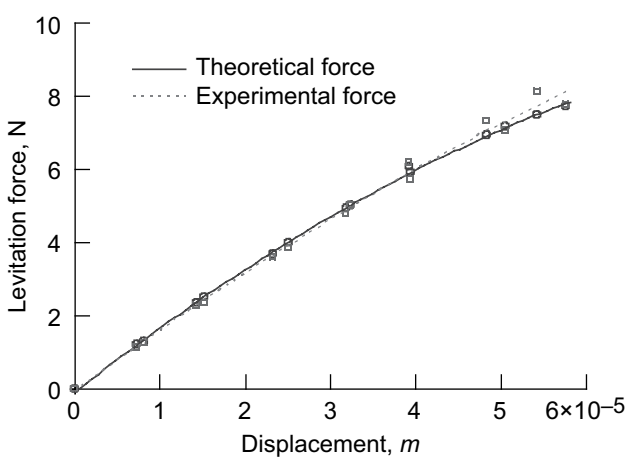


*Theoretical and experimental levitation radial forces.*

The graph shows that the theoretical and experimental results are in very close agreement. Hence, we have developed a very valuable analysis tool for designing future motors of this type for different mission applications. A pending publication (ref. 3) will give a complete description of the levitated and nonlevitated magnetic field and force characteristics of the motor and its rotor.

**References**


1. Morrison, Carlos R.: Bearingless Switched Reluctance Motor. U.S. Patent 6,727,618 B1, Apr. 27, 2004.
2. Morrison, Carlos R.: Improved Bearingless Switched-Reluctance Motor. NASA Tech Briefs, vol. 27, no. 10, 2003, pp. 68–70.
3. Morrison, Carlos R.; Siebert, Mark W.; and Ho, Eric J.: Electromagnetic Radial Forces in a Hybrid Magnetic-Bearing Switched-Reluctance Motor. NASA/TP—2007-214818 (to be published in IEEE Trans. Magnetics), 2007.



**Glenn contacts:**
Carlos R. Morrison, 216–433–8447, Carlos.R.Morrison@nasa.gov

Dr. Gerald V. Brown, 216–433–6047, Gerald.V.Brown@nasa.gov

**Authors:**
Carlos R. Morrison, Mark W. Siebert, Eric J. Ho, and Dr. Gerald V. Brown


**Headquarters program office:**
Aeronautics Research Mission Directorate

**Programs/Projects:**
Alternate Energy Foundation Technologies, Alternate Fuels Foundation Technologies

**Special recognition:**
2004 R&D 100 Award, Patent 6727618 B1, 2004 Space Act Award

# Ironless High-Power-Density Permanent Magnet Electric Motor Evaluated for Non-Combustion-Based Air Vehicles

The NASA Glenn Research Center has been investigating non-combustion-based aircraft propulsion through experimental and system tradeoff studies. Conventional electric motors are too heavy for use in large aircraft propulsion. To address this deficiency, a team at Glenn designed an ironless motor to evaluate flight applications.

In this design, the rotating magnetic flux is generated by two sets of axial Halbach arrays using high-energy-density permanent magnets. The magnetic flux is a maximum 1.2-tesla flux density at the center of a 0.5-in. gap (ref. 1) and approximately sinusoidal with respect to angle. The arrangement of the magnets eliminates the need for backiron in the motor, which is heavy and lossy.

In fiscal year 2006, one stator design was evaluated for static torque as a function of current and current-carrying capacity with and without forced air convection. Static torque measurements were made as a function of angle and current up to 104 A. A one-dimensional prediction of the torque was compared with the experimental data at 1.0-, 1,1-, and 1.2-tesla maximum flux in the gap. The graph shows good agreement between the experiment and the analytic one-dimensional prediction. Forced-air convection was demonstrated to increase the steady-state current-carrying capacity of the stator by 140 percent, from 42 to 104 A.

The effect of stator packing factor on the specific power of the motor was determined using the motor setup in the photograph. The packing factor is the percentage of the stator that is occupied by conductors.

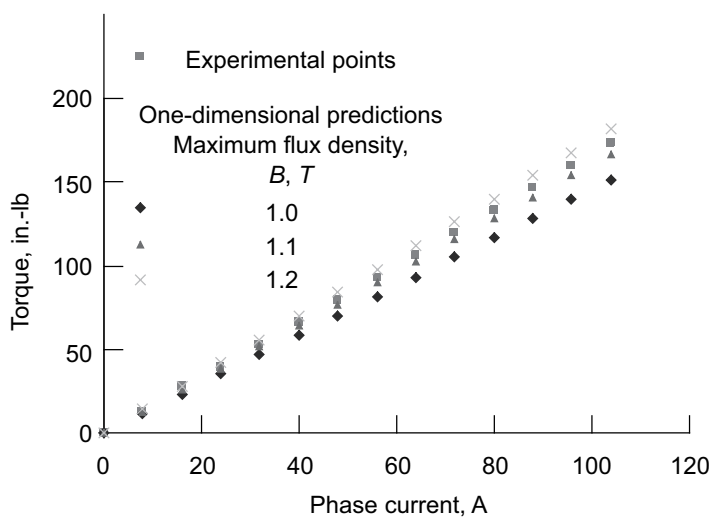


*Experimental results and one-dimensional predictions of torque as a function of current in one phase of the ironless motor at an angle of maximum torque. The one-dimensional predictions are for 1.0-, 1.1-, and 1.2-tesla maximum flux density.*

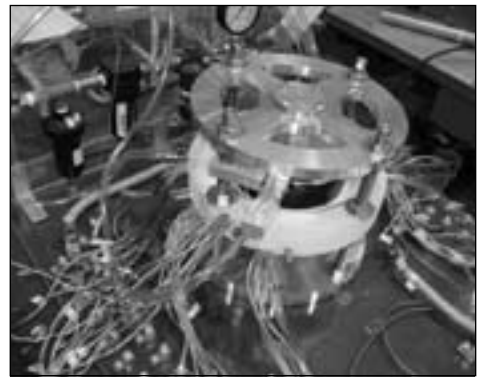

*Ironless motor setup for evaluation of static torque as a function of current and rotor angle. The current stator has a ~10-percent packing factor.*

The electromagnetic (EM) weight is defined as the weight of just the EM components (i.e., stator copper and permanent magnets). The total weight of a prototype motor is taken to be 50 percent more than the EM of the motor to account for structural support. The current stator (ref. 1) has only a 10-percent packing factor. As shown in the graph on the following page, the specific power of the current motor is 0.6 hp/lb using total weight and increases to 5 hp/lb for a 75-percent packing factor. A packing factor of 50 percent is more realistic and indicates that 3.4 hp/lb is realizable for this ironless motor running at room temperature and high speed. For comparison, the estimated horsepower per pound of the 98-percent-efficient Halbach motor designed by the Commonwealth Scientific and Industrial Research Organization (CSIRO) that was used in a solar-powered car in the World Solar Challenge race across Australia is shown. This work was supported by the Subsonic Rotary Wing Project.

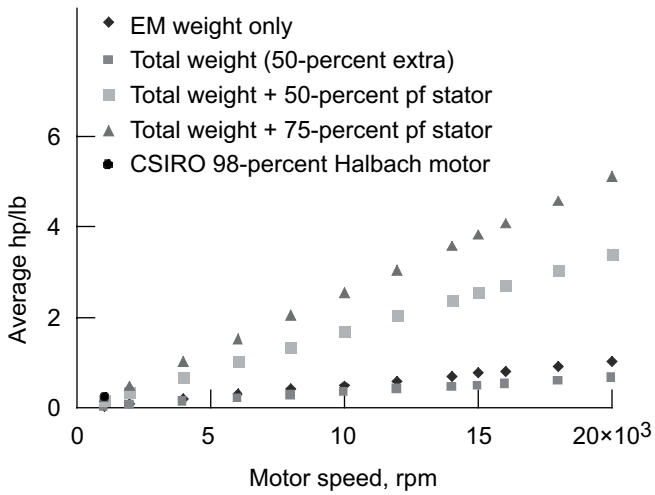


*Horsepower per pound as a function of packing factor (pf) in the stator and motor speed.*

**Glenn contact:**
Andrew J. Provenza, 216–433–6025, Andrew.J.Provenza@nasa.gov

**U.S. Army Research Laboratory at Glenn contact:**
Albert F. Kascak, 216–433–6024, Albert.F.Kascak@nasa.gov

**Authors:**
Mark W. Siebert and Andrew J. Provenza

**Headquarters program office:**
Aeronautics Research Mission Directorate

**Programs/projects:**
Propulsion and Power, Vehicle Systems Program, Revolutionary Aeropropulsion Concepts, Alternate Energy Foundation Technologies, Subsonic Propulsion, Subsonic Rotary Wing Project

**Reference**

1. Provenza, Andrew J.: Stator and Rotor Designed and Manufactured for an Ironless High-Power-Density Permanent Magnet Electric Motor for Pollution-Free Aircraft Propulsion. Research & Technology 2005, NASA/TM—2006-214016, pp. 162–163, 2006. http://www.grc.nasa.gov/WWW/RT/2005/RX/RX46S-provenza.html

## Liquid-Hydrogen-Cooled Electric Motors Test Facility Completed for Aircraft Propulsion

The NASA Glenn Research Center investigated, both through feasibility studies and experimental research, the possibility of using turbogenerators to produce electric power to drive electric motors to turn the propulsive fans or propellers of aircraft. Either jet fuel or hydrogen would power the turbogenerators. The demonstration of a hydrogen-powered aircraft would accomplish a NASA 21st century goal of pollution-free aircraft; and electrically driven fans or propellers offer alternative wing placements that could reduce noise, which continues to be a significant environmental problem. Conventional electric motors and their electronics are too heavy to use in these new systems and will likely require cryogenic cooling. Using superconducting coils on the rotor would eliminate the need for heavy rotor iron, and the cooling would be provided by a small cryocooler or would be available free if hydrogen fuel was stored on the airplane as a liquid.

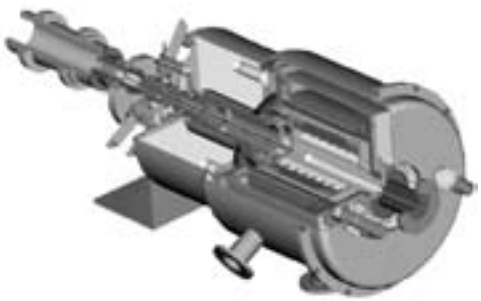

*Liquid-hydrogen-cooled, superconducting electric motor.*

The superconducting alternating-current generator shown in the illustration on the preceding page is being fabricated by Long Electromagnetics, Inc., (LEI), through NASA and U.S. Air Force contracts to serve as a testbed for evaluating superconducting and conventional materials in coil form in a realistic environment. The initial design will test second-generation bismuth strontium calcium copper oxide ($Bi_2Sr_2CaCu_2O_{8+\delta}$, or BSSCO) superconducting rotor coils. Testing in coil form is important because current densities typically are reduced by an order of magnitude from wire form. The design accommodates easy replacement of the coils and windings.

Glenn's Small Multi-Purpose Research Facility (SMiRF), shown in the photographs and used for general liquid hydrogen ($LH_2$) testing, has been modified to allow $LH_2$-cooled electric motor/generator testing. The modifications include concrete containment walls (see the bottom photograph), $LH_2$ supply lines, and data acquisition and control. The generator test stand design (see the figure on the next page) is complete. This work was supported by the Alternative Energy Foundation Technologies Project.

*Glenn's SMiRF location for $LH_2$ testing, and SMiRF modified for aeropropulsion electric motor testing.*

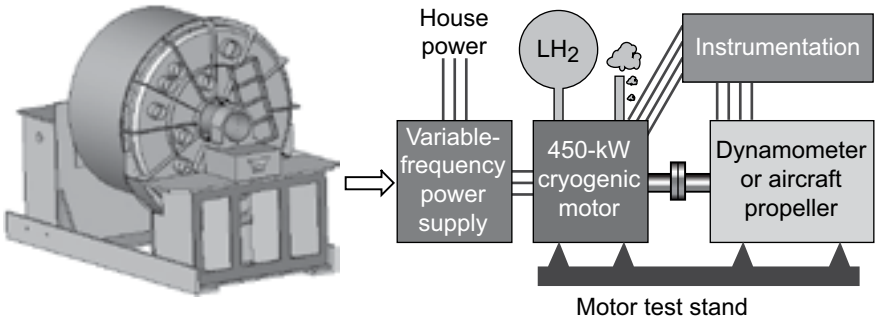


*Motor test stand for $LH_2$ testing.*

**Glenn contact:**
Jeffrey J. Trudell, 216–433–5303, Jeffrey.J.Trudell@nasa.gov

**Jacobs-Sverdrup Technologies, Inc., contact:**
Helmut H. Bamberger, 216–977–7450, Helmut.H.Bamberger@nasa.gov

**Gilcrest Electric & Supply Company contact:**
Timothy M. Czaruk, 216–433–3296, Timothy.M.Czaruk@nasa.gov

**U.S. Army Research Laboratory at Glenn contact:**
Albert F. Kascak, 216–433–6024, Albert.F.Kascak@nasa.gov

**Authors:**
Jeffrey J. Trudell and Albert F. Kascak

**Headquarters program office:**
Aeronautics Research Mission Directorate

**Programs/projects:**
Propulsion and Power, Vehicle Systems Program, Revolutionary Aeropropulsion Concepts, Alternate Energy Foundation Technologies, Subsonic Propulsion

## High-Temperature Active Clearance Control System Concept Performance Tests Successfully Completed at NASA Glenn

Seal leakage performance of an active clearance control (ACC) system concept (see the photographs on the next page) was characterized at elevated test temperatures and pressure differentials (up to 1000 °F and 120 psi, respectively) at the NASA Glenn Research Center. The ACC test rig was designed and fabricated to examine the feasibility of incorporating a fast-acting, mechanically actuated control system into the high-pressure turbine (HPT) section of a modern gas turbine engine to actively regulate the clearance between the blade tips and the surrounding sealing shroud. The rig simulates the HPT environment (temperatures and pressure differentials) present at the backside of the sealing shroud, and it facilitates the evaluation of actuators, clearance sensors, secondary seals, and other hardware needed to implement the clearance control concept into an actual engine.

Current gas turbine engines utilize scheduled cooling of the outer case flanges during cruise conditions to reduce blade-tip clearance. Reduced clearance decreases the volume of combustion gas spilling over the blade tips, thus improving engine performance and efficiency. Current case-cooling methods, however, are limited by slow response times and the inability to monitor dynamic, asymmetric blade-tip to sealing-shroud clearances. As such, tip clearances must remain conservative to prevent collisions between the blade tips and sealing shroud during extreme engine condition transients such as takeoff and reacceleration. The ACC under evaluation at Glenn couples a fast-acting mechanical actuation system with advanced high-temperature clearance sensors through a closed-loop control scheme. This system would detect and

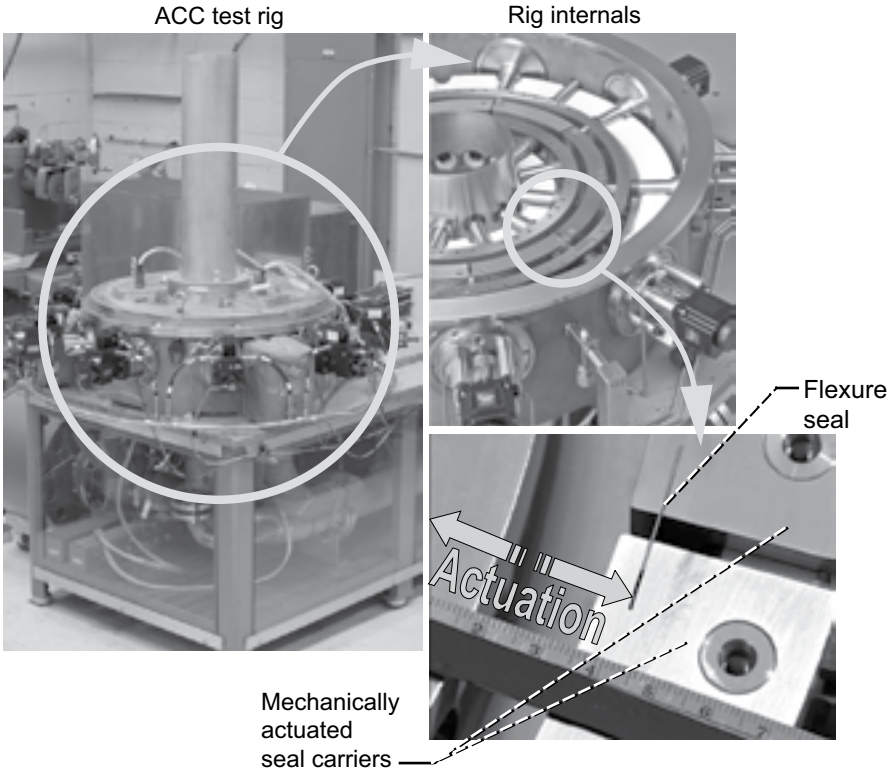


*ACC test rig at Glenn showing the rig exterior, the internal structure of the rig with the cover plate removed, and a closeup of two adjoining, mechanically actuated sealing-shroud carriers.*

quickly accommodate sudden clearance transients, allowing tighter, more stable tip-clearance levels at all engine operating stages. With ACC, a tip-clearance reduction of 0.010 in. would decrease specific fuel consumption by approximately 0.8 to 1.0 percent; significantly decrease $NO_x$, CO, and $CO_2$ emissions;[1] and lower exhaust gas temperatures by approximately 10 °C. In addition, reduced tip clearance would lead to increased engine time-on-wing, decreased operating and maintenance costs, and enhanced mission range and payload capabilities.

Building on previous room-temperature investigations, tests were completed at Glenn to evaluate the performance of the ACC secondary seals at elevated temperatures, including 500, 800, and 1000 °F, with pressure differentials up to 120 psi. System secondary seal leakage continuously decreased as test temperature was increased (see the bar chart to the right). At 1000 °F with a 120-psig pressure differential across the seals, system leakage was 0.038 lbm/sec: a 64-percent decrease from the room-temperature leakage rate. To obtain a practical performance benchmark, researchers converted representative ACC leakage rates for multiple test temperatures to effective clearance values and compared them with a reference level provided by engine industry manufacturers (see the bar chart on the next page). This reference value is based on an acceptable mass flow rate of 0.2-percent core (W25)[2] flow for seal locations (forward and aft combined) needed to implement the ACC concept into an engine. As shown in the bar chart, on the next page, ACC effective clearances were lower than the industry reference for all evaluated test conditions, with the largest decrease, 70 percent, occurring at 1000 °F.

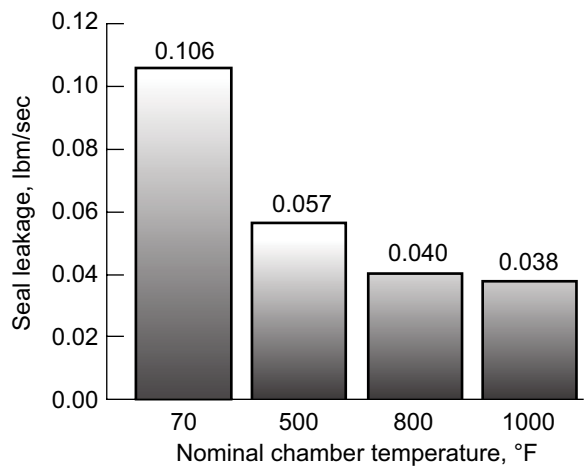


*ACC seal leakage dependence on chamber test temperature.*

[1]Emissions of oxides of nitrogen, carbon monoxide, and carbon dioxide.

[2]Industry designation for core flow through the engine.

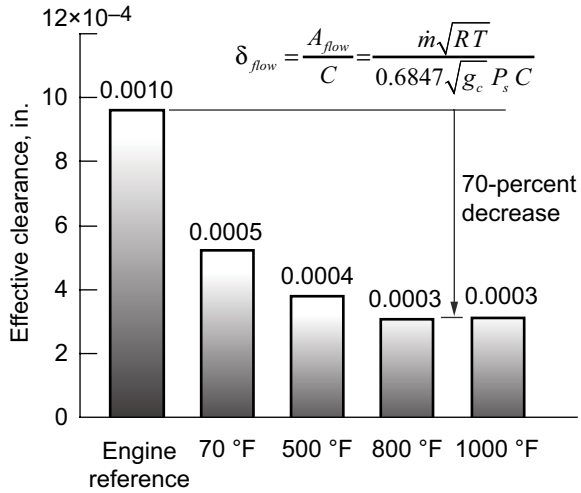


*Calculated effective clearances for the ACC rig are lower than the industry engine reference level at all temperatures evaluated; $\delta_{flow}$, effective clearance where flow is choked (in.); $A_{flow}$, area where flow is choked (in.$^2$), $\dot{m}$, measured mass flow rate (lbm/sec); R, gas constant for air, 53.3 lbf-ft/lbm-°R; T, temperature (°R); C, circumference of seal test section (in.); $g_c$, gravitational constant, 32.2 lbm-ft/lbf-sec$^2$; $P_s$, supply pressure (psia).*

**Find out more about this research:**

**Turbine seals:**
http://www.grc.nasa.gov/WWW/TurbineSeal/

**Structural seals and thermal barriers:**
http://www.grc.nasa.gov/WWW/structuralseal/

**Mechanical Components Branch:**
http://www.grc.nasa.gov/WWW/5900/5950/

**University of Toledo contact:**
Shawn C. Taylor, 216–433–3166, Shawn.C.Taylor@nasa.gov

**Glenn contact:**
Dr. Bruce M. Steinetz, 216–433–3302, Bruce.M.Steinetz@nasa.gov

**Authors:**
Shawn C. Taylor, Dr. Bruce M. Steinetz, and Jay J. Oswald

**Headquarters program office:**
Aeronautics Research Mission Directorate, Fundamental Aeronautics

**Programs/projects:**
Ultra-Efficient Engine Technology, Propulsion 21, Subsonic Fixed Wing

**Bibliography**

Taylor, S.; Steinetz, B.; and Oswald, J.: High Temperature Evaluation of an Active Clearance Control System Concept. AIAA–2006–4750 (NASA/TM—2006-214464), 2006. http://gltrs.grc.nasa.gov/Citations.aspx?id=187

# Leak Rates of Candidate Docking System Seal Materials Determined After Simulated Space Exposure

A Low Impact Docking System (LIDS) is being developed by the NASA Johnson Space Center to support future missions of the Crew Exploration Vehicle (CEV). This system will allow in-space assembly and rendezvous of vehicles, modules, and structures to enable mission profiles that will ensure the success of NASA's Vision for Space Exploration.

All docking and berthing mechanisms currently in use are composed of two different halves that can mate only with structures having the opposite configuration. LIDS, however, is androgynous: each system half is identical. Thus, any two vehicles or modules with LIDS can mate with each other without regard to "gender." Because LIDS is also a "smart system," both manned and unmanned autonomous vehicles and structures can be joined.

The androgynous nature of LIDS creates challenges for the sealing interface—the main interface seals must seal against each other instead of against a conventional flat metal surface. These sealing surfaces will also be exposed to the space environment when vehicles are not docked. The NASA Glenn Research Center is supporting this project by developing the main interface seals for LIDS and determining the durability of candidate seal materials in the space environment.

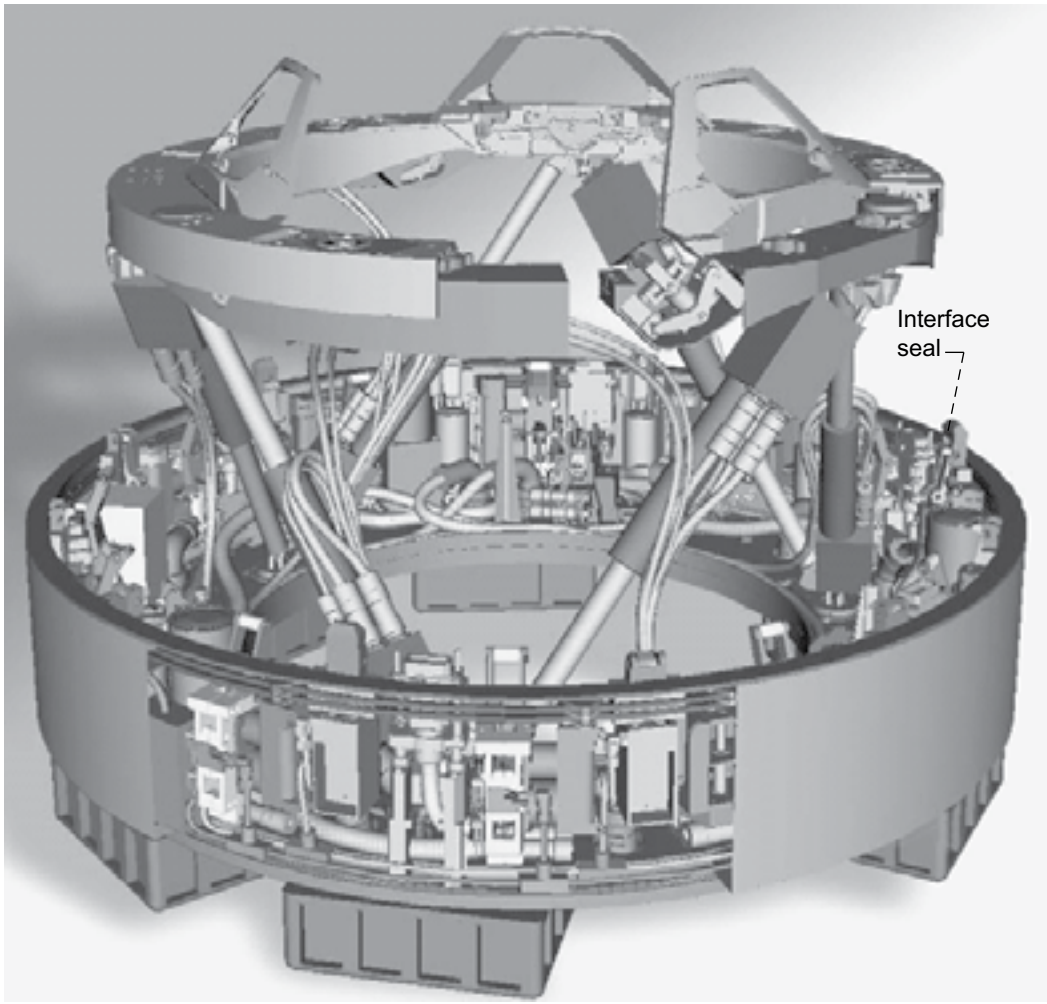


*Advanced Docking and Berthing System highlighting the main interface seal location.*

LIDS is expected to be exposed to operating temperatures from –50 to 50 °C (–58 to 122 °F). Since silicone rubber is the only class of seal elastomer that functions across this temperature range, Glenn is focusing on three silicone elastomers: two provided by Parker Hannifin (S0899–50 and S0383–70) and one from Esterline Kirkhill (XELA–SA–401). Because LIDS is designed for a service life of up to 15 years, the system may undergo as many as 120 docking/undocking operations that would expose it to vacuum, atomic oxygen (AO), particle and ultraviolet (UV) radiation, and micrometeoroid and orbital debris (MMOD). Glenn is engaged in determining the effects of these environments on our candidate elastomers.

The primary test done before and after simulated space exposure is a leak test on an o-ring of the candidate material. A vacuum is pulled on the outer side of the o-ring, and atmospheric pressure is applied to the inner side of the seal. The leak rate of the seal is measured and scaled up to estimate the leak rate for the full LIDS seal. The top plot on the next page shows leak rates measured for each elastomer after exposure to simulated space AO. The leak rates for all three materials increased at similar rates up to about 1.5 years of space AO. Beyond that point, the leak rate of the S0899–50 silicone increased significantly.

For testing the combined effects of AO and UV radiation, a set of o-rings was first exposed to an average AO fluence of about $5.77\times10^{21}$ atoms/cm$^2$ and then to increasing UV radiation. This amount of AO is what one might expect after being in space for 1 to 2 years. Of the three materials tested, S0899–50 showed the highest increase in leak rate after exposure to UV radiation.

Longer exposures of the candidate seal materials to AO and UV radiation are underway. Plans include completion of electron particle radiation exposures and testing as well as MMOD testing. Ultimately, the best material will be selected for this application, and full-scale seals will be fabricated for further evaluation.

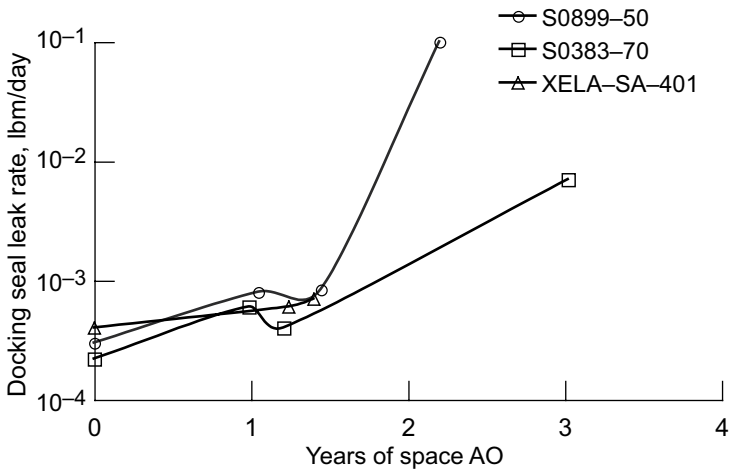


*Effect of simulated AO on the ability of silicone o-rings to seal; 1 year of space AO exposure was defined as an oxygen fluence of $5\times10^{21}$ atoms/cm$^2$.*

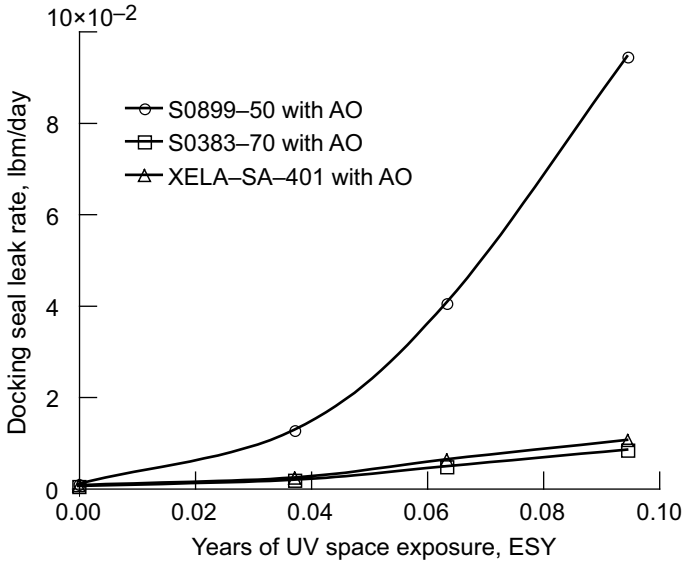


*Effect of AO and UV radiation on seal leak rate; elastomers were exposed to an AO fluence of ~$5.77\times10^{21}$ atoms/cm$^2$ prior to UV exposures.*

**Find out more about the research of Glenn's Mechanical Components Branch:**
http://www.grc.nasa.gov/WWW/5900/5950/

**Glenn contacts:**
Henry C. de Groh III, 216–433–5025 or 216–433–2788, Henry.C.deGroh@nasa.gov

Patrick H. Dunlap, Jr., 216–433–3017, Patrick.H.Dunlap@nasa.gov

Dr. Bruce M. Steinetz, 216–433–3302, Bruce.M.Steinetz@nasa.gov

**University of Akron contact:**
Chris C. Daniels, 216–433–6714, Christopher.C.Daniels@nasa.gov

**Authors:**
Henry C. de Groh III,
Dr. Christopher C. Daniels,
Patrick H. Dunlap, Jr., and
Dr. Bruce M. Steinetz

**Headquarters program office:**
Constellation

**Programs/projects:**
Crew Exploration Vehicle

# Preliminary Turbomachinery Seal Power Loss Data Completed for Competing Engine Seal Applications

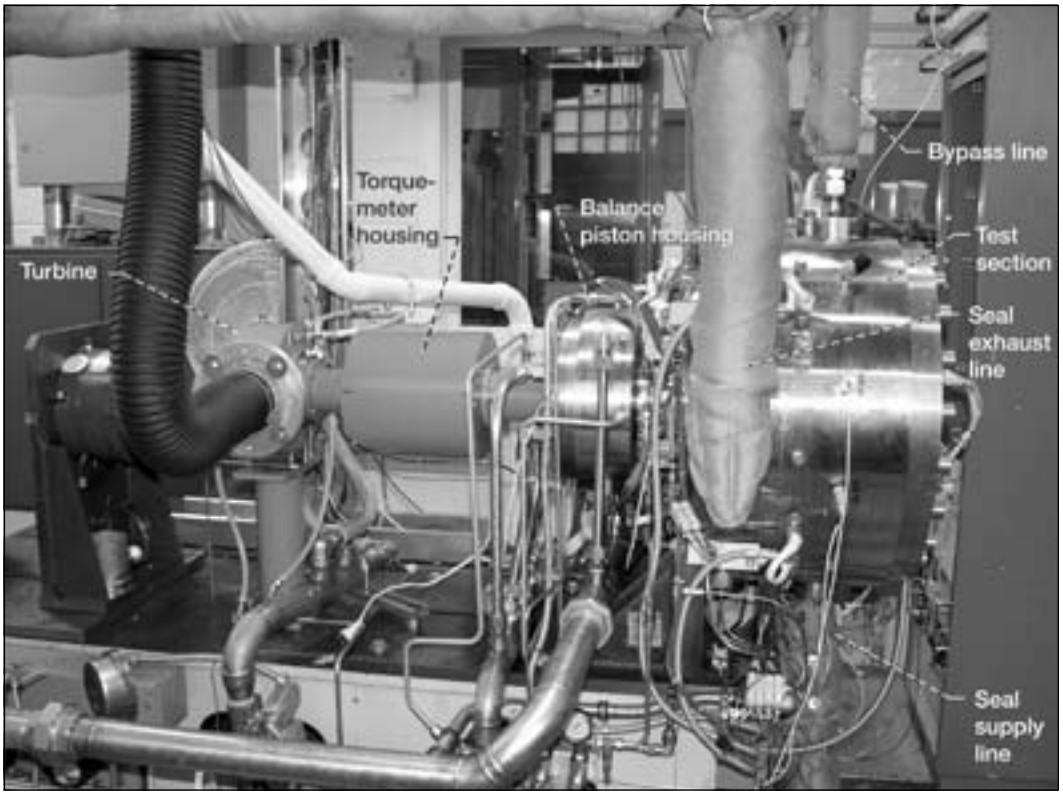


*Glenn's High-Temperature, High-Speed Turbine Seal Test Rig can test engine seals at advanced gas turbine engine operating conditions.*

Maintaining jet engine efficiency is vital to extracting as much power out of the engine cycle as possible. Unwanted disk windage, or "viscous drag on rotating components" in the secondary airflow system results in additional heat input into the secondary cooling system, which reduces the fatigue life of downstream engine components. Engine seals provide a means of controlling parasitic air leakage into the secondary flow path, separating air and oil cavities, preventing hot gas ingestion into the turbine/stator cavities, and preventing air leakage around compressor and turbine blades. However, engine seals may also cause unwanted heat input into the flow path.

To determine how much heat is produced by engine seals, U.S. Army and NASA researchers at the NASA Glenn Research Center tested four types of seals in Glenn's High-Temperature, High-Speed Turbine Seal Test Rig (see the photograph), where the torque produced by each seal was measured. Care was taken to account for the rig tare torque, disk windage, and bearing losses at different operating conditions. From these seal torque measurements, the preliminary baseline seal power loss was calculated. Data were taken over a range of temperatures, pressures, and speeds up to 922 K, 517 kPa, and 32,600 rpm. The geometry of each seal type (annular, labyrinth, brush, and finger) is shown in the table on the next page.

The following conclusions are given for the seals tested. Also see the graphs.

- Seal power loss is not strongly affected by inlet temperature.
- Seal power loss increases with increasing surface speed, seal pressure differential, mass flow rate or flow factor, and radial clearance.
- The brush and finger seals had nearly the same power loss.
- Annular and labyrinth seal power loss data were higher than finger or brush seal power loss data. The brush seal power loss data were the lowest and were 15- to 30-percent lower than annular and labyrinth seal power loss data.

BUILD GEOMETRY FOR EACH SEAL

| Seal type | Seal/disk cross section | Material | Seal inner diameter, mm | Radial clearance at 297 K, mm | Axial length, mm | Other |
|---|---|---|---|---|---|---|
| Annular | 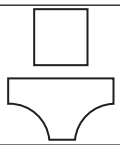 | INCONEL 625 | 216.5096 | 0.3048 | 11.2 | Not applicable |
| Four-knife labyrinth | 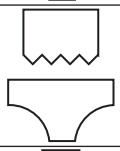 | INCONEL 625 | 216.5096 | 0.3048 | 11.2 | Tooth height, mm . . . 0.762<br>Pitch, mm . . . . . .1.016<br>Tip width, mm . . . . . 0.318<br>Tooth angle, deg . . . . . 7.9 |
| Brush | 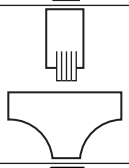 | Haynes 25 bristles<br>INCONEL 625 sideplates | 215.6968 | –0.0965 | 0.953 bristle pack width<br>4.27 total | Bristle lay angle, deg . . 50<br>Bristle diam, μm . . . . . 102<br>Density, wires/mm . . . . 68<br>Fence height, mm . . . 1.27 |
| Finger | 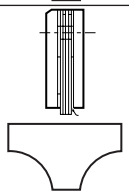 | Haynes 25 sheet per AMS5537 | 215.5520 | –0.165 | Similar to brush seal | Pressure-balance design |

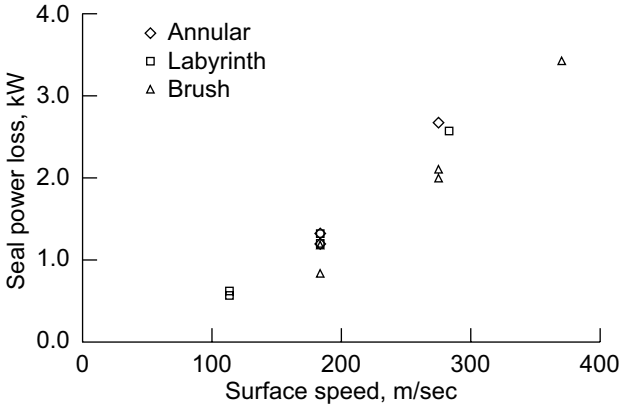


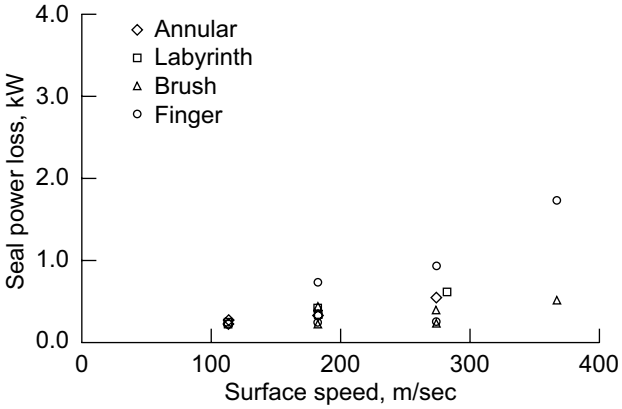


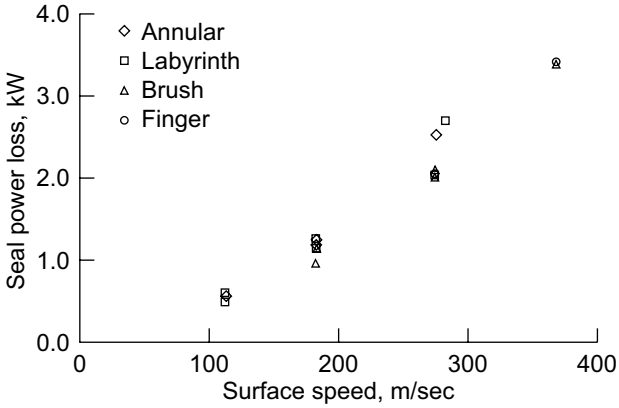


*Comparison of seal power loss for annular, four-knife labyrinth, brush, and finger seals as a function of speed at three temperature and pressure differentials. Top left: 297 K, 276 kPa. Top right: 700 K, 68.9 kPa. Bottom: 700 K, 276 kPa.*

Further analytical and experimental work is needed to understand the effect of seal axial length and preswirl on seal power loss. These findings along with future work will aid seal designers in minimizing the seal heat generation and subsequent efficiency losses in jet engine applications. This work is a collaborative effort between NASA and the U.S. Army Research Laboratory in support of the NASA Aeronautics program as well as U.S. Army platforms (i.e., helicopters, tanks, and unmanned aerial vehicles).

**References**

1. Millward, J.A.; and Edwards. M.F.: Windage Heating of Air Passing Through Labyrinth Seals. J. Turbomach., vol. 118, no. 2, 1996, pp. 414–419.
2. Proctor, Margaret P.; and Delgado, Irebert R.: Leakage and Power Loss Test Results for Competing Turbine Engine Seals. NASA/TM—2004-213049 (ASME GT2004–53935), 2004. http://gltrs.grc.nasa.gov/cgi-bin/GLTRS/browse.pl?2004/TM-2004-213049.html
3. Delgado, Irebert R.; and Proctor, Margaret P.: Continued Investigation of Leakage and Power Loss Test Results for Competing Turbine Engine Seals. NASA/TM—2006-214420 (ARL–MR–0643 and AIAA–2006–4754), 2006. http://gltrs.grc.nasa.gov/Citations.aspx?id=168

**Find out more about Glenn's turbine seal research:**
http://www.grc.nasa.gov/WWW/TurbineSeal/

**U.S. Army Research Laboratory at Glenn contact:**
Irebert R. Delgado, 216–433–3935, Irebert.R.Delgado@nasa.gov

**Glenn contact:**
Margaret P. Proctor, 216–977–7526, Margaret.P.Proctor@nasa.gov

**Authors:**
Irebert R. Delgado and Margaret P. Proctor

**Headquarters program office:**
Aeronautics Research Mission Directorate

**Programs/projects:**
Fundamental Aeronautics, Subsonic Fixed Wing

# Influence of Operational Parameters on the Thermal Behavior of High-Speed Helical Gear Trains Studied

In the future, high-speed, heavily loaded, and lightweight gearing components will be a part of all propulsion systems for rotorcraft. These systems are expected to deliver high power from the gas turbine engines to the high-torque/low-speed rotor with high reduction ratios. Gearing systems in these extreme duty applications can have thermal behavior issues because of the high pitch-line velocities. Although design considerations for gear-tooth bending and contact capacities are usually considered initially, a high-speed gearing design needs to carefully consider the consequences of pitch-line velocities approaching 25,000 ft/min and beyond. Unfortunately the thermal behavior characteristics of mechanical components have been shown to be the least understood or developed part of gearing analysis in the open literature.

In rotorcraft drive systems, such as that of tiltrotors, a helical gear train (see the illustration) is used to provide the required separation between the parallel engine and rotor shafting on the aircraft. The thermal behavior of the gear system includes all the loss mechanisms within the gearbox. These include the gear meshing, bearing, and seal losses along with the windage losses (power lost by the system due to the air-lubricant environment that the gears rotate within). Windage losses become substantial at high rotational speeds as seen in some rotorcraft transmissions. The amount of heat that has to be rejected from the sum of the loss mechanisms mentioned above directly affects the efficiency.

In the present study conducted by U.S. Army researchers at the NASA Glenn Research Center, two speed conditions, hover and forward flight, were tested for the gear train along with three levels of torque. For the six conditions of interest in this study, the results from analysis and experiment are shown in the graph on the next page. The results indicate that the efficiency increases with increasing load and decreases with increasing input rotational speed. For the analytical results shown in the graph, the windage losses can reach 50 percent of the losses. The windage losses are not dependent on load but are dependent on rotational speed, gear dimensions, and lubrication conditions. For this study, the air-lubricant environment was chosen to match the maximum power loss at the highest speed condition and then fixed. The results followed the experimental trends for the conditions under study, but the results diverged at lower power levels.

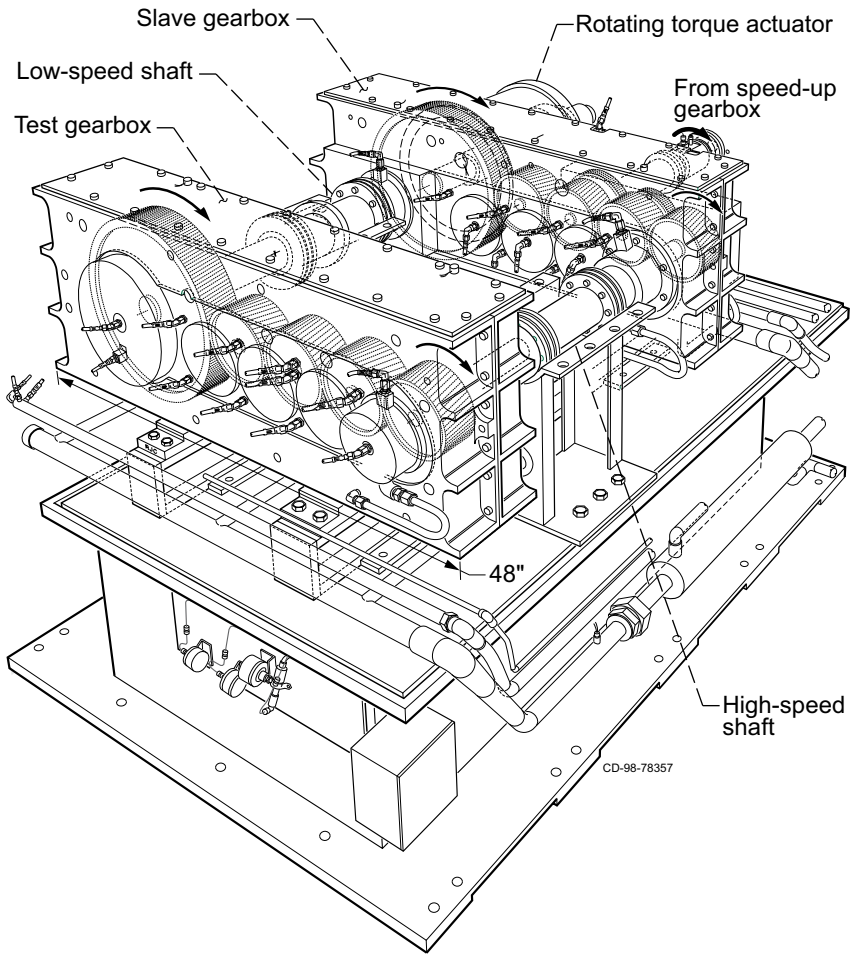


*High-speed helical gear test facility.*

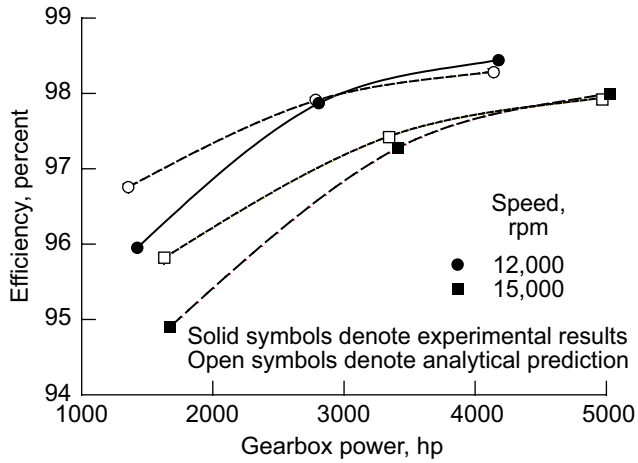


*Analytically predicted and experimentally obtained gearbox efficiency as a function of operational load and speed.*

**Find out more about the research of Glenn's Mechanical Components Branch:**
http://www.grc.nasa.gov/WWW/5900/5950/

**U.S. Army Research Laboratory at Glenn contact:**
Dr. Robert F. Handschuh, 216–433–3969, Robert.F.Handschuh@nasa.gov

**Author:**
Dr. Robert F. Handschuh

**Headquarters program office:**
Aeronautics Research Mission Directorate

**Programs/projects:**
Fundamental Aeronautics, Subsonic Rotary Wing

## Testing Began in New Wave Bearing Test Facility

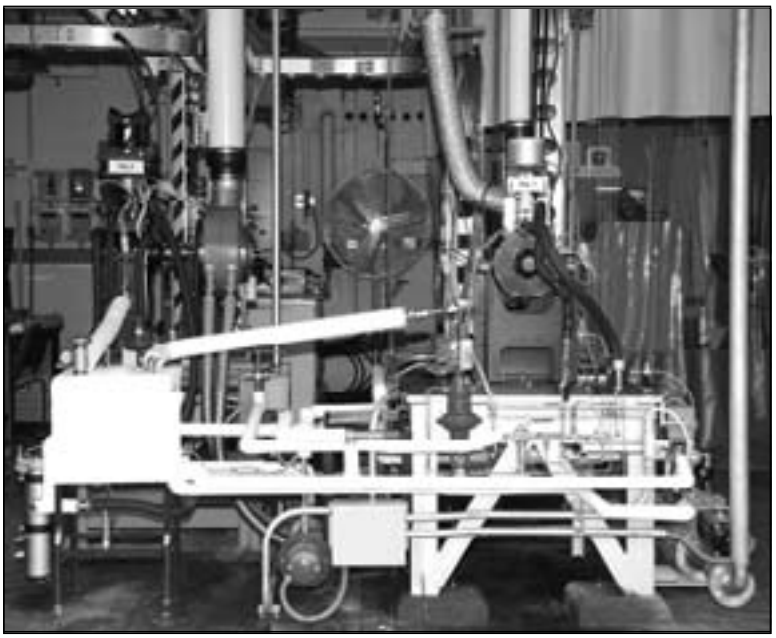

*Wave bearing test facility.*

A new test facility was developed at the NASA Glenn Research Center to test advanced fluid-film wave bearings up to 68 mm in diameter and 38 mm in length at a maximum speed of 15,000 rpm and with a maximum load of 30,000 lb. This facility (see the photograph) was designed to test wave bearings under heavily loaded conditions, simulating the loading conditions that would be experienced by bearings

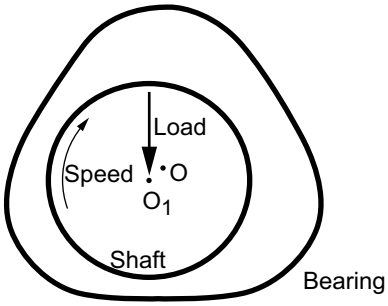


*Wave bearing.*

installed in the transmissions for rotorcraft or geared turbofan jet engines. The new wave bearing test facility is instrumented for oil pressure, oil temperature, oil flows, shaft position, vibration, speed, and load.

A wave bearing is similar to a journal bearing but has a wave profile circumscribed on the bearing sleeve inner diameter. The bearing clearance and the wave amplitude are largely exaggerated in the sketch on the preceding page to visualize the concept. Wave bearings with liquid lubricants can support very high loads and run thermally and dynamically stable. These bearings have been tested to 1500-psi specific load and are planned to be tested to 3500 psi in the new facility. The bearings can overcome start-stop difficulties and oil starvation. Tests have demonstrated that, with the application of physical-vapor-deposition coatings on both bearing surfaces, the wave bearing can perform 1000 start-stop cycles without significant damage to the bearing surfaces and can survive without oil supply for more than 2 hr. The wave bearing is a promising technology for reducing the size, weight, and noise of aeronautical transmissions.

One major benefit of wave bearings is their potential to significantly reduce the noise and vibration transmitted to the housing. Preliminary tests in the new facility showed a significant reduction in vibration transmission through the bearing and a reduction in radiated noise. The final figure shows the signals from four accelerometers installed in the new test facility. Channel 1 (Ch1) is located on the turbine, Ch2 and Ch4 are located close to the ball bearings that support the rig shaft, and Ch3 is close to the test wave bearing. As seen in the figure, the vibration through the wave bearing has a root mean square (rms) value more than 15 times less than the vibrations through the turbine ball bearings and the ball bearings that support the shaft.

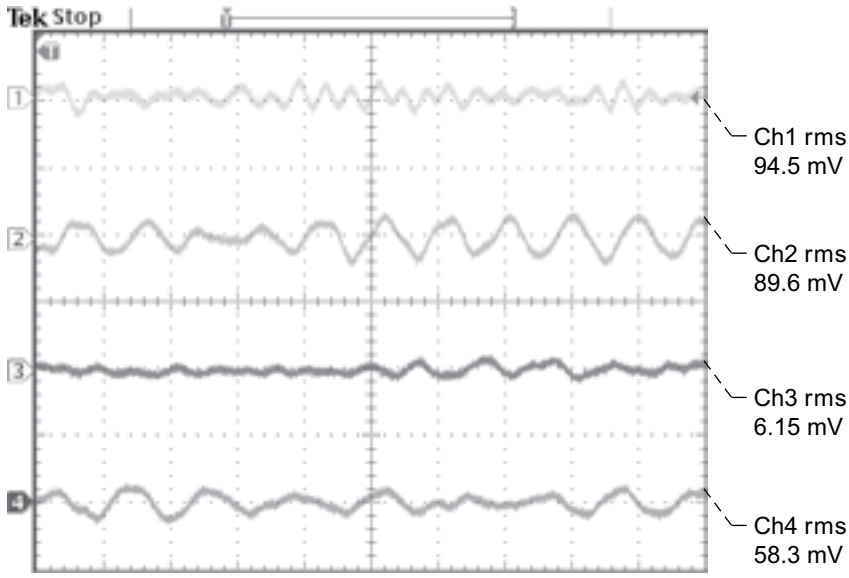


*Plots of vibration generated by the turbine and transmitted through wave bearing from accelerometers mounted on the turbine housing (Ch1), near the shaft support bearing close to the turbine (Ch2), on the test wave bearing loading rod (Ch3), and near the second shaft support bearing (Ch4).*

**Bibliography**

Dimofte, Florin; and Addy, Harold E.: Waved Journal Bearing Demonstrates Greater Stability and Load Capacity. Research & Technology 1993, NASA TM–106376, 1994, p. 63.

Dimofte, Florin: Gas Wave Bearings: A Stable Alternative to Journal Bearings for High-Speed Oil-Free Machines. Research & Technology 1996, NASA TM–107350, 1997, pp. 114–115. http://www.grc.nasa.gov/WWW/RT1996/5000/5340d.htm

Dimofte, Florin, et al.: Wave Fluid Film Bearing Tests for an Aviation Gearbox. NASA/TM—2000-209766, 2000. http://gltrs.grc.nasa.gov/cgi-bin/GLTRS/browse.pl?2000/TM-2000-209766.html

**Find out more about the research of Glenn's Mechanical Components Branch:**
http://www.grc.nasa.gov/WWW/5900/5950/

**University of Toledo contact:**
Dr. Florin Dimofte, 216–977–7468, Florin.Dimofte-1@nasa.gov

**U.S. Army Research Laboratory at Glenn contact:**
Dr. Robert F. Handschuh, 216–433–3969, Robert.F.Handschuh@nasa.gov

**Authors:**
Dr. Florin Dimofte and
Dr. Robert F. Handschuh

**Headquarters program office:**
Aeronautics Research Mission Directorate

**Programs/projects:**
Fundamental Aeronautics, Subsonic Rotary Wing

# Face Gear Endurance Testing Conducted

Commercial and military requirements continuously drive the need for reduced weight and increased power density for aircraft drive systems. The use of face gears in transmissions emerged as a way to achieve this. Previous studies showed that a split-torque, face-gear transmission gave a 40-percent decrease in weight in comparison to a convention design for an advanced attack helicopter application. Face gears, however, had no previous experience in high-power systems, and much work had to be done to establish design guidelines. The objective of this study was to determine the surface durability life of a face gear in mesh with a tapered involute spur pinion gear.

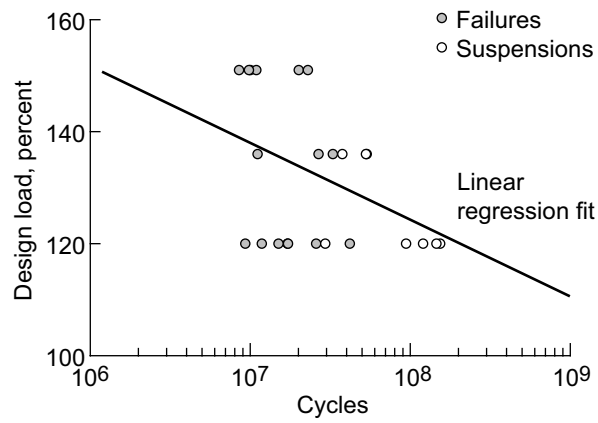


*Endurance test results for tapered involute spur gear with meshing face gear.*

Experimental fatigue tests were performed in the spiral-bevel/face-gear fatigue test facility at the NASA Glenn Research Center to determine the surface durability life of a face gear in mesh with a tapered involute spur pinion gear. The gears were carburized and ground, shot-peened, vibrohoned, and made from Pyrowear 53 steel per Aerospace Material Specification (AMS) 6308. Twenty-four sets of gears were tested. Tests were performed at three load levels and various speeds, either to the point of failure or to a predefined runout condition. The tests produced 17 gear-tooth spalling failures and 7 suspensions. For all the failed sets, spalling occurred on at least one tooth of the pinion gear. In some cases, the spalling initiated a crack in a pinion tooth that progressed to tooth fracture. Spalling also occurred on some face gear teeth. This testing resulted in the determination of a design endurance allowable stress for a tapered involute spur pinion in mesh with a face gear. For a tapered involute spur pinion in mesh with a face gear, experience was gained as how to best adjust assembly procedures to optimize the contact pattern and backlash. Proper use of pinion-gear-tooth tip and root relief modifications minimized the occurrence of hard lines.

*Test hardware used for endurance tests of tapered involute spur gear with meshing face gear.*

**Find out more about the research of Glenn's Mechanical Components Branch:**
http://www.grc.nasa.gov/WWW/5900/5950/

**U.S. Army Research Laboratory at Glenn contact:**
Dr. David G. Lewicki, 216–433–3970, David.G.Lewicki@nasa.gov

**Glenn contact:**
James J. Zakrajsek, 216–433–3968, James.J.Zakrajsek@nasa.gov

**Author:**
Dr. David G. Lewicki

**Headquarters program office:**
Aeronautics Research Mission Directorate

**Programs/projects:**
Fundamental Aeronautics, Subsonic Rotary Wing Program

# Foil-Bearing Research Capabilities Expanded in Support of Oil-Free Turbomachinery

Compliant foil bearing technology is at the center of NASA's Oil-Free Turbomachinery program, which aims to replace the oil-lubricated rolling-element bearings in high-speed rotating machines with maintenance-free foil gas bearings, substantially reducing weight and cost while increasing reliability and efficiency. Because of these advantages, oil-free rotor supports are demanded for long-duration space power applications and are highly desirable for ground- and air-based rotating machinery. To support further development of this technology, the NASA Glenn Research Center added two new foil bearing test facilities that target specific gaps in previously available test capabilities.

*High Pressure Journal Bearing Test Rig.*

The High Pressure Journal Bearing Rig (see the top photograph) consists of a high-speed electrical motor with an overhung journal operating within a pressure vessel. In this configuration, foil bearing performance from 0 to 42,000 rpm can be measured at pressures from moderate vacuum up to 4.8 MPa (700 psi) at room temperature. Foil bearing power loss, typically much lower than in rolling-element bearings, can be mapped over this wide pressure and speed range, simulating a broad range of operating conditions for potential oil-free turbomachines. This test rig also supports variable-pressure testing in inert gases such as carbon dioxide, helium, and xenon, which are candidate working gases for several power cycle turbomachines, including a Brayton-cycle turboalternator for high-electrical-power space missions.

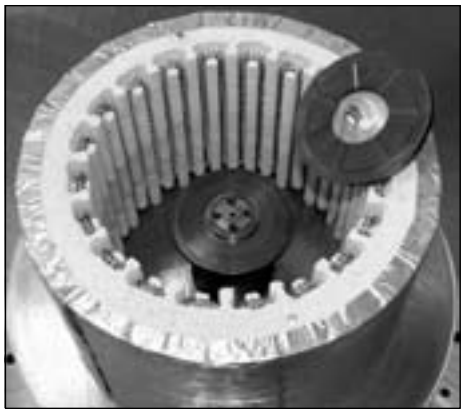

*Core of Low Speed Thrust Bearing Test Rig.*

Testing of foil thrust bearings (see the bottom photograph) will be augmented with a new test rig that can subject oil-free thrust bearings to tens of thousands of start-stop cycles, verifying endurance of the solid lubricant coatings that have been developed at Glenn and by industry. The rig also will provide very stable operation at speeds up to 21,000 rpm and temperatures from room temperature to over 540 °C (1000 °F) to measure bearing performance at the lower speed range of their operational envelope. Solid-lubricant coating systems will be further matured by this new facility, adding a valuable experience base for designers of next-generation turbomachines. Although foil thrust bearing development lags that of foil journal bearing counterparts, this added test rig will foster a more rapid advance of foil thrust bearing technology.

Thrust bearing operational performance and durability, as well as journal bearing performance at high pressure, can now be determined experimentally. The addition of these new test capabilities further diversifies NASA's portfolio of Oil-Free Turbomachinery research assets, supporting numerous applications for ground, air, and space power and propulsion.

**Find out more about the research of Glenn's Oil-Free Turbomachinery program:**
http://www.grc.nasa.gov/WWW/Oilfree/

**Glenn contacts:**
Dr. Robert J. Bruckner, 216–433–6499, Robert.J.Bruckner@nasa.gov

Dr. Christopher DellaCorte, 216–433–6056, Christopher.DellaCorte@nasa.gov

**Authors:**
Dr. Robert J. Bruckner, Dr. Brian D. Dykas, Daniel W. Tellier, and Maxwell H. Briggs

**Headquarters program office:**
Aeronautics Research Mission Directorate, Prometheus Program

**Programs/projects:**
Space Power, Subsonic Rotary Wing—Drive System

# Integrating Sphere Used With Fourier Transform Infrared Spectroscopy To Characterize Lubricants on Ball Bearings

Fourier transform infrared (FTIR) spectroscopy is used extensively to characterize lubricants and their degradation products. The introduction of microscope attachments facilitated examination of degradation products by allowing spectra to be acquired from selected areas of ball bearings and races. FTIR microscopy allowed small particles of wear debris or aggregated materials to be examined. For surfaces evenly coated with a homogeneous material, this technique provided estimates of film thickness, but it was limited because curved surfaces had to be centered in the objective. Quantification of nonuniform films was another limitation. Analysis required spectral information from at least a statistically significant fraction of the sample. Over a million spectra were required to examine the surface of a 0.5-in.-diameter ball bearing.

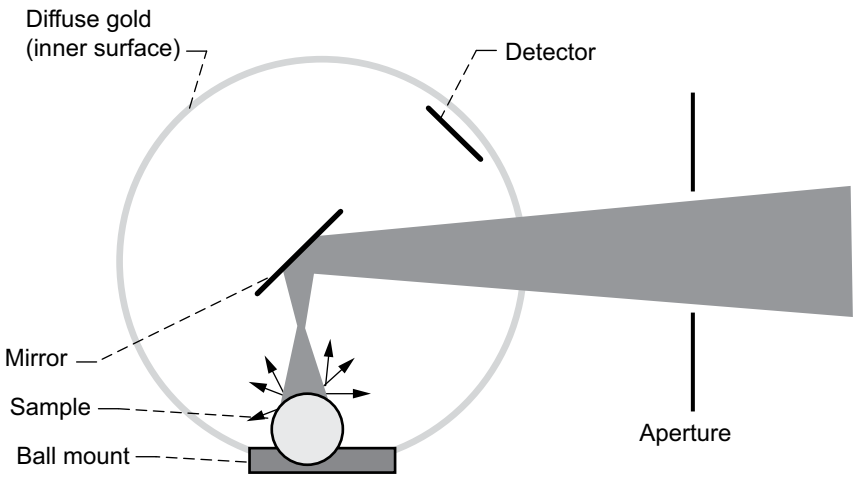


*Integrating sphere with ball sample.*

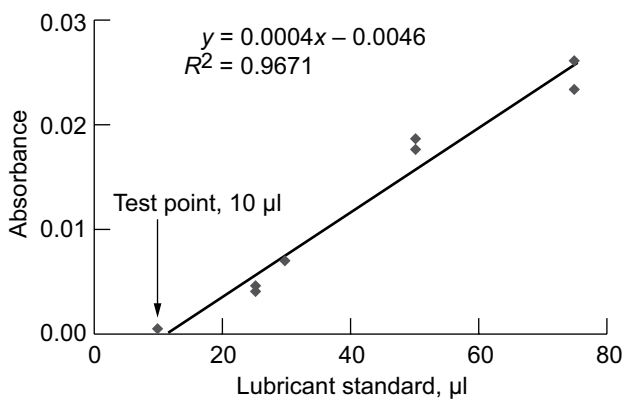


*Plot of the absorbance from a 0.5-in.-diameter ball versus the lubricant charge, expressed as volume of solution delivered; x, volume of solution in microliters; y, absorbance; $R^2$, correlation coefficient.*

Integrating sphere attachments traditionally used for scattering transmission or reflectance measurements have long been available. At the NASA Glenn Research Center, we began using an integrating sphere to characterize lubricants and degradation products that were not distributed uniformly over a ball bearing surface. For objects, such as balls, information could be obtained from significant portions of the surface in a single spectrum, thus averaging over local heterogeneity. Quantification of a single substance and qualitative chemical characterization of mixed substances became possible. Glenn researchers completed instrument modification, parameter optimization, and other changes needed for obtaining quantitative information from ball bearings.

The schematic shows an integrating sphere with a ball bearing sample. The intensity of the incoming beam was a complex function of the beam steering optics. It was estimated that the beam covered between 20 and 50 percent of the surface of the ball and depended on (1) the aperture setting of the bench, (2) the ball diameter, and (3) the positioning of the ball within the sphere. Therefore, five spectra were determined as the optimum number to obtain information from the entire surface: the top, the bottom, and three evenly spaced positions about the equator.

The plot shows the averaged absorbance for the five spectra on a ball versus the lubricant charge expressed as the volume of solution delivered onto a ball. The volumetric calculation of lubricant charge was at least as accurate as gravimetry and was far less time consuming. Furthermore, smaller lubricant amounts could be determined reliably. The test point, at 6.5 µg lubricant by volumetric calculation (10 µl), was well below the

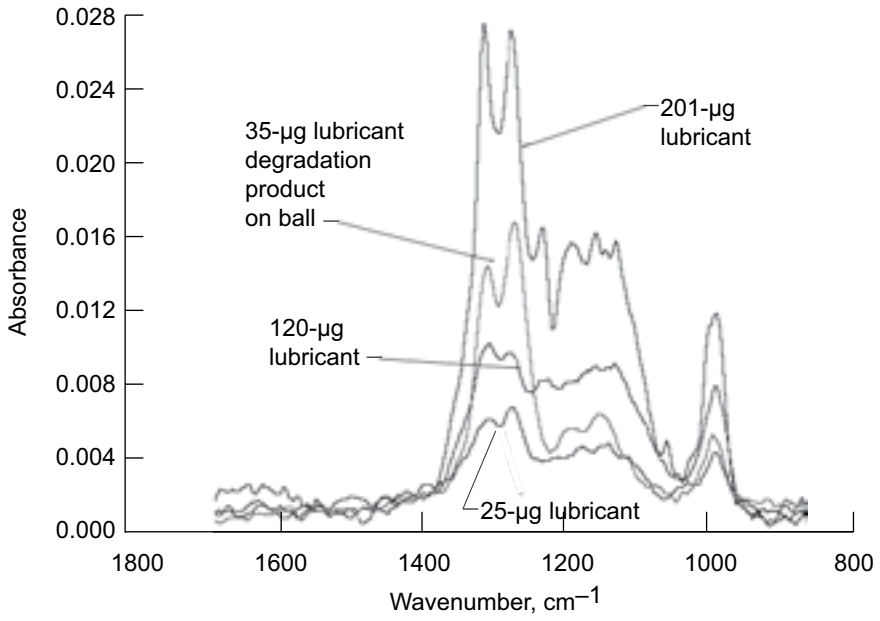


*Spectra of lubricant and degradation product on a 0.5-in.-diameter ball.*

**Glenn contacts:**
Dr. Kenneth W. Street, Jr., 216–433–5032, Kenneth.W.Street@nasa.gov

Dr. Stephen V. Pepper, 216–433–6061, Stephen.V.Pepper@nasa.gov

**Authors:**
Dr. Kenneth W. Street, Jr.,
Dr. Stephen V. Pepper, Alisha A. Wright, and Brianne Grady

**Headquarters program office:**
Exploration Systems Mission Directorate

**Programs/projects:**
Exploration Systems Research and Technology, Aeronautics Propulsion and Power Project, Revolutionary Aeropropulsion Concepts, Advanced Mechanisms and Tribology Technologies for Durable Lightweight Actuation and Mechanical Power Transmission Systems, Advanced Materials and Structural Concepts Element Program, Advanced Space Technology Program

gravimetric determination limit. The negative offset of the calibration plot is probably due to a bias encountered when determining the baseline-corrected absorbance using software.

The final figure illustrates the ability of the method to characterize material on a ball after lubricant failure. These spectra represent 35 µg of lubricant degradation product compared with lubricant standard spectra. A 35-µg lubricant load would not have experienced tribological failure, which indicates that the material was a degradation product rather than residual lubricant.

Using this integrating sphere technique, we determined that the lubricant charge on balls was not typically uniform as were the degradation products. Smaller loadings could be determined than could be quantified by weighing. This technique has extended the usefulness of FTIR spectroscopy in tribological research.

# Long-Term Compression and Recovery Tests Completed on Space Shuttle Main Landing Gear Door Seals

As part of the investigation into the loss of the *Space Shuttle Columbia*, the Columbia Accident Investigation Board requested an evaluation of the main landing gear (MLG) door environmental seals on the remaining shuttle orbiters. During this evaluation, a visual inspection of the seals on the *Space Shuttle Discovery* revealed that the seal bulbs were permanently deformed, which necessitated their replacement. At the request of the NASA Johnson Space Center, a series of tests was performed at the NASA Glenn Research Center beginning in 2004 to help guide installation and maintenance of these seals. A part of these evaluations involved determining how quickly and to what extent the seals recover their original shape after being compressed for varying durations. During many shuttle missions, the seals are compressed for long periods because of launch delays and other reasons. The degree and rate of recovery for these seals have implications for their maintenance procedures and replacement criteria. If the seals recover too slowly, they may not meet the minimum compression criteria during a preflight check and may need to be replaced.

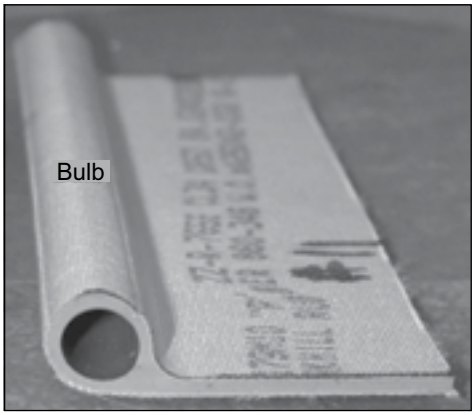


*Shuttle MLG door environmental seal.*

To better understand the recovery behavior of these seals, researchers at Glenn performed a series of tests in 2006 in which the seals were compressed for long durations and then their rate of recovery was measured upon rapid unloading. As shown in the following photograph, a laser fixture was used to measure the recovery response of the seals with respect to time after they had been compressed for a specified duration.

Representative results from the recovery tests are presented in the plots on the next page. These graphs show the amount of seal recovery as a function of elapsed time after the seal is quickly unloaded. For the tests shown, the seals were compressed by approximately 40 to 45 percent relative to their bulb diameter for durations ranging from 1 hr to 90 days before the recovery was measured.

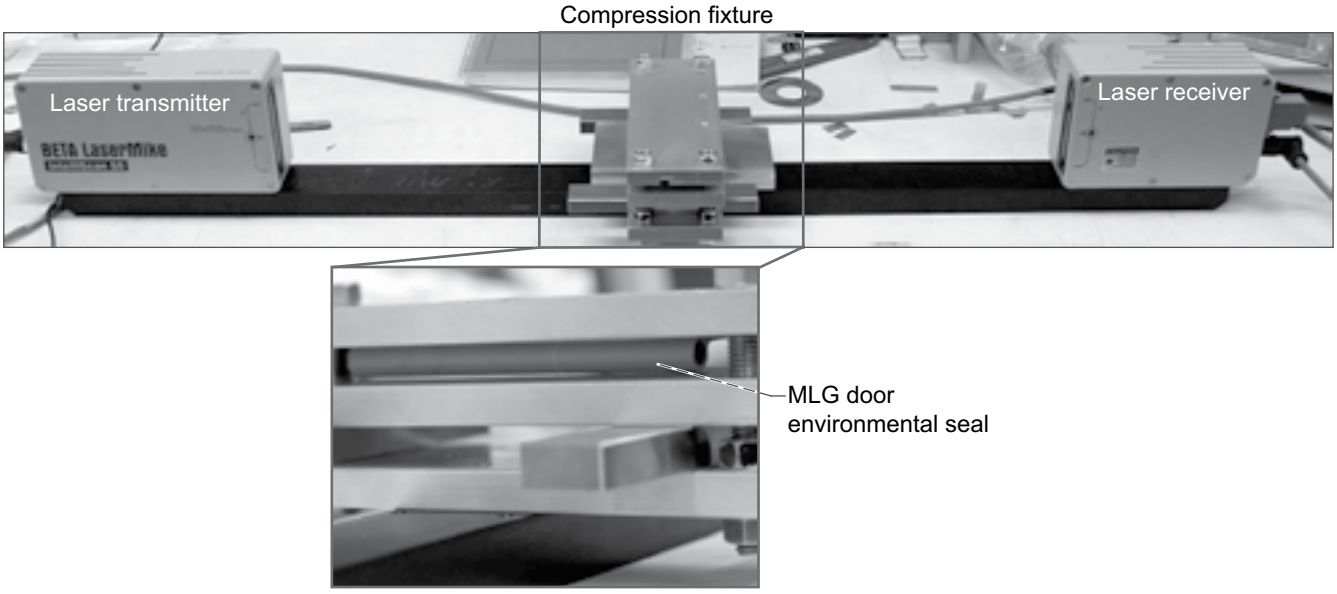


*Laser test fixture used to measure amount of seal recovery for shuttle MLG door seals.*

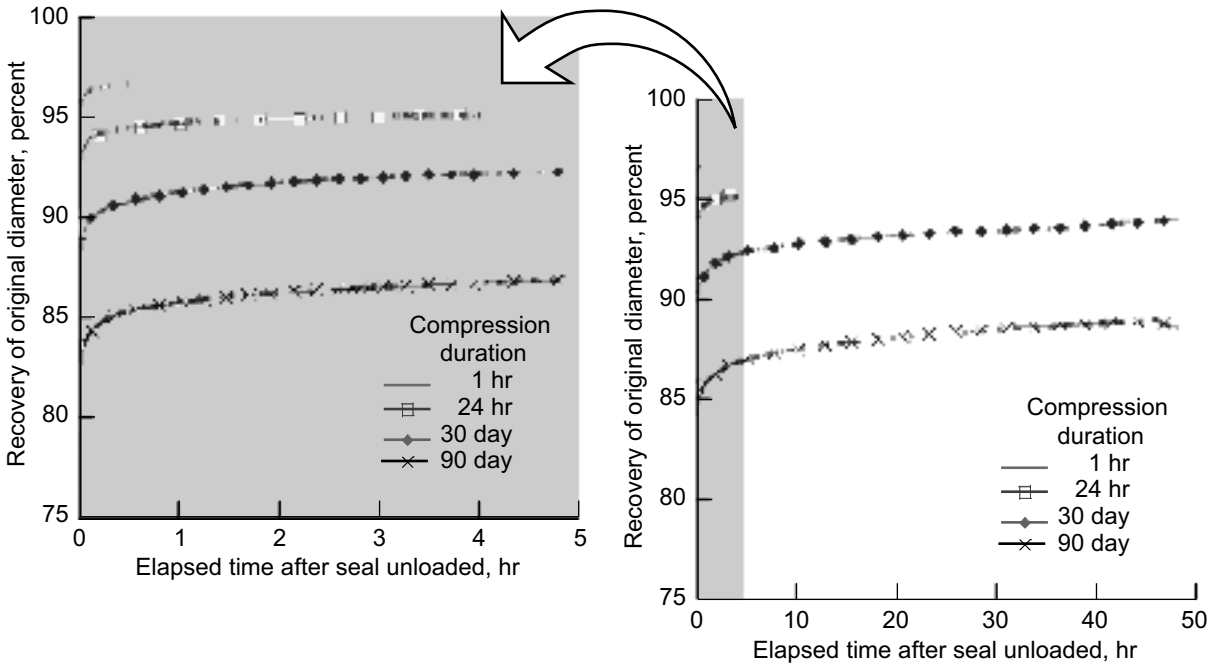


*Amount of seal recovery as a function of elapsed time after compression for various durations. The graph on the left is a "zoomed-in" area of the graph on the right.*

As shown in the graphs, seals that were held in a compressed state for longer times exhibited significantly less recovery than those that were compressed for shorter periods. For example, the seal that was compressed for 1 hr recovered to about 97 percent of its original diameter 1/2 hr after it was unloaded. By contrast, a seal that was compressed for 90 days recovered to about 86 percent during the same time. Even after 48 hr of data collection, this seal only recovered to about 89 percent of its original diameter. For all cases, it appeared that most of the recovery occurred during the first hour after unloading.

Using Glenn's test data, shuttle technicians now have guidance on (1) how long to wait before measuring seal conformance criteria (i.e., bulb height/compression) and (2) when to replace the MLG door environmental seals.

**Find out more about the research of Glenn's Mechanical Components Branch:**
http://www.grc.nasa.gov/WWW/5900/5950/

**University of Toledo contact:**
Jeffrey J. DeMange, 216–433–3568,
Jeffrey.J.Demange@nasa.gov

**Glenn contacts:**
Patrick H. Dunlap, Jr., 216–433–3017,
Patrick.H.Dunlap@nasa.gov

Dr. Bruce M. Steinetz, 216–433–3302,
Bruce.M.Steinetz@nasa.gov

**Authors:**
Jeffrey J. DeMange, Joshua R. Finkbeiner,
Patrick H. Dunlap, Jr., and
Dr. Bruce M. Steinetz

**Headquarters program office:**
Space Operations

**Programs/projects:**
Space Shuttle

# Mechanical Response Experiments Designed for Full-Scale Testing of Orbiter Composite Overwrap Pressure Vessels

The NASA Glenn Research Center in partnership with the Ohio Aerospace Institute (OAI) collaborated with Cornell University and the NASA White Sands Test Facility to lead the effort in designing experiments and specifying test requirements for a series of full-scale vessel tests to be conducted on the Centaur and the space shuttle Orbital Maneuvering System flight hardware. The work was directed by the Orbiter Projects Office as part of a concerted effort to certify shuttle composite overwrap pressure vessel (COPV) flight hardware for the remaining mission schedule.

*Test setup: 40-in. Kevlar/epoxy overwrap COPV.*

Previous mechanical response analyses conducted by Glenn for the NASA Engineering and Safety Center had indicated that the Kevlar (DuPont)/epoxy composite vessel was operating at higher percentages of its burst strength than originally assumed. Concerns were raised on reliability issues given the increased ratio of operating fiber stress to burst fiber stress along with the existing long-term stress rupture data. Two factors contributed to the higher relative fiber stresses at operating pressure: (1) manufacturing data indicated that processing-induced residual strains were greater than expected, and (2) a lower-than-expected fiber failure strength was computed for the COPVs when the load share of the metallic liner was accounted for. The mechanical response of a COPV is difficult to predict owing to the presence of metallic load-sharing liners and complex manufacturing procedures. Life would be extended if there was an accurate theoretical framework for the mechanical response calibrated by careful full-scale vessel tests.

It was reasoned that the large residual manufacturing strains were indicative of a more compliant Kevlar composite than assumed in the manufacturer's analysis. This conclusion was supported by early experiments conducted by the NASA Johnson Space Center, which had measured larger-than-expected through-the-thickness compression of filament-wound overwrap on pressurized COPVs. When three-dimensional elasticity was applied for a transversely isotropic spherical shell, inner-wall deformation per unit pressure increased with decreasing transverse modulus despite constant in-plane properties. Cornell-Glenn versions of the three-dimensional model were extended to demonstrate that low transverse stiffness and compressive "crushing" could also lead to the misconception of low nominal fiber strength despite the presence of high inner-wall fiber stresses. These findings guided the design of full-scale experiments to provide data verifying the possible role of through-the-thickness compression in large residual strains and apparently low burst fiber strengths.

In addition to standard internal pressure, external surface strains were measured by foil strain gauges. A number of integrated deformation measurements were required that were unique to this program of full-scale tests:

(1) Total internal volume measurement
(2) Through-the-thickness compression measurement by eddy-current probe technology
(3) Digital image correlation (DIC) to measure full-field strains at high frame rates
(4) Raman spectroscopy to measure total elastic fiber strains including residual elastic strains to determine stress in the fiber at zero applied pressure

Glenn-developed DIC and Raman spectroscopy methods are described in references 1 and 2. The eddy-current probe technology was developed by the NASA Langley Research Center. The test setup and remaining instrumentation were developed and installed at the White Sands Test Facility. This photograph shows the test setup without the DIC grid, and the graph on the next page shows a typical volumetric deflection plot as a function of pressure as the vessel goes beyond liner yield. The initial slope of the curve reflects the total compliance of the vessel until the metallic liner yields. The post-yield slope is the compliance of the composite alone if the metal is uniformly yielding without hardening. After unloading, the residual volume indicates an increment of additional residual strain stored in the vessel.

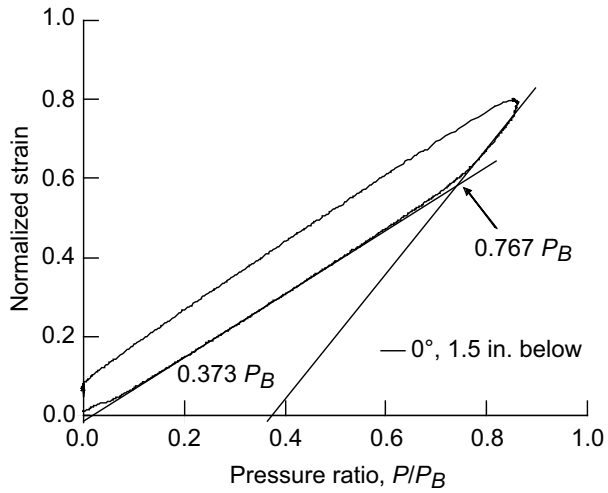


*Typical normalized volumetric strain response as a function of normalized pressure.*

**Ohio Aerospace Institute (OAI) contact:**
Dr. John C. Thesken, 216–433–3012, John.C.Thesken@nasa.gov

**Glenn contact:**
Dr. James K. Sutter, 216–433–3226, James.K.Sutter@nasa.gov

**Authors:**
Dr. John C. Thesken, Dr. Leigh Phoenix, Dr. James K. Sutter, Dr. Pappu L. Murthy, Regor Saulsberry, Nate Greene, Duane M. Revilock, Jr., and Dr. Jeffrey I. Eldridge

**Headquarters program office:**
Space Shuttle

**Programs/projects:**
Orbiter

Thus far, the Centaur vessel and a 40-in.-diameter shuttle vessel have been tested to burst. The acquired data are enabling accurate calibration of mechanical response models to predict stress states as a function of pressure so that the appropriate stress-rupture life-extension reliability can be determined.

**References**

1. Revilock, Duane M., Jr.; Thesken, John C.; and Forsyth, Bradley S.: Digital Image Correlation Utilized To Obtain Full-Field Strains of a Full-Scale Orbiter Composite Overwrapped Pressure Vessel During Stress Rupture Life Testing. Research & Technology 2006. NASA/TM—2007-214479, 2007, pp. 312–313. http://www.grc.nasa.gov/WWW/RT/2006/RX/RX69S-revilock.html
2. Eldridge, Jeffrey I.; and Thesken, John C.: Raman-Based Strain Measurements Successfully Incorporated Into Composite Overwrapped Pressure Vessel Pressurization Tests. Research & Technology 2006. NASA/TM—2007-214479, 2007, pp. 309–310. http://www.grc.nasa.gov/WWW/RT/2006/RX/RX67D-eldridge.html

# Mechanical Characteristics of Kevlar/Epoxy Overwrap From Columbia's Composite Overwrap Pressure Vessels Investigated

The NASA Glenn Research Center in partnership with the Ohio Aerospace Institute (OAI) collaborated with the NASA Kennedy Space Center and Cornell University to lead an experimental investigation to extract crucial mechanical characteristics from the *Space Shuttle Columbia*'s remaining composite overwrapped pressure vessels (COPVs). The work was focused on (1) determining manufacturing residual strains due to the overwrap/liner interference fit and (2) measuring the mechanical properties of Kevlar (DuPont)/epoxy strands extracted from *Columbia*'s composite overwrap.

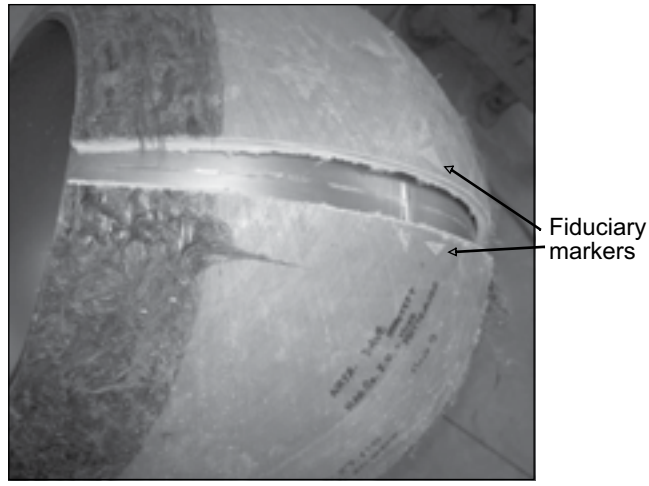


*Saw cut through overwrap showing expanded gap.*

The investigation began with the development and approval of plans to section two of *Columbia*'s Main Propulsion System (MPS) COPVs: a 40-in.- and a 26-in.-diameter vessel. Glenn researchers were onsite at Kennedy to participate in and document the tank dissections. Researchers measured residual strains by placing several fiduciary markers on a tank's surface and measuring the arc length between them. As the dissection proceeded, the manufacturing residual strains were relaxed, producing significant gaps in the progressing saw cuts. This photograph shows a finished meridian cut with the fiduciary markers. After the complete section was removed, significant residual strains were recovered. The bar chart compares the strains measured to those available from manufacturer's data sheets. These data were the first available experimental verifications of the residual strains and were of significant value to the Orbiter COPV Team.

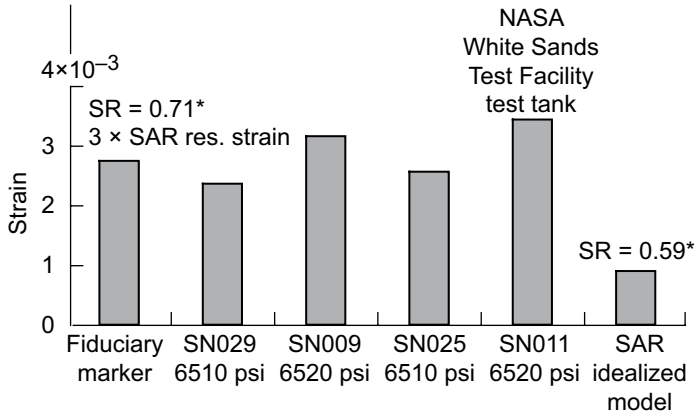


*Summary of zero-pressure overwrap residual strains. Columbia MPS 40-in. overwrap linear fiduciary marker measurements and individual volumetric changes from data packs. SR, ratio of operating fiber stress to burst fiber stress; SAR, original manufacturer's stress analysis report (1978 Stress Analysis Report); SN, vessel serial number; asterisk (*), original thin-shell analysis of 68-percent load share, with no adjustments for creep, rate effects, or through-the-thickness gradients.*

Sections of the composite were sent to Glenn, where techniques were developed to extract individual fiber strands from the solid composite sections. These strands were then mounted on specially designed cardboard picture frames to provide support and alignment for mechanical testing. Strand specimen testing is often used only to provide strength data since it is difficult to apply extensometry without disturbing the specimen. This was overcome by employing Glenn's unique digital imaging correlation (DIC) technology to obtain strains in the specimen gauge length without contact. The photograph on the next page shows the typical test setup for the specimen along with the resolved DIC strain distribution and the digital wave acoustic emission sensors. The resolved strains show a shear concentration on one side of the specimen because of the preferential failure of a portion of the filaments. Together with the acoustic emission data, these results demonstrate that failure in these strands was progressive. The graph on the next page summarizes the strength-versus-failure strain for the distinct vessels.

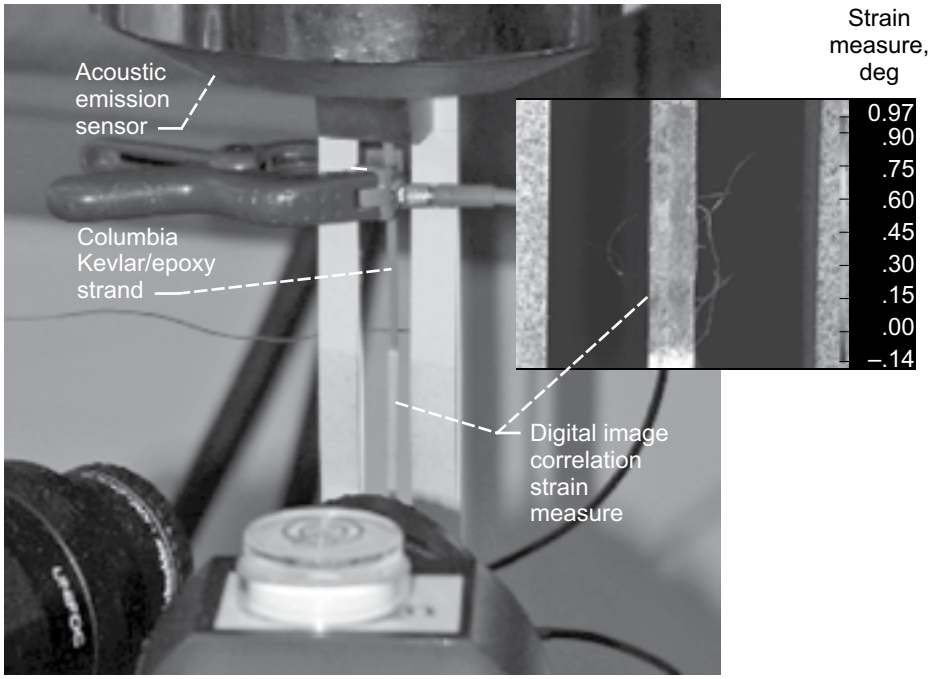


*Tensile property testing of Columbia strands.*

These experiments have been extremely valuable in understanding the mechanical characteristics of COPVs. The data are being used in modeling efforts to assess the performance of COPVs on the remaining shuttle fleet.

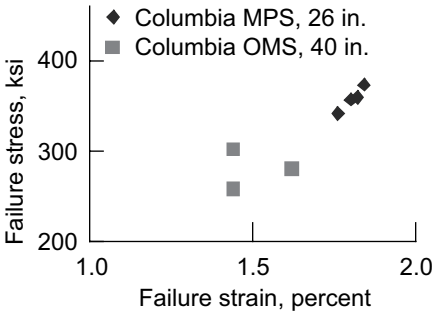


*Columbia strand test results. Vendor minimum strength, 490 ksi; stresses were based on 0.000542 in.$^2$ per roving. OMS, orbital maneuvering system.*

**Ohio Aerospace Institute (OAI) contact:**
Dr. John C. Thesken, 216–433–3012, John.C.Thesken@nasa.gov

**Glenn contact:**
Dr. James K. Sutter, 216–433–3226, James.K.Sutter@nasa.gov

**Authors:**
Dr. John C. Thesken, Dr. James K. Sutter, Richard Russell, Bill Wendorf, Fred Banke, Phil Stroda, Dr. Leigh Phoenix, Justin Littell, and Dr. Gregory N. Morscher

**Headquarters program office:**
Space Shuttle

**Programs/projects:**
Shuttle Orbiter

# Raman-Based Strain Measurements Successfully Incorporated Into Composite Overwrapped Pressure Vessel Pressurization Tests

The stress rupture life of the composite overwrapped pressure vessels (COPVs) used on the space shuttle was reevaluated as part of the return-to-flight effort because of concerns that COPV stress rupture life may be significantly lower than the original predictions. Pressurization testing of shuttle COPVs was performed at the NASA White Sands Test Facility (WSTF) as the critical assessment of the risk of COPV rupture. Because the total elastic strain, including the residual manufacturing contribution, sustained by the Kevlar fibers in the Kevlar (DuPont)/epoxy composite overwrap is a key factor in the rupture strength of the COPVs, monitoring the Kevlar fiber strain during pressurization was an essential component of the testing. However, the standard strain-gauge-based strain measurements previously employed during pressurization tests only measured the applied strain and did not account for the contribution of residual manufacturing strain in the fibers, which can have a large effect on COPV stress rupture life.

Researchers from the NASA Glenn Research Center utilized the well-known strain-dependent peak shifts (0.23-percent strain per $cm^{-1}$ shift of the Kevlar Raman peak at 1610 $cm^{-1}$) observed in Raman spectra of Kevlar fibers to provide a measurement of total elastic strain, including residual strain. After demonstrating residual stress measurements in the Kevlar/epoxy overwrap on an unpressurized Centaur rocket COPV at Glenn, Glenn researchers worked onsite at the WSTF to install and demonstrate Raman strain measurement as part of the critical COPV pressurization tests.

Many problems were overcome to incorporate these measurements. The risk of COPV burst necessitated remote control of probe positioning and measurement acquisition from a control room well removed from the concrete block house where the pressurization tests took place. In addition, Raman strain measurements could not interfere with any of the other measurements being performed simultaneously, such as the conventional strain gauge measurements and digital image correlation.

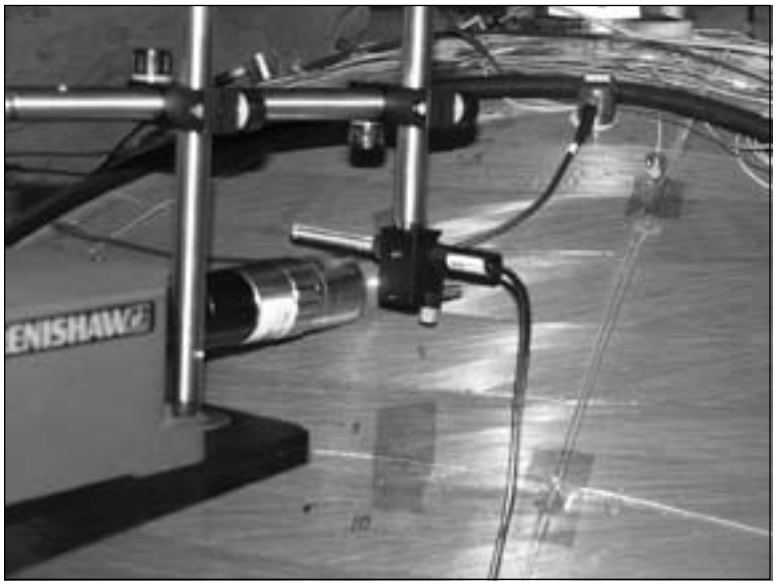


*Top: Tripod-mounted Raman strain probe positioned in front of shuttle COPV. Bottom: Closeup view.*

The photographs show the tripod-mounted Raman strain probe aimed at the shuttle COPV that was instrumented for pressurization tests at the WSTF. This Raman strain probe successfully monitored (see the graph on the next page) total elastic strain in the Kevlar fibers up to the COPV maximum operating pressure of 4860 psi, where the total fiber elastic strain was measured to be 0.58 percent, with negligible residual strain upon depressurization. These results agreed quite well with resistance strain gauge measurements and theoretical predictions. The residual manufacturing strains were measured by comparing the Raman spectra of fibers on the tank at zero pressure to fibers removed from a similar tank and, hence, free of residual manufacturing strain. The residual strains did not agree well with theoretical predictions, suggesting that the residual strain field may be less uniform than assumed in the theoretical analysis. These Raman strain measurements are providing critical input for the prediction of COPV stress rupture life.

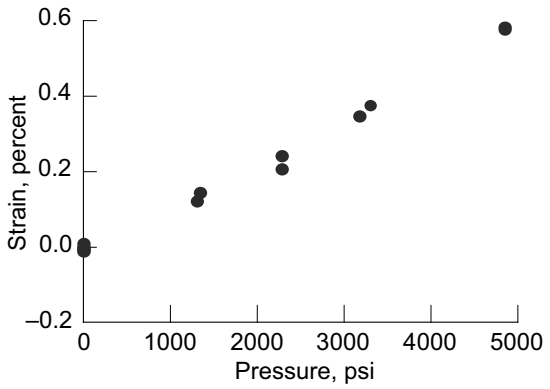


*Total elastic strain of Kevlar fibers measured with Raman strain probe plotted versus COPV pressure during pressurization tests at the WSTF.*

**Glenn contact:**
Dr. Jeffrey I. Eldridge, 216–433–6074, Jeffrey.I.Eldridge@nasa.gov

**Ohio Aerospace Institute (OAI) contact:**
Dr. John C. Thesken, 216–433–3012, John.C.Thesken@nasa.gov

**Authors:**
Dr. Jeffrey I. Eldridge and Dr. John C. Thesken

**Programs/projects:**
Space Shuttle Program

## Microstructure of Kevlar Fibers Used in Composite Overwrapped Pressure Vessels Characterized

Composite overwrapped pressure vessels (COPVs) are composed of a fiber-based composite overwrapping a polymeric or metallic liner. The liner serves as a permeability barrier, and the composite provides structural integrity and strength. The vessels are used as pressurization systems and to contain a variety of fluids on the space shuttle orbiter and on the *International Space Station*. Main propulsion system vessels supply helium for manifold repressurization, purging, pneumatic valve actuation, emergency shutdown, and propellant dumps. Reaction control system (RCS) tanks store and provide helium for the pressurization of RCS thrusters, and orbital maneuvering system (OMS) vessels provide propellant to the OMS engines.

An effort led by NASA White Sands Test Facility (WSTF) is underway to characterize spare fleet leader COPVs, including burst tests to compare residual and design strengths and to assess the possibility of the creep deformation of Kevlar (DuPont) fibers. The NASA Nondestructive Evaluation Working Group is fabricating new Kevlar bottles for accelerated aging tests. The NASA Glenn Research Center supported both of these efforts by performing fractography of samples from ruptured fleet leader vessels, as well as from stress-ruptured Kevlar strand tests at Texas Research Institute. Techniques for polishing Kevlar fibers and composites were developed, enabling Glenn to characterize polished cross sections of composites and mounted strands. As bottles from the accelerated aging program become available, they will undergo microstructural characterization.

Microstructural analysis (optical and field emission scanning electron microscopy is being used at Glenn to support the development of nondestructive evaluation methods, as well as additional Glenn efforts focused on characterizing constitutive properties and residual stresses.

The micrographs from ruptured fleet leader COPVs illustrate representative findings. Deformation of fibers in transverse compression resulted in regions in which the fiber cross section began to deviate from round to “square” (see the top left figure on the next page), with little matrix seen between adjacent fibers. Some cross-sectional areas show

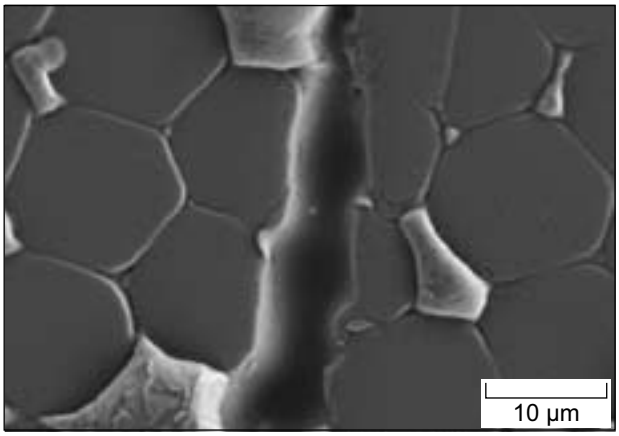


*Polished cross section from fleet leader tank serial number (S/N) 032 showing close packing of fibers and fiber deformation.*

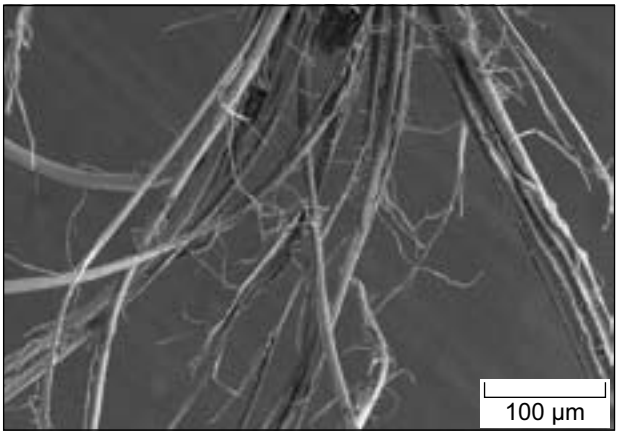


*Fractography of ruptured fiber from fleet lead tank S/N 011 showing branchlike fracture arising from hierarchical structure of Kevlar fiber.*

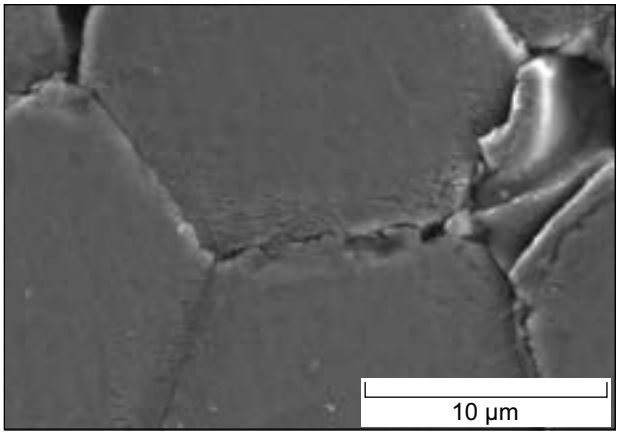


*Polished cross section from fleet leader tank S/N 007 showing fiber damage at edges.*

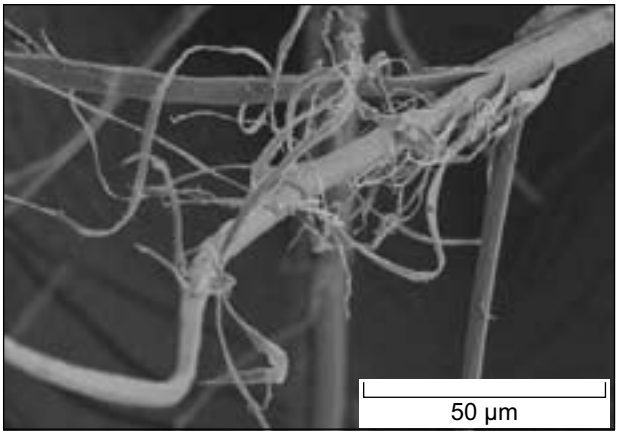


*Fractography of ruptured fiber from fleet lead tank S/N 011 showing "string-cheese" failure.*

damage around fiber edges, which may denote actual fiber damage or weaker fibers, which are more readily damaged in polishing (see the bottom left figure).

Fractography of ruptured fiber bundles illustrates the hierarchical structure of Kevlar fibers, which is composed of bundles of fibrils that split apart upon fracture (see the figures on the right).

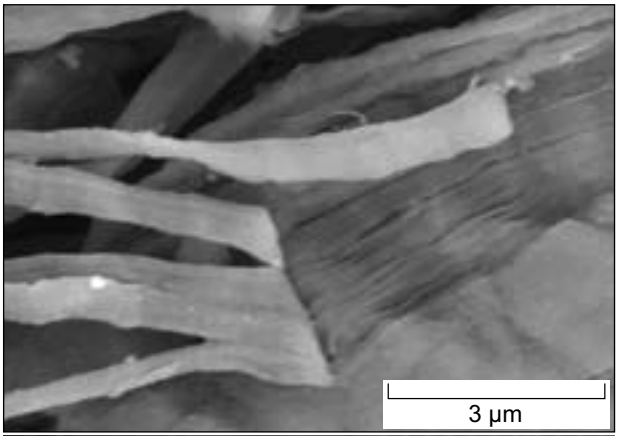


*Fractography of ruptured fiber from fleet lead tank S/N 011 showing parallel sheet structure within Kevlar fiber.*

**Glenn contact:**
Frances I. Hurwitz, 216–433–5503, Frances.I.Hurwitz@nasa.gov

**Authors:**
Dr. Frances I. Hurwitz and Joy A. Buehler

**Headquarters program office:**
Office of Safety and Mission Assurance, NASA Nondestructive Evaluation Working Group

**Programs/projects:**
Shuttle Orbiter

# Digital Image Correlation Utilized To Obtain Full-Field Strains of a Full-Scale Orbiter Composite Overwrapped Pressure Vessel During Stress Rupture Life Testing

An assessment by the NASA Engineering and Safety Center showed that composite overwrapped pressure vessels (COPVs) used on the space shuttle orbiters faced an increased risk of stress rupture of the Kevlar (DuPont)/epoxy overwrap because of their long-term usage. Stress rupture in Kevlar is not well understood, but the experimental data show that stress rupture life is a function of time at operating stress and temperature. Owing to the presence of load-sharing metallic liners and manufacturing procedures that induce significant residual stresses, the state of stress in the Kevlar is difficult to define. Analytical models developed by the NASA Glenn Research Center and others would benefit from full-scale mechanical response test data for calibration purposes.

The NASA Johnson Space Center's White Sands Test Facility (WSTF) conducted ambient-temperature hydrostatic pressurization testing of a COPV to improve understanding of the fiber stresses in the COPV components. One of Glenn's roles was to provide full-field displacement and strain data of each pressurization test, utilizing the Glenn Ballistic Impact Laboratory's three-dimensional digital image correlation (DIC) system, ARAMIS, with high-speed cameras. This system was shipped to WSTF for the pressurization tests, and the data were analyzed by Glenn personnel.

*COPV dot pattern painted on vessel for DIC.*

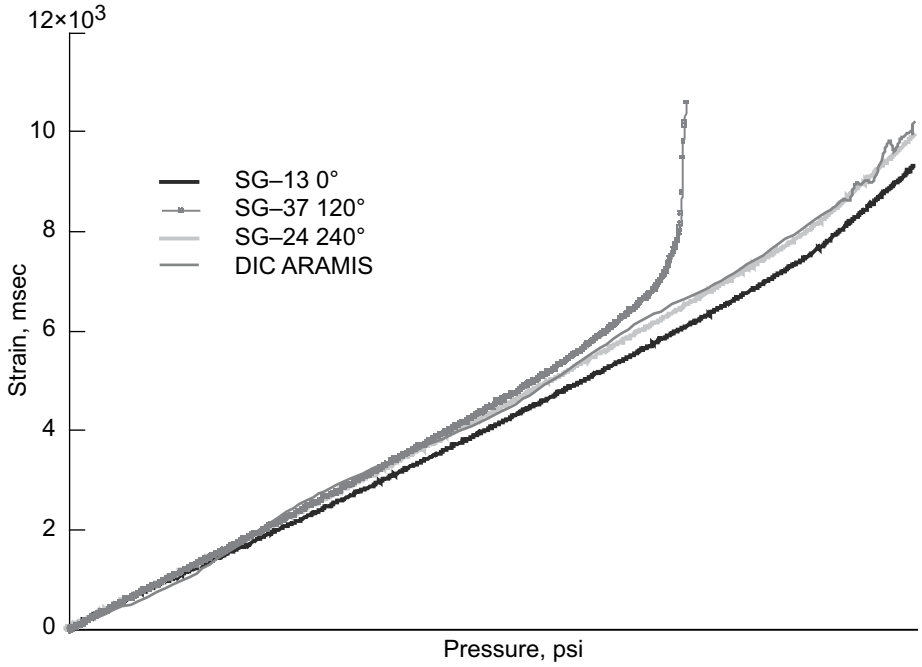


*Comparison of DIC strain to gauges (strain gauge SG–13, –37, and –24) at the equator of the COPV.*

The ARAMIS software uses principles of three-dimensional image correlation photogrammetry that give full-field displacement and strain measurements. The system was developed by GOM mbH of Braunschweig, Germany, and is distributed by Trillion Systems in North America. The basic principles of three-dimensional image correlation photogrammetry have been known for about 15 years, and ARAMIS has been commercially available for about 10 years. The system requires spraying random high-contrast dot patterns onto a sample; this pattern is then tracked in ARAMIS by thousands of unique correlation areas known as facets (see the photograph). The center of each facet is a measurement point that can be thought of as a three-dimensional extensometer. Arrays of facets form in-plane strain rosettes. The facet centers are tracked in each successive pair of images, with accuracy up to one hundredth of a pixel.

Two high-speed systems were used in the tests, one focusing on the upper boss area and the other on the equator of the vessel. Each system gave a field of view of approximately 70 in.$^2$ Strain gauges were mounted on the vessel to show strains in the hoop direction of the fiber. The strain data from ARAMIS followed the same trend as the mounted strain gauges during pressurization cycles (see the graph on the preceding page and the top figure on this page). However, the data showed some abnormalities at the edges of the solved areas and at areas where the vessel had cables and other instrumentation devices. The full-field principle strain data for the burst pressurization cycle show strains over 2 percent on the right side of the vessel, indicating a weak spot in that section (see the bottom figure). These high strains were not picked up by the mounted gauges since they only could provide strains in the hoop direction. Overall, the two systems provided an accurate measurement of strain in the COPVs during multiple pressurization tests.

The data have been extremely useful in establishing the degree of uniformity in the biaxial strain field present in the structure. This is important because rotational symmetry and spherical symmetry assumptions are used in finite-element and thin-shell models, respectively. In regions where strains were uniform and in agreement with resistance strain gauges, the results were valuable in calibrating the existing mechanical response models.

**Glenn contacts:**
Duane M. Revilock, Jr., 216–433–3186,
Duane.M.Revilock@nasa.gov

**Ohio Aerospace Institute (OAI) contact:**
John C. Thesken, 216–433–3012, John.C.Thesken@nasa.gov

**Authors:**
Duane M. Revilock, Jr., Dr. John C. Thesken, and Bradley S. Forsyth

**Headquarters program office:**
Space Shuttle Program

**Programs/projects:**
Space Operations

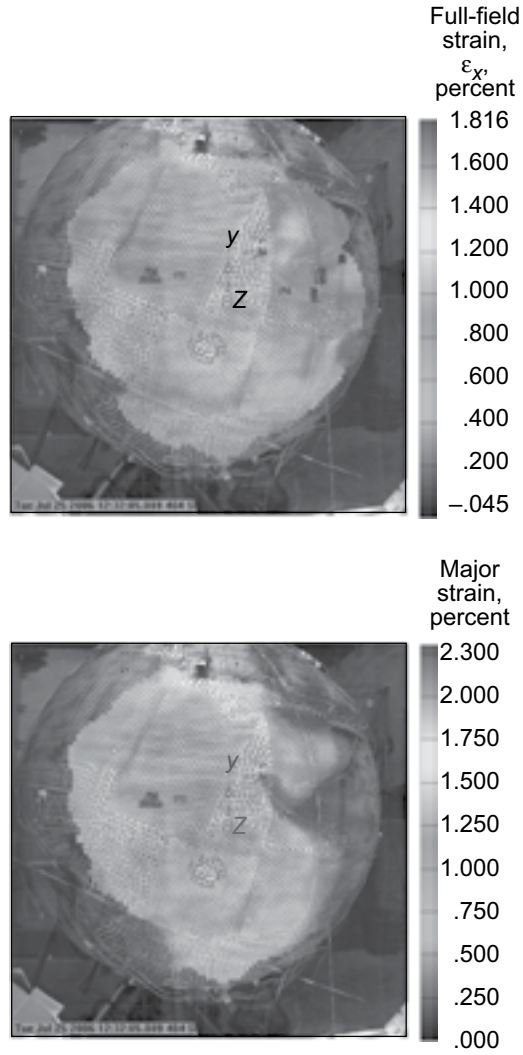


*Top: Full-field strain x of the vessel before burst. Bottom: Full-field principal strain of the vessel before burst. These figures are shown in color in the online version of this article (http://www.grc.nasa.gov/WWW/RT/2006/RX/RX69S-revilock.html).*

# Ballistic Impact Response of Kevlar and Zylon Evaluated

Ballistic impact tests were conducted at the NASA Glenn Research Center on layered dry fabric rings to measure their impact strength and to provide data for developing improved numerical models for simulating impact events. The rings were representative of containment systems that are used in all commercial jet engines to prevent a fan blade from penetrating the engine case in the event of an accident that causes the blade to be released during operation. New materials and structures are being evaluated by NASA to increase aviation safety. The impact energy absorption of two different fabrics, Kevlar 49 (DuPont) and Zylon–AS (Toyobo Co., Ltd.) in two different fabric architectures were compared. The test specimens consisted of layers of plain woven cloth, 25-cm- (10-in.-) wide, wrapped around a ring-shaped fixture.

This series of still photographs depicts a typical impact test. The fixture was steel and had an outer diameter of 102 cm (40 in.), a thickness of 2.5 cm (1 in.), and a height the same as the fabric width (25 cm, ~10 in.). The fabric was rolled around the fixture under a controlled tension of 25 N (5.5 lb) to make up the desired number of layers. The fixture had a 25.4-cm (10-in.) circumferential gap at the impact location. It was placed in front of the gun barrel at an incline of 15° so that the projectile, after exiting the gun barrel, passed over the front edge of the ring, passed through the gap in the ring fixture, and impacted the fabric from the general direction of the center of the ring. The projectiles were various sized pieces of flat stainless steel that represented fan blades. The orientation of the projectiles at impact was controlled and measured.

We found that for the same fabric architecture and under the given impact and environmental conditions, Zylon was able to absorb over twice the energy of the equivalent weight Kevlar. The normalized energy absorbed was independent of the number of layers of fabric and was approximately linearly related to the presented area of the projectile. These results are illustrated in the graph on the next page.

**Bibliography**

Pereira, J. Michael; and Revilock, Duane M.: Ballistic Impact Behavior of Kevlar® and Zylon® Fabrics in Jet Engine Blade Containment Applications. 56th Meeting of the Aeroballistic Range Association, NASA Johnson Space Center, Houston, TX, Oct. 2005. (Available only on CD.)

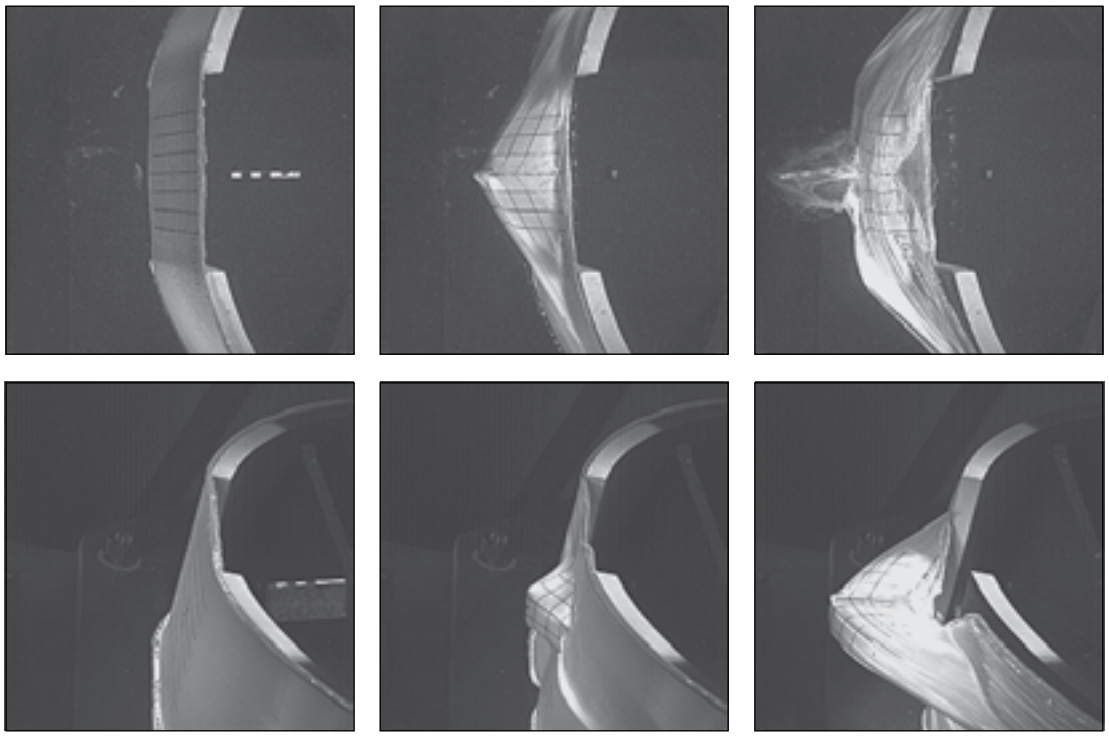

*Series of photographs showing two views of a typical test. The projectile is impacting the fabric from the right.*

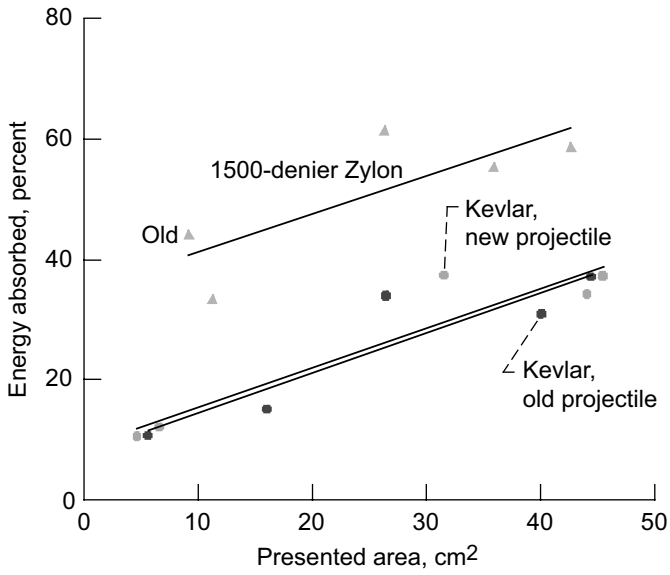


*Percent of energy absorbed as a function of presented area.*

**Glenn contacts:**
Duane M. Revilock, Jr., 216–433–3186, Duane.M.Revilock@nasa.gov

J. Michael Pereira, 216–433–6738, J.M.Pereira@nasa.gov

Matthew E. Melis, 216–433–3322, Matthew.E.Melis@nasa.gov

**Authors:**
Duane M. Revilock, Jr., Dr. J. Michael Pereira, and Matthew E. Melis

**Headquarters program office:**
Aviation Safety Project

**Programs/projects:**
Aircraft Aging and Durability Program

## Candidate Materials Examined for Ice Mitigation on the External Tank Liquid Oxygen Feedline Bracket

Five brackets located along the axis of the 17-in.-diameter liquid oxygen (LOx) feedline secure it to the exterior of the space shuttle external tank (ET). The brackets are used to provide stability for the line, but must also accommodate feedline movement during the expansion and contraction experienced at tanking, during prepressurization, and finally during launch and ascent. Since the early 1980s, ice has been observed to build up in the gaps between the tank and the bracket and between the bracket and the feedline (see the photographs on the next page). Because the launch loads and articulation that the feedline undergoes are sufficient to liberate the ice, the debris threat that ice poses is a significant concern. By filling the gap between the feedline and its bracket, ice can also damage the insulating foam during prelaunch movement of the feedline.

In October 2005, the NASA Engineering and Safety Center assembled an intercenter team with members from the NASA Glenn Research Center, NASA Kennedy Space Center, NASA Marshall Space Flight Center, NASA Johnson Space Center's White Sands Test Facility (WSTF), and NASA Langley Research Center to address this problem. The team underwent a thorough review of available documentation on specific bracket motions, bracket design, and tolerances to better understand the constraints. Throughout fiscal year 2006, the team worked to provide a flexible foam solution that would fill any gaps and thereby minimize and/or prevent ice formation.

Researchers in Glenn's Materials and Structures Division were responsible for the thermal and mechanical testing and for general evaluation of candidate materials to establish desired properties and guide material development. From the document review, certain limits were established that successful materials must pass to be considered. Specifically, the material must withstand thermal environments from cryogenic temperatures through 300 °C and must remain flexible throughout this range. It also must be able to withstand repeated compressions of 20 percent without failing. Within these boundaries, scientists and engineers tested several foam types—including (1) methyl phenyl silicone foams, (2) friable glass microsphere foams, (3) aerogel-silicone foams, and (4) polyimide-based foams—and benchmarked the results versus the standard BX–265 polyurethane ET closeout foam.

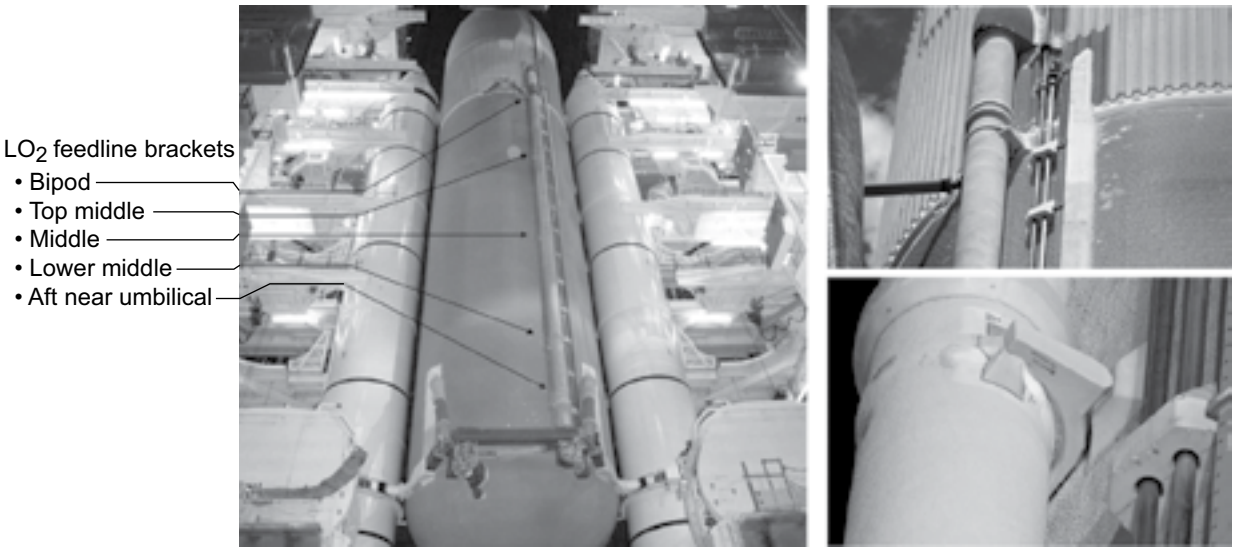


*Left: View of space shuttle during STS–114 prior to orbiter attachment reveals the five attachment brackets securing the LOx feedline to the ET. Top right: Closeup view of topmost bracket before tanking. Bottom right: Closeup view of the same bracket after tanking with obvious ice seen in the gap between the bracket and the feedline, and in the area between the tank and the bracket.*

All the materials tested boasted initial decomposition temperatures several hundred degrees higher than the benchmark BX–265 foams, with several past 500 °C. Ultimately, the first three classes of foams failed for different reasons including stiffening at cryogenic temperatures and unacceptable thermal transitions (thermodynamic chemical restructuring) in the specified temperature range. Additional testing with the Polyumac foam on an engineering test article is planned. If successful, the technology will be transferred to the Space Shuttle Program for potential implementation.

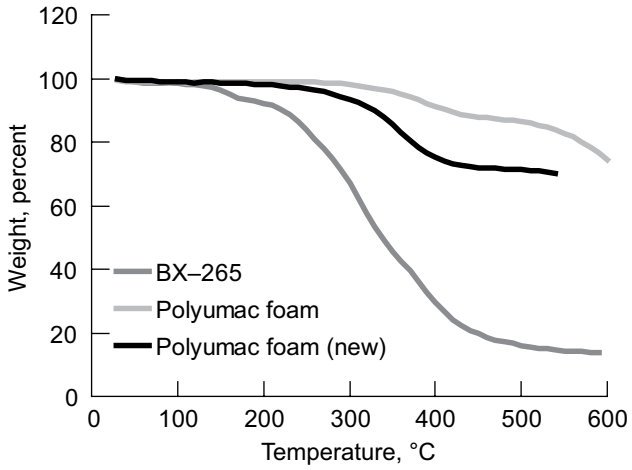


*Thermogravimetric analysis of two versions of the leading candidate foam produced by Polyumac Inc. (Hialeah, FL) compared with the standard shuttle polyurethane closeout foam BX–265. Both versions performed extremely well, with the onset of decomposition beginning around 250 °C and material degradation well past 300 °C.*

**Find out more about LOx feedline bracket ice mitigation:**
http://www.grc.nasa.gov/WWW/NESC/PDF_files/LOXFeedline_icemit.pdf

**Glenn contacts:**
Dr. Lynn Capadona, 216–433–5013, Lynn.A.Capadona@nasa.gov

Dr. Brad Lerch, 216–433–5522, Bradley.A.Lerch@nasa.gov

**Authors:**
Dr. Lynn A. Capadona,
Dr. Bradley A. Lerch, Paul A. Trimarchi, and George R. Harpster

**Headquarters program office:**
NASA Engineering and Safety Center

**Programs/projects:**
NASA Engineering and Safety Center, Bracket Ice Mitigation

# Methodology Based on Vertical Scanning Interferometry Developed for Space Shuttle Window Inspection

As a result of the *Space Shuttle Columbia* accident, a number of safety-related concerns have emerged in the Space Shuttle Program. One such concern involves the ability to adequately locate and measure window defects, which accumulate from several types of debris sources during shuttle missions. Of particular interest is the ability to accurately and precisely determine defect depth because this parameter dictates whether or not a window needs to be taken out of service.

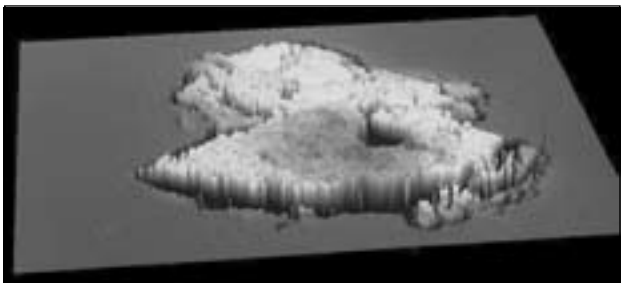

*Three-dimensional surface produced by performing a typical scan with the VSI tool. Note that both detailed height information and morphological information are produced via this method.*

In the past, a two-dimensional section-based approach was used to assess window defects for depth: an optical microscope outfitted with a micrometer stage used a replica to ascertain defect depth. This technique had been shown to have a depth-resolution capability on the order of ~5 μm with a variation on the same order. Until recently, this level of accuracy was considered to be acceptable, but recent changes in the program requirements dictated a higher degree of resolution capability. To meet this requirement, a new methodology/technique based on vertical scanning interferometry (VSI) was developed at the NASA Glenn Research Center. This approach utilizes changes in fringe modulation to accurately determine the point of focus on a three-dimensional object during a scan, thereby allowing for the full three-dimensional reconstruction of the object or defect.

The top photograph shows the typical result of performing a scan using the VSI technique. Using this technique, depth measurements on shuttle window defects were shown to be resolvable to within 0.5 μm of the actual depth. The technique was validated by comparing the three-dimensional reconstruction results from the VSI technique to independent measurements made in a field emission gun-scanning electron microscope. The results, which can be seen in the following figures, show that the VSI technique produced the salient features of the defect with a high degree of accuracy. The results taken from the VSI-based technique constitute an order of magnitude improvement in sensitivity over measurements taken via the former method. Along with the improved sensitivity gains, the technique also provides both quantitative and qualitative morphology information, which can aid in determining the root cause associated with the creation of the defect.

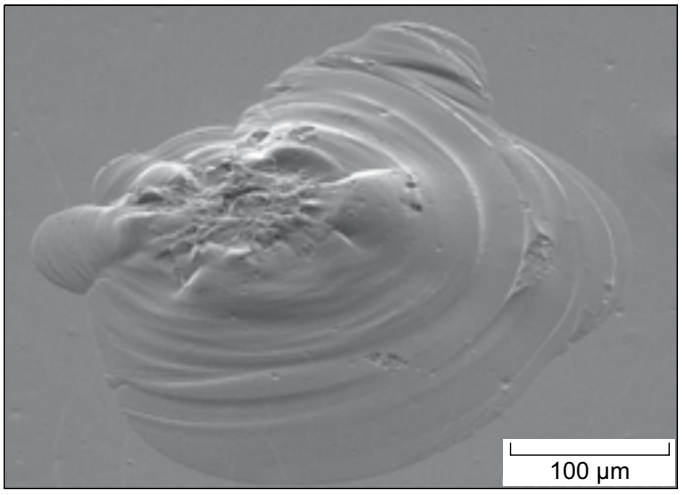


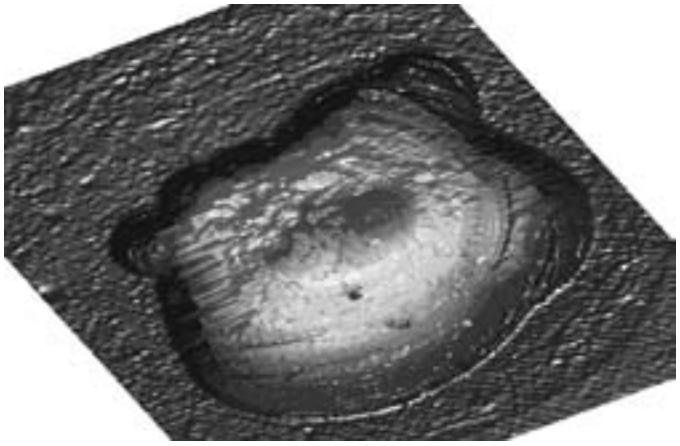

*Comparison of the defect morphology. Left: Image taken with field emission gun-scanning electron microscope. Right: Three-dimensional surface produced by performing a scan with the VSI tool. All features of the defect were captured by the VSI technique.*

The VSI-based methodology also showed a significant reduction in operator-to-operator depth-measurement variability. With the initial feasibility study on the technique demonstrated successfully, the technique was transferred to the NASA Kennedy Space Center, where work is underway to certify the instrument and technique for use. Once completed, the VSI-based methodology will be adopted as the technique used to recertify all shuttle windows for flight.

**Glenn contacts:**
Dr. Santo A. Padula II, 216–433–9375, Santo.A.Padula@nasa.gov

Dr. Michael V. Nathal, 216–433–9516, Michael.V.Nathal@nasa.gov

**Authors:**
Dr. Santo A. Padula II and Terry R. McCue

**Headquarters program office:**
Space Operations

**Programs/projects:**
Space Shuttle

## Composite Crew Module Designed and Sized for Orion

The Crew Exploration Vehicle, or *Orion*, will replace the space shuttle for ferrying crews to and from the *International Space Station*; and in the future, it is planned to take part in manned lunar and Mars missions. The spacecraft consists of three components (see part (a) of the figure beginning on the next page): (1) the Launch Abort System, (2) the Crew Module (CM), and (3) the Service Module. Although *Orion* will ultimately be constructed by Lockheed Martin Corporation, NASA developed an independent CM design as part of a smart buyer exercise. The current design is predominantly metallic, relying heavily on NASA's past experience with the Apollo program configuration. Early in 2006, the NASA Engineering and Safety Center assembled a team to examine the possibility of an alternative composite-dominated CM design. As part of this activity, NASA Glenn Research Center personnel and contractors took the lead on designing and sizing a potential monocoque CM concept and performed sizing analysis on a geometrically stiffened CM concept designed by the NASA Ames Research Center (see parts (b) to (e) of the figure).

The NASTRAN finite-element code and the HyperSizer structural sizing code were used for the design and sizing (ref. 1). HyperSizer identifies structural components (e.g., beams, bars, and panels) from a finite-element model and, on the basis of the loads on each component from the finite-element analysis results, along with specified factors of safety, sizes the components for minimum weight. Specializing in composite materials and stiffened sandwich panels, HyperSizer checks a large number of static failure and buckling criteria, enabling rapid design with a high level of confidence. HyperSizer's new HyperFEA module (ref. 2), which automates the process of sizing all components in a structure and of iterating with NASTRAN to capture the effects of load redistribution, was employed for rapid turnaround. Load cases representing internal pressure, 15g Launch Abort System acceleration, and 16g late abort reentry deceleration were considered in the analyses.

The monocoque composite CM concept combines the CM aeroshell and pressure vessel over part of the CM acreage (see part (b)). Starting with an existing CM finite-element model provided by the NASA Langley Research Center that had a separate aeroshell and pressure vessel, the pressure vessel wall was moved outward to merge with the aeroshell as shown. The original conceptual design involved TEEK (low-density polyimide closed-cell foam designed and patented at Langley) sandwich panels with hybrid composite laminate facesheets composed of IM7/8552 graphite/epoxy, Kevlar (DuPont)/epoxy, glass/epoxy,

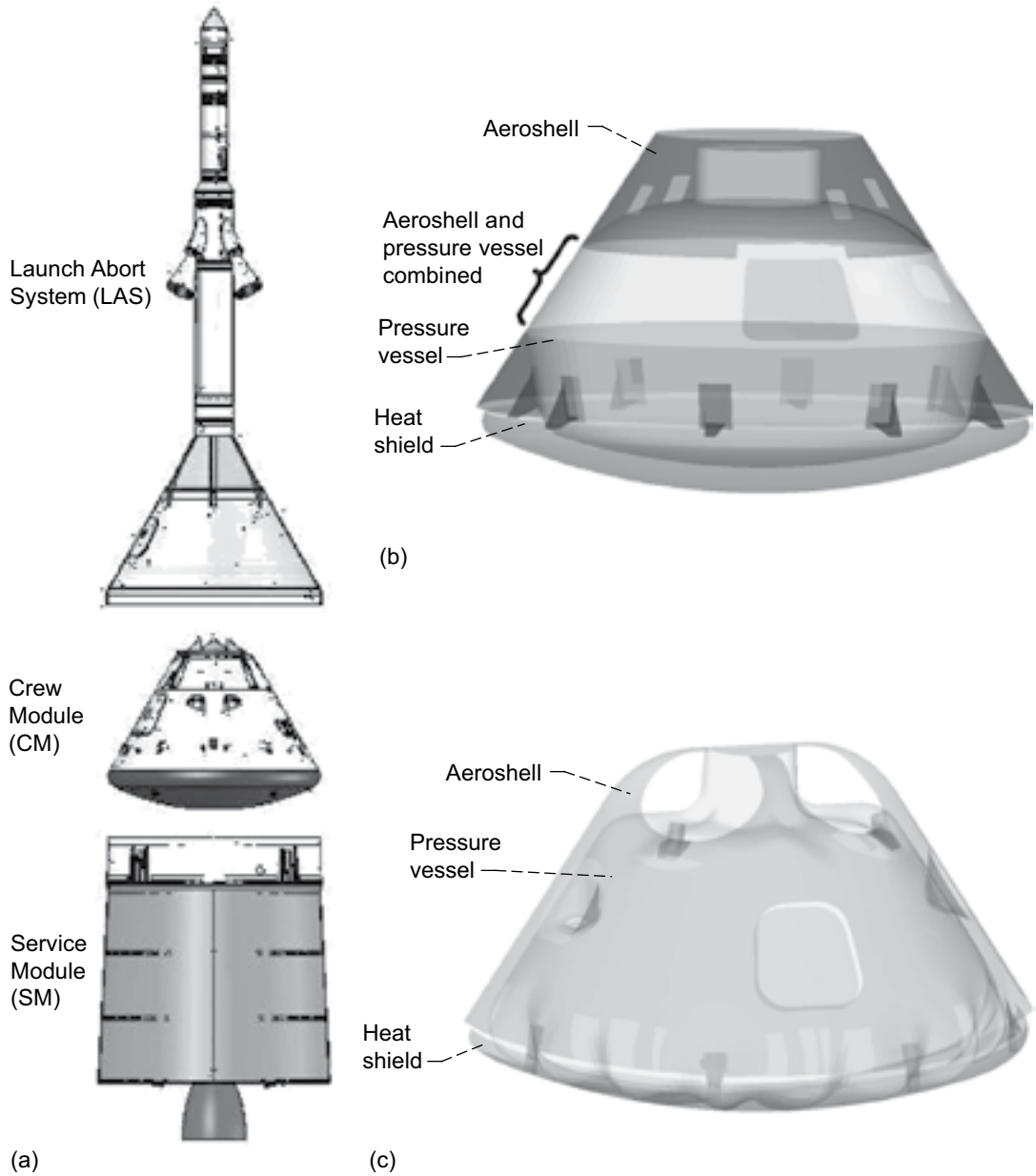


*Proposed design for composite crew module. (a) Orion. (b) Monocoque CM design led by Glenn. (c) Geometrically stiffened CM design led by Ames.*

and T300/934 carbon/epoxy plies. The facesheet construction was chosen to provide micrometeoroid impact resistance. A total CM weight of 1965 lb resulted from the HyperSizer-NASTRAN sizing of the CM with these TEEK sandwich panels. Next, an alternative design involving webcore (ref. 3) sandwich panels with identical facesheets was sized. The resulting weight was 1538 lb—427 lb less than the original sandwich construction concept. Finally, a third design was considered involving IM7/977–2 graphite/epoxy facesheets in conjunction with webcore sandwich panels. The resulting weight was 1081 lb—an additional savings of 457 lb. Part (d) shows the webcore sandwich panel core thickness resulting from the sizing.

The geometrically stiffened CM concept is based on corrugating the top and bottom of the pressure vessel (similar to the bottom of a plastic 2-liter soft drink bottle) to derive stiffness from the geometry itself (see parts (c) and (e)). Ames designed this concept and provided a NASTRAN finite-element model for the concept to Glenn. Glenn performed the HyperSizer-NASTRAN sizing. The original concept

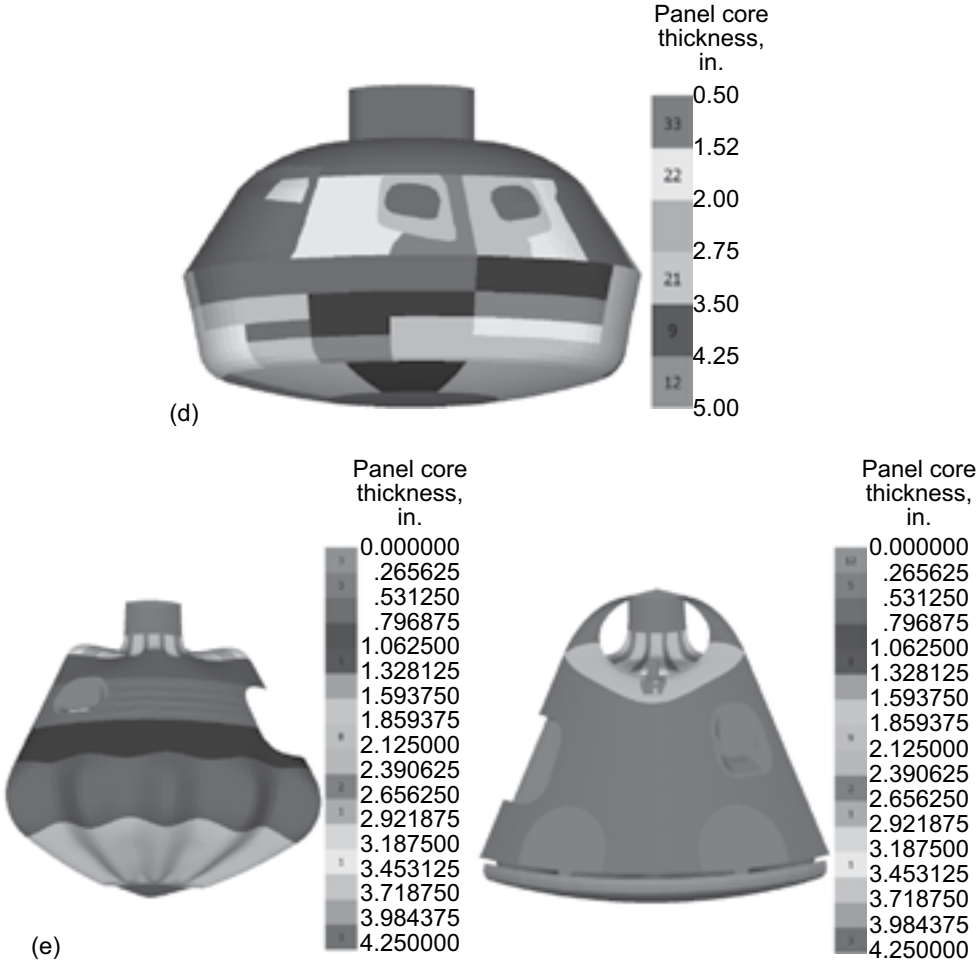


*Proposed design for composite crew module. (d) Sized webcore sandwich panel core thickness for monocoque CM design. (e) Sized webcore sandwich panel core thickness for geometrically stiffened CM design (one-fourth model). This figure is shown in color in the online version of this article (http://www.grc.nasa.gov/WWW/RT/2006/RX/RX73L-arnold3.html).*

for the geometrically stiffened design called for the pressure vessel to be composed almost exclusively of solid IM7/977–2 graphite/epoxy laminates rather than sandwich panels. This configuration resulted in a total sized CM weight of 1851 lb. As an alternative design, webcore sandwich panels with IM7/977–2 graphite/epoxy facesheets were introduced, reducing the sized CM weight to 1330 lb—a weight savings of 520 lb. Part (e) shows the webcore sandwich panel core thickness resulting from the sizing.

**References**


1. HyperSizer Structural Sizing Software. Collier Research and Development Corporation, Hampton, VA, 2005. http://hypersizer.com/Products/products.htm
2. HyperFEA Product Brochure. Collier Research Corporation, Hampton, VA, 2005. http://www.hypersizer.com/documents/brochure_HyperFEA.pdf
3. Stoll, Frederick, et al.: Advancements in Engineered Composite Sandwich Core Materials. SAMPE 2006, Long Beach, CA, 2006. http://www.sampe.org/store/paper.aspx?pid=3520 Accessed May 24, 2007.



**Glenn contact:**
Dr. Steven M. Arnold, 216–433–3334, Steven.M.Arnold@nasa.gov

**Ohio Aerospace Institute (OAI) contact:**
Dr. Brett A. Bednarcyk, 216–433–2012, Brett.A.Bednarcyk@nasa.gov

**Authors:**
Dr. Brett A. Bednarcyk,
Dr. Steven M. Arnold, Peter J. Bonacuse, Craig S. Collier, Phillip W. Yarrington, and Robert J. Allen


**Headquarters program office:**
NASA Engineering and Safety Center

**Programs/projects:**
Composite Crew Module

# Polymer Matrix Composites Evaluated for Advanced Space Radiators

High-temperature polymer matrix composites (PMCs) based on high thermal conductivity (~1000 W/mK) pitch-based carbon fibers (e.g., K1100, Cytec Industries Inc., and K13D2U, Mitsubishi Chemical Corp.) are being considered for facesheet/fin structures in next-generation large-area space radiators such as the heat-rejection system for the Jupiter Icy Moon Orbiter and the Service Module radiator for the Crew Exploration Vehicle (CEV) (refs. 1 and 2). Replacement of conventional metallic structures with PMC structures could lead to significant weight reductions along with improved thermal performance, tailorability and manufacturability, and structural integrity. However, several challenges, including establishing the reliability and space durability of these PMC structures, must be addressed. Various commercial resin systems including cyanate esters (e.g., RS–9D, YLA, Inc.), bismaleimides, and polyimide were selected for this application because of their high-temperature capability and processability. To improve the thermal conductivity (TC) and microcracking resistance of PMCs, nanocomposites modified with vapor-grown carbon nanofibers (VGCNFs) and/or exfoliated graphite flakes (ExGfs) were evaluated at the NASA Glenn Research Center (see the following figure).

PMC laminates were designed to match the thermal expansion coefficient of various metal heat pipes or tubes. Large, thin composite panels were successfully fabricated after the cure conditions for the brittle, highly anisotropic fibers were optimized. The space durability of these PMCs was assessed by accelerated thermal aging tests in high vacuum (1 to $3\times10^{-6}$ torr) at 227, 277, and 316 °C for up to 10,000 hr (see the photographs on the next page). Various thermal, physical, and mechanical properties were monitored systematically as a function of aging time and temperature to determine potential degradation mechanisms. High-quality nanocomposites were fabricated and evaluated for TC and durability. TC was measured in both in plan and through the thickness. The effects of microcracking on TC also were investigated in collaboration with Prairie View A&M University. Laminates were subjected to up to 1250 thermal spiking conditioning cycles (from 177 to –196 °C) to generate microcracks, and TC is being measured. The radiation resistance of PMCs including nanocomposites was evaluated by electron beam irradiation testing at –20, 200, and 400 Mrad. Weight changes after irradiation were minimal regardless of material,

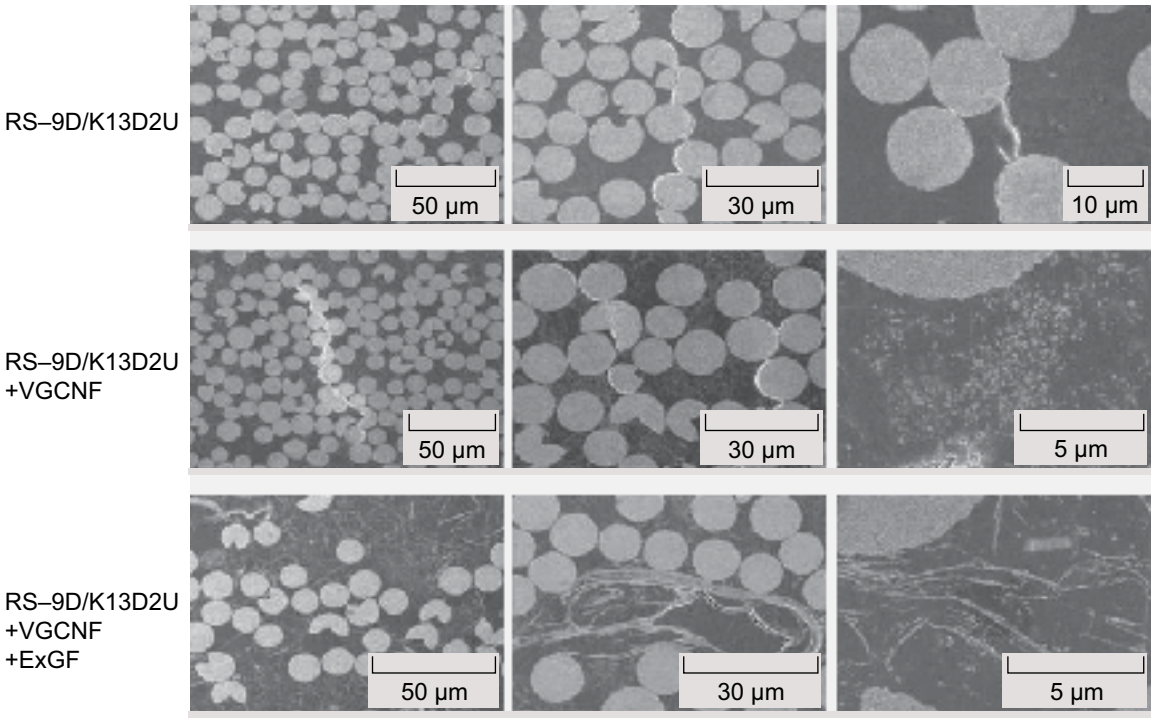


*Typical scanning electron microscope micrographs of RS–9D/K13D2U PMC that was modified with vapor-grown carbon nanofibers (VGCNF) and/or exfoliated graphite flakes (ExGF), showing fiber/filler distribution, connectivity, and defects.*

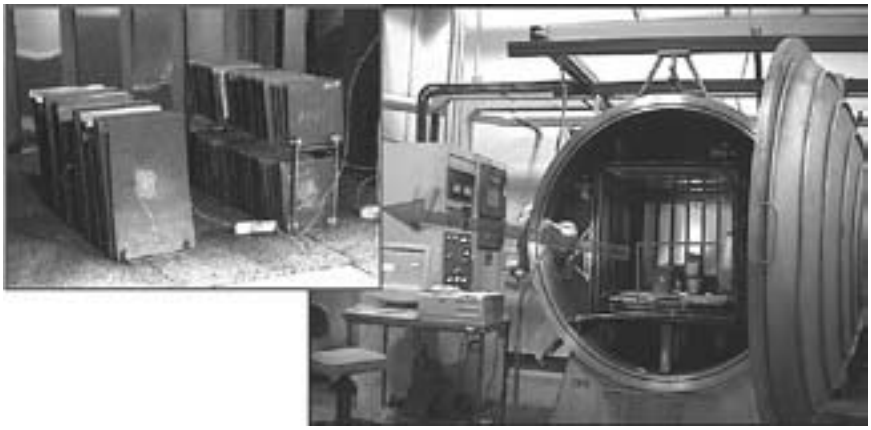

*Long-term vacuum thermal aging test setup for PMC facesheet candidates.*

but more extensive residual property measurements are being conducted to ascertain any sign of degradation.

A joint program with the NASA Johnson Space Center for the Advanced Technology Demonstration Radiator project was initiated to develop and demonstrate a PMC radiator for the CEV. In this project, the fabrication of prototype substructures based on feasible material-design-fabrication concepts for the PMC-heat tube attachment such as the PMC facesheet design; the heat tube type, geometry, and radius; and heat tube-PMC bonding mechanisms are being pursued; and the structural integrity of the substructures prepared from these methods is being evaluated. A commercial CE film adhesive (RS–4A, YLA Inc.) rated for up to 230 °C cure was used to bond heat tubes to PMC facesheets, along with higher use temperature CE adhesives modified with conductive nanofillers to improve TC. A full-scale, a single quarter-cylinder panel based on the results of these studies and representing one-fourth of a CEV radiator is planned to be fabricated and tested in fiscal year 2007.

**References**


1. Bowman, Cheryl L.; Ellis, David L.; and Singh, Mrityunjay: Material Options for Fabricating Radiator Facesheets in Support of Dynamic Power Conversion. Proceedings of Space Technology and Applications International Forum (STAIF–2006), Albuquerque, NM, 2006.
2. Shin, E. Eugene; Bowman, Cheryl; and Beach, Duane: High Thermal Conductivity Polymer Matrix Composites (PMC) for Advanced Space Radiators. Proceedings of High Temple Workshop 2007, Sedona, AZ, 2007.


**Find out more about this research:**

**Glenn's Polymers Branch:**
http://www.grc.nasa.gov/WWW/5000/MaterialsStructures/polymers/

**Glenn's Advanced Metallic Branch:**
http://www.grc.nasa.gov/WWW/5000/MaterialsStructures/metallics/

**Glenn's Thermal Energy Conversion Branch:**
http://www.grc.nasa.gov/WWW/tmsb/


**Ohio Aerospace Institute (OAI) contact:**
Dr. E. Eugene Shin, 216–433–2544, Euy-Sik.E.Shin@nasa.gov

**Glenn contacts:**
Dr. Cheryl L. Bowman, 216–433–8462, Cheryl.L.Bowman@nasa.gov

Duane E. Beach, 216–433–6285, Duane.E.Beach@nasa.gov

**Authors:**
Dr. E. Eugene Shin,
Dr. Cheryl L. Bowman, and
Duane E. Beach


**Headquarters program office:**
Space Mission and Exploration Systems Mission Directorate

**Programs/projects:**
Prometheus, Crew Exploration Vehicle

# Crew Exploration Vehicle Landing Concept Designed

The NASA Exploration program is investigating the merits of water and land landings for the Crew Exploration Vehicle (CEV). For land landings, four options are under investigation: (1) retrorockets, which fire and slow the CEV before landing; (2) deployable crushable material, which deploys just before and crushes during landing, thus absorbing energy; (3) airbags; and (4) deployable legs, which deploy before landing and contain material that absorbs energy during landing. The NASA Glenn Research Center investigated the effectiveness of the deployable leg concept. Structural models of the deployable leg concept were integrated with the Crew Model (CM), and computational simulations were performed to determine vehicle and component loadings, acceleration levels, and astronaut risk.

The simulations needed to simulate the complex transient dynamic behavior of the CM and the attached deployable legs impacting a landing surface. The deployable leg-CM model consists of a collection of structural parts. The main portion of the vehicle, which consists of the pressure vessel, associated structure, and internal components, is modeled as a rigid part having inertia properties equivalent to the Design Analysis Cycle II CM design. Since this part is modeled as rigid, it exhibits no structural deformation and no structural loadings are computed for it. Although the actual landing surface will be some form of soil that will deform on impact and absorb energy, for this study, the landing surface was assumed to not deform or absorb energy from landing, so it also was modeled as a rigid part. The landing surface was made large enough so that the vehicle would not leave the surface during the range of landing simulations performed in this study.

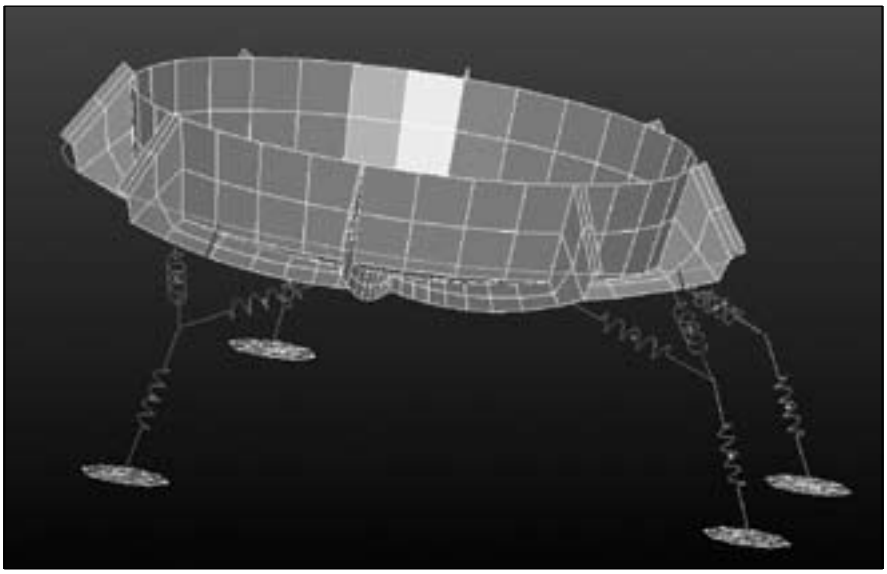

*CM model with deployable legs.*

Four sets of deployable legs are attached to the pressure vessel and all are centered about the direction of the horizontal landing velocity. The two front sets are 45° apart, and the two rear sets are 135° apart. The locations were determined from the design of the vehicle underbody and the availability of space and attachment points. Having the two front sets closer together is advantageous for horizontal landing velocities, and having the two rear sets more spread out adds to overall vehicle stability.

The primary and secondary landing leg designs are fundamentally similar to those used for the Apollo Lunar Module: the primary legs are designed for compression only, and the secondary legs are designed for both compression and tension. Both the primary and secondary landing legs have an outer housing that contains crushable material which is designed to provide a constant force regardless of leg displacement. The appropriate crushable material could provide constant deceleration to the CEV and could maintain acceleration levels at or below design criteria. However, the material can only be designed for a single design condition, and performance at off-design conditions will be less than optimal. The length of the legs, the crushable force, and the stoke length were altered several times until an optimal design was obtained.

SUMMARY OF MAXIMUM ACCELERATIONS[a]
[Vertical velocity, 25 ft/sec]

| Pitch, deg | Maximum acceleration, g | | | |
|---|---|---|---|---|
| | Horizontal velocity, ft/sec | | | |
| | 0 | 20 | 40 | 60 |
| –15 (nose down) | 4 | 8 | 8 | 10 |
| 0 | 9 | 8 | 8 | 8 |
| +15 (heel down) | 8 | 7 | 9 | 6 |

[a]Maximum of *x*, *y*, or *z* body-fixed position.

The table depicts the overall effectiveness of the deployable legs, summarizing the maximum accelerations in the x- and y-directions for each of the 12 load cases. The maximum acceleration levels were fairly constant regardless of the loading conditions. For large horizontal landing velocities, the maximum acceleration did not exceed 10g; and for zero horizontal velocity, the maximum acceleration was 9g. Pitch angle also had only a limited effect on the acceleration levels. The maximum acceleration was 10g for a nose-down landing and 9g for a heel-down landing. The results show that the deployable legs effectively accommodated the 12 landing conditions.

**Glenn contacts:**
Dr. Charles Lawrence, 216–433–6048, Charles.Lawrence-1@nasa.gov

Paul A. Solano, 216–433–6518, Paul.A.Solano@nasa.gov

Karen F. Bartos, 216–433–6478, Karen.F.Bartos@nasa.gov

**Authors:**
Dr. Charles Lawrence, Paul A. Solano, and Karen F. Bartos

**Headquarters program office:**
Exploration Systems Mission Directorate

**Programs/projects:**
Crew Exploration Vehicle

## Lightweight Cryogenic Hydrogen Storage Tanks—Preliminary Design for Unmanned Aerial Vehicle Applications Evaluated

Unmanned aerial vehicles (UAVs) are a proven asset in tactical military applications, providing remotely operated surveillance and reconnaissance in battlefield operations. The civil aviation sector also envisions an expanding role for UAVs including atmospheric science research. Power and propulsion systems for UAVs currently being investigated use fuel cells with electric motors and internal combustion engines. Many of the uses for UAVs require high-altitude, long-endurance platforms, necessitating low vehicle dry weight. In addition, low to zero emissions of environmentally harmful products is desired. Because of its high specific energy content and near zero harmful emission, liquid hydrogen ($LH_2$) is emerging as a possible fuel for these propulsion systems. A large, lightweight, reusable cryogenic liquid storage tank that can store fuel for several days would be needed for $LH_2$ UAVs.

$LH_2$ storage tanks have many challenges and design issues, including determining the optimal geometrical shape and size for the tank, maintaining cryogenic temperature for preventing hydrogen boiloff, hydrogen permeation, and hydrogen embrittlement. Currently insulation systems use foams (including advanced aerogels) and multilayer insulation (MLI) systems with vacuum. Potential tank wall materials include monolithic metals, polymer matrix composites, and discontinuously reinforced metal matrix composites.

Over the past few years, NASA has supported some development of crosslinked silica aerogels and nanoclay-enhanced graphite/epoxy composites for potential use in advanced, lightweight, durable tank designs. For nanoclay-enhanced graphite/epoxy composites, clay platelets are added to the epoxy prior to fiber impregnation to reduce matrix microcracking and permeation. A

nanoclay-enhanced graphite/epoxy composite has been proposed for cryogenic tanks because these tanks may weigh less than metal tanks and may provide sufficient hydrogen permeation resistance.

Engineering analyses were performed to assess the possibility of using these materials in UAV tank applications. Analyses were performed to assess the benefits of these materials and to provide material property value targets for the continued development of these materials. To investigate the use of crosslinked silica aerogels and nanoclay-enhanced graphite/epoxy composites in cryogenic hydrogen tank designs, we considered two tank designs: (1) a vacuum-jacketed tank design and (2) a sandwich tank construction consisting of an inner and outer shell and an aerogel insulating core. For a common set of design specifications, we performed thermal and structural analyses of each design to compare tank architectures, materials, and insulation. The tank size was based on 1323 lb of propellant with an ullage volume of 5 percent. A vacuum-jacketed tank with an MLI blanket offered the most efficient thermal design. Spray-on-foam insulation and high- or low-strength aerogels resulted in a much heavier tank system because of a higher rate of heat penetration and thus propellant boiloff (see the figure). Analyses showed that a sandwich construction with an aerogel core is not a viable design solution for long-duration applications. A vacuum-jacketed design is far superior to aerogel, although a design using aerogel insulation may be feasible for shorter duration missions. The results also revealed that the application of nanoclay-enhanced graphite/epoxy should be limited to the construction of outer tanks in a vacuum-jacketed design, since a graphite/epoxy inner tank does not provide enough weight savings over an aluminum tank and since the ability of nanoclay-enhanced graphite/epoxy to limit hydrogen permeation is still in question.

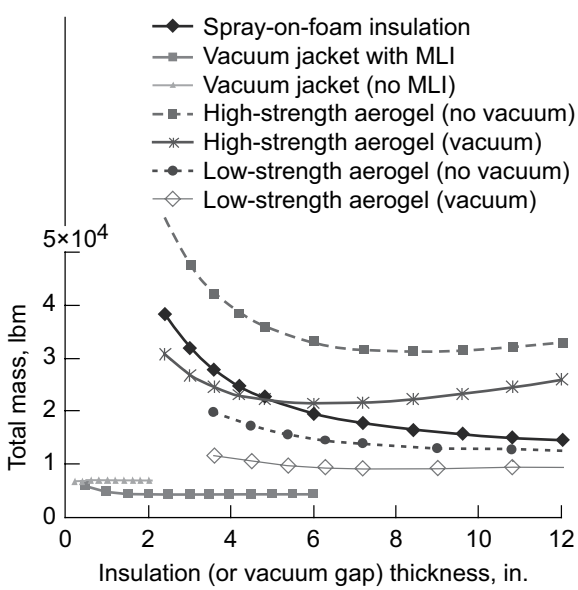


*Combined weight estimates for tank, propellant (including boiloff), and insulation for 14-day mission plotted versus insulation thickness for various insulating schemes (–70 °F ambient temperature).*

**Bibliography**

Brewer, G.D.: Hydrogen Aircraft Technology. CRC Press, Boca Raton, FL, 1991.

Mital, Subodh K., et al.: Review of Current State of the Art and Key Design Issues With Potential Solutions for Liquid Hydrogen Cryogenic Storage Tank Structures for Aircraft Applications. NASA/TM— 2006-214346, 2006. http://gltrs.grc.nasa.gov/Citations.aspx?id=143

Sullivan, R.M., et al.: Engineering Analysis Studies for Preliminary Design of Lightweight Cryogenic Hydrogen Tanks in UAV Applications. NASA/TP—2006-214094, 2006. http://gltrs.grc.nasa.gov/Citations.aspx?id=206

**Glenn contacts:**
Dr. Roy M. Sullivan, 216–433–3249, Roy.M.Sullivan@nasa.gov

**Authors:**
Dr. Subodh K. Mital and
Dr. Roy M. Sullivan

**Headquarters program office:**
Aeronautics Research Mission Directorate

**Programs/projects:**
Unmanned aerial vehicles

# Nanoindentation Hardness of Compacted JSC–1 Lunar Soil Simulant Determined

Structural and functional reliability is vital for lunar surface operations using moving mechanical assemblies, such as life-support machinery, rovers, and scientific equipment. Lunar dust has been identified as the most important obstacle to this reliability, so the NASA Glenn Research Center, in collaboration with the Nippon Institute of Technology, studied the hardness of a lunar dust simulant (JSC–1) for future comparison with lunar materials. When contact surface material is removed by hard lunar dust particles, abrasive wear occurs. Particles may adhere to a second surface or may exist as loose particles between two contacting surfaces. The rate of abrasive wear is at least one to two orders of magnitude greater than that of other mechanisms, such as adhesive wear and fatigue. A material's static hardness has been related to its abrasive wear resistance, and abrasive wear rate is inversely proportional to Vickers hardness for many annealed pure metals. Therefore, a hardness study of JSC–1 is important in determining how the hardness and elastic modulus of lunar dust will affect the wear behavior of materials proposed for lunar mechanisms.

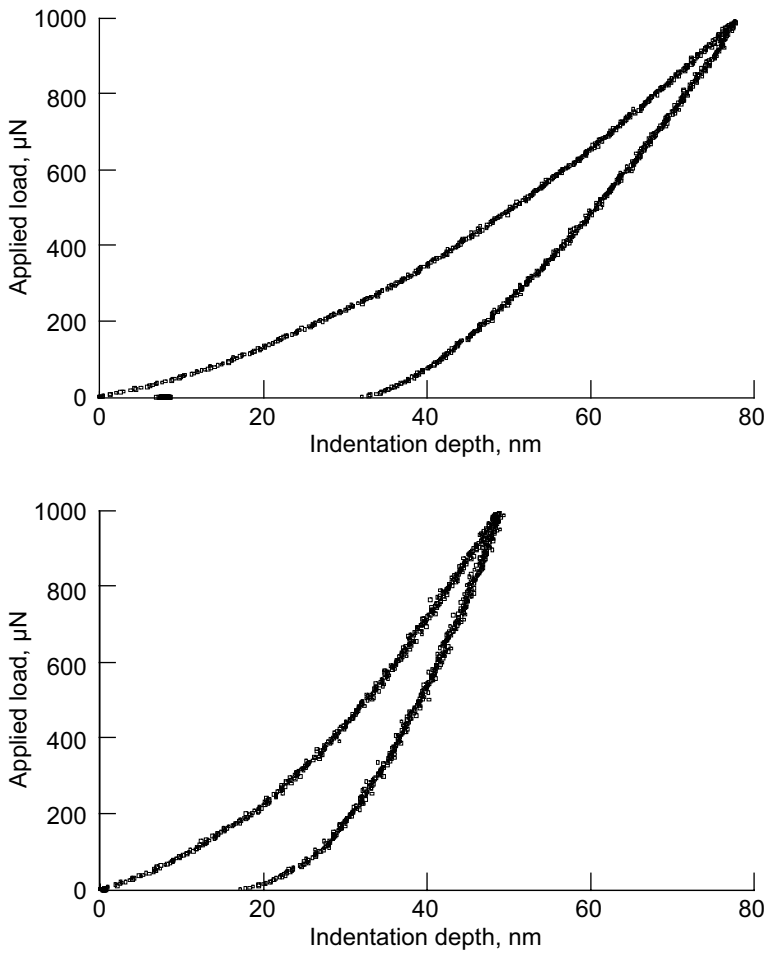


*Examples of load-displacement data for compacted JSC–1. Top: Cold-pressed JSC–1. Bottom: Hot-pressed JSC–1.*

Tests showed that JSC–1 is cohesive: its particles stick together under cold or hot pressing at compaction pressures of 4 to 6 GPa. Hot pressing at 1473 K produced a higher bulk density than cold pressing at 296 K did. The surfaces in contact with JSC–1 were flats polished with 1-μm diamond powder, and the root mean square roughness of the cold- and hot-pressed JSC–1 surfaces were 0.1 μm.

A Berkovich indenter was used for nanoindentation measurements up to a predefined load of 1000 μN with the cold- and hot-pressed JSC–1, and load/unload curves were recorded for each indentation with a nanoindentation device mounted in an atomic force microscope (AFM). Reference measurements were conducted with fused silica, silicon, silicon carbide, amorphous silicon carbide films on silicon, and polycrystalline boron carbide. Both cold- and hot-pressed JSC–1 were characterized by low-vacuum scanning electron microscopy (SEM), three-dimensional measurements with SEM, and AFM for morphological and topographical analysis; x-ray diffraction for phase analysis; and x-ray fluorescence, energy dispersive x-ray spectroscopy with SEM, and electron probe microanalysis or x-ray microanalysis using wavelength dispersive x-ray spectrometers for chemical and elemental analysis.

Measurements similar to those in the graphs gave the nanoindentation hardness for cold- and hot-pressed JSC–1, fused silica, silicon, silicon carbide, amorphous silicon carbide films on silicon, and polycrystalline boron carbide. The photomicrographs on the next page show the resulting nanoindentations.

The measured hardness value of the cold-pressed JSC–1 was 2/3rd, 1/8th, and 1/9th, respectively, of that of silicon, silicon carbide, and polycrystalline boron carbide. The harder ceramics, such

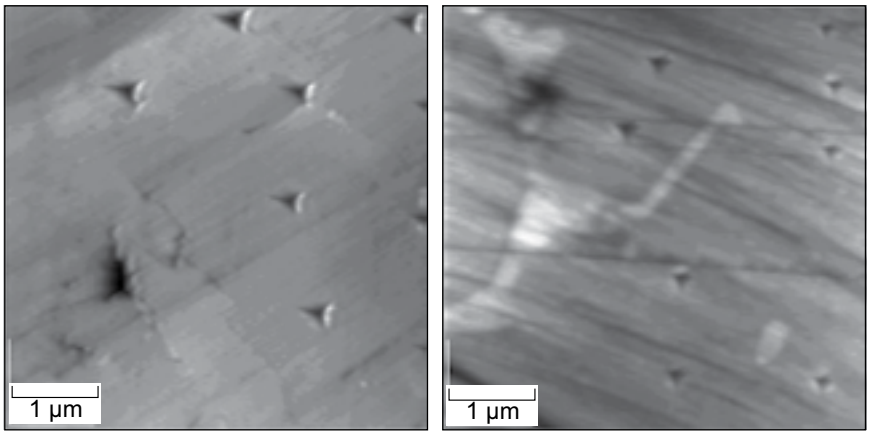


*Scanning probe microscope images of the nanoindentations obtained by in situ imaging using the Berkovich indenter tip to scan the surface. Left: Cold-pressed JSC–1. Right: Hot-pressed JSC–1.*

as boron carbide and silicon carbide, most likely possess greater abrasive resistance to JSC–1. In a separate investigation, the authors found that JSC–1 did readily abrade silicon. Thus, boron carbide and silicon carbide may be needed to provide suitable antiabrasion surfaces for long-life, lightweight components in surface mobility and power systems for lunar operations.

**References**

1. McKay, David S., et al.: JSC–1: A New Lunar Soil Simulant. Proceedings of the 4th International Conference on Engineering, Construction, and Operations in Space, American Society of Civil Engineers, New York, NY, 1994, pp. 857–866.
2. Carrier, W. David, III; Olhoeft, Gary R.; and Mendell, Wendell: Physical Properties of the Lunar Surface. The Lunar Sourcebook: A User's Guide to the Moon, Grant H. Heiken, David T. Vaniman, and Bevan M. French, eds., Ch. 9—Cambridge University Press, New York, NY, 1991, pp. 475–594.
3. Miyoshi, Kazuhisa: Abrasion: Plowing and Cutting. Solid Lubrication Fundamentals and Applications, Ch. 5, Marcel Dekker, New York, NY, 2001, pp. 221–256.

**Glenn contacts:**
Dr. Kazuhisa Miyoshi, 216–433–6078, Kazuhisa.Miyoshi@nasa.gov

Dr. Kenneth W. Street, Jr., 216–433–5032, Kenneth.W.Street@nasa.gov

Dr. Phillip B. Abel, 216–433–6063, Phillip B. Abel@nasa.gov

**Nippon Institute of Technology contacts:**
Manabu Suzuki, 0480–33–7535, m-suzuki@nit.ac.jp

Kenichi Ishibashi, 0480–34–4111, m3061001@mstu.nit.ac.jp

**Authors:**
Dr. Kazuhisa Miyoshi, Manabu Suzuki, Kenichi Ishibashi, Dr. Kenneth W. Street, Jr., and Dr. Phillip B. Abel

**Headquarters Program Office**
Advanced Space Technology Program, Exploration Systems Mission Directorate

**Programs/projects**
Advanced Space Technology Program, Exploration Systems Research & Technology, Advanced Materials and Structures Concepts Element Program, Advanced Mechanisms and Tribology Technologies for Durable Lightweight Actuation and Mechanical Power Transmission Systems Project

# INDEX OF AUTHORS AND CONTACTS

Both authors and contacts are listed in this index. Articles start on the page numbers following the names.


**A**

Abdul-Aziz, Dr. Ali 72
Abel, Dr. Phillip B. 326
Agui, Dr. Juan H. 193
Aksay, Dr. Ilhan 234
Allen, Robert J. 318
Anderson, Bernhard H. 164
Anderson, Robert C. 140, 143
Ansari, Dr. Rafat R. 176
Arnold, Dr. Steven M. 258, 264, 318
Arrington, Lynn A. 174
Asipauskas, Marius 177
Asmus, Amy R. 42
Assaad, Mahmoud C. 92

**B**

Baaklini, Dr. George Y. 77
Bakhle, Dr. Milind A. 272, 273
Bamberger, Helmut H. 286
Banke, Fred 307
Banks, Bruce A. 123, 131
Barlow, Karen L. 15
Bartos, Karen F. 323
Batur, Dr. Celal 212
Baumeister, Joseph F. 6
Beach, Duane E. 111, 321
Bednarcyk, Dr. Brett A. 258, 264, 318
Beeson, Dr. Harold 190
Beheim, Dr. Glenn M. 90, 97
Beltran, Luis R. 338
Bennett, William R. 245
Bents, David J. 99
Bigelow, Glen S. 211
Birchenough, Arthur G. 112
Bizon, Thomas P. 31
Blaha, Charles A. 92
Blaser, Tammy M. 34
Bonacuse, Peter J. 318
Bowman, Dr. Cheryl L. 197, 200, 222, 321
Bowman, Dr. Randy R. 247, 250
Bridges, Dr. James E. 138, 338
Briggs, Maxwell H. 300
Briones, Janette C. 34
Britton, Doris L. 101
Brooker, John E. 182, 191
Brown, Dr. Gerald V. 274, 276, 279, 281, 284
Bruckner, Dr. Robert J. 300
Buehler, Joy A. 310
Burkardt, Leo A. 6

**C**

Cable, Dr. Thomas L. 240
Capadona, Dr. Lynn A. 226, 229, 232, 315
Capece, Dr. Vincent R. 272
Carek, David A. 42, 56
Caruso, John J. 75
Cerny, Jennifer 225
Chamberlin, Roger 339
Chamis, Dr. Christos C. 20, 22, 24
Chang, Bei-Jiann 99
Chen, Prof. Da-Ren 185
Chen, Dr. Liang-Yu 97
Chima, Dr. Rodrick V. 163
Choi, Dr. Benjamin B. 276, 279
Chuang, Dr. Kathy 220
Collier, Craig S. 318
Connolly, Joseph W. 46, 48, 51
Connors, Timothy R. 164
Cooper, Beth A. 332
Culley, Dennis E. 62
Cummings, Steve 202
Cuy, Michael D. 218
Czaruk, Timothy M. 286

**D**

Daniels, Dr. Christopher C. 290
DeCastro, Jonathan A. 63
de Groh, Henry C., III 290
de Groh, Kim K. 123, 124
Delgado, Irebert R. 293
DellaCorte, Dr. Christopher 300
DelRoso, Richard L. 339
DeMange, Jeffrey J. 303
Dever, Joyce A. 124, 127
Dever, Timothy P. 274, 281
DiCarlo, Dr. James A. 206, 207
Diedrick, Dale M. 174
Dietrich, Daniel L. 183
Dimofte, Dr. Florin 297
Dogan, Dr. Numan S. 32
Downey, Alan N. 42
Draper, Susan L. 255
Duffy, Dr. Kirsten P. 270
Dunlap, Patrick H., Jr. 290, 303
Dykas, Dr. Brian D. 300
Dynys, Dr. Frederick W. 212, 241, 254

**E**

Easton, John W. 183
Eichenberg, Dennis J. 330, 331
Elam, Kristie A. 81
Eldridge, Dr. Jeffrey I. 305, 309
Ellis, Dr. David L. 202
Ensworth, Clinton B. 12
Evans, Laura J. 90, 95

**F**

Farmer, Dr. Serene C. 240
Faykus, Eric W. 148
Finkbeiner, Joshua R. 303
Fischer, Dr. David G. 177
Fisher, Kenneth L. 2
Fite, E. Brian 134
Fitzgerald, Prof. Eugene 122
Flatico, Joseph M. 74
Forsyth, Bradley S. 312
Fox, Dennis S. 208
Fralick, Gustave C. 92
Frate, David T. 13
Freeh, Joshua E. 148
Fujikawa, Gene 32

**G**

Gabb, Dr. Timothy P. 197, 199
Gaier, Dr. James R. 130
Gallo, Christopher A. 148
Garcia, Christopher P. 99
Gayda, Dr. John 197, 200
Gaydosh, Darrell J. 211
Georgiadis, Dr. Nicholas J. 165
Gerber, Scott S. 117
Ghosn, Dr. Louis J. 208
Gonzalez, José M., III 92

Good, Dr. Brian S. 231
Grady, Brianne 301
Graham, Scott R. 11, 12, 13
Green, Robert D. 148
Greenberg, Paul S. 185
Greene, Nate 305
Greer, Lawrence C. 75, 83
Gubinyi, Zoltan 212
Guynn, Mark D. 103
Gyekenyesi, Dr. Andrew L. 77
Gyekenyesi, Dr. John P. 262

**H**

Haase, Dr. Wayne C. 77
Halbig, Michael C. 224
Hall, Charles S. 34
Haller, William J. 3
Hambourger, Prof. Paul 193
Hamilton, David F. 339
Hammoud, Dr. Ahmad 132
Handler, Louis M. 34
Handschuh, Dr. Robert F. 296, 297
Harpster, George R. 315
Hasan, Dr. Mohammad M. 195
Hegde, Dr. Uday G. 187, 191
Hervol, David S. 112
Hickman, Mark 13
Hicks, Michael C. 187
Hicks, Dr. Yolanda R. 140, 143
Hirt, Stephanie M. 164
Ho, Eric J. 284
Hoberecht, Mark A. 104
Hojnicki, Jeffrey S. 10
Hopkins, Dale A. 260
Howe, Donald C. 164
Huff, Dennis L. 338
Hunter, Dr. Gary W. 93, 95
Hurst, Janet B. 238
Hurwitz, Dr. Frances I. 80, 214, 310

**I**

Ilhan, Dr. Faysal 219
Irimies, David P. 56
Ishibashi, Kenichi 326

**J**

Jakupca, Ian J. 99
Jansen, Ralph H. 274, 281
John, Jeremy W. 174
Johnson, Dereck F. 200
Johnson, Donald W. 99
Jones, Dr. Jeffrey A. 176
Jones, Dr. Kevin D. 272
Jones, Robert E. 36
Joseph, James 36
Juergens, Jeffrey R. 183
Jurns, John M. 169
Just, Marcus L. 334

**K**

Kacpura, Thomas J. 37, 39
Kalluri, Dr. Sreeramesh 72, 248, 250
Kamhawi, Dr. Hani 108
Kaminski, Sharon 124
Kascak, Albert F. 277, 285, 286
Kiser, J. Douglas 80, 206, 224
Kobayashi, Takahisa 65
Kohout, Lisa L. 103
Kojima, Dr. Jun N. 149, 152, 154
Kollar, Thaddeus J. 58
Kory, Dr. Carol L. 28
Krasowski, Michael J. 75, 83
Krause, David L. 72, 248, 250
Kreeger, Richard E. 168
Kubat, Gregory 59
Kuczmarski, Dr. Maria A. 218
Kudlac, Maureen T. 169

**L**

Lambert, Kevin M. 28
Landis, Dr. Geoffrey A. 118, 120
Lang, Dr. Jerry 207
Lawrence, Dr. Charles 323
Lazbin, Jennifer 36
Lebron-Colon, Dr. Marisabel 235
Lee, Dr. Chi-Ming 146
Lee, Dr. Richard Q. 26, 28
Lekki, John D. 78
Lerch, Dr. Bradley A. 256, 315
Leventis, Dr. Nicholas 226
Lewandowski, Beth 17
Lewandowski, Dr. Edward J. 116
Lewicki, Dr. David G. 299
Lewis, Michael J. 183
Licata, Dr. Angelo 17
Lichter, Michael J. 183
Lindamood, Glenn R. 42
Linne, Diane L. 148
Litt, Jonathan S. 66
Little, Justin 307
Liu, Dr. Nan-Suey 160
Locci, Dr. Ivan E. 200, 222
Lock, Dr. James A. 89
Locke, Dr. Randy J. 140, 143
Loewenthal, William S. 200
Long-Davis, Mary Jo 166
Loyselle, Dr. Patricia L. 104

**M**

MacKay, Dr. Rebecca A. 199
Manning, Dr. Robert M. 29
Manzella, Dr. David H. 108, 255
Manzo, Michelle A. 101
Martin, Richard E. 80
Mason, Lee S. 111, 112, 113
Maul, William A. 68
McCarthy, Catherine E. 124
McCue, Terry R. 317
Meador, Dr. Mary Ann B. 226, 229, 232, 245
Meador, Dr. Michael A. 219, 234, 235
Melcher, Kevin J. 63, 68
Melis, Matthew E. 314
Mercer, Dr. Carolyn R. 3
Merret, Dr. Jason M. 164
Meyer, Michael L. 173
Mielke, Amy F. 81
Miles, Dr. Jeffrey Hilton 136
Miller, Dr. Fletcher J. 189
Miller, Dr. Robert A. 208, 218, 270
Miller, Sandi G. 234
Miller, Sharon K. 123, 127, 131
Miller, Thomas B. 11, 101
Milliser, Myrna 40
Min, Dr. James B. 266, 268, 272, 273
Miranda, Dr. Félix A. 26, 28
Mital, Dr. Subodh K. 214, 324
Miyoshi, Dr. Kazuhisa 326
Morrison, Carlos R. 284
Morscher, Dr. Gregory N. 206, 225, 307
Mueller, Dr. Carl H. 28
Murthy, Dr. Pappu L. 305
Myers, Dr. Jerry 17

**N**

Nagorny, Dr. Aleksandr S. 281
Nall, Marsha M. 334
Nathal, Dr. Michael V. 199, 254, 317
Nawash, Nuha S. 117

Nayagam, Dr. Vedha 195
Nelson, David A. 332
Nelson, Dr. Emily S. 17
Nemeth, Noel N. 262
Nesbitt, Dr. James A. 204, 222, 254
Neudeck, Dr. Philip G. 97
Nguyen, Nam T. 40
Nguyen, Dr. Quang-Viet 74, 78, 149, 152, 154
Nguyen, QuynhGiao N. 270
Nickol, Craig L. 103
Niederhaus, Dr. Charles E. 15
Noebe, Dr. Ronald D. 211

**O**

Oberle, Lawrence G. 93
Okojie, Dr. Robert S. 97
Olson, Dr. Sandra L. 189, 190
Opila, Dr. Elizabeth J. 254
Oriti, Salvatore M. 115
Oswald, Jay J. 288

**P**

Padula, Dr. Santo A., II 211, 317
Pai, Dr. Shantaram S. 260
Palaszewski, Bryan A. 1 56, 157
Palko, Joseph L. 214
Panda, Dr. Jayanta 138
Paris, Stephen W. 8
Parsons-Wingerter, Dr. Patricia A. 179
Passe, Paul J. 332
Pastel, Robert T. 208
Patnaik, Dr. Surya N. 260
Patterson, Michael J. 109
Patterson, Richard L. 132
Paxson, Dr. Daniel E. 70
Pepper, Dr. Steven V. 301
Pereira, Dr. J. Michael 314
Perusek, Gail P. 334, 335
Pham, Nang T. 11, 12, 13
Phoenix, Dr. Leigh. 305, 307
Platzer, Dr. Max F. 272
Plencner, Robert M. 6
Podboy, Gary G. 134
Popovic, Zoya 26
Proctor, Margaret P. 293
Prokop, Norman F. 83, 83
Prokopius, Kevin P. 104
Provenza, Andrew J. 285
Prud'homme, Robert K. 234

**Q**

Quinn, Todd M. 39

**R**

Raj, Dr. Sai V. 204
Rapoport, Allison L. 124
Reddy, Dr. T.S.R. 273
Regan, Timothy F. 116
Reid, Concha M. 106
Reinhart, Richard C. 34, 37, 39
Revilock, Duane M., Jr. 305, 312, 314
Richter, Dr. Hanz 66
Riehl, John P. 8
Rindfleish, Matt 282
Ringel, Prof. Steven 122
Ritzert, Frank J. 222
Robinson, Raymond Craig 208
Romanofsky, Dr. Robert R. 28
Rondineau, Sebastien 26
Ross, Raymond C. 337
Roth, Dr. Don J. 85
Rucker, Rochelle N. 124
Russell, Richard 307

**S**

Samorezov, Sergey 335
Sands, Dr. O. Scott 42, 46, 48
Sankovic, Dr. John M. 179
Sawicki, Prof. Jerzy T. 77
Sayir, Dr. Ali 212, 241, 254
Scardelletti, Maximillian C. 43
Schmitt, Jeff G. 332
Schmitz, Paul C. 103
Schneider, Dr. Steven J. 174
Schreiber, Jeffrey G. 115, 116, 117
Sechkar, Edward A. 127
Seidel, Jonathan A. 6
Setlock, John A. 240
Severt, Gwynn A. 337
Shin, Dr. E. Eugene 252, 321
Shpargel, Tarah P. 224
Siebert, Mark W. 276, 279, 284, 285
Simon, Donald L. 65
Singh, Dr. Mrityunjay 224, 225
Sjauw, Waldy K. 8
Slywczak, Richard A. 58
Smialek, Dr. James L. 199, 208, 216
Snyder, Dr. Aaron 124
Solano, Paul A. 323
Sookdeo, Steven 262
Soulas, George C. 109
Spina, Danny C. 83
Spry, David J. 97
Steffen, Christopher J., 148
Stefko, George L. 273
Steinetz, Dr. Bruce M. 288, 290, 303
Stocker, Dennis P. 191
Street, Dr. Kenneth W., Jr. 301, 326
Stroda, Phil 307
Suh, Dr. Kwang I. 176
Sullivan, Dr. Roy M. 214, 256, 324
Surgenor, Angela D. 146, 159, 171
Sutter, Dr. James K. 252, 305, 307
Suzuki, Manabu 326

**T**

Tacina, Dr. Kathleen M. 164
Taylor, Linda M. 117
Taylor, Shawn C. 288
Tellier, Daniel W. 300
Thesken, Dr. John C. 256, 305, 307, 309, 312
Thieme, Lanny G. 252
Tigelaar, Dr. Dean M. 243, 245
Tomsic, Michael 282
Tomsik, Thomas M. 146, 159, 171
Tong, Michael T. 3, 5
Tornabene, Robert T. 13
Torres, Felix J. 6
Towne, Dr. Charles E. 165
Trimarchi, Paul A. 315
Trudell, Jeffrey J. 274, 277, 281, 282, 286
Tyson, Dr. Daniel S. 219

**U**

Urban, Dr. David L. 182

**V**

Vaden, Karl R. 44
Vander Wal, Dr. Randall L. 95
Van Drei, Donald E. 59
Van Dresar, Dr. Neil T. 173
Van Zante, Dr. Dale E. 273
Varaljay-Spence, Vanessa A. 43
Vickerman, Mary B. 168
Vivod, Stephanie L. 232

**W**
Weaver, Harold F. 113
Welch, Bryan W. 46, 48, 51, 53, 54
Wendell, Jason C. 174
Wendorf, Bill 307
Wernet, Dr. Mark P. 87
Wey, Changlie 140
Wey, Dr. Thomas 160
Whitlow, Darryl 272
Wichman, Indrek S. 189
Wilt, David M. 122
Wittberg, Thomas N. 127
Wnuk, Stephen P. 338
Woike, Mark R. 339
Woodward, Richard P. 134
Woytach, Jeffrey M. 10
Wrbanek, John D. 92
Wrbanek, Susan Y. 89
Wright, Alisha A. 301

**X**
Xu, Dr. Jennifer C. 93, 95

**Y**
Yarrington, Phillip W. 318
Yen, Chia H. (Judy) 143, 146, 159, 171
Yun, Dr. Hee Mann 206

**Z**
Zakrajsek, James J. 299
Zaman, Dr. Khairul B. 166
Zhu, Dr. Dongming, 208 218
Zimmerli, Dr. Gregory A. 44, 173, 177
Zoeckler, Joseph G. 174

| REPORT DOCUMENTATION PAGE | | Form Approved<br>OMB No. 0704-0188 |
|---|---|---|

The public reporting burden for this collection of information is estimated to average 1 hour per response, including the time for reviewing instructions, searching existing data sources, gathering and maintaining the data needed, and completing and reviewing the collection of information. Send comments regarding this burden estimate or any other aspect of this collection of information, including suggestions for reducing this burden, to Department of Defense, Washington Headquarters Services, Directorate for Information Operations and Reports (0704-0188), 1215 Jefferson Davis Highway, Suite 1204, Arlington, VA 22202-4302. Respondents should be aware that notwithstanding any other provision of law, no person shall be subject to any penalty for failing to comply with a collection of information if it does not display a currently valid OMB control number.
PLEASE DO NOT RETURN YOUR FORM TO THE ABOVE ADDRESS.

| | | |
|---|---|---|
| **1. REPORT DATE** *(DD-MM-YYYY)*<br>10-07-2007 | **2. REPORT TYPE**<br>Technical Memorandum | **3. DATES COVERED** *(From - To)* |
| **4. TITLE AND SUBTITLE**<br>Research & Technology 2006 | | **5a. CONTRACT NUMBER**<br>**5b. GRANT NUMBER**<br>**5c. PROGRAM ELEMENT NUMBER** |
| **6. AUTHOR(S)**<br>Riddlebaugh, Stephen, M., editor(s) | | **5d. PROJECT NUMBER**<br>**5e. TASK NUMBER**<br>**5f. WORK UNIT NUMBER**<br>None |
| **7. PERFORMING ORGANIZATION NAME(S) AND ADDRESS(ES)**<br>National Aeronautics and Space Administration<br>John H. Glenn Research Center at Lewis Field<br>Cleveland, Ohio 44135-3191 | | **8. PERFORMING ORGANIZATION REPORT NUMBER**<br>E-15771 |
| **9. SPONSORING/MONITORING AGENCY NAME(S) AND ADDRESS(ES)**<br>National Aeronautics and Space Administration<br>Washington, DC 20546-0001 | | **10. SPONSORING/MONITORS ACRONYM(S)**<br>NASA<br>**11. SPONSORING/MONITORING REPORT NUMBER**<br>NASA/TM-2007-214479 |

**12. DISTRIBUTION/AVAILABILITY STATEMENT**
Unclassified-Unlimited
Subject Categories: 01 and 31
Available electronically at http://gltrs.grc.nasa.gov
This publication is available from the NASA Center for AeroSpace Information, 301-621-0390

**13. SUPPLEMENTARY NOTES**

**14. ABSTRACT**
This report selectively summarizes NASA Glenn Research Center's research and technology accomplishments for fiscal year 2006. It comprises 198 short articles submitted by the staff scientists and engineers. The report is organized into three major sections: Programs and Projects, Research and Technology, and Engineering and Technical Services. A table of contents and an author index have been developed to assist readers in finding articles of special interest. This report is not intended to be a comprehensive summary of all the research and technology work done over the past fiscal year. Most of the work is reported in Glenn-published technical reports, journal articles, and presentations prepared by Glenn staff and contractors. In addition, university grants have enabled faculty members and graduate students to engage in sponsored research that is reported at technical meetings or in journal articles. For each article in this report, a Glenn contact person has been identified, and where possible, a reference document is listed so that additional information can be easily obtained. The diversity of topics attests to the breadth of research and technology being pursued and to the skill mix of the staff that makes it possible. For more information, visit Glenn's Web site at http://www.nasa.gov/glenn/. This document is available online (http://www.grc.nasa.gov/WWW/RT/). For publicly available reports, visit the Glenn Technical Report Server (http://gltrs.grc.nasa.gov).

**15. SUBJECT TERMS**
Aeronautics; Aerospace engineering; Space flight; Space power; Materials; Structures; Electronics; Space experiments

| **16. SECURITY CLASSIFICATION OF:** | | | **17. LIMITATION OF ABSTRACT** | **18. NUMBER OF PAGES** | **19a. NAME OF RESPONSIBLE PERSON** |
|---|---|---|---|---|---|
| **a. REPORT** | **b. ABSTRACT** | **c. THIS PAGE** | | | Cynthia L. Dreibelbis |
| U | U | U | | 357 | **19b. TELEPHONE NUMBER** *(include area code)*<br>214-433-2912 |